Martin Storheim

Structural Response in Ship-Platform and Ship-Ice Collisions

Doctoral thesis
for the degree of philosophiae doctor

Trondheim, January 2016

Norwegian University of Science and Technology
Faculty of Engineering Science and Technology
Department of Marine Technology

NTNU
Innovation and Creativity

NTNU

Norwegian University of Science and Technology

Doctoral thesis
for the degree of philosophiae doctor

Faculty of Engineering Science and Technology
Department of Marine Technology

Abstract

Collision events may have severe consequences, and it is important to design both ship and offshore structures so that they have sufficient resistance to a collision event. The main purpose of the work herein is to improve the methods for description of the material behavior in nonlinear finite element analysis (NLFEA), and to study the physics of the collision process through numerical simulations of both experiments and full-scale scenarios. Simplified methods are proposed based on the findings.

The shape of the stress-strain curve of the steel material is found to have a large effect on how strains localize in a deformation process, and thereby on the fracture initiation and propagation. Strain-rate hardening is found to be challenging with shell elements, especially w.r.t. dynamic fracture strain, and can increase the uncertainty if not carefully calibrated. Determination of the *design material* concept is discussed, ensuring that the materials representing load and resistance are given appropriate safety factors. A novel way of separating two different mesh scale effects termed *geometric* and *material* is proposed.

The micromechanical process of fracture is discussed, and related to the macromechanical process that can be captured with coarse shell elements. The dependence of strain-state and length scale is investigated. Many of the popular fracture criteria are implemented in LS-DYNA and a large simulation program is conducted with different experiments and many mesh sizes. The accuracy of the fracture criteria is assessed.

An extension of the BWH fracture criterion is proposed, in which post-necking effects can be included. Through a combination of coupled damage and a strain-state dependent erosion criterion, a more robust fracture prediction with reduced mesh dependence is achieved.

NLFEA is used as virtual experiments to study supply vessel collisions with offshore platforms. A pressure-area relation is proposed for the pressures required to initiate crushing of the bulbous bow of a supply vessel. A simplified model is proposed for strength-design of stiffened panels, combining a roof-top mechanism with the stiffener shear capacity in an incremental approach. A refined method for strength-design of jacket legs and braces is proposed, based on the characteristic strength R_c.

Various challenges related to simulation of ice collision events are discussed, especially with respect to the material behavior of ice during fast compressive loading. The material behavior of ice is not well known, and has large statistical variations in properties. During a collision with damage to the ship, the changed geometry

of the ship side will increase the confinement of the ice, thereby increasing its crushing pressure. All ice loads given in current rules and standards disregard this effect.

Two experimental campaigns are performed to study the coupled deformation process as both ice and structure deforms, thereby investigating the effect of the confinement. The load exerted from the ice increases significantly when the structure deforms plastically, indicating that the coupled effect is important. The effect should be considered in updated rules and standards.

Preface

This thesis is submitted to the Norwegian University of Science and Technology (NTNU) for partial fulfillment of the requirements for the degree of philosophiae doctor. The doctoral work has been performed at the Department of Marine Technology, NTNU, Trondheim, with *Jørgen Amdahl* as main supervisor and with *Sveinung Løset* as co-supervisor. The primary funding for the PhD thesis was through strategic university funds.

Acknowledgments

This work has been carried out under the supervision of Professor Jørgen Amdahl at the Department of Marine Technology at the Norwegian University of Science and Technology. I am very grateful for the opportunity to pursue a PhD degree under his supervision. The supervision has been a good mix of useful input and guidance, freedom to pursue ideas I found interesting and valuable discussions throughout the Thesis work. Jørgen is a fun and inspiring person to work with.

I would also like to thank my co-supervisor Professor Sveinung Løset at the Department of Civil and Transport Engineering for supervision on the Arctic aspects in my work. He has been available for counseling when needed, and enthusiastically contributed both technically and with financial support for the experiments. Through his leadership in the SAMCoT center, he has facilitated a good technical and social work environment among the Arctic PhDs, Post Docs and Professors.

During the thesis work, I have collaborated with may devoted and skilled colleagues. I would especially like to thank

- Dr. Hagbart S. Alsos for valuable input and help during my time at NTNU, and his openness towards sharing both his knowledge and data from his PhD work. The novel idea of coupling a necking-dependent damage to the BWH criterion originated from him.
- Prof. Odd Sture Hopperstad for his significant contributions to further developing the damage model for the BWH criterion.
- Prof. Sören Ehlers for guidance in the PhD role and many rewarding discussions about aspects of material modeling, collision simulations, Arctic challenges and Land Rovers.
- Dr. Ekaterina Kim for a rewarding collaboration and many interesting discussions about both cold and hot topics.
- Tobias Olsson at *Dynamore Nordic* and Torodd Berstad at *SIMLab* for valuable assistance regarding LS-DYNA implementation issues.
- Dr. Zhenhui Liu at Reinertsen AS for sharing his implementation of the external collision mechanics model and for fruitful discussion about the usage together with Prof. Jørgen Amdahl.
- Dr. Ingo Martens (formerly Ingo Tautz) for sharing his experimental data and valuable insights related to indentation experiments.
- Håvard Nyseth and Per Olav Moslet at DNV for valuable discussions and input to the simplified ice collision calculations.
- Drs. Lin Hong, Mohammed T. Tavakoli and Tan-Hoi Nguyen, and Reny Watan, MSc., Kjetil Qvale, MSc. and Line Kristiansen, MSc. for their contributions to the FE modeling in Chapter 6. Some parts of the numerical

Article contributions

The PhD work has resulted in significant contributions to several articles. For all articles where the candidate was first author, the candidate was responsible for modeling, numerical implementation, simulation, interpretation of results and writing the manuscript. The main ideas in each article evolved through discussions and the numerical work as a cooperation between all the authors. Especially, Dr. Hagbart Alsos and Prof. Odd Sture Hopperstad are acknowledged for their significant contributions to the extension of the BWH damage model.

Journal papers

JP-1   Storheim, M. and Amdahl, J. Design of offshore structures against accidental ship collisions. *Marine Structures*, 37:135–172, 2014b

JP-2   Storheim, M., Alsos, H. S., Hopperstad, O. S., and Amdahl, J. A damage-based failure model for coarsely meshed shell structures. *International Journal of Impact Engineering*, 83:59–75, 2015b

JP-3   Storheim, M., Amdahl, J., and Martens, I. On the Accuracy of Fracture Estimation in Collision Analysis of Ship and Offshore Structures. *Journal of Marine Structures*, 44:254–287, 2015. doi: 10.1016/j.marstruc.2015.09.006

JP-4   Storheim, M. and Amdahl, J. On the sensitivity to work hardening and strain-rate effects in nonlinear fem analysis of ship collisions. *Ships and Offshore Structures*, 2015b. doi: 10.1080/17445302.2015.1115181

JP-5   Kim, E., Storheim, M., Amdahl, J., Løset, S., and von Boch und Polach, R. Laboratory experiments on shared-energy collisions between freshwater ice blocks and a floating steel structure. In Review

Conference papers

CP-1   Storheim, M., Kim, E., Amdahl, J., and Ehlers, S. Iceberg shape sensitivity in ship impact assessment in view of existing material models. In *Proceedings of the ASME 2012 31st International Conference on Ocean, Offshore and Arctic Engineering OMAE2012 Volume 6.*, 2012

CP-2   Storheim, M. and Amdahl, J. Accidental ice management–platform vs. ice breaking supply vessel collision. In *Proceedings of The Twenty-third International Offshore and Polar Engineering Conference*, pages 1195–1202, ISOPE-I-13-046, 30 June-5 July, Anchorage, Alaska, 2013

CP-3   Storheim, M. and Amdahl, J. Non-conservative consequences of "conservative" assumptions in ship-platform collision analysis. In *Proceedings of the 33rd International Conference on Ocean, Offshore and Arctic Engineering*, pages OMAE2014–24457, San Francisco, California, USA, June 2014a

CP-4   Storheim, M. and Amdahl, J. On the effect of work hardening on strain-localization and fracture initiation in collision simulations. In *Proceedings of the 34rd International Conference on Ocean, Offshore and Arctic Engineering*, St. Johns, Newfoundland, Canada, June 2015a

CP-5   Storheim, M., Alsos, H., Hopperstad, O., and Amdahl, J. An extension of the BWH instabilitiy criterion - Numerical study. In *Proceedings of the 34rd International Conference on Ocean, Offshore and Arctic Engineering*, St. Johns, Newfoundland, Canada, June 2015a

CP-6   Storheim, M., Nord, T., Kim, E., Høyland, K., Langseth, M., Amdahl, J., and Løset, S. Pilot Study of Ice-Structure Interaction in a Pendulum Accelerator. In *Proceedings of the International Conference on Port and Ocean Engineering Under Arctic Conditions*, 2015c

CP-7   Kim, E., Storheim, M., und Polach, R. v. B., and Amdahl, J. Design and modelling of accidental ship collisions with ice masses at laboratory-scale. In *ASME 2012 31st International Conference on Ocean, Offshore and Arctic Engineering*, pages 495–505, 2012b

CP-8   Kim, E., Storheim, M., Amdahl, J., Løset, S., and von Bock und Polach, R. Drop tests of ice blocks on stiffened panels with different structural flexibility. In *Proceedings of the 6th International Conference on Collision and Grounding of Ships and Offshore Structures*, pages 241–250, 2013

CP-9   Kim, E., Amdahl, J., Storheim, M., and Løset, S. Understanding the Effect of Assumptions on Shell Plate Thickness for Arctic Ships. In *Proceedings of the International Conference on Port and Ocean Engineering Under Arctic Conditions*, 2015a

Contents

List of Abbreviations

1D	One dimensional
1FB	One flatbar stiffener (Alsos and Amdahl 2009)
2D	Two-dimensional
2FB	Two flatbar stiffeners (Alsos and Amdahl 2009)
3D	Three-dimensional
ALE	Arbitrary Lagrangian Eulerian
ALS	Accidental Limit State
BWH	Bressan-Williams-Hill fracture criterion
CCGS	Canadian Coast Guard Ship
CL	Cockroft-Latham fracture criterion
COG	Center of Gravity
COV	Coefficient of Variation
CP	Conference Paper
DHF	Dynamic Hardening Factor
DIC	Digital Image Correlation
DMU	Dynamic Motion Unit
DNV	Det Norske Veritas
FB	Flat bar (stiffener)
FEM	Finite Element Method
FLC	Forming Limit Curve (in an FLD)
FLD	Forming Limit Diagram
FSI	Fluid-Structure Interaction
GL	Germanischer Lloyd
HP	Bulb profile (stiffener)
IACS	International Association Of Classification Society
IIP	International Ice Patrol
IMO	International Maritime Organization

JP	Journal Paper
L	L profile (stiffener)
LNG	Liquified Natural Gas
M-K	Marciniak and Kuczyiski fracture criterion
MMC	Modified Mohr-Coulomb fracture criterion
MPP	Massively Parallel Processing
NLFEA	Nonlinear Finite Element Analysis
NSR	Northern Sea Route
NTNU	Norwegian University of Science and Technology
RMRS	Russian Maritime Register of Shipping
RTCL	Rice-Tracey Cockroft-Latham fracture criterion
SG	Strain Gauge
SMP	Symmetric multiprocessing
SOLAS	International Convention for Safety of Life at Sea
STD	Standard Deviation
T	L profile (stiffener)
ULS	Ultimate Limit State
US	Unstiffened panel (Alsos and Amdahl 2009)
UTS	Ultimate Tensile Strength

Chapter 1

Introduction

1.1 Motivation

Wherever there is ship traffic, collisions may occur. Ship collisions are fortunately rare events, but as the global trade continues to grow, avoiding accidents becomes more and more challenging. The *International Maritime Organization* (IMO) reports for the last 10 years an average of 23.8 collisions pr. year with very serious casualties, i.e., collisions involving loss of ship, loss of life or severe pollution (IMO:GISIS (2015)). As the consequences of a collision event can be severe, it is important to be able to predict the outcome of such events with high precision, and design crash-worthy structures that can withstand the probable collision events without severe casualties.

The most well-known ship collision of all times may be the *Titanic*, which collided with an iceberg and sunk in 1912. Impacts into ice masses are still frequent events, but normally with smaller consequences than the Titanic. Increasing interest in Arctic operations make ice collisions a hot topic.

Recently, tanker collisions have attracted special public attention due to the high impact oil leakage might have on the environment and local communities. Examples of events with oil tankers are numerous, among others the Exxon Valdez accident in 1989 in Alaska, with an oil spill of more than 40 000 ton crude oil, and the 146,000-tonne tanker Heibei Spirit which collided with a crane-carrying barge outside South Korea's West coast in December 2007, causing oil spillage in the range of 10 000 tonnes crude oil. The tanker Full City came adrift during a storm near the Norwegian coast, and the grounding caused rupture and oil spill. Several large damages were observed, see Figure 1.1a. Collisions often lead up to

dramatic scenes, as in Figure 1.1b.
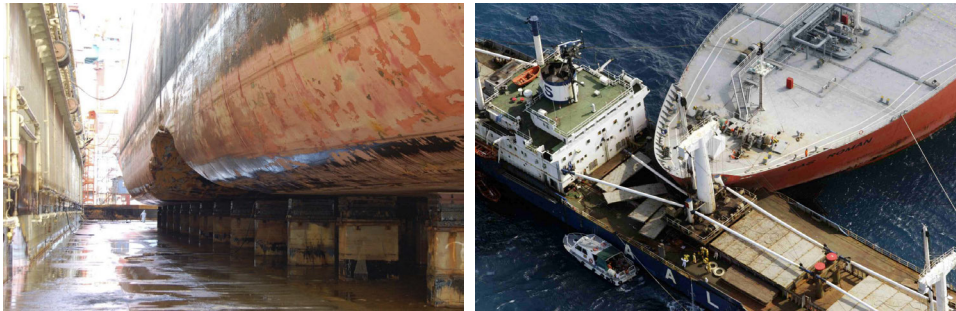
(a) Full City, from the report of the Accident Investigation Board Norway (2013)

(b) M/T Gas Roman vs. M/V Springbok, from Countryman and McDaniel (2003)

Figure 1.1: Example of ship damage from grounding (left) and collision (right)

Though receiving less public attention, offshore collisions are also frequent events with potentially catastrophic outcomes. Kvitrud (2011) reports that there were 115 collisions on the Norwegian Continental Shelf from 1982 to 2010. Fortunately, none of these collisions caused loss of life, but the economic consequences were significant. Some of the collisions *barely* avoided large-scale damage and pollution, notably the Big Orange collision with the Ekofisk platform in 2007 (Figure 1.2a). The outcome was significantly worse in the collision between the support vessel Samundra Suraksha and the Mumbai North High jacket platform in 2005 (Walker 2005). The helideck of the ship hit the platform riser, which ruptured and caused a catastrophic fire (Figure 1.2b).

(a) Damage to Big Orange after impact to Ekofisk jacket

(b) Mumbai High North on fire

Figure 1.2: Example of recent offshore collision events

The Titanic accident led to the establishment of the first SOLAS convention, the *In-*

ternational Convention for Safety of Life at Sea in 1914. The convention is ratified by IMO, and is still one of the major conventions that govern design requirements to ships (SOLAS (2014)).

Other regulatory bodies that control design requirements are typically classification societies and national regulations. For the offshore industry in Norway, typical standards are then the NORSOK N-003 and NORSOK N-004, which, combined with the SOLAS (2014) convention, governs the design requirements. Recommended procedures for design are given in DNV RP-C204 and DNV RP-C208.

Documents like NORSOK N-004, DNV RP-C204 and DNV RP-C208 give some guidance on how to address these challenges, but are, in order to be general, either difficult to fulfill or overly simplified in a prescriptive manner. Refined methods may be required. Accidental Limit State (ALS) scenarios allows for significant damage to the struck body, provided that the damage does not lead to progressive collapse of the structure or prevent safe evacuation due to factors such as loss of stability. The *Alexander L. Kielland* accident in 1980 is an example of the opposite, in which a minor event led to a progressive collapse and loss of stability, causing capsizing and loss of 123 lives (Moan 1985).

In the design process, the size and speed of the vessel shall be determined by a risk analysis, in which the best estimate of a design impact event should not exceed an annual probability of occurrence of 10^{-4}. See Pedersen (2010) for an overview of the risk analysis methods. Risk analysis can generate a set of collision scenarios with associated probability of occurrence, which should be the governing cases in design. In lieu of establishing scenarios, a standard minimum design collision event has been widely adopted. This consists of an impact from a supply vessel of 5000 ton displacement suffering from power blackout, drifting uncontrolled into the installation at a speed of 2 m/s (NORSOK N-003). Considering the added mass, the associated kinetic energy is 11 MJ and 14 MJ for bow/stern collisions and broad side impacts, respectively. Recent collision events on the Norwegian Continental Shelf with energies in the 40-70 MJ range indicate that the current requirement for the standard design collision event is far from an annual probability of 10^{-4} (Kvitrud 2011).

A significant increase in the standard design collision event is expected in the next revision of NORSOK N-003. There are two primary reasons for this anticipated change. First, the size of the vessels servicing the installations on the Norwegian Shelf has increased significantly up to 7500 to 10000 ton displacements, and this size is not reflected in the current requirements. Second, the high energy bow impact events documented by Kvitrud (2011) had a significantly higher velocity than the 2 m/s requirement in the NORSOK code. The aforementioned accidents

with kinetic energies above the current requirements were caused by human errors and control system malfunction or interaction errors, and not drift during power blackout. The requirement to collision energy has already been increased in DNV-OSS-201, where drilling and production units on the Norwegian continental shelf are required to withstand a collision of at least 35 MJ.

Another important consideration is that the standard force deformation curve for bow impact (Figure 1.3), which was developed in 1981, is based on a raked bow where crushing occurs in the relatively weak bow superstructure. Pettersen and Soegaard (2005) calculated the collision energy for the impact between the supply vessel *Far Symphony* and the semi-submersible drilling rig *West Venture* (Figure 1.4) with the NORSOK design curve for bow impact. The energy associated with crushing of the bow up to the observed indentation level corresponded well to the demand calculated using external collision mechanics. The forecastle structure of *Far Symphony* dissipated most of the energy before the vessel bulb obtained contact, thus experiencing a similar deformation mode as that assumed for a raked bow in Figure 1.3.
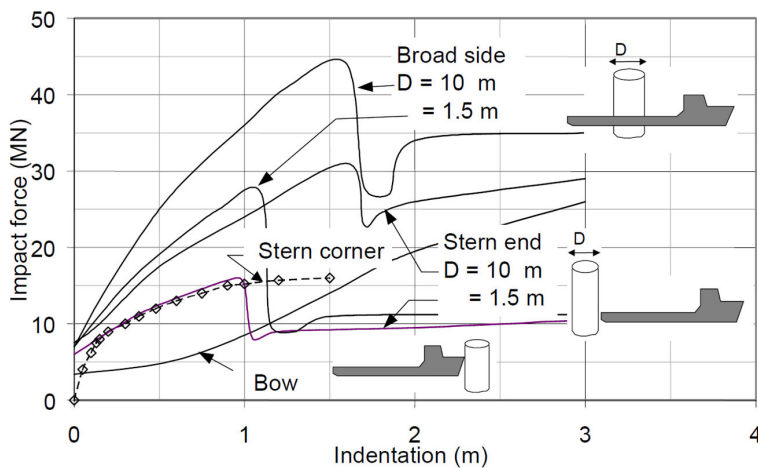
Figure 1.3: Force-deformation curves for a 5000 ton supply vessel, NORSOK N-004

Supply vessels are now built with a variety of bow shapes (i.e., bulbous bows, X-bows, etc.), which have crushing characteristics that differ widely from that of the standard vessel considered in NORSOK N-004. Ice reinforcements are also common for supply vessels on the Norwegian Continental Shelf. If ice-reinforced vessels serve installations that are not ice-reinforced, the installation will sustain greater damage than from a non-reinforced vessel under otherwise similar impact conditions. This scenario is especially challenging for non-conventional bow designs such as the X-bow (Notaro et al. 2015), causing impact loads far above

(a) Far Symphony   (b) West Venture
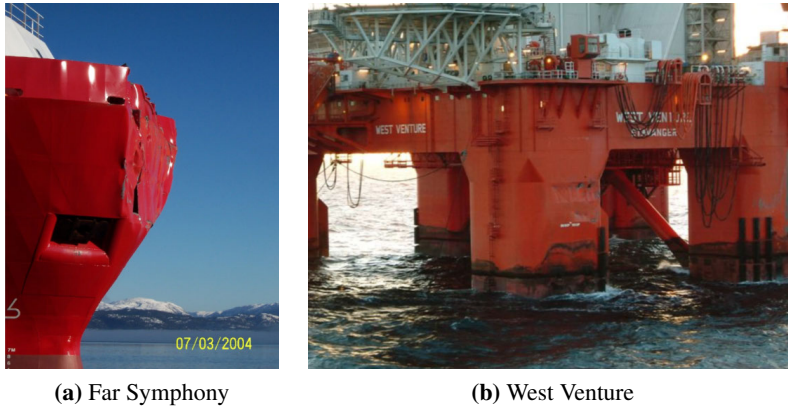
Figure 1.4: Damage to *Far Symphony* and *West Venture* after a 39 MJ collision, from Pettersen and Soegaard (2005)

the curves in Figure 1.3 and distributed over a narrow width (thereby acting like an axe). Notaro et al. shows that a jacket may be able to resist such an impact by inflicting local crushing of the sharp bow. A stiffened panel such as a semi-submersible platform it not likely to withstand such an impact, and the damage to the platform may be significant both in terms of global structural integrity and damage stability.

If the NORSOK standard is read from a crashworthiness point of view, it links the impact scenario to the actual operation of supporting vessels around a platform. Thus, if a platform is designed to resist impact from a 5000 ton vessel, it should only be allowed to operate with supporting vessels up to this size. However, this seems not to be enforced in actual operations, and larger vessels with stronger and sharper bows are currently operating around the platforms. Thus, the potential collision scenarios are far beyond the standard design event.

Offshore structures operating in ice-infested waters should be designed with their collision performance in mind, whereas ships are normally designed according to prescriptive ice class rules. The design load level for low ice classes has a significantly higher return period than conventional design loads (Riska and Kämäräinen 2011), and may easily exceed the structural capacity.

The methods for assessing ship-ice and ship-ship/platform collisions are similar, but the ice introduces additional uncertainties. Its shape and strength is associated with large uncertainties, and the mechanical behavior of ice during deformation is coupled with the structural response. Further, as probable ice masses are smaller with respect to the wave length and have low drift speeds, the wave-induced motion

of the ice mass is a significant contribution to the total collision energy.

1.2   Challenge : Assess the Consequence of Collision Events

The consequences of a ship collision event (ship-ship/platform or ice-ship/platform) can be severe, varying from local deformations to large-scale fracture and associated environmental pollution due to rupture of cargo tanks or complete loss of the ship and crew. There is a need for a robust method to assess the consequences of a ship collision in the design phase of both ships and offshore structures. No consensus has so far been established for how the industry should conduct such analysis, notably how to describe the material strength and how to predict fracture in coarsely meshed stiffened panel structures. A designer is thus left with the challenge of either conducting a large experimental test program (not realistic) or to make conservative assumptions in order to document the structural resistance to and the damage extent from a typical collision event.

Engineers often turn to Non-Linear Finite Element Analysis (NLFEA) to assess the consequence of an ALS event. NLFEA has become the primary tool for collision design for a number of reasons. Mainly, computational resources are now so cheap that detailed collision simulations with millions of degrees of freedom can easily be run on a desktop computer in hours. Secondly, finite element models are often established anyway, and the additional cost of a collision simulation is thus reduced. If this is done correctly, NLFEA enables increased reliability in the results and a better utilization of the actual structural capacity compared to what can be achieved with simplified methods.

The main challenge with NLFEA is that the softwares are now quite robust, and a stable solution with nice colors is most often obtained almost regardless of the amount of input errors. Solland (2014) compared simplified calculations to riding a bicycle, linear finite element analysis to driving a car and non-linear finite element analysis to flying a plane. Thus, while many designers and analysts carry out advanced simulations, they are not necessarily conducted in accordance with *state-of-the-art* principles. Until standardized procedures have been established, the simulation results will depend strongly on the craftsmanship of the engineer performing the simulations. The results of such simulations are often reported unsatisfactory, thereby making quality control a difficult task; in turn placing high demands on the classification societies and other regulatory bodies.

In order to obtain reliable results, the mesh discretization of the structures should be sufficiently refined to capture the governing deformation modes, the collision scenario sufficiently represented through the analysis setup, and the material behavior sufficiently accurate to properly capture strain localizations and fracture.

Further, a typical ship structure can have a multitude of material types and qualities, whose plastic properties can have a wide scatter. This necessitates a material representation that is easily calibrated towards simple material tests or standard material grades for ships and offshore use.

Material scientists have for many years known the fundamental aspects of fracture behavior of sheet metals, but this knowledge is not widely adopted in the ship-engineering community. To bridge the gap, the principal knowledge from material science should be extracted, and adjusted to that it can be applied in an engineering scale.

Prototype testing is limited to scale models due to the size and cost of the structures involved. This implies that material failure (fracture) must be calibrated in a domain that is outside of the structural application domain, presupposing that the response predictions are transferable from the small-scale calibration models to the large-scale structural.

It should be kept in mind that real collision events will differ substantially from design collision events with respect to the shape and structural layout of the striking ship, structural imperfections, the impact location, velocity and material strength. Accurate simulations of idealized collision events can never remove this uncertainty. However, inaccurate simulations due to deficient modeling will add significantly to the total uncertainty. Plastic hardening, fracture initiation and propagation are key factors in such simulations, for which uncertainties should be reduced by improved techniques.

1.3 Thesis Objectives

The aim of this thesis is to improve methods for modeling of material behavior in simulations of events that exceed the linear structural capacity, with special application to ship collisions. The collision process is studied through numerical simulations of both experiments and full-scale scenarios. In particular, the following research questions are addressed:

- How does the material behavior depend on strain, strain-state and strain rate?
- How can the material behavior be described based on statistical parameters of properties from different material grades?
- How can fracture of steel plates in FE simulations be considered in a robust way with low mesh dependence and low computational cost?
- How should stiffened panels and tubular members be designed to resist an impact?
- How can abnormal ice collision events be assessed with better accuracy?

By addressing these issues, the technical safety level of the structure can be evaluated in a better manner and measures can be taken during both the design and operational stage to minimize the risk of unacceptable consequences from a collision event. A detailed investigation of material behavior and its modeling in NLFEA are likely to help engineers to improve the accuracy of their simulations, will hopefully help regulatory bodies to understand and question misleading assumptions, and in the end contribute to development of improved regulations to ensure consistent results with a known uncertainty.

Measures to increase the accuracy of ship and offshore collisions are

1. The material behavior needs to be described in a reliable manner with low mesh dependence and in a way that allows for simple calibration of the governing parameters by the engineer. A prerequisite for accurate fracture prediction is a sufficiently refined mesh so that the structural stiffness and strain localizations are captured.
2. The procedure to conduct full-scale simulations needs to be improved, and guidance on assumptions that have to be made during the design process should be enhanced. A recommended procedure should be developed.
3. With an accurate procedure in place, the physical behavior of collision events can be investigated in a systematic way through simulations, and the results can help to create and verify simplified methods for use in early-phase design.

This thesis attempts to address all these measures. The primary concern is on point 1 for steel material behavior, point 2 for all types of collisions (ship-ship/platform, ship-ice) and point 3 for ship-ship/platform collisions.

Special attention is placed on assessment from an *engineering state of mind*, in which procedures and assumptions are applicable to a design situation. The governing physics should be captured in a pragmatic way. This differs from the *research state of mind*, in which enormous efforts may be put into minor details; with more accurate results, but not necessarily methods applicable for design. With an *engineering state of mind*, a method cannot be calibrated towards a known solution, as this does not exist in a design phase. Thus, the assumptions and numerical parameters should only be calibrated to data that is either known or can be determined with reasonable accuracy.

1.4   Methodologies and Assumptions

The primary goal of this thesis is to enable increased accuracy in numerical simulations of nonlinear structural response. When the accuracy of NLFEA simulations is increased, they may either solve specific problems with a known accuracy,

or be used as numerical experiments to further understand the physics of collision events. In turn, this can pave the way for improved simplified methods. To achieve this, accurate methods for material behavior should be a first priority. For steel, this will primarily relate to work hardening and fracture, whereas for ice, a broader approach is needed as the fundamental aspects of its behavior are not yet fully understood.

An extensive literature study was conducted, spanning several research fields. Key aspects from each field were discussed, and applied to collision problems. NLFEA simulations of published experiments, both from material testing and large-scale indentation, were used to extend and verify engineering methods suited for fracture prediction in stiffened panel structures. Simulations of full-scale events were used as numerical experiments to create and improve simplified calculation methods.

The literature review of the ice behavior in a collision reveals that glacial ice as a material is not well enough understood for scenarios in which both the ice and the structure undergo significant damage, which will be the case in most ALS ice encounters. Experimental methods were used to provide more data that can be employed to develop improved material models for glacial ice, and the findings compared to previously published experiments.

1.5 Thesis Organization

The thesis is organized into chapters with separate topics. The chapters are based on the papers published during the thesis work, both journal papers (JP) and conference papers (CP), but the contents has evolved further since the original publications.

Chapter 2 reviews the historical background of collision assessments and describes key aspects and methods required for such assessments.

Chapter 3 describes the steel material behavior relevant for ship collision simulations. The chapter is based on JP-2, JP-3, JP-4 and CP-4.

Chapter 4 describes a novel extension of the BWH damage criterion. The chapter is based on JP-2.

Chapter 5 describes benchmark tests of various fracture criteria against material tests and large-scale indentation experiments. The objective is to reveal how the various criteria behave with changing mesh discretization, stress state, type of strain concentration etc. The various criteria are tested with an *engineering state of mind*, and their reliability discussed. The chapter is based on JP-3.

Chapter 6 uses NLFEA as numerical experiments to investigate the behavior of

ship and offshore structures during accidental collisions. The behavior is described and simplified methods are proposed. The chapter is based on JP-1, CP-2 and CP-3, but also contain new parts that have not been published.

Chapter 7 address various additional challenges related to ice-structure collisions, including key aspects of ice material behavior. Simplified and advanced methods for assessment of such problems are discussed.

Chapter 8 describes experiments that have been performed during the Thesis work. The experiments pave the way for a better understanding of the material behavior of granular ice in collisions in which both the ice and the structure deforms significantly. They highlight a path for further experimental studies. Chapters 7 and 8 are loosely based on JP-5, CP-1, CP-6, CP-7 and CP-8, but also contain unpublished work.

Figure 1.5 shows how the different parts of the work link together.
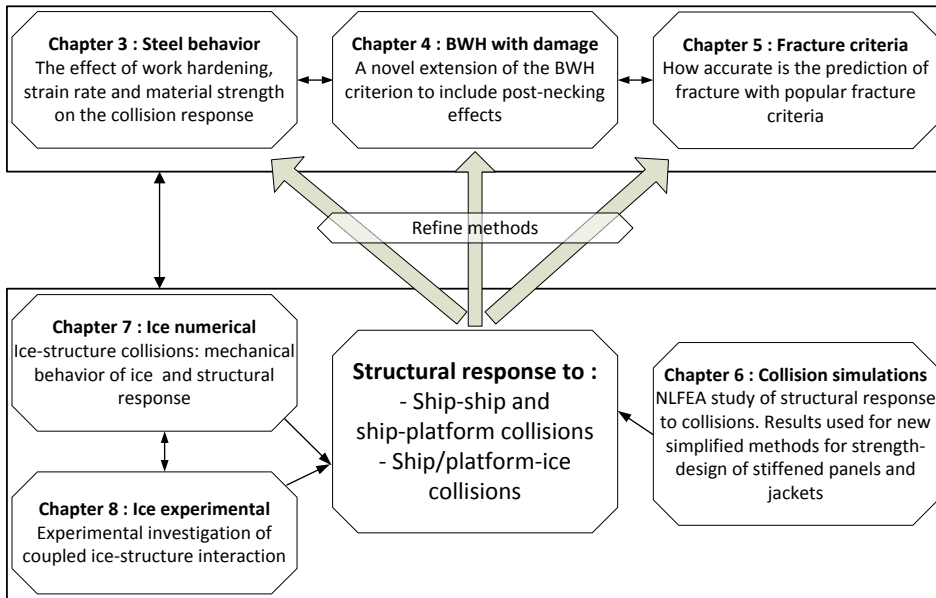
Figure 1.5: Diagram showing the relation between different activities performed in the PhD study.

1.6   Summary of Original Contributions

The work on the thesis has been on several levels. To advance the field of ship collision simulations, the following original contributions are given in this thesis:

  - An extension of the BWH criterion in the post-necking region is proposed,

with improved mesh and strain-state dependence. The robustness of the fracture prediction in coarsely meshed shell structures is significantly enhanced.
- Separation between different mesh-scale effects is proposed, so that they can be treated individually in a rational manner. They are termed *geometrical* and *material* mesh dependence.
- A broad investigation of the reliability of commonly used fracture criteria is conducted. The statistical evaluation allows for selection of the most robust criterion, and a better knowledge of the accuracy level to be expected for a given fracture criterion.
- A new pressure-area relation for crushing of a bulbous bow or stern corner is developed, that can be used for strength design of a side structure.
- A simple strength-design procedure for early-phase design of stiffened panels is proposed, using the pressure-area relation and mechanism consideration.
- The dent normalizing factor $R_c > \eta$ is proposed as a requirement for a leg or brace to initiate crushing of a striking vessel. This relates the relative strength of the jacket to the striking vessel. η can be determined based on the crushing resistance of the relevant striking vessel.
- A revised design procedure for impact to brace/legs that are strength-designed is proposed. If crushing of the striking vessel is achieved, the requirement to global capacity of the brace/leg can be reduced.
- The first ice impact experiments to show coupled ice-structure interaction in brittle ice regime were conducted, highlighting that this is an important effect with respect to the development of structural damage.

Further, work has focused on evaluating some of the assumptions that often are used by both researchers and engineers. The outcome of this work does not necessarily represent new knowledge, but deals with challenges that should be addressed in a better way during design. The assumptions are discussed, and their effects highlighted. Recommendations to the design approach are given on

- Determination of work hardening parameters for the striking and struck vessel
- The use of strain-rate hardening in ship collision simulations.
- Accuracy of fracture prediction based on the plastic properties, structural configuration, fracture criterion and the mesh size.
- Non-conservative effects of assuming a rigid striking vessel.
- The effect of wave-induced velocity of ice masses to the collision energy.
- The importance of the coupled effect of ice-structure interaction, currently not considered in design rules.

Chapter 2

Review of Methods for Collision Assessments

Samuelides (2015) described the history of crashworthiness assessments of ship structures, and separated *high-energy* and *low-energy* impacts. For high-energy impacts, the available kinetic energy is so great that very large-scale fracture and damage is expected, whereas a low-energy impacts should cause no or low fracture. Thus, for high-energy impacts one need only to approximate the overall behavior, whereas for low-energy impacts the actual deformation mechanism and fracture limits should be described in more detail.

The first to express the idea of a collision model in a semi empirical formula was Minorsky (1959). He applied only one parameter to represent all of the damage modes, calibrated to data from 26 full-scale collisions. Minorsky's formula relates the amount of absorbed energy to the volume of damaged structural elements that are parallel to the indentation direction (Figure 2.1). It is seen that for high-energy impacts, the empirical data correlates to the linear relationship proposed by Minorsky, but in the region of lower energy (shaded area) the empirical results deviate. Minorsky's method is thus good for high energy impacts of structures similar to those in the empirical data. Hence, the Minorsky model implicitly involves all factors of actual collision phenomena of the ships in service at that time, namely bow shape, friction, strain-rate effects, velocity of struck ship, variation of as built material properties and rupture of the material. If a ship side is to be strengthened to resist an impact, the designer simply needs to increase the volume of material of structural elements such as girders, stringers, decks and frames. Notably, the membrane effects in the outer ship shell plating were not considered by Minorsky. This is probably acceptable for high-energy impacts, but is an important effect

prior to fracture in low-energy impacts.
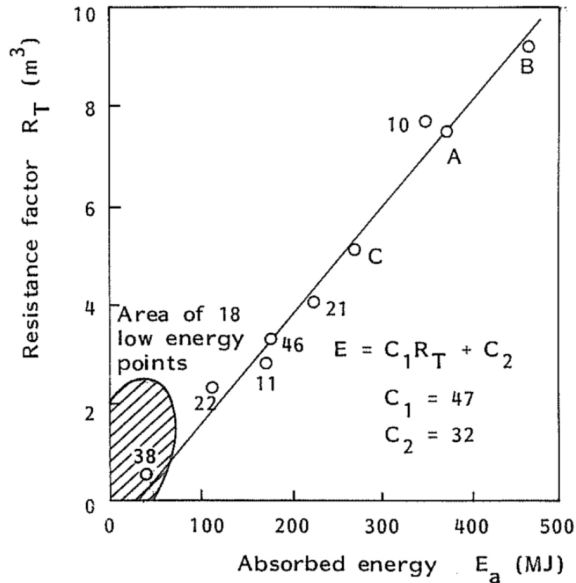
Figure 2.1: Absorbed energy vs. volume of damaged structure, from Minorsky (1959)

Using empirical data to assess novel ship designs can easily be problematic. Pedersen and Zhang (2000) attempted to mitigate this by improving the Minorsky model to account for structural arrangement, material properties etc.

Samuelides (2015) reported that large oils spills from accidents such as the Exxon Valdez grounding in 1989 shifted the focus towards *low-energy* impacts. This means impacts that should be resisted by the vessel in order to avoid unacceptable consequences such as oil spill. This led to requirements to double hulls in oil tankers, such that the outer shell could be damaged without rupture of the oil tank barrier.

The initiation and propagation of fracture became more important for low-energy impacts in order to assess the possible puncturing of the shell plate. The method by Minorsky cannot consider such problems, and a more direct approach to estimating the strength of the ship was needed. The remainder of this thesis focuses on low-energy impacts.

2.1   Accidental Limit State Design

Regulatory bodies such as classification societies have issued some general criteria for assessment of accidental actions[1]. The overall goal for the design of the structure against accidental loads is to prevent an incident from developing into an accident disproportional to the original cause. Care should be taken to apply sound engineering judgment and pragmatic evaluation of the design for two reasons: There are large uncertainties in both magnitude and frequency of accidental loads, and the methods for determination of accidental effect have an approximate nature. The governing principle is that the accidental event shall not impair the basic safety functions such as

- Usability of escape ways
- Integrity of shelter areas
- Global load bearing capacity

To achieve this, several performance criteria are derived, which typically are related to

- Energy dissipation
- Local strength
- Resistance to deformation (e.g., braces in contact with risers/caissons, use of escape ways)
- Endurance of fire protection
- Ductility (allowable strains) to avoid cracks in components, fire walls, passive fire protection etc.

2.2   Relative Strength

During a collision event the instantaneously weaker body deforms. A typical collision between two bodies of similar strength may start with the bow penetrating slightly into the ship side, until sufficient membrane forces are mobilized in the ship side to start crushing the incoming vessel bow. This effect of the relative strength of the colliding structures is an important consideration that is too often neglected in the analysis of ship-ship or ship-platform collision. The deformation of the bodies is normally very sensitive to changes in the relative strength, and small changes in the resistance to deformation of one of the bodies can change the interaction regime completely. In NORSOK N-004, analysis or design against ship collision is categorized into three regimes that depend on the relative strength, illustrated in Figure 2.2.

---

[1] Accidental actions are mainly collisions, grounding, explosion, fire and dropped objects.
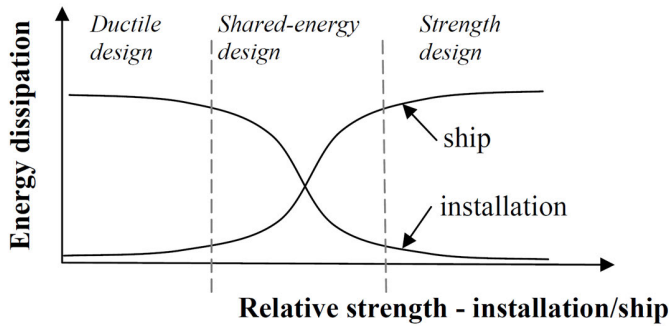
Figure 2.2: Characterization of design principles in terms of relative strength

In *ductile design*, the bow or side of the striking ship is considered to be infinitely rigid, such that all of the energy is dissipated by the struck ship/installation. This assumption can simplify the calculations because the shape of the striking ship largely dictates the form of the damage to the struck ship/installation. However, this frequently used assumption results in the struck ship/installation sustaining damage regardless of how much it has been strengthened, resulting in overly strong and expensive structures.

In *strength design*, the striking ship is considered to have a finite strength, and the struck ship/installation can be strengthened to crush the striking ship. The striking ship has to dissipate the major part of the collision energy. This objective is achieved if the struck ship/installation can resist the total crushing force as well as local hot spots, i.e., local areas with high force intensities. These design principles resemble those adopted in conventional Ultimate Limit State (ULS) design. Strength design may be a relevant option in certain cases but often yields an overly conservative and costly solution. It may be necessitated by operational limitations, such as unacceptably high costs due to downtime while repairing the structure. It should be noted that true strength design, in which the struck body suffers *no* damage, is not possible to achieve with reasonable structural scantlings. Strength design should be associated with a criterion of acceptable damage, typically related to what can easily be repaired without large downtime or off-hire.

In *shared-energy design*, both the striking ship and the struck ship/installation are allowed to deform significantly. During the impact, the instantaneously weaker body deforms. This makes the distribution of the damage and energy dissipation considerably more difficult to estimate by simple methods, as the bow resistance to crushing cannot be assessed independently of the deformation state of the ship side/installation and vice versa. In other words, the resistance to the penetration of the struck ship/installation depends on the crushing state of the bow. A clear

example of such behavior was observed in experiments conducted by Tautz et al. (2013) in which a stiffened double side structure was impacted by a rigid and deformable indenter, thereby involving ductile and shared-energy scenarios.

It has been generally observed that the transition between strength design and ductile design may be quite narrow: a moderate strengthening of one of the structures may cause the other structure to deform. Consequently, it is essential to properly capture the governing physical effects during a collision interaction to reduce the risk of overly conservative and costly designs, or even worse, to significantly overestimate the resistance of the struck body to the collision.

Lützen et al. (2000) investigated the energy absorption capability of a ship bow, and concluded that a large bow with longitudinal stiffening will dissipate small amounts of energy, whereas the bow of a small ship against a larger vessel or vessel bows with transverse stiffening system may dissipate large amount of energy. Yamada et al. (2005) investigated the concept of buffer bows that are strong enough to resist normal operational loads, but weak enough to dissipate large amounts of energy in a collision.

2.3   The Mechanics of a Ship Collision

The total available kinetic energy will govern the mechanics of a ship-ship collision. During the collision, the kinetic energy is absorbed in several ways; strain energy dissipation, hydrodynamic dissipation and acceleration of structural and hydrodynamic added mass. All these effects should be included in the assessment of the accidental limit state. However, the effects may be treated separately if the coupling between the effects is limited.

A distinction is commonly made between *external* and *internal* mechanics, first suggested by Minorsky (1959). The *external* mechanics deals with the global motion of the two interacting bodies prior to, during and after the collision. The main outcome of an external mechanics assessment is the energy that is expected to be dissipated by the deformation processes. This is input to the *internal* mechanics assessment. The internal mechanics deals with the local recoverable and unrecoverable deformation in each interacting body, and how they interact during the collision event. Thus, the energy to be dissipated is distributed between the two bodies.

2.3.1   External Mechanics

The external mechanics of ice-ship and ship-ship collisions have over the years been addressed by many researches, e.g., Brown (2002); Liu and Amdahl (2010); Pedersen and Zhang (1998); Popov et al. (1967); Stronge (2004); Tabri et al. (2008,

2009).

Using simple calculation methods, the part of the collision energy that needs to be dissipated as strain energy can be calculated by means of the principles of conservation of momentum and conservation of energy. Both NORSOK N-004 and DNV RP-C204 have guidance on assessing the strain energy dissipation based on the type of structure and their initial velocities. It is distinguished between compliant and fixed structures. For a fixed structure, such as a stiff jacket or other bottom-founded structures, all the energy from the striking ship have to be dissipated. The energy of the striking vessel is found as

$$E_s = \frac{1}{2}(m_a + a_a)v_a^2 \tag{2.1}$$

where m_a is mass of striking ship, a_a is added mass of striking ship and v_a is initial velocity of striking ship.

Contrary to this, a compliant structure will be free to move and the energy to be dissipated is also a function of the mass and velocity of the struck ship/installation as

$$E_s = \frac{1}{2}(m_a + a_a)v_a^2 \frac{\left(1 - \frac{v_b}{v_a}\right)^2}{1 + \frac{m_a + a_a}{m_b + a_b}} \tag{2.2}$$

where v_b is the initial velocity, m_b the mass of struck ship and a_b the added mass of struck ship/installation.

Both these formulations assume that the impact is head-on so that only one degree of freedom is required, which will result in the most conservative estimate of the requirement to energy dissipation. This is rarely the case in real collisions, and more degrees of freedom are needed to properly describe the behavior. This can conveniently be described with a combination of translational and rotational impulse theory, see Liu and Amdahl (2010); Pedersen and Zhang (1998); Stronge (2004).

de Jonge and Laukeland (2013) developed a closed form solution for energy dissipation in a collision between a spar platform and a large tanker considering the eccentricity of the impact on the spar's center of gravity (COG). This method can be applied for the energy dissipation in a head on collision between a vessel and a platform with varying impact location on the platform, such that both translational and rotational degrees of freedom are excited. The energy to be dissipated can then

be found as

$$E_s = \frac{1}{2} \left[\frac{m_a(1 + a_a)v_a^2}{1 + \frac{m_a(1+a_a)}{m_b(1+a_b)} + \frac{m_a}{m_b}\left(\frac{R}{\rho}\right)^2 (1 + a_a)} \right] \qquad (2.3)$$

where R is the eccentricity distance and ρ the struck body's gyration radius in the relevant plane.

The external mechanics methods usually assume that the impact duration is short, so that there is no change in force direction during the impact. Further, the impact force is assumed to be so large that other forces are negligible, and that deformations are limited to the contact surface.

2.3.2   Internal Mechanics

The internal mechanics calculation starts with the requirement to energy dissipation from the external mechanics assessment. The main goal is to distribute that energy dissipation as correctly as possible between the interacting bodies, so that the damage extent to each structure can be evaluated. This can either be performed with simple calculation methods or with more advanced NLFEA simulations, the latter being the primary focus of this thesis.

Sajdak and Brown (2005) states that the majority of the energy absorbed by damage to the structure is absorbed by either the side shell, longitudinal bulkheads, decks, stringers, web frames, transverse bulkheads, longitudinal girders and transverse girders. Struts, columns and brackets are of little importance, but may in some cases delay failure of other structural members such as girders. This can in turn have some effect on the total energy absorption, especially for low-energy impacts.

Simplified methods attempt to describe the governing deformation mechanism, and uses plastic analysis methods to establish a simplified model. Compared to NLFEA, the user has significantly smaller possibilities of making errors, and the cost vs. accuracy is usually very good. Some of the key methods are described briefly in the following.

Simplified Methods for Striking Bow

Yamada and Pedersen (2008) presented a benchmark study of the main methods divided into two principally different groups; the *intersection method* and the *plate unit method* (Figure 2.3) depending on which parts are assumed to contribute mostly to the energy dissipation during crushing. Many of the simplified methods

are described in further detail in Amdahl (1983); Lehmann and Yu (1995); Lützen (2001); Lützen et al. (2000); Pedersen et al. (1993); Yamada and Pedersen (2008, 2007).

(a) Intersections   **(b)** Plate Units
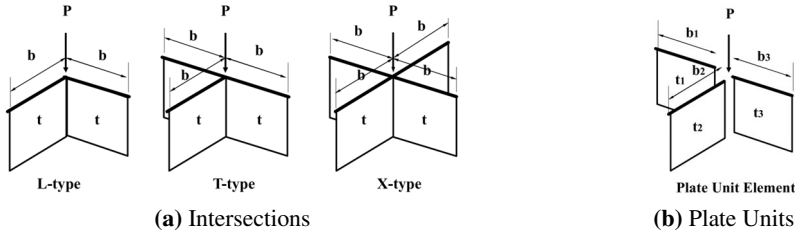
Figure 2.3: General simple methods, from Yamada and Pedersen (2008)

Using the method proposed by Amdahl (1983) as an example, a typical calculation routine is then to count the number of different types of intersections (as marked with colors in Figure 2.4), associate each type of intersection with an typical force and sum up to estimate a total force level. This is performed for several transverse cuts of the vessel to produce a force-indentation curve, and the corresponding energy vs. indentation relation is thus established. The comparison by Yamada and Pedersen (2008) shows that many of the simple methods give fairly good results with crushing energy and force in the correct order of magnitude.
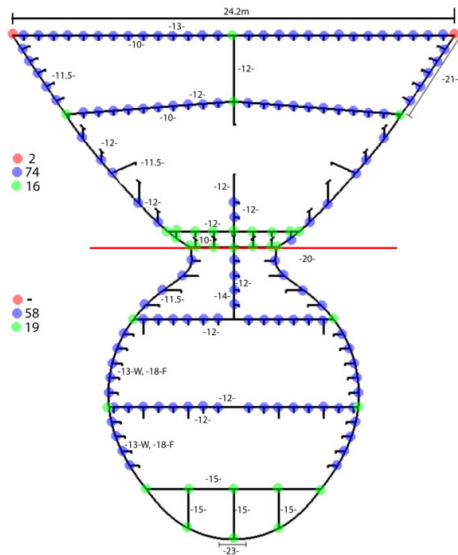
Figure 2.4: Identification of types of cross sections in an oil tanker bow, from Storheim (2008). Different colors represent different intersection types.

Simplified Methods for the Struck Side Structure

Pedersen (2010) summarize observations from full-scale accidents and model-scale experiments, and list the primary energy absorption mechanisms of a ship side structure as

- Membrane deformation of shell plating and attached stiffeners
- Folding and crushing of transverse frames and longitudinal stringers
- Folding, cutting and crushing of horizontal decks
- Cutting and crushing of ship's bottoms
- Crushing of bulkheads

Notably, bending and shear response of stiffeners attached to the shell are not mentioned, as these fail at low force levels and then primarily give a contribution to the membrane capacity of the stiffened plate. Each of the different mechanisms can be treated with simplified plastic deformation models.

The load to be applied to such a mechanism can either be found from a pressure-area relation derived from a relevant load (such as from crushing of a bulbous bow in Hong et al. (2009) and Section 6.3), or through a crushing strength load model such as those described in Lützen et al. (2000).

Membrane shell plate response becomes relevant for finite deflections to the plate. Jones (1971) proposed a theoretical model for the study of dynamic plastic behavior of plates with finite deflections, extending the work of Sawczuk (1964a,b). A rigid-plastic behavior was assumed, in which all yielding took place inside yield hinges. By predefining a yield line pattern, the energy absorption in each yield line could be expressed through considerations of internal and external work, and a relation between the plate deflection w and the pressure load could be obtained. Different yield line patterns can be assumed (such as in Figure 2.5).

(a) Roof top   **(b)** Double diamond
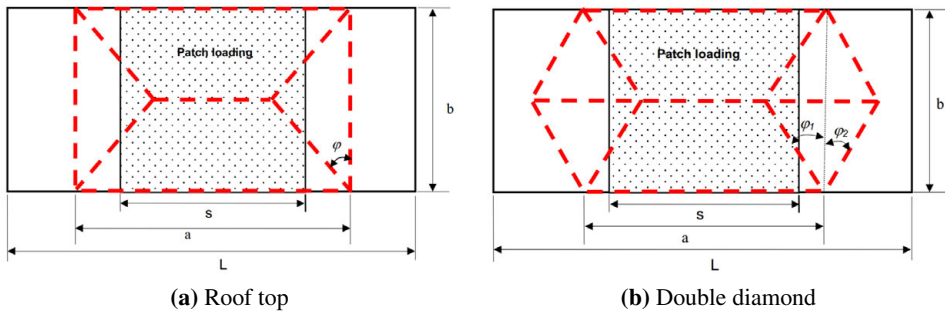
Figure 2.5: Yield line models, from Hong (2008)

The stiffeners may be designed with a simple three-point bending plastic mechanism such as in Hong et al. (2009). The load distribution over the stiffener is assumed (Figure 2.6a), and a mechanism model is then established (Figure 2.6b). The interaction between shear and bending is accounted for by allowing a full plastic moment capacity M_p in the center yield hinge, whereas the capacity of each stiffener end M_{pr} is reduced due to shear in the web. A simplified calculation approach is demonstrated in Section 6.5.

(a) Two different load distributions assumed for stiffener

(b) Plastic mechanism model
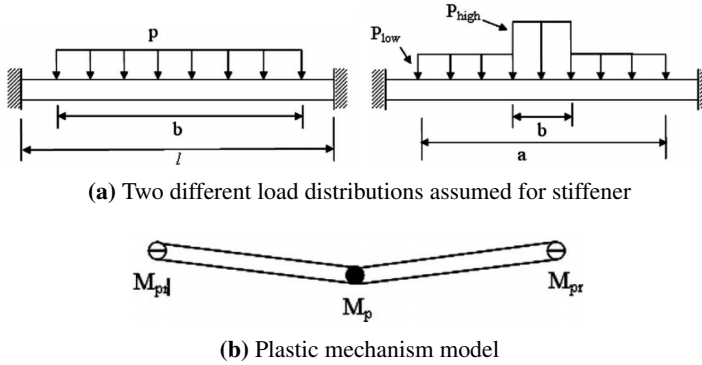
Figure 2.6: Three point bending mechanism for stiffener design, from Hong et al. (2009)

Stringers and girders may be assessed with similar methods (Figure 2.7), but due to their short length to height ratio, shear, buckling, folding and local denting should be properly taken into account. Some of the proposed methods may be found in Hong and Amdahl (2008); Wierzbicki and Driscoll (1995).
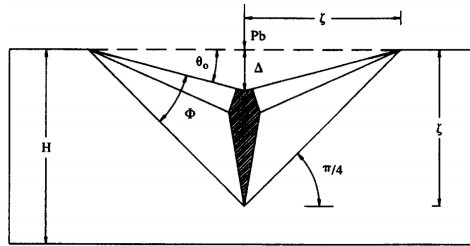
Figure 2.7: Local denting of the web of a web frame, from Wierzbicki and Driscoll (1995).

Many researchers, such as Lützen et al. (2000); Sajdak and Brown (2005); Yamada and Pedersen (2007), have proposed methods that combine several types of mechanisms so that the total resistance of the ship side can be estimated in a simplified manner. These methods will often assume that the stiffeners are weak, and include them by increasing the plate thickness. This is often termed smeared stiffeners (Paik and Pedersen 1995), and is an adequate assumption for collisions in which

large damage is expected, but not if strength design is the design goal.

Nonlinear Finite Element Analysis

NLFEA can be used to solve both the internal and external collision mechanics, and is nowadays the preferred solution. Methods, assumptions and challenges for NLFEA collision simulations are discussed throughout the remainder of this thesis, with some links back to simplified methods.

2.3.3   Validity of the Split Between Internal and External Mechanics

The validity of the split between internal and external mechanics has not been discussed in great detail in the literature. For the simple cases, the validity is obvious, but for cases in which the force direction changes during the collision the split can be erroneous. A typical example of this is an oblique impact (Figure 2.8) in which large forces can be expected both in the longitudinal and transverse direction of the vessel, thereby changing the vessel heading towards the platform during the collision. Sajdak and Brown (2005) argue that oblique collisions occur more often than perpendicular collisions. Further, if the striking bulb penetrates the struck side-shell, the collision force direction will be even more difficult to predict. External mechanics methods may fail, and a coupled external/internal approach is necessary.

(a) Near perpendicular impact   (b) Oblique impact
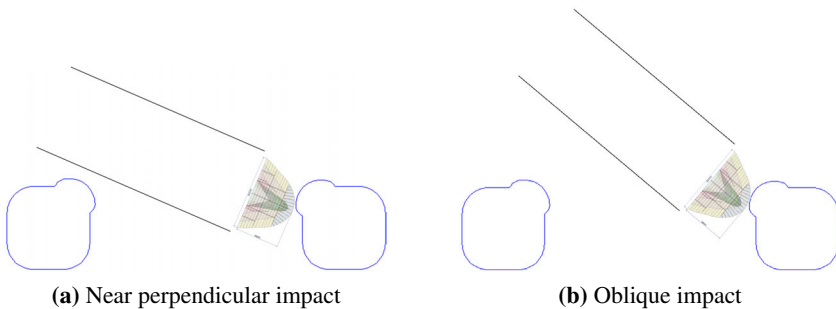
Figure 2.8: A near perpendicular and an oblique impact scenario of a supply vessel bow between two columns of a semi-submersible platform

The split is also challenging for ship-ship collisions in which both vessels have considerable velocities at impact. Lee et al. (2013) used complex simulations using Fluid-Structure-Interaction (FSI) and modelling of both the colliding vessels in an integrated manner to study the behavior of such events (Figure 2.9). The internal mechanics was found to be very dependent on the vessels velocities, and the collision force changed both magnitude and direction during the collision process.
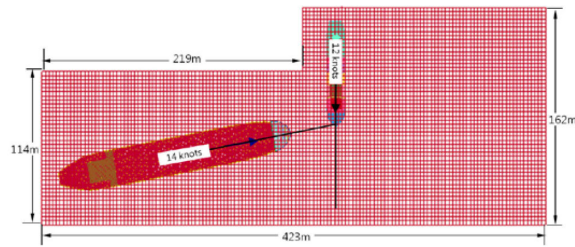
Figure 2.9: Integration collision simulations using FSI, from Lee et al. (2013)

2.4   Mitigation Measures

Risk analysis establishes a design scenario with a known probability. From the design scenario, the external and internal mechanics can be estimated. If the structure is found to not withstand the scenario, mitigation measures have to be taken. Pedersen (2010) argue that the cheapest risk-reducing measure is to lower the probability of impact, typically by operational procedures or constraints.

If the strength of the struck ship should be increased, typical measures are to

- Increase the distance between the outer and inner shell in a double-sided structure (ductile design). This can in turn increase the volume of the damaged structure, and thereby the energy dissipation according to Minorsky (1959) for high-energy collisions
- Increase the strength of the struck vessel to rather initiate crushing of the striking vessel (strength design)
- Dividing the structure into small enough compartments so that sufficient stability is ensured after flooding (damage stability)
- Moving dangerous or pollutive cargo and consumables away from the zone of expected damage

Accurate simulations are necessary to determine the effectiveness of measures to improve the crashworthiness of a structure in a cost-efficient and safe manner.

2.5   Common Assumptions

Several assumptions are made when using plane stress shell elements for simulations where crack initiation and propagation are important. Simonsen and Törnqvist (2004) lists some of the most important:

- Plane stress is assumed regardless of thickness or structural configuration. In reality, the crack-tip mechanics may be closer to plane strain.
- Shell models cannot predict necking accurately, as the out-of-plane stress

components are neglected.
- In-plane dimensions of the elements are normally such that the stress and strain concentrations at the crack tip cannot be captured accurately.
- With element erosion, the possible directions of the crack are limited by the mesh discretization.

The lack of through-thickness stiffness will also impose challenges with strain-rate dependent fracture models. Further, the effect of cracks, welds, perforation of plates, heat affected zones and other minor imperfections are typically not considered in a simulation. Their effect on the total collision outcome has yet to be assessed by the research community.

2.6   Numerical Setup

A wide range of numerical parameters have to be determined when conducting NLFEA. A thorough investigation of each parameter is often not feasible, and the numerical influence on the simulation results may be significant. Further, when conducting simulations of an experiment with a known solution, it may be tempting to tune some numerical parameters to get a better match. Such temptations are resisted herein, and focus is kept on only tuning parameters that can also be tuned in a full-scale design case in which the solution is not already known.

Some general recommendations for NLFEA simulations and a sensitivity study of the numerical sensitivity to warping and drilling stiffness, as well as a range of other numerical parameters, are presented in Appendix A. The full control parameter deck as used in most of the simulations herein is also given in the appendix.

Chapter 3

Material response

3.1 Introduction

When assessing the structural strength during a collision by NLFEA, the analyst needs to describe the complete material behavior up fracture. This includes the stress-strain relation, strain-rate effects, the strain-state dependence of fracture and in special cases also the thermal response. The predicted response of the structures is very sensitive to the material behavior, and this chapter investigates this dependence.

Hogström and Ringsberg (2012) discuss the effect of variance in work hardening on the damage extent in a collision based on a set of uniaxial tests performed on the same material grade (DOMEX 240 YP, similar to NV A). By using the mean and mean $\pm$ two standard deviations, they found that the work hardening significantly influence the force-displacement relation and the predicted damage in a given impact scenario. The modeled side structure was more sensitive to material properties if the modeled striking vessel was rigid as opposed to an integrated analysis. Paik (2007) also recognize that the NLFEA simulation results can be highly dependent of the shape of the material stress-strain curve.

When assessing the resistance of a struck vessel, the striking vessel represents a *load*. The struck vessel shall resist this load. Due to the high sensitivity to material parameters on the collision response of a vessel, it is important to have a consistent method to assess the behavior of materials in collision simulations. This *design material behavior* should be defined so that the predicted consequences of the collision are conservative, in other words that the damage to the struck vessel is not underpredicted.

Normally, the yield strength of materials for the struck ship or offshore platform is based upon a low characteristic value, typically at the 5% percentile of the probability distribution of mechanical tests. As for the striking vessel, the material's yield strength at 95% percentile would be more appropriate as this would render a higher collision force. It is emphasized that the *design material behavior* differs substantially from the *expected material behavior*. In a real collision event the expected damage to the struck vessel will be smaller than the "design" damage.

How can this *design material behavior* be complied with? What is the appropriate shape of the stress-strain curve? How should strain-rate effects be treated? How to consider fracture and its mesh dependence? These questions will be discussed in the following based on literature review, engineering judgment and numerical simulations.

3.2   Plastic Material Behavior

The response of ductile metals in collisions can be described in several stages: elastic behavior up to yielding (yield strength), a yield plateau without significant hardening, followed by plastic hardening until the maximum tensile strength is reached, after which the specimen strength decrease. In a uniaxial tension test (Figure 3.1a), the maximum strength occurs at the point of diffuse necking, in which localized contractions in the width direction occur (Figure 3.1b) and balance the increased strength due to strain hardening. A local neck will then form, and the specimen rapidly becomes thinner without large contractions in the width direction. Eventually, fracture occurs in the local neck.

(a) Stress-strain curve   **(b)** Diffuse (top) and localized (bottom) necking
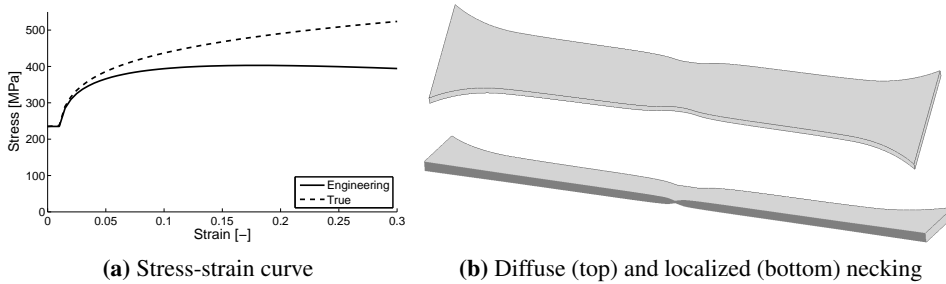
Figure 3.1: Material behavior in a uniaxial tensile test

The point of fracture is for most materials dependent on the multi-axial state of stresses and strains. A *strain state* is defined as the ratio of the minor and major principal strain rates, $\beta = \dot{\varepsilon}_2/\dot{\varepsilon}_1$. Similarly, a *stress state* is defined as the ratio between the minor and major principal stresses, $\alpha = \sigma_2/\sigma_1$. The stress state is also commonly defined in terms of the stress *triaxiality* T

$$T = \frac{\sigma_1 + \sigma_2 + \sigma_3}{3\sigma_{eq}} \tag{3.1}$$

through the principal stresses σ_i and the equivalent (von Mises) stress σ_{eq}. The stress triaxiality describes the ratio between the volume change (hydrostatic) and the shape change (deviatoric). For bi-axial stress states (as in shell elements) with proportional strain paths[1], a relation among T, α and β can be obtained. Thus, the strain state and stress state describe the same material state. Such relations are provided in Appendix B. In the following, these terms are used interchangeably to describe the dependence with respect to a multi-axial state of loading and/or deformation.

3.3 Yield Criterion and Hardening

All simulations herein uses J2 flow theory; i.e., the von Mises yield criterion, the associated flow rule and isotropic hardening are adopted. The yield criterion is given by

$$f = \sigma_{eq} - \sigma_f(\varepsilon_p) = 0 \tag{3.2}$$

where σ_{eq} is the von Mises equivalent stress. The current flow stress σ_f is assumed as a function of the equivalent plastic strain ε_p via the Hollomon-type power-law hardening rule, i.e.,

$$\sigma_f(\varepsilon_p) = \begin{cases} \sigma_0 & \text{if } \varepsilon_p \leq \varepsilon_{plateau} \\ K(\varepsilon_{0,eff} + \varepsilon_p)^n & \text{if } \varepsilon_p > \varepsilon_{plateau} \end{cases} \tag{3.3}$$

where K and n are the hardening parameters and σ_0 is the initial yield stress. To account for the existence of a strain plateau, the hardening is delayed until the plastic strain reaches the plateau strain $\varepsilon_{plateau}$. Thus, $\varepsilon_{0,eff}$ is defined by the relation

$$\varepsilon_{0,eff} = \varepsilon_0 - \varepsilon_{plateau} = \left(\frac{\sigma_0}{K}\right)^{1/n} - \varepsilon_{plateau} \tag{3.4}$$

where ε_0 is the strain at initial yield. Up to the point of diffuse necking, the true and engineering stress-strain values can be converted as

---

[1]A proportional strain path gives a constant β-value throughout the deformation. Thus, $\beta = \dot{\varepsilon}_2/\dot{\varepsilon}_1 = \varepsilon_2/\varepsilon_1$

$$\varepsilon_{true} \; = \; \ln\left(1 + \varepsilon_{eng}\right) \tag{3.5}$$

$$\sigma_{true} \; = \; \sigma_{eng}\exp\left(\varepsilon_{true}\right) \tag{3.6}$$

For structural steels commonly used in marine applications, the power-law harden-
ing rule gives good correlation with actual material test data, especially when it is
combined with a yield plateau. Example simulations of uniaxial tensile tests are
shown in Figure 3.2 for different materials. The curve for NV A36 is typical for
medium strength steel, with a significant yield plateau and moderate hardening up
to the tensile strength. The DP450-material (test from Colla et al. (2009)) is a
special steel alloy with low yield but steep hardening. The curve marked Tautz is
from a uniaxial test by Tautz et al. (2013). The material parameters used in the
simulations are given in Table 3.1.

(a) NV A36   **(b)** DP450   **(c)** Tautz plate
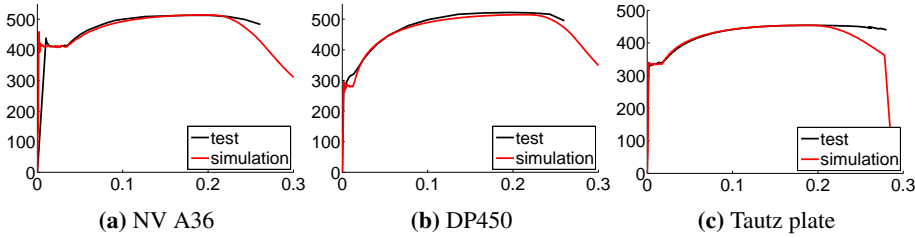
Figure 3.2: Example calibrations of power law material to structural steels with low and
high hardening. Engineering strain [-] vs. engineering stress [MPa].

Table 3.1: Material parameters used in Figure 3.2.

	σ_0 [MPa]	E [GPa]	K [MPa]	n	$\varepsilon_{plateau}$
NV A36	418	206	845	0.175	0.033
DP450	282	206	870	0.195	0.012
Tautz plate	338	204	758	0.19	0.015

3.4 Strain Rate

Strain rate (defined as velocity of deformation or time derivate of strain) affects the
initial yield stress, the hardening and the fracture limit. This effect is understood
to be relevant to ballistic impacts, but its importance is more debated for ship
collisions.

Strain rates increase the initial yield stress and the hardening, thereby increasing
the flow stress and the resistance to further deformation. Strains localize when a

diffuse neck starts, and the strain rates in the localization zone increase. Strain-rate hardening then stabilizes the strain localization, and thereby the necking process. The ductility of the material can thus be extended. On the other hand, an increase in strain rate is often believed to decrease the ductility (see Jones (2006); Paik (2007)). Experimental results on this show decreasing, constant or increasing elongation at fracture for high strain rates, which complicates the assessment of dynamic fracture strain significantly. The effects of increased flow stress and reduced ductility may, to some extent, cancel each other with respect to the predicted energy dissipation in a collision.

If samples of the actual material used in a structure is available, it is possible for a well-equipped laboratory to perform dynamic material testing for calibration of strain-rate models. However, assumptions are often required in the design phase, as either the material samples are not available or the cost of performing such tests on multiple material batches can not be justified.

3.4.1 Range of Strain Rates in Ship Collision

Figure 3.3 shows the plastic strain and strain rate for initial crushing of a bulb tip against a rigid plate at 4 m/s. The strain-rates associated with plastic strain are large, in the range of 5-15 s^{-1} for a mesh size of around 100 mm. Typically, high rates are observed over a short period of time when a structural member fail by e.g. buckling of a stiffening member.

(a) Equivalent plastic strain $[-]$ **(b)** Effective strain rate $[s^{-1}]$
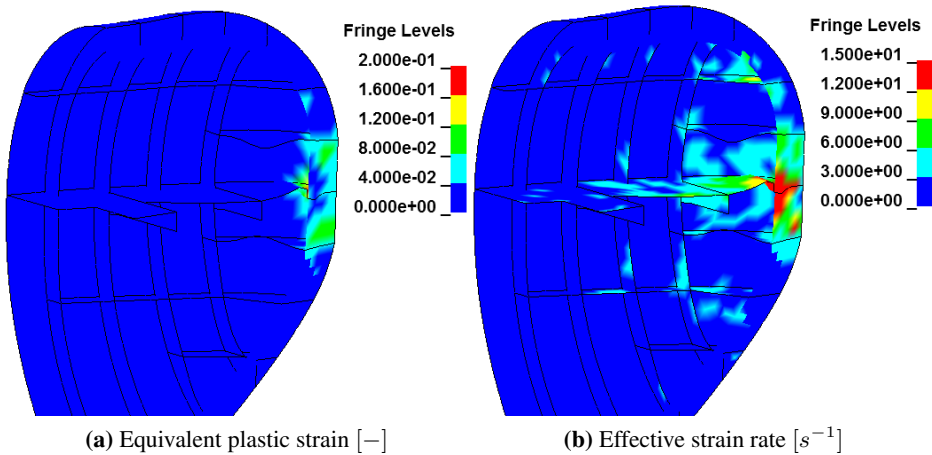
Figure 3.3: Plastic strain and strain rate for initial crushing of a bulb tip against a rigid plate

Choung et al. (2010) found strain-rates in a numerical simulation of a model scale impact test from a sharp wedge into a stiffened plate in the range of 400 s^{-1}, with a mesh size of 2 mm. These examples illustrate two important points; the local instantaneous strain rate in ship impacts may be significant even at low collision velocity, and the strain rate is (similar to strains) mesh-size dependent. In collision simulations with mesh size in the range of five to ten times the plate thickness, simulated strain rates will be in the range up to 100 s^{-1}, whereas the true strain rate may be significantly higher in the local neck. The high strain rates often have a short time duration.

3.4.2   Methods for Strain-rate Dependence

There are many advanced methods for strain-rate dependence on plastic flow and fracture, see e.g. Roth and Mohr (2014) for an overview. They often require calibration against material tests.

A commonly used model was developed by Cowper and Symonds (1957), in which the dynamic stress is found by scaling the static stress with a dynamic hardening factor (DHF)

$$\sigma_{dynamic} = \sigma_{static} \left[1 + \left(\frac{\dot{\varepsilon}}{C} \right)^{\frac{1}{p}} \right] \tag{3.7}$$

where $\dot{\varepsilon}$ is the strain rate and C and p are calibration parameters. The model scales all static stresses with the same DHF, defined as the ratio between the response at elevated strain-rates compared to the response at 0.001 s^{-1}. Based on experimental data, Cowper and Symonds (1957) suggested $C = 40.4$ s^{-1} and $p = 5$ for initial yield stress of mild steels, a recommendation that is widely adopted for ship collision analysis. For initial yield stress of high tensile steels, Jones (2012); Paik and Thayamballi (2003) suggests C=3200 and p =5.

Experiments show that the DHF varies significantly from initial yield to large plastic strains (Jones 2006). Strain energy dissipation is the important factor for ship collisions, and the DHF should properly represent the response for large plastic strains. DNV RP-C208 recommends to calibrate the DHF to the maximum expected stress and strain, and not the initial yield stress. In lack of test data, the RP suggests parameters $C = 4000$ s^{-1} and $p = 5$ for common offshore steel materials.

The C-parameter can be defined as a function of the plastic strain, as proposed by Jones (1989b) as

$$C = F + G\varepsilon_p \tag{3.8}$$

where F and G are new parameters. Choung et al. (2013) suggested to modify the above equation to include the plastic strain squared; this worked well for DH36 and EH36 steels.

Another popular strain-rate model is the model by Johnson and Cook (1983), in which the yield stress is decomposed multiplicatively with the effect of strain hardening, strain rate and temperature as

$$\sigma = \left(K(\varepsilon_{0,eff} + \varepsilon_p)^n \right) \left(1 + D \ln \dot{\varepsilon} \right) \left(1 - T^{*m} \right) \tag{3.9}$$

where the coefficients D and m are needed in addition to the power law parameters K and n. T^* is a temperature parameter relative to a reference temperature. This model is widely used for very-high strain-rate applications such as ballistic simulations, in which the coupled thermo-mechanical behavior becomes important.

3.4.3 Strain Rates in Uniaxial Tests

Many experiments on strain-rate response of structural steels have been published. DH-36 high strength steel has been investigated by Choung et al. (2013); Guo and Gao (2013); Nemat-Nasser and Guo (2003); Su et al. (2013) among others. Some high-strength steels used in the automotive industry have been investigated by Roth and Mohr (2014) (DP590) and Anderson et al. (2014) (DP780).

Choung et al. (2013) conducted a range of tests of DH-36, EH-36 and 2W50 steels at strain rates between 0.001 and 200 s^{-1} at various temperatures. Figure 3.4 shows the stress-strain curve for steel grade DH36 for various strain rates at room temperature. The rate-effect on initial yield stress is high, but moderate on hardening. From 0.001 to 100 s^{-1}, the flow stress increases by approximately 20%.

The DHFs extracted from Choung et al. (2013)'s experiments at room temperature are plotted in Figure 3.5. Figure 3.5a shows the increase of initial yield stress and Figure 3.5b the increase of flow stress with increasing strain rates. The plotted values for the flow-stress DHF are averaged between 5 and 15% plastic strain for each test. This is compared to the multiplicative strain-rate factor for the Cowper-Symonds and Johnson-Cook strain-rate models.

It appears that the Cowper-Symonds model with parameters given in DNV RP-C208 is somewhat correlated to the ratio of yield stresses (Figure 3.5a), but not for the average increase in plastic strain during the full strain range of a uniaxial test. The same applies for C=3200 as suggested in Jones (2012). Thus, using this as
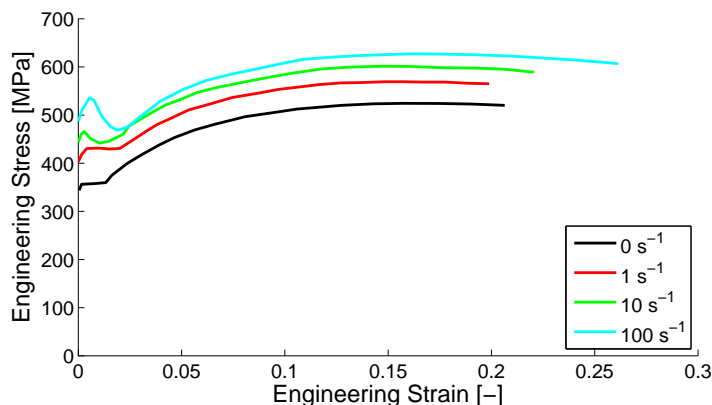
Figure 3.4: Uniaxial tensile test of DH36 steel at different strain rates in room temperature, from Choung et al. (2013).
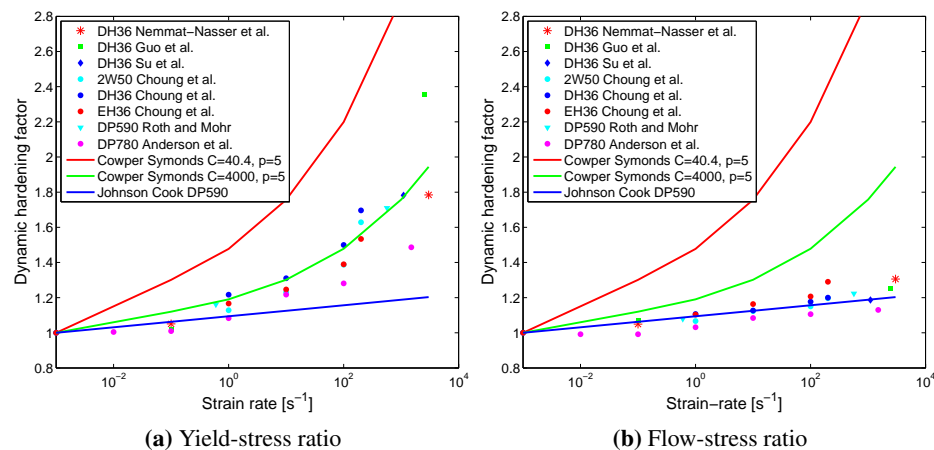
Figure 3.5: Dynamic hardening factors for initial yield stress and average flow stress at different strain rates.

a multiplicative factor on the flow stress will overestimate the specimen strength, and thereby the energy dissipation prior to fracture.

When compared against the flow stresses in Figure 3.5b, the Johnson-Cook model fitted to DP590 steel show a better correlation with the average increase of flow stress for the range of strain-rate ratios considered, while at the same time underestimating the yield stress ratio. Similarly, the Cowper-Symonds model can be calibrated to achieve satisfactory results for flow stress. However, when both the initial-yield and the flow-stress rate effects are needed, methods similar to Jones (1989b) and Choung et al. (2013) should be used, or *calibrated* tabular input of the complete stress-strain curve for varying strain rates be given directly as input to the NLFEA code.

The shape of the engineering stress-strain curve in Figure 3.4 remains similar for the tested strain rates, but may alter for very high rates. Thus, for simulation of ship collisions, a constant multiplicative increase in dynamic flow stress vs. strain rate can be assumed with sufficient accuracy.

3.4.4 Simulations of a Uniaxial Tensile Test with Strain-rate Hardening

Simulations of the uniaxial tensile test in Choung et al. (2013) was performed using LS-DYNA with shell elements. The Cowper-Symonds parameters[2] are calibrated to fit the experimental results in Figure 3.4. The calibrated C-parameter in Eq. 3.7 was 400000, compared to the value of 40.4 in Cowper and Symonds (1957) or 4000 in DNV RP-C208. The p parameter was, for simplicity, set to 5 for all cases.

(a) C=40.4   **(b)** C=4000   **(c)** C=400000
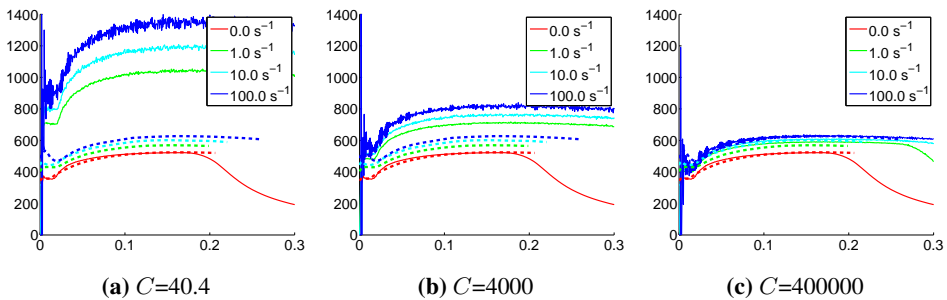
Figure 3.6: Simulations (thin continuous lines) vs. experiment (thick dashed lines) of uniaxial tensile test of DH36 steel with varying C-parameter in Cowper Symonds.

---

[2]Note that the visco-plastic option for Cowper-Symonds in LS-DYNA is not used, rather the simpler version with a constant DHF is adopted. This allows for comparison with hand calculations directly. The visco-plastic method is generally recommended (VP=1), and will require re-calibration for dynamic amplification of the plastic flow stress. Generally, the strain-rate effect is less for the visco-plastic implementation for the same set of parameters.

Figure 3.6 shows the simulation results. If strain-rate hardening is included based on the parameters in Cowper and Symonds (1957) ($C = 40.4$), the DHF on flow stress was considerably overestimated: a 160% increase at a strain rate of 100 s^{-1} versus the observed 20%. With the parameters in DNV RP-C208 ($C = 4000$), the simulated DHF for dynamic flow stress was 58%, and with parameters actually calibrated to the test ($C = 400000$) the simulated DHF match the experiments. The calibration of strain-rate parameters will be somewhat mesh sensitive (especially in the post-necking phase). This sensitivity is significantly less than the large differences in the calibration of C and p.

Figure 3.6 further shows that the simple check of simulating the experiment that was used to calibrate the strain-hardening model is important to conduct; errors introduced by calibrating to DHFs from initial yield stress rather than plastic flow stress are easily identified.

3.4.5   The Strain-rate Effect on Dynamic Fracture Strain

The effect of strain rate on fracture initiation is a matter of discussion, and is often disregarded in ship collisions (Jones 2006). It is often argued that fracture will occur earlier at higher strain rates, but many tests on high strength steels actually show the opposite. Roth and Mohr (2014) summarize different experiments in which an increase in elongation to fracture (engineering strain) was obtained at increasing strain rates. Their own experiments showed that the elongation to fracture was almost independent of the loading rate in tests of DP590 advanced high-strength steel. However, when examining the fracture surface of the test specimens, it was observed that the thickness reduction increases with the speed of loading. Li and Chandra (1999) showed results where the elongation to fracture increased with the increase in strain rate, whereas the elongation in Choung et al. (2013)'s results show no clear dependence of strain rate.

Strain-rate hardening stabilize the deformations such that the area with elevated strains is extended, notably when higher strain rates are obtained in a diffuse or localized neck. At the same time, the elongation to fracture is not largely affected. Thus, while the elongation to fracture (engineering strain) can be assumed constant, the true strain to fracture inside the necked region may change significantly with increasing strain rates. When simulating a uniaxial tensile test, strain-rate hardening will increase the elongation at fracture considerably (as in Figure 3.6). Consequently, the dynamic fracture strain should also be scaled if the elongation to fracture is to be preserved.

During the necking process, through-thickness effects inside the neck becomes important and the assumption of plane stress is no longer valid (Walters and

Voormeeren 2014). With the complicated process of stabilized necking and increased thinning at higher strain rates (as observed by Roth and Mohr (2014)), shell elements will require a different method to include strain-rate-dependent fracture than solid elements, in which shortcomings of the plane stress-assumption are accounted for.

To study the effect of stabilization of necking and the true dynamic fracture strain when using shell elements, the strain results in the simulations in Figure 3.6c (with C=400000) was used. Figure 3.7 shows the principal and thickness strain in the uniform part of the specimen, as well as within the diffuse neck. Figure 3.7a clearly shows the stabilization effect with delayed diffuse necking with increasing strain rate. Up until local necking, a linear relationship is observed between the uniform strain and the engineering strain. Once necking initializes, the strain in the neck increases quickly with increasing elongation, and the remaining specimen show negligible further straining. The thickness strain in Figure 3.7b does not show increased values with increasing strain rates (as observed in the experiments in Roth and Mohr (2014)). The simulated slope of the thickness strain in the neck seems to be fairly insensitive to strain-rate effects.

(a) Principal strain   **(b)** Thickness strain
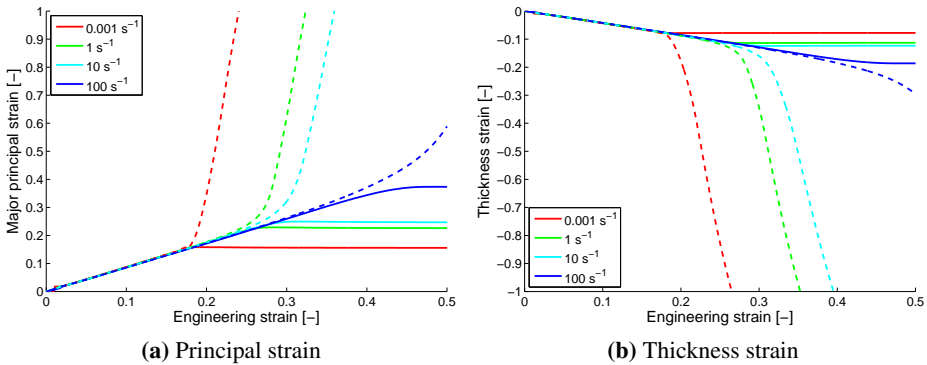
Figure 3.7: True strains in uniform and necked region of a uniaxial test specimen, from the simulations in Figure 3.6c. Continuous lines represent the uniform strain, dashed lines the strain in the neck.

Figure 3.7 shows that the true strain in the uniform part of the specimen (prior to diffuse necking at ultimate tensile strength) is practically unaffected by increasing strain rates. Thus, dynamic fracture strains less than the diffuse necking strain can be considered independent of the strain-rate. However, when strains localize after diffuse necking, the stabilizing effect of strain-rate hardening cause large differences in the true strain in the neck vs. the specimen elongation (engineering strain) due to delayed necking. This makes post-necking dynamic fracture strains

in shell elements a challenge, as the dependence of true strain vs. the elongation is a highly nonlinear function of strain rate and its stabilizing effect on necking. The dynamic fracture strains should be compensated accordingly to preserve the same elongation at fracture, or a safe value of the dynamic fracture strain that is below the diffuse necking strain should be adopted.

Jones (1989a) used an inverse Cowper-Symonds model to scale the critical strain ε_f as

$$\varepsilon_{f,dynamic} = \varepsilon_{f,static}\, \xi \left[1 + \left(\frac{\dot{\varepsilon}}{D}\right)^{\frac{1}{q}}\right]^{-1} \tag{3.10}$$

where ξ is the ratio of the total energies to rupture for dynamic vs. static uni-axial loading, and D and q new parameters. Paik and Thayamballi (2003), Paik (2007) and Jones (2013) argues that the strain-rate effect is smaller on the fracture strain than on the stresses. Hence, the same Cowper-Symonds parameters C and p cannot be used for both the dynamic yield stress and the dynamic fracture strain. Samuelides (2015) uses D=800 and q=1.25, whereas Paik (2007) recommends D from 7000 - 10000 and q from 2 to 4.

Scaling the dynamic fracture strain as in Eq. 3.10 does not comply with the non-linearity of the true strain to fracture in Figure 3.7. Utilizing this scaling prior to diffuse necking is not needed according to Figure 3.7. In the post-necking phase, the scaling is insufficient to account for the delayed localization and the corresponding nonlinear relation between true strain and the specimen elongation.

Table 3.2 shows the estimates of dynamic fracture strains using Eq. 3.10 for a static critical strain of 0.2 and 0.5. Comparing this to Figure 3.7a reveals that Eq. 3.10 may be used for moderate plastic strains without significant necking. However, the scaling of the dynamic strain fails if high static critical strains are allowed (including post-necking ductility), as commonly used in modern fracture criteria with mesh dependence.

3.4.6 Discussion

Jones (2013) discuss the credibility of structural analysis with high dynamic loading. He argues that the dynamic properties are sensitive to a wide range of factors, such as plate thickness, surface finish, heat treatment and chemical composition of the test specimen. Experimental testing of dynamic material parameters is challenging, and a wide range of results have been obtained for the same material grade in different laboratories. The shape of test specimens also affects the dynamic rupture strain. Using notched axisymmetric specimens, Alves and Jones (1999) observed

Table 3.2: Dynamic fracture strain using inverse Cowper-Symonds with varying parameters of D and q for static fracture strains of 0.2 and 0.5.

	D/q	40.4/5	4000/5	400000/5	800/1.25	7000/4
	Rate 1 s^{-1}	0.14	0.17	0.19	0.2	0.18
Static strain 0.2	Rate 10 s^{-1}	0.11	0.15	0.18	0.19	0.17
	Rate 100 s^{-1}	0.09	0.14	0.17	0.17	0.15
	Rate 1 s^{-1}	0.34	0.42	0.46	0.5	0.45
Static strain 0.5	Rate 10 s^{-1}	0.28	0.38	0.45	0.49	0.42
	Rate 100 s^{-1}	0.23	0.34	0.42	0.42	0.37

that the dynamic rupture strain decreased with increasing hydrostatic stress.

Jones (2006) argues that dynamic fracture does not scale according to classic geometric scaling laws, similar to the size-effect in linear elastic fracture mechanics. Thus, a full-scale specimen may sustain dynamic fracture even though a geometrically similar small-scale experiment concluded that no fracture was expected.

Considering the limited effect of strain rate on plastic flow as opposed to initial yield stress in Figure 3.5, the use of parameters for strain-rate hardening calibrated to initial yield stress (e.g., $C = 40.4\,\mathrm{s}^{-1}$ and $p = 5$) would significantly overestimate the strain-rate hardening during plastic flow. A properly calibrated strain-rate model yields a drastically lower effect of strain-rate hardening.

Based on the investigated experiments, the true dynamic fracture strain in NLFEA should be adjusted so that the same elongation to fracture is maintained for different strain rates. This is challenging, as the onset of necking is delayed by strain-rate hardening. Post-necking effects, that are often accounted for with quasi-static fracture models, will thus not scale with the inverse Cowper-Symonds equation.

It may be argued that a proper treatment of strain-rate effects including both the stabilizing effect of the increased hardening and a dynamic fracture strain is not feasible with shell elements due to the assumption of plane stress.

Further research on the dynamic properties of metals is needed before strain-rate effects can be properly included in full-scale simulations. The sensitivity of strain-rate assumptions in a full-scale collision scenario is investigated in Section 3.8.2.

3.5   Fracture

A fracture occurs at a length scale orders of magnitude smaller than the plate thickness. In comparison, FEM element lengths are often 5-10 times the plate thickness. This tremendous span in length scale is difficult to handle when modeling ductile fracture. The micromechanical response is controlling the macromechanical re-

sponse, and it is thus worthwhile to investigate.

3.5.1   Micromechanical Fracture

Garrison Jr and Moody (1987) gives a very comprehensive overview of the experimental and theoretical work related to the micromechanical ductile fracture process. The micromechanical process is in essence split in three phases that to some extent occurs sequentially; void nucleation, void growth and coalescence of voids (illustrated in Figure 3.8).
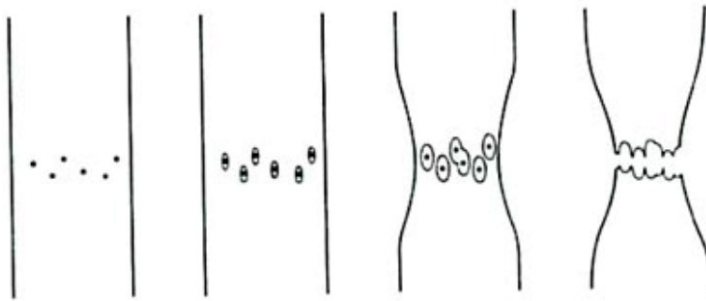
Figure 3.8: Void nucleation, growth and coalescence in ductile failure, from Weck (2015).

Void nucleation refers to the initiation of micro-voids, which usually occurs close to larger particles within the material. The strain at which void nucleation occurs is strongly dependent on the stress state; voids typically nucleate at lower strains for higher triaxialities. Void nucleation also occur at lower strains in higher strength materials, explaining the often observed reduction in ductility for high-strength alloys.

After nucleation, a void will grow in volume and its shape depends on material properties and the experimental conditions. This has been an intensive area of research. Among many proposed methods, the Rice and Tracey (1969) method is widely used, as in the RTCL fracture criterion developed by Törnqvist. For constant stress states, void growth decelerates as the work hardening coefficient increases. The rate of void growth increases with increasing strain. Triaxiality is important in determining both the rate of void growth and the void shape, and the relative growth rates are amplified with increasing stress triaxiality. Voids can also deform in pure shear, see Nahshon and Hutchinson (2008) for a discussion.

After sufficient void growth, the voids coalesce (grow together), which is the process in which the actual fracture propagates. Based on various experiments, Garrison Jr and Moody (1987) states that the coalescence event in general is rapid, and occurs over a small interval of macroscopic strain. Figure 3.9 shows the detailed fracture surface of a DH36 tensile round bar from Xue et al. (2010).
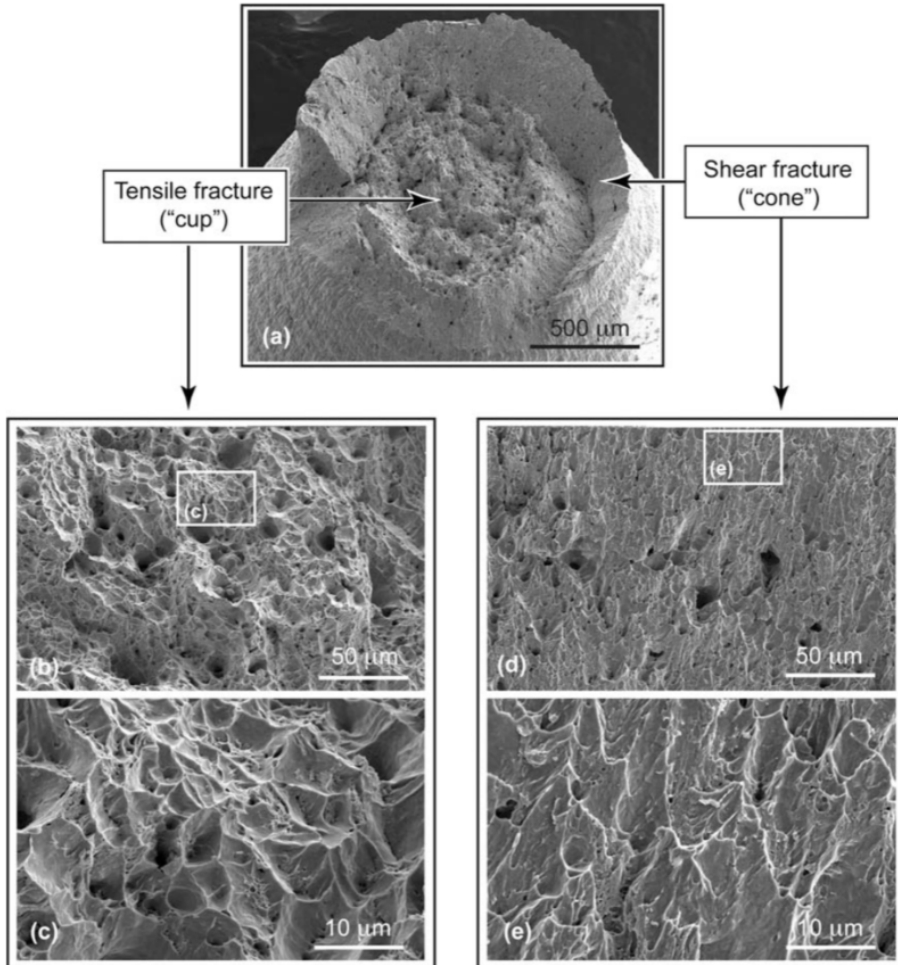
Figure 3.9: Fracture surface of DH36 tensile bar showing: (a) cup-cone failure mode; (b, c) equi-axed dimples caused by void growth and coalescence in the central region; and (c, d) elongated dimples formed by void coalescence during shear lip formation. From Xue et al. (2010).

In a typical uniaxial tensile test, a neck forms once the critical uniform strain is reached. Further straining is localized in the neck, and the stress-state changes from uniaxial tension towards plane strain tension. Void nucleation is found to initialize well before fracture, and the volume fraction of voids is highest in the center of the tensile neck, which has both the highest triaxiality and strain. Fracture usually initiates in this concentration of voids.

The fracture initiation toughness K_{IC} in fracture mechanics can also be explained by theories of void nucleation, growth and coalescence. The stress at the crack tip is high, and the local strain, stress and stress-state close to the crack tip affect how the micro-mechanical void process develops. Compared to conventional ductile fracture, K_{IC} is also significantly influenced by the particle spacing, arising from the steep gradients in strain, stress and stress-state ahead of the crack tip; see Garrison Jr and Moody (1987) for a comprehensive overview of the methods, and how they link to experimentally observed micro- and macromechanical behaviors.

Thus, the micromechanical process leading up to fracture is strongly dependent on the stress triaxiality. This micromechanical process cannot be treated adequately with large elements, typically used in ship collision analysis.

Constitutive models which explicitly account for void nucleation, growth and coalescence are available for refined solid elements, e.g., the Gurson (1977) model. This model was recently extended by Woelke et al. (2015) for shell element simulations.

Simonsen and Törnqvist (2004) highlights that the near-tip plasticity and material separation dissipate insignificant amounts of energy. The primary effect of fracture is the reduction in resistance due to released boundary conditions. In a numerical simulation that is focused on energy dissipation, both the initiation and propagation of a crack should be estimated as accurately as possible to predict the resistance to further indentation with good accuracy.

3.5.2   Macromechanical Fracture

On a macroscale, failure criteria can conveniently be separated into diffuse or localized necking, ductile failure and shear failure. Diffuse necking refers to necking over a range larger than the plate thickness, whereas localized necking is over an area about the plate thickness.

The material behavior in collisions and sheet metal forming is similar, with thin plates subjected to large in-plane and out-of-plane deformation. Plane stress is usually assumed in a simulation. However, as Walters and Voormeeren (2014) point out, this assumption is valid only up to necking, after which the through-thickness

behavior becomes important. In terms of the numerical value of stress triaxiality (Eq. 3.1), plane stress elements can only reach as high as 2/3, whereas the actual triaxiality for refined volumetric elements considering the through-thickness stress may reach 1.

The local necking preceding fracture causes vanishing strain along the neck; The strain state in the local neck is best described as plane strain conditions (Refs. (Hill 1952; Hosford and Caddell 1983)). Within the local neck, the failure mechanisms are either shear fracture (due to shear band localization) or ductile fracture (due to nucleation, growth and coalescence of voids). A local neck requires very detailed mesh using solid elements. In comparison, a ship collision analysis is feasible using elements with dimensions around five to ten times the plate thickness. Apparently, this mesh size may be refined enough to track strain localization in diffuse necking, but is very crude for a detailed local necking analysis. However, out-of-plane strain concentrations close to stiffening members are normally not captured with coarse shell element meshes.

The Keeler-Goodwin approach (Goodwin 1968; Keeler and Backhofen 1964) has been the predominant method for analyzing sheet metal forming. A forming limit diagram (FLD) is created by plotting the principal strains ε_1 and ε_2 at the onset of plastic instability. A compilation of some experimental data available in literature is shown in Figure 3.10, with NVA mild steel by Hogström et al. (2009), DOCOL 600DL steel by Gruben et al. (2013b) and AISI-1012 low carbon steel by Nurcheshmeh and Green (2011). The general trend (indicated with a dashed line) is decreasing fracture strain for increasing negative minor strains (a decreasing absolute value of the compressive minor strain), and increasing fracture strain for increasing positive minor strains (increasing absolute value of the tensile minor strain). For the NVA and DOCOL steels, the onset of necking was also identified to occur at less than half of the fracture strain, indicating significant post-necking ductility.

It is often assumed that fracture occurs when the strain reaches a critical value. This critical fracture strain can be estimated from material testing. The assumption is easy to adopt with the NLFEA method, but can pose some limitations on the accuracy. Figure 3.10 shows that necking occurs at a critical equivalent plastic strain, but the critical strain will be a function of the applied strain mode. Bai and Wierzbicki (2010) argues that the plane stress critical strain reaches a maximum for compression, uniaxial tension and bi-axial tension, whereas minimum critical strains are found for pure shear and plane strain. Thus, using a material model with critical plastic strain obtained from uniaxial testing may be non-conservative in some cases, particularly if the critical strain is larger than the critical strain value in plane-strain tension
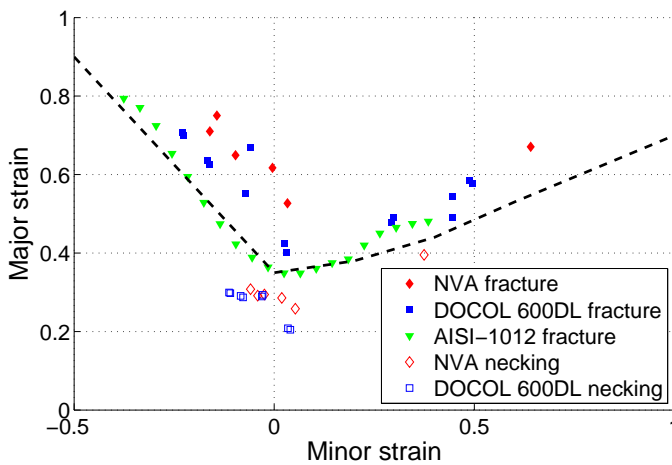
Figure 3.10: FLD from formability experiments. Dashed line indicate the generally observed trend for most steels.

Alsos et al. (2008) and Aretz (2007) summarized methods for assessing fracture in sheet metal forming applications. Strain-based FLDs can be constructed from a range of material tests at different strain states. Analytically, the forming limit curve (FLC) in the FLDs can be constructed from different proposed theories, e.g. Hill (1952), Swift (1952), Bressan and Williams (1983) and Marciniak and Kuczyiski (1967). FLD methods presuppose proportional strain paths. However, this is not necessarily the case for large plastic deformations due to non-linearities from strain hardening, geometrical changes and contact between different structural components.

A simple alternative to the strain-based FLD is the stress-based FLD proposed by Stoughton (2001), assuming that the stress-based criterion is less affected by changing strain paths. Yoshida et al. (2007) investigated the strain-path dependence based on M-K analysis, and found that the stress-based FLDs are not independent of the stress-path if abrupt changes in the path are imposed without unloading.

For coarsely meshed shell structures, Alsos et al. (2008) proposed the stress-based BWH instability criterion combining the Bressan and Williams (1983) and Hill (1952) necking criteria. This criterion is easy to implement numerically. Alsos et al. (2008) demonstrated that numerical simulations with this criterion gave good agreement with experimental data, which was also supported by Paul (2013). Törnqvist proposed the RTCL criterion, which was later confirmed by many researchers to work well for stiffened panel structures.

Several fracture criteria are compared in Chapter 5.

3.6   Mesh Dependence

The fracture strains, as determined in experiments such as those represented in Figure 3.10, can be used directly with solid elements with many elements spanning the direction of the plate thickness, e.g., in Gruben et al. (2013a). These critical strain values must be adjusted if shell elements are used.

The stress-strain curve is practically mesh-independent up until the point of strain localization. After this, mesh dependence is observed in simulations. Based on DIC measurements, Ehlers (2010a); Ehlers et al. (2012) adopted mesh-dependent stress-strain curves to account for this. Ehlers (2010b) investigated the effect of these differences in simulations of uniaxial tensile tests and full-scale scenarios.

Length-scale effects have been studied by many researchers: Ehlers (2010a,b); Ehlers and Varsta (2009); Hogström et al. (2009); Kõrgesaar et al. (2014); Marinatos and Samuelides (2015, 2013a,b); Simonsen and Törnqvist (2004); Walters (2013); Yamada et al. (2005). Mesh-size dependence is taken into account in the BWH criterion proposed by Alsos et al. (2008) and in the RTCL criterion proposed Törnqvist, both suitable for coarsely meshed shell structures.

Shell elements with length l_e equal to thickness t_e can capture local necking fairly accurately. Yet, larger elements, in the range of five to ten times the plate thickness, is often preferred in a collision analysis. Elements larger than ten times the plate thickness are not recommended for ship collision simulations as they fail to capture the stiffness of the structure prior to fracture. This would mean a minimum of three elements over the stiffener webs and five to six elements in the plate between stiffeners. If severe folding takes place, eight elements pr. half fold is recommended (Paik 2007).

Figure 5.5 shows simulations of a uniaxial tensile test, with the engineering stress-strain curves in Figure 5.5a and the true strain in the neck in Figure 5.5b. After the onset of necking, the strains localize to a small zone and the true strain in this zone shows a strong mesh dependence. This relates to several different aspects, among others that the strain in general is length-scale dependent and that localization of strains can be smaller than the mesh-size used. This type of mesh dependence is herein termed *material mesh-dependence*, mostly relevant to the local zone at and near necking. This scaling is important in the prediction of the post-necking phase.

In a stiffened panel, local strain concentrations can take place in the plate close to the stiffening members. The magnitude of the strain concentrations will increase with increasing local deformations, e.g., upon local plate bending between two stiffeners. With a coarse mesh discretization, the simulation will not be able to resolve these local strain concentrations, and the simulated onset of fracture will be

(a) Engineering stress-strain

(b) True strain in the neck
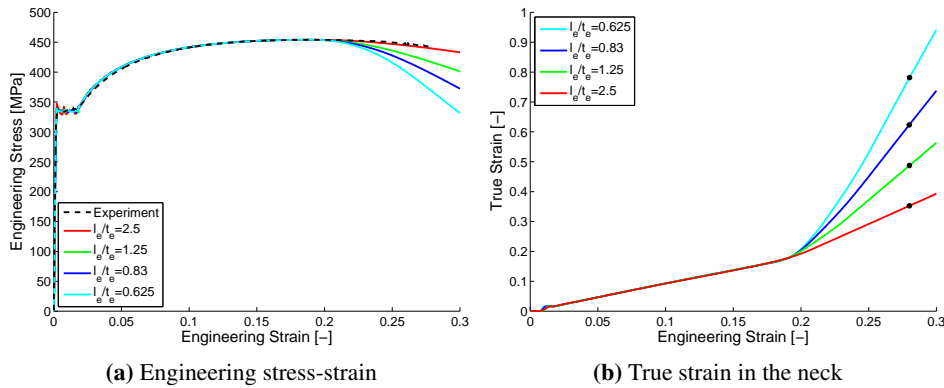
Figure 3.11: Uniaxial tensile test simulation results for element length vs. plate thickness $l_e/t_e = 0.63 - 2.5$

delayed compared to the actual behavior. Thus, the strength of the stiffened panel will be overestimated. This type of mesh dependence is herein termed *geometric mesh-dependence*, i.e., the case in which the discretized geometry does not capture the correct strain concentration prior to local instability. Compensating this mesh dependence is important to predict the onset of necking.

To obtain a robust fracture model for impact assessment of coarsely meshed shell structures, both these mesh dependencies must be considered. Calibration of a fracture criterion to simulations of a uniaxial tensile test with different mesh sizes will capture a mixture of the *material* and *geometric* mesh scaling effects, and it's applicability to different scenarios may thus be questioned if the ratio between the different effects change with the application.

Walters (2013) proposed a framework for adjusting the critical fracture strain of shell structures with both stress triaxiality and mesh size. The procedure, if properly calibrated, is general and may potentially improve fracture strain prediction. By combining the MMC fracture criterion (Bai and Wierzbicki (2008)) with the Swift diffuse instability (Swift 1952), large differences in the mesh-size scale effect was found for varying triaxiality, with low dependence for plane strain but high dependence for uniaxial and equi-biaxial straining. Körgesaar and Romanoff (2014) used a similar approach, with good results for fracture when the pre-necking strain concentrations were properly captured.

The methods by Walters (2013) and Körgesaar and Romanoff (2014) consider only the mesh size effect on diffuse necking, and not the geometric mesh size effect. The disadvantage of this is overestimation of the critical strains, and a too high

predicted structural resistance for stiffened panel structures.

Plates will have defects from the manufacturing process, and these defects increases in magnitude with an increase in plate thickness. Consequently, the fracture strain may not scale proportionally with the length-to-thickness ratio of the element. This phenomenon is taken into account by decreased requirements on, e.g., the initial yield stress for very thick plates in DNV-OS-B101 and NORSOK M-120. Moreover, Peschmann (2001) applied different mesh-scaling laws depending on the plate thickness to account for this effect.

3.7   Choice of Plastic Hardening Model for Design

The procedure to calibrate material parameters to a uniaxial tensile test is straightforward. However, when designing a vessel, the actual plastic behavior is not know a priori. Thus, the analysts are required to assume material parameters for design.

Example of material parameters ranges based on DNV-OS-B101 are shown in Table 3.3 (for minimum yield stress, ultimate tensile strength range and minimum elongation at fracture). Specific ranges are given for the ultimate strength, but not for the upper values of initial yield stress or elongation at fracture. Thus, the actual material may have a significantly higher yield strength, and may also be more ductile. Note that for high-strength steels with yield stress above 420 MPa, NORSOK M-120 gives additional values to the maximum initial yield stress (values in parentheses in Table 3.3).

Table 3.3: Example material parameters from DNV-OS-B101 and NORSOK M-120 (in ()).

Grade	Minimum σ_Y [MPa]	Tensile strength [MPa]	Minimum elongation [%]
NV A	235	400-520	22
NV A36	355	490-630	21
NV A46	460 - (580)	570-720	19
NV A50	500 - (600)	610-770	18

The yield ratio is defined as the ratio of initial yield stress σ_0 to the ultimate tensile strength σ_{UTS}. The yield ratio increases with an increase in yield strength. Billingham et al. (2003) reports yield ratio data from Willock (1992) (Figure 3.12). In steels with yield strength of 350 MPa, the yield ratio varies from 0.6 to 0.8. For steel with 450 MPa in initial yield stress, the yield ratio ranges from 0.7 to 0.87.

When designing a structure against impact loads, the material properties of the impacting body represent a *load*, and should be based on high characteristic values. The material parameters of the struck body will affect the resistance and deforma-
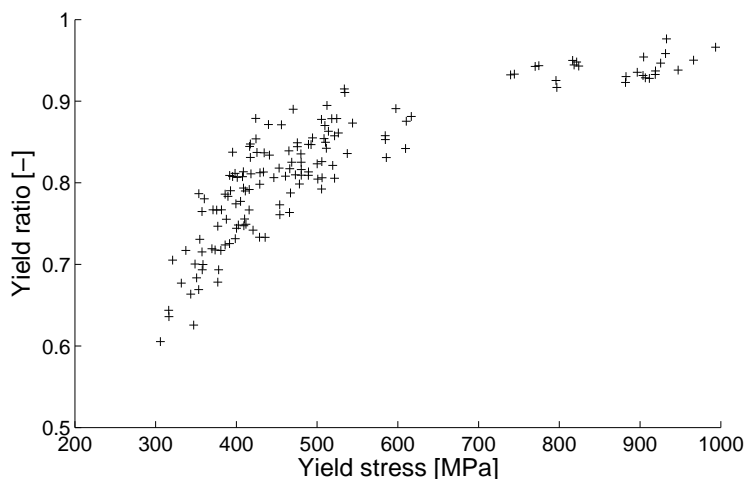
Figure 3.12: Yield ratio for high-strength steels, data from Willock (1992)

tion, and low characteristic values should be used.

For offshore structures, NORSOK N-001 gives some governing principles for assessment of material strengths. When a high resistance is favorable with respect to design, a low characteristic value, typically the 5% percentile, of the material strength is used. When a high resistance is unfavorable, a high characteristic value, typically the 95% percentile, is used. This definition is useful for both ship-platform and ship-ship collision assessments. With elastic analysis, the yield stress is easily adjusted to comply with these percentiles. However, the complete stress-strain relation is needed for NLFEA.

Design codes give some input on the range of material behavior for a given material grade. For the 5% percentile, the lower values in Table 3.3 could be used. Unfortunately, the 95% percentile of the yield strength distribution is not known, and will have to be assumed based on engineering judgment. As concerns the ultimate tensile strength, it is natural to choose the upper limit of the specified range of tensile strength in Table 3.3 in lieu of quantitative data.

Thus, there is considerable bias and variation in the characteristic yield- and ultimate stresses. In lieu of relevant material tests of the actual materials used, the analyst needs to assume the plastic properties based on requirements such as those given in Table 3.3 combined with sound engineering judgment.

3.7.1 Variations Observed in Coupon Tests

Billingham et al. (2003) discussed the performance of high strength steels, and ar-

gued that the stress-strain behavior for higher strength steels is somewhat different
from lower strength steels, with a relatively smaller work hardening because the
strengthening mechanisms that are introduced to increase the yield strength have
little influence on the subsequent strain-hardening behavior. Billingham et al. fur-
ther states that old high-strength steels generally show a decreased elongation as
the yield ratio increase, whereas modern clean steels with low carbon content and
low levels of impurity have significant elongation even at high strength and high
yield ratios. This should be kept in mind when deciding the minimum elongation
to ultimate stress.

Figure 3.13 shows uniaxial tensile test data from a selection of steels from the
manufacturer SSAB (2014). Hogström et al. (2009) states that DOMEX 355 is
increasingly used by the shipbuilding industry, while DOMEX240 is similar to
NV A steels. All the tested materials exhibit an initial yield plateau followed by
a high rate of work hardening (gradient of stress-strain curve) which decreases
towards the point of ultimate tensile strength. The elongation at ultimate tensile
strength is in the range of 20% for material grades lower than 355, but decreases
somewhat for higher grades. The yield ratios range from 0.63 to 0.85, with the
highest ratios for the higher material grades.
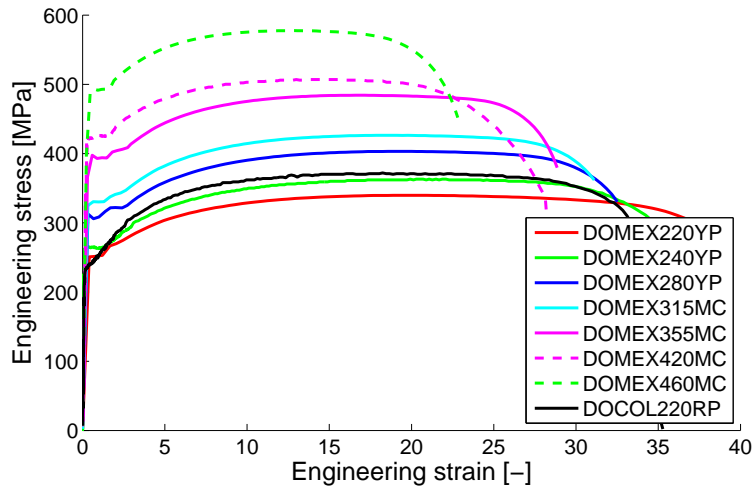
Figure 3.13: Uniaxial tensile test data from the database of SSAB (2014).

VanDerHorn and Wang (2011) presented a thorough review of modern shipbuild-
ing steels from about 140000 coupon tests from five different steel manufactures,
sampled during the period 2004-2009. The statistical parameters are listed in Table
3.4 for mild steel, high-strength steel (HS) and thermo-mechanically rolled high
strength steel (HS-TM). They also noted that modern steels show less statistical

variation in properties than older studies suggest.

Table 3.4: Statistical distribution parameters for steel material properties, from VanDer-Horn and Wang (2011).

Variable	Steel type	Mean	COV	Distribution
Yield strength σ_0*	Mild	1.28	0.07	Log-normal
	HS	1.18	0.06	
	HS-TM	1.30	0.06	
Tensile strength σ_0*	Mild	1.12	0.03	Normal**
	HS	1.16	0.03	
	HS-TM	1.14	0.04	
Elongation e*	Mild	1.54	0.08	Normal**
	HS	1.35	0.08	
	HS-TM	1.23	0.12	

*σ_0, σ_{UTS} and e represent IACS nominal rule values (same as minimum yield,
minimum tensile stress and minimum elongation in Table 3.3)
** truncated a zero

Coherent distributions of yield and tensile stress, yield ratio and elongation to fracture are shown in Figure 3.14 for material grade E450, based on data from the compilation in Billingham et al. (2003). The width of the initial yield stress and tensile stress distributions are approximately the same in Figure 3.14a. The high yield ratios show that very few material samples have a high tensile strength compared to their actual yield stress, with the lowest value at 0.76. However, as the yield ratio increases linearly with initial yield stress, the variation of work hardening for mild steels can be significantly larger than for the 450-grade steel in Figure 3.14. The elongation to fracture in Figure 3.14c is large for most of the tests, but the minimum value is close to the values given in Table 3.3 based on DNV-OS-B101.

The material behavior in Figures 3.13 - 3.14 and Table 3.4 can be compared to the requirements in Table 3.3. In order to comply with the distribution of yield ratios, the upper bound tensile strength in Table 3.3 should be associated with a high initial yield strength.

Estimates of the range of yield and tensile stress and elongation to fracture can be found using the data in Table 3.4 within the 5 and 95 percentiles. For mild steel, the yield and tensile stress ranges from 272-329 MPa and 428-468 MPa, respectively. This gives a higher yield stress and a smaller range of tensile stress than the material requirements in Table 3.3 suggests. This may indicate that few materials will have a tensile strength close to the upper limit in DNV-OS-B101. Thus, it may be overly conservative to use the upper values to characterize the material of the striking ship.

The elongation to fracture show a higher mean value in Table 3.4 and a signi-
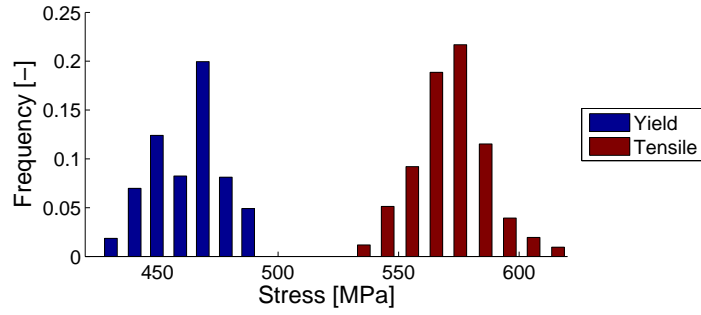
(a) Yield and tensile stress
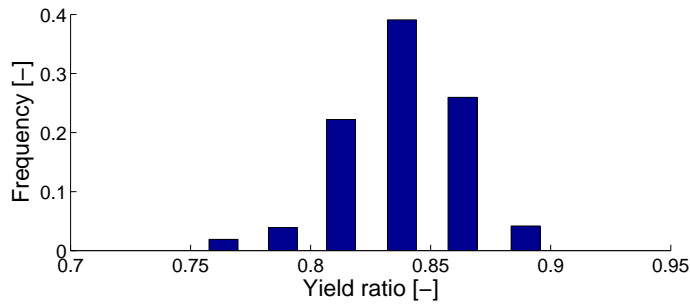
(b) Yield ratio
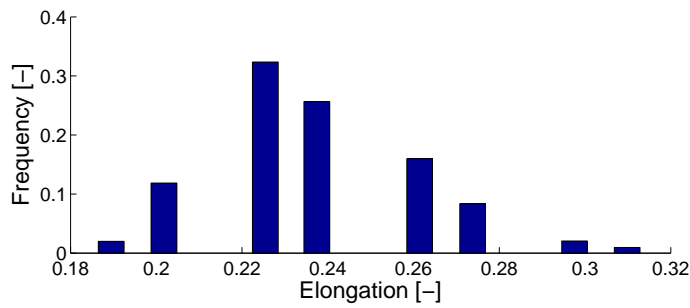
(c) Elongation to fracture

Figure 3.14: Variation in material data from E450-steel.

ficantly larger standard deviation than for the stresses. The material can thus be expected to be significantly more ductile than the minimum requirements in Table 3.3, which in turn also affect the slope of the stress-strain curve.

The combined probability of having both an extreme low material strength for the struck vessel and an extreme high strength for the striking vessel is low. It may be argued that using both the 5% (for the struck vessel) and 95% (for the striking vessel) percentiles is more stringent than the intention of NORSOK N-001. An alternative approach may be to select material parameters such that the combined probability of material strengths has a 5% probability of exceedance.

3.7.2   Plastic Hardening Model

Hardening controls where strains localize. A vast amount of plastic hardening models are available. Here, the discussion is limited to isotropic hardening (assuming that the collision does not give cyclic plastic loading), and the simple bi-linear model (as in DNV RP-C208) and power law models following Eq. 4.17.

If the upper bound behavior of mild steel (NV A) is the target behavior, one may assume that the actual yield limit is say $1.15\sigma_0 = 270$ MPa, the maximum ultimate tensile strength $\sigma_{UTS} = 520$ MPa, the corresponding minimum elongation to fracture is 0.22 and the minimum strain up to necking is 0.18. The lower bound values can be assumed to be $\sigma_0 = 235$ MPa and $\sigma_{UTS} = 400$ MPa.

Figure 3.15 shows the assumed engineering stress-strain curves for mild steel NV-A material for a power law hardening (with and without yield plateau) and a piecewise linear hardening model. Even though the plastic behavior is calibrated to the same initial yield and tensile strength, there is a considerable difference in the assumed hardening behavior. In fact, the upper bound bi-linear curve and the lower bound power law curve will give fairly similar results up to 10% plastic strains.

A material curve from a uniaxial tensile test is also plotted in Figure 3.15. Compared to the curves calibrated from Table 3.3, the tested material shows a larger initial yield stress but lower hardening, and a larger elongation at fracture.

The rate of strain hardening is initially very large for the upper bound values when using a power law work hardening, and the material approaches a linear elastic - perfectly plastic material with a high initial yield stress (as in Figure 3.16). This reduces the ductility of the structures, as plastic strains localize faster with higher rates of strain hardening. Compared to the material data in Figures 3.2 and 3.13, it is evident that the yield ratio of 0.52 of the upper bound material is extreme. A higher initial yield stress should probably be assumed for the upper bound values of tensile strength. Though, with the very steep initial hardening of the power law
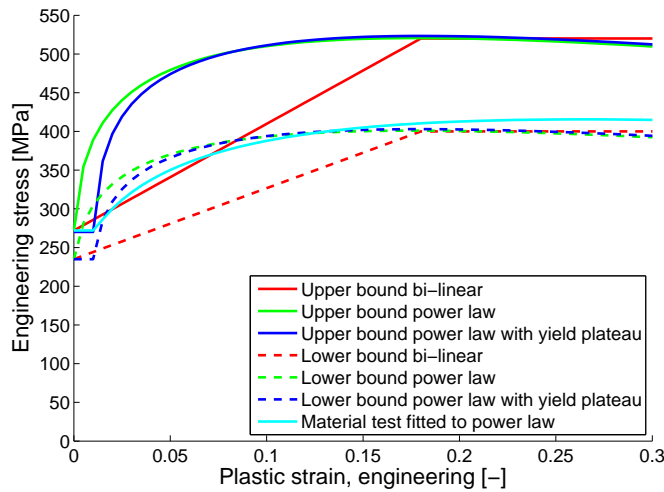
Figure 3.15: Engineering stress-strain curves for NV A material from DNV-OS-B101.

models calibrated to upper bound work hardening, increasing the yield strength somewhat will not make a big difference on the rate of work hardening.
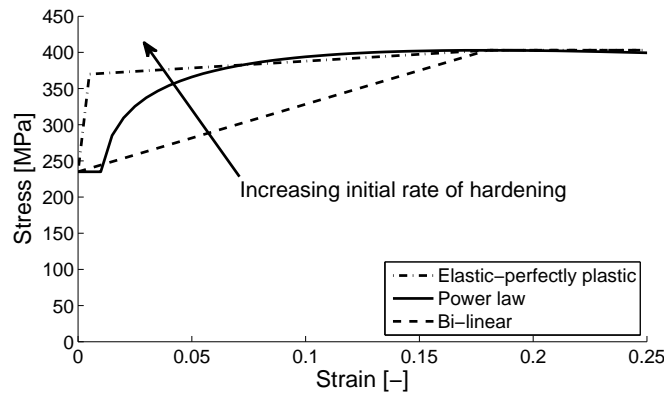
Figure 3.16: Engineering stress-strain curves with varying initial rate of hardening. Bi-linear is a lower bound, elastic-perfectly plastic an upper bound.

3.7.3   Calibrating Power-law Parameters to Prescriptive Material Requirements

Zhang et al. (2004) shows how the power law parameters K and n can be fitted to a tensile test by considering range of the maximum uniform strain ε_{UTS} related to the ultimate tensile strength σ_{UTS} as defined in the governing equations as

$$n \quad = \quad \ln(1 + \varepsilon_{UTS}) \tag{3.11}$$

$$K \quad = \quad \sigma_{UTS}\,(e/n)^n \tag{3.12}$$

in which e is the base of the natural logarithm. Power law parameters calculated with Eqns. 3.11 and 3.12 based on the material requirements in DNV-OS-B101 are shown in Table 3.5.

Table 3.5: Example material parameters from DNV-OS-B101 with calculated power law parameters based on Eqns. 3.11 - 3.12.

Grade	Min σ_Y [MPa]	σ_{UTS} [MPa]	$\varepsilon_{fracture}$ [%]	$\varepsilon_{necking}$ [%]	n -	K [MPa]
NV A	235	400-520	22	18	0.166	636-827
NV A36	355	490-630	21	17	0.157	767-986
NV A46	460	570-720	19	15	0.140	863-1091
NV A55	550	670-830	16	12	0.113	960-1189

If a yield plateau is to be included based on the material data in Table 3.5, the power law modulus K remains unchanged, but the power law exponent n can be modified by subtracting the yield plateau strain from the maximum uniform strain in Eq. 3.11.

Both bi-linear and power-law material models are readily available in most general purpose NLFEA codes. If a yield plateau is to be used, the strain-hardening can normally be given as a true stress-strain curve.

3.8 Effect of Material Parameters in a Full-scale Scenario

The bow of a 7500-ton displacement supply vessel and the side of a 115000-ton displacement membrane LNG tanker were utilized in the following studies, see Figure 3.17. In the bow model, the plate thickness varies from 7 mm in decks to 12.5 mm in bulb. The stiffener spacing is approximately 600 mm, with ring stiffeners and breast hooks of approximately 250×15 mm in the bulb. In the forecastle structure, HP220×10 stiffeners were used, simplified to 220x12.8 flatbars in the model. The forecastle extends about 1.2 m forward of the bulb. For the vessel side at the impact location, an outer plate thickness of 17 mm is used, with stiffener spacing of 880 mm and stiffeners T335×125/12×15. Web frames are spaced with 3360 mm, and are made of 20 mm plates. Both ships are assumed to be built of mild steel, NV A.

Three test cases are considered in order to assess the choice of plastic hardening model w.r.t. the structural response; a bulbous bow against a rigid wall, a rigid

(a) Supply vessel bow   (b) Vessel side
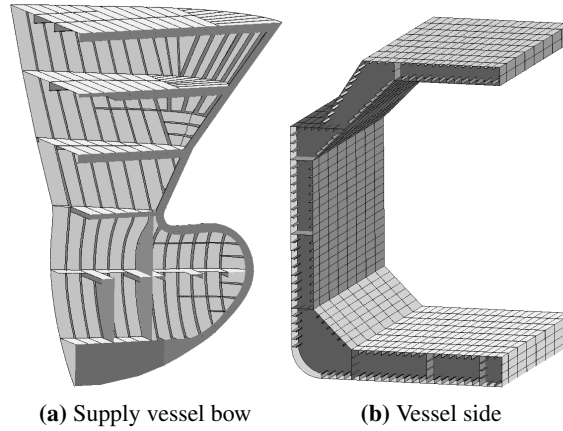
Figure 3.17: FE models used for simulation. The figures are not to scale.

bulbous bow against a deformable ship side and a deformable bow vs. deformable side (integrated analysis).

3.8.1 Plastic Work Hardening

Upper bound values of the plastic hardening parameters are chosen for the striking bow, and lower bound for the side. A yield plateau of 1% is included as a separate case for the power law simulations. To compare the material parameters calibrated from the rule requirements in DNV-OS-B101 with a more realistic material, a material set is investigated with plastic parameters based on test data from Alsos and Amdahl (2009). Note that this material is above minimum yield, but has a low tensile stress. The material parameters are listed in Table 3.6.

Table 3.6: Upper and lower bound material parameters for comparison of ship side response.

	σ_Y [MPa]	σ_{UTS} [MPa]	E [GPa]	K [MPa]	n [-]	$\varepsilon_{plateau}$ [-]
Power law	235-270	400-520	206	636-827	0.166	0.00
Power law w. plateau	235-270	400-520	206	636-827	0.157	0.01
Power law mat. test	275	411	206	740	0.24	0.01
	σ_Y	σ_{UTS}	E	ε_{neck}		
Bi-linear	235-270	400-520	206	0.18		

For the struck vessel, a critical failure strain is of 20% was defined. An integration point is failed once this strain is reached by setting the stress to zero. An element will be removed by erosion when the middle integration point through thickness reach the failure strain. For the striking bow, no fracture limit was defined as the

stress-state will be more dominated by compression and shear. Frictionless penalty contacts were assumed for simplicity.

Vessel Against Rigid Plate

Figure 3.18 shows the force-displacement curves for the bow striking a rigid vertical wall. For the stem contact (Figure 3.18a), the response is governed by the bending and buckling collapse of the structural members. The material models have relatively low influences. There is some variation in the load peaks, but the dissipated energy (calculated as the area under the force-displacement curve) has small variations.

Larger variations are observed in the peak force in the bulb curves (Figure 3.18b), with peak crushing force varying from 21.6 MN with a bi-linear hardening to 26.1 MN for a power law hardening. The low-hardening power law from material tests and the upper-bound bi-linear assumption show similar results. Both the upper-bound power-law calibrations gives significantly higher contact force estimates. The variation is significant both in terms of maximum crushing force of the bulb and the energy dissipation during crushing.

Rigid Vessel against Deformable Ship Side

Figure 3.19 shows the force-displacement curves for impact of a rigid bow into a deformable side with lower-bound plastic parameters.

The stem force-displacement curves in Figure 3.19a from a rigid vessel into a deformable side show a rapid drop in contact force after the side shell is punctured by the sharp rigid stem structure. All the hardening models predict approximately the same displacement at fracture, though the bi-linear curve as expected show a lower peak force. Note that comparing a rigid stem vs. a deformable side structure has a limited physical relevance as the relative strength is low; hence the stem will be crushed by the side. See Section 6.4.2 for further details.

The bulb force-displacement curves in Figure 3.19b agree well with respect to the magnitude of the force peak. As the rate of hardening is small for the bi-linear model, the resistance to indentation is delayed compared to the power-law materials. Thus, the indentation of the bulb at initiation of side shell fracture varies significantly depending upon the chosen material parameters, thereby significantly changing the energy dissipation. For the bi-linear model and the power-law model calibrated to test data, a peak force occurs at first longitudinal rupture (small sharp drop), which then propagates (at almost constant force) until the next frame where a vertical rupture initiates, giving a pronounced sharp drop in resistance. By contrast to this, the power-law models from lower bound assumptions yields a shorter
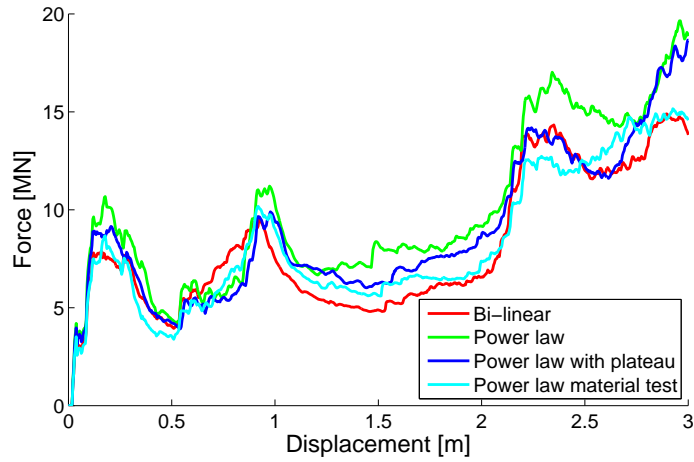
(a) Stem/forecastle
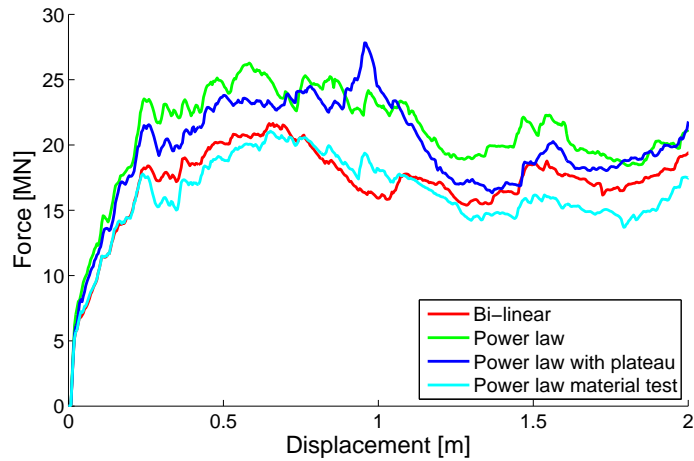
(b) Bulb

Figure 3.18: Force-displacement from simulations for the stem and bulb crushing force against a rigid vertical wall.
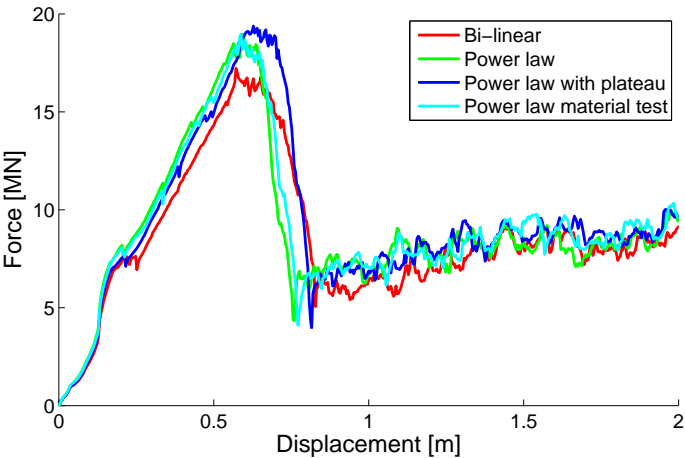
(a) Stem
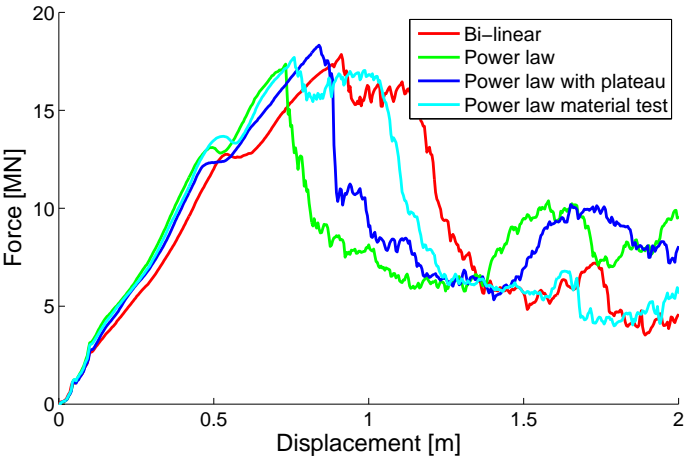
(b) Bulb

Figure 3.19: Force-displacement from simulations for the rigid bow impacting a deformable ship side.

longitudinal fracture, and transverse fracture occurs rapidly in way of the bulb close to the beam mid-span. This causes a sharp drop in the resistance, and a significantly lower energy dissipation prior to fracture.

(a) Bi-linear   **(b)** Power law   **(c)** Power law with plateau   **(d)** Power law from material test
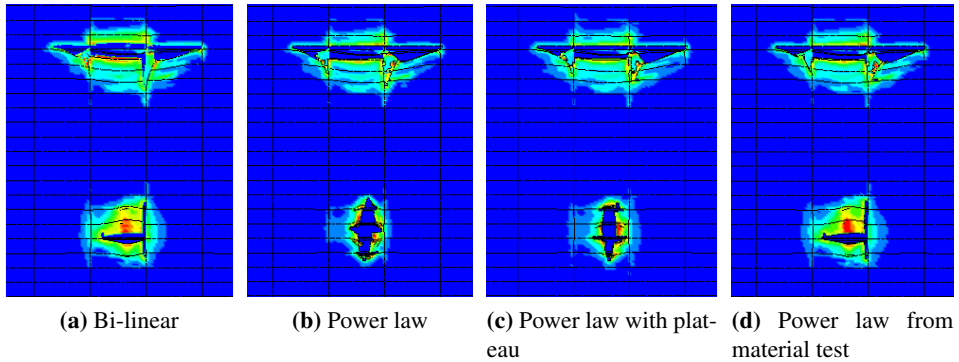
Figure 3.20: Plastic strain in ship side after 1.3 meters indentation of bulb into side. Fringes are equivalent plastic strain, from blue (0) to red (0.2).

Figure 3.20 shows the deformation pattern. The bi-linear material model in Figure 3.20a have a low rate of hardening, and the strains spread out to a very large area. Fracture is observed along the stiffener, and at the intersection with the vertical web frame. The power law hardening models show a much smaller strain localization (Figures 3.20b and 3.20c), with fracturing mainly at the stiffener midspan. When including a yield plateau, the initial rate of hardening is low, and the strains spread out to a somewhat larger area. The power law model with parameters calibrated to a material test in Figure 3.20d show a similar behavior as the bi-linear assumption. However, this material test was not representative of a lower bound plastic strength.

The simulations shows that capturing the initial phase of the work hardening as well as the rate of hardening has a large effect on the response of the struck vessel. Assuming a too small rate of hardening will likely underestimate the peak resistance from the struck ship, but will also significantly overestimate the energy dissipation capacity in the struck structure. This may be *nonconservative* with respect to the design strength of the struck vessel.

Integrated Analysis

Integrated analysis was performed, where both the striking bow and the struck vessel were deformable. Upper-bound values were used for the bow and lower-bound for the side structure.

Figure 3.21 shows the predicted force-displacement curves. The displacement measure is now the local crushing of the bow or indentation into the ship side. The stem was crushed by the vessel side, but the bulb was stronger. The side of the struck vessel was capable of crushing the bulb only when material parameters calibrated to test data were used, i.e., with a lower strength of the bulb and a more ductile response of the side.

Predicted fracture in the bulb impact zone varies. Figure 3.22 shows the plastic strain and fracture after the significant drop in peak force for the different simulations. The bi-linear and power law simulations show the same fracture prediction for the case with a rigid bulb, whereas the power law with yield plateau changes fracture pattern when damage to the bulb is allowed. The contact force vs. indentation at fracture is changed from 18.3 MN at 0.84 m to 19.6 MN at 0.87 m in the integrated analysis, even though the bulb is deformed less than 40 mm. This small change is sufficient to shift fracture from the midspan of the stiffener over to the web frame. However, the simulations shows that fracture was imminent at the beam mid span, and the fracture localization is very sensitive to the assumed work hardening.

Analytical Consideration of the Effect of Work Hardening on Strain Localization

The effect of the rate of hardening can be studied through a simple axisymmetric problem. A contraction process is assumed to occur in the center of the model, causing plastic straining in the surrounding areas (this represents a bulb impact to a non-stiffened panel). When the same contraction is assumed for lower bound bi-linear, power law and power law with yield plateau (Figure 3.15), the strains will spread out differently. Figure 3.23 shows this effect. With low initial hardening, the yield zone extends to a larger area, and the dissipated energy increases.

Discussion

The choice of plastic work-hardening model significantly affects the simulated response in a collision event. Hence, the hardening parameters need to be considered from a holistic point of view where their effects on the relative strength and the distribution of energy dissipation to the striking and struck vessel are carefully considered in view of the target safety level.

The rate of hardening (slope of the stress-strain curve) was identified as a crucial factor controlling how strains localize. The slope is affected greatly by the statistical variations of yield and tensile stress and the elongation to fracture (Table 3.4). Underestimating the slope is conservative with respect to the peak resistance of a struck vessel, but *nonconservative* with respect to the energy dissipation prior to peak resistance.

(a) Stem

(b) Bulb
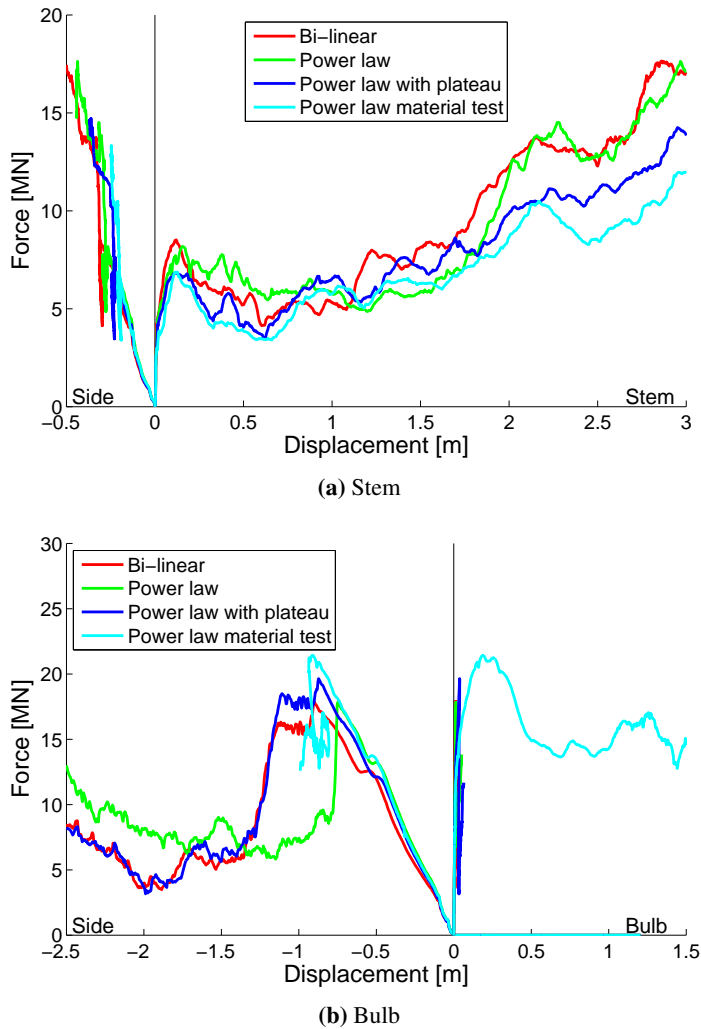
Figure 3.21: Force-displacement from simulations for integrated analysis between a deformable stem and bulb crushing against a deformable ship side. The displacement is local crushing for the side (negative values) and bow (positive values), respectively.

(a) Bi-linear   **(b)** Power law   **(c)** Power law with plateau   **(d)** Power law from material test
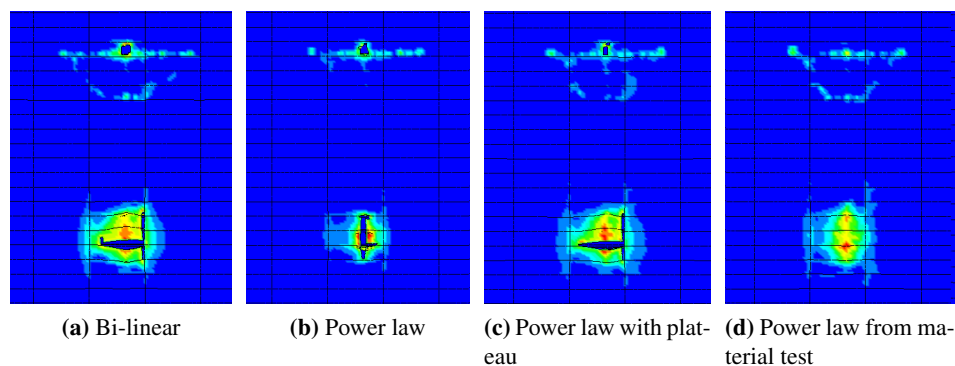
Figure 3.22: Plastic strain in ship side after peak force for integrated analysis. Fringes are equivalent plastic strain, from blue (0) to red (0.2).

3.8.2 Strain-rate Effects

As the focus of a full-scale collision simulation is on energy dissipation, the strain-rate model should be optimal for high plastic strains and not the initial yield strain.

The parameters calibrated to the plastic flow stress on DH36 steel to the tests of Choung et al. (2013) were applied in the simulations of bow against rigid plate, rigid bow against deformable ship side and an integrated analysis with deformation on both bodies. This was compared to parameters found in literature (calibrated to initial yield stress). For simplicity, a constant dynamic fracture strain of 20% was assumed in the ship side. This is close to the strain at maximum tensile strength, and thus show low dependence on strain rate. Upper and lower bound plastic parameters were chosen for the striking bow and struck vessel respectively, using power law hardening with a yield plateau. The parameters are listed in Table 3.6.

Figure 3.24 shows the predicted force and energy v.s. displacement of the deformable bow crushing against a rigid plate, the rigid bow crushing against a deformable side and the deformable bow crushing against the deformable side (integrated analysis). Figures 3.24a - 3.24d are plotted against the vessel displacement, whereas Figures 3.24e - 3.24f are plotted against the actual indentation into the bow or the side structure. Table 3.7 shows the increase in bulb crushing force and dissipated energy at end of simulation with the different strain-rate assumptions.

With $C = 400000$, the predicted strain energy dissipation increases by 4-12%, whereas $C = 40.4$ predicts an increase of 43-65%. The damage to the side is more affected by the strain-rate behavior. Figure 3.24e shows that the bulb is stronger than the vessel side for all assumptions of C. The level of dissipated energy in

(a) Bi-linear   (b) Power law   (c) Power law with plateau

(d) Strain vs. radius curve
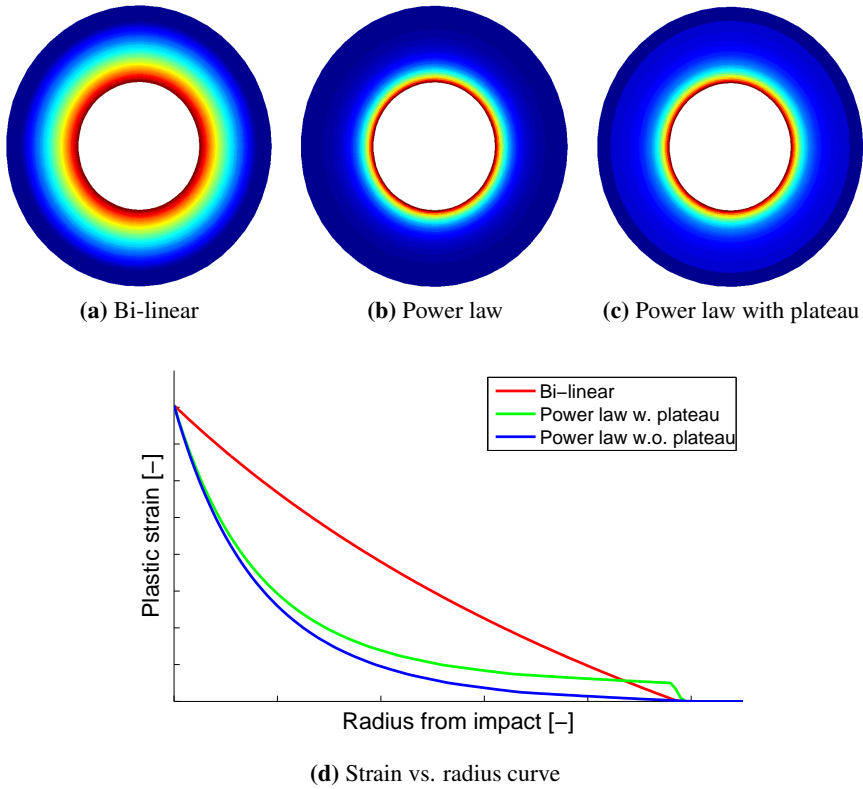
Figure 3.23: Effect of rate of hardening on strain localization for an axisymmetric problem.

Figure 3.24g shows significant differences, and the estimated indentation into the structure at a given level of dissipated strain energy decrease with the decrease in the C-parameter (decreasing indentation with increasing strain-rate effect).

As the employed dynamic fracture strain limit of 20% is slightly larger than the diffuse necking strain, the allowable elongation for high strain rates is somewhat overestimated (ref. Figure 3.7). The effect of strain rate on the total simulation results is thus smaller than that listed in Table 3.7.

Discussion

It is important to calculate the maximum indentation into the side of a vessel. A quasi-static material model gives the most conservative estimate, whereas the increasing strength caused by strain-rate effects reduces the predicted indentation. Using the strain-rate hardening parameters for mild steel as proposed by Cowper

(a) Bow force-displacement (rigid side)

(b) Bow energy-displacement (rigid side)

(c) Side force-displacement (rigid bow)

(d) Side energy-displacement (rigid bow)

(e) Integrated force-indentation, bulb

(f) Integrated force-indentation, stem

(g) Integrated energy-displacement
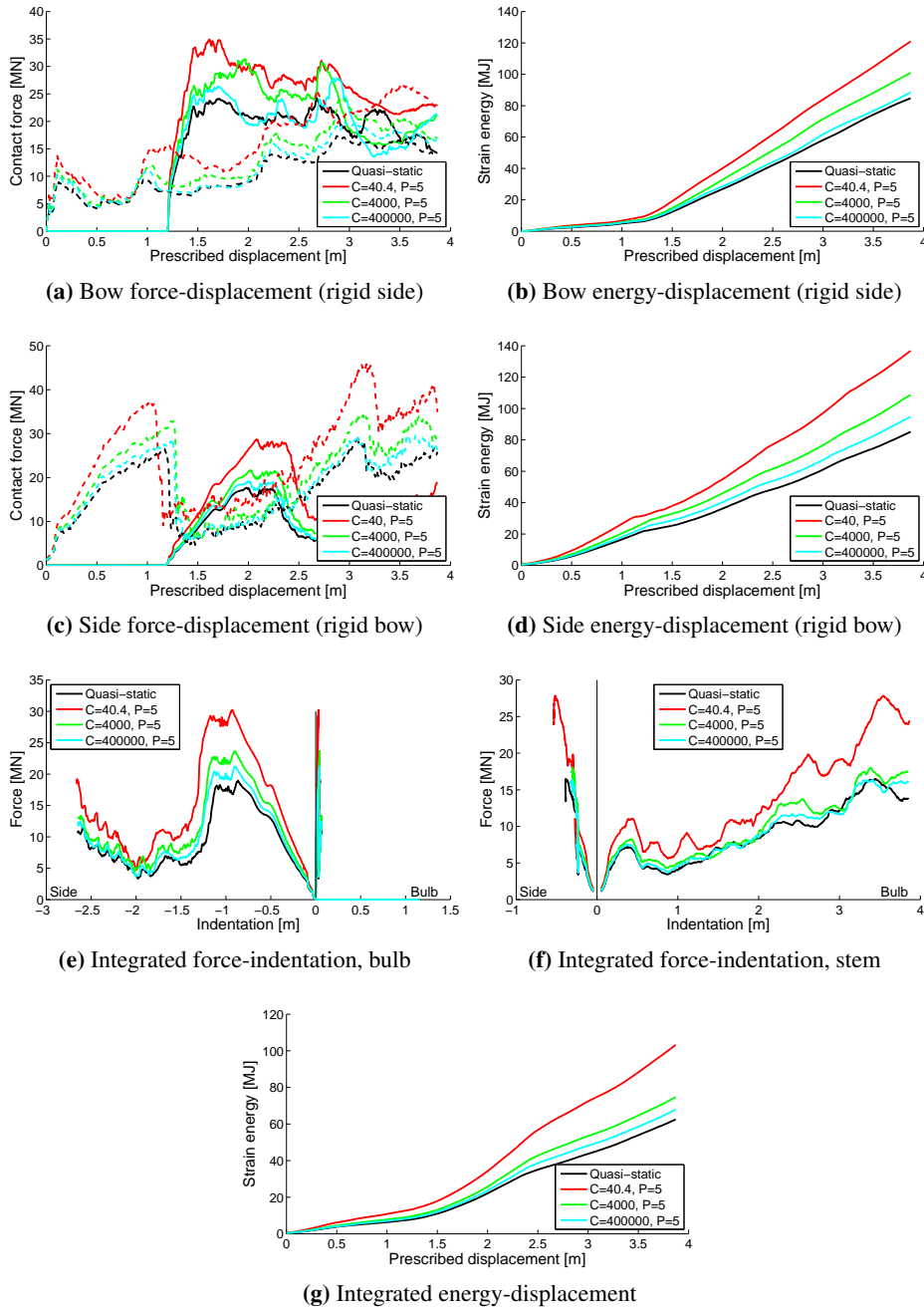
Figure 3.24: Results for bow against a rigid plate with varying strain-rate hardening parameters. In (a) and (c): dashed lines represent stem contact, continuous lines bulb contact.

Table 3.7: Percentage increases in the predicted response (peak force and energy dissipation) with strain-rate hardening compared to the quasi-static solution.

	Peak bulb force			Total dissipated energy		
	Bow	Side	Integrated	Bow	Side	Integrated
C=40.4	45%	62%	59%	43%	61%	65%
C=4000	30%	23%	25%	19%	28%	20%
C=400000	9%	8%	12%	4%	12%	9%

and Symonds (1957) for initial yield stress gives a significant overestimation of the predicted flow stress, and thereby the energy dissipation in the collision assessment.

If strain-rate hardening is included based on parameters calibrated to flow stress, the increase in energy dissipation is about 10%. If parameters calibrated to the initial yield stress are used, the predicted energy dissipation increase by about 60%, and the predicted indentation decrease significantly. Thus, it is conservative to neglect strain-rate effects if the goal is to assess the maximum indentation into the structure. If including strain-rate effects without careful calibration, the simulation results are *far less accurate* than if strain-rate hardening is neglected. If strain-rate effects must be included, a practical approach to avoid the shortcomings of plane stress elements is to define a critical strain that is less than the diffuse necking strain (including any effects from strain concentrations not captured by a coarse mesh).

3.9   Conclusions

The literature study and the numerical investigations have shown that some mechanical properties of shipbuilding steel and the work hardening model adopted for NLFEA have a large effect on the predicted resistance and the energy dissipation during a collisions. The important features of the stress-strain response are

1. *Tensile stress* : For components subjected to large plastic deformations, the tensile stress is more important than the yield strength.
2. *Yield ratio* : For a fixed yield stress, a low yield ratio gives high hardening, and thereby a significant capacity up to ultimate strength. For a fixed ultimate tensile stress, a low yield ratio will determine the minimum initial yield stress that can be associated with the tensile stress level.
   To preserve the lower elongation to fracture normally found for higher strength steels, a low yield ratio should also be combined with a low elongation at failure.
3. *Rate of work hardening* : If the initial rate of work hardening (slope of the stress-strain curve) is high, strains will localize quickly and fracture initiates

early.

If the rate of work hardening is underestimated, especially in the initial phase of hardening, strain localization will be delayed and the energy dissipation in the structure overestimated. This is *nonconservative*.

A low yield ratio results in a steeper slope of the stress-strain curve, thereby a more rapid strain localization. A low yield ratio is generally beneficial due to the high capacity from yield to tensile stress, but a too low yield ratio may give a less ductile response due to the effect of rate of work hardening on fracture.

A yield plateau increase the extent of the plastic zone.

4. *Elongation at ultimate strength* : A short elongation gives a high rate of hardening, resulting in rapid strain localization. The slope effect on global resistance may be as important as the local change in critical fracture strain due to the rapid localization of strains. The elongation is associated with larger statistical variation than yield and tensile stress for modern steels.

5. *Strain-rate hardening* : The effect of strain-rate hardening can be significant but it is uncertain. Simulations show that the full-scale results are substantially less dependent on strain-rate hardening than a uniaxial tensile test. Not including strain-rate hardening is conservative, as the estimated indentation into the struck vessel decreases with increasing strain-rate hardening. If included, the strain-rate hardening parameters should be calibrated to the plastic flow stress and not the initial yield stress.

6. *Strain-rate effect on fracture* : The strain-rate effect on the dynamic fracture strain is challenging. The true strain at fracture decreases somewhat at higher strain rates, but this effect is difficult to include in a simulation with shell elements. Strain-rate hardening stabilizes the necking process, thereby delaying the strain localization. Due to the nonlinear relation between true strain in the neck and the engineering strain (elongation of the specimen), small changes in true critical strain gives large changes in the elongation at fracture.

The static fracture strain should be less than the diffuse necking strain in order to avoid overestimation of the critical elongation at fracture for high strain rates. If the static fracture strain contains the post-necking response, scaling of the dynamic fracture strain is dependent on rate, strain state, mesh and geometry. Possible shortcomings of the selected scaling method are revealed when simulating dynamic material tests. There is a lack of relevant experimental data to quantify the strain-rate effect on dynamic fracture strain in an accurate manner. A robust method for inclusion of these effects in simulations with shell elements is required.

7. *Fracture* : Fracture depends on the multi-axial stress state of the material,

arising from the micromechanical processes of void nucleation, growth and coalescence. Stress states with triaxialities in the range of $1/3$ to $2/3$ (based on shell finite element modeling) predominate the most important fracture modes in ship collisions. It is recommended to adopt fracture models that are good for this triaxiality range.

8. *Mesh-dependence* : Relevant for estimation of fracture are the *geometric* dependence and the *material* dependence. Both should be considered in a collision simulation.

To improve the accuracy of numerical simulations of accidental events such as ship collisions, the following points should be further studied:

- *Yield ratio* : The material parameters given in design codes should include an estimate of the range of possible yield ratios to enable better choices of initial yield stress relative to the ultimate tensile stress for NLFEA.
- *Elongation at tensile stress* : The elongation at tensile stress should be given in design codes. A range of values is beneficial. Lower elongation gives higher initial rate of hardening.
- *Rate of work hardening* : The rate of work hardening should be investigated for typical "design materials". How does actually a low-yield - high-tensile stress material behave for the entire strain range? The lower bound values are more certain than upper bound values.
- *Strain-rate hardening and dynamic fracture* : The combined effect of strain-rate hardening and dynamic fracture should be further studied. Especially, a robust method for treating post-necking dynamic fracture strain with shell elements is needed.

Figure 3.25 is a proposal for describing the stress-strain relationship of steel materials that is consistent with observed material behavior. First, determine the tensile strength. Second, use the yield ratio to find the yield strength (a low value for high hardening (striking) and a high value for low hardening (struck) material). Third, determine the yield plateau. Fourth, use power law hardening to describe the curve between these points.
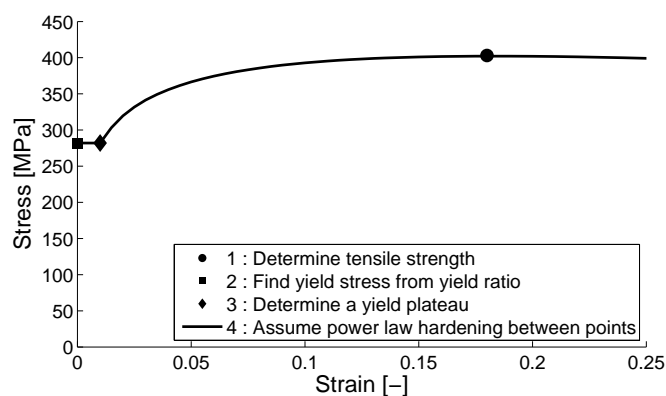
Figure 3.25: Proposed model for stress-strain relationship for a ship collision analysis.

Chapter 4

An Extension of the BWH Instability Model

In the following a combined local necking instability criterion with post-necking damage is proposed. The novel damage model considers the local necking phenomenon in a virtual neck inside a large element, and is coupled with the plastic response in the post-necking phase. This allows numerical simulation of the pre- and post-necking failure process in coarsely meshed shell structures with low mesh dependency and reasonable accuracy. The formulation is valid for materials with low anisotropy.

The BWH local instability criterion from Alsos et al. (2008) is used to predict the onset of necking. The BWH criterion assumes no initial defects. A strong argument for the criterion is that it can be calibrated from the power law hardening parameters, and can thus be used without an extensive test program for regular structural steel with low anisotropy.

After instability is identified, strains will localize in a narrow band in and close to the local neck, as shown by digital image correlation (DIC) measurements by Hogström et al. (2009). Post-necking damage is included on the basis of a geometric consideration of the reduction in load-carrying capacity of a shell element, which is calculated from the thickness reduction in a virtual local neck. The damage evolution rule is formulated so that the strength degradation by damage increases with larger element size (as more compensation is needed when the local instability is a small part of a large element).

The failure prediction will be regarded as conservative if failure is initiated earlier than in experiments. If failure is predicted later, the strength of a struck body will

be overestimated, and thus give a non-conservative prediction of the resistance against collision.

Due to the simplicity of the proposed model formulation, the required parameters can be found with good accuracy from a single uniaxial tensile test, or calculated on the basis of the material requirement limits in rules and standards of yield stress, ultimate strength and elongation at ultimate strength for coarse estimates.

The proposed material model is based on the J2 flow theory; i.e., the von Mises yield criterion, the associated flow rule and isotropic hardening are adopted (as described in Section 3.3). The hardening rule accounts for the yield plateau frequently exhibited in mild steels. In addition, the BWH criterion is applied to determine the onset of local necking, and coupled damaged is used in the post-necking phase to reduce the load-carrying capacity of the shell element.

The BWH instability criterion searches for local instability on the middle integration point of the shell element (i.e., only membrane stresses are accounted for). When instability is reached in an element, the coupled damage model reduces the load-carrying capacity of the element on all integration points through the thickness based on the assumed reduction in cross-sectional area of a virtual neck inside the element.

4.1   Local Instability Criterion

The BWH instability criterion from Alsos et al. (2008) combines Hill's local necking analysis (Hill 1952) and the Bressan-Williams shear stress criterion (Bressan and Williams 1983). The BWH criterion searches for instability at the mid integration point of the shell element, and triggers damage coupling when fulfilled. The full derivation of the BWH criterion can be found in Alsos (2008).

For negative values of β, Hill's criterion gives the angle between the major principal stress direction and the normal to the local neck as $\varphi = tan^{-1}(\sqrt{-\beta})$. Within the neck the strain increments along the necking band will be zero, thereby giving a plane-strain condition. At the point of necking, the traction in the material will reach a maximum value as the strain hardening and reduction in thickness balance. The condition for localized necking can be derived as

$$\frac{d\sigma_1}{d\varepsilon_1} = \sigma_1(1 + \beta) \tag{4.1}$$

where for plane-stress conditions β is calculated from the principal stresses via the stress-ratio α as

$$\beta = \frac{\dot{\varepsilon}_2}{\dot{\varepsilon}_1} = \frac{2\alpha - 1}{2 - \alpha} \quad , \quad \alpha = \frac{\sigma_2}{\sigma_1} \tag{4.2}$$

which is valid for the von Mises yield criterion and the associated flow rule.

The Bressan-Williams criterion is valid for positive values of β. It postulates that local shear instability is initiated when a critical shear stress is reached, in a direction inclined through the thickness at which the sheet element experiences no change in length. This gives the critical value of the major principal stress as

$$\sigma_1 = \frac{2\tau_{cr}}{\sqrt{1 - (\beta/(2 + \beta))^2}} \tag{4.3}$$

Calibration against the Hill criterion for $\beta = 0$ and assuming powerlaw hardening defines the critical shear stress τ_{cr} by

$$\tau_{cr} = \frac{1}{\sqrt{3}} K \left(\frac{2}{\sqrt{3}} \hat{\epsilon}_1 \right)^n \tag{4.4}$$

where K and n are the hardening parameters and $\hat{\epsilon}_1$ is a critical strain. Combined, the BWH criterion for sheet metal instability can be expressed as

$$\sigma_1 = \begin{cases} \dfrac{2K}{\sqrt{3}} \dfrac{1 + \frac{1}{2}\beta}{\sqrt{\beta^2 + \beta + 1}} \left(\dfrac{2}{\sqrt{3}} \dfrac{\hat{\epsilon}_1}{1 + \beta} \sqrt{\beta^2 + \beta + 1} \right)^n & \text{if } -1 < \beta \le 0 \\[4mm] \dfrac{2K}{\sqrt{3}} \dfrac{\left(\frac{2}{\sqrt{3}} \hat{\epsilon}_1 \right)^n}{\sqrt{1 - \left(\frac{\beta}{2 + \beta} \right)^2}} & \text{if } 0 < \beta \le 1 \end{cases} \tag{4.5}$$

where the critical strain $\hat{\epsilon}_1$ can be assumed equal to the power law exponent n. Alsos et al. (2008) reports that measured values of $\hat{\epsilon}_1$ sometimes yield better correlation with experimental results. No instability is predicted for $\beta \le -1$, as the material will not experience thinning strains.

In the application of ship collisions, coarse meshes will not capture local strain concentrations (e.g., due to out-of-plane bending close to a stiffener). This implies that the coarse mesh will not detect the proper stress concentration, and the BWH criterion will predict instability too late. As a remedy, geometric mesh scaling is incorporated as a user-selectable option, in which $\hat{\epsilon}_1$ in Eq. 4.5 is scaled with the factor $\frac{1}{2}(t_e/l_e + 1)$, where t_e is the element thickness and l_e the element length

measured at the initial condition of the element. This mesh scaling was proposed by Alsos et al. (2009), and significantly improves the mesh scalability for stiffened panel structures.

If strain concentrations are properly captured by the mesh, the proposed mesh scaling rule will underestimate the stress at instability, and trigger damage and failure too early. Consequently, the collision resistance of a ship side will be underestimated, thereby giving a conservative estimate of the damage extent on the struck ship. On the other hand, if geometric mesh scaling is not applied to the ship side, its resistance to damage could be overestimated and fracture predicted too late, as the strain concentration not captured by the mesh remains unaccounted for.

As suggested by Alsos et al. (2009), geometric mesh scaling for stiffened panel structures could be applied only to intersection elements so that the out of plane strain concentration is compensated for only where necessary. This would require special pre-processing tools in order to be feasible for large-scale simulations. For other applications, in which coarse meshes adequately capture the strain concentrations, the unscaled BWH criterion does not need assistance from geometric mesh scaling.

4.2 Damage Evolution

A virtual neck with length scale equal to the thickness is assumed to evolve after onset of local instability. The underlying assumption in the proposed damage model is that a mesh with element length equal to the plate thickness gives an adequate treatment of this local phenomenon in terms of the stress-strain response of the element (within the limitations of plane stress shell elements). However, larger elements cannot capture local instability, and the response should be compensated accordingly.

To achieve this, the scalar damage variable D is defined, that considers the reduction in thickness inside a virtual local neck within the element as a function of the element length vs. thickness ratio. By coupling this damage to the element response, a damage degradation is achieved that accounts for the presence of a narrow local neck within the larger element. D is zero for an undamaged and unity for a fully damaged shell section. Note that the damage variable D does not represent material damage, but rather the reduced capacity of the shell section due to the thinning within a developing virtual local neck inside the element. The damage is coupled with the elastic-plastic model by substituting the stress tensor $\boldsymbol{\sigma}$ with the effective stress tensor $\tilde{\boldsymbol{\sigma}}$ in all constitutive relations, where

$$\tilde{\boldsymbol{\sigma}} = \boldsymbol{\sigma}/(1 - D) \tag{4.6}$$

Consider an element with characteristic length l (i.e., the diameter of the circle in Figure 4.1a) and thickness t subjected to proportional straining. Assume that the element contains a local neck of width b and thickness h (Figure 4.1b), and that at initiation of necking $b_0 = h_0 = t_0$, where sub-index 0 indicates incipient necking. The characteristic element length at necking is then l_0. The angle between the major principal strain direction and the normal to the local neck is denoted φ.

(a) Top view of element   **(b)** Plane perpendicular to neck
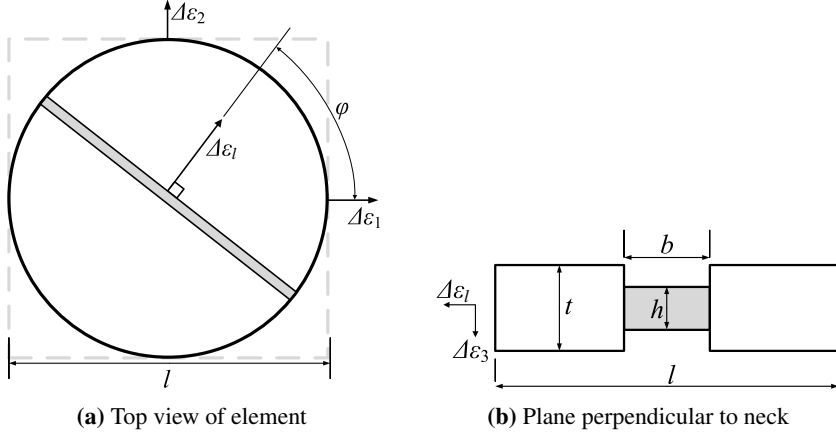
Figure 4.1: Element with local virtual neck.

4.2.1   Case I: Negative Minor Principal Strains

Hill's analysis shows that for negative principal strains a local neck will form at an angle φ that is defined by the strain-rate ratio β as

$$\varphi = \tan^{-1} \sqrt{-\beta}, \quad -1 < \beta \leq 0 \tag{4.7}$$

The assumptions of plane-strain conditions within the neck and plastic incompressibility gives

$$\ln \frac{b}{t_0} = -\ln \frac{h}{t_0} \Leftrightarrow \frac{h}{t_0} = \frac{t_0}{b} \tag{4.8}$$

After onset of local necking it is assumed that the deformation is concentrated inside the neck. The characteristic element length is expressed as

$$l = l_0 + \Delta l = l_0 \exp \Delta \varepsilon_l \Leftrightarrow \Delta l = l_0 \left[\exp \left(\Delta \varepsilon_l \right) - 1 \right] \tag{4.9}$$

where $\Delta\varepsilon_l$ is the normal strain of the element in the direction perpendicular to the local neck measured with the configuration at local necking as reference, and Δl is the post-necking elongation of the element, assumed to take place within the neck. Thus, the width of the local neck is obtained by

$$b = b_0 + \Delta b = t_0 + \Delta l = t_0 + l_0 \left[\exp\left(\Delta\varepsilon_l\right) - 1\right] \tag{4.10}$$

Combining Eqns. 4.8 and 4.10 gives

$$\frac{h}{t_0} = \frac{t_0}{b} = \frac{1}{1 + \frac{l_0}{t_0}\left[\exp\left(\Delta\varepsilon_l\right) - 1\right]} \tag{4.11}$$

Since h/t is unity at incipient local necking and then decreases towards zero with further elongation of the element, the damage D is defined as

$$1 - D \equiv \frac{h}{t} = \frac{h}{t_0}\frac{t_0}{t} = \frac{\exp\left(-\Delta\varepsilon_3\right)}{1 + \frac{l_0}{t_0}\left[\exp\left(\Delta\varepsilon_l\right) - 1\right]} \tag{4.12}$$

where $\Delta\varepsilon_3$ is the principal strain in the thickness direction of the element measured with the configuration at local necking as reference. Using plastic incompressibility, we get $\Delta\varepsilon_l = (1+\beta)\Delta\varepsilon_1$, and the final expression for the damage for negative minor strains becomes

$$1 - D = \frac{\exp\left((1+\beta)\Delta\varepsilon_1\right)}{1 + \frac{l_0}{t_0}\left[\exp\left((1+\beta)\Delta\varepsilon_1\right) - 1\right]} \tag{4.13}$$

4.2.2   Case II: Non-negative Minor Principal Strains

In this case, there is no direction of the neck that gives plane strain inside the neck. Instead, it is assumed that the neck is normal to the major principal strain direction ($\varphi = 0$) and that the minor strain within the neck is equal to $\Delta\varepsilon_2 = \beta\Delta\varepsilon_1$. Using plastic incompressibility, we get

$$\ln\frac{b}{t_0} + \Delta\varepsilon_2 = -\ln\frac{h}{t_0} \Leftrightarrow \frac{h}{t_0} = \frac{t_0}{b}\exp\left(-\beta\Delta\varepsilon_1\right) \tag{4.14}$$

Eqns. 4.9 and 4.10 are still valid, but with $\Delta\varepsilon_1$ instead of $\Delta\varepsilon_l$. Combining Eqns. 4.14 and 4.10, we get

$$\frac{h}{t_0} = \frac{t_0}{b} \exp\left(-\beta \Delta\varepsilon_1\right) = \frac{\exp\left(-\beta\Delta\varepsilon_1\right)}{1 + \frac{l_0}{t_0}\left[\exp\left(\Delta\varepsilon_1\right) - 1\right]} \tag{4.15}$$

and further

$$1 - D \equiv \frac{h}{t} = \frac{h}{t_0}\frac{t_0}{t} = \frac{\exp\left(-\Delta\varepsilon_3\right)\exp\left(-\beta\Delta\varepsilon_1\right)}{1 + \frac{l_0}{t_0}\left[\exp\left(\Delta\varepsilon_1\right) - 1\right]} = \frac{\exp\left(\Delta\varepsilon_1\right)}{1 + \frac{l_0}{t_0}\left[\exp\left(\Delta\varepsilon_1\right) - 1\right]} \tag{4.16}$$

4.2.3 Summary

The final damage rule reads as

$$1 - D = \begin{cases} \frac{\exp\left((1+\beta)\Delta\varepsilon_1\right)}{1+\frac{l_0}{t_0}\left[\exp\left((1+\beta)\Delta\varepsilon_1\right)-1\right]} & \text{if } -1 < \beta \leq 0 \\[2ex] \frac{\exp\left(\Delta\varepsilon_1\right)}{1+\frac{l_0}{t_0}\left[\exp\left(\Delta\varepsilon_1\right)-1\right]} & \text{if } 0 \leq \beta \leq 1 \end{cases} \tag{4.17}$$

or in more compact form

$$1 - D = \frac{\exp\left((1 - \langle -\beta \rangle)\Delta\varepsilon_1\right)}{1 + \frac{l_0}{t_0}\left[\exp\left((1 - \langle -\beta \rangle)\Delta\varepsilon_1\right) - 1\right]} \tag{4.18}$$

where $\langle x \rangle = \max\left(x, 0\right)$. It is seen that the damage D vanishes if $l_0/t_0 = 1$ and increases with increasing value of l_0/t_0 for a given value of $\Delta\varepsilon_1$.

The resulting damage rule is in essence a mesh-dependent scaling of the post-necking element response, thereby reducing the *material* mesh sensitivity for elements larger than the width of the local neck. Figure 4.2 shows the evolution of the damage function for different ratios of l_0/t_0.

4.3 Erosion Criterion

After onset of necking, the coupled damage gradually reduces the strength of an element. At some point, fracture will occur and the element has to be eroded. This will introduce additional strain concentrations to the surrounding elements, and thus contribute to the speed and direction of crack propagation.

Final fracture and thus erosion of an element is assumed to be controlled by the total thickness strain within the virtual neck $\tilde{\varepsilon}_3$. This can be expressed through the
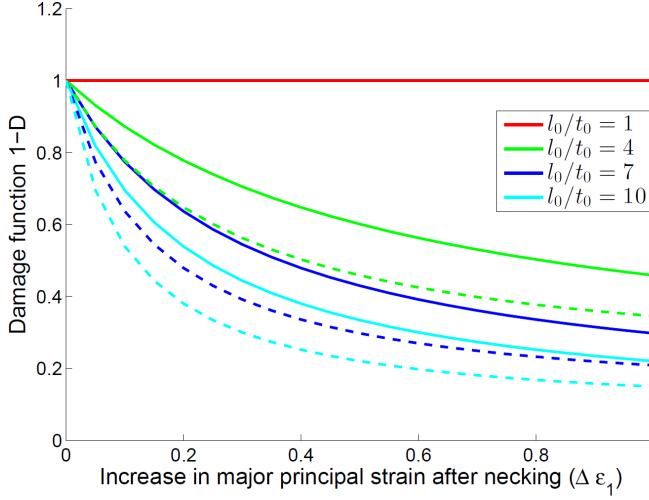
Figure 4.2: Damage function $1-D$ for different mesh sizes. Solid lines are for $\beta = -0.5$, dashed lines for $\beta = 0$.

element strain at incipient necking ε_3^0 and the increase in strain in the virtual neck from onset of necking $\Delta\tilde\varepsilon_3$. From the definition of damage, we have that

$$\Delta\tilde\varepsilon_3 = \ln\frac{h}{t_0} = \ln\left(\frac{t}{t_0}(1-D)\right) = \Delta\varepsilon_3 + \ln(1-D) \qquad (4.19)$$

The total thickness strain in the neck is then expressed as

$$\tilde\varepsilon_3 = \varepsilon_3^0 + \Delta\tilde\varepsilon_3 = \varepsilon_3^0 + \Delta\varepsilon_3 + \ln(1-D), \ \ l_0 \geq t_0 \qquad (4.20)$$

As indicated by Walters (2013) and Kõrgesaar et al. (2014), the mesh sensitivity is less in equi-biaxial tension than in uniaxial tension. Further, the strain from local instability to fracture is reduced for high strain-rate ratios ($\beta > 0$) where local necking is not the dominant fracture mechanism.

As a pragmatic rule, the local virtual neck in plane strain is assumed to evolve with damage degradation until its thickness strain is increased by a given percentage ξ from incipient necking. The same percentage is assumed for all negative minor strains. To account for the reduced ductility for positive minor strains, the allowable change in thickness strain is reduced linearly with the β-ratio until equi-biaxial strain. The erosion criterion is then defined as

$$
\tilde{\varepsilon}_{3,max} = \begin{cases} \varepsilon_3^0 \left(1 + \xi\right) & \text{if } -1 < \beta \le 0 \\ \varepsilon_3^0 \left(1 + \xi \left(1 - \psi\beta\right)\right) & \text{if } 0 < \beta \le 1 \end{cases} \tag{4.21}
$$

The factors ξ and ψ are input parameters to the model. The ξ parameter can be calibrated from e.g. uniaxial tension tests. Physically, the parameter can be understood as a measure of the length of the ductile region with softening after incipient necking prior to fracture. Smaller values will give a less ductile response. In lack of test data, ξ can be assumed equal to unity, which works well for normal marine structural steels. The ψ parameter can be calibrated to equi-biaxial tests, or assumed close to 1 for a conservative estimate. In the present study, $\psi = 0.9$ is assumed for all simulations, i.e., 10% of the post-necking ductility is allowed for equi-biaxial straining.

An integration point is assumed to fail once the total thickness strain $\tilde{\varepsilon}_3$ reaches the critical strain $\tilde{\varepsilon}_{3,max}$. The element is then eroded once the mid integration point through the thickness reach the critical strain.

The erosion criterion is plotted under the assumption of proportional straining in Figure 4.3a for different ratios of l_0/t_0. Figure 4.3b shows the effect of varying the parameters ξ and ψ for fixed l_0/t_0 ratio. The energy dissipation in a large simulation will not be overly sensitive to the exact point of erosion as the elements are subjected to softening from the damage formulation. Thus, the proposed model is robust with respect to the calibrations of the ξ and ψ parameters, and generic values can normally be used. The simulation results of stiffened panels will be more sensitive to small variations in ψ than to ξ, as failure occurs for high values of β.

4.4 Discussion of the Proposed Extension of the BWH Criterion

Gruben et al. (2013b) investigated the fracture response of a DOCOL 600 steel sheet with both Marciniak–Kuczynski and Nakajima formability tests combined with DIC-measurements. Local necking was observed for uniaxial tension and plane strain, but not for equi-biaxial tension, in which shear fracture was observed. After onset of local necking, the ductility of the specimens was slightly larger than what is obtained by assuming $\xi = 1$. The ductile range from plane strain towards uniaxial tension increased slightly. However, for equi-biaxial straining, no local necking was observed prior to shear fracture, giving an unstable response after onset of through-thickness shear instability. Hogström et al. (2009) investigated a softer NVA-grade material, and found local necking and significant post-necking ductility also for near equi-biaxial straining. Törnqvist investigated another soft steel of grade EN 10025 S275 in a giant bulger test apparatus, which was later
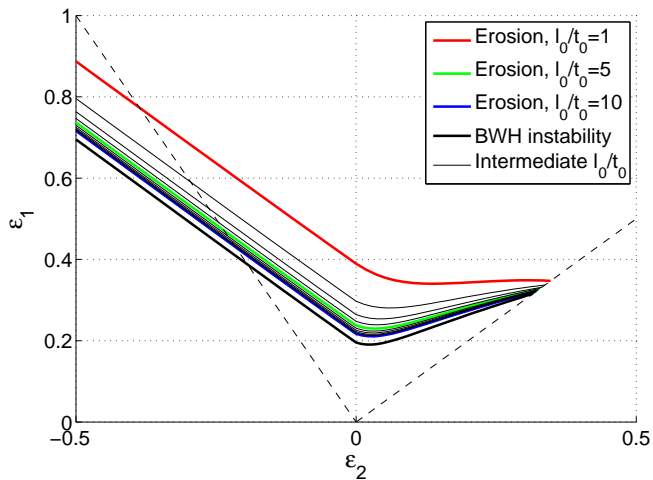
(a) Effect of varying mesh size for $\xi = 1.0$, $\psi = 0.9$
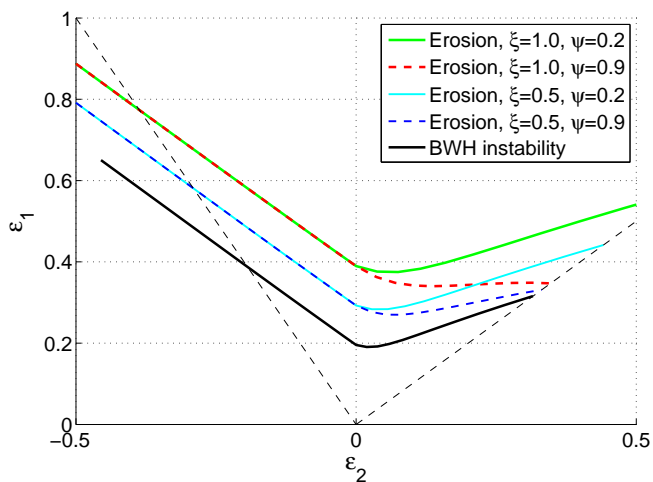
(b) Effect of varying erosion parameters for $l_0/t_0 = 1$

Figure 4.3: Example forming limit plots of local instability and erosion assuming proportional strains and no geometric strain concentrations.

simulated using the BWH criterion without damage by Alsos et al. (2008). Comparison of simulations and experiments revealed that some post-necking ductility was present after the BWH criterion was triggered in equi-biaxial straining.

In the proposed damage model, the same virtual local necking mechanism is assumed to occur for $-1 < \beta \leq 1$. This is a valid assumption for negative minor strains, but not necessarily for positive strains in which through-thickness shear failure takes place prior to local necking. With the combination of the damage and the strain-state dependent erosion criterion, this is partly mitigated. Further, the gradual decrease in allowable ductility after onset of local instability for positive β-values in Eq. 4.21 provides a transition between the rather ductile necking regime and the less ductile through-thickness shear regime.

Note that for strain states dominated by shear ($\beta < -0.5$), local thinning is not dominant and the Hill part of the BWH criterion does not give reasonable results, see Li et al. (2010) for a detailed discussion. This can be important for some specific applications. In the application of ship collision, structural members will normally fail by buckling prior to exceedance of the fracture criterion when they are subjected to shear and compressive stress states. The structural member most prone to fracture, the outer shell plate, will fail in a strain-state with $\beta > 0$.

4.5   Numerical Implementation

The proposed model is implemented into the explicit FE code LS-DYNA MPP version 971 R7.0.0. The numerical implementation consists of several parts. First, the temporal integration of the rate constitutive equations for the elastic-plastic material is obtained by use of the cutting plane algorithm from Ortiz and Simo (1986). Second, local necking is checked with the BWH criterion, which is evaluated for the mid integration point through the thickness of the shell element. Third, if local necking is detected, the damage evolution is computed and coupled with the elastic-plastic constitutive equations in all integration points by introducing the effective stress. Finally, the erosion criterion is evaluated.

4.5.1   Plasticity

Small strain plasticity is assumed, in which the strain-rate tensor $\dot{\varepsilon}$ can be decomposed to an elastic and plastic part as

$$\dot{\varepsilon} = \dot{\varepsilon}^{e} + \dot{\varepsilon}^{p} \tag{4.22}$$

Associated plastic flow gives the flow rule

$$\dot{\varepsilon}^p = \dot{\lambda}\mathbf{a} \tag{4.23}$$

where $\mathbf{a}$ is the derivative of the yield function f (Eq. 3.2) with respect to the stress tensor $\boldsymbol{\sigma}$ as

$$\mathbf{a} = \frac{\partial f}{\partial \boldsymbol{\sigma}} \tag{4.24}$$

Hence, $\mathbf{a}$ represents the flow direction and $\dot{\lambda}$ the flow magnitude. The stress rates $\dot{\boldsymbol{\sigma}}$ can then be calculated by the generalized Hooke's law with the elastic stiffness tensor $\mathbf{C}^e$ as

$$\dot{\boldsymbol{\sigma}} = \mathbf{C}^e \dot{\boldsymbol{\varepsilon}}^e = \mathbf{C}^e (\dot{\boldsymbol{\varepsilon}} - \dot{\lambda}\mathbf{a}) \tag{4.25}$$

The Kuhn-Tucker equations

$$f \leq 0, \quad \dot{\lambda} \geq 0, \quad \dot{\lambda}f = 0 \tag{4.26}$$

needs to be satisfied pr. definition. During plastic flow ($\dot{\lambda} > 0$) the yield function f is zero. Thus, $\dot{f}$ is zero and the plastic parameter can be found from the consistency equation as

$$\dot{\lambda}\dot{f} = 0 \tag{4.27}$$

As $\dot{\lambda} > 0$, $\dot{f}$ have to be zero and we get

$$\dot{f} = \frac{\partial f}{\partial \boldsymbol{\sigma}}\dot{\boldsymbol{\sigma}} - \frac{\partial f}{\partial R}\dot{R} = 0 \tag{4.28}$$

where the last term represent the change of f due to hardening given by $H_R\dot{\lambda}$. Using power law hardening, the hardening rate is defined as

$$H_R = Kn\langle \varepsilon_{0,eff} + \varepsilon_p \rangle^{n-1} \tag{4.29}$$

Inserting the stress rate tensor $\dot{\boldsymbol{\sigma}}$ and the hardening rate H_R, $\dot{f}$ can be expressed as

$$\dot{f} = \frac{\partial f}{\partial \boldsymbol{\sigma}}\mathbf{C}^e (\dot{\boldsymbol{\varepsilon}}^e - \dot{\lambda}\mathbf{a}) - H_R\dot{\lambda} = 0 \tag{4.30}$$

Solving this for the plastic parameter $\dot{\lambda}$ gives the flow magnitude as

$$\dot{\lambda} = \frac{\mathbf{a}^T \mathbf{C}^e \dot{\boldsymbol{\varepsilon}}}{\mathbf{a}^T \mathbf{C}^e \mathbf{a} + H_R} \tag{4.31}$$

4.5.2 Incremental Stress Update

The stresses are updated using the cutting plane algorithm, which consists of an elastic predictor step and a plastic corrector step. The elastic predictor is calculated from Hooke's law for plane stress. The effective trial stress increment $\Delta\tilde{\boldsymbol{\sigma}}$ is calculated as

$$\Delta\tilde{\boldsymbol{\sigma}} = \begin{bmatrix} \Delta\tilde{\sigma}_{xx} \\ \Delta\tilde{\sigma}_{yy} \\ \Delta\tilde{\tau}_{xy} \end{bmatrix} = \frac{E}{1-\nu^2} \begin{bmatrix} 1 & \nu & 0 \\ \nu & 1 & 0 \\ 0 & 0 & 1-\nu \end{bmatrix} \begin{bmatrix} \Delta\varepsilon_{xx} \\ \Delta\varepsilon_{yy} \\ \Delta\varepsilon_{xy} \end{bmatrix} = \mathbf{C}^e \Delta\boldsymbol{\varepsilon} \tag{4.32}$$

based on the strain increment $\Delta\boldsymbol{\varepsilon}$; E and ν being the elastic constants for the isotropic material. Damage coupling is obtained by the method outlined by de Borst (2004) for elastic-plastic materials. The effective trial stress at time step $n+1$ is calculated as

$$\tilde{\boldsymbol{\sigma}}_{trial}^{(n+1)} = \frac{\boldsymbol{\sigma}^{(n)}}{1-D} + \Delta\tilde{\boldsymbol{\sigma}} \tag{4.33}$$

where the damage $1-D$ used to predict stresses for time step $n+1$ is calculated at time step n. The damage variable D equals zero until the BWH instability criterion is fulfilled and local instability is initiated.

Equivalent stress is calculated from the trial stress, and the yield criterion is checked. If the yield criterion $f > 0$, a cutting plane algorithm is used to return to the yield surface. The stress increment from plastic iteration step k to $k+1$ can be calculated as

$$\begin{aligned} \Delta\boldsymbol{\sigma}^{(k)} &= (\boldsymbol{\sigma}^{(k+1)} - \boldsymbol{\sigma}^{(k)}) \\ &= -\mathbf{C}^e \Delta\boldsymbol{\varepsilon}^{p(k)} = -\Delta\dot{\lambda}^{(k)} \mathbf{C}^e \mathbf{a}^{(k)} \end{aligned} \tag{4.34}$$

The yield function is then linearized at every iteration step k as

$$f^{(k+1)} = f^{(k)} + \mathbf{a}^{(k)T}(\Delta\boldsymbol{\sigma}^{(k)}) + H_R\Delta\lambda^{(k)} \tag{4.35}$$

Inserting the stress increment $\Delta\boldsymbol{\sigma}^{(k)}$ into the linearized yield function, demanding $f^{k+1} = 0$ and solving for $\Delta\dot{\lambda}^{(k)}$ gives

$$\Delta\dot{\lambda}^{(k)} = \frac{f^{(k)}}{\mathbf{a}^T\mathbf{C}^e\mathbf{a} + H_R} \tag{4.36}$$

To return back to the yield surface, the stresses and strains can be updated as

$$\begin{aligned}
\tilde{\boldsymbol{\sigma}}^{(k+1)} &= \tilde{\boldsymbol{\sigma}}_{trial}^{(k+1)} - \Delta\dot{\lambda}\mathbf{C}^e\mathbf{a} \tag{4.37}\\
\varepsilon_p^{(k+1)} &= \varepsilon_p^{(k)} + \Delta\dot{\lambda}^{(k)} \tag{4.38}
\end{aligned}$$

Once the yield criterion is satisfied, the new stresses are returned as

$$\boldsymbol{\sigma}^{(n+1)} = \begin{cases} \tilde{\boldsymbol{\sigma}}_{trial}^{(n+1)}(1-D) & \text{if step was elastic} \\ \tilde{\boldsymbol{\sigma}}^{(k+1)}(1-D) & \text{if step was plastic} \end{cases} \tag{4.39}$$

where the damage variable D is zero until instability by the BWH criterion is reached. The damage variable D remains constant during the plastic return.

4.5.3 Evaluation of the BWH Criterion

The BWH criterion is checked after the stress update is completed, and is evaluated in the mid integration point through the thickness of the shell element using Eqns. 4.2 and 4.5. The critical strain $\hat{\epsilon}_1$ is here assumed to be equal to the power law exponent n, in accordance with the Hill criterion. If the BWH criterion is fulfilled for the mid integration point, damage starts to evolve and will be coupled in the next time step for the element in all integration points, and the post-necking evolution of $\Delta\varepsilon_1$ and $\Delta\varepsilon_3$ is calculated.

4.5.4 Damage Evolution

The damage parameter is updated if the BWH criterion is reached. Damage is applied in all integration points through the thickness. The quantity $1 - D$ is calculated from Eq. 4.18, in which $\Delta\varepsilon_1$ is the change of major principal strain after incipient necking. The element length and thickness ratio l_0/t_0 is evaluated at incipient necking.

The element length for the mesh size scaling is calculated from the square root of the element area. This strictly limits the validity of the current implementation to shell elements with nearly quadratic shape, as high aspect ratios will predict inaccurate element lengths.

4.5.5 Erosion Criterion

An integration point is set to fail by setting all the stress values to zero once the thickness strain in the virtual neck (Eq. 4.20) reaches the critical value in Eq. 4.21. When the mid integration point through the thickness fails, the element is removed from the simulation by erosion. Thus, for a bending-dominated stress state, the integration points fail sequentially from one surface towards the mid-thickness integration point, and then the element is removed by erosion when over half of the through-thickness integration points have failed.

4.6 Numerical Validation Study

The proposed material model is evaluated for large-scale structural impact simulations based on several published experimental results:

1. Uniaxial tensile test by Tautz et al. (2013)
2. Formability tests of ship construction steel with varying triaxiality by Broekhuijsen (2003)
3. Indentation tests on unstiffened and stiffened panels by Alsos and Amdahl (2009)
4. Indentation tests on double-sided shell structure by Tautz et al. (2013)

The proposed criterion is benchmarked against other fracture criteria on more experiments in Chapter 5.

In the numerical investigations the following numerical setup in LS-DYNA R7.0.0 was used according to good practice for full-scale analysis of marine collisions.

- Quadrilateral Belytschko-Lin-Tsay shell elements with five integration points over the thickness
- Standard stiffness-based hourglass control (Flanagan-Belytschko, option 4 in LS-DYNA). No drilling stiffness is applied
- Automatic surface-to-surface contact for contact between bodies
- Automatic single-surface contact for internal self-contact (e.g. stiffener touching plate after tripping)

No special numerical adjustments are made to improve agreement with the experimental data other than fitting the hardening parameters and the ξ parameter to the relevant uniaxial material tests. The ψ parameter is assumed equal to 0.9 in

all simulations. Thus, the numerical results display the prediction accuracy of the proposed material model for different structures and stress states, and thereby its potential for application in structural design.

4.6.1   Uniaxial Tensile Test

A uniaxial test is often used for calibration of a tensile fracture criterion, and should thus be captured well. A uniaxial test performed in the experiments by Tautz et al. (2013) is used herein. The sample is 4 mm thick, 10 mm wide and has a gauge length of 50 mm for calculation of the engineering strain. Four mesh sizes are used, where the ratio l_e/t_e between the initial element length and the initial element thickness ranges from 0.63 to 2.5.
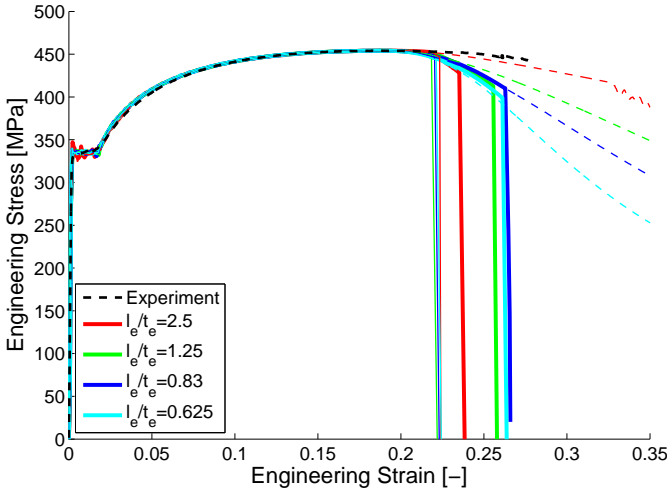
Figure 4.4: Uniaxial tensile test simulation results for various element lengths. Thick lines represent the BWH model with damage, thin continuous lines the BWH model without damage. Thin dashed lines are from a simulation without damage or fracture.

Table 4.1: Material parameters for the uniaxial tensile test.

σ_0 [MPa]	E [GPa]	K [MPa]	n	$\varepsilon_{plateau}$	ξ
338	204	728	0.167	0.015	1.0

Figure 4.4 shows the experimentally obtained curve and the simulation results with material parameters as in Table 4.1. If fracture is not considered (thin dashed lines), the different meshes show similar response up to the point of diffuse necking at an engineering strain of 0.19. After this, the results diverge, and the post-necking strain is reduced with decreasing element size. To capture diffuse necking, it is

important that the work hardening around ultimate tensile strength is defined accurately.

In Figure 4.4 the coarsest mesh apparently simulate the experiment accurately, but this is just a coincidence. Strain-rate effects are needed in order to get the correct softening of the material in the post-necking region. Typically, the strain-rate is about ten times higher in the localized neck than in the uniform part of the specimen, which is sufficient to stabilize the neck growth. If this effect is not included, the post-necking work hardening will be underestimated.

When the BWH criterion without damage is used (thin continuous lines), the point of local instability is determined and the elements are immediately eroded. Coupling post-necking damage (thick continuous lines) improves the correlation with experimental data while suppressing most of the mesh dependency.

The simulation with mesh size $l_e/t_e = 2.5$ has only one element over the width of the specimen, and suffers somewhat from hourglass deformations. This affects the post-necking response to some degree, and final fracture is predicted earlier than for the finer meshes.

4.6.2   Formability Tests of Ship Construction Steel with Varying Triaxiality

Broekhuijsen (2003) reported results of material tests with varying stress triaxiality for 12 mm thick plates of mild steel. The material is of a similar grade to that used in the full-scale collision experiments reported by Peschmann (2001). Six different geometries were tested with a spherical indenter of 60 mm in diameter to obtain a forming limit diagram (FLD), with strain-rate ratios β between -0.19 and 0.66. The FE mesh of the geometries with mesh size 10 mm ($l_e/t_e = 0.8$) are shown in Figure 4.5, together with the simulation setup of a formability test with indenter.

The specimens were assumed to be clamped in the out-of-plane direction outside a radius of 140 mm from the specimen center. In-plane constraints were applied to the bolt holes. Numerical simulations were performed using shell elements. The test specimens were thick compared with their width, and this limited the mesh size to a range from 0.8 to 2.4 times the plate thickness to ensure the proper capture of the strain response and the stability of the contact between the indenter and the specimen. The material parameters used in the simulations were calibrated based on a uniaxial tensile test and are listed in Table 4.2. A friction coefficient of 0.2 was assumed between the indenter and the specimen. The same hardening and friction parameters were used in the simulations performed by Broekhuijsen (2003).

Results are presented in Figures 4.6a to 4.6f for the different specimen geometries.
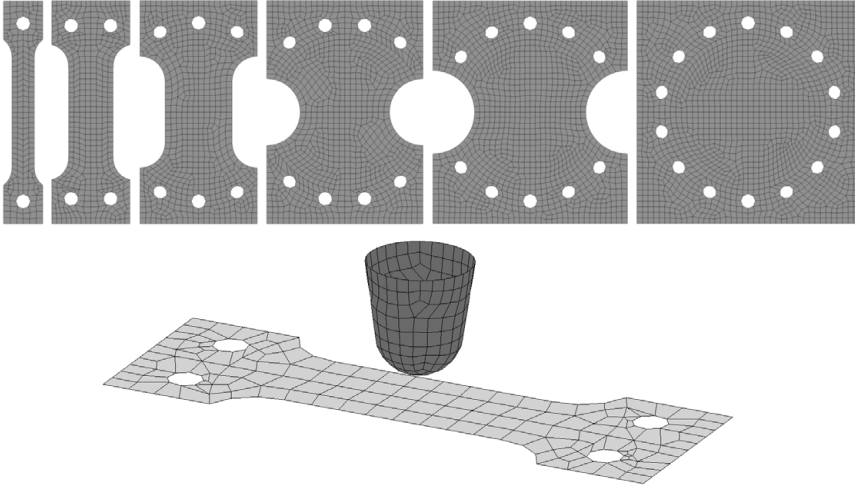
Figure 4.5: Formability models 1 (left) to 6 (right) with mesh size 10 mm ($l_e/t_e = 0.8$), and view of test setup with indenter (bottom) with mesh size 20 mm ($l_e/t_e = 1.6$).

Table 4.2: Material parameters for the Broekhuijsen experiments

σ_0 [MPa]	E [GPa]	K [MPa]	n	$\varepsilon_{plateau}$	ξ
284	196.5	680	0.195	0.0	1.0

Solid lines represent results from the BWH criterion with damage, while dashed lines represent results obtained with the original BWH criterion without damage (similar to Alsos et al. (2008)). In the figures, l_e/t_e is the initial ratio between the characteristic element length and the plate thickness.

For FLD tests 1 and 2 the meshes capture diffuse necking, while for FLD tests 3-6 diffuse necking is constrained. The contact interaction between the indenter and the test specimens is challenging with the coarse mesh discretization, and the simulations will not be able to capture all strain concentrations. The geometric mesh scaling rule of the BWH criterion thus becomes important. Omitting mesh scaling will lead to an overestimation of the experimentally obtained force, as the inability of the mesh to capture strain concentrations leads to an underestimation of the principal stress checked against the BWH instability criterion.

Considering the coarse shell element discretization of the test specimens, the overall agreement between simulations and test results is good. The extension of the BWH criterion with coupled damage shows increased accuracy compared to the original BWH criterion from Alsos et al. (2008). The smallest mesh size ($l_e/t_e = 0.8$) appears to give higher forces and larger deformations to failure than

the results compared to the coarser meshes.

4.6.3   Indentation Experiments with Unstiffened and Stiffened Panels

Alsos and Amdahl (2009) performed indentation experiments using a rigid indenter and a panel with dimensions of 1200×720 mm. The plate thickness was 5 mm, and the stiffeners were flat-bars, FB120$\times$6. The experimental results from the panels without stiffeners (US) and with one (1FB) and two (2FB) flat-bar stiffeners are considered in the following. The stiffener spacings were 360 and 240 mm for 1FB and 2FB, respectively. The welds had overmatching strength and were modeled as thin shell elements with increased thickness in the plate and stiffeners (+2 mm for the plate, +4 mm for the stiffeners). The panel configurations are depicted in Fig. 4.7a, and the FE mesh, including the 12.5 mm thick support frame, is shown in Fig. 4.7b. The hardening parameters for the material were selected based on the data reported in Alsos et al. (2009); see Table 4.3. A static friction coefficient of 0.3 was assumed.

The hardening parameters for the material as reported in Alsos et al. (2009) were utilized, see Table 4.3. The simulations were conducted with and without mesh scaling of the BWH criterion. Geometric mesh scaling was applied to all elements, not only to intersection elements (plate-stiffener junction). Post-necking damage was used in all simulations.

Note that the experiments were unloaded after about 130 mm displacement due to limited crosshead displacement stroke of the hydraulic jack used in the test setup. This was not accounted for in the simulations.

Table 4.3: Material parameters for the Alsos and Amdahl experiments

	σ_0 [MPa]	E [GPa]	K [MPa]	n	$\varepsilon_{plateau}$	ξ
Plate	285	210	740	0.24	0.00	1.0
Stiffener	340	210	760	0.225	0.015	1.0
Supporting frame	390	210	730	0.18	0.01	1.0

The numerical results are compared with the experimental data in Figure 4.8. In the case of the non-stiffened plate, strain localization is properly captured with all the meshes, and the BWH criterion identifies the onset of necking well without mesh scaling for most mesh sizes. With mesh scaling, the strength is underestimated for coarse meshes. Adding damage softening to the material delays the element erosion and softens the fracture process compared to the original BWH criterion. As one stiffener is added, the BWH criterion without mesh scaling still gives better results. For the experiment with two stiffeners, the BWH criterion without mesh scaling overestimates significantly the strength of the plate for coarser meshes, whereas the mesh-scaled version provides more consistent results for the mesh

(a) FLD 1, $\beta = -0.19$

(b) FLD 2, $\beta = 0.03$

(c) FLD 3, $\beta = 0.28$

(d) FLD 4, $\beta = 0.43$

(e) FLD 5, $\beta = 0.44$

(f) FLD 6, $\beta = 0.66$
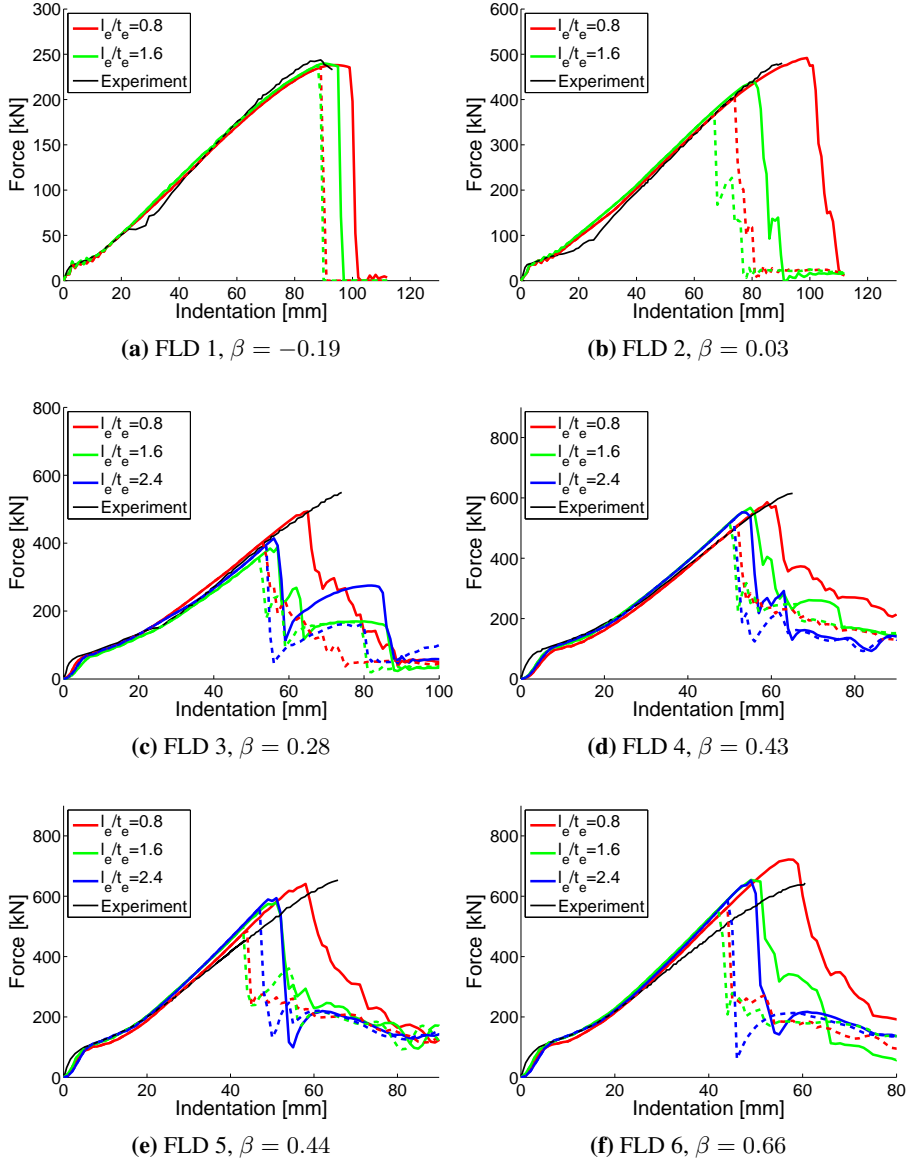
Figure 4.6: Force-displacement relation from formability tests and simulations with varying mesh size vs. thickness ratio l_e/t_e. Solid lines represent simulations using the BWH criterion with coupled damage, dashed lines the original BWH criterion without damage.

(a) Panel cross sections

(b) Mesh of panel with two flatbars. 25 mm mesh size ($l_e/t_e = 5$)
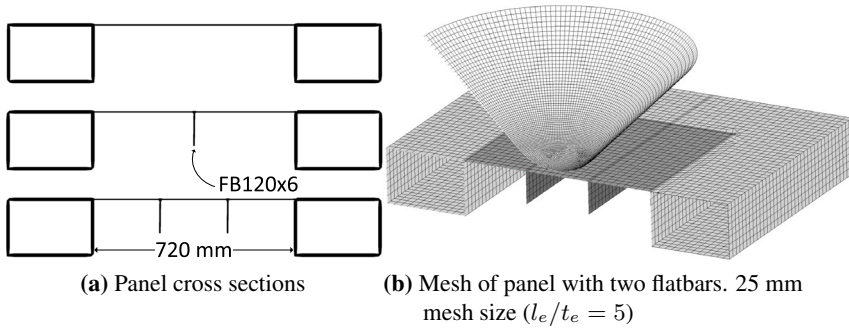
Figure 4.7: Geometry and mesh of deformable panels tested by Alsos and Amdahl.

sizes tested. Similar as for the formability tests in Figure 4.6, using mesh size with $l_e/t_e = 1$ gives a higher peak force compared to the other mesh sizes.

When failure occurs close to a stiffener (as for the panel with two flatbar stiffeners), the stress triaxiality is limited by the stiffener to values slightly above plane strain conditions. When failure occurs in a free plate field with constraints on all sides, the stress triaxiality is higher, and can approach equi-biaxial strain conditions. Fracture occurring close to a stiffener is typically not captured by the coarser meshes, and compensation is necessary. For the non-stiffened plate, even the coarse mesh is capable of resolving the out-of-plane behavior and obtains a good estimate of the strain concentration. For the plate with one stiffener two strain concentrations occur in parallel; the first close to the stiffener (where experimental fracture was observed) and the second in the free plate. Using geometric mesh scaling on the entire model leads to a fracture prediction in the free plate rather than near the stiffener, thereby explaining the scatter in Figure 4.8c.

Figure 4.9 shows the deformed plate sections at the maximum indentation level in the experiments. Comparison with the experimental deformation shows that the simulations with $l_e/t_e = 1$ and 2 are able to reproduce the curved fracture path. Simulations with coarser meshes capture the correct initiation point of fracture, but the propagation continues along the stiffener until transverse fracture occurs. Considering the coarse meshes involved, the force-displacement curve and the overall deformation of the test specimen are still simulated with acceptable accuracy for the experiment with two flat bar stiffeners.

4.6.4   Indentation Experiments with Double-sided Shell Structure

Tautz et al. (2013) conducted indentation experiments using a model of a double-sided shell structure. The scale was approximately 1/3; see Figure 4.10. The plate
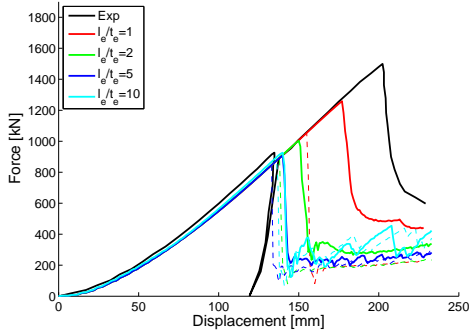
(a) Plate US, mesh scaling of BWH
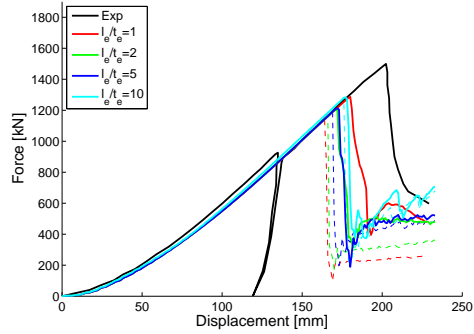
(b) Plate US, no mesh scaling of BWH
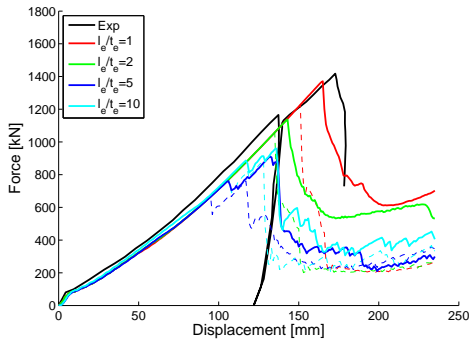
(c) Plate 1FB, mesh scaling of BWH
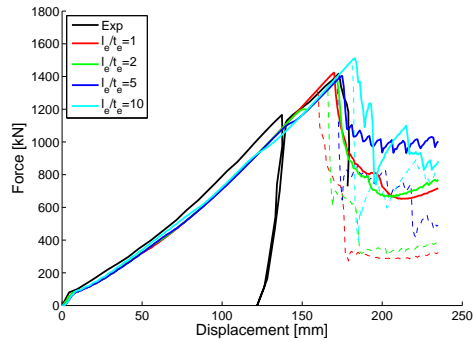
(d) Plate 1FB, no mesh scaling of BWH
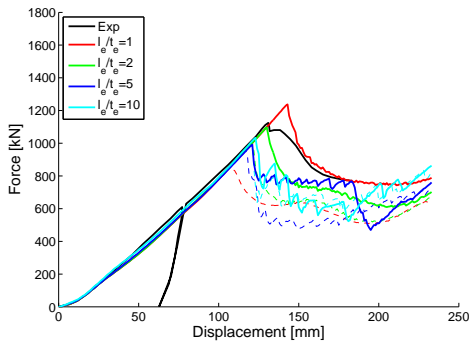
(e) Plate 2FB, mesh scaling of BWH
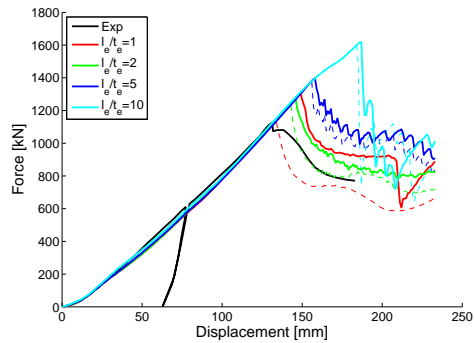
(f) Plate 2FB, no mesh scaling of BWH

Figure 4.8: Force-displacement curves from test and simulations of the Alsos and Amdahl test with varying mesh size. Thin dashed lines mark the original BWH criterion without damage, thick continuous lines the BWH criterion with damage.
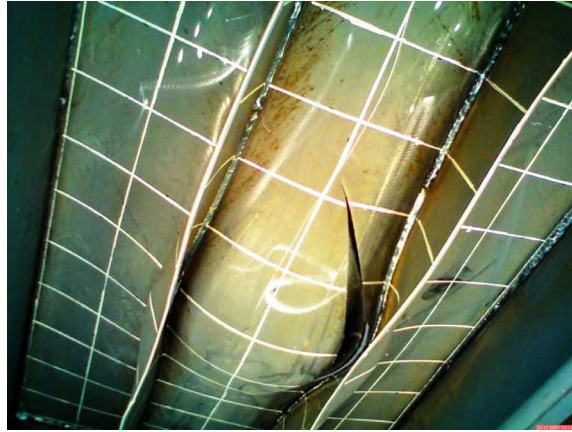
(a) Experimental failure mode, from Alsos (2008)
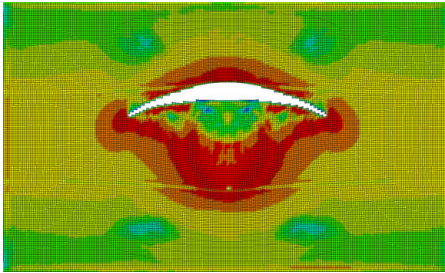
(b) $l_e/t_e = 1$
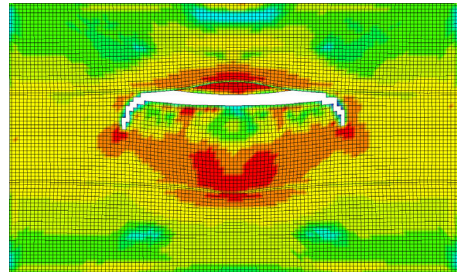
(c) $l_e/t_e = 2$
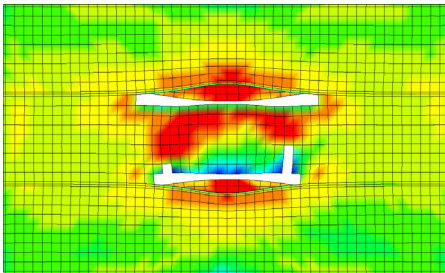
(d) $l_e/t_e = 5$
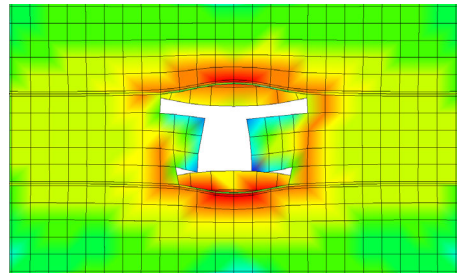
(e) $l_e/t_e = 10$

Figure 4.9: Deformed plate at end of experimental indentation of plate with two flatbars with different mesh sizes. Colors represent the equivalent von Mises stress from zero (blue) to 500 MPa (red). Mesh scaling of the BWH criterion is applied.

of 4 mm thickness had bulb profile stiffeners (HP140×7) with a spacing of 280 mm. The frame spacing was 800 mm, with 5 mm plates containing 600×400 mm manholes. The total height from the outer to the inner shell was approximately 900 mm, and the total length of the deformable region was 4000 mm. Steel plates with a thickness of 20 mm were utilized at the boundary, creating a strong support frame around the panel. The experiments were performed using two types of indenters: rigid and deformable. Herein, only the experiment with the rigid indenter is considered for verification of the material model. Further details of the experiments can be found in Fricke et al. (2014) and Martens (2014) (both available in German only).

During construction of the tested shell structure, cutouts around the stiffeners were made in the web frames according to normal ship manufacturing procedures, see Figure 4.10. The cutouts were included in the numerical model. Two meshes were investigated, with $l_e/t_e = 3.1$ and 6.3.
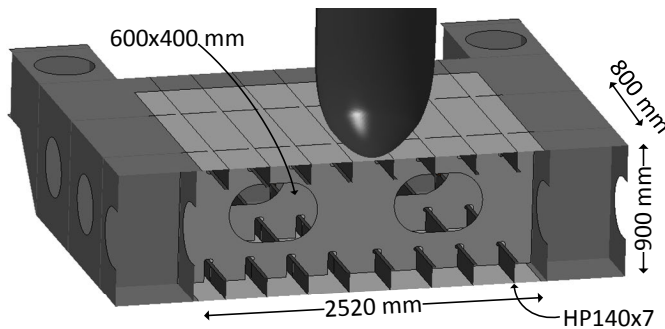
Figure 4.10: Transverse view of the experimental setup from Tautz et al. (2013), with manholes and cutouts around the stiffeners in accordance with standard ship design procedure.

The material properties were calibrated based on uniaxial tensile tests of the materials involved, and the parameter values are shown in Table 4.4. The friction coefficient was assumed to be equal to 0.23, similar to the assumption adopted in Tautz et al. (2013). This assumption was based on an investigation by Karlsson et al. (2009), in which the average value of the kinetic friction for non-lubricated mild steel was found to be 0.23. The supporting frame was assumed to be rigid.

Figure 4.11a compares the force-displacement curves obtained using the proposed material model with the experimental data. The predicted results are in good agreement with the experiments, with a slight underestimation of the peak force. The mesh dependence is small for the first peak force (rupture of outer hull). If mesh scaling is omitted, the contact force will be overestimated and this overestimation

Table 4.4: Material parameters for the tests of Tautz et al. (2013)

	σ_0 [MPa]	E [GPa]	K [MPa]	n	$\varepsilon_{plateau}$	ξ
Plate	338	204	728	0.167	0.015	1.0
Stiffener	330	211	755	0.149	0.010	0.5
Frame	331	196.5	728	0.158	0.012	1.0
Supports	331	196.5	760	0.184	0.009	1.0

increases with increasing mesh size, see Figure 4.11b. This leads to an overestimation of the energy dissipation during indentation.

Figure 4.12 compares the deformed structure and fracture path after penetration of the outer hull of the test section at approximately 400 mm of indentation. Both simulations capture the overall experimental fracture path, but the coarsest mesh gives a cruder approximation. The behavior is similar to that observed in the simulations of the Alsos experiments (Figure 4.9), and the fracture path seems to converge to the experimentally observed path with decreasing mesh size.
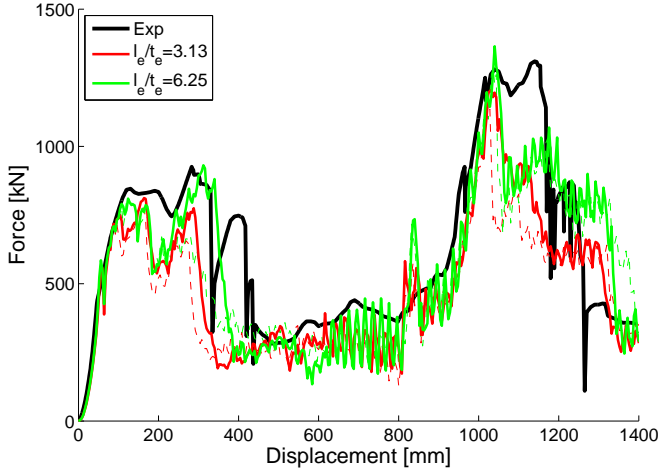
(a) Mesh scaling of BWH
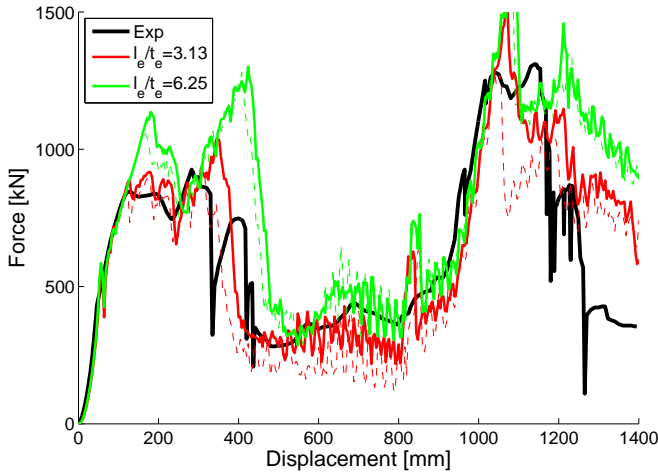
(b) No mesh scaling of BWH

Figure 4.11: Force-displacement curves comparing numerical simulations with experimental results from Tautz et al. for two different mesh sizes. Thin dashed lines mark the original BWH criterion without damage.

(a) Experimental failure mode, figure from Fricke et al. (2014)
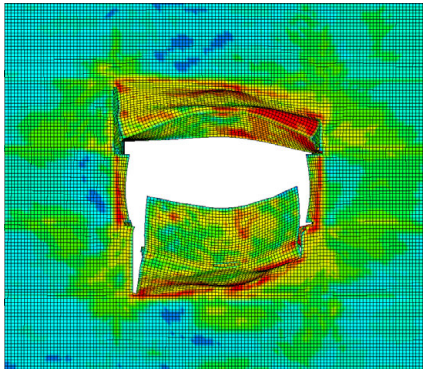
(b) Simulation with $l_e/t_e = 3.1$
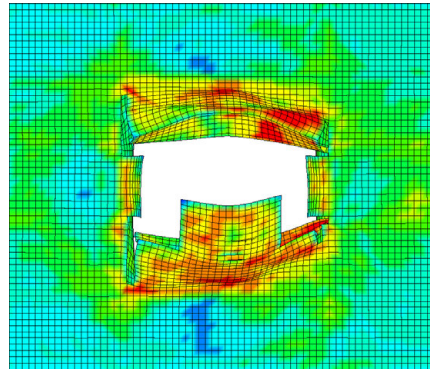
(c) Simulation with $l_e/t_e = 6.3$

Figure 4.12: Comparison of fracture path from tests and simulation. Colors represent the equivalent von Mises stress from zero (blue) to 500 MPa (red). Mesh scaling of the BWH criterion is applied.

4.7   Discussion of Damage Extension

The practical consequence of introducing the damage term to the BWH criterion is that the energy dissipation subsequent to local instability can be captured approximately even when the elements are significantly larger than the width of the assumed local neck (i.e., larger than the plate thickness). This implies that the global model can dissipate additional energy also after local necking. The proposed material model with J2 flow theory, the BWH instability criterion and post-necking damage shows improved predicted peak force for the simulated experiments compared to the original BWH criterion without damage. The average prediction of energy dissipation (area under the force-displacement curve) for the entire simulation is also improved drastically. The effect of adding damage to the BWH criterion is both that the initial fracture by erosion is delayed, and that the fracture propagation speed is reduced so that the remaining capacity after first fracture is better in line with the experiments.

Due to the post-necking stiffness reduction imposed by the damage coupling, the simulation results are not overly sensitive to the exact numerical value of ξ and ψ. Except for the stiffener material in the experiments by Tautz et al. (2013), $\xi = 1$ worked well in calibrations to all the material tests used in this study. The ψ-parameter was set constant to 0.9 for all materials, which seems to be a good value for marine steels. Other materials with different multi-axial fracture behavior might require a more careful calibration of ξ and ψ.

In the experiments where strain localization is not close to stiffeners, but rather in the free plate field (i.e., the tests of unstiffened plate and plate with one flatbar stiffener by Alsos and Amdahl (2009)), the coarsely meshed shell structures will capture the in-plane strain concentrations adequately. Using geometric mesh scaling, which assumes that the strain concentrations are not captured, will thus cause fracture to be predicted too early for the coarser meshes. The BWH criterion without mesh scaling will then give the best prediction of fracture.

When compared against larger impact experiments of stiffened plate structures (all tests except the unstiffened plate and the plate with one flatbar mentioned above), the proposed mesh-scaled criterion shows an improved prediction of fracture and subsequent energy dissipation, with low mesh dependency when scaling of the BWH criterion is used for element length to thickness ratios l_e/t_e between 1 and 10. If mesh scaling is not used, the criterion will significantly overestimate the experimental force level (see Figure 4.8f and 4.11b), as the strain concentrations due to out-of-plane bending are not captured. Thus, in design it is safe to apply mesh scaling on the struck object, as this will give a conservative prediction of the struck object's resistance to impact.

From the experiments where element failure occurs in a free plate field rather than at the intersection between the plate and a stiffener, the stress triaxiality is observed to be closer to that of equi-biaxial tension than plane-strain tension. When failure occurs close to a stiffener, the stiffener will constrain the element's stress triaxiality to be somewhat above that of plane-strain tension. However, the simulated triaxiality is dependent on the element length, as larger elements capture more of the response of the plate away from the actual fracture location.

Chapter 5

Benchmark of Fracture Models

The robustness and prediction uncertainty of various fracture criteria are investigated in the following. Multiple experiments with varying structural configuration, strain state and loading, each with several different mesh sizes, are simulated to obtain a challenging numerical test bench. Each criterion is calibrated only towards data from a uniaxial tensile test, so that the obtained results show how the criteria would behave in a design situation, where calibration to a known solution is impossible.

5.1 Simple Strain-state-independent Fracture Criteria

Strain-state-independent criteria often specify a critical equivalent, principal or thinning strain as a fixed parameter. Because of the differences among strain types, these criteria will behave differently when plotted in diagrams such as the FLD shown in Figure 3.10. To illustrate this behavior, J2 plasticity with proportional loading is assumed. The strain types can then be calculated using the stress ratio α as follows:

$$\varepsilon_1 = \varepsilon_{eq}\frac{1 - \alpha/2}{\sqrt{1 - \alpha + \alpha^2}} \tag{5.1}$$

$$\varepsilon_2 = \varepsilon_{eq}\frac{\alpha - 1/2}{\sqrt{1 - \alpha + \alpha^2}} \tag{5.2}$$

$$\varepsilon_3 = -(\varepsilon_1 + \varepsilon_2) = -\varepsilon_{eq}\frac{1 + \alpha}{2\sqrt{1 - \alpha + \alpha^2}} \tag{5.3}$$

Figure 5.1 illustrates how the choice of strain parameter affects the critical strain

for all strain states when calibrated against the same fracture limit determined from a uniaxial tensile test. From a comparison of these curves to the experimental values in Figure 3.10, it appears that the major principal strain is the best candidate for positive minor strains, whereas the through-thickness strain could be a good candidate for negative minor strains. The assumption of a constant critical equivalent strain contradicts experimental observations for both negative and positive minor strains, yet it is the most widely adopted assumption for fracture estimation in the ship and offshore community.
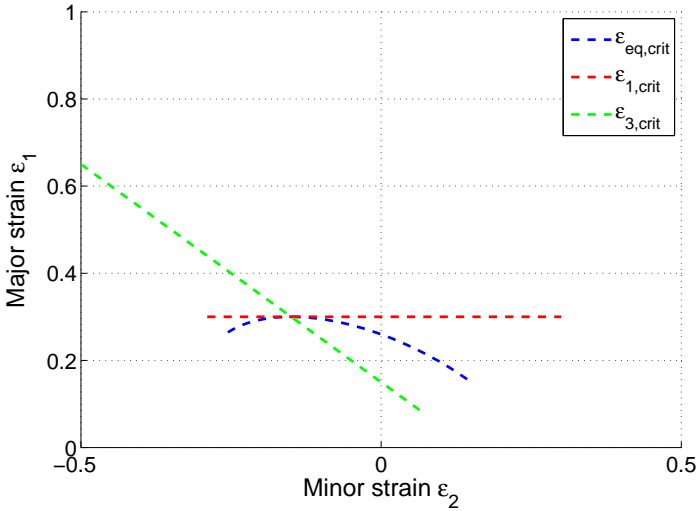
Figure 5.1: Constant critical strain curves deduced from strain-state-independent fracture criteria compared in an FLD.

The criteria are often defined to be mesh dependent. In a typical model, the critical strain ε_f combines a uniform strain ε_u and a local mesh-dependent strain ε_l. The latter scales with the thickness t_e and the element length l_e as follows:

$$\varepsilon_f = \varepsilon_u + \varepsilon_l \frac{t_e}{l_e} \tag{5.4}$$

where the subindex e indicates an initial value. The constants ε_u and ε_l are determined through calibration.

From the experimental data in Figure 3.10, the minimum critical strain is observed for plane strain (in which the minor strain is zero). When calibrating a strain-state-independent criterion with respect to uniaxial experiments, one must ensure that the defined critical strain is not greater than the minimum critical strain that will occur for plane strain. Körgesaar et al. (2014) have noted that to ensure this,

the maximum allowable t_e/l_e ratio in Eq. 5.4 must be specified together with the strain-state-independent failure criterion. For a strain-state-dependent criterion, the actual failure strain can be included in the analysis because this effect is compensated for by the strain-state dependence.

5.1.1 Barba's Relation

As reported by Jernkvist et al. (2004), Barba (1880) found through empirical methods that the uniform elongation of a specimen is a material property, whereas the necking extension in a uniaxial test is proportional to the linear dimensions of the cross-sectional area of the test specimen. Thus, the total strain at failure in the uniaxial elongation of a specimen is dependent on the cross-sectional area, the gauge length and the uniform elongation strain. Hogström et al. (2009) formulated Barba's relation for the prediction of fracture strain as

$$\varepsilon_{cr} = ln\left(e^{\varepsilon_n} + C\frac{\sqrt{W t_e}}{l_e}\right) \tag{5.5}$$

where e is the base of the natural logarithm, ε_n is the strain at the onset of necking, W is the width of the tested specimen, t_e is the thickness, l_e is the element length (corresponding to the gauge length) and C is a parameter that is used to fit the critical strain relation to the experimental results. Because $\varepsilon_1 = \varepsilon_{eq}$ in a uniaxial test until necking occurs, this criterion can be used for either strain measure. Yamada et al. (2005) has applied the criterion to the equivalent plastic strain.

When this relation is applied to uniaxial test results, the W parameter in Barba's relation has a physical meaning. However, when it is applied to a large FE mesh, the width term loses its physical meaning. It is common to fix the W parameter during calibration, but the fracture estimation in full-scale simulations is then dependent on the geometry of the uniaxial test specimen.

5.1.2 Considère's Criterion for Diffuse Necking

Considère's criterion is derived from the maximum force and states that the ultimate strength of a material is described by the point at which the increase in stress due to strain hardening perfectly balances the reduction in cross-sectional area due to diffuse necking. Consider a uniaxial sample of length l and cross-sectional area A, with the subindex 0 indicating the initial configuration. The stretch ratio can be defined as $\lambda = l/l_0$, and the corresponding logarithmic strain is $\varepsilon = \ln(l/l_0)$. The force applied to the specimen is $F = \sigma A_0/\lambda$, where σ is the current flow stress. At the ultimate strength of the material, the load reaches a maximum value, and the strains begin to localize. Further straining occurs predominantly in the diffuse

neck of the specimen with decreasing force. The point of maximum force can be found by taking the derivative of the force as follows:

$$\frac{\partial F}{\partial \varepsilon} = A_0 \frac{\partial \sigma}{\partial \varepsilon} \exp(-\varepsilon) - \sigma A_0 \exp(-\varepsilon) = 0 \tag{5.6}$$

Rearranging this expression yields Considère's criterion

$$\frac{\partial \sigma}{\partial \varepsilon} = \sigma \tag{5.7}$$

which is visualized in Figure 5.2. A similar derivation of this criterion can be found in Petrie (2009).
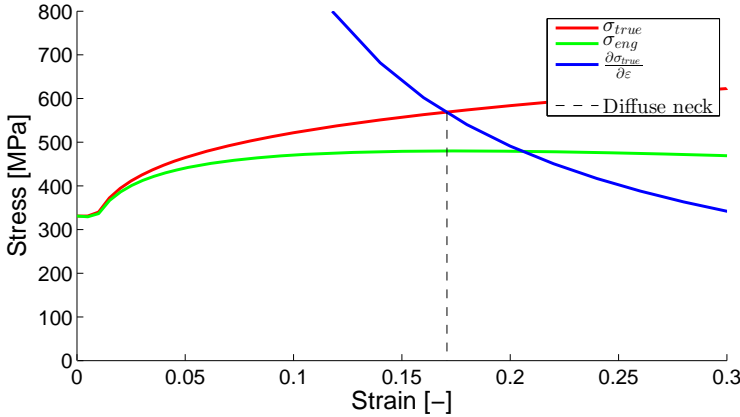
Figure 5.2: Stress-strain diagram for a uniaxial tensile test showing the Considère criterion. Diffuse necking begins when Eq. 5.7 is satisfied.

5.1.3   DNV RP-C204

A simple fracture criterion is given in DNV RP-C204, based on the simple relation described in Eq. 5.4 with the following coefficients:

$$\varepsilon_f = 0.02 + 0.65 \frac{t_e}{l_e}, \qquad l_e/t_e \geq 5 \tag{5.8}$$

It is not specified whether this is an equivalent- or principal-strain criterion. The same criterion is also given in NORSOK N-004 and applied to axially loaded plate material in which yielding occurs in the parent material (not in welds).

5.1.4 Peschmann

Peschmann (2001) defined a two-step criterion for small and large plate thicknesses as follows:

$$\varepsilon_f = \begin{cases} 0.1 + 0.8\frac{t_e}{l_e} & \text{if } t \leq 12 \\ 0.08 + 0.65\frac{t_e}{l_e} & \text{if } t > 12 \end{cases} \tag{5.9}$$

This criterion was derived from experimental results, including, among others, those reported in Wevers and Vredeveldt (1999), and an iterative numerical approach with a varying mesh size. A reduction in critical strain was observed for larger plate thicknesses. This criterion is to be applied to the equivalent plastic strain.

5.1.5 GL

The GL criterion (Radon (2014); Scharrer et al. (2002)) was derived based on thickness measurements sampled from a large number of ruptured plates from damaged ship structures. Therefore, this criterion has the added advantages that several imperfections are included in the results and that the limit strains correspond to a stress state similar to that found in actual collisions. The criterion is defined in two parts based on the principal strain ε_1 at failure,

$$\varepsilon_{1,fail} = \begin{cases} 0.056 + 0.54\frac{t_e}{l_e} & \text{if plate structures} \\ 0.079 + 0.76\frac{t_e}{l_e} & \text{if beams or trusses} \end{cases} \qquad l_e/t_e \geq 5 \tag{5.10}$$

and the critical through-thickness strain $\varepsilon_{3,fail}$ given by

$$|\varepsilon_{3,fail}| = \frac{\varepsilon_{1,fail}}{1 + \varepsilon_{1,fail}} \tag{5.11}$$

As shown in Figure 5.1, the principal-strain criterion dominates for low minor strains and the thickness-strain criterion dominates for high minor strains. Thus, the GL criterion differs from other simple criteria in that it has some strain-state dependence.

5.1.6 SHEAR

Marinatos and Samuelides (2013b) utilized the SHEAR criterion. They calibrated a polynomial critical strain rule combined with a change in the work hardening model after incipient necking, and they verified this approach against various indentation experiments in Marinatos and Samuelides (2015, 2013a,b).

To calibrate the fracture criteria, a uniaxial test is modeled using various mesh sizes. The element strain is measured at the experimentally observed elongation at fracture for the various mesh sizes. A third-order polynomial curve is fitted to these critical strain data to obtain a continuous estimate of the critical equivalent strain ε_{cr} as a function of l_e/t_e. The advantage of using the SHEAR criterion is that the fracture limit can be scaled in accordance with the material properties, in contrast to criteria formulated based on Eq. 5.4. To achieve more robust calibration of the parameters, the criterion is herein modified to a power-law relationship, similar to the assumption in Paik (2007). This yields a critical strain as

$$\varepsilon_{cr} = A \left(\frac{l_e}{t_e} \right)^B \tag{5.12}$$

Marinatos and Samuelides (2013b) recommend using the SHEAR criterion in combination with a tangential hardening stress-strain curve after incipient necking. To the authors' understanding, this is performed to account for the strain-rate effect on the post-necking response of the element. In the following, only the power-law hardening curve is used throughout the plastic regime, which is also in line with the later recommendation by Marinatos and Samuelides (2015).

5.1.7 Coupled Ductile Damage

ABAQUS (2012) provides a method for damage modeling in ductile materials. The method assumes that the onset of damage occurs at a given strain (which may be a function of strain state and strain rate). Subsequently, a softening model is used to perform a mesh-dependent damage calculation that is coupled to the element response. This method is commonly used by researchers and the offshore industry, e.g., for a constant initiation strain by Notaro et al. (2013) and Hogström and Ringsberg (2012).

In its simplest form, this model assumes that damage is initiated at a critical equivalent strain ε_{fs} and follows a linear damage evolution after this point. A critical post-necking failure elongation $u_{pl,f}$ is assumed rather than a critical failure strain (following Hillerborg et al. (1976)). The post-necking equivalent plastic strain to failure is a function of the element length and thus corresponds to a *material* mesh dependence. The rate of effective plastic displacement u_{pl} is defined as

$$\dot{u}_{pl} = l_e \dot{\varepsilon}_{eq} \tag{5.13}$$

where l_e is the initial element length and $\dot{\varepsilon}_{eq}$ is the rate of equivalent plastic strain after damage initiation. The rate of damage is defined as $\dot{D} = \dot{u}_{pl}/u_{pl,f}$, and the

total damage D is obtained as follows:

$$D = \int \dot{D} dt = \int \frac{l_e \dot{\varepsilon}_{eq}}{u_{pl,f}} d\varepsilon_{eq}$$

(5.14)

An integration point has failed once the damage D reaches 0.99.

5.2 Advanced Strain-state-dependent Fracture Criteria

5.2.1 Swift Criterion for Diffuse Instability

Considère's criterion was derived based on uniaxial stress considerations. Swift (1952) extended this criterion to account for a peak force in both principal directions of plane stress under the assumption that both in-plane principal forces F_1 and F_2 reach a maximum, i.e.,

$$\dot{F}_1 = 0 \quad \text{and} \quad \dot{F}_2 = 0$$

(5.15)

By assuming proportional loading paths and neglecting elastic strains, Altmeyer (2013) expressed the Swift criterion as

$$\frac{\dot{\sigma}_{eq}}{\sigma_{eq}\dot{\varepsilon}_{eq}} = \frac{4 - 3\alpha - 3\alpha^2 + 4\alpha^3}{4(1 - \alpha + \alpha^2)^{3/2}}$$

(5.16)

More conveniently, power law hardening can be assumed and the criterion can be expressed as a critical equivalent plastic strain as follows:

$$\varepsilon_{eq,crit} = \frac{4n(1 - \alpha + \alpha^2)^{3/2}}{4 - 3\alpha - 3\alpha^2 + 4\alpha^3}$$

(5.17)

This criterion predicts the maximum force (diffuse necking) for various stress states. Note that even when diffuse necking is constrained by adjacent structures, the maximum force criterion is valid and is automatically present in a simulation, provided that the plastic hardening is properly described close to the ultimate tensile strength.

5.2.2 Bressan-Williams-Hill Criterion with and without Damage

The BWH criterion without damage and the BWH criterion extended with post-necking damage are both viable candidates for collision assessment of stiffened panel structures. For completeness, the main equations are given below. The reader is referred to Chapter 4 for the derivation of the criteria.

The BWH criterion can be expressed as follows:

$$\sigma_1 = \begin{cases} \frac{2K}{\sqrt{3}} \frac{1+\frac{1}{2}\beta}{\sqrt{\beta^2+\beta+1}} \left(\frac{2}{\sqrt{3}} \frac{\hat{\epsilon}_1}{1+\beta} \sqrt{\beta^2+\beta+1} \right)^n & \text{if } -1 < \beta \leq 0 \\ \frac{2K}{\sqrt{3}} \frac{\left(\frac{2}{\sqrt{3}} \hat{\epsilon}_1 \right)^n}{\sqrt{1-\left(\frac{\beta}{2+\beta} \right)^2}} & \text{if } 0 < \beta \leq 1 \end{cases} \tag{5.18}$$

The BWH criterion without damage erodes an element once the BWH criterion is reached (i.e., at onset of local instability). For inclusion of post-necking behavior, a damage D can be determined as

$$1 - D \equiv \frac{h}{t} = \frac{\exp\left((1 - \langle -\beta \rangle) \Delta\varepsilon_1 \right)}{1 + \frac{l_0}{t_0} \left[\exp\left((1 - \langle -\beta \rangle) \Delta\varepsilon_1 \right) - 1 \right]} \tag{5.19}$$

and coupled to the element response to reduce the strength of a large element due to the formation of a virtual local neck within the element. Post-necking erosion takes place when the virtual thickness strain in the neck

$$\tilde{\varepsilon}_3 = \varepsilon_3^0 + \Delta\tilde{\varepsilon}_3 = \varepsilon_3^0 + \Delta\varepsilon_3 + \ln(1 - D), \ \ l_0 \geq t_0 \tag{5.20}$$

reach a critical thickness strain defined by

$$\tilde{\varepsilon}_{3,max} = \begin{cases} \varepsilon_3^0 (1 + \xi) & \text{if } -1 < \beta \leq 0 \\ \varepsilon_3^0 (1 + \xi (1 - \psi\beta)) & \text{if } 0 < \beta \leq 1 \end{cases} \tag{5.21}$$

5.2.3 RTCL: Rice-Tracey Cockroft-Latham Damage Criterion

In the RTCL criterion proposed by Törnqvist, the stress triaxiality T is used to distinguish between shear- and tension-dominated damage. The damage rate $\dot{D} = \dot{D}(T)$ is defined as

$$\dot{D} = \begin{cases} 0 & \text{if } T < -1/3 \quad \text{(compression)} \\ \frac{\sigma_1}{\sigma_{eq}} \dot{\varepsilon}_{eq} & \text{if } -1/3 \leq T < 1/3 \quad \text{(shear)} \\ exp\left(\frac{3T-1}{2} \right) \dot{\varepsilon}_{eq} & \text{if } 1/3 \leq T \quad \text{(tension)} \end{cases} \tag{5.22}$$

Fracture is simulated via element erosion when the accumulated damage D reaches a critical level, where D is defined as

$$D = \frac{1}{\varepsilon_{cr}} \int \dot{D}dt \tag{5.23}$$

The critical strain ε_{cr} is mesh scaled in accordance with the relationship

$$\varepsilon_{cr} = n + (\varepsilon_n - n)\frac{t_e}{l_e} \tag{5.24}$$

where ε_n is the failure strain in terms of uniaxial tension for a mesh size $l_e = t_e$ and n is the power-law exponent. The plasticity formulation is assumed to be independent of the strain rate. The damage D is not coupled with the plastic response; it is used only for fracture prediction. For proportional strain paths, the RTCL criterion can be expressed as a critical equivalent plastic strain:

$$\varepsilon_{eq,crit} = \begin{cases} 0 & \text{if } T < -1/3 \\ \varepsilon_{cr}\sqrt{1 - \alpha + \alpha^2} & \text{if } -1/3 \leq T < 1/3 \\ \varepsilon_{cr}/exp\left(\frac{3T-1}{2}\right) & \text{if } 1/3 \leq T \end{cases} \tag{5.25}$$

5.2.4 CL: Cockroft-Latham Criterion

The criterion from Cockcroft and Latham (1968) predicts fracture when the tensile principal stress integrated over the strain path, W, reaches a critical value W_c as follows:

$$W = \int \langle\sigma_1\rangle\dot{\varepsilon}_{eq}dt \leq W_c \tag{5.26}$$

where only positive values of the major principal stress are used. The integration point has failed when $W/W_c = 1$. W_c is the critical plastic dissipation per unit volume and can be calculated as the area under a true stress-strain curve for the material (see Gruben et al. (2012)). Under the assumptions of proportional strain paths and plane stress, the criterion may be described as follows:

$$\varepsilon_{eq} = \left(\frac{(n+1)W_c}{K}\sqrt{1 - \alpha + \alpha^2}\right)^{\frac{1}{n+1}} \tag{5.27}$$

No scaling for coarsely meshed shell structures is proposed for the CL criterion, but it has been shown to work well for fine solid meshes by Gruben et al. (2012, 2013a), among others.

5.2.5   MMC: Modified Mohr-Coulomb Criterion

Bai and Wierzbicki (2008) proposed a modified Mohr-Coulomb failure model that depends on both the stress triaxiality T and the lode parameter $\bar{\theta}$, resulting in a critical strain ε_f for von Mises yield:

$$
\varepsilon_f(T, \theta) = \left\{ \frac{K}{C_2} \left[C_3 + \frac{\sqrt{3}}{2 - \sqrt{3}} (1 - C_3) \left(sec\left(\frac{\bar{\theta}\pi}{6} \right) - 1 \right) \right] \right.
$$
$$
\left. \times \left[\sqrt{\frac{1 + C_1^2}{3}} cos\left(\frac{\bar{\theta}\pi}{6} \right) + C_1 \left(T + \frac{1}{3} sin\left(\frac{\bar{\theta}\pi}{6} \right) \right) \right] \right\}^{-1/n} \quad (5.28)
$$

where K and n are the power-law parameters and C_1, C_2 and C_3 are material parameters governing the fracture process. When plotted in a 3D space (Figure 5.3a), this criterion yields a fracture locus, which Bai and Wierzbicki (2010) calibrated for several types of materials using a range of tests.

Under the assumption of plane stress, the lode parameter $\bar{\theta}$ can be expressed in terms of the stress triaxiality as

$$
-\frac{27}{2}T\left(T^2 - \frac{1}{3} \right) = sin\left(\frac{\pi\bar{\theta}}{2} \right) \quad (5.29)
$$

Using this relation, the 3D fracture surface described by Eq. 5.28 can be reduced to 2D; it is plotted as a 3D line in Figure 5.3a and in 2D in Figure 5.3b. It can be observed from the figure that with this failure model, the critical strain reaches peak values for compression ($T = -1/3$), uniaxial tension ($T = 1/3$) and biaxial tension ($T = 2/3$), whereas it reaches minimum values for pure shear ($T = 0$) and plane strain ($T = 1/\sqrt{3}$) and for $T = -1/\sqrt{3}$.

To remain conservative, a strain-state-independent criterion (such as Eq. 5.4) should not exceed the plane-strain fracture limit (dashed line in Figure 5.3b).

Bai and Wierzbicki (2008) note that the effect of the lode angle varies significantly for different materials and steel types. They report that DH36 steels demonstrate a low sensitivity to the lode angle, which has also been confirmed by MacLean (2012) and Gao et al. (2009). Choung et al. (2012) performed tests of EH36 material and concluded that for high stress triaxialities, the effect of the lode parameter is not important. This simplifies the shape of the fracture locus significantly.

No mesh scaling is proposed for the MMC criterion with respect to coarsely meshed shell structures.

(a) 3D fracture surface

(b) 2D fracture curve, plane stress
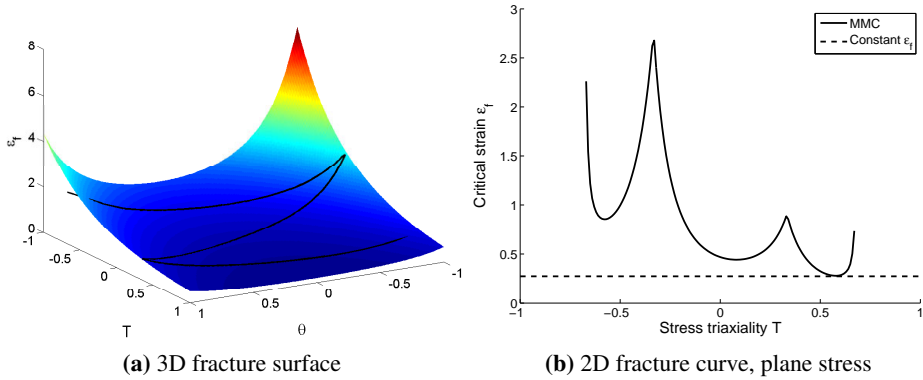
Figure 5.3: Fracture locus based on the modified Mohr-Coulomb model Bai and Wierzbicki (2010), not calibrated to a specific material.

5.2.6 Comparison of Stress- and Strain-state-dependent Fracture Criteria

The strain-state-dependent fracture criteria discussed above are plotted together in Figure 5.4 in principal stress and strain space and also as the critical equivalent strain vs. the strain-rate ratio and the stress triaxiality. To obtain a common reference for comparison of the strain-state dependence, all criteria in the figure are calibrated to yield the same value of critical strain in a plane strain state, as this is the lowest strain value than can be obtained through tests performed at different triaxialities.

In sheet metal forming, the FLD shown in Figure 5.4a is often used. Comparison of these criteria to the general trends observed in the experimental data in Figure 3.10 reveals that all criteria behave acceptably for negative minor strains. However, for increasing positive minor strains, the RTCL and CL criteria contradict the experimental results, predicting a decreasing fracture strain for increasing positive minor strains. This is an important discrepancy, considering that most fracture conditions for stiffened panel structures are characterized by positive minor strains (triaxialities above plane strain).

5.2.7 Safety Margin for Design

In the design of vessels, it may be desirable to add a safety margin, γ, to the fracture criterion for a number of reasons, including natural variations in material strength, material defects, weld defects, structural misalignment, small cutouts, and other effects that are not included in the numerical simulations. For the BWH criterion, this can be achieved through a reduction of the $\hat{\epsilon}_1$ parameter, e.g., $\hat{\epsilon}_1 = n/\gamma$. For RTCL, the ε_n parameter can be scaled down. Scaling of the strain-state-

(a) Principal strain space (FLD)

(b) Principal stress space

(c) Equivalent strain vs. strain-rate ratio

(d) Equivalent strain vs. stress triaxiality
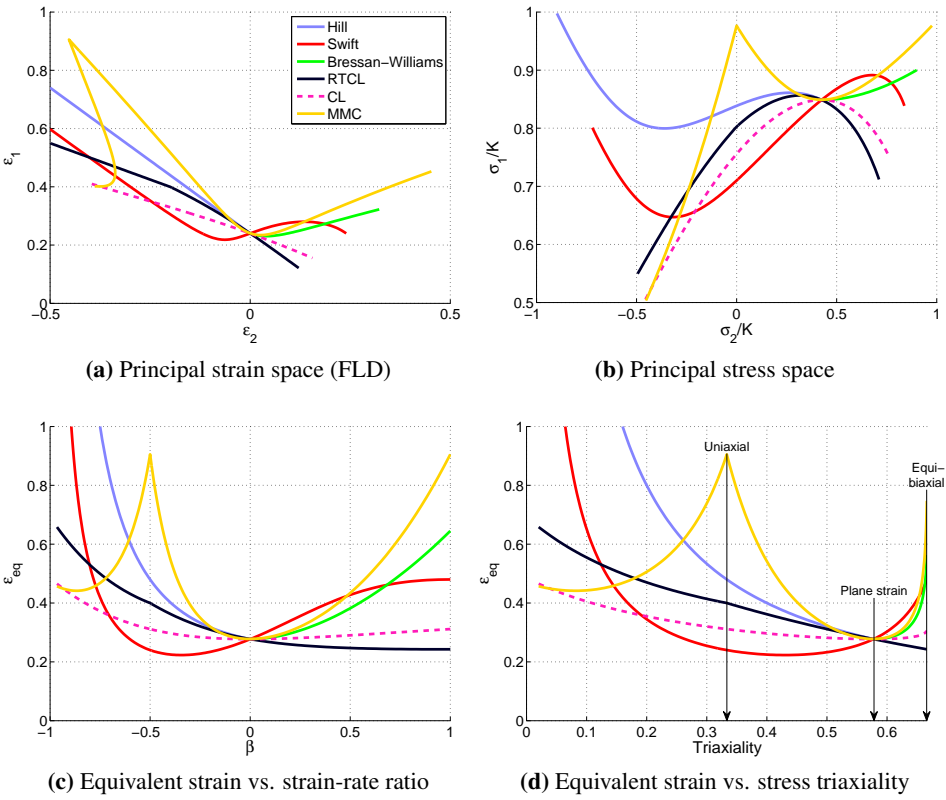
Figure 5.4: Fracture criteria visualized in various stress and strain spaces.

independent criteria can be performed directly on the critical value. No safety factor is included in the simulations presented below. In design, the value of γ is subject to determination.

5.3   Numerical Validation

To achieve a broad numerical validation of the material models, a multi-scale verification approach based on different types of experiments was selected. The simulations were performed using the explicit nonlinear finite element solver LS-DYNA MPP R7.0.0 (Hallquist 2006). The same numerical setup, based on proven best practices for the full-scale analysis of marine collisions, was used in all simulations.

- Quadrilateral *Belytschko-Lin-Tsay* shell elements with Belytschko-Wong-Chiang warping stiffness and five integration points over the thickness. No drilling stiffness.
- Automatic surface-to-surface contacts between bodies.
- Automatic single-surface contact for internal contacts on each body (e.g., the self-contact from a stiffener touching the plate after tripping).
- Standard stiffness-based hourglass control (Flanagan-Belytschko, option 4 in LS-DYNA).

No special numerical adjustments were made to match the experimental data for each test other than fitting the plastic parameters to the results of uniaxial tensile tests for each experiment. Thus, the achieved simulation results demonstrate the prediction accuracy of the material models given assumptions that can be made during design, when the correct solution is not known a priori. The tested criteria are listed in Table 5.1. The CL and MMC criteria were not investigated because of the lack of a mesh-scaling method.

The Damage criterion suffers from numerical instabilities, which caused a few simulations to crash before the end of the simulated experiment, namely, for the Alsos US, 2FB and Tautz experiments with certain mesh sizes. Such failures occur because damage is initiated in a circular pattern around the indenter and the strength is reduced sufficiently that erosion eventually creates an unconnected plate part that gains infinite velocity upon further contact. This instability worsens when the critical failure elongation is increased or the mesh size is decreased, and it is especially challenging in symmetric problems. Nevertheless, this criterion was included in the simulations, and its behavior is discussed up to the point of numerical instability. Strain-state dependence could mitigate this behavior.

A through-thickness integration point is failed by setting the stresses to zero once a failure criterion is satisfied. Final element erosion occurs once the middle integ-

Table 5.1: Fracture criteria used in the simulations

Name	Description
BWH w. dam	BWH criterion with damage and geometric mesh scaling
BWH no dam	BWH criterion without damage but with geometric mesh scaling
RTCL	RTCL criterion with geometric mesh scaling
GL	GL criterion on ε_1 and ε_{thin}
SHEAR	SHEAR criterion on ε_{eq}
RPC204	RP-C204 criterion on ε_{eq}
Peschmann	Peschmann's criteria on ε_{eq}
Damage	Ductile failure with coupled linear damage evolution

ration point fails. This approach is preferred over requiring all integration points to fail prior to erosion because nodal fiber rotations in elements undergoing large strains may limit the strains in the remaining integration points, thus resulting in no erosion of the element (see Hallquist (2006)). All criteria were implemented in user-defined subroutines. Although certain criteria (such as the RPC204 and GL criteria) have a minimum allowed mesh size, they were used for simulations in the same range of mesh sizes as the more general criteria.

The simulations considering the various criteria for all experiments, each with several meshes, produced a wealth of data. In a design situation, the force-indentation relation is of interest. If this relation is correct, then the energy dissipation vs. indentation behavior is known, and the extent of damage from a given collision scenario can be found. Both the energy dissipation at peak force and the total energy dissipation at the end of the experiment were used as assessment criteria for the various fracture criteria. All the force-displacement curves for all experiments, fracture models and mesh sizes are also shown in Appendix C.

The energy dissipation at peak force indicates how accurately a criterion can predict the capacity prior to rupture (important for shared-energy design), whereas the energy dissipation at the end of the experiment indicates the overall behavior of a criterion for a given test. For experiments with low resistance after peak force (such as the 1FB experiment from Alsos and Amdahl (2009)), the simulations may delay the peak force and thus also the final failure of the test specimen. In such cases, the simulated energy dissipation at end of experiment is measured at the simulated failure of test specimen rather than the point of experimental failure of the test specimen. Thus, if the peak force found in a simulation is delayed with respect to that in the experiment, the energy dissipation will be overestimated. The extracted energy dissipation levels are normalized to their experimental equivalents:

$$E_{norm} = E_{simulation}/E_{experiment} \qquad (5.30)$$

such that a normalized energy of 1.0 indicates a perfect match with the experiment for energy dissipation up to the peak force or throughout the entire simulation.

5.3.1   Material Tests

Uniaxial Tensile Test

Uniaxial tensile tests are often used for calibration of different fracture criteria, and should thus be captured well by all the tested criteria. The uniaxial tensile test from Tautz et al. (2013) is considered. as described in Section 4.6.1.

(a) Engineering stress-strain curve

(b) True strain in the neck
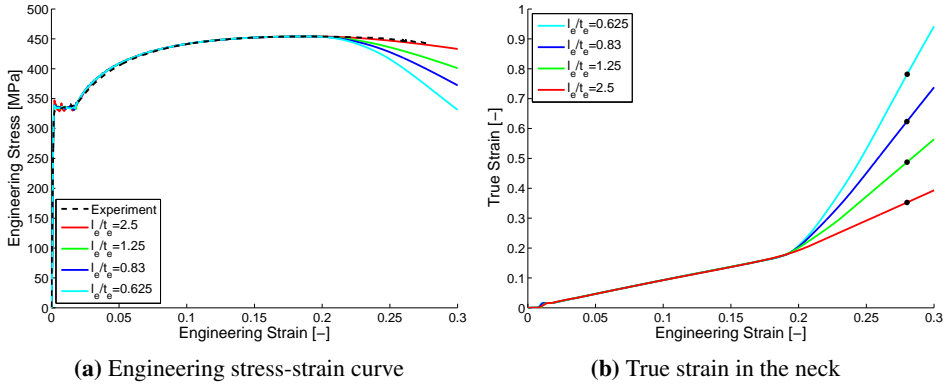
Figure 5.5: Uniaxial tensile test simulation results for element length vs. plate thickness ratios of $l_e/t_e = 0.63 - 2.5$.

Figure 5.5a shows the experimentally obtained curve and the simulation results for the material parameters given in Table 4.1. The different meshes exhibit similar responses up to the point of diffuse instability, near an engineering strain of 0.19. After this point, the results diverge, and the post-necking strength decreases with decreasing element length. To capture diffuse necking, it is important that the plastic hardening close to the ultimate tensile strength is defined accurately.

In Figure 5.5a, the coarsest mesh appears to simulate the experiment accurately, but this is merely coincidence. The response is simulated increasingly accurately with decreasing mesh size (this assertion is strictly valid only for solid elements), but strain-rate effects are needed to obtain the correct softening of the material in the post-necking region. Typically, the strain rate is approximately ten times higher in a localized neck than in the uniform part of the specimen, which is sufficient to

stabilize the neck growth. If this effect is not included, then the post-necking strain will be underestimated.

Figure 5.5b shows the true strain in elements in the neck for each mesh size. The divergence in strain rate as the neck forms is clearly revealed by the change in slope. The divergence of the true strain curves will primarily reflect the *material mesh dependence*, as the deformation localizes to the width of a single element. If the width of a local neck is smaller than the element, the element will be overly stiff and requires compensation on the fracture strain. A simple mesh correction can be applied by defining the critical strain as a function of the element length, e.g., by considering the true strain at fracture vs. element length (marked points in Figure 5.5b), as is done when calibrating the SHEAR criterion.

Figure 5.6 shows the engineering stress-strain curves for the tested fracture criteria in a uniaxial tensile test. The curves are identical up to the maximum force, but the subsequent strengths exhibit different mesh dependencies among the tested fracture criteria.

Formability Tests

The formability tests in Broekhuijsen (2003), as described in Section 4.6.2, is used in the following.

Figure 5.7a shows the experimental force-indentation curves. Figure 5.7b shows the normalized energy at peak force. A clear variation in the prediction accuracy is observed among the different fracture criteria. The RTCL criterion yields the smallest scatter and is closest to the experimental results.

Plate Tearing Tests

Simonsen and Törnqvist (2004) investigated fracture propagation in shell structures through a tearing experiment, in which a mode-I crack was driven approximately 400 mm through a plate under controlled conditions. Many tests were performed using various materials and thicknesses; in the following, the experiments on 5 and 10 mm plates of normal-strength steel are considered.

Plates of 700×580 mm were modeled, with an initial crack extending 150 mm into the long edge of the plate. The experimental crack had a blunt crack tip with a radius of 5 mm. In the simulations, this crack was created by simply removing elements 150 mm into the plate, leaving the crack tip sharp. This simplification is expected to lead to somewhat premature erosion of the initial elements. Four meshes were investigated; with characteristic element lengths of 5, 10, 20 and 40 mm. Figure 5.8 shows the model in the initial and intermediate configurations during the simulation. The material parameters are given in Table 5.2 and are the

(a) BWH w. dam

(b) BWH no dam

(c) RTCL

(d) GL

(e) Peschmann

(f) RP-C204

(g) SHEAR

(h) Damage
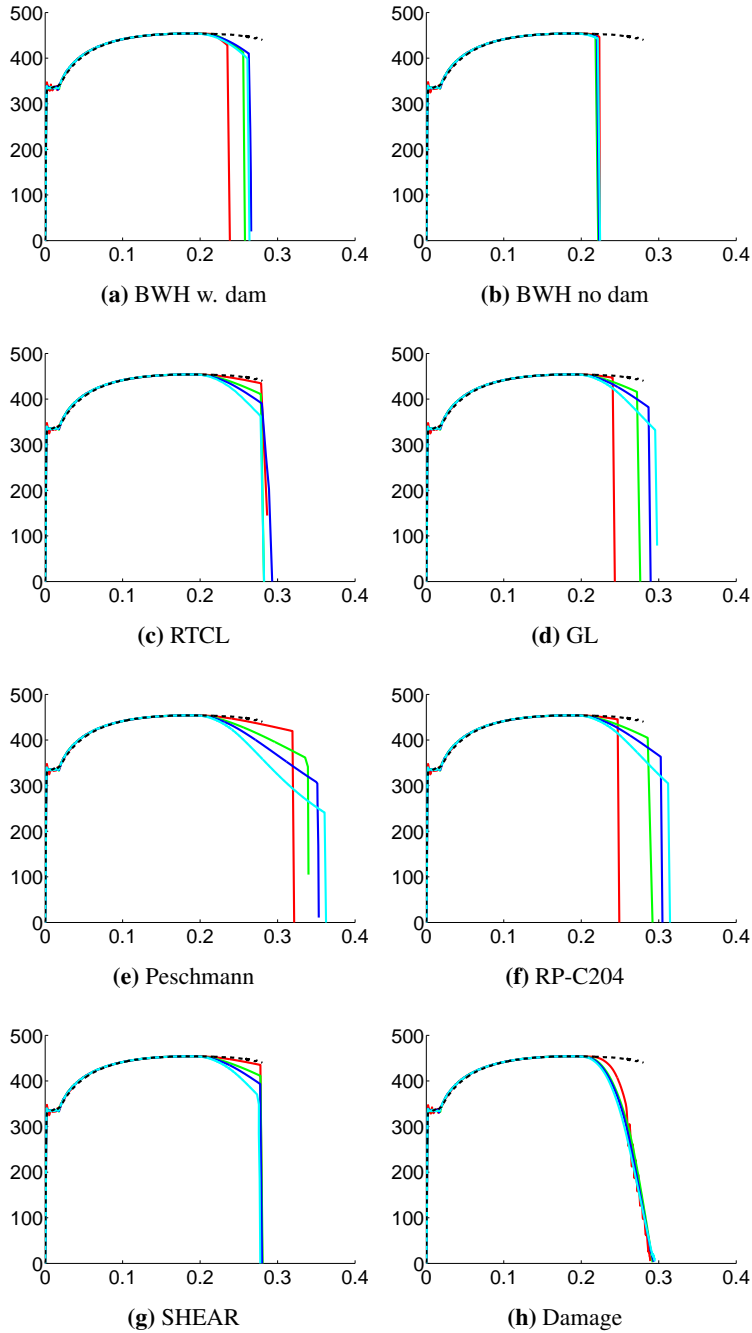
Figure 5.6: Engineering stress [MPa] vs. strain [-] curves from uniaxial tests for various fracture criteria and mesh sizes. The tested mesh sizes are indicated by the same colors used in Figure 5.5.

(a) Experimental force-indentation curves

(b) Normalized energy at peak force
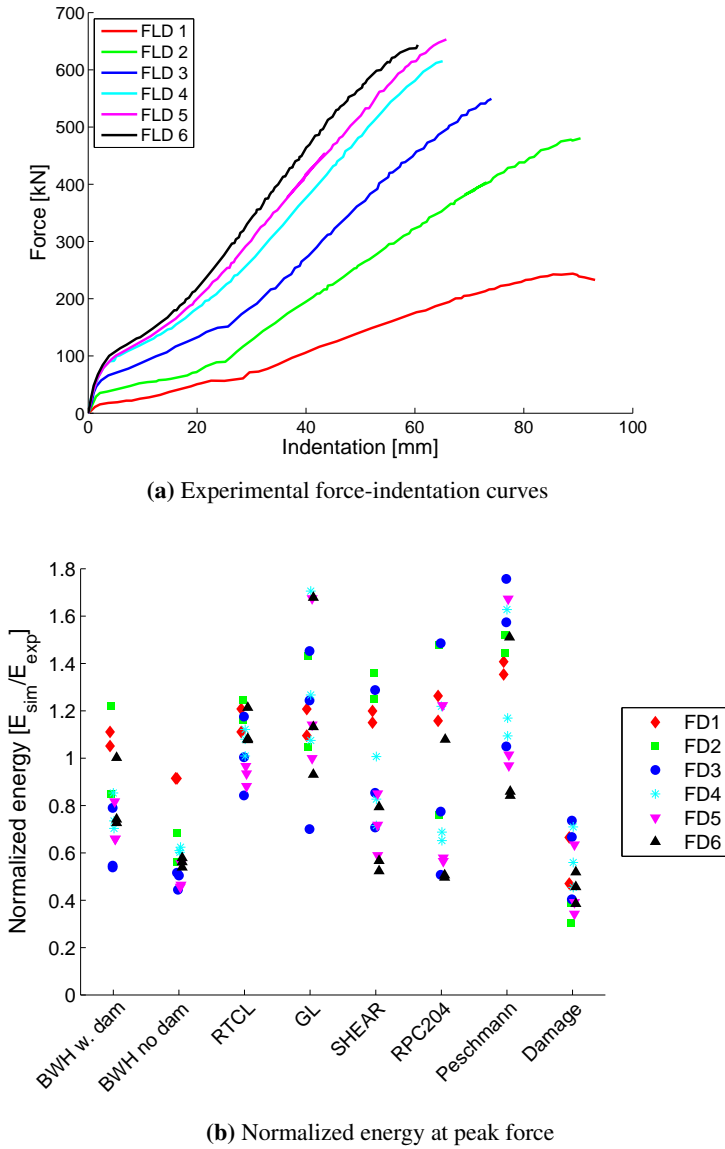
Figure 5.7: Force-indentation curves and normalized energy dissipation at peak force for the formability simulations. FD1-6 marks the different formability experiments, and each mesh size has a separate data point for each experiment.

same as those used in Simonsen and Törnqvist (2004).

Table 5.2: Material parameters for the plate tearing experiments Simonsen and Törnqvist (2004)

σ_0 [MPa]	E [GPa]	K [MPa]	n	$\varepsilon_{plateau}$
273	210	650	0.23	0.01

| (a) | (b) | (c) | (d) |
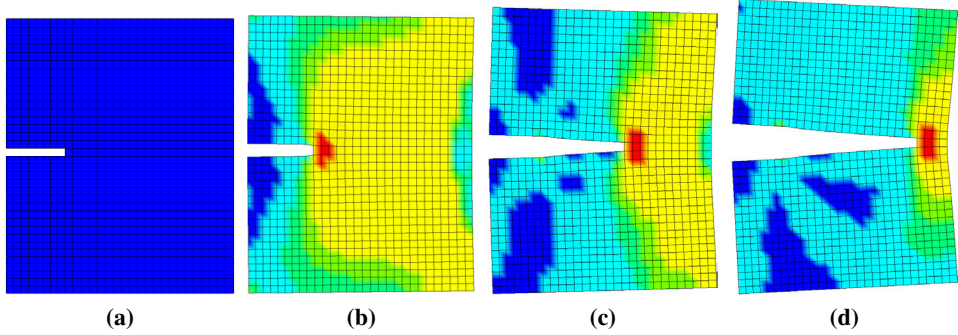
Figure 5.8: FE mesh (20 mm) and crack propagation behavior for the tearing experiments. The fringes represent equivalent stress, ranging from 0 (blue) to 400 (red) MPa.

Figure 5.9 shows the experimental force vs. crosshead displacement and the normalized energy dissipated at the end of the experiment for the various fracture criteria. The strain-state-dependent criteria exhibit less scatter, and both RTCL and BWH with damage yield good average results. Of the simpler criteria, the SHEAR and Peschmann criteria exhibit the least scatter.

Summary of Material Tests

Table 5.3 shows the means μ and standard deviations σ_{STD} of the normalized energy for the simulations of material tests with the various fracture criteria (based on the data presented in Figs. 5.7b and 5.9b). The performances of the strain-state-dependent criteria are superior with respect to the standard deviations of their predictions, but there is also significant scatter with respect to the mean predicted energy. If a fracture criterion demonstrates good performance in these simple material tests, its reliability is also likely to be good for other types of tests.

5.3.2 Impact Tests

Alsos and Amdahl Indentation Experiments

The indentation experiments from Alsos and Amdahl (2009), as described in Section 4.6.3, are used in the following.

(a) Experimental force-indentation curves

(b) Normalized energy at fracture
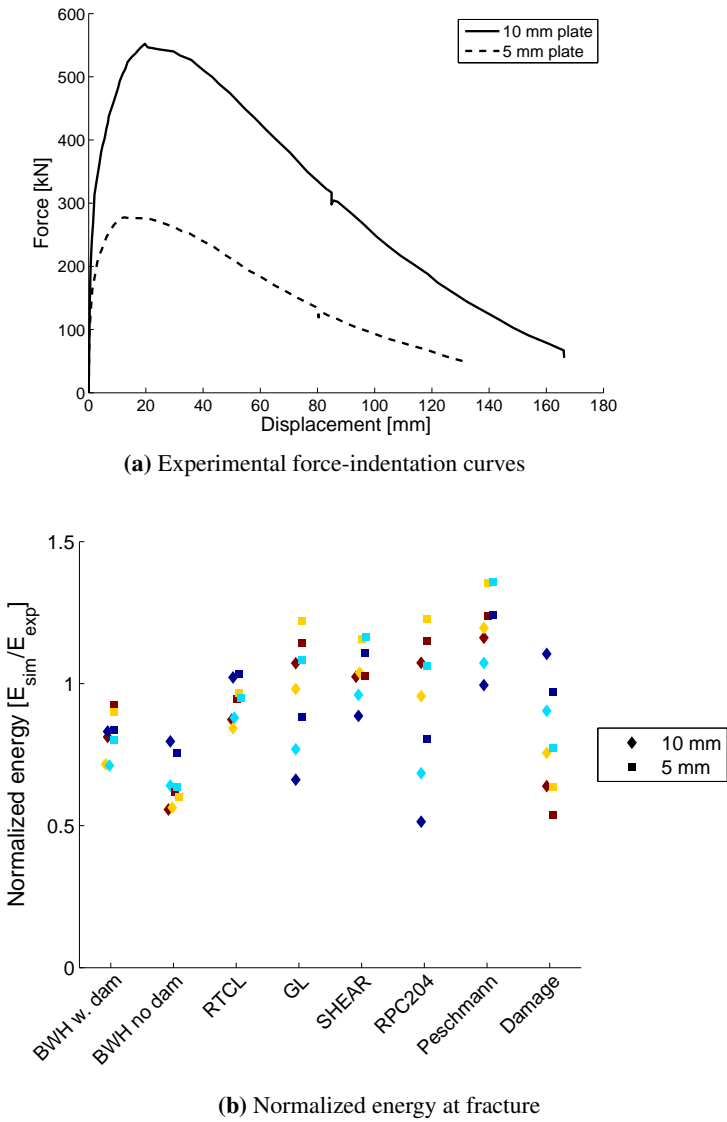
Figure 5.9: Force-displacement curves and normalized energy dissipation at peak force for the tearing simulations. The colors from dark blue to dark red represent decreasing mesh sizes of 40, 20, 10 and 5 mm.

Table 5.3: Means and standard deviations of the normalized energy for the material tests

	BWH w. dam	BWH no dam	RTCL	GL	SHEAR	RPC204	Pesch-mann	Damage
μ	0.81	0.61	1.03	1.15	0.95	0.91	1.27	0.6
σ_{STD}	0.16	0.13	0.12	0.28	0.24	0.32	0.26	0.21

Figure 5.10 shows the normalized energies at peak force and at the end of the experiment for the US, 1FB and 2FB simulations with mesh sizes of $l_e/t_e = 1$, 2, 5 and 10. None of the criteria exhibits consistent prediction behavior for the US simulations, in which fracture occurred in a free plate field. The simulations demonstrate that all meshes are capable of properly resolving the strain gradients. Geometric mesh scaling of the fracture behavior is therefore not necessary, and when it is applied, it increases the scatter in the US experiments. In the 2FB experiments, fracture initiation occurred at the stiffeners, resembling a full-scale scenario, and was captured with less scatter using the *BWH w. dam, BWH no dam, RTCL* and *SHEAR* criteria. High strain concentrations were observed in the 1FB experiments, both in the free plate and at the stiffener-plate interface. This test is more difficult to model because only strain concentrations close to the stiffener should be accounted for through geometric mesh scaling.

The stress-state-independent criteria predict an increase in the peak force with decreasing mesh size. The US simulations converge toward the experimental solution but, for the stiffened panels, strain-state-independent criteria significantly overestimate the peak force in the case of fine meshes. Applying the minimum mesh requirement of $l_e/t_e \geq 5$ mitigates this problem, but the peak force is still overestimated. The strain-state-dependent criteria approach the experimental values as the mesh is refined.

Tautz et al. Indentation Experiments

The experiments from Tautz et al. (2013), as described in Section 4.6.4, are used in the following, but now with modeling of the supporting structure (near rigid) and with new meshes over a larger range of l_e/t_e-ratios.

During construction of the test specimens, cutouts around the stiffeners were created in the web frames in accordance with typical ship manufacturing procedures. FE models were created with and without these cutouts, each with mesh sizes of 2.5, 5, 8.25 or 10 times the plate thickness, resulting in eight simulations per criterion. The FE models contained the supporting structure with boundary conditions close to the experimental ones, similar to what was done by Tautz et al. (2013). Material parameters are listed in Table 4.4.

Figure 5.11a shows the normalized energies for all criteria. The scatter of the predictions is smaller for the Tautz experiments than for the Alsos tests, both at first peak force and for the entire simulation. The mean energy at first peak force varies significantly among the criteria, with the strain-state-dependent criteria yielding results closest to the experimental values and with significantly less scatter. However, when the entire experiment is considered, the simpler criteria exhibit less
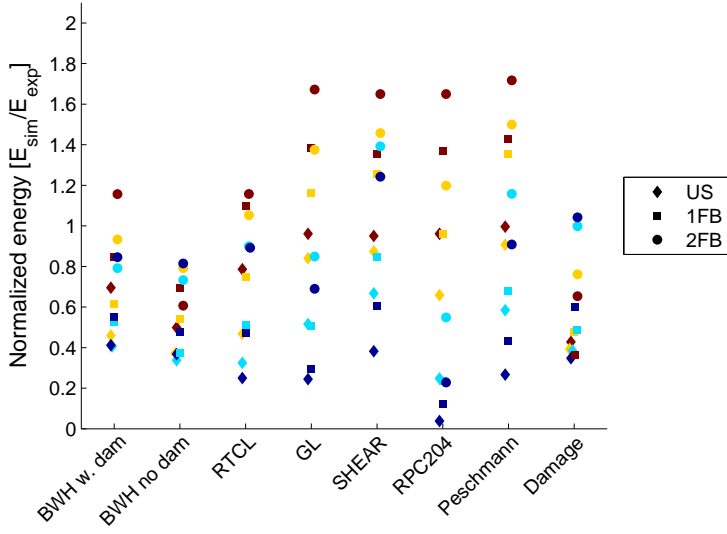
(a) Normalized energy at peak force
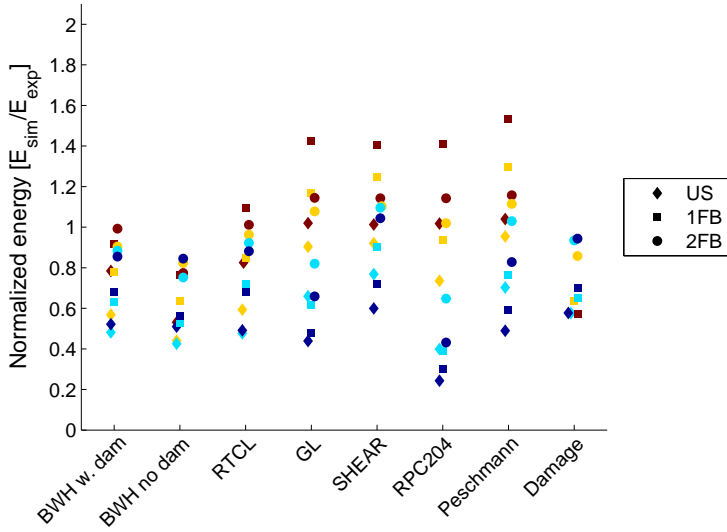
(b) Normalized energy at end of experiment

Figure 5.10: Force-displacement relation and normalized energy at peak force for simulations of the experiments performed by Alsos and Amdahl (2009). The colors from dark blue to dark red represent decreasing mesh sizes of $l_e/t_e = 10, 5, 2$ and 1.

scatter among the various mesh sizes. None of the criteria demonstrates a clear trend of convergence in the dissipated energy as the mesh size is decreased.

Impact Experiments Reported by Peschmann

Peschmann (2001) reported data from large-scale collision tests performed on two inland waterway barges in the Netherlands during 1997 and 1998 by the research organization TNO, also documented in their report Wevers and Vredeveldt (1999). An 800-ton tanker struck another 1400-ton tanker at a $90°$ angle at approximately 4 m/s. The striking vessel was fitted with a rigid bulb, and the struck vessel had a total of four different deformable side panels. The collision with test section 3 is considered for comparison herein because this panel most closely resembled a full-scale ship structure.

Figure 5.12 shows the structures of the test section and the indenter. The tested section had a plate thickness of 5 mm, vertical flat bar stiffeners (FB100×5) spaced 225 mm apart and 6 mm thick web frames with large manholes spaced 1125 mm apart. Horizontal stringers, also with a 5 mm plate thickness, were placed approximately 1130 mm apart. The scale was approximately 1/3 that of typical full-scale ship structures. The material parameters used are listed in Table 5.4. A static friction coefficient of 0.3 was assumed.

Table 5.4: Material parameters for the experiments reported by Peschmann (2001)

σ_0 [MPa]	E [GPa]	K [MPa]	n	$\varepsilon_{plateau}$
284	206	680	0.195	0.0

Because the collision experiment was performed under floating conditions without laboratory control of the boundary conditions, the exact impact location and impact angle are uncertain. Consequently, it was assumed that the impact occurred perpendicular to the struck hull and at the most probable location identified by Ehlers et al. (2008). Thus, the simulated conditions might not match perfectly with the experimental conditions. The simulations were performed for a constant velocity of the rigid bulb of 4 m/s.

Figure 5.13 shows the normalized energies for mesh sizes of $l_e/t_e = 5$ and 10. Most criteria yield good estimations of the peak force for these mesh sizes. However, the fracture estimate obtained using the RPC204 criterion is premature compared with the experimental findings. The Peschmann criterion exhibits superior consistency vs. mesh size, but it should be noted that this criterion was calibrated against these tests.
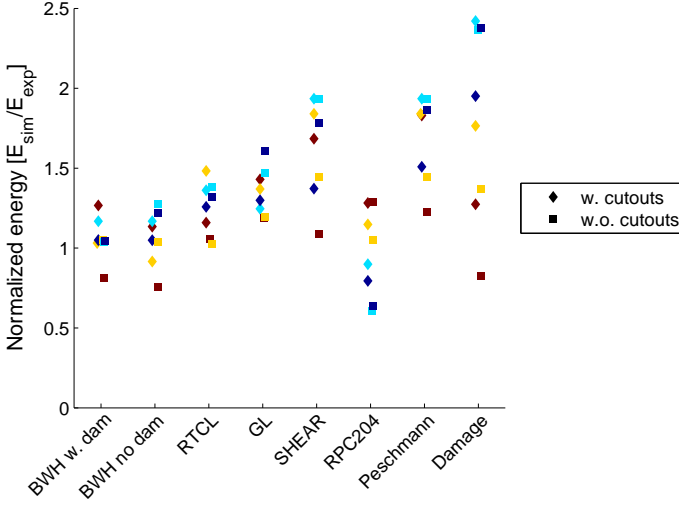
(a) Normalized energy at first peak force
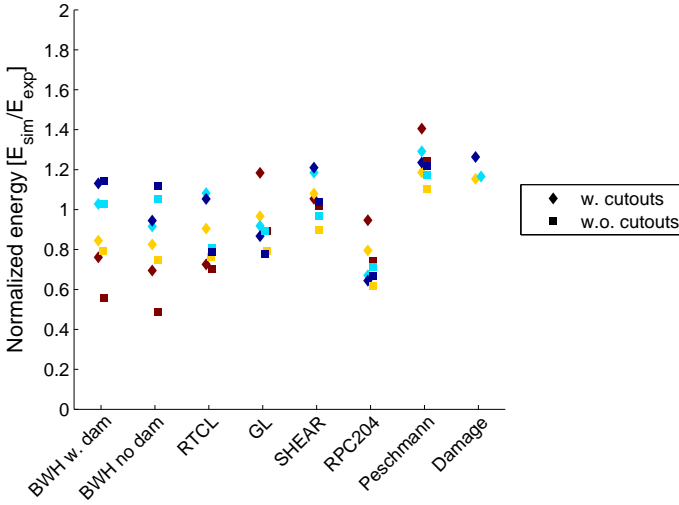
(b) Normalized energy at end of experiment

Figure 5.11: Normalized energies for simulations of the Tautz experiments. The colors from dark blue to dark red represent decreasing mesh sizes of $l_e/t_e = 10$, 8.25, 5 and 2.5.

(a) Cut along the centerline of
the impact

(b) Frame and stringer layout
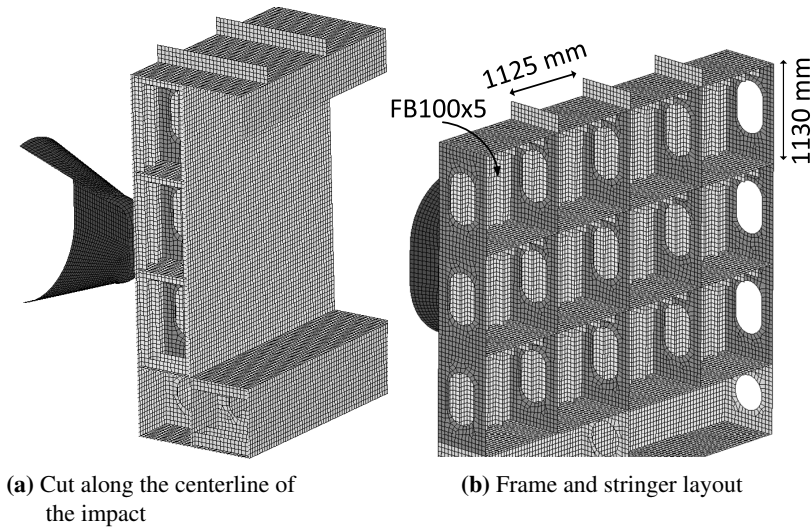
Figure 5.12: Large-scale collision experiments on test section 3 in Peschmann (2001), meshed with 50 mm elements ($l_e/t_e = 10$).

5.3.3 Discussion of Mesh Scaling

Figure 5.14 shows the strain at peak force obtained from simulations of the indentation experiments without including fracture, from which a mesh-dependent fracture strain could be reverse engineered. For most of the stiffened panels, the critical strain decreases with increasing mesh size. The equivalent strains at the top surface exhibit a stronger dependence on mesh size than that at the mid-surface of the element. Note that the initiation of fracture will begin prior to the peak force; hence, the fracture initiation strain is generally lower than the values in Figure 5.14.

For the Alsos and Amdahl tests, both the US and 1FB simulations demonstrate a limited mesh dependence, whereas the 2FB experiment exhibits a clear decreasing trend with increasing mesh size. For the US experiment, fracture occurred in the free plate field, and the strain concentrations were captured adequately by the various meshes used in the simulations. For the 2FB panel, fracture occurred in the plate close to the stiffener, and the various meshes did not capture the strain concentration with sufficient accuracy. The 1FB panel represents, in some sense, a combination of the two fracture locations; fracture occurred close to the stiffener, but the numerical simulations show a higher strain concentration in the unsupported plate field. The 1FB results exhibit a fairly low dependence on element length.

Thus, for the 2FB test of Alsos and Amdahl (2009), strain localizations are not cap-
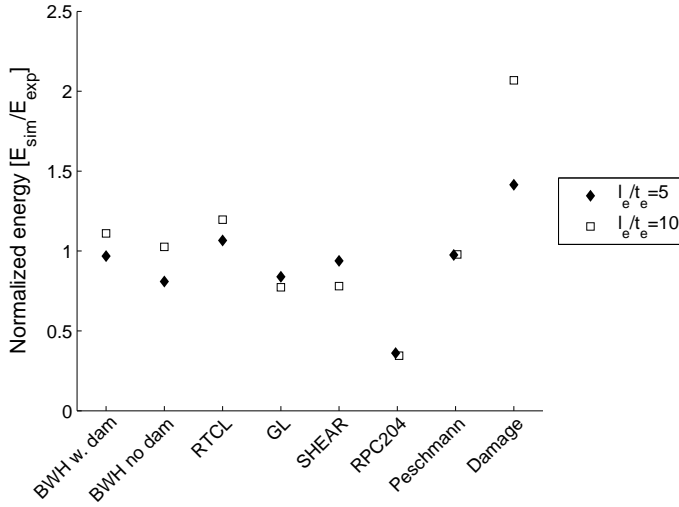
(a) Normalized energy at peak force
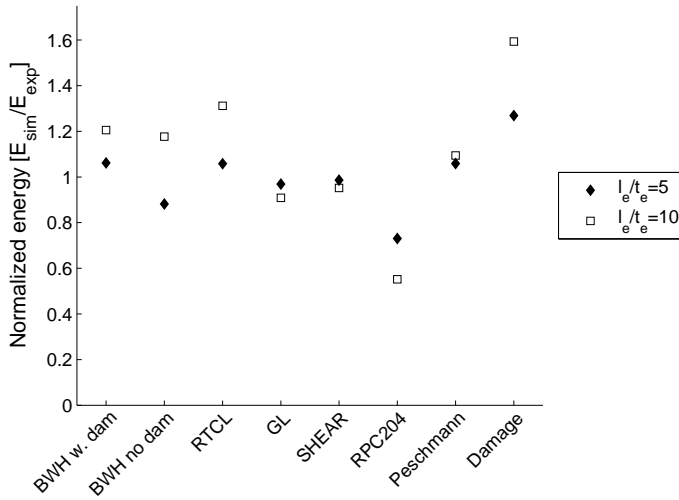
(b) Normalized energy at end of experiment

Figure 5.13: Normalized energies for simulations of the Peschmann experiments.
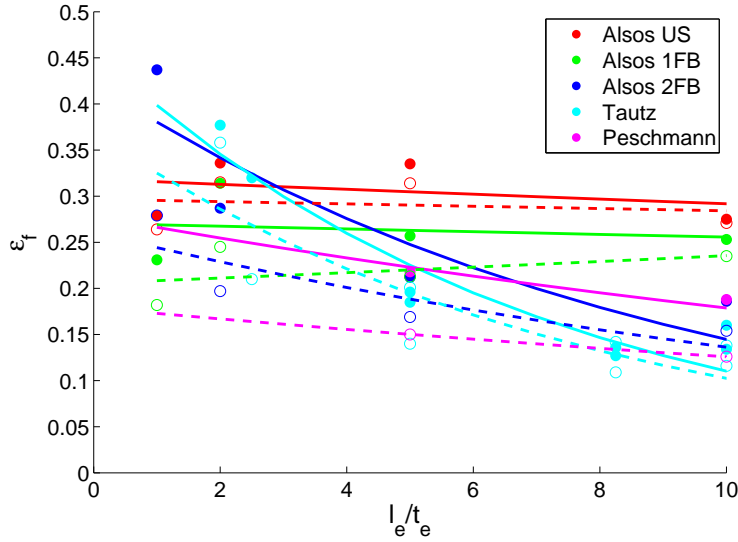
Figure 5.14: Equivalent strain at peak force vs. mesh size. The filled circles correspond to the plate surface, and the open circles correspond to the middle integration point. The solid lines are curves fitted to the top-surface data, and the dashed lines are curves fitted to the mid-surface data. No fracture criterion is applied.

tured properly by large meshes, and geometric mesh scaling is needed. However, the US simulations show that the strains are properly captured, and including the geometric mesh-scaling effect serves only to reduce the estimate of the plate capacity. Both the US and 1FB experiments require material mesh scaling. Fracture criteria that do not distinguish between the mesh-dependence effects will not be able to capture this difference. No solution has been proposed for a mesh-scaling approach that adequately accounts for the difference between the US and 2FB experiments, with the exception of applying geometric mesh scaling to intersecting elements only.

The simulations of the experiments performed by Tautz et al. (2013) show a strong dependence on mesh size, even stronger than that of the 2FB panel. From the simulations of the Peschmann (2001) experiment, a slightly lower dependence is observed. The simulated triaxiality at fracture will change somewhat with the mesh size, as more of the behavior around the local neck is included with an increasing element size.

Figure 5.15 shows the geometries of the indenter with respect to the 2FB and Tautz panels at peak experimental force. These tests represent the two most controlled experiments among the available impact experiments on stiffened panels. The de-
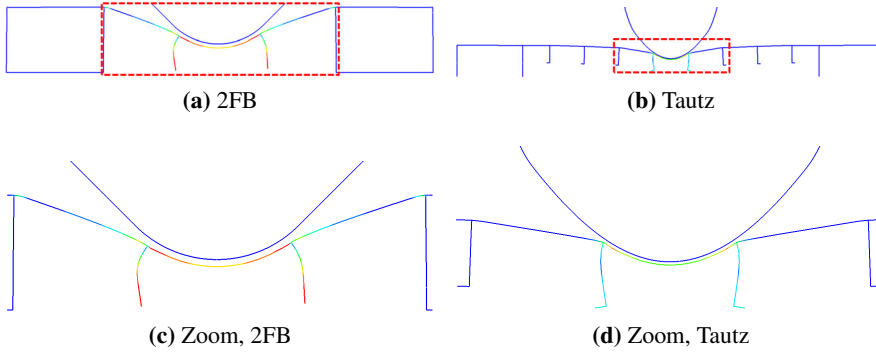
Figure 5.15: Cross sections of stiffened panels at peak experimental force. The contours represent plastic strains from 0 (blue) to 0.2 (red). The areas marked in (a) and (b) are enlarged in (c) and (d).

formation mode in the Tautz simulation is more localized between two stiffeners, inducing large strain concentrations in the plate inside of the stiffener, which leads to fracture. The deformation mode in the Alsos 2FB simulation is more global throughout the panel, mobilizing more membrane forces at significantly elevated plastic strains, and the local plate curvature between the stiffeners is smaller than that in the Tautz simulation. The difference in local curvature arises from the relative strength of the plate and stiffeners; in the model of the Tautz experiments, the stiffeners were considerably stronger than the plate strength compared to the Alsos experiments. The increased local curvature explains the increased mesh sensitivity of the Tautz experiments that is evident in Figure 5.15. It may also explain the decreased mesh sensitivity of most fracture criteria for these tests, as the fracture is localized over a smaller area and is thus less sensitive to the simulated fracture path.

A typical full-scale bulbous bow of a supply vessel has a radius of curvature in the range of two meters in the vertical plane and approximately one meter in the horizontal plane (these radii are smaller for high-speed vessels). Compared with these values, the radius of the indenter is relatively small with respect to the stiffener spacing for both the Alsos and Tautz experiments. For the 1FB and US experiments, the full-scale equivalent would be an even sharper object penetrating on or between two stiffeners or a large panel with very weak stiffeners undergoing global deformation. Several stiffeners will be deformed in a longitudinally stiffened vessel or in the case of a blunt bulb. For a transversely stiffened vessel or a sharp bulb, the indentation may be more local. Thus, both the 2FB and Tautz experiments should be captured well by a fracture criterion that is suitable for coarsely

meshed stiffened panel structures.

The mesh sensitivity shown in Figure 5.14 is increasing for an increasing local curvature of the plate close to a stiffener. To achieve general applicability to all tested experiments, the mesh scaling should be capable of accounting for the interaction between the bow and the side, including the instantaneous strain states and the local plate curvatures. At present, such a mesh-scaling law does not exist. Improving the prediction of the *geometric* mesh dependence is a valuable topic for further research.

5.3.4   Discussion of the Prediction Accuracy

Based on the 47 different simulations performed for each criterion (simulated experiments with different element sizes), the normalized energy was tabulated to assess the robustness of each fracture criterion at first peak force and at the end of the experiment/simulation. Table 5.5 shows the calculated means μ and standard deviations σ_{std}, and Figure 5.16 shows the results graphically.

Table 5.5: Means and standard deviations of the normalized energy. The stiffened panel results contain only data from the Alsos 2FB, Tautz and Peschmann experiments. The Damage criterion is not included for the end of simulation results because of the few available stable simulations.

	All simulations at first peak force		Stiffened panels at first peak force		Stiffened panels at end of simulation	
	μ	σ_{std}	μ	σ_{std}	μ	σ_{std}
BWH w. dam	0.83	0.22	1.02	0.14	0.94	0.18
BWH no dam	0.69	0.24	0.95	0.21	0.86	0.18
RTCL	0.99	0.26	1.16	0.18	0.93	0.17
GL	1.1	0.35	1.21	0.31	0.92	0.14
SHEAR	1.09	0.38	1.47	0.36	1.06	0.09
RPC204	0.84	0.4	0.86	0.43	0.74	0.19
Peschmann	1.26	0.39	1.49	0.38	1.15	0.14
Damage	0.85	0.59	1.52	0.63	-	-

Considering all the simulations, the mean value at first peak force is predicted within 30% for all criteria, and the standard deviation is between 22 and 59%. The high standard deviations indicate that the criteria in general are not sufficiently accurate with respect to the strain-state and mesh dependence.

If only the first peak forces in the stiffened panel experiments are considered, for which the strain localization and failure mode are closer to those of a full-scale collision scenario, the strain-state-dependent criteria behave significantly better than the strain-state-independent criteria in terms of both the mean and standard deviation. The difference in the prediction accuracy of the peak force is similar to

that seen in the material test results in Table 5.3.

The situation changes when the total energy at the end of the simulation is investigated. All criteria show a reduction in mean energy. The strain-state-dependent criteria have almost the same standard deviation, but the strain-state-independent criteria now show a significant improvement in standard deviation. Thus, as the total deformation process becomes increasingly complex, with the occurrence of several large fractures, buckling, etc., the simpler criteria are able to represent the combined process better than the strain-state-dependent criteria.

When the energy dissipation is in the ductile regime with respect to the struck vessel, the choice of fracture criterion is of little importance provided that the striking bow will penetrate significantly into the side of the ship. This is the case for slender bulbous bows that are significantly stronger than the side of the struck ship. This result is not particularly surprising; if a rigid bulb penetrates a double-sided structure, it will create a hole of a similar shape as long as *any* fracture criterion is applied. However, in the shared-energy regime, in which both the striking and struck bodies are expected to dissipate significant energy, large membrane stresses will activate prior to fracture. Such conditions have generally not been achieved in indentation experiments because the complexity of the tests is limited by both cost and the test apparatus. The results of experiments with larger membrane stresses and realistic boundary conditions may affect the conclusions regarding the simulated fracture responses for such cases as well as energy dissipation in the ductile regime.

In the shared-energy regime, it is important to obtain good predictions of the struck ship's capacity prior to the fracture of the outer shell. Strain-state-dependent criteria are therefore preferred. Both the BWH criterion with damage and the RTCL criterion perform quite well in this regard. The safety margin should most likely be increased in the case of the RTCL criterion, considering its overestimation of the mean energy at peak force.

Figure 5.17 shows the convergence of the mean and standard deviation with decreasing mesh size. With decreasing mesh size, the strain-state-dependent criteria exhibit decreasing standard deviations and convergence toward the experimental results for the dissipated energy. The strain-state-independent criteria also exhibit decreasing standard deviations with decreasing mesh size, but they converge to values of energy dissipation that are too high compared with the experimental findings. Fine meshes capture the strain state more accurately and thus improve the accuracy of the strain-state-dependent criteria. Note that the dataset shown in Figure 5.17 is limited and that the represented values are only indicative of the qualitative behavior of the criteria.
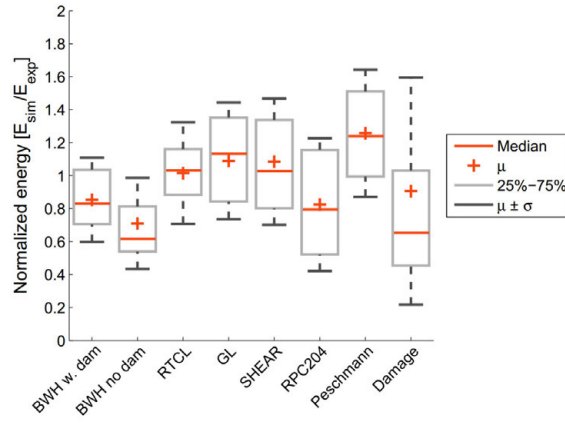
(a) All simulations, peak force
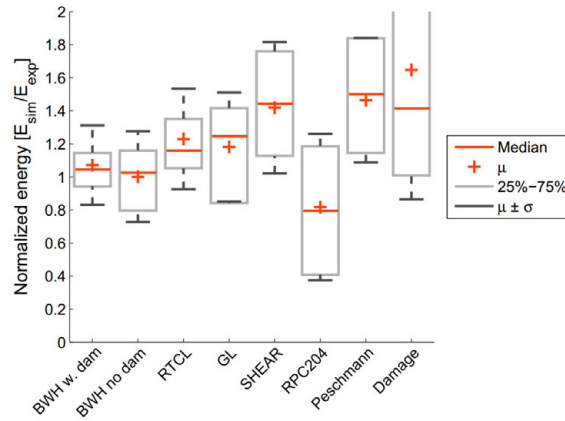
(b) Stiffened panels, peak force
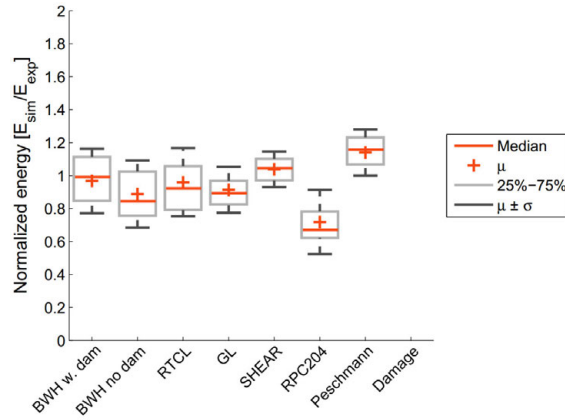
(c) Stiffened panels, entire simulation

Figure 5.16: Distributions of normalized energy for all tested fracture criteria. The Damage criterion is not included in (c) because of the few available stable simulations.
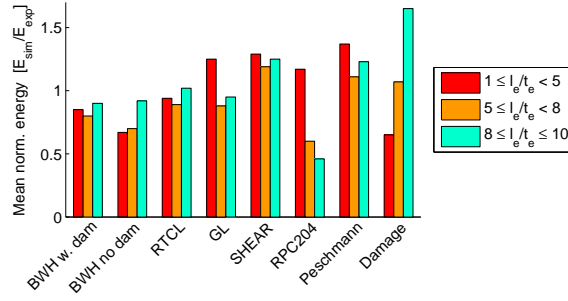
(a) Mean energy at peak force
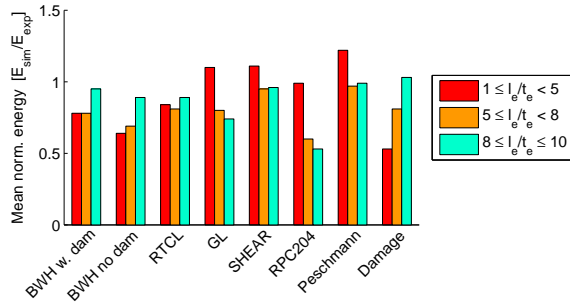
(b) Mean energy at end of simulation
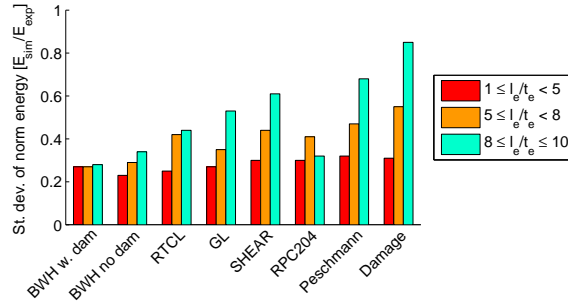
(c) Standard deviation of energy at peak force
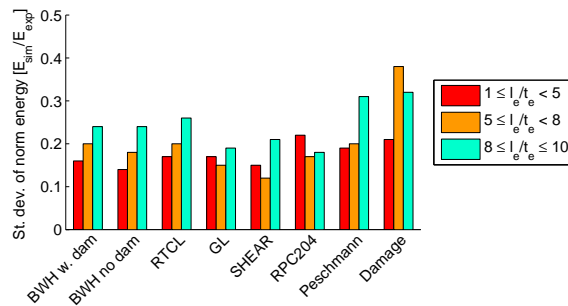
(d) Standard deviation of energy at end of simulation

Figure 5.17: Evolution of the normalized means and standard deviations as functions of mesh size.

For most of the experiments, initial fracture occurred at a triaxiality somewhat above plane strain. According to the material formability experiments represented in Figure 3.10, the critical strain should increase from plane strain toward equi-biaxial tension. Kõrgesaar et al. (2014) showed that the material mesh dependence is reduced with the transition from plane strain to equi-biaxial tension. The RTCL criterion exhibits a decrease in the critical strain from plane strain toward equi-biaxial tension, and the mesh-scaling technique is constant for all stress states. Theoretically, therefore, this criterion should produce premature fracture predictions. Despite these "deficiencies", however, the RTCL criterion performs surprisingly well. The success of this criterion may be attributable to two competing effects, namely, the strain-state-independent mesh scaling may be balanced by the tendency toward premature fracture.

For the strain-state-independent criteria, the convergence toward an excessively high resistance can be explained in terms of the low actual critical strain near plane-strain conditions, as observed in material tests (Figure 3.10). In the case of more refined meshes, higher strains are allowed, and the critical strain to fracture is overestimated between uniaxial and equi-biaxial tension. A minimum mesh size allowance is thus required for all strain-state-independent criteria, similar to the $l_e/t_e \geq 5$ limit that is imposed on both the GL and RP-C204 criteria, to ensure that the maximum critical strain does not exceed the critical strain in plane-strain tension.

The energy up to the first peak force for stiffened panels is not notably different in the case of the SHEAR criterion, which is individually calibrated for each specific material used, compared with that in the case of the prescriptive GL criterion. When the entire simulation is considered, the performance of the SHEAR criterion is somewhat better than that of the GL criterion.

Marinatos and Samuelides (2015) recently investigated the SHEAR criterion, the RTCL criterion and the BWH criterion without damage in simulations of several experiments using ABAQUS with user-defined materials. Several of the same tests are simulated herein with the same fracture criteria and similar meshes. Generally, the agreement is good, small differences arise in the force-displacement relation for some of the criteria. Marinatos and Samuelides (2015) did not use the mesh-scaled version of the BWH criterion, and their simulations do not match the original simulations using the BWH criterion reported in Alsos et al. (2009). The discrepancies indicate that even the application of the same fracture criterion to the same experiments still involves certain human factors in calibration and implementation, which further add to the total simulation uncertainty for an engineer in a design situation. Compared with Marinatos and Samuelides (2015), the simulations presented herein cover a wider range of mesh sizes, with more meshes per

experiment, but fewer experiments in total.

5.3.5 Discussion of Experimental Uncertainty

These investigations have revealed significant variations in the abilities of the proposed criteria to correctly predict fracture initiation in various experiments using coarse element meshes. There are several reasons for this variation:

1. The criteria do not include all effects that contribute when the mesh is large ($l_e/t_e >> 1$). This is most relevant to geometric effects, i.e., pre-necking strain concentrations that are not captured due to the too coarse mesh discretization.
2. The considered experiments were conducted by different researchers in different laboratories. Most likely, they are not "perfect" in all respects: for example, how well the material properties were measured; how well the samples were fabricated with respect to welding, imperfections, etc.; and how well the results were measured.
3. All considered experiments are unique; if two nominally identical tests had been performed, the results would not have been exactly identical, thereby demonstrating the inherent natural uncertainties in the measurements.

Given a sufficient number of parameters, it is obviously possible to calibrate most of the criteria to accurately match a particular test. Given a known solution, several numerical parameters can also be tuned to improve the agreement with the test results. However, extreme care should be exercised in doing so for the following reasons:

- the fracture criterion may be calibrated against a "bad" test, or
- the deficiencies of the fracture criterion may be disguised, and the criterion may perform poorly for other structures, strain states or scales.

Finally, bias and statistical variations in structural resistance predictions are not unique to the present application to fracture initiation and propagation in ship collision analysis. Even for such a comparatively simple problem as the maximum bending moment (stress) in a fabricated pipe, the design formula provided in the ISO-19902 (2007) for offshore structures has a bias of 1.1 and a coefficient of variation of 8.5%. From this perspective, we consider the fracture criteria to perform reasonably well, as long as the accuracy is properly considered when evaluating simulation results.

5.4 Analysis of a Full-scale Collision

Martens (2014) conducted a simulation of a full-scale collision that occurred in 2012 in the German harbor *Travemünde* between the RoPax vessels *URD* (struck) and *NILS HOLGERSSON* (striking). The struck vessel was moored alongside the quay when the striking vessel lost control during maneuvering and impacted the struck vessel at 6.5 knots. The impact direction and velocity were determined from AIS data and documented in the accident investigation report (Bundesstelle für Seeundfalluntersuchung 2012). The struck ship suffered considerable damage both above and below the waterline (Figure 5.18a), whereas the striking ship received only minor plate dents (Figure 5.18b). This was to be expected, as the NILS HOLGERSSON is ice strengthened to class E2 in GL notation, equivalent to the Baltic ice class ICE-1B. The maximum indentation into the struck vessel was 7.6 m according to Martens (2014).

The mass of the NILS HOLGERSSON was 20500 tons at the draft she had at impact. The added mass of the vessel is not known; the added mass may have increased as a result of shallow water effects due to the shallow depth (10 m) of the harbor. Under the assumption of 10% added mass, the total available kinetic energy was 126.5 MJ. In the following simulations, the struck vessel is simply supported along its centerline, and the striking vessel assumed to have only a longitudinal degree of freedom. Martens (2014) estimated that with these assumptions, 12.1 MJ of the dissipated energy was not included in the simulations, being consumed in the motions of the striking and struck vessels and the deflection of the fender system along the quayside. This leaves 114.4 MJ to be dissipated through strain and friction. Figure 5.19a shows the impact geometry.

(a) URD. Red line indicates puncture by bulbous bow

(b) NILS HOLGERSSON

Figure 5.18: Damaged structures after collision, from Martens (2014).

(a) Impact scenario, from Martens (2014)

(b) Vessel deformation after simulation
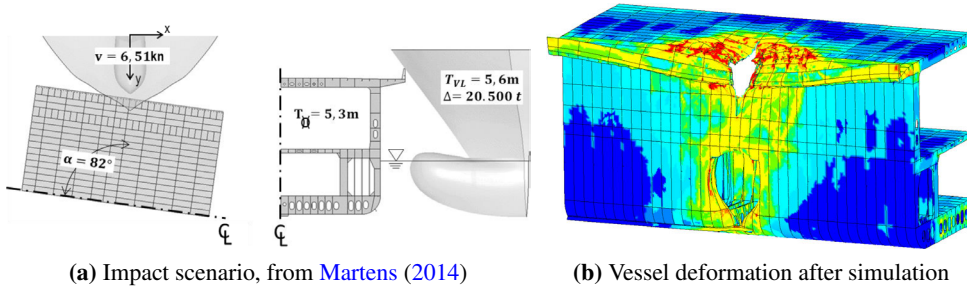
Figure 5.19: Impact scenario and vessel deformation after simulation. The fringes represent equivalent stresses from 0 (blue) to 500 (red) MPa.

The simulations were performed under the assumption of a friction coefficient of 0.23 (similar to Martens (2014)) and a constant impact velocity rather than an initial kinetic energy to reduce computational costs. Because the damage to the striking vessel was minor, this vessel was assumed to be rigid. The structural model of the ship side was based on the structural drawings provided in Martens (2014), including all relevant stiffening. Two meshes were investigated: a coarse mesh with elements of approximately 95 mm and a refined mesh with 48 mm elements. The shell plate thickness of the struck vessel ahead of the bulb was 19 mm, and that ahead of the forecastle was 13-15 mm, resulting in ratios of element length to thickness for the coarse and refined meshes of respectively 5 and 2.5 for the bulb impact and approximately 7 and 3.5 for the forecastle impact. Because no material tests were available, the material parameters were assumed based on engineering judgment of the applied material grades; with parameters given in Table 5.6.

Table 5.6: Material parameters used for the full-scale collision simulation

σ_0 [MPa]	E [GPa]	K [MPa]	n	$\varepsilon_{plateau}$
314	210	745	0.22	0.01

Figure 5.19b shows the deformed model after the simulation, with damage similar to that apparent in Figure 5.18a. Contact was established first with the cantilevered weather deck and then with the bulbous bow. The forecastle created a deep V-shaped indentation into the side of the ship, causing large energy dissipation. The bulb cut a cleaner hole, giving rise to a high initial energy dissipation followed by predominantly frictional dissipation until contact with the inner hull was established.

Figure 5.20 shows the force-displacement curves for the most reliable strain-state-

dependent criterion (BWH with damage) and the most reliable strain-state-independent criterion (GL) considering both the peak force and the total energy for stiffened panel structures. In the case of the BWH criterion, peaks are observed corresponding to the indentation into the weather deck (0-3 m displacement), whereas the GL criterion indicates a nearly constant force. The force and energy dissipation for the bulb are fairly similar for both criteria. After the puncture caused by the bulb (displacement > 3.5 m), the GL criterion exhibits a similar slope as the BWH criterion in the force-displacement curve related to crushing ahead of the stem/-forecastle, but delayed in terms of displacement. This discrepancy arises from the difference in the tearing of the weather deck and its effects on the subsequent structural resistance.

Figure 5.21 shows the dissipated energies at 7.6 m indentation for all fracture criteria and both mesh sizes. Interestingly, most of the criteria estimate similar energy dissipations ahead of the bulbous bow. Larger differences are observed ahead of the forecastle. Fracture ahead of the bulb occurred under conditions similar to those of the indentation experiments, with a strain state between plane strain and equi-biaxial tension. The cantilevered weather deck, which was less constrained by surrounding structures, exhibited triaxialities between uniaxial tension and plane strain. The deviations in the behavior of the criteria between these states (Figure 5.1 vs. Figure 5.4) indicate that the constant equivalent-strain criteria underestimate the energy dissipation for the weather deck.

For collision scenarios with large indentation, the frictional dissipation will be an important parameter. On average, the frictional dissipation in the simulations amounts to approximately 22% of the total energy for the assumed coefficient of 0.23. A small change in this coefficient will induce a significant change in the total energy dissipation during the simulation. Martens (2014) discussed the sensitivity to frictional dissipation in greater detail. Combined with the uncertainty in the added mass due to shallow water effects and the actual material strength, it is not possible to conclude with certainty which fracture criterion performs best for this full-scale scenario. However, the qualitative differences among the criteria are unaffected by these uncertainties.

5.5   Concluding Remarks

A set of fracture criteria that are commonly used in the analysis of ship collisions and grounding via NLFEA were tested. A multi-scale validation scheme was employed, with a common method of calibration for all criteria similar to what can be achieved in a design situation. The 392 simulations performed constituted a challenging test bench with varying impact geometry, strain localization, strain state, etc. Based on the simulation results, the robustness of each criterion was assessed
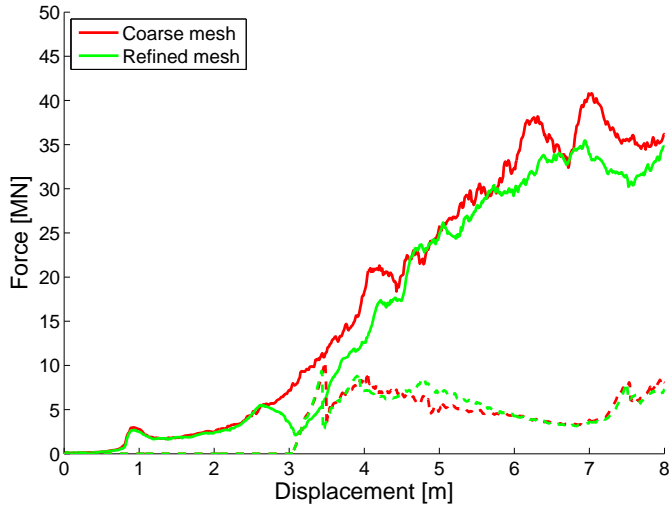
(a) BWH with damage
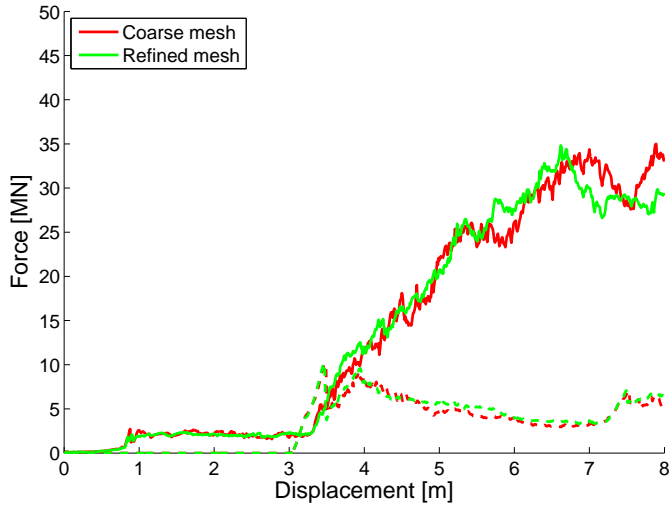
(b) GL

Figure 5.20: Force-displacement curves obtained using the BWH and GL criteria for two mesh sizes. The solid lines correspond to contact with the stem, and the dashed lines correspond to contact with the bulb.
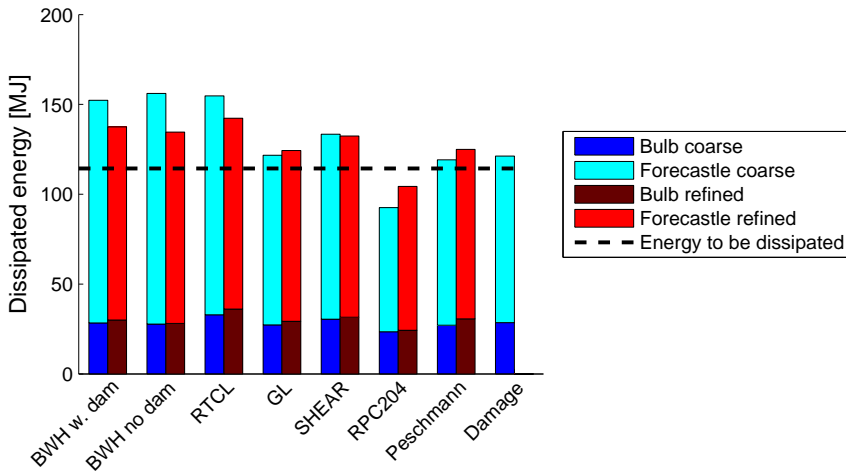
Figure 5.21: Dissipated energy ahead of the bulb and forecastle for two mesh sizes and the tested fracture criteria at 7.6 m indentation. Results for the Damage criterion with the finer mesh are not included because of the instability of the simulations.

in a quantitative and rational manner. For the analyst, it is useful to know whether the coefficient of variation is in the range of 15 or 60% with the fracture criterion that is used.

Of the advanced strain-state-dependent criteria that were tested, the BWH criterion with damage and the RTCL criterion demonstrated the best overall performance. The results indicated that if it is important to know the *capacity up to the first fracture* of the ship's shell plate, a strain-state-dependent criterion yields the best prediction of the initial fracture (and therefore the peak force). Simple strain-state-independent criteria produce a wider scatter in the initial fracture predictions and should therefore be used in combination with more generous safety factors. An analogy can be made to the separation between high and low energy impacts by Samuelides (2015); for low energy impacts the actual resistance of the different structural members are important, whereas for high-energy impacts more processes are mixed and simpler methods (such as in Minorsky (1959)) can yield acceptable results.

Strain-state-dependent fracture criteria will generally converge to the correct solution with decreasing mesh size. The same does not hold for strain-state-independent criteria, which often converge to an excessively high resistance for stiffened panel structures.

Mesh scaling should be performed to account for two different effects: a *material* mesh scaling to compensate for the case in which a local neck represents only a

small part of a larger element (typically with the length of the neck equal to the plate thickness) and a *geometric* mesh scaling to compensate for strains that are not captured by the coarsely discretized geometry up until the onset of necking. Material mesh scaling can be achieved using many methods, such as coupled ductile damage. Geometric mesh scaling is more difficult to predict in a robust way and is shown to depend on the relative size of the impacting body vs. that of the struck body's stiffening system. Further work to improve the rules for geometric mesh scaling is strongly recommended.

Comparisons performed on a single full-scale collision were not conclusive, but they did reveal certain differences between strain-state-dependent and strain-state-independent criteria on the upper side of the struck ship. Knowledge obtained from experiments regarding known material behavior at various triaxialities indicates that strain-state-independent criteria may underestimate the energy dissipation in the upper structure of the ship side, in which the strain state prior to failure differs from that in indentation experiments. Furthermore, if the ship side was to be re-designed to avoid fracture ahead of the bulb of a striking ship, strain-state-dependent criteria would offer increased reliability in predicting fracture initiation and thus, in turn, the capacity to fracture.

Finally, it is of utmost importance that the uncertainty in fracture predictions be considered when evaluating the results of a collision simulation. This is an important concern for all fracture criteria.

Chapter 6

Application to Ship and Offshore collisions

6.1 Introduction

The objective of this chapter is use numerical simulations to investigate the behavior of a platform subjected to ship collisions by accounting for the ship-platform structure interaction. An up-to-date supply vessel was analyzed; the bow, side and stern of a 7500 ton displacement supply vessel were modeled. Notably, the vessel has a bulb that can hit the platform below the water line. As a significant increase in the design energy for head-on collisions is expected in the revised NORSOK N-003, the study was conducted for collision energies that are typically in the 50 MJ range, which is substantially larger than the present standard event of 11 and 14 MJ. The increase in the collision energy will place much heavier demands on the resistance and/or ductility of the offshore structure, which may be difficult to meet using the methods described in NORSOK N-004. Some of the requirements have been based on idealized considerations that may not be entirely realistic and are sometimes too conservative for real collisions. The validity of such requirements was investigated using integrated nonlinear finite element analysis. In this context, *integrated analysis* means that deformations of both the striking and struck body are considered simultaneously, thereby capturing the interactions in the deformation process.

The following collision scenarios will be investigated:

- a bulbous bow impact against a semi-sub platform column,
- a stern corner impact against a semi-sub platform column,

- a bulbous bow impact against a jacket brace and
- a beam impact against a jacket leg.

The physics of the interaction between the bodies were investigated and used in the validation and further development of hand calculation methods for early phase design of collision resistant structures with emphasis on strength design.

6.2   FE Modeling

6.2.1   General Setup

Numerical simulations of collisions were performed by means of the explicit finite element software LS-DYNA 971 R7600, using Belytschko-Lin-Tsay shell elements. The mesh size was maintained within 5-10 times the plate thickness to obtain sufficiently accurate predictions of the strain and fracture. Standard viscous hourglass control was used. Penalty-based contact algorithms were used to model the contact between the vessel and the platform and the internal contact of either the vessel or the platform. A static friction coefficient of 0.3 was used in all of the contact formulations. In the simulations, the vessel travels with a constant velocity of 4 m/s until the desired deformation level is reached. This speed is sufficiently low to avoid large inertial effects and dynamic buckling. The level of damage can then be analyzed based on the demand for energy dissipation, which is obtained from external mechanics analysis.

When strain-rate effects are neglected, there are only small differences in the end deformation for a stiffened panel subject to a perpendicular ship collision where either the velocity or the initial kinetic energy is fixed (constant vs. decreasing velocity), provided that the fixed impact velocity is sufficiently low. For jacket braces and legs, the inertial forces of the leg may become significant, and the estimated capacity of the leg can be significantly overpredicted if the velocities used in the analysis are unrealistically high.

A power law hardening with yield plateau is assumed, together with the mesh-scaled RTCL fracture criterion (Section 5.2.3). High characteristic strength is assumed for the striking vessel. The steel in the struck platforms consists of high-strength steel with characteristic yield stresses of 355, 420 and 460 MPa. As the primary objective is to assess the damage sustained by the platform column, it is important to use the specified (characteristic) yield strength with moderate strain hardening. The engineering stress strain curves for the materials used are shown in Figure 6.1. The uncertainty in the material modeling is by far the most significant source of uncertainty in collision analysis, both in terms of the actual ultimate capacity and the accuracy of fracture prediction, ref. Chapter 3.
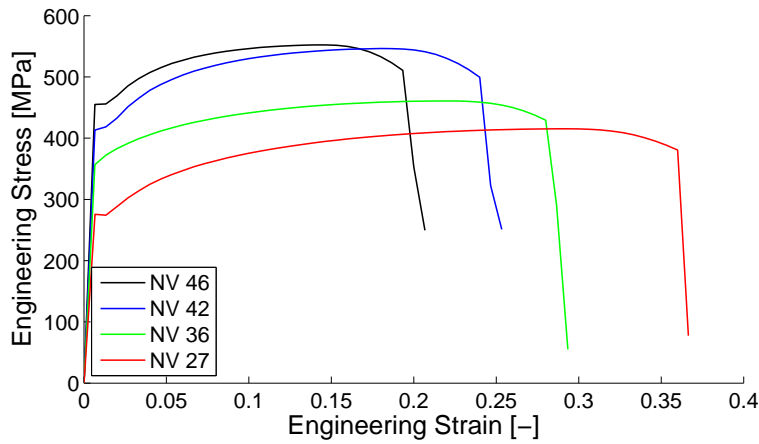
Figure 6.1: Engineering stress strain curves used in numerical studies in this chapter.

6.2.2   Ship and Platform Finite Element Models

Approximately 1/3 of the front section of the column of a floating production platform is modeled, as shown in Figure 6.2a. The column is 17 m wide, has decks with a plate thickness of 12 mm and ring frames (T1100×300/12×20) spaced approximately 3 m apart. The vertical stiffeners are typically HP300×12 with a spacing of 0.65 m. In the rounded corners of the column, the outer shell stiffener spacing is approximately 800 mm. The net shell plate thickness is in the 16-17 mm range in the collision region. All of the degrees of freedom of the rear of the modeled section are fixed. The element size is approximately 100-120 mm, which corresponds to a minimum of three elements over the stiffener web and five elements in the plate between each stiffener.

Figures 6.2b and 6.2c show the FE models that were established for the bow and stern of a modern 7500-ton displacement offshore supply vessel. The main dimensions of the vessel are as follows: Length overall 91 m, length between perpendiculars 79 m, breadth 19 m, molded depth of 7.6 m and scantling draught of 6.2 m. The bow model (described in Section 3.8) has a bulb radius along the centerline of approximately 2 m and 1 m along the stringer deck in the middle of the bulb.

The stern corner model has a shell plate thickness of 11 mm with a 25 mm thick vertical plate strip around the outermost region (which is shown in white in Figure 6.2c). Large open frames are located every 650 mm in both the transverse and longitudinal directions, with a plate thickness of 10 mm (intermediate) and 20 mm for the main frames towards the shell.

(a) Platform column   **(b)** Platform column and bow FE models, showing details of bulb stiffening

(c) Stern corner FE model with and without shell plating
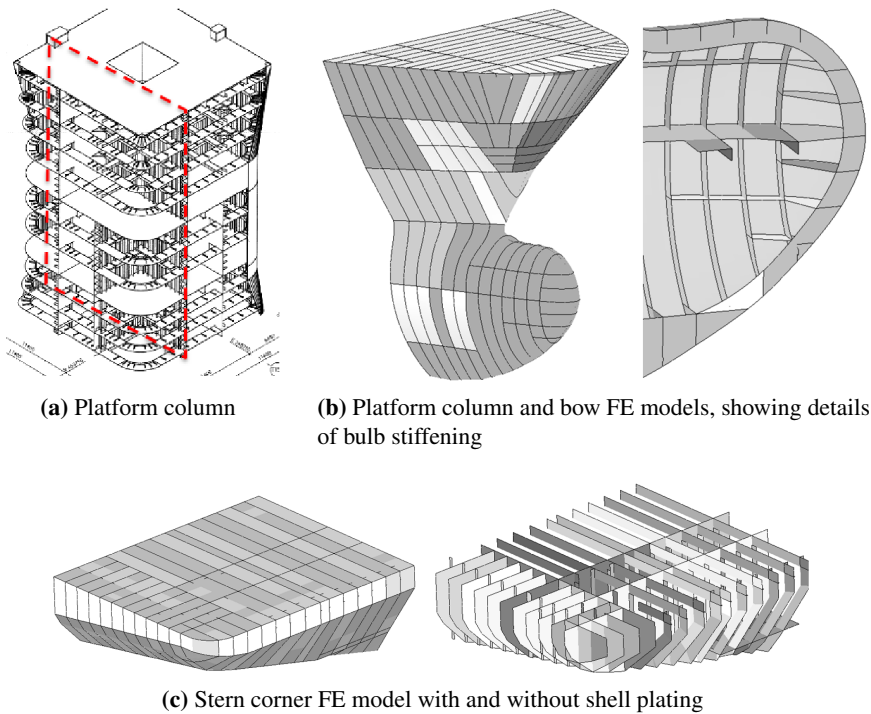
Figure 6.2: FE models of platform column, supply vessel bow and stern corner.

6.3   Bow Collision Against a Rigid Wall

As a first step, the bow is crushed against a rigid wall. The crushing force versus deformation of the bulb and the stem is plotted in Figure 6.3. The stem force increases steadily as the contact area grows. The bulb force, which engages after 1.2 m crushing of the stem, is significantly larger than that of the stem. The crushing force of the bulb attains a peak value at an early stage, followed by subsequent peaks. Characteristic features of the stem deformation are marked in the figure. The initial contact with the uppermost deck, which bends upwards, is denoted by *1*. The subsequent global buckling of the uppermost deck, which reduces the force capacity of the superstructure significantly, is denoted by *2*. The engagement of the second deck, which significantly increases the collision force, is denoted by *3*. For the bulb, the first large load peak marked with *A* occurs when the front part of the bulb crushes. Then, the bulb folds sequentially between transverse frames, with large folds created at the peaks marked with *B* in Figure 6.3.

Note that the stem deformation curve by itself is smaller than the present NORSOK N-004 design curve (Figure 1.3), but the bulb force is larger and more concentrated
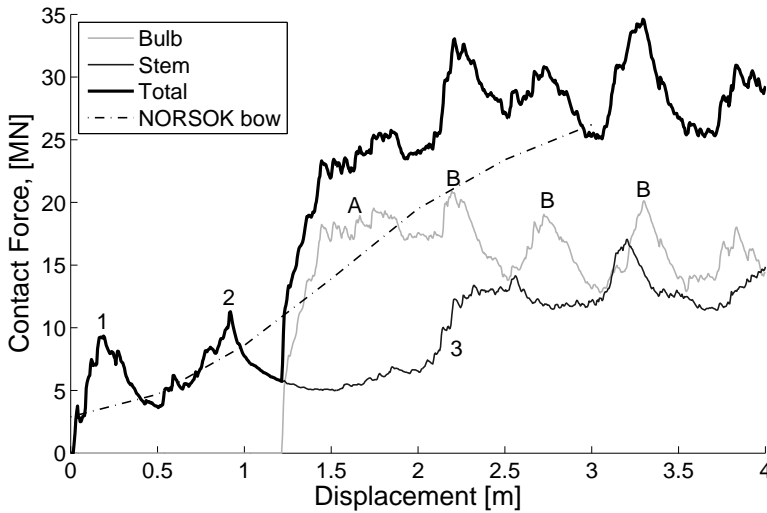
Figure 6.3: Force vs. deformation of supply vessel bow against a rigid planar wall.

than the stem force. The stem structure is defined from the uppermost deck and down towards the top of the bulb (about half the total height) and cannot be compared directly to the NORSOK curve, which was determined for the total height of a raked bow. Because the bulb has a much smaller cross-sectional area than the stem while crushing at a higher force, the intensity (average force per area) is much larger. Hence, the bulb has the highest potential to damage the platform, and is thus the main focus in the following study.

When the stem and bulb hits cylindrical columns or braces, the force-deformation relationship could change compared to that from a rigid plate. To investigate this behavior, rigid cylinders with radius R ranging from 0.5 m to 10 m were subjected to perpendicular impacts from the bow model. Figure 6.4 shows the deformation pattern of the bow for a cylinder with $R = 1$ and $R = 10$ m.

Figure 6.5 show the force-displacement relationship for the stem and the bulb, respectively. The stem force varies significantly with the radius, with lower force peaks for the smaller cylinders. The curve for R = 5 m is fairly representative for large cylinders (e.g., the curvature of a semi-sub column), and the results for smaller cylinders may be used for jacket legs and braces (e.g., $R = 0.5$- 2.0 m). The bulb force is fairly independent of the column radius because the global deformation mode is similar for the various radii (see Figure 6.4b), but some differences are observed in the local crushing of the bulb tip.

The contact force distributions for bulb impact against a plane wall at various

(a)

(b)
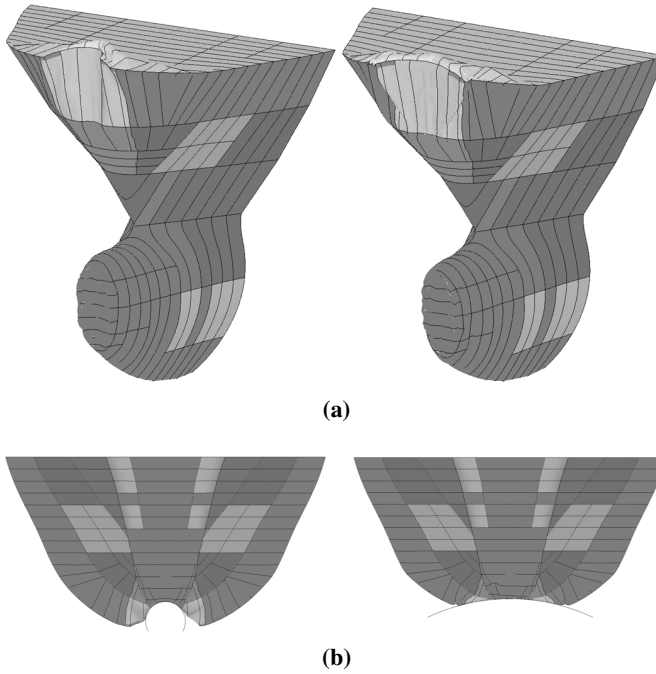
Figure 6.4: Deformation of bow from collision with a rigid cylinder of radius 1 m (left) and 10 m (right)

stages of deformation are shown in Figure 6.6. Contact occurs over limited areas, notably around the bulb perimeter, whereas the central areas are not in constant contact. Very high local pressures in the 40-80 MPa range are observed over small areas. Large areas carry the main load with moderate pressures in the 5-15 MPa range. The mesh size in the figure is 100x100 mm. From Figure 6.6c, the contact area can be determined to be 2.4 m^2 with an average pressure of 7 MPa.

Hong et al. (2009) calculated the maximum average pressure versus contact area for the same supply vessel bulb using similar force distributions. The relationship between the pressure P and the contact area A was represented by the following expression (for units of MPa and m^2):

$$P = 7A^{-0.7} \tag{6.1}$$

This relationship is similar to that for local ice pressures from thick multi-year ice features, which is often used in the design of Arctic structures (ISO-19906 (2010)).

A drawback of the pressure calculation method used by Hong et al. (2009) is that

(a) Stem

(b) Bulb
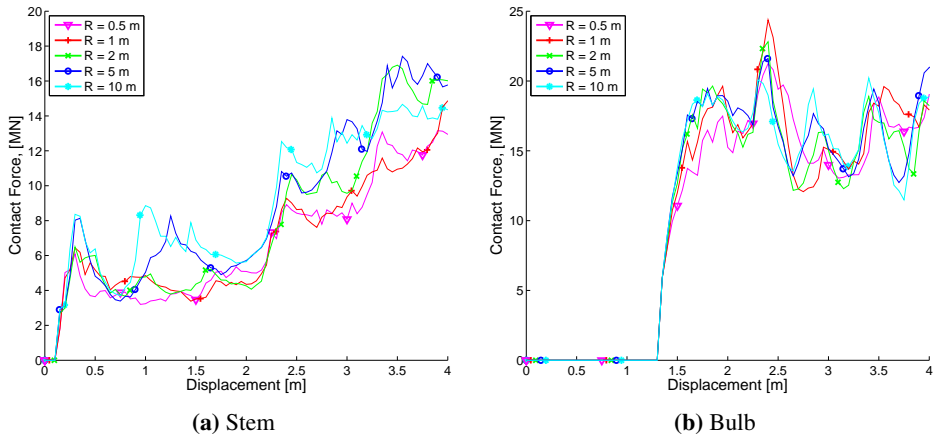
Figure 6.5: Force-displacement curves for bow impact with rigid cylinders of varying radii.

(a) Displacement: 1.36 m
    Deformation: 0.03 m
    Force: 4.8 MN

(b) Displacement: 1.48 m
    Deformation: 0.15 m
    Force: 9.3 MN

(c) Displacement: 1.88 m
    Deformation: 0.57 m
    Force: 18 MN
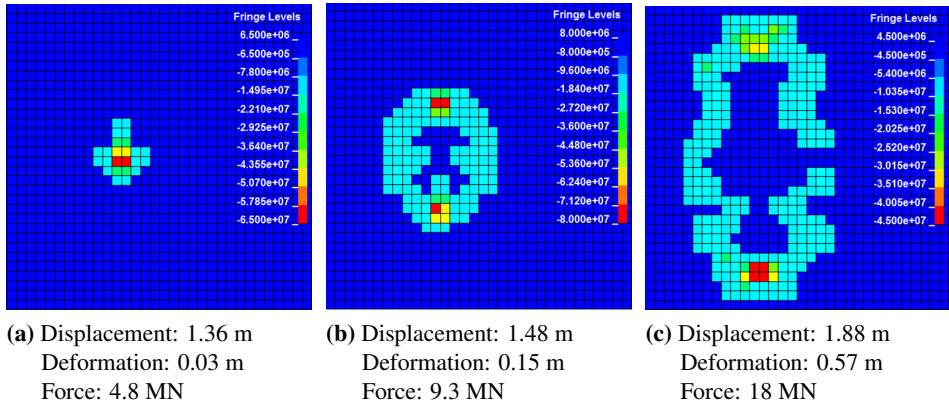
Figure 6.6: Simulated contact forces and its distribution for crushing of the bulb. The displacement corresponds to the overall vessel displacement (see Figure 6.5b) and the deformation to the actual crushing of the bulb (as the stem extends forward of the bulb).

the load area is a function of the discretization of the impacted body and not just the striking body. If a small fraction of an element on the struck body is in contact, the estimated force per element area is smaller than the actual local contact pressure. With many such elements, the total estimated area can be grossly underpredicted. Thus, the area is easily overpredicted when contour plots of the impacted rigid face are used, and the mesh sizes for both bodies are similar.

Measuring the contact area from the struck body is another alternative for impact against a relatively flat object, which gives a more accurate view of the actual contact dimensions. Table 6.1 compares the extent of contact measured on either the striking or struck body. The maximum contact width and height was measured for selected time steps, and the area was calculated by assuming an elliptical contact surface over the width and height of the contact. The corresponding contact pressure was calculated as the force divided by the total area. Large differences in area were predicted when using either the struck or striking body, giving large variations in the pressure estimates. The mesh sizes of the striking and struck objects are maintained at similar levels (approximately 100 mm). A simply remedy for the area prediction error is to refine the mesh of the struck object.

With the updated pressures calculated from the area measured on the striking body, the following curve is proposed used for bulbous bows of modern conventional designs (for units of MPa and m^2):

$$P = 12A^{-0.7} \tag{6.2}$$

Table 6.1: Contact size calculated from striking and struck bodies and corresponding nominal pressure prediction.

Indentation [m]	Deformation	Width [m]	Height [m]	Area $[m^2]$	Pressure [MPa]
0.11	Deformation of striking body	0.66	1.2	0.62	15
	Mapped pressure on struck body	1	1.3	1.02	9.1
0.27	Deformation of striking body	1.27	1.76	1.76	8.5
	Mapped pressure on struck body	1.4	2.1	2.31	6.5
0.35	Deformation of striking body	1.3	2.1	2.14	7.8
	Mapped pressure on struck body	1.6	2.3	2.89	5.8

DNV RP-C204 and NORSOK N-004 provide recommendations for strength design of large diameter columns of floating platforms that are also relevant for ship-type installations. NORSOK N-004 specifies the magnitudes of concentrated collision forces for local plate design, which may be assumed to be uniformly distributed over the contact surface (listed in Table 6.2).

Table 6.2: Local concentrated collision force F evenly distributed over a rectangular area of width a and height b, from NORSOK N-004. A and P are the corresponding areas and pressures.

Stern corner					Stern end				
a [m]	b [m]	F [MN]	A [m^2]	P [MPa]	a [m]	b [m]	F [MN]	A [m^2]	P [MPa]
0.35	0.65	3	0.23	13	0.6	0.3	5.6	0.18	31.1
0.35	1.65	6.4	0.58	11	0.9	0.5	7.5	0.45	16.7
0.2	1.15	5.4	0.23	23.5	2	1.1	10	2.2	4.55

Figure 6.7 shows the pressure-area points obtained from a NLFE analysis of a stern corner and a bulb against a rigid plate, which is calculated as a contact force over a predicted area on the striking body. The pressure-area curve proposed by Hong et al. (2009) (Eq. 6.1) is plotted in Figure 6.7 together with the revised pressure-area curve (Eq. 6.2), which is based on a more accurate definition of the area. The developed nominal or process pressure-area curve is analogous to those adopted for design against ice actions. The pressure-area combinations recommended for strength design of columns against stern corner and stern end collisions in NOR-SOK N-004 are shown as triangles. Note that the simulation results generally lie above the NORSOK pressure-area recommendation. This is partly attributed to the different strain-hardening model that was used in the simulations behind the original NORSOK points.

The high local pressures from a collision event varies temporary and spatially (Figure 6.6). If a stiffener fails under high local loads the shape of the impacting structure forces the surrounding structure to carry the load. Hence, one single stiffener will not be required to carry a local high-pressure patch load, but only deform until sufficient portions of the surrounding structure are activated. Thus, the structure might not be required to support the highest pressures over the smallest areas, but instead to support medium pressures over larger areas.

6.4   Collision with a Deformable Floating Platform Column

6.4.1   Bow Collision Against Platform Column

Figure 6.8 shows the simulated damage for a bow impact against the corner of the column, with the bulb impacting on a ring frame. Figure 6.9 shows the contact force, which is split into a stem contribution and a bulb contribution, together with the force-displacement relationship for a bow against a rigid column with a 5 m radius (similar to the platform corner radius). The stem force-deformation curve is close to that obtained for crushing against a rigid column with the same diameter as the platform column, and witness of a behavior according to strength design.
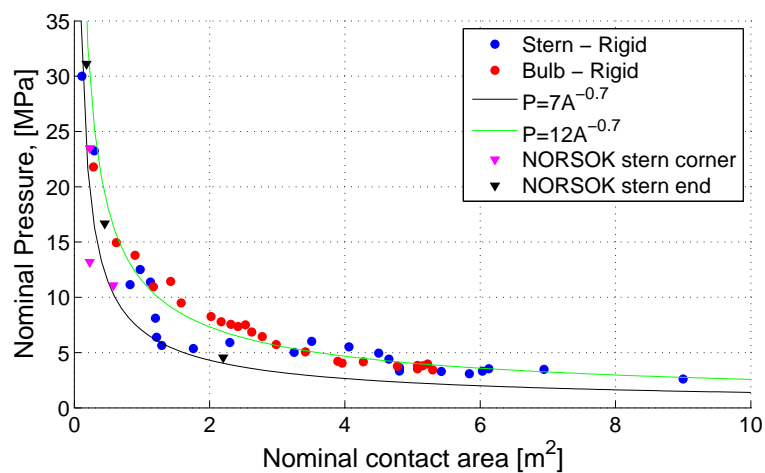
Figure 6.7: Pressure-area relationships for bulb and stern impacts against a rigid plate.
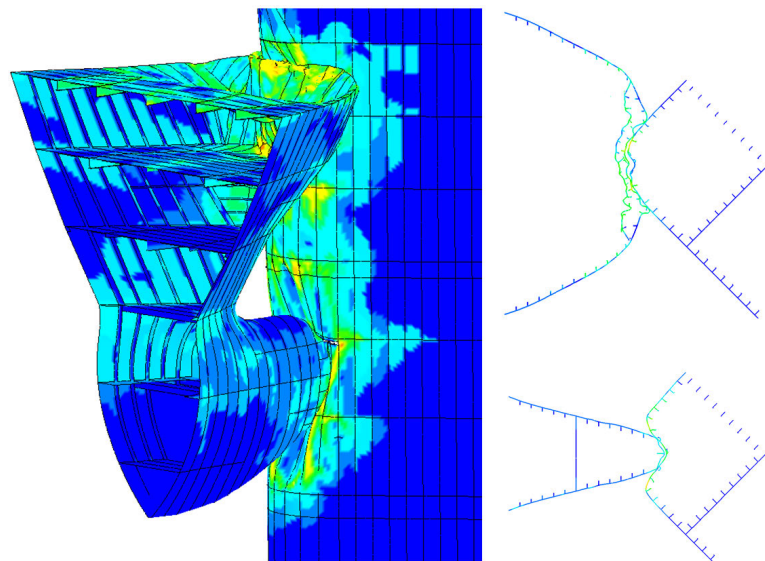
Figure 6.8: Simulated damage for bow and column after 51 MJ of energy has been dissipated (which corresponds to a 4 m global displacement in Figure 6.9).
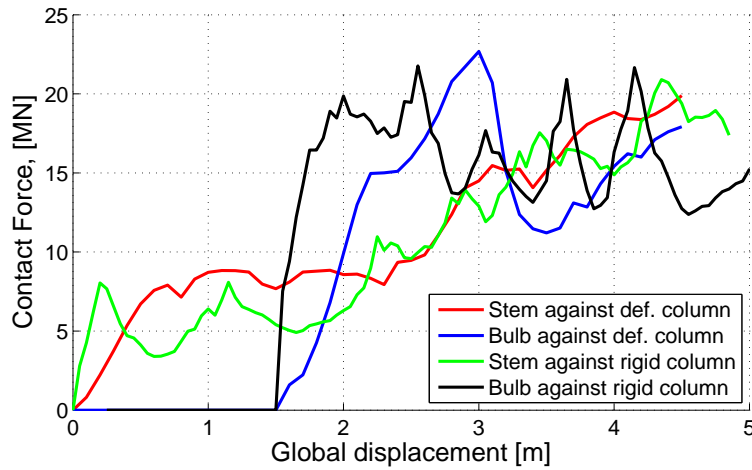
Figure 6.9: Force vs. total displacement of a deformable bow for a corner impact to deformable and rigid columns.

In the initial phase of the collision, the bulb is stronger than the platform, and the force-displacement relationship is thus governed by the strength of the platform column, as can be seen from the gradient of the force-deformation curve being lower than that for rigid column impact. As the membrane strength of the platform shell is mobilized, the bulb starts to crush at a peak force of 22 MN. The corresponding peak force for crushing against a rigid column is 20 MN. This illustrates an important interaction effect: the column tends to wrap around the bulb such that the resistance to crushing of the bulb exceeds the resistance for crushing against a rigid column. If the force-deformation curve for impact against a rigid column had been used, it would have been predicted that the crushing would switch from the column to the bulb when the contact force exceeded 20 MN, thereby underpredicting the load and damage to the platform.

The strain and fracture model does not predict fracture in the shell until 37 MJ of strain energy have been dissipated. However, fracture may occur earlier at the hard points not included in the FE model (anchors, bollards, etc.), as observed in the *West Venture* accident (Pettersen and Soegaard 2005).

6.4.2   Consequences of Assuming a Rigid Bow

Figure 6.10 shows the force-displacement relationship for a head-on bow impact to the platform column between frames where both bodies deform, and an impact where the bow is assumed to be *rigid*. Due to the large difference in the relative strength between the platform column and the vessel stem, the stem force-displacement curve is fairly similar to crushing against a rigid vertical wall. If the

stem is assumed rigid, the *magnitude* of the collision force is significantly overestimated. Consequently, a rigid stem may be highly **non-conservative** in terms of the potential penetration of the *bulb* into the column, as too much energy is dissipated by the overprediction of collision force from the stem contact. The column will sustain more damage at forecastle deck level, but the more critical puncturing the column below the water line is underpredicted.

The integrated response for the vessel bulb exhibits a significantly larger contact force than for a rigid bulb because the contact area is increased by the deformations of the bulb, thereby increasing the platform resistance. Thus, significantly more energy will be dissipated in the bulb contact per meter of deformation by considering the actual strength of the bulb.
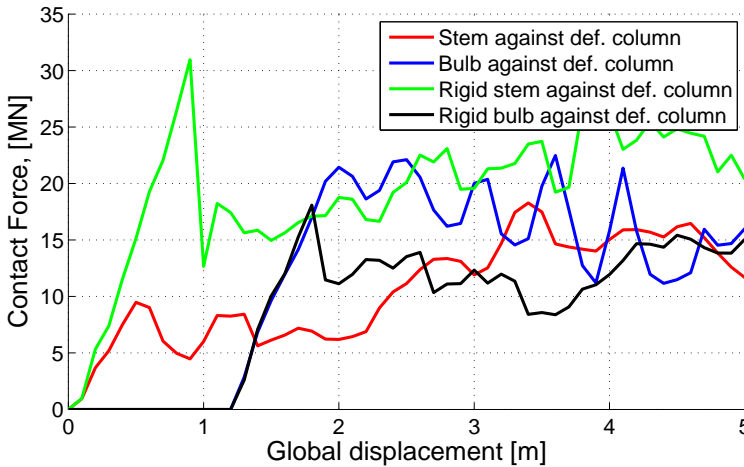
Figure 6.10: Force-displacement for mid-column impact using an integrated analysis and a rigid bow analysis. Global displacement is measured at the undeformed section of the vessel, as the total longitudinal movement of the ship.

As simulations with different assumptions dissipate different amounts of energy pr. meter global displacement of the vessel, it is difficult to directly assess the consequence of the rigid assumption in Figure 6.10. In order to get a better comparison, the indentation into the platform in way of the stem and bulb is plotted vs. the dissipated energy in Figure 6.11 for the integrated analysis and the rigid vessel vs. the deformable platform. For the stem, the initial response is similar for both analysis runs, but deviate quickly as the stem is crushed. Further indentation into the platform is limited in the integrated analysis, whereas it increases quickly for the rigid vessel vs. deformable platform.

Due to the differences in dissipation of energy in way of the stem, the rigid bulb
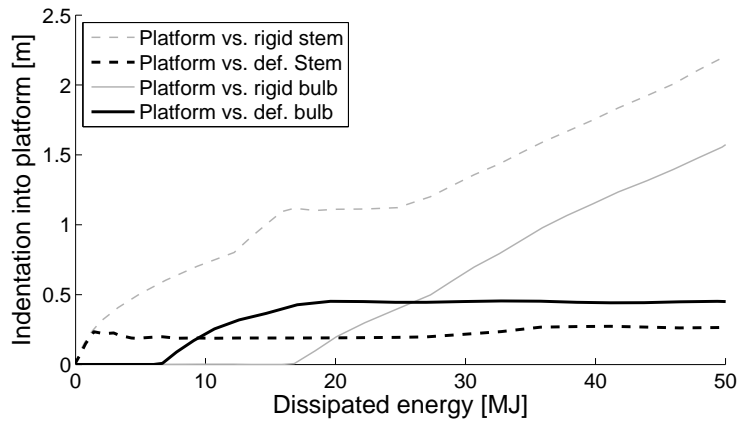
Figure 6.11: Indentation into platform vs. dissipated energy in way of stem and bulb.

hits the platform after 17 MJ dissipated energy, whereas the deformable bulb hits the platform after only 6.5 MJ of dissipated energy. The rate of indentation into the platform in way of the bulb is similar for both the rigid bulb and deformable bulb initially, but as the crushing force of the bulb is reached the curves deviate.

The findings in Figure 6.11 is also demonstrated by Figure 6.12, which shows the deformation pattern along the centerline of the vessel for integrated analysis (top) and rigid vessel vs. deformable platform (bottom). Large differences are visible in the predicted damage in way of the stem. Differences in way of the bulb are more difficult to read from the figure, and can be more easily understood by Figure 6.11.

Significant differences in the deformation pattern can be observed, and the assumption of rigid vessel leads to an error in the estimation of dissipated energy vs. indentation into the platform in way of the vessel stem. Due to this error, the indentation into the platform in way of the bulb is smaller from the rigid bow than the deformable bow until 26 MJ of energy is dissipated. This is problematic, as the underpredicted deformation below waterline is worse for the integrity of the platform with respect to hydrostatic stability than damage many meters higher in way of the stem.

Only after 26 MJ of dissipated energy, the rigid bow assumption will result in larger indentation than the deformable bow for both the stem and bulb contacts. With a realistic strength of the striking bow, the deformation mode should have switched from the side to the bow, and the simulated deformation pattern becomes increasingly unrealistic with increasing indentation with the rigid bow. Thus, when the rigid vessel assumption actually is conservative ($E > 26$MJ), the predicted damage to the platform is not realistic, and any strengthening efforts are misguided.

(a) Deformable bow   (b) Rigid bow
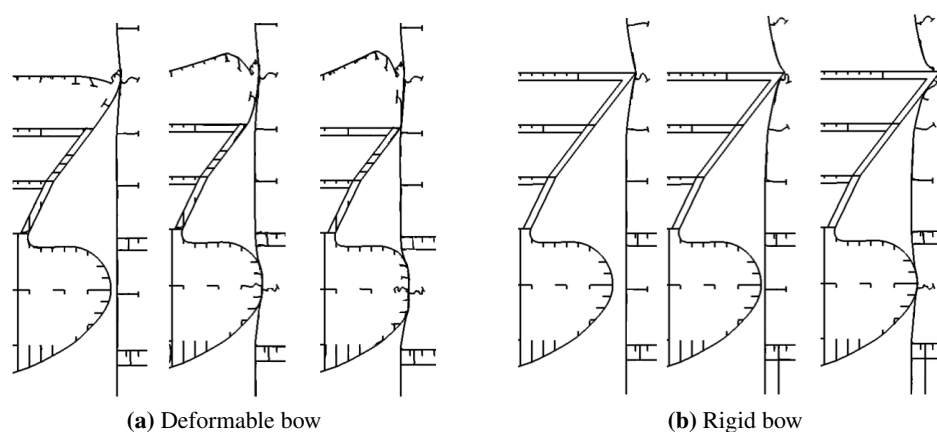
Figure 6.12: Deformation at 5, 15 and 25 MJ dissipated energy, for deformable and rigid bow vs. deformable platform. Some details are removed for clarity. For higher energies, the rigid bulb will penetrate further, whereas the deformable bulb is crushed.

Variations of the distance from the front of the stem to the bulb tip would change the level of dissipated energy before the bulb comes into contact with the platform. If this distance is large, the damage to the platform will decrease. However, if a rigid bow is assumed, the results will be increasingly non-conservative when the distance from front of stem to the bulb tip is increasing. The higher the available kinetic energy, the worse the rigid assumption can be.

6.4.3   Stern Collision Against Platform Column

Figure 6.13 illustrates the impact scenario. Contact takes place at the junction of a vertical bulkhead and a web frame, which has the potential to puncture four adjacent compartments. The stern is assumed to move perpendicularly to the shell. The potential yaw motion of the supply vessel induced by the contact force is neglected.

The simulation is conducted up to a 5 m displacement of the stern corner, which corresponds to a dissipated energy of 122 MJ. Two impact locations are investigated. They are both in the same vertical position above an internal deck, but are spaced 2 m apart in the horizontal plane. The force deformation curves for the two impact locations are shown in Figure 6.14. The column has sufficient capacity to crush the stern corner, but not without undergoing significant local damage. Small variations in the impact location produce large changes in the local damage to the platform column, witnessing of the high sensitivity to the relative strength of the column and the stern corner.
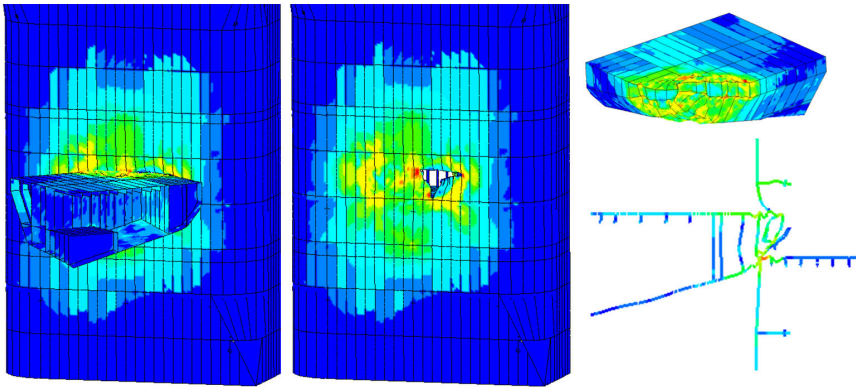
Figure 6.13: Stern corner scenario and deformed configuration of the column and stern corner for 50 MJ of dissipated energy.

Although significant damage is sustained in the initial phase of the deformation (see Figure 6.13), the contact area increases sufficiently fast so that the collision force is efficiently redistributed away from the most damaged and ruptured areas for both the impact locations. Thus, the stern corner is crushed, and very high energies can be dissipated. For deformations up to 1 m, the force curve is in good agreement with the design curve for stern corner impacts given in NORSOK N-004, but the NORSOK curve tends to be too "weak" for larger deformations.
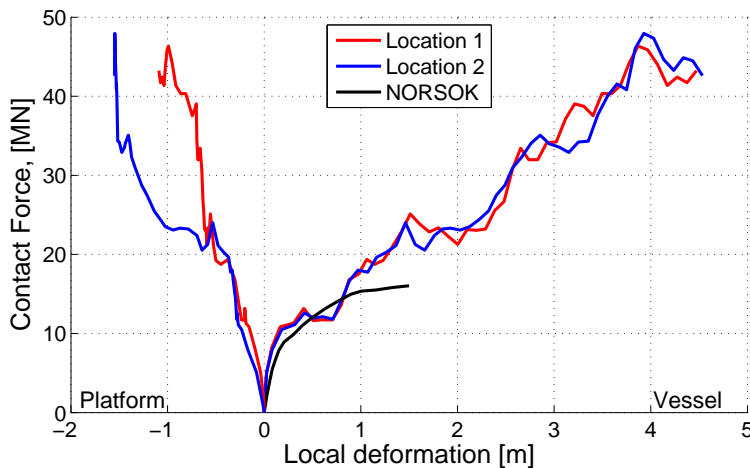
Figure 6.14: Force deformation curve for stern corner and column at two impact locations compared with recommended NORSOK stern corner curve.

6.4.4   Pressure-area Relationships Obtained from Integrated Analysis

Figure 6.15 shows the pressure-area relations from the integrated simulations compared to crushing against a rigid wall. The pressure is calculated as the contact force over the estimated total enclosed area of the striking body. In the initial phases, the pressure for impact against a rigid column is very large and significantly larger than the capacity of the column. Consequently, in the integrated analysis, the contact pressures are governed by the capacity of the platform column. After a contact area of 1 m^2 is reached, the pressure-area relationship from the integrated and rigid analyses follow the same overall trend: however, as the platform shell wraps around the incoming object, the contact area obtained from the integrated analysis increases faster than that obtained from the rigid analysis. The pressure-area relation for crushing of a ship's bulb and stern corner (as given in Eq. 6.2) seems to be a sound assumption also for integrated analysis.
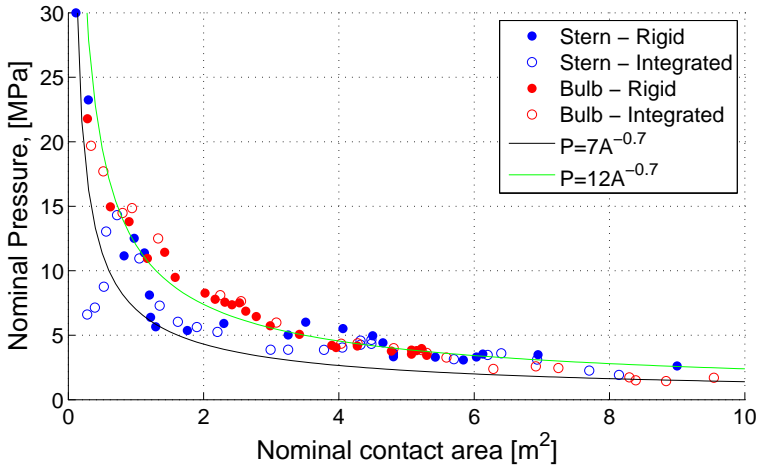
Figure 6.15: Pressure-area relation for stern corner and bulb impact on platform column: impact from deformable vessel to rigid platform is denoted by "rigid"; impact with deformable platform and deformable vessel is denoted by "integrated"

6.4.5   Stiffener Response to Bulb Impact

To determine how strength design should be applied, the response of a stiffener designed according to standard ULS requirements was considered. An impact to the middle of the stiffener span was assumed. The load is distributed uniformly as a line load $q = Ps$ on the stiffener, where P is the pressure, and s is the stiffener spacing. The load has to be carried by a combination of shear and bending before the membrane forces of the panel are mobilized. The shear force is transferred to both sides of the panel and is given by $qL/2$, where L is the loaded length of the

stiffener. For a NV36 material, the yield stress in pure shear is 205 MPa.

For high pressures over small areas, the initial phase of the stiffener deformation is governed by shear. This behavior is well illustrated by the shear stress plots in Figure 6.16, where almost the entire stiffener yields in shear at a contact force of 1.2 MN in the early phase of the contact. Carrying this force with small deformations requires a web area of 6000 mm^2, nearly twice the capacity of the HP300 $\times$ 12 stiffener used in the existing rig design.

After significant stiffener deformation, shear hinges form at the stiffener ends and longitudinal (membrane) stresses dominate in the middle of the stiffener span. To support the load at this contact level by pure shear, the required web area is 36000 mm^2. At this deformation stage, the induced curvature of the panel mobilizes additional stiffeners to carry the load. Only three stiffeners are in direct contact with the bulb (Figure 6.16d), but the load is distributed over five stiffeners through the curvature of the shell plating. Thus, the 36000 mm^2 web area can be distributed over five stiffeners with 7200 mm^2 each, corresponding to a required 24 mm thickness for each 300 mm high stiffener.

In rigorous strength design the stiffener web should be designed to support the local distributed loads for all increments of the impact; from a point load to a distributed load over the entire stiffener. This design method places stringent demands on the stiffener shear area, thereby enabling the stiffener to withstand the load with minor deformation.

Provided that the stiffener ends are properly supported and some deformation is allowed, shear alone may not be the relevant design variable. With proper support, the shear stresses quickly change to longitudinal stresses in the stiffener, and the load is carried by a combination of shear, plastic bending in the stiffener and membrane stresses in the plate and the stiffener. Figure 6.17 shows the yield stress utilization of the longitudinal and shear stresses vs. the stiffener indentation over the stiffener length. The stresses are sampled at the top, middle (above and below the bulb tip) and bottom of the stiffener web, as shown in Figure 6.16a. The shear stress initially dominates: however, after only a 5% deflection, the middle of the stiffener is in almost pure tension, and the shear has localized to the top and bottom ends of the stiffener. This behavior resembles that of a typical collapse mechanism.

6.5   Strength Design of a Stiffened Panel Against Impact

As an example, a vertically stiffened plate field in a platform column is to be designed to resist impact from a bulb with a peak force of 20 MN. The height and width of the contact surface at the peak force is about 4 m and 1.3 m respectively.

(a) Schematic of model showing stress sampling points

(b) 1.2 MN contact force

(c) 7.5 MN contact force

(d) 1 m contact width carried by 5 stiffeners for a 7.5 MN contact force
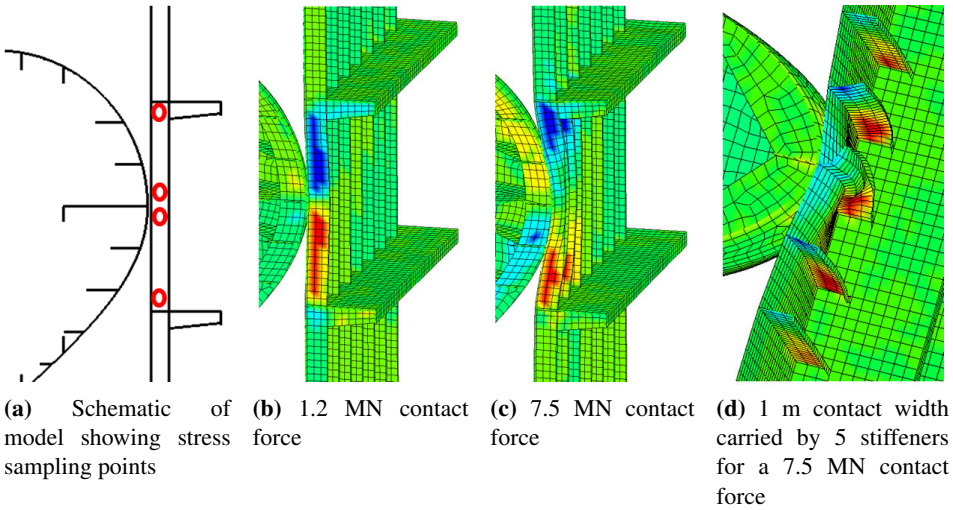
Figure 6.16: Deformation of stiffener in initial phase: fringes show shear stresses ranging from -205 to +205 MPa
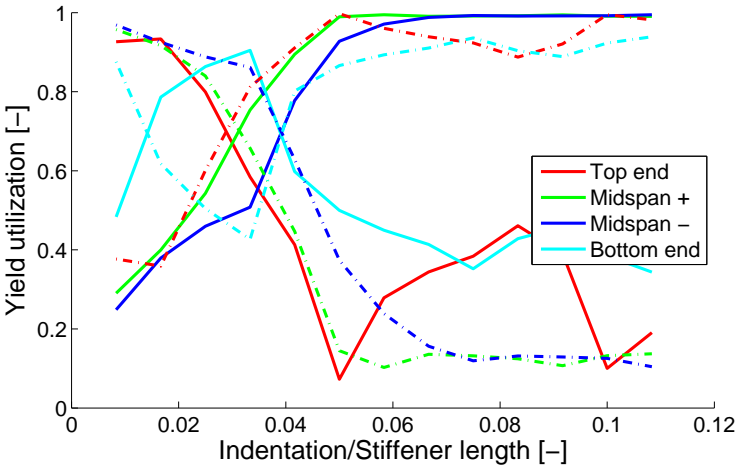
Figure 6.17: Normalized utilization of stiffener web in longitudinal and shear stress: solid lines denote the longitudinal stress and dashed lines denote the shear stress utilization.

Based on this, three stiffeners will be in direct contact with the bulb, possibly over the height of two stiffener spans. Assuming an elliptical contact surface yields a contact area of 5.2 m^2 and a corresponding average pressure of 3.8 MPa.

The pressure distribution plots in Figure 6.6 shows that the pressure is not evenly distributed over the total contact area. If small deformations are required, the local areas should be designed for the local contact pressure rather than the average over the entire contact. A reasonable assumption may be that the pressure-area relation in Eq. 6.2 has to be complied with over one single stiffener. Using a stiffener length of 3 m and a spacing of 0.65 m yields a local design pressure of 7.5 MPa over the stiffener plate flange.

The plate will only fail locally between each stiffener if the stiffener capacity is sufficient to prevent failure through plastic shear or bending of the stiffener. The extent of the deformation is thus limited to the total contact zone. However, if the stiffener is weaker and deforms, the plate curvature will increase, and the curvature may mobilize the strength of adjacent stiffeners. The plate deformation can then be described with methods such as yield-line models.

Provided that fracture/tearing of the plate does not occur, plastic deformation of the shell plating – on the order of 1-3 times the plate thickness – is considered to be acceptable and should not require immediate repair. For further loading, stiffeners will fail and large panel deformations may occur. Adjacent girder webs may also fail to support large plate membrane stresses, and the web may undergo local deformation. In addition, as the plate undergoes finite deflections, the direct contact with the stiffeners and/or web frames continues to increase. Due to the large plate membrane capacity, the crucial components for *strength design* are the stiffener and girder systems.

In the following, the governing capacity mechanisms for such a scenario is discussed, and a simplified calculation method is described. Various panel scantlings are investigated through NLFEA simulations using an actual bulb model and with the simplified approach.

6.5.1   Governing Mechanisms

Stiffeners

The ULS capacity of the stiffeners may be estimated using plastic analysis and a three-hinge mechanism model (Figure 2.6). The collapse resistance in bending for a uniformly distributed load can be expressed as follows:

$$q_c = \frac{16M_p}{L^2 \left(1 - \frac{s}{2L}\right)} \tag{6.3}$$

where M_p is the plastic moment, and L and s are the frame spacing (stiffener span) and the stiffener spacing, respectively. The second factor in the denominator accounts for the effect that some of the collision forces are transferred directly to the web frames and not via the stiffeners. The resistance q_c should be compared with the line load demand Q, calculated from the exponential pressure-area relation in Eq. 6.2

$$Q = Ps = C_1 A^{C_2} s = 12(Ls)^{-0.7} s \tag{6.4}$$

The required stiffener section modulus z_p becomes

$$z_p \geq \frac{sL^2 \left(1 - \frac{s}{2L}\right) C_1 (Ls)^{C_2}}{16f_y} \tag{6.5}$$

where f_y is the yield stress. The above expression does not account for stiffener webs that are highly utilized in shear at the supports. In this case, the contribution to the bending resistance from the web at the stiffener ends has to be reduced, and the required stiffener section modulus can be expressed as follows:

$$z_p + z_{flanges} + z_{web} \left\{ 1 - \left[\frac{C_1(Ls)^{C_2} sL \left(1 - \frac{s}{2L}\right)}{2\frac{f_y}{\sqrt{3}} A_{web}} \right]^2 \right\} \geq \frac{sL^2 \left(1 - \frac{s}{2L}\right) C_1 (Ls)^{C_2}}{8f_y} \tag{6.6}$$

where $z_{flanges}$ and z_{web} are the contributions from the plate flanges and the web to the plastic stiffener section modulus, and A_{web} is the web shear area. The term in the {}-brackets must remain positive for the shear capacity to be sufficient[1]. An iterative procedure is needed to determine exactly when this requirement is met. The above expression is similar to the requirement for stiffeners subjected to ice loads according to IACS-UR-I (2011).

Eq. 6.6 could be used for a rigorous strength design. The equation implies that the allowed stiffener deformation after collision is negligible. However, this is considered to be overly conservative for most structures, and unnecessarily expensive.

---

[1]Eq. 6.6 is only valid when the shear stress in the web is smaller than or equal to the shear yield stress. If a shear hinge is created at the supports, the resistance is limited by the yield shear force of the stiffener web.

A pragmatic approach is to allow the stiffener to undergo collapse but to limit the deformations such that there is ample margin before fracture in the shell plating. The damage should be sufficiently small to allow repair at a convenient time (preferably on site for permanent installations).

It is reasonable to assume that the resistance of the stiffeners remains constant during the allowable deformation range. It is difficult to set exact values on the allowable deformation; however, a plastic strain in the shell plate that is 1/3 of the fracture strain can be assumed to be a safe limit. From the simulations in this chapter, the strain reaches this level for a deformation approximately equal to a 10% deflection of the stiffener normalized to the stiffener length. This deformation mobilize membrane stresses in the panel which may contribute substantially to the resistance.

Plate

Yield-line theory was used to derive a new rooftop collapse model suitable for strength-design of stiffened panel structures with moderate deformations, extending the work of Jones (1971). The rooftop model is herein assumed to be constrained by stiffeners and the impacting bulbous bow. The dimensions of the bulb controls the width of the central part of the mechanism (U). The neighboring stiffeners constrain the angle of the yield lines ($\tan \phi$). As the indentation progress, the neighboring stiffeners fails sequentially, and the angle $\tan \phi$ changes. The total mechanism width is given as a_i.

The internal and external work was derived for this scenario (see Appendix D for details). Solving for the mechanism load yields

$$Q_{rt} = M_p \left[\frac{w}{h} \left\{ 32 \frac{(1 + i/n)}{b^2} + \frac{8}{nis^2} \right\} + \frac{2}{3w/h} \left\{ \frac{8}{nbs} + \frac{4}{nis^2} \right\} \right] \qquad (6.7)$$

where M_p is the plastic moment of the plate, w the indentation, h the plate thickness, b the mechanism height (stiffener length) and s the stiffener spacing. The integer n represents the width of the contact in number of stiffener spacings s. The integer i represents the number of stiffeners that carry load outside of the loaded area. In an integration regime, i will increase from 1 as a stiffener fails to support the membrane loads from the mechanism.

If large indentations are assumed, the latter part (containing $1/(w/h)$) of Eq. 6.7 may be neglected.
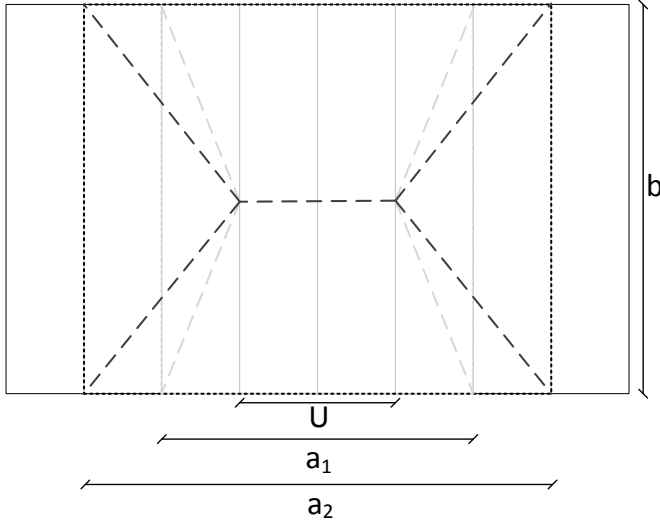
Figure 6.18: Roof top collapse mechanism between frames, spreading out due to failure of stiffeners outside of the loaded area. In the figure, $i = 2$ in Eq. 6.7 for the black dashed lines.

6.5.2   Proposed Method for Progressive Failure of Stiffeners with Increasing Indentation

The above rooftop model and the stiffener strength were combined to yield an integration procedure that accounts for the progressive failure of stiffeners as the indentation increases. Motivated by the stiffener response in Figure 6.17, in which the shear capacity of the stiffener was governing, the progressive indentation model assumes that a stiffener carries load by shear alone. Bending and membrane action in the stiffeners are thus disregarded. Rolling of yield lines for each increase in the mechanism width is disregarded.

A neighboring stiffener to the deflection zone has to carry the load transferred through membrane stresses in the deforming plate. As a simple assumption, it is postulated that all the edges of the roof top pattern carry equal amounts of membrane force. Each neighboring stiffener thus has to carry $b/(2(b + a_i))$ of the total load. The vertical shear force transferred to one stiffener is then

$$Q_{shear,neighbor} = Q_{rt}\frac{b}{2(b + a_i)} \tag{6.8}$$

If this shear force exceeds the shear capacity of the web, i is increased and the width of the mechanism increases with one stiffener on each side. The integration

is continued until the required total force is reached.

6.5.3   Investigated Side Shell Scantlings

Four different panel scantlings were determined based on the impact scenario and assumed deformation mechanisms. To represent the collision load, the pressure-area relation proposed in Eq. 6.2 was used, assumed to be evenly distributed over parts of the stiffened panel. The different scantlings were based on different assumptions of loaded area:

1) A model based on an existing platform designed according to conventional ULS requirements.
2) A model in which three stiffeners are assumed to carry the distributed load (the pressure is calculated over three stiffener spacings, with a total area close to the estimated contact area of the bulbous bow at peak force. Eq. 6.5 is used)
3) A model in which one stiffener is assumed to carry the local load (using Eq. 6.5)
4) A model in which the reduced plastic section modulus for shear is assumed to be satisfied when only one stiffener carry the local load (using Eq. 6.6)

The scantlings of the different models are listed in Table 6.3. The stiffened panels were assumed to have a yield stress of 355 MPa. Contact over the entire stiffener height was assumed. The weight per meter of the stiffener with plate flange is increased by a factor of five from the ULS design to the shear-resistant panel.

Table 6.3: Scantlings of panel configurations used to verify the strength design procedure: all values are in SI base units.

		Model 1 Existing stiffener	Model 2 Three stiffeners bending	Model 3 One stiffener bending	Model 4 One stiffener incl. shear
Frame spacing	L	3	3	3	3
Stiffener spacing	s	0.65	0.65	0.65	0.65
Plate thickness	t_{plate}	0.017	0.017	0.021	0.033
Web height	h_{web}	0.3	0.45	0.5	0.5
Web thickness	t_{web}	0.011	0.013	0.025	0.075
Flange width	w_{flange}	0.05	0.2	0.2	0.3
Flange thickness	t_{flange}	0.035	0.02	0.04	0.08
Plastic modulus	z_p	0.00113	0.00325	0.00696	0.0139
Weight of plate field	kg/m^2	198	257	420	1021

To investigate the effect of the plate and stiffeners alone, a very strong girder is modeled (T1200 $\times$ 400/30 $\times$ 30). In a design scenario, the girder must be suffi-

ciently strong to hold the forces from the stiffeners both as a global beam and as a local plate, but deflections of the girder (i.e., the whole panel) as a global beam are allowed. That would result in a girder with significantly smaller scantlings than the one applied in the analysis, thereby producing larger global deflections of the stiffened panel. The connection between the stiffener web and the girder needs to have a sufficient shear capacity to support the stiffeners locally.

6.5.4   Panel Responses Found Through NLFEA Simulations

To investigate the effectiveness of the structural scantlings found above, integrated NLFEA simulations were performed, in which the bulb of the supply vessel in Figure 6.2b collides with the four different panel models.

Figure 6.19a shows the stiffener indentation vs. the contact force for the different models, and Figure 6.19b the deformation state of the models in the stiffener mid-span at the peak crushing force. The key simulation results are listed in Table 6.4. The non-reinforced platform (model 1) shows approximately 17% deformation, and the stiffeners are not strong enough to initiate crushing of the bulb before contact with the stringers is well established. For model 2, in which the load is assumed to be uniformly distributed over three stiffeners, the stiffener deformation is somewhat reduced, and the crushing of the bulb starts directly after initial contact with the girders. Model 3, in which the plastic capacity in bending is sufficient to resist a uniform load over one stiffener, shows approximately 5% deformation. Model 4, which also satisfies the shear capacity requirement, shows less than 1% indentation (30 mm). Note that increasing the panel strength decreases the maximum force as the interaction effects are reduced.

Table 6.4: NLFEA simulation results for the four models subjected to bulb impact.

Maximum force [MN]	24.7	24.2	20.4	17.9
Indentation w [m]	0.5	0.45	0.15	0.03
Normalized indentation w/L [-]	17%	15%	5%	1%
Plate strain $\varepsilon_{eq,max}$ [-]	9.7%	8.5%	2.6%	0.1%

The equivalent plastic strain levels in the most strained plate surface are listed in Table 6.4. From the investigation in Chapter 5, the simplified tensile strain limit in DNV RP-C204 (Eq. 5.8) is found to give overall conservative estimates of the critical fracture strain. Using this criterion as a rough lower limit yields a maximum tensile strain of $\varepsilon = 0.02 + 0.65 t_e/l_e = 0.13$ for model 1. All of the models are below that limit, but not with sufficient safety margin. Both models 1 and 2 have strains $> 50\%$ of the limit, indicating that using three stiffeners for the load distribution may be a too loose requirement for rough hand calculations of the collision strength.

(a) Stiffener indentation up to initial crushing of bulb

(b) Deformation state for models 1 to 4 at peak force
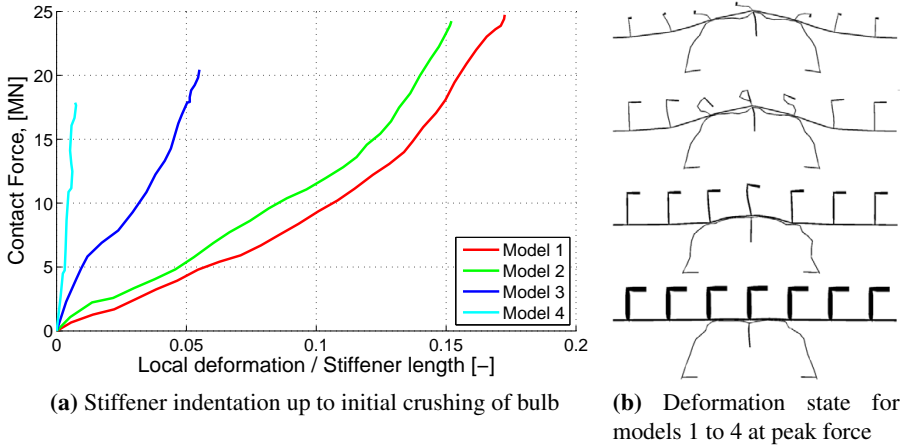
Figure 6.19: Force-indentation curves and deformation states for models 1 to 4 subject to bulb impact. Thicknesses of lines in (b) corresponds to plate thickness in each member.

Note that all of the models, including the non-reinforced (model 1), would be characterized as sufficiently safe designs according to the current rules, but not necessarily by strength design. The differences among the models are associated with how urgently repair work would be required and thus, the extent to which repair work could be planned without unnecessary interruptions of production.

The results in Figure 6.19 show that the requirement that the stiffeners should resist the collision load without undergoing shear failure is too strict for practical strength design. Very large web areas or very short stiffeners would be required to prevent stiffener collapse. It may be more useful to accept a partial collapse of the stiffeners, which is often governed by shear deformations, but the combined resistance of the collapsed stiffener and the shell membrane forces should balance the maximum crushing force.

Some additional plots from the simulation are shown in Appendix D.2.

6.5.5 Panel Responses Found Through a Simplified Procedure

The proposed rooftop + stiffener shear model in Section 6.5.2 was utilized, and the results of the NLFEA simulations in Figure 6.19 and Table 6.4 can be compared to the simplified approach.

The results obtained with the simplified approach are shown in Table 6.5. The maximum indentation w is captured well (19% in NLFEA vs. 14% simplified for model 1, 15% vs. 13% for model 2, 5% vs. 6% for model 3 and 1% vs. 0% for

model 4) . The width of the contact zone (a) compares well with the deformations observed in Figure 6.19b.

Table 6.5: Hand calculation of estimated indentation depth for bulb impacts with generic platform side models.

	Model 1	Model 2	Model 3	Model 4
b	3.0	3.0	3.0	3.0
U	1.3	1.3	1.3	1.3
a_i	6.5	3.9	2.6	2.6
$N_{stiff\ in\ shear}$	9.0	5.0	3.0	3.0
w	0.41	0.40	0.17	0.00
w/L	0.14	0.13	0.06	0.00
Q_{shear}	12.2	12.0	15.4	46.1
$Q_{rooftop}$	8.0	9.0	4.6	14.5
Q_{total}	20.2	20.9	20.0	60.6

Significant differences are present in the NLFEA simulations and the simplified approach:

- The NLFEA simulations consider the integrated deformation of an actual bulb, whereas the simplified approach considers a uniform pressure to act over two stiffener spacings. The total load is similar.
- Work hardening was included in NLFEA, whereas only elastic-perfectly plastic material was considered in the simplified approach.
- NLFEA captures the actual stiffener resistance, whereas the simplified approach only consider it's shear capacity.

Thus, the good correlations between Tables 6.4 and 6.5 does not mean that the rooftop+shear model gives excellent results. It may however indicate that the main load-bearing features of the panel are included, and that the progressive collapse of the stiffeners surrounding the impact is captured adequately.

6.5.6 Discussion

The NLFEA and simplified calculation method shows that the scantlings of model 3 may be regarded as a safe strength design. Thus, determining the strength-designed scantlings based on a plastic section modulus requirement without shear corrections (Eq. 6.5) with a uniform load over one stiffener (as given by Eq. 6.2) could serve as an efficient way to achieve practical strength design in the early design phase. This assumption ensures that the deformations are small, and repairs can likely be performed at a convenient time without affecting the operation of the platform.

The main difference between model 2 and 3 is the web thickness. If the stiffener

shall remain relatively intact when subjected to such high loads, it must be *compact* far beyond typical requirements used in ULS design. It is suggested that a web height to thickness ratio $h_{web}/t_{web} \geq 20$ is sufficient. This is likely maintained with a design approach as in model 3. Ice rules, such as IACS-UR-I (2011), have similar requirements to ensure buckling stability of the web of stiffening members. For flatbars, it is required that $h_{web}/t_{web} \leq 282/\sqrt{\sigma_0}$. Bulb, T and L profiles are required[2] to have $h_{web}/t_{web} \leq 805/\sqrt{\sigma_0}$.

The strength-designed scantlings in model 3 yields a weight increase factor of 2.1 compared to the ULS scantlings. For a large semi-sub-platform with three legs per pontoon, this results in a weight increase of approximately 400 tons for a 10 m high reinforced area, i.e., < 1% of the lightship weight. To reduce the extent of the strength-designed panels, operations could be planned such that the approach of the incoming vessels serving the platform is on one side of the platform only. A collision-resistant strength design could be applied on this side only, while the other sides could remain unstrengthened because of the lower probability of impact.

If a lighter structure is required, it may be reasonable to use the approach of model 2 combined with $h_{web}/t_{web} \geq 20$. This will give a response somewhere between model 2 and 3, thereby crushing a bulbous bow, but with a lower weight penalty and somewhat larger damage than model 3.

Assuming that the load carrying depends on the stiffener shear capacity combined with the plate membrane capacity produces reasonable agreement with the numerical simulations of actual impacts. It is emphasized that the proposed mechanism serves only as an illustration of possible load bearing mechanisms and is not a validated design tool. However, the resistance predicted by the model is similar to that obtained from the numerical analysis, indicating that it is relevant for strength design based on moderate stiffener deformations.

A simple method to determine strength-designed scantlings can be very beneficial in the early design phase. It is then required to determine the capacity to given impact events. A simple calculation method allows for better decisions on whether to increase structural scantlings or to increase the allowable damage to allow for the required collision energy to be dissipated.

In conjunction with strength design, it is clearly more effective to increase the stiffener shear capacity in the initial phase of the deformation, before tensile membrane forces dominate, rather than increasing the shell plate thickness. For ductile

---

[2]Note that exceptions to these criteria are allowed in the IACS rules provided that the web is stiffened (especially relevant to deep stringers or web frames).

or shared-energy design, a larger plate thickness may be preferable in order to exploit the beneficial plate membrane effect of large indentations.

6.6   Collision Between Ice-reinforced Vessels and Non-reinforced Platforms

6.6.1   Impacting Vessels

A wide variety of anchor handling or supply vessel designs are currently in operation. Due to prospects of Arctic supply operations, many vessels are constructed according to the ICE-1C class (capable of 0.4 m level ice), some with ICE-1A (1.0 m level ice) and some few offshore vessels with icebreaker class. Some of these vessels operate in ice during the winter and are used for normal open water operations during the summer, while other vessels primarily see open water operation. If an ice-reinforced vessel impacts a non-reinforced platform, the relative strength between the two is changed drastically compared to if both had ice reinforcements. Possible structural consequences of this are discussed in the following.

Two typical conventional vessels with bulbous bows will be compared; a normal supply vessel with no ice reinforcement and a ICE-1C strengthened vessel. Both vessels are assumed to have similar displacements and mass distribution, so that the external mechanics remain similar. Both vessels are constructed of regular mild steel.

The non-ice-reinforced vessel has a gross outer shell plate thickness of 12.5 mm in the bulb and between 9 and 11 mm in the bow superstructure. The ICE-1C vessel has a gross plate thickness of 17 mm in the bulb and 15 mm above the bulb. The stiffening system of the ICE-1C vessel is also more elaborate; with about half the stiffener spacing and shorter stiffener lengths. The vessel bows are shown in Figure 6.20.

Figure 6.21 compares the force-displacement response of the ICE-1C-strengthened vessel to a conventional vessel. The crushing strength is about twice that of a conventional vessel, both for stem and bulb contacts.

6.6.2   Drilling Platform

Impact with a modern semi-submersible drilling rig is used as a case study. The Moss Maritime CS60 rig design is a slightly larger version of the West Venture drilling rig, and is constructed with three columns on each pontoon. The operational draught is 23.5 m, at which the waterline is about halfway up the columns and the displacement is approximately 67000 ton. The total height of the column is 25 m. A transverse impact to the corner column is assumed, for which the sway

(a) Profile view   **(b)** Front view
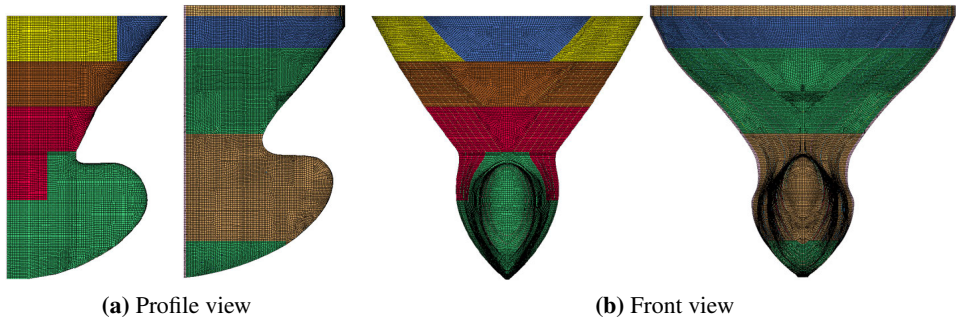
Figure 6.20: Vessel bows, non-strengthened (left) and ICE-1C-strengthened (right) from two different viewing angles.
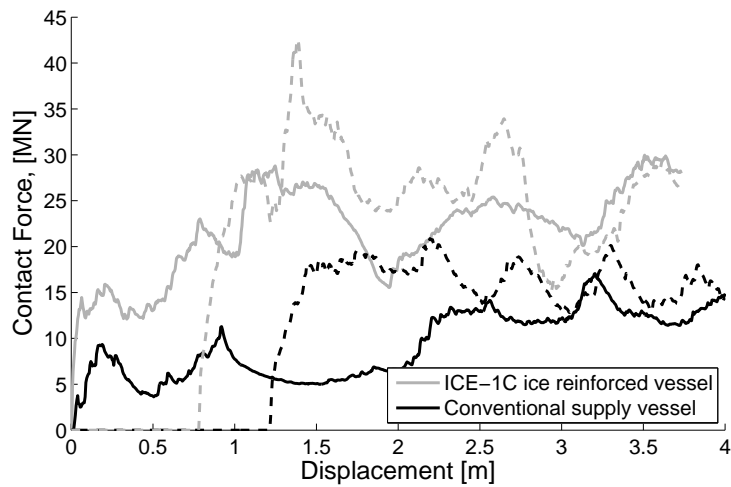
Figure 6.21: Force-displacement curves for non-strengthened and ICE-1C-strengthened vessel. Continuous lines represent the stem contact, dashed lines the bulb contact.

added mass coefficient of the platform is 0.64. The platforms radius of gyration in yaw is about 40 m.

The corner column is a simple steel grillage structure with 14 mm plate thickness and L250×90×10/15 and L300×90×11/16 vertical stiffeners spaced 640 mm apart. Stringers of approximately 1000 mm depth are fabricated from 12 mm plates, with 200×20 mm flanges, 400×12 mm tripping brackets and stringer spacing between 1.7 and 2.65 m, see Figure 6.22 and Figure 6.23. In way of the bulb contact, the stringer spacing is 2.1 m. Watertight decks are spaced up to five stringer decks apart. All material in the platform is of grade NV-36.

Figure 6.22: Platform column stringer, typical structural layout.

6.6.3   Impact Scenario

A variety of impact conditions could be considered in the horizontal plane with large differences in the required energy dissipation. A transverse impact to the platform column is assumed, with the supply vessel normal to the platform shell, see Figure 6.23. This will maximize the eccentricity of the impact with respect to the platform center of gravity, and is similar to the West Venture collision. External mechanics calculations using Eq. 2.3 and the radius of gyration in yaw shows that platform surge and yaw motions reduce the required energy dissipation by about 10%. Increasing the mass of the striking vessel will increase the reduction due to eccentricity.

With a total height of the platform column of 25 m, a regular supply vessel could impact the column from all outwards directions without hitting the pontoon or topside structures. Impacting at an angle of 145° from the forward centerline would give an impact to the starboard aft column with no eccentricity to the center of gravity of the platform. Consequently, the damage should be evaluated both for zero and maximum eccentricity.

Two impact locations are investigated locally on the platform column (Figure 6.24):

  a) A central impact on the column allows the bulb to interact with a single compartment. This creates the maximum indentation into the column.
  b) An impact to the side of the centerline allows the bulb to interact with two
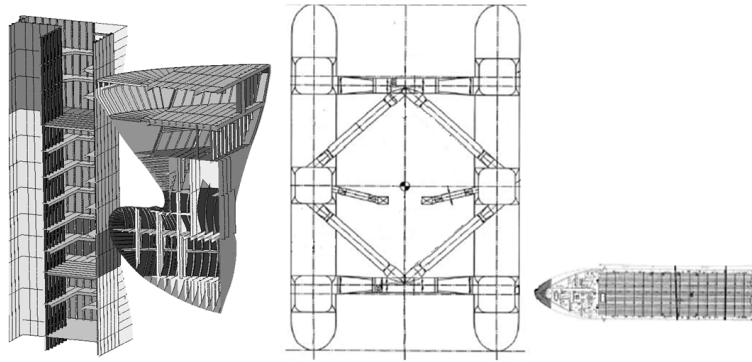
Figure 6.23: Vertical and horizontal global impact location.

compartments via an internal bulkhead in the column. With the actual compartment layout of the rig three compartments are put at risk of being punctured; two in way of the bulb and one in way of the stem.

(a) Mid compartment impact   **(b)** On internal bulkhead
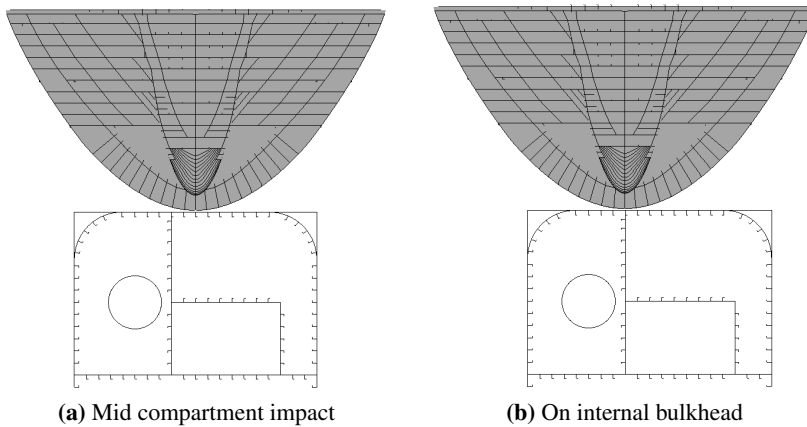
Figure 6.24: Horizontal impact locations on platform column.

6.6.4 Results

The simulations shows that the platform is able to resist the stem of both the conventional and ice-reinforced vessel (Figure 6.25). However, the bulb of the ice-reinforced vessel is significantly stronger than the platform, and easily pierces the platform shell with near rigid behavior if sufficient kinetic energy is available.

Figure 6.26 shows the dissipated energy in the platform and the supply vessel for both vessel bows. With the ice-reinforced vessel, significantly more energy has to

be dissipated by the platform compared to the conventional vessel. More energy is dissipated in the supply vessel for impacts on the internal bulkhead due to the increased local strength of the platform in this area.

For the ICE-1C vessel, a 1.4 m long rupture of the platform shell have developed in front of the bulb along the platform's internal bulkhead after 15 MJ of dissipated energy. Large-scale fracture was not observed in the other impact simulations.

6.6.5 Discussion

The collision resistance of a drilling rig was explored by means of integrated NLFEA according to the recommendations in the NORSOK N-004 code. Damages similar to those observed in the West Venture collision were found, though the bulb of the vessels used in this study is protruding more than for the Far Symphony vessel and thus causes larger damages below the waterline.

Collision with the ICE-1C strengthened vessel give larger damage than with the non-reinforced vessel. Three-compartment damage is probable, which is outside of the normal damage stability requirements. Even with three-compartment damage, the stability of the specific drilling rig was maintained within the current rule requirements of 17° heel angle. This is due to the rig's tank layout. Similar results may not be obtained for other rig designs with different tank layout and COG.

The difference in the platform resistance to impact from a conventional supply vessel and an ice-reinforced vessel is significant. Even a light ice class, like ICE-1C, can significantly alter the relative strength of the two interacting bodies in a platform - supply vessel collision. This leads to a significant increase of the energy dissipation in the platform, and thus a significantly larger damage potential, especially for high-energy collisions.

Another observation is the importance of the location of the bulbous bow with respect to the forecastle deck. The bulb of the ice-reinforced vessel is less protruding, thus allowing significantly more energy to be dissipated before it hits the platform. This is favorable and delays the onset of severe damage to the submerged areas.

Further ice strengthening than an ICE-1C class will significantly affect the integrated collision response, and the vessel will behave more rigid compared to a regular non-reinforced platform. If these vessels don't have a superstructure that can dissipate some energy from the impact, the strength of the ice-reinforced vessels may well be so high that they must be considered rigid.

Unconventional vessels can cause larger damage to the platform. Unconventional vessels with ice reinforcement can cause an even larger damage. Selecting which vessels that operate around the platform with their collision performance in mind

(a) Non-reinforced vessel   **(b)** ICE-1C vessel
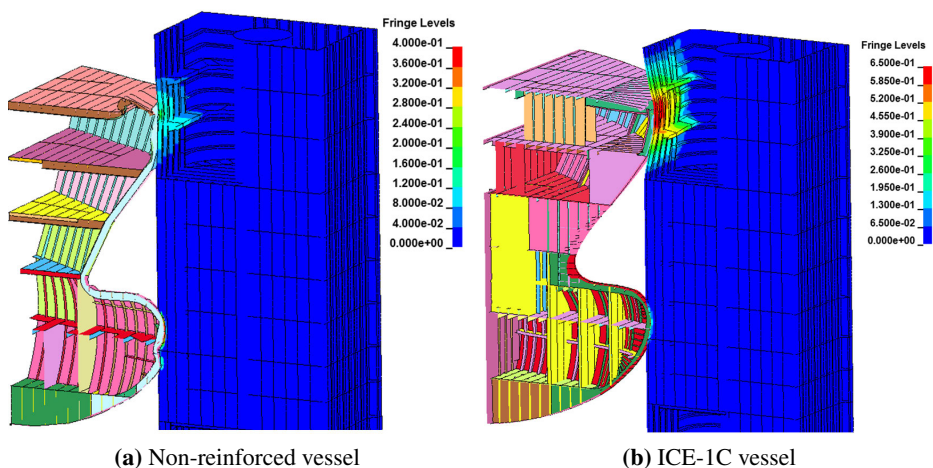
Figure 6.25: Indentation normal to shell of platform column after a 15 MJ impact on the internal tank bulkhead, fringe unit [m]

(a) Non-reinforced vessel   **(b)** ICE-1C vessel
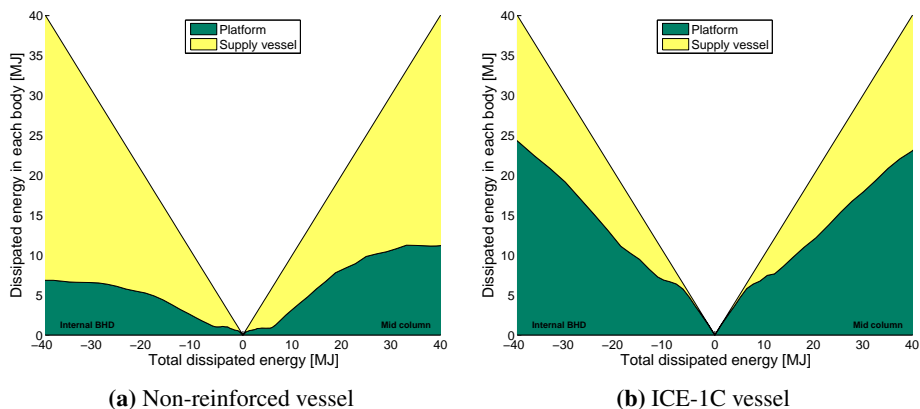
Figure 6.26: Dissipated energy in platform and supply vessel as a function of total dissipated energy, for mid column impact (positive energy) and impact on internal bulkhead (negative energy).

is likely the most cost-efficient and least expensive risk reducing measure.

6.7   Collisions with Jacket Platforms

Jackets are bottom-supported truss-work structures (Figure 6.29), comprised of *legs* (the main load bearing trusses) and *bracings* (the smaller interconnecting trusses that supports the legs and transfers shear forces). Due to their smaller size, jacket braces will sustain the largest damage from bow collisions. Ship side impacts to a brace are less likely, as the leg will prevent significant contact. Legs can be impacted by all parts of a ship. Although the legs are significantly stronger, they should not be neglected in damage prevention schemes. A high-speed central bow impact is a potentially serious event because the legs play the primary role of carrying the functional loads. Contact to the legs is also likely to occur in sideways impacts, whereas both the legs and braces are exposed in stern collisions.

A design impact event cannot be allowed to result in direct collapse of the jacket, and the damaged platform must be capable of resisting the design environmental actions (where all of the partial safety factors are equal to unity). Further, impact on the risers and the conductors may result in environmental pollution, and the accident may escalate into a catastrophic fire. Hence, the risers and conductors in the collision prone zone should not be located towards the outer perimeter of the jacket, but rather at a safe distance inwards to ensure that the impacting vessel can be stopped before environmental damage or fire is likely to occur. Collision design places heavy demands on a single or a few braces if these braces are assumed to dissipate most of the collision energy, and may become a major concern if the bow collision energy is increased in the revised requirements in NORSOK N-003.

6.7.1   Resistance of Jacket Braces and Legs

Ductile design is often assumed for bow or stern impacts with jacket braces, i.e., the brace must dissipate all of the strain energy. This assumption is also motivated by the observation that a ship bow is relatively sharp such that the struck brace is subjected to local denting, which further reduces the plastic resistance of the brace in bending. To dissipate a substantial amount of energy, the brace must be able to deform over a large deflection range (in the order of the brace diameter) so as to develop the beneficial tensile membrane force. This deformation can occur provided that the joints and the adjacent structure have sufficient strength to anchor the membrane forces. Tensile fracture limits energy dissipation in the brace. Using common fracture strain criteria, non-strengthened braces are typically found to only absorb energies in the range of 5 to 10 MJ. Therefore, it is often necessary to assume impact with multiple braces to stop a ship with a kinetic energy above 11 MJ.

The collision resistance can be substantially improved by assuming that the brace also damages the bow of the ship. This assumption is accepted within the requirements of NORSOK N-004, provided that the plastic collapse resistance in bending for the brace, R_0, exceeds a certain level, as shown in Table 6.6. The higher values of R_0 can only be achieved for relatively short or compact braces.

Table 6.6: Energy dissipation in bow for different brace resistances (NORSOK N-004 Table A3.3).

| Contact location | Energy dissipation in bow if brace resistance R_0 | | | |
	> 3 MN	> 6 MN	> 8 MN	> 10 MN
Above bulb	1 MJ	4 MJ	7 MJ	11 MJ
First deck	0 MJ	2 MJ	4 MJ	17 MJ
First deck - oblique brace	0 MJ	2 MJ	4 MJ	17 MJ
Between forecastle/first deck	1 MJ	5 MJ	10 MJ	15 MJ
Arbitrary location	0 MJ	2 MJ	4 MJ	11 MJ

One may assume the following response history for impact against a jacket leg: As the contact force increases, the brace/leg starts to deform by local denting. When the contact force, R, exceeds the plastic bending resistance of the brace/leg, R_0, the brace/leg will collapse. The collapse typically occurs via a three-hinge mechanism. During the local denting phase, the plastic resistance R_0 decreases because of the detrimental effect of the dent on the plastic bending moment M_p at the contact point. If the brace/leg is hit at mid-section and has constant dimensions, the plastic resistance is given by

$$R_0 = \frac{4M_p}{L}(1+k) \tag{6.9}$$

where $k = M_{p,red}/M_p$ is the relative magnitude of the plastic bending capacity at the dented section.

If little restraint is exerted on the brace/leg against pull-in at adjacent joints, the local denting process ceases, and the plastic resistance is virtually constant during further beam deformation. If a significant restraint against pull-in is exerted on the leg, membrane forces develop, the contact force increases and denting increases. Figure 6.27 illustrates the plastic resistance versus the beam deformation for a leg with and without an axial restraint, showing different denting regimes.

The effect of the dent is two-fold: first, energy is dissipated in the denting process, and second, the dent reduces the effective bending capacity of the leg.

The resistance to local denting of tubular specimens has been described in some detail by Amdahl (1980) and Skallerud and Amdahl (2002). In the aforementioned

(a) No axial restraint
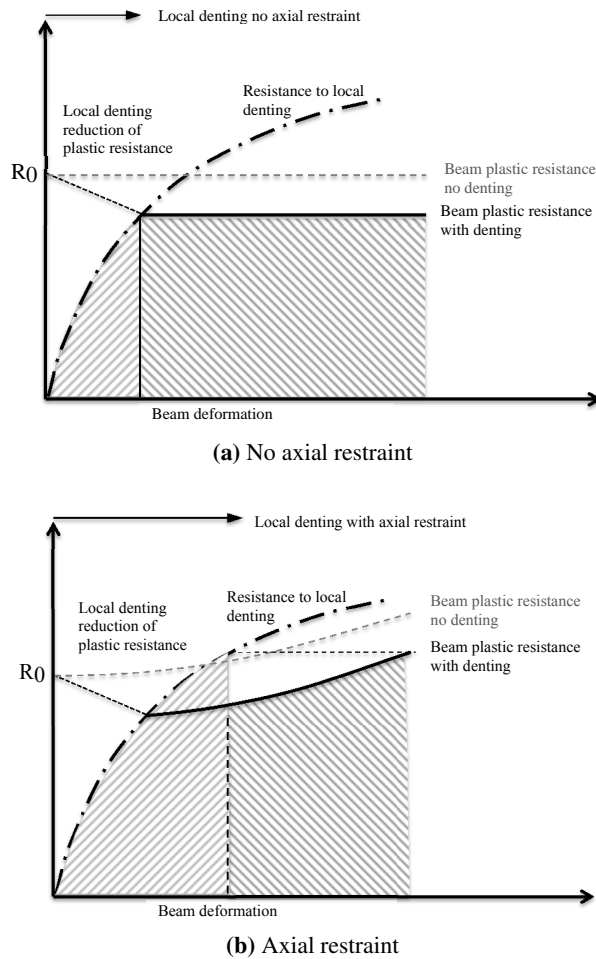
(b) Axial restraint

Figure 6.27: Plastic resistance vs. beam deformation for varying axial restrain

(a) Deformed cross-section

(b) Yield line model

(c) Resistance to local denting
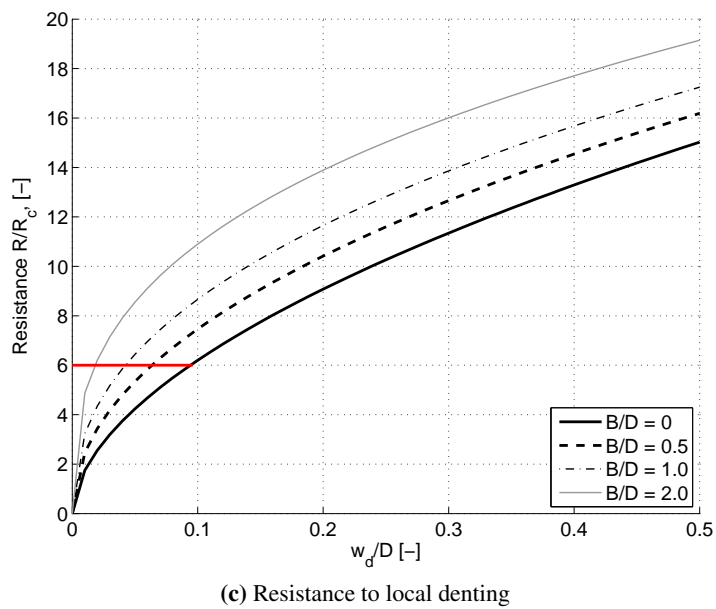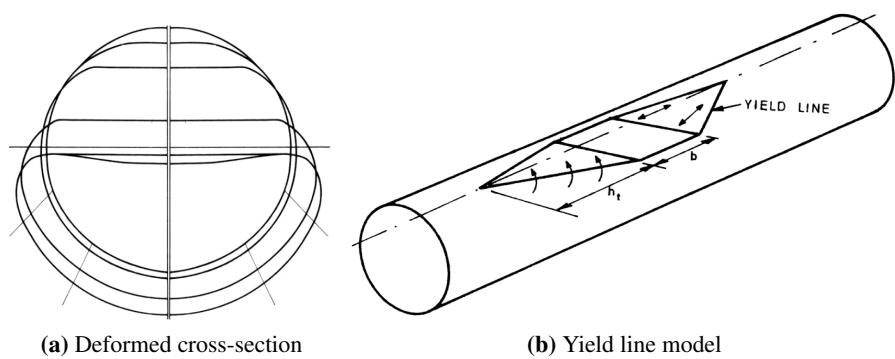
Figure 6.28: Plastic model for normalized resistance to local denting.

studies, plastic analysis based on the simplified yield line model shown in Figure 6.28a and 6.28b was performed. The flattened section of the model was assumed to be in direct contact with the ship. The resulting expression, which is adopted in NORSOK N-004, is plotted in Figure 6.28c and has the following form:

$$\frac{R}{R_c} = c_1 \left(\frac{w_d}{D}\right)^{c_2} = \left(22 + 1.2\frac{B}{D}\right) \left(\frac{w_d}{D}\right)^{\frac{1.925}{3.5+\frac{B}{D}}} \sqrt{\frac{4}{3}\left(1 - \frac{1}{4}\left[1 - \frac{N}{N_p}\right]^3\right)}$$

(6.10)

where w_d is the indentation, D is the tube diameter, t is the wall thickness, and B is the contact height. The last term accounts for the interaction between the denting and the axial loads in the leg, N, (e.g., functional loads) and was proposed by Wierzbicki and Suh (1988). N_P is the plastic axial force. The normalizing factor (characteristic strength) R_c is defined by

$$R_c = f_y \frac{t^2}{4} \sqrt{\frac{D}{t}}$$

(6.11)

where f_y is the yield stress. According to NORSOK N-004 denting may be disregarded if the brace fulfills the compactness criterion

$$f_y t^{1.5} \sqrt{D} \geq \frac{2}{3} R_0$$

(6.12)

where R_0 is calculated using Eq. 6.9. This criterion can alternatively be expressed as

$$\frac{R_0}{R_c} \leq 6$$

(6.13)

and is plotted as a red line in Figure 6.28c. The figure shows that the requirement is related to a dent depth $w_d/D \leq 0.1$ for $B = 0$ (thereby assuming a point load). Thus, the effect of denting on the plastic capacity can be disregarded if $w_d/D \leq 0.1$. If the load is distributed over a larger length ($B > 0$), the requirement in Eq. 6.13 can be relaxed.

The idea behind the requirement is that local denting can be neglected provided that the collapse load in bending is sufficiently small compared to the denting force. This requirement was developed by assuming local denting for a concentrated load. Table 6.6 was developed for typical supply vessel bows in the 1990s,

i.e., raked bows with no bulb, and is used in conjunction with Eq. 6.10 in the current NORSOK rules. The question arises: Is this local denting requirement also appropriate for bulb impacts, especially if crushing of the bulb is achieved?

Several assumptions that were used in the calculation procedure could also be questioned, e.g., what width should be assumed for the contact area? Most often, a concentrated collision force is assumed ($B = 0$). This assumption is always conservative. Assuming a larger contact width B would significantly increase the resistance of the leg. However, are the resistance curves for a large contact width at all realistic? A ship is not a rigid structure like the solid beams that were used in the tests (Amdahl 1980) and assumed in the plastic yield line model.

Jacket legs are typically designed with inclination, e.g., a batter of 1:8. In these cases, the initial contact in a sideways collision probably occurs at the bilge. Upon further deformation, the contact height is likely to increase because of the deformation of the structure and/or by ship rolling.

6.7.2 Numerical Analysis of Brace Impact with a Bulbous Bow

To investigate these issues, a series of nonlinear finite element simulations of jacket impacts were carried out using LS-DYNA. The jacket used for this study was intentionally designed to be resistant to ship collision.

Figure 6.29 shows a global finite element model of the jacket. The vertical brace in position 1 is 50 mm thick, has a diameter of 1.3 m and is 21 m long, as measured from the chord-to-chord intersection. The diagonal brace in position 2 is 60 mm thick, has a diameter of 1.2 m and a chord-to-chord length of 24.4 m. The braces are fabricated of high-strength steel with a yield strength of 460 MPa.

The jacket may be exposed to collision on all sides. Herein, two impact positions are considered, both shown in Figure 6.29. Assuming that the collision force acts as a concentrated load at mid-span, the collapse resistance in bending, R_0, is 13.7 MN and 11.8 MN respectively for positions 1 and 2. According to Table 6.6, the ship bow will be substantially damaged and dissipate more than 11 MJ of strain energy. The value of R_0/R_c is calculated to be 9.3 and 6.4 for positions 1 and 2, with R_c values of 1.47 and 1.85, respectively. This result implies that local denting cannot be ruled out and that the value used for the resistance in bending, R_0, may be too optimistic for position 1. For position 2, the calculated resistance is more likely close to the limit value, and local denting is expected to be small.

To determine the resistance to local denting, a submodel of the impacted braces was developed in LS-DYNA using shell elements. Ship rolling and pitch motions are neglected such that the ship is assumed to float in upright position during the
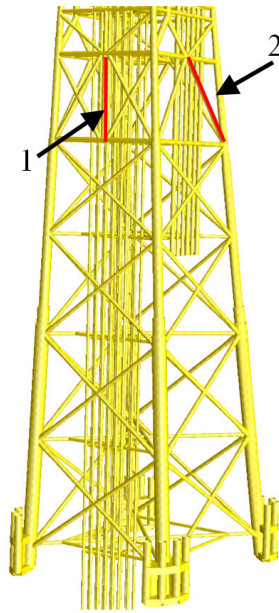
Figure 6.29: FE model of jacket with collision positions.

collision. Only deformations of the bulb are considered due to the significantly lower contact load and higher contact area exerted from the bow stem to the brace. In all of the calculations, local denting is defined as the original diameter of the leg less the distance of the reduced "diameter" of the dented section.

Figure 6.30 shows the force deformation curve for the bow colliding against the brace in position 1. The local deformation (indentation) of the cross section of the brace is above 0.5 m (40% of the diameter), and the global deflection is approximately 1.1 m. The bulb crushes with a maximum force of approximately 18-20 MN against a *rigid* brace. However, for a *deformable* 50-mm brace, the integrated crushing force exceeds 22 MN, because the brace wraps around the bulb during deformation (thereby making the bulb "stronger"). Consequently, the collapse resistance in bending, R_0, should be at least 20 MN to avoid the development of substantial lateral, plastic deformations. In the present case, the brace thickness should preferably be increased slightly to reduce the dent depth.

Figure 6.31 shows the force-deformation relationship for the bulb and the lateral (beam) deformation at the contact point when the brace thickness varies from 50 mm to 65 mm. The curves show that there is a significant change from shared energy design to strength design as the thickness increases. Local denting is substantial for a thickness of 50 mm, but becomes very small for thicknesses of 55

(a) Force-displacement
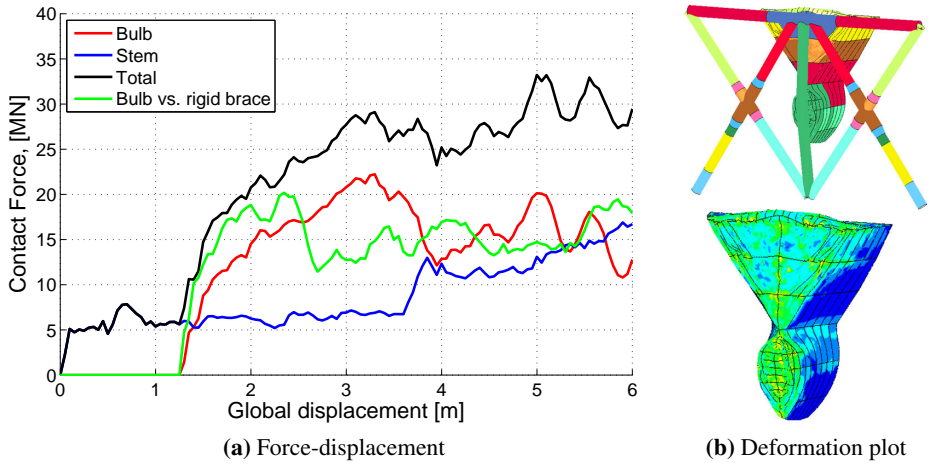
(b) Deformation plot

Figure 6.30: Force vs. deformation for position 1 and a 50-mm brace thickness.

mm and above. Global deflection is still significant for a thickness of 55 mm, but is very limited for 60 mm thickness. In practice, a 55-60 mm thickness may be categorized as strength design. These results illustrate the rapidity of the transition from shared energy to strength design.

(a) Global deflection

(b) Local deformation
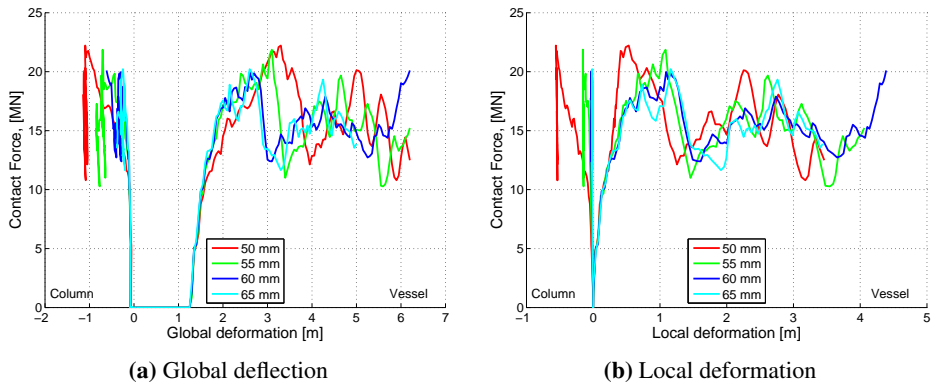
Figure 6.31: Force vs. deformation for position 1.

Simple hand calculations of the plastic resistance (Eq. 6.9) confirm these results. In the present case the jacket nodes have overmatching strength. This justifies measuring the beam length as the chord-to-chord intersection (rather than as the center-to-center length of the beam). Further, because the leg can crush the bulb with minor denting, the crushing force may be assumed to be uniformly distributed

over a height of 4 m, thus reducing the effective beam length used in the collapse mechanism by 4 m (assuming two hinges with equal displacement that are spaced 4 m apart at the contact point). Using a 55 mm thickness and a 17 m length for the brace, we obtain $R_c = 1.7$, $R_0 = 18.5$ MN and the ratio of the collapse load to the local denting parameter $R/R_c = 10.9$. In conclusion, a sufficiently thick brace ensures k $\approx$ 1 in Eq. 6.9 (only minor denting), and crushing of the bulb significantly increases the contact length. Both effects increase the collapse load of the brace.

Figure 6.32 shows the contact force versus the total ship displacement for a collision at position 2. Only the bulb is in contact with the brace. The brace crushes the bulb significantly but undergoes a global plastic deformation of 0.6-0.7 m before the bulb crushing force levels out. No local denting of the brace is observed. The contact force is similar to impact against a rigid brace, but at a larger global displacement of the beam. The contact length in position 2 is smaller than the contact length in position 1. In addition, the chord-to-chord length is larger in position 2 than in position 1, so it is reasonable to assume that the collision force for practical purposes is concentrated in position 2. Assuming a concentrated load, the plastic collapse resistance for the brace is 11.9 MN, which compares well with the simulation results. Hence, the brace in position 2 is not strong enough to withstand an impact from the bulbous bow without global deflection of the brace, but is locally strong enough to initiate crushing of the bulb tip once sufficient membrane forces are activated to resist the total force.

(a) Force-displacement   **(b)** Deformation plot
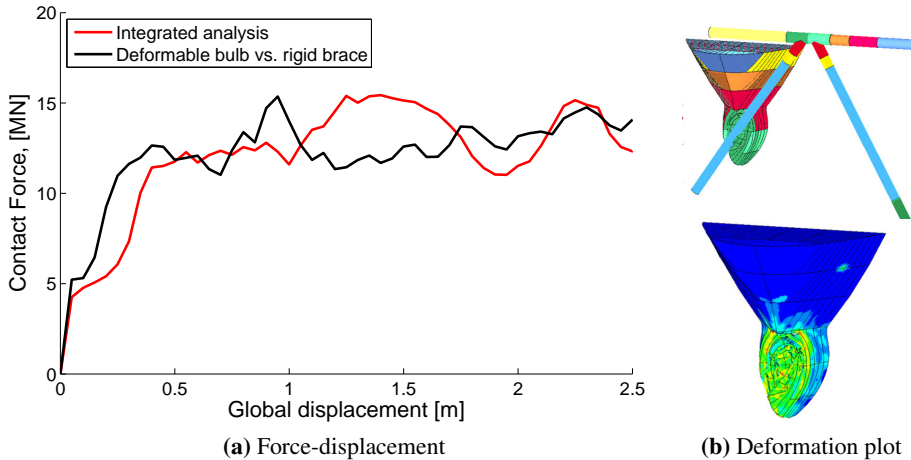
Figure 6.32: Force vs. deformation for collision of a bow against a deformable and rigid brace at position 2.

The compactness requirement from NORSOK N-004 is not met in either case, but

local denting is only evident for position 1 (for the 50- and 55-mm thicknesses). If the brace in position 1 is to be strengthened to satisfy the compactness criterion $(R_0/R_c \leq 6)$, the thickness has to be increased from 50 to 103 mm for the same diameter, which also doubles the plastic capacity R_0. Crushing of the bulb tip occurs at a thickness ≥ 60 mm, thereby distributing the load over a larger length of the brace. This in turn increase both the global brace resistance and the resistance to further local denting. In view of this, the NORSOK requirement of using a point load to estimate the resistance to denting seems to be unreasonable for strength-designed jackets than can initiate local crushing of the bulb.

The NORSOK requirement is based on local denting considerations for impact by a rigid, plane object. This requirement substantially underestimates the resistance to denting when the deforming bulb "wraps" around the brace. The difference between the idealized concentrated load and the actual distributed load can be understood by inspecting Figure 6.33, which shows how the bulb wraps around the column for the impact position 1. The force-displacement relationship in Figure 6.34 shows that the response is similar to crushing from a rigid bulb up to approximately 1-1.5 m, but when the bulb crushing resistance is reached the bulb deformation starts to govern the resistance. When the brace is rigid, bulb crushing starts immediately, and the force is higher for moderate deformations. For a fully integrated analysis in which both bodies deform, the crushing of the bulb is delayed compared to crushing against a rigid brace because the brace deforms locally and globally. Only a small increase in the crushing force is observed for the integrated simulation compared to with a rigid brace. The actual capacity of the brace impacted by a rigid bulb by far exceeds the bulb crushing force when the membrane contribution is accounted for, and fracture does not occur until 3 m global deflection.

Figures 6.35 and 6.36 show the normalized resistance to local indentation for the brace subject to a bulb collision for positions 1 and 2 with varying brace thicknesses. The NORSOK local denting expression (Eq. 6.10) is also plotted. Local denting ceases if the brace thickness is above 55 mm for position 1 and above 50 mm for position 2. The corresponding R_c values are 1.7 and 1.4, respectively. The brace at position 2 is inclined such that the contact width is lower than for position 1.
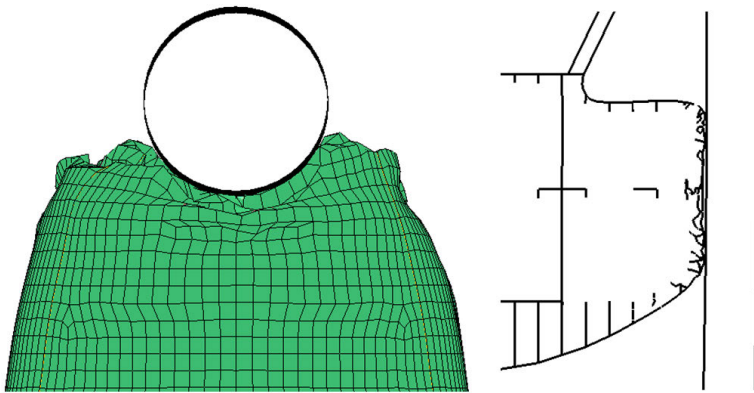
Figure 6.33: Typical deformation of bulb against a strength-designed column at position 1.
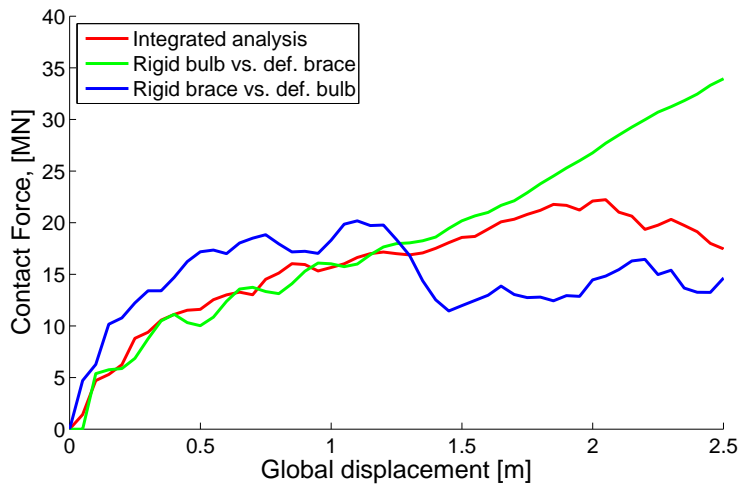
Figure 6.34: Force-displacement relationship for integrated analysis for a collision of a rigid bulb against a deformable brace, a rigid brace against a deformable bulb and a deformable bulb against a deformable brace in position 1 for a 50-mm brace thickness: the displacement corresponds to the global displacement of the vessel (not considering deformations).
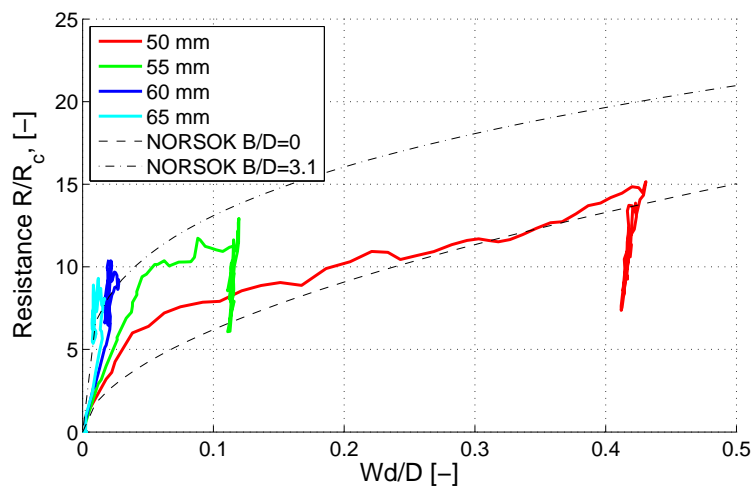
Figure 6.35: Normalized resistance to local indentation for collision of bulb against brace in position 1.
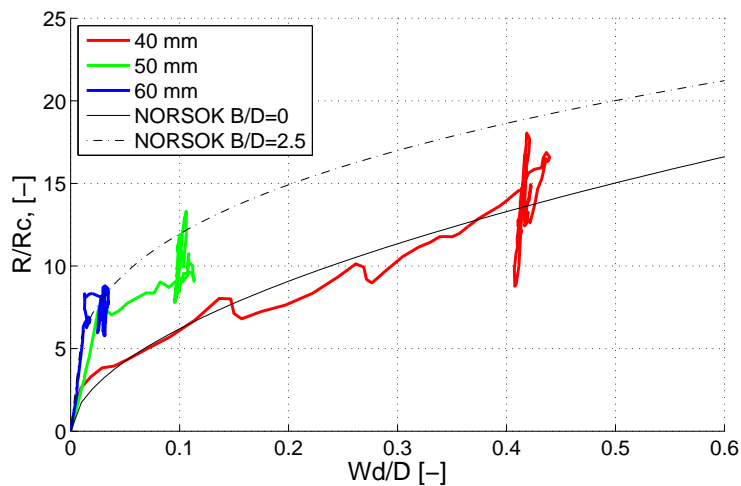
Figure 6.36: Normalized resistance to local indentation for collision of bulb against brace in position 2.

6.7.3   Numerical Analysis of Broadside Collisions Against Jacket Legs

A broadside collision of the four-leg jacket shown in Figure 6.37 by a supply vessel was investigated. The jacket leg interacts with the adjacent platform structure. The adjacent joints are assumed to be stronger than the leg, such that plastic hinges occur in the leg inward from the joints. The rotational degrees are assumed to be fixed (because elastic rotational flexibility plays a minor role). In the axial direction, the leg is typically subjected to compression induced by the functional loads. If the leg deforms by plastic bending, the adjacent joints will move inwards such that the functional loads may be redistributed to other legs in a redundant jacket structure. This effect is modeled by linear axial springs. The spring stiffness of the two ends is estimated by replacing the leg by unit inward forces at the two joints and calculating the inward motion. The leg is meshed using 100 mm shell elements. The material has yield strength f_y = 355 MPa. The power law model is used with a strength coefficient of K =790 MPa and a hardening exponent n = 0.19. In the parametric study, the brace diameter is 1, 1.5 and 2 m, and the wall thickness is 30-70 mm. The jacket has a batter of 1:8 (inclined legs).

(a) Impact location   **(b)** Boundary conditions
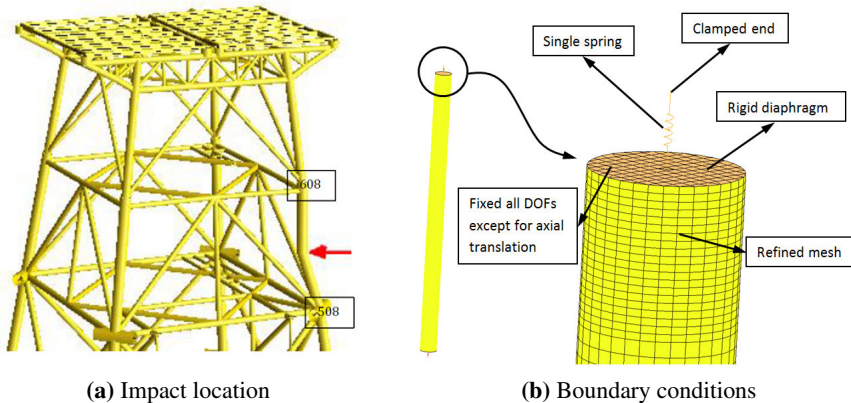
Figure 6.37: Modeling of jacket leg.

Two supply vessel sides are investigated with displacements of 7500 and 2250 tons, as shown in Figure 6.38. The height from the keel to the main deck of the vessels is 7.6 and 6.9 meters. Contact heights of approximately 6.8 and 6.1 meters are obtained in the analysis because of the bilge shape. The 7500-ton vessel has a shell thickness of 9 mm and closed frames of 9.5 mm in the bilge area. Above the bottom deck, longitudinal HP200×8 stiffeners are spaced 600 mm apart with a frame spacing of 2.6 m. The 2250-ton vessel has a shell plate thickness of 9.5 mm

(a) 7500 ton displacement   **(b)** 2250 ton displacement
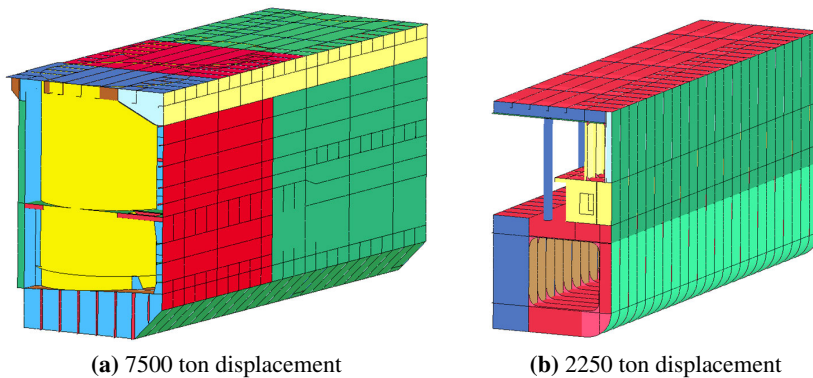
Figure 6.38: Finite element models of supply vessel sides.

and L400×50/80×10 stiffeners every 600 mm. The deck thickness is 8 mm, with a deck spacing of approximately 2.6 m.

The ship sides are supported along the centerline and at the ends of the modeled sections, because the global bending effects are considered to be minor. The analyses are conducted with a constant prescribed displacement without allowing for any roll motion of the vessel. This may be reasonable as the distance between the impact location and the center of gravity is small.

The ship side models impacts rigid columns with three different diameters, D=1, 1.5 and 2 m. The deformation pattern and the resistance to penetration of the side are virtually independent of the column diameter. Thus, results for are discussed interchangeably between the various diameters in the following discussion. Figure 6.39 shows the force-deformation relationships for the two side models for a vertical cylinder and a battered cylinder with D= 1 m. The 7500 ton vessel shows considerably higher strength at large deformations because of its internal structures, whereas the 2250 ton vessel is considerably weaker because of its smaller and more open design. For impact against a battered leg, the initial force is considerably smaller than the NORSOK curve with $D = 1.5$ m for both vessels. However, the NORSOK curve was developed assuming that contact occurs over the entire side and is reasonably representative for impact against a vertical leg. The sudden drop in the NORSOK curve for the 1.1 m penetration, caused by the assumed fracture in the side plating, is not observed in the finite element simulations.

Next, the effect of local denting is investigated for impacts against a battered leg for varying leg diameters and thicknesses. Figure 6.40a shows the damage condition at the end of simulation for 30 mm leg thickness. Contact has developed over the entire ship side, and the leg has undergone extreme denting/flattening over a
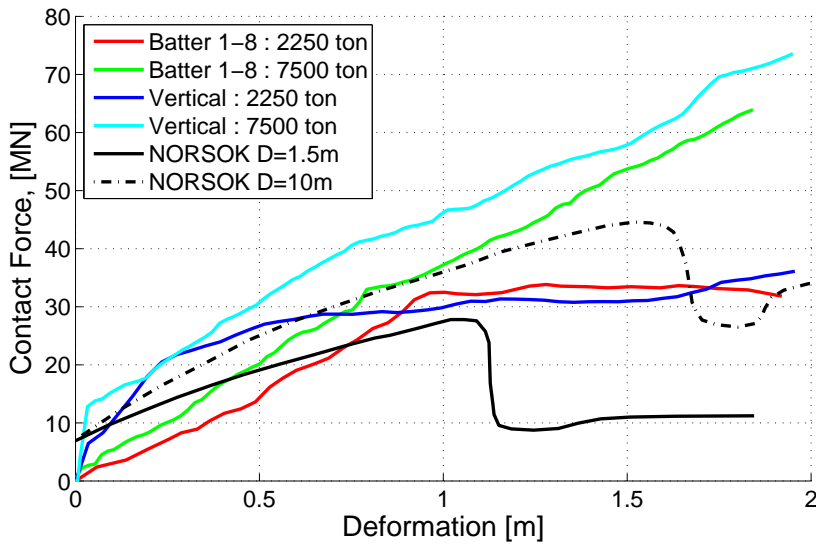
Figure 6.39: Deformation of side models for 1 m rigid column with and without batter angle.

very large portion of its span. When the leg thickness is increased to 70 mm, the deformation switches from the leg to the ship hull. The leg undergoes some plastic bending but no significant denting (see Figure 6.40b).

Corresponding pairs of collision forces versus deformation of the contact point for the jacket and the side of the 7500 ton vessel are plotted in Figure 6.41 for various leg thicknesses. For the jacket leg, the displacement consists of a contribution from the denting and a contribution from the leg deformation. For the ship, the displacement represents the maximum penetration of the jacket leg into the ship hull. The curves demonstrate that there is a strong interaction between the two structures and that there is no unique force-deformation curve for the ship: if the leg undergoes significant denting, the side becomes stronger with respect to the penetration, and the force vs. indentation distance increases. The force-displacement curves may change somewhat if roll is allowed in the simulations.

Figure 6.42 shows the normalized collision force R/R_c vs. the local denting of the leg for a side impact. The measured value thus includes the local denting and the possible ovalization of the column (these effects cannot be separated). The point at which contact is established over the entire ship side is indicated by a solid circle in the plots.

The normalized contact force-deformation relationships show that it is reasonable

(a) 30 mm, 22 MJ   (b) 70 mm, 58 MJ
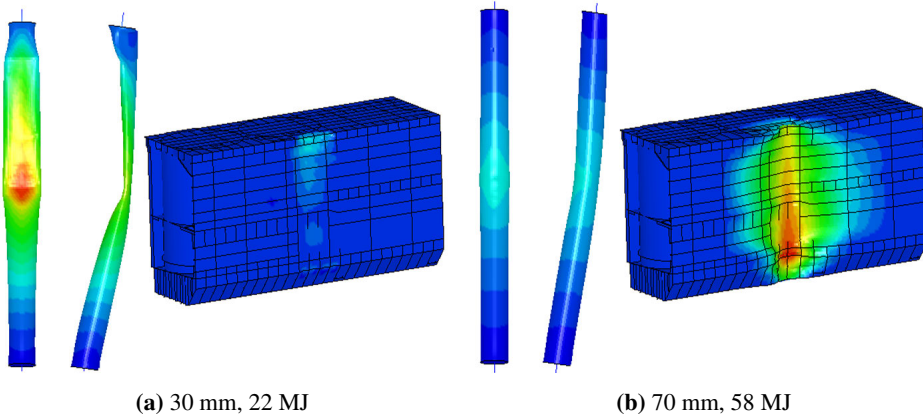
Figure 6.40: Simulated damage for two leg thicknesses and the corresponding total energy dissipation (leg+side).

to assume that the load is concentrated for leg thicknesses of 30 mm and 40 mm, because the leg undergoes significant local denting. For leg thicknesses of 50 mm and above, the denting is substantially reduced, and it is appropriate to use the resistance curve for contact over the entire ship side. Local denting interacts with beam collapse for $R/R_c > 15$ for a leg thickness of 50 mm.

This trend is similar to that observed for a column diameter of 2 meters (see Figure 6.43), except that the transition thickness is 40 mm. For a 1 meter column diameter, the NORSOK curve at the full contact height apparently overestimates the resistance to local indentation. However, the distinct increase of denting at $R/R_c \sim$ 8-10 is caused by interaction with global collapse, which occurs long before the full contact height is reached.

Table 6.7 shows the R_0/R_c relation for different combinations of thicknesses and diameters of the jacket legs investigated in the study of the vessel side impacts, and Table 6.8 shows the R_c values. Only the 1 m leg diameter with leg thickness above 50 mm satisfy the local denting requirement with $R_0/R_c \leq 6$.

Table 6.7: R_0/R_c for impacted legs in parametric study.

D/t	30 mm	40 mm	50 mm	60 mm	70 mm
1 m	7.6	6.4	5.6	5	4.6
1.5 m	14.2	12.1	10.7	9.6	8.8
2 m	22	18.9	16.7	15.1	13.9

The numerical analysis shows that the transition where the brace local denting pro-
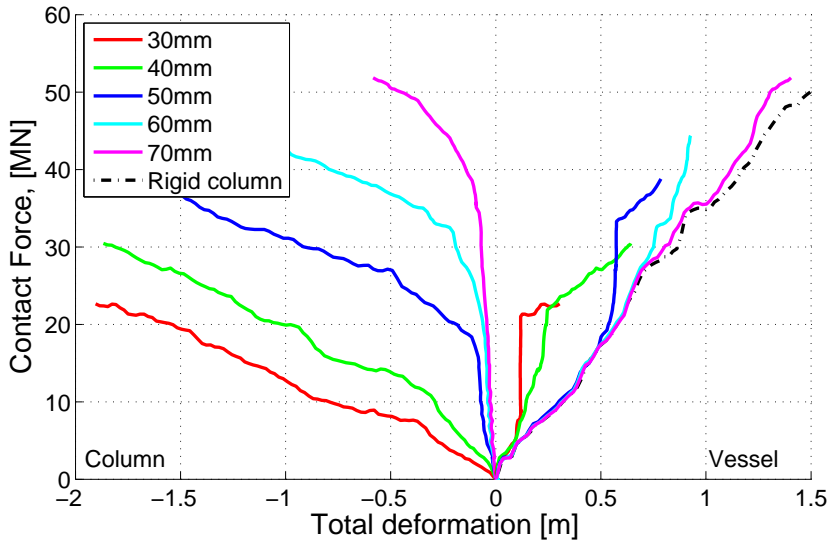
Figure 6.41: Contact force versus deformation for D= 1.5 m, 7500 ton vessel.
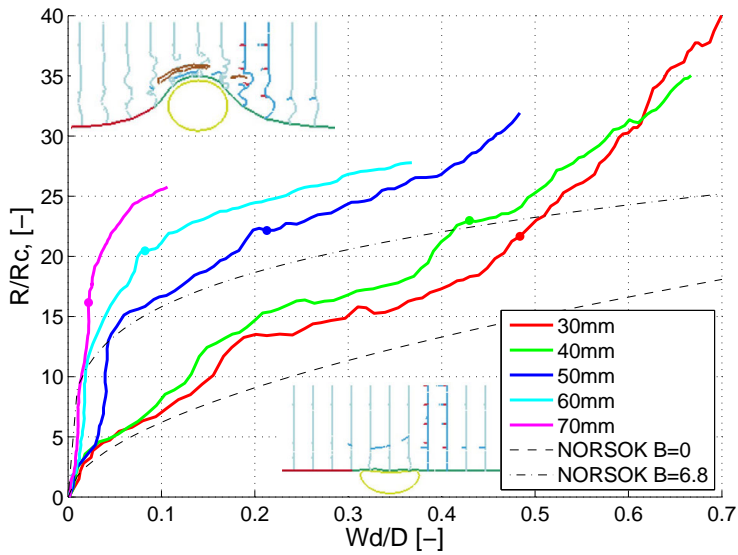
Figure 6.42: Normalized contact force versus local denting for D=1.5 m; the full contact height is marked with a solid circle, 7500 ton vessel

(a) D=1.0 m

(b) D=2.0 m
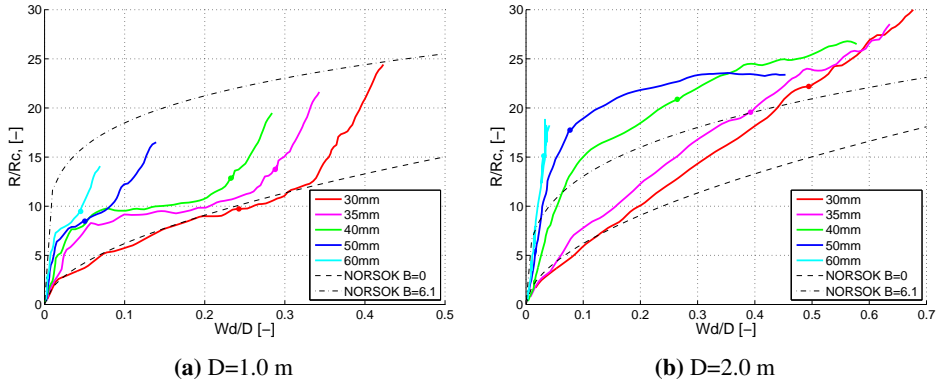
Figure 6.43: Normalized contact force versus local denting for varying leg diameter, 2250 ton vessel.

Table 6.8: R_c for impacted legs in parametric study.

D/t	30 mm	40 mm	50 mm	60 mm	70 mm
1 m	0.46	0.71	0.99	1.3	1.64
1.5 m	0.56	0.87	1.22	1.6	2.01
2 m	0.65	1	1.4	1.84	2.32

cess ceases is fairly constant at 40-55 mm (larger thickness for smaller diameter). This is also supported by the findings of Travanca and Hao (2014). The R_0/R_c relation is not by itself enough to consistently estimate whether the jacket satisfies strength design in terms of the resistance to local denting. Simply using the normalizing factor R_c appears to fit the numerical results better, where the incoming vessel is crushed if $R_c > 1.2$.

If the batter is reduced, the resistance to local indentation will change significantly because of the increased probability of a flat impact. The full contact height is then established at an earlier stage, and approaches the NORSOK resistance curve quickly (see the results in Figure 6.44 for a leg with diameter 1.5 m). With no batter, the full contact height can also be more safely utilized for smaller leg thicknesses, though with some uncertainty for small local indentations. However, it may not be a conservative design assumption that a flat contact is the relevant design event.

Note that using the curves for the rigid ship or column could lead to highly distorted conclusions in terms of the collision resistance of the leg if the objective is strength design. The error will be to the safe side if the contact height is assumed to be zero, but any effort to strengthen the platform leg by increasing the stiffness,
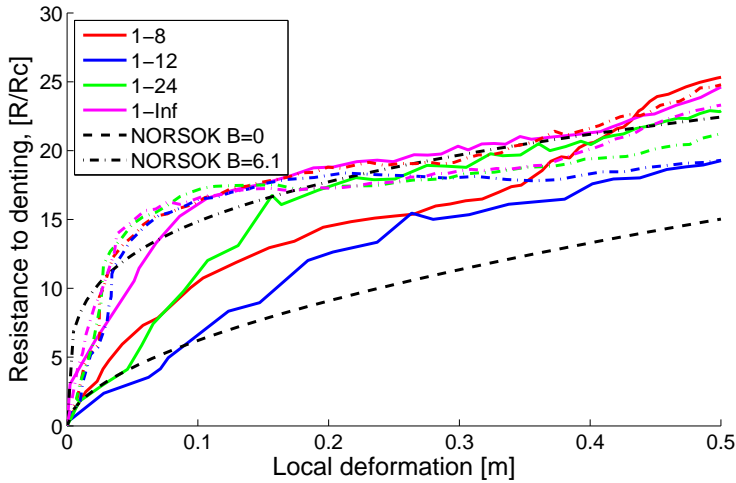
Figure 6.44: Normalized contact force versus local denting for varying batter angles, D= 1.5 m and wall thicknesses of 35 mm (solid line) and 50 mm (dashed line). 2250 ton vessel.

for example from 45 mm to 55 mm, is not given the credit it deserves.

The NLFEA simulations confirms that strength design of the jacket braces for high energy impacts can be achieved using reasonable brace dimensions when accounting for the relative strength between the vessel and the column.

6.8   Strength Design Procedure for Jacket Broadside and Bulbous Bow Collisions against Jackets

If a jacket is to be strength designed to resist impacts from typical bulbous bows, the brace/legs plastic resistance in bending R_0 (Eq. 6.9) should be above the crushing force of the bulb including any effects of local denting. NORSOK N-004 postulates that local denting can be disregarded if $R_0/R_c \leq 6$ (thereby ensuring that $w_d/D \leq 0.1$).

For large values of R_0, the R_0/R_c requirement may yield impractically thick pipes. Through numerical simulations, the transition from local denting to crushing of the striking ship was observed to be rapid, and occurred if R_c surpassed an absolute limit η. This is suggested as a new compactness criterion for initiation of crushing of the striking ship, as $R_c \geq \eta$. For the investigated supply ships, $R_c \geq 1.7$ for bulb and $R_c \geq 1.2$ for supply vessel sides was found to be sufficient to initiate crushing of the striking ship.

For strength design, the plastic resistance R_0 should be large enough to crush the

striking ship. For the supply ship used in this study, the peak crushing force is around 20 MN for the bulb. Further, the brace/leg must fulfill the compactness criterion; $R_c \geq \eta$, where η is a function of the striking ship's design. Satisfying both these requirements ensures that both global and local deformations of the brace/leg are small.

If the brace/leg is not strong enough to crush the ship, i.e., $R_0 <$ the crushing force of the ship, the brace/leg will fail globally, but it will absorb significant amounts of energy. Membrane forces will be mobilized, and the globally deformed brace/leg may then become strong enough to resist the striking ship.

If the compactness criterion $R_c \geq \eta$ is violated, the striking ship should be treated as a point load, and the reduced capacity of the brace/leg due to denting should be evaluated. This will in essence create a plastic hinge in way of the point load.

When the compactness criterion $R_c \geq \eta$ is complied with, the cross-section of the brace is strong enough to initiate crushing of the striking ship, and the load will be distributed over a finite length. The plastic capacity of the brace/leg may then be calculated by considering the length of the distributed load (rather than a point load). This may be envisaged as two plastic hinges spaced B meters apart, where B is the length of the distributed load.

A practical strength-design may be achieved by first evaluating the compactness criterion $R_c \geq \eta$. When this is satisfied, the plastic resistance R_0 may be calculated with a reduced length L_{red} as

$$L_{red} = L - B \qquad (6.14)$$

Satisfying the compactness requirement $R_c \geq \eta$ distributes the load along the beam, causing two beneficial effects:

  - Increasing resistance to local denting with high B/D-ratio
  - Increasing plastic resistance of the beam with $L_{red} = L - B$

For the bulb used herein, the contact height B was found to be around 4 meters. For ship side impacts, the height from upper deck to the bilge (length of the vertical ship side) was found to be about 6 meters for conventional supply vessels with displacement of 7500 ton.

As a practical design limit including a safety margin to account for different bulb designs, $R_c \geq 1.9$ is assumed to be sufficient to crush a striking bulbous bow. Similarly, $R_c \geq 1.4$ can be used for a vessel side. If a vessel with a significantly different crushing strength is used, the R_c requirement may be scaled. For

example, if crushing of the bulbous bow of the ICE-1C reinforced vessel (Figure 6.21) is required, the R_c requirement may scale as $R_c \geq 1.9 F_{icebulb}/F_{bulb} = 1.9 \ 40/20 = 3.8$.

6.9 Concluding Remarks

Current design guidelines for ship collisions with offshore structures were developed thirty years ago for supply vessels of 5000 ton displacements with a raked bow. The guidelines need to be revised in view of significant increases in the supply vessel sizes and a wide variety of bow configurations (bulbous bows, X-bows etc.) that can exert significant collision forces over small areas on platforms. In addition, if ice-reinforced supply vessels are used to serve offshore platforms, significantly stronger bows will be used than that assumed in NORSOK N-004.

The expected increase in the requirement for the kinetic energy from accidents will place heavy demands on the energy dissipation. There are several scenarios for which it may be difficult to meet these demands without sizing platform members in the collision-prone area to obtain shared-energy or strength design; i.e., the impacting vessel must dissipate a significant amount of energy. This consideration is especially relevant for jackets for which there is a limited potential for energy dissipation in single braces with normal dimensions.

This study demonstrates the importance of accounting for interaction effects. A rigid bow is an overly conservative assumption for most scenarios and does not give appropriate credit to strengthening efforts. On the other hand, neglecting interaction effects may lead to an underprediction of the collision load exerted on the platform. For bulbous bow impacts on floating platforms, the rigid bow assumption results in larger damage and energy dissipation at the less critical forecastle deck level, whereas more dangerous penetrations of the bulb into the platform below sea level may be grossly underestimated.

The numerical analysis shows that current design rules produce structures that can resist collision forces from conventional vessels without causing catastrophic damage. The predicted extent of damage complies with the damage stability requirements. However, such damage may necessitate urgent repair work, resulting in costly downtime. The consequences of a collision may worsen with the expected increases in collision energy. Strength design does not necessarily lead to huge weight increases, but will give increased collision resistance, increased safety levels and less downtime in the event of an accidental impact.

At the same time it is recommended that vessels that frequently operate around platforms should be designed with their collision performance in mind. This includes avoiding extremely sharp and strong bows, and where possible facilitate that

the bow can dissipate the majority of the collision energy (as this is the cheaper vessel to repair). The platform operators face to same challenge. If they are aware of the collision performance of the vessels frequenting the platform, operational limitations can be tailor-made for each vessel type, thereby reducing the risk of critical high-energy impacts from the vessels with the worst collision performance. It is very likely that some offshore facilities currently in operation will suffer catastrophic failure if they are impacted by some of the worst bow designs; in other words : certain vessels should not service certain platforms.

Strength design of stiffened panels may be achieved provided that local crushing force intensities (pressures) are designed for. A new pressure-area relationship is proposed for use in early phase design for collision resistance. The proposed formulation can be used for bulbous bows and stern corners, and represents a significant increase compared to present strength design requirements in NORSOK N-004.

Different criteria for strength design are discussed in some detail. It is argued that local plate deformations between stiffeners are not likely to be critical when large deformations are allowed, and do not require particular consideration. Consequently, the stiffener and panel strengths are of higher importance. One strength design option is to size the stiffeners such that they do not undergo plastic collapse in bending (by accounting for shear in the web) when subjected to the local force intensities. However, this alternative is very rigorous and calls for heavy stiffeners. A more pragmatic resistance formulation is proposed, whereby a few stiffeners are allowed to undergo plastic collapse and deformations in the range of 10% of the stiffener length, for which the resistance is provided by shear in the stiffeners and membrane stresses in the plate. A sufficiently safe strength-designed platform with higher collision resistance can be achieved for a reasonable weight penalty.

For jacket structures, the study shows that many of the simplified methods given in NORSOK N-004 are valid. Satisfactory agreement is obtained between the NORSOK formulation for the resistance to local denting and that obtained from numerical simulations given the simplicity of the method. For strength design, the present requirement to R_0/R_c may yield impractically thick pipes, and crushing of the bulbous bow can be initiated for lower thicknesses.

An additional compactness requirement of $R_c \geq \eta$ is proposed for tubular members (brace/leg). η can be taken as 1.9 for bulbs and 1.4 for ship sides of conventional supply vessels. Satisfying this criterion gives sufficient strength of the brace/leg to crush the striking vessel, and the contact load is distributed over a larger length. This in turn increases both the global beam capacity and the local resistance to further local denting. If $R_c \geq \eta$ is not fulfilled, the collision force

should be assumed to be a point load, and the effect of local denting considered when assessing the plastic capacity of the leg or brace.

The present conclusions depend significantly on the conventional supply vessel bow shape with the bulbous bow used in the analysis and do not apply to unconventional bow shapes such as sharp axe shapes.

Chapter 7

Ice Impacts to Ship and Offshore Structures

7.1 Introduction

We are currently experiencing a significant increase in Arctic activities, related to transport along *The Northern Sea route* (NSR) and exploitation of the vast hydrocarbon and mineral resources in the region. The diminishing ice cover provides increased access to these sailing routes in the years to come, making the *NSR* a viable alternative to the Suez Canal for ship transit between Europe and Asia, and exploitation of natural resources along the route more feasible.

At the moment, a vessel is to comply with the Arc4 ice class in the RMRS Ship Rules (2014) in order to transit the *NSR*. This ice class is similar to the Baltic ice class ICE-1A (DNV SHIP RULES (2011)). This ice class is for operation in Northern Baltic Sea and in similar areas, with difficult ice conditions up to 0.8 meter thick level ice. Icebreaker assistance is often required.

The local design loads are low when designing low ice-class vessels (such as the Baltic ice class 1A), and the vessels are expected to sustain damage during their service life, see Riska and Kämäräinen (2011). An example of damage to a 1A-classed vessel is shown in Figure 7.1. If the damage is small, repair can be performed on the next classification of the vessel, whereas larger damages should get immediate attention. As discussed by Kujala and Ehlers (2013), the choice of a design load level that causes an acceptable damage will then be a matter of cost optimization. For the vessel owner, the minimum design load level is defined by the selected ice class. Additional reinforcements may be cost efficient in terms of

increased operability of the vessel.
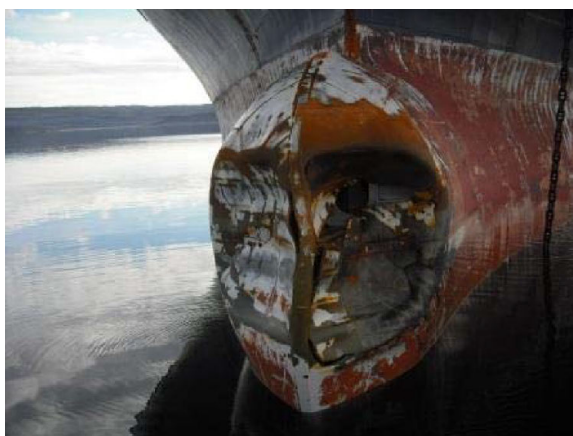
Figure 7.1: Bow damage from ice action to a 1A-classed vessel, June 2012, from Canadian Coast Guard (2012)

As damages are expected during the service life of the vessel in the Baltic ice classes, the design load philosophy differs from conventional ULS design. Using low design loads and allowing for frequent repairs gives cost-effective ships, at least if only parts of their service life is in ice covered waters. The alternative, to calculate the load with a 100-year return period, would significantly increase the vessel scantlings. Thereby, the investment cost increase and the cargo capacity decrease for a fixed vessel size. Utilizing low ice classes is also discussed for offshore field developments in which ice has a higher return period than 100 years. Otherwise, an offshore installation should normally be designed to resist the expected ice loads with minimal damage.

Increased activity in ice-covered waters will increase the probability of ice encounters which are outside of the vessels elastic capacity. However, the loads from these encounters are still within the *Ultimate Limit State* (ULS), with an annual probability typically $\leq 10^{-2}$. For offshore structures operating in ice infested waters, requirements will also be made to assess the *Accidental Limit State* (ALS) capacity (annual probability typically $\leq 10^{-4}$), in which damage to the structure is allowed as long as there is sufficient residual strength to prevent progressive collapse, and safety of the crew and environment can be maintained. However, there is no defined ALS criterion for ships, and the strength of the vessel will be solely dependent on the classification rules applied. An impact that causes significant damage to the vessel is in the following termed an ALS event regardless of its probability of occurrence.

The challenge for classification societies is then to provide for adequate resistance of the vessel hull, suitable for the intended operation. The normal ULS loads should not cause significant damage. Sufficient structural strength can easily be achieved by increasing the scantlings in a conservative manner. However, the economic consequences of too strict design requirements are in many cases not feasible.

Loads that exceed the given ULS threshold should not cause progressive collapse or insufficient stability due to flooding. For offshore structures, this is already considered through the ALS requirements. For ships with low ice classes, for which damage is expected also from ULS loads, an additional extreme damage requirement would be beneficial. This requirement should ensure that events with 100-year return period does not cause unacceptable damage.

Having such an additional requirement to ships is especially relevant for vessels transiting the *NSR*, for which low ice-class vessels are allowed provided light ice conditions and icebreaker assistance. Marchenko (2013, 2014) reports on observed damages from operations in the Russian Arctic. Along the NSR, several scenarios with loading above the design point are to be expected, typically by traveling with excessive speed compared to the plausible impact loads from first or multi-year ice floes or bergy bits, or impacts with the edges of the broken channel. Marchenko (2014) reports that even ice breakers has suffered terminal damage due to collision with ice floes, causing large water ingress than eventually sank the vessel. This highlights the hazards for low ice class vessels during ice navigation. A recent example of potentially critical damage from ice collisions is the oil tanker Nordvik, which collided with an ice mass in 2013 causing water ingress (Pettersen 2013). The vessel had a low ice class, but was still permitted to sail in Arctic conditions during the summer season.

As these extreme load scenarios could involve severe damage to both the ice and vessel, the coupled behavior of ice and structure during deformation is important. The impact force will then depend on the evolution of structural deformations and the extent of ice crushing.

Interaction with ice gives loads that are commonly split into different limit scenarios:

- *Limit stress* : The maximum load is limited by a maximum stress, such as the crushing stress of a level ice sheet that is so large compared to the structure that the energy can be considered unlimited. This is relevant to fixed installations.
- *Limit force* : The maximum force than can be transferred from the driving

force (such as a moving ice sheet) onto the structure. Typically, the limit force is the weakest link in the force chain, e.g., by failure of the driving ice sheet behind a large ice ridge. This is relevant primarily for fixed installations, but can occur also for floating vessels.

- *Limit energy*: The maximum energy that a process can deliver to a structure, typically impact events from isolated ice floes and icebergs. Both the ship and the ice contribute to the total energy, and their relative mass governs the interaction process.

By definition, most of these scenarios are impact processes at varying velocities. In the following, only *limit energy*-scenarios are considered. For these scenarios, the severity of the ice and sea conditions combined with the shape and speed of the vessel dictates the required structural strength, or inversely, the structural strength dictates the maximum allowable operating conditions.

It is further separated between global and local ice loads; global accounts for loads on the entire structure such as icebreaking resistance, and local loads dictate the local structural scantlings. Only local loads are considered in the following.

Most typical full-scale impact scenarios that can lead to structural damage will occur at high indentation velocities, either caused by the vessel speed or wave-induced motions of the ice. Another common damage process is from compressive forces from an ice sheet that closes around a ship stuck in ice, occurring under near quasi-static conditions, with ductile ice behavior (Hänninen 2005). Realistic impact events, which is the focus herein, are in the brittle ice regime. The separation between brittle and ductile ice behavior is used as defined in Schulson and Duval (2009).

There are currently two main methods to design a structure to locally withstand impact loads from ice:

- Using existing pressure-area information from experiments (or rules and standards) to generate loads to patches of predefined sizes that can be employed in simplified elastic or plastic hand calculations or in NLFEA
- To conduct integrated NLFEA simulations in which the structure and the ice is modeled directly either as a continuum or with discrete elements. Only continuum methods are in focus herein.

The former method is chosen mostly in ship rules due to its simplicity, whereas the latter can be employed to improve the realism of the impact assessment and thereby more accurately reward design optimization.

In the following, published research on relevant background for ice-structure col-

lisions is presented. Each topic is a research field by itself, so the goal is only to obtain an overview of relevant background for design of an ice-resistant structure. Later, the resistance of a vessel is estimated using either pressure-area information combined with NLFEA or integrated NLFEA directly. The benefits and limitations of both approaches are discussed.

This chapter discuss some of the required basis to establish relevant design scenarios.

7.2 Special Considerations for Ice-Structure Collision Assessments

Many pieces of information should be assembled to be able to accurately assess an impact scenario; mainly the ice shape, its probability of occurrence, mechanical behavior and impact velocity. Relevant impact scenarios can be defined by combining these fields of research.

As a pragmatic approach to collision design evaluation, the vehicle industry has adopted a few representative scenarios which should be assessed (EURONCAP). Similar cases are at the moment not agreed upon for ship-ship or ice-ship impacts. Hence, it is up to the designer and regulatory body to choose the relevant realistic scenarios that should be used in design. Such approaches are used behind the rule formulations in IACS rules for polar ships, IACS-UR-I (2011) and RMRS Ship Rules (2014), but are hidden behind simplifying assumptions (see CP-9 for a discussion). Due to the high variability in ice shape and strength, selecting a few governing scenarios for direct design is significantly more challenging with ice than for ship collisions.

Having a good probabilistic design method for assessment of the structural resistance of a vessel subject to ice impacts would be preferable. With NLFEA, a large number of scenarios needs to be investigated, and their probability of occurrence will be low. An industry example of this is the design of the gravity based platform *Hebron*, in which the Canadian research company *C-CORE* used Monto Carlo simulations to establish 192 million impact scenarios, from which design impacts could be established at given probability limits. Probability distributions of iceberg shape, size, velocity and trajectory were utilized, see Widianto et al. (2013) for details.

7.2.1 Ice Shape and Probability of Occurrence

The first and major challenge in determining a realistic impact scenario is to evaluate ice feature shapes for the selected area of operation. Both the global and local shape is of interest; the global (the overall shape of the ice mass) giving the
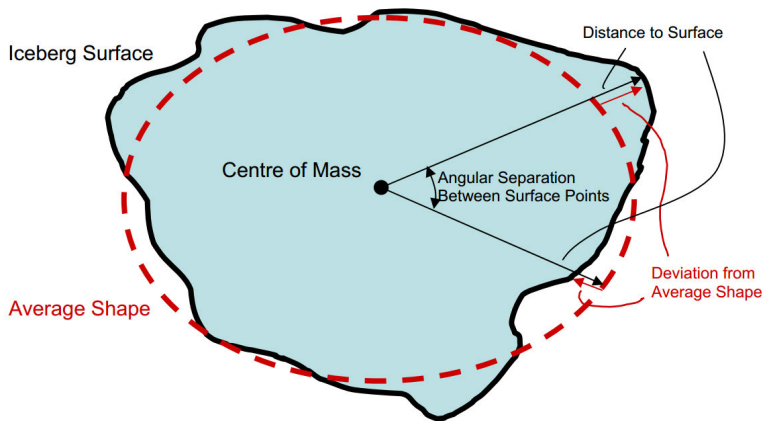
Figure 7.2: Schematic of the iceberg shape representation, from McKenna (2005)

external collision mechanics and the energy limits, the local (the actual shape interacting with the ship structure) determining how the forces are transferred and energy dissipated. The ice masses could be :

- Pieces of first and multi-year ice
- Broken-off pieces of ice ridges
- Glacial ice masses (icebergs) typically denoted
    - growlers (size of a large car)
    - bergy bits (size of a large house)
    - small, medium and large icebergs (size of small ships and upwards).

Small ice masses calve from larger icebergs, and have a high probability of occurrence. Shape and size data is available for a range of medium to large icebergs in a structured manner in the *International Ice Patrol* (IIP) database (NSIDC (1995)) and McKenna (2015); Timco (1999), and can be used for design. However, the probability of not detecting a large iceberg by visual observations or radar is low, and the probability of occurrence for such events is consequently small.

Due to ice melting, dependent on effects from the sea temperature, wave and current action etc., any initially sharp features of the ice are rounded off during the life of the ice mass. The end result is an ice feature with a somewhat smooth global shape and local protrusions with different curvatures. This also creates a thermal gradient in the ice with lower temperatures in the middle than at the outer surfaces of the ice, causing variations in mechanical properties with increasing indentation. McKenna (2005) characterized the shape of icebergs based on a range of measurements, and generalized the iceberg shape into a statistically definable shape as shown in Figure 7.2.

Fuglem et al. (1996) outlines some of the challenges when applying the collected shape data to a probabilistic model, among others that the size classification in the *IIP* data is limited. Due to the limited data resolution, Fuglem et al. (1996) further states that the number of small icebergs are somewhat underestimated and the number of growlers is significantly underestimated.

Smaller ice features may be more difficult to detect using radar (due to waves and precipitation) and difficult to observe visually (due to fog and darkness). A common rule of thumb is that it is not possible to detect an ice feature with vertical height above stillwater level of less than 2 meters. Freshwater ice has a density of up to $917 \, \text{kg/m}^3$, which typically gives a draft of 9-10 times the height above water. The height limitation for detection defines the vertical extent of a realistic ice mass to encounter, but the horizontal size and shape is to a limited degree documented for ice masses smaller than medium-sized icebergs.

Fuglem et al. (1999) developed a framework for determining the expected number of annual encounters of icebergs given known distributions of iceberg size and density in an area, the vessel geometry and operational characteristics.

Based on the above, it is possible to establish "realistic" impact shapes, but this cannot easily be limited to a few critical cases.

7.2.2   Ice Material Behavior

Ice as a material is warm, i.e., with homologous temperature close to 1. Further, it is highly strain-rate dependent, with ductile response at low and brittle response at high strain rates (Figure 7.3). The transition is not clearly defined (as it depends on many parameters, such as temperature, confinement etc.) but typically strain rates less than $0.001 \, \text{s}^{-1}$ are considered to be in the ductile regime. Consequently, most of the realistic impact scenarios yield ice response in the brittle regime. Many failure mechanisms are possbile depending on the scale of deformation, from large scale splitting and spalling (flaking) of the ice, to micro-mechanical fractures (in essence giving a *damage* degradation of the material).

There are many different types of ice; freshwater ice, saltwater ice (separated into first year and multi-year ice) and glacial ice (icebergs), each with a specific structure and mechanical behavior. When an ice sheets forms on a lake or the sea, the top layer (primary ice) is mostly granular. Below this layer (i.e., the secondary ice), the ice grains grow primarily as columns down into the water, thereby giving an anisotropic structure. This differs significantly from glacial ice, which starts out as snow that is then compacted over the years to produce a granular structure without a clearly defined grain direction (thereby an isotropic structure). Glacial and multi-year sea ice poses the highest risk to ship structures due to the their size
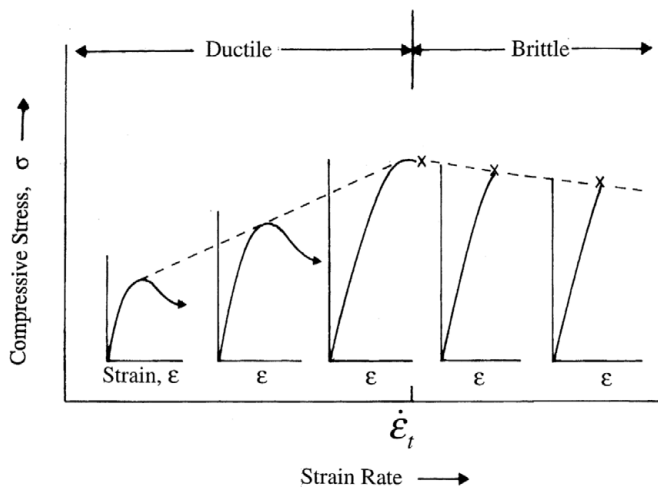
Figure 7.3: Ductile to brittle transition of ice dependent on strain rate, from Schulson (2001).

and high compressive strength, and is therefor focused in the following.

Ice as a material has a clear stochastic nature. The crushing strength is governed by a range of variables (temperature, grain size, loading direction, salinity, imperfections, cracks, strain rate, internal friction and the failure mode), each of which has significant variations. There is a significant scatter in the experimental data. The grain size of glacial ice is large, in the range of 1-50 mm compared to micrometer values for steel (Schulson and Duval 2009). Consequently, for both mechanical testing and numerical modeling, large volumes are needed in order to treat it as a "true" continuum. Otherwise, the internal grain behavior may be important.

Because of these challenges, the material response of ice is difficult to generalize, and even more difficult to represent numerically. Many researchers have addressed the mechanical behavior of ice during compressive loading. It can be argued that a general agreement has yet to be established. Some works discussing the mechanical behavior of ice in compression are Gagnon and Gammon (1995b, 1997); Jordaan and Timco (1988); Jordaan et al. (1992, 1999); Kim et al. (2012a); Muggeridge and Jordaan (1999); Schulson (1997, 2001); Schulson and Duval (2009). Some researchers argue that fracture mechanics approaches are well suited to characterize the mechanical behavior ice (Bazant and Xiang 1997; Dempsey et al. 1999; Mulmule and Dempsey 2000; Palmer et al. 2009), thereby explaining some of the size-effect from model scale to full scale experiments. Such approaches are not considered herein.

The strength of the ice is strongly depending on the confinement. In the following, confinement is defined as the local triaxial compressive stress state in the ice. If the ice is highly confined then the sides of the ice are supported, thereby preventing large cracks from propagating. Consequently, the resistance of the ice against crushing is increased locally in the highly confined regions. This, in turn, can have a large effect on the total impact response.

The presence of confinement can be envisaged in many different scenarios. An ice feature may confine itself provided that the thickness of the ice around the contact surface is sufficiently large. Thus, the larger the contact area, the higher is the confinement in the center of the ice contact. This is to a large extent captured by large-scale testing of an ice block against a rigid panel. Another important effect is the increase in confinement that occurs when the impacted panel is not rigid; the ice load causes the panel to bend inwards, thereby changing the panel geometry such that the panel will provide lateral support of the ice (as in Figure 7.4).
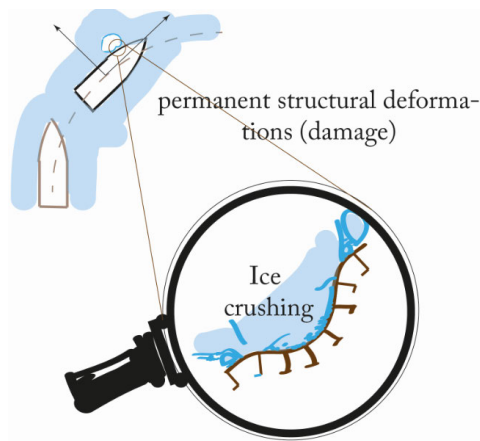
Figure 7.4: Changing geometry of the stiffened panel during an impact changes the confinement of the ice, from Kim (2014).

The pressure transferred from the ice to the structure is a crucial factor for design. Representing the ice strength solely by one pressure variable does not capture the true mechanical behavior. If sufficient safety margins are added, it may however be a relevant simplification for design. Based on experimental data collected on ice compression of glacial and multi-year ice, ISO-19906 (2010) suggest a pressure-area curve to be applied in local design for impacts with thick multi-year ice features, refer Figure 7.5. This curve is commonly used for strength design of offshore structures, i.e., scenarios when the structure shall have small deformations and resist whatever ice load that is expected during the service life.
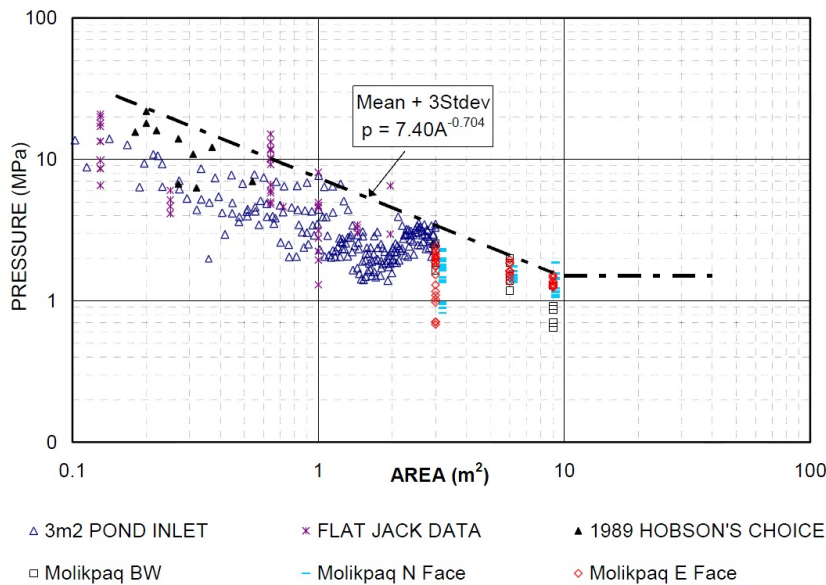
Figure 7.5: Compilation of pressure-area data from experiments on multi-year and glacial ice together with a design curve, from ISO-19906 (2010)

It can be argued that a fundamental understanding of the behavior of ice in terms of pressure-area relation ($p = CA^x$) does not exist. Experiments, such as those in Figure 7.5, show a wide scatter. Measured pressure data for the same area may differ by one order of magnitude. Kim and Schulson (2015) discussed these issues for ice deformed by spherical indenters in the brittle regime. By accounting for the strain-softening behavior of ice, they showed that the pressure decrease with increasing indentation (i.e., increasing contact area). The C-parameter was found to depend on the indenter radius (increasing pressure with increasing radius of the indenter). Further, they suggested that the exponent x depends on temperature, indentation velocity and grain size. The total pressure is then a function of the instantaneous conditions at impact.

Ice-structure interaction may be categorized as strength, shared-energy and ductile design regimes, similar to ship-platform collisions (Section 2.2). Most experiments are carried out in the strength design regime; this represents nearly all the data in Figure 7.5. A few experiments have been conducted with flexible structures; among them are Daley and Kim (2010); Määttänen et al. (2011); Sohdi (2001). Full-scale ice impacts were conducted with the icebreaker Kigoriak (Varsta and Riska 1982), in which a few cases exceeded the elastic load limit. In the field test campaign at the Hobson's Choice ice island, flat flexible indenters were pushed

against an ice wedge at constant speeds (Masterson et al. 1993). Quasi-static experiments in the shared-energy regime have been performed in the STePS^2 program (Kim et al. 2015b; Manuel et al. 2013, 2015), where the ice failure was ductile, far from what normally is experienced in actual full-scale impacts.

High-strain-rate brittle behavior of ice has been investigated by several researchers, e.g., field drop-rig experiments on rigid pipes (Saeki et al. 1977), pendulum impact experiments with a spherical indenter into confined ice (Oldford et al. 2014), conically shaped ice into a flat structure (Gagnon et al. 2015; Sopper et al. 2015) or using a split Hopkinson pressure bar (Shazly et al. 2009), but none of these are coupled to inelastic structural response.

Except from the experiments by Manuel et al. (2013), all experiments with flexible indenters were in the strength design regime, with only small plastic structural deformations. This effectively limits the potential coupling effect between the ice and structure deformations. In the strength-design regime, the structural strength can be assessed mechanism analysis. Daley (2002a,b) derives plastic framing requirements for polar ships based on this approach, which are now implemented in the IACS rules for polar ships, IACS-UR-I (2011).

As all the tests in Figure 7.5 were performed with near rigid structures, the pressure-area curve is applicable for strength design only. If the structure deforms significantly, the pressure required to crush the ice will increase due to the increased confinement.

The coupled response between ice and a structure undergoing substantial damage is of importance, as this represents the critical scenario for ships and offshore structures. The coupled response causes an increase of the confinement in the ice (change of local stress state) due to changing local geometry of the ship during the impact, thereby increasing the crushing strength of the ice. This can cause a *progressive increase* in the severity of the impact event;

- The structure deforms when the crushing pressure of the ice surpasses the plastic bending capacity of the structure.
- Membrane forces are mobilized in the deforming ship structure, and additional resistance to withstand the initial ice load is mobilized.
- Due to the changing geometry of the ship structure, the local confinement of the ice increases, thereby increasing the pressure required to crush the ice.
- The increased ice strength due to ship-induced confinement causes further indentation, which in turn increase the confinement of the ice etc.

Thus, if the ice load surpasses the structural strength by a small amount and causes moderate damage, the structural damage will in turn increase the ice strength, and

further damage is likely in a self augmenting fashion.

Recent experiments on crushing of ice have shed more light on the physical crushing behavior, with varying local shape in Gudimetla et al. (2012), varying confinement in Ulan-Kvitberg et al. (2011), rate effects in Habib et al. (2014) and shared-energy deformation in Manuel et al. (2013). However, none of the experiments have investigated the coupled ice-structure interaction in the brittle ice regime. More experimental work is needed to provide data for development of proper models of the physical mechanisms, and further to improve continuum material models for integrated analysis using NLFEA.

Experiments to study the coupled interaction between ice and structures have been conducted at NTNU, and are described in Chapter 8.

7.2.3   Velocities and Kinetic Energies

For a vessel in transit, the kinetic energy will be governed by the relative normal velocity between the vessel surge and the ice. In addition, significant contributions can come from the other vessel motions (mainly heave, pitch and roll) and the ice motions (slowly varying drift and first order wave motion).

Fylling (1994) investigated the influence of wave induced motion of drifting ships in an accidental collision with a platform, and developed a framework to assess the impact velocity and distribution of vertical impact location. The model accounts for the effect of the ratio between wave-induced and drift velocity of the ice to establish a probability distribution of the actual impact velocity of the ice to the structure. For low drift velocities, the impact will most probably occur in phase with the wave, whereas higher drift velocities may cause impacts in which the induced wave velocity component can act both towards and away from the structure (Figure 7.6). A similar approach may be employed to create a probability distribution for the impact velocity and location in ice-ship collision.

Arunachalam et al. (1987) investigated the short term motion of icebergs in linear waves, and presented the relative velocity of the ice vs. the wave particles as a function of the horizontal iceberg length to the wave length and the iceberg draft to water-depth ratio. The results in Figure 7.7 are valid for draft/depth ratio of 0.1, and for cylindrical and cubical ice masses.

As shown in Figure 7.7a, the surge velocity of small icebergs closely follows the wave particle velocity, but as the size of the iceberg increase to half of the wave length, the ice surge velocity is decreased to close to half the wave particle velocity. In Figure 7.7b the heave velocity shows a dynamic amplification with increasing iceberg length up to a length ratio of 0.33.
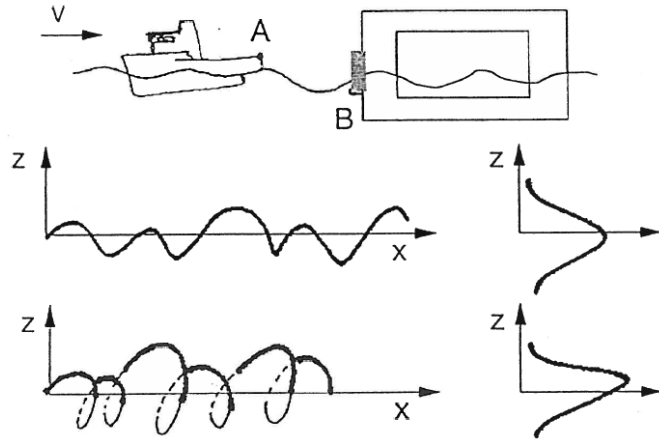
Figure 7.6: Illustration of impact problem for high (top) and low (bottom) drift velocity, from Fylling (1994). Z and X are vertical and horizontal coordinates in the projection of the ship trajectory. To the right is a probability distribution of vertical impact location.

The wave particle velocities for infinite water depth can be calculated as

$$u = \omega\zeta_a e^{kz}sin(\omega t - kx) \tag{7.1}$$

$$v = \omega\zeta_a e^{kz}cos(\omega t - kx) \tag{7.2}$$

where ω is the wave angular frequency, ζ_a is the wave amplitude, k is the wave number and z and x are the vertical and horizontal coordinates.

7.2.4 External Mechanics

Popov et al. (1967) proposed the limit momentum theory for ice impacts, in which the load history during an impact event could be described until the two impacting bodies reach a common velocity. This has together with ice load models formed the basis of the design pressure loads in the current IACS-UR-I (2011) and RMRS Ship Rules (2014).

The use of external mechanics principles enables determination of the energy that has to be dissipated in a collision event (see Section 2.3.1 for details). By considering the principle of conservation of momentum, the impulse and momentum equation can be written as

$$\int_o^{t'} F(t)dt = M(\mathbf{V}' - \mathbf{V}) \tag{7.3}$$
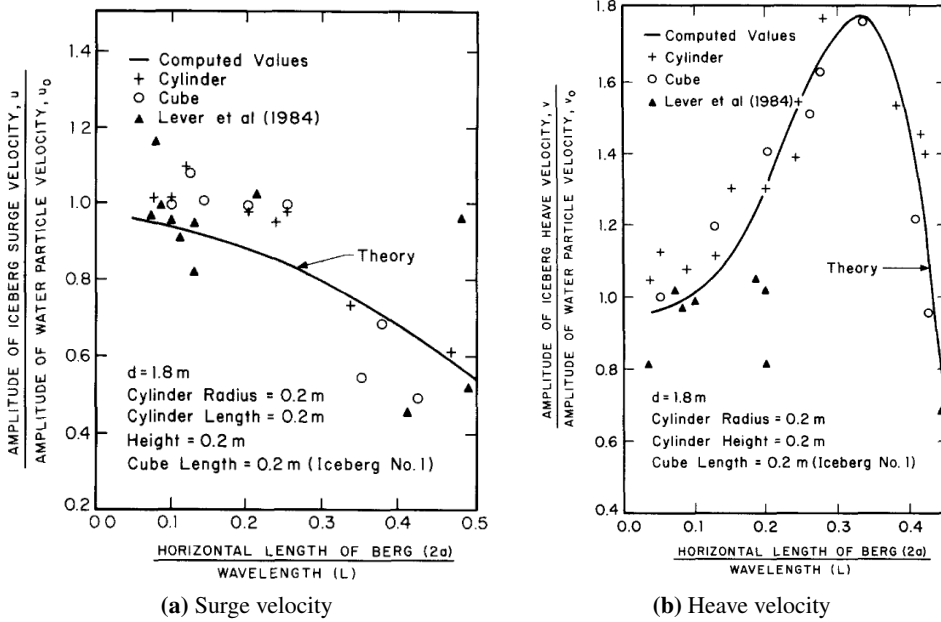
Figure 7.7: Ice velocity vs. wave particle velocity, from Arunachalam et al. (1987)

where $F(t)$ is the impact force, t' is the impact duration, M is the dynamic mass of the ship (including added mass), $\mathbf{V}'$ is the ship velocity vector after impact and $\mathbf{V}$ is the ship velocity vector prior to impact. For a 1D collision between an ice mass and a ship, the equation can be simplified to

$$MV + mv \;=\; MV' + mv' \qquad (7.4)$$

in which M and V is dynamic mass and velocity of the ship and m and v dynamic mass and velocity of the ice prior to impact. V' and v' denotes velocities after impact.

During the impact, a force component in the direction normal to the impact surface will be present until the two bodies have the same velocity in this direction. At the point of equal normal velocity, the change in kinetic energy can be found. If the impact is purely elastic, this energy will be returned to the motion of the system. If there is plastic damage, parts of the energy has been dissipated. A coefficient of restitution can be defined as

$$e = \frac{V' - v'}{V - v} \tag{7.5}$$

A fully elastic impact ($e = 1$) gives no change in the system's kinetic energy, whereas a fully plastic impact ($e = 0$) gives the same velocity after impact of the two bodies, and thus a change in total kinetic energy. This change will then have to be absorbed by local deformation in either body during the collision.

Stronge (2004) defined the coefficient of restitution more generally based on the energies in a collision event, by taking the ratio of the energy released during restitution to the internal energy absorbed during compression.

Simplified to a 1D case, the dissipated energy can be determined as

$$\delta E = \frac{1}{2} \frac{Mm}{M + m} (1 - e^2)(V - v)^2 \tag{7.6}$$

Liu and Amdahl (2010) describes a 3D formulation of a similar impact theory based on the work of Stronge (2004). The benefit of doing this assessment in 3D is large for impacts between icebergs and ships; the impact eccentricity, friction and rotational energy can be treated in a better way, thus removing otherwise conservative assumptions in 1D and 2D.

The 3D theory is formulated in a rotated coordinate system with origo in the contact point and directions along the impact normal direction, longitudinal aft and transverse down along the hull. To define the coordinate transformation, the vessel geometry in the contact location is described by the angles in Figure 7.8. The mathematical formulation of the 3D impact theory is rather lengthy, and the reader is referred to Stronge (2004) for a general derivation and Liu and Amdahl (2010) for application to ship-ice collisions.

The impact mechanics model assumes that the impact duration is short, that the impact direction does not change during the impact, that the impact force is so large that other external forces are negligible during the impact and that deformations are limited to the contact surface.

(a) Coordinate frame

(b) Hull angles
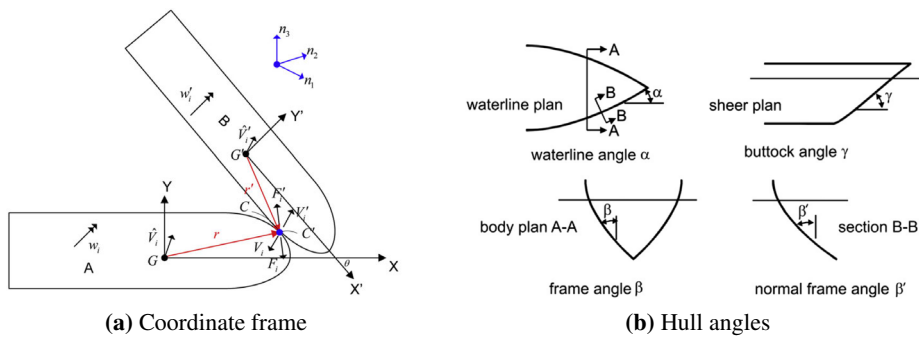
Figure 7.8: Geometric definition of rotated coordinate frame, from Liu and Amdahl (2010)

7.2.5   Case Study on External Mechanics

In the following, the results from Arunachalam et al. (1987) and Liu and Amdahl (2010) are combined to investigate the energy that has to be dissipated in typical collisions considering ship and ice velocity, ice mass size and the shape of the vessel relative to the impact direction.

The initial kinetic energy of ice masses of varying sizes is checked based on the short term wave motion from Arunachalam et al. (1987). A mean drift speed of 1 m/s is assumed, along with deep-water waves with varying period and amplitude. A spherical ice shape is assumed for the mass calculation, but the hydrodynamic response is for simplicity assumed to be similar to a cylinder with radius equal to sphere radius. This neglects the change in waterplane stiffness due to changing waterplane area of the sphere in heave, thereby allowing use of the data set in Figure 7.7. As a conservative estimate, it is assumed that the impact will occur when horizontal wave velocity is at a maximum towards the vessel.

The obtained velocities are shown in Figure 7.9a for three different small waves with peak periods T_p of 5, 6 and 8 seconds and significant wave heights H_s of 2, 3 and 5 meters. From this, the corresponding kinetic energy of the ice is calculated as in Figure 7.9b. It is observed that even with moderate wave heights, wave-induced velocities are important for smaller ice masses but diminish for larger ice masses. A peak kinetic energy can be observed for the smaller ice masses depending of their length relative to the wave length. For large ice masses, the kinetic energy converges to the drifting kinetic energy. With increasing wave height, the kinetic energy will increase significantly for all but the largest ice masses.

Liu and Amdahl (2010)'s external mechanics theory was then used to investigate the change in kinetic energy (i.e., energy to be absorbed during impact) for a refer-

(a) Wave-induced velocity of ice
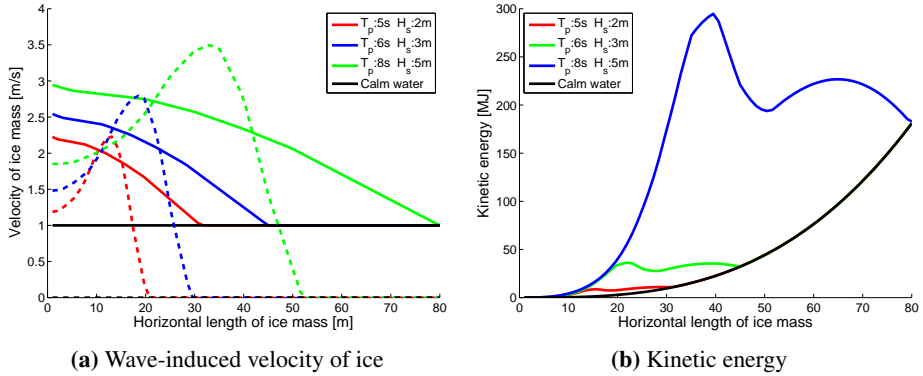
(b) Kinetic energy

Figure 7.9: Wave-induced velocity and kinetic energy of an ice mass as a function of horizontal dimension. Dashed lines in (a) indicate vertical, continuous lines horizontal velocity.

ence vessel impacting varying ice masses. A 170 000 m^3 Moss type LNG carrier is used as reference vessel, representing either a large ship in transit or a ship-shaped stationary offshore structure.

Six impact locations were selected (Figure 7.10), with parameters given in Table 7.1. To simplify the assessment, only spherical ice features are considered. The ice velocity at impact is taken from Figure 7.9. The ship velocity is set to 15 knots. The friction coefficient between the ice and the vessel is assumed to be 0.15.

Table 7.1: Parameters for the impact locations in Figure 7.10. L is longitudinal and B transverse coordinates normalized to the maximum length and breadth. The angles α and β are defined as in Figure 7.8.

ID	$\frac{L_{impact}}{L}$	$\frac{B_{impact}}{B}$	α	β'
1	0.65	1.00	2	11
2	0.72	0.94	6	8
3	0.81	0.71	18	21
4	0.87	0.45	22	33
5	0.91	0.24	23	40
6	0.96	0.00	90	64

Figure 7.11 shows the energy to be dissipated in a fully plastic impact (coefficient of restitution $e = 0$) vs. the mass of iceberg and impact location for either a ship in transit (Figures 7.11a and 7.11b) or a stationary floating offshore installation (Figures 7.11c and 7.11d). It is observed from the figures that the dissipated energy is very sensitive to the impact location, or more specifically to the normal direction of the contact surface compared to the impact direction; a head-on im-
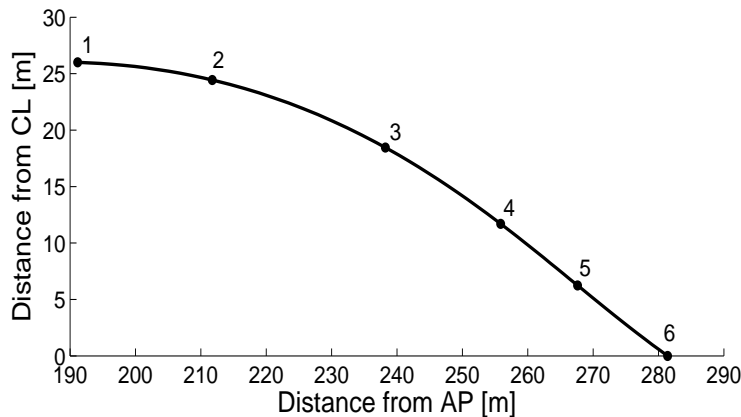
Figure 7.10: Waterline profile of the bow of the selected vessel with impact locations marked. AP is the aft perpendicular of the vessel, CL the centerline.

pact gives significantly higher requirements to energy dissipation than a glancing impact. The effect of ice drift speed and wave-induced velocity is significant for a ship in transit, especially if the ice mass is close to heave resonance. For stationary vessels, ice drifting into the structure causes low energy dissipations, whereas even benign sea states significantly increases the energy that has to be dissipated in an impact. The impact energy from ice with wave-induced velocity is in the same range as for supply ship collisions to offshore installations.

It is thus of importance to include the ice kinematics when determining the design impact loads, both for stationary platforms and transiting vessels.

7.3   Assessment of Structural Resistance using Pressure-area Curves

As a simple approach to ice strengthening, the structure can be designed according to a defined pressure-area relationship. Simplified resistance calculations can be used. Kivisild (1971) investigated the effect of iceberg impact on a drillship in 1971, and concluded with a limit curve of the mass of ice vs. velocity of vessel that would give an elastic structural response. More recently, Daley and Liu (2010) shows the same type of analysis for ships in pack ice with up-to-date ice knowledge.

In the following, application of pressure-area curves was explored using NLFEA to assess the structural resistance of a vertically stiffened vessel with DNV ICE-1A class to an impact event.

(a) All impact locations, 15 knots ship speed, calm seas

(b) Impact location 4, 15 knots ship speed, varying sea conditions

(c) All impact locations, no ship speed, calm seas, 1 m/s ice drift

(d) Impact location 4, no ship speed, varying sea conditions
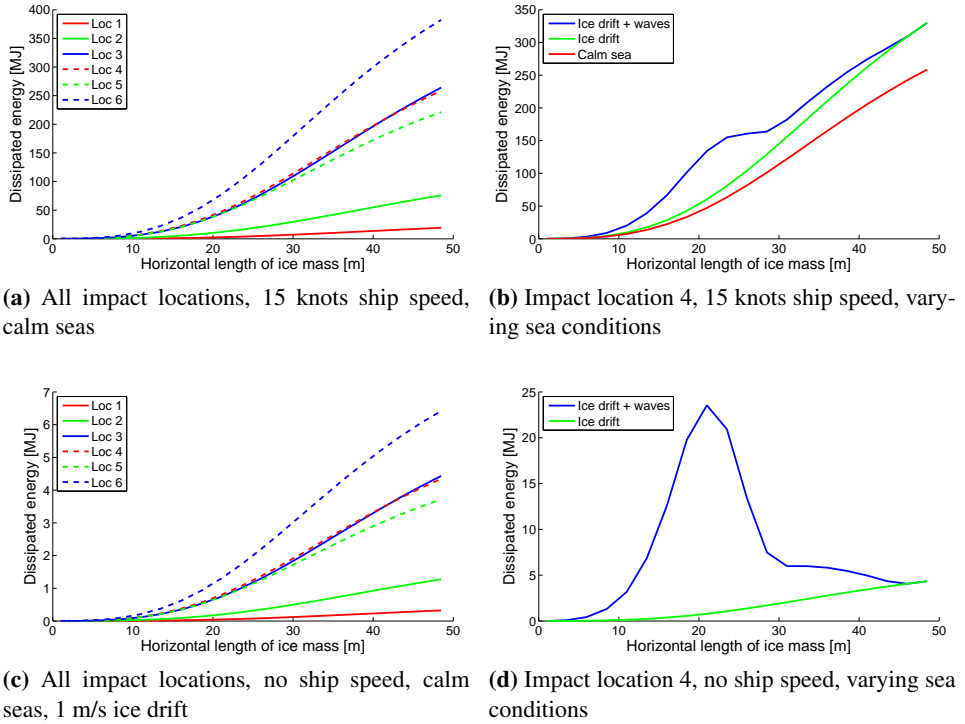
Figure 7.11: Requirement to dissipated energy for varying ice mass, impact location, sea state and ship velocity. Wave conditions used : $T_p = 6$ s, $H_s = 3$ m.

To determine a realistic loaded area, a flat multi-year ice sheet with a given mass and contact zone with constant radius of curvature was assumed to impact perpendicular to a stiffened panel structure. During the interaction, the failure mode in the ice was assumed to be pure crushing in the ice zone (i.e., no in-plane global splitting, local spalling, bending or rotation of the ice floes), thereby giving a steadily increasing loaded area. A power law process[1] pressure-area curve is used to predict the contact pressure. With these assumptions the force-time history of the impact between the ice floe and the ship can be established.

Peak events in this force-time history are then checked with NLFEA to verify the structural resistance (or lack thereof) for the vessel. From such an assessment, the maximum envelope of the impact resistance can be established based on different acceptable limits; the elastic response, the plastic bending capacity, the acceptable

---

[1]Process pressure area is defined as total force over nominal (enclosed) area, as opposed to a spatial pressure area that considers the local hot spots within the nominal area.

damage, the damage before collapse etc. Similar results can be achieved with simplified plastic calculation methods.

7.3.1   Impulse Integration Procedure

Realistic impact areas were established using the impulse theorem, Eq. 7.3. The time integral of the force $F(t)$ can be found equal to the change in momentum of the retarding mass M from initial velocity V to final velocity V'. A time integration scheme is established to solve the retardation problem and find a set of realistic impact forces, pressures and areas for different ice masses.

In the following, a multi-year ice floe of random size, see Figure 7.12, is assumed to impact a vessel to its side structure. The vessel is assumed so strong that the ice mass takes all the energy absorption, and so heavy that the retardation of the vessel is negligible with respect to the ice. A perpendicular impact is assumed, i.e., a 1D collision without rotations in either the ship or the ice.

The relative velocity between the ice and the vessel is 2 m/s. For a large ship such as the LNG carrier in Section 7.2.5, the retardation of the vessel will be negligible. Ice crushing will continue until the ice mass has the same velocity as the ship. The ice crushing energy is thus equal to the kinetic energy of the ice mass with the relative velocity between the two bodies.
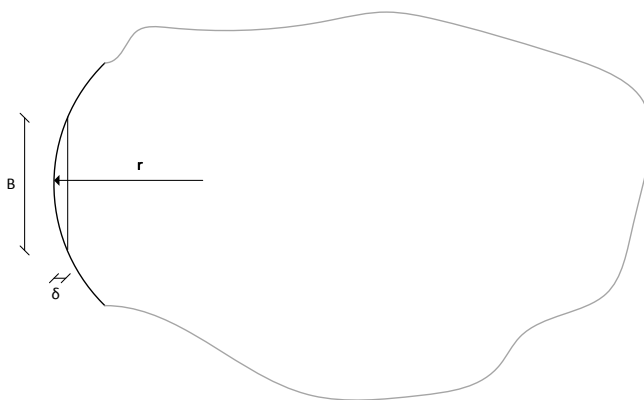
Figure 7.12: Multi-year ice feature with contact curvature, horizontal view

The impact zone is assumed to be described by a radius of curvature r, so that the contact area can be found as the curve segment B times the ice thickness h. The length of B can be found as a function of the ice crushing distance δ by assuming a constant radius of curvature of the ice as

$$B = 2\sqrt{\delta(2r - \delta)} \tag{7.7}$$

A numerical procedure from time step n to $n + 1$ with interval Δt is then established. The increment in ice crushing displacement $\Delta\delta$ is found from the current velocity as

$$\Delta\delta = V_n\Delta t \tag{7.8}$$

When the total displacement $\delta_{n+1} = \delta_n + \Delta\delta$ is found, the area of the contact zone A can be calculated as

$$A_{n+1} = hB = 2h\sqrt{\delta_{n+1}(2r - \delta_{n+1})} \tag{7.9}$$

The pressure p and force F can be found from a pressure-area relation

$$p_{n+1} = CA_{n+1}^x \tag{7.10}$$
$$F_{n+1} = p_{n+1}A_{n+1} \tag{7.11}$$

where C and x are assumed to be constants. To prevent very high or very low pressures, the pressure is assumed constant if the area is larger than 10 m^2 or smaller than a load patch of the stiffener spacing square. The coefficients C and x are assumed to follow the pressure-area relation $p = 7.4A^{-0.7}$ (in Figure 7.5)[2].

The acceleration and velocity to the next time step can then be expressed as

$$a_{n+1} = F_{n+1}/M \tag{7.12}$$
$$v_{n+1} = v_n - a_{n+1}\Delta t \tag{7.13}$$

The numerical integration continues until the force impulse is equal to the change in momentum, ref. Eq. 7.3. The last time step represents the peak force exerted on the structure from the ice, and can now be checked against the structural resistance.

---

[2]This pressure-area relation, proposed in ISO-19906 (2010) for thick multi-year ice features, is assumed valid also for 1 m high contacts (thin ice), e.g., representing a smaller contact zone from a thick ice feature.

Using this numerical procedure, realistic loaded areas and corresponding pressures can be determined for an ice impact with a strong vessel. The ice mass is varied from 250 to 1000 ton. To be conservative, an added mass coefficient of 1.0 is used. The load vs. area vs. time can now be found, and used as input to either a simple calculation method or a numerical simulation.

Figure 7.13 shows calculation results using the impulse integration scheme. A few peak forces are extracted for further analysis, summarized in Table 7.2. The peak force occurs at the end of the impact process (with maximum penetration into the ice). The corresponding pressures are the average pressures over the contact zone. The actual local pressure is higher over certain areas of the structure, but this is not considered in the simulations.
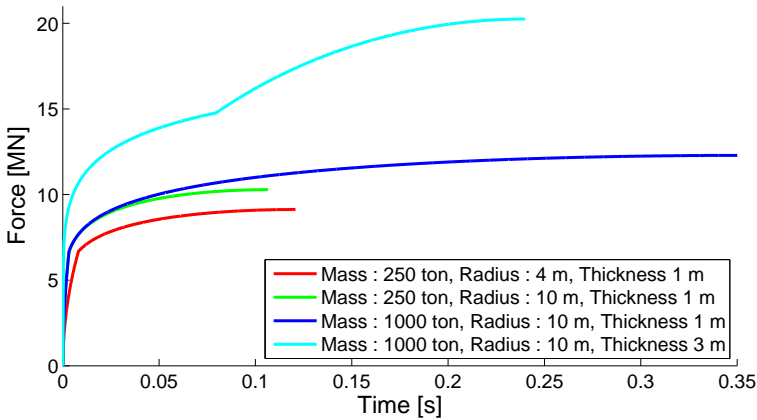
Figure 7.13: Force vs. time curves from the impulse integration calculation for the runs in Table 7.2.

Table 7.2: Ice feature properties and corresponding peak pressures, forces and dissipated energies from the simulations in Figure 7.13.

	Mass [tonne]	Thickness [m]	Radius [m]	Area [m^2]	Average pressure [MPa]	Force [MN]	Energy [MJ]
Run 1	250	1	4	2	4.5	9	1
Run 2	250	1	10	3	3.5	10.5	1
Run 3	1000	1	10	5.5	2.3	12.7	4
Run 4	1000	3	10	13	1.6	20.8	4

The above calculations were performed for a vertical ship side with an impact perpendicular to the surface normal. If 3D external mechanics theory was used (as in Section 7.2.5) for impacts in the bow area, significant reductions in the forces and energies would be achieved due to the difference between the impact direction and the surface normal of the struck bow plating.

7.3.2   NLFEA Simulations

The areas and pressures found in Table 7.2 were then applied in NLFEA calculations to assess the structural capacity before damage, the possible exceedance of the elastic resistance and the actual capacity of the structure before collapse of the double side of the ship.

A finite element model of an ICE-1A ship side was established (Figure 7.14). The ice belt (yellow part in Figure 7.14a) was a 30 mm plate, with T350×12/150×15 stiffeners spaced about 880 mm apart. Frames behind the ice belt were 20 mm thick and stiffened with 200×12 flatbars, with a frame spacing of 3360 mm. All parts of the main structure were modeled with four-noded Belytschko-Tsay shell elements. The mesh size was sufficiently refined to capture the strain localization during plastic deformation, see Figure 7.14b.

(a) Ship structure   (b) Mesh details
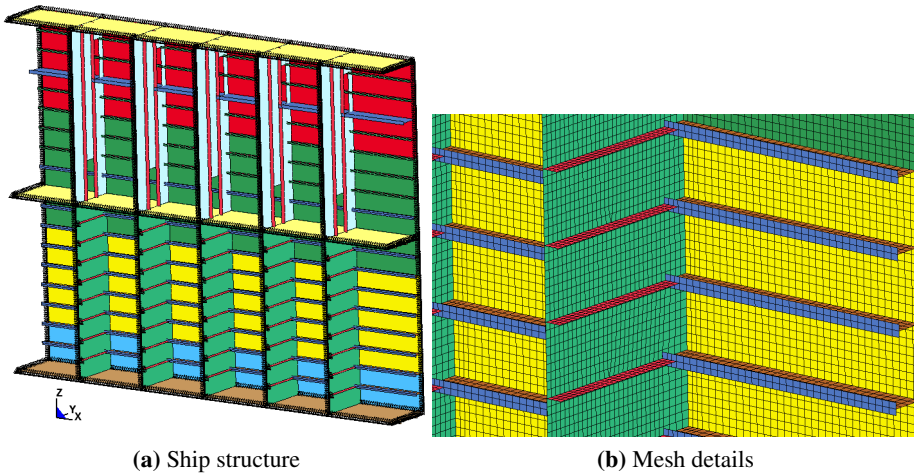
Figure 7.14: NLFEA model of a ICE-1A-strengthened vessel side.

The model was simply supported along the boundaries, marked with a black line in Figure 7.14a. The material was assumed to be similar to NV DW27. A mean value of the tensile strength was used, and the corresponding material properties are listed in Table 7.3. The RTCL fracture criterion (Section 5.2.3) was used.

The peak contact forces from Table 7.2 were applied to the finite element model in square patches with length and height similar to the stiffener spacing. Fifteen patches were defined for simplicity, five horizontal by three vertical, in which the impact pressure was applied. Figure 7.15 shows the load-area combinations used for the different analysis runs.

In the analyses, the pressure was distributed as constant pressure over as many

Table 7.3: Material properties for NV DW27 material used in ICE-1A side structure.

σ_0 [MPa]	σ_{UTS} [MPa]	E [GPa]	K [MPa]	n	$\varepsilon_{plateau}$
275	478	210	850	0.24	0.0

(a) Run 1

(b) Run 2

(c) Run 3

(d) Run 4
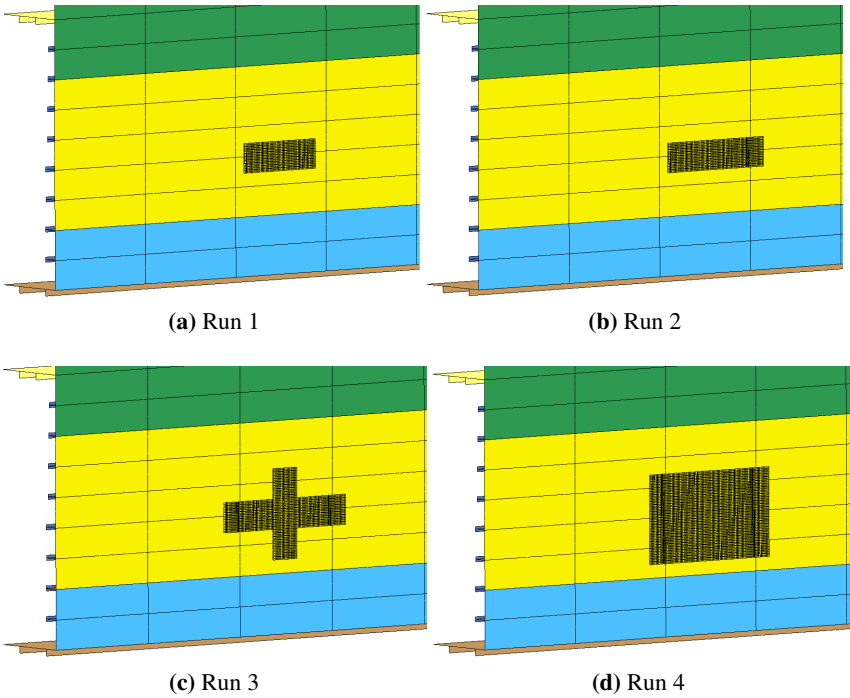
Figure 7.15: Loaded area for the different runs

patches as required to reach the loaded area. As the patch area does not exactly match the desired areas from Table 7.2, the pressure was slightly adjusted so that the force applied to the vessel was identical to that in the table, though over a slightly different area. In the simulations, the pressure is ramped up to and beyond the load level that was found in the impulse integration scheme (Table 7.2). The expected response to the impact event, and the actual ultimate capacity, can thus be determined.

Figure 7.16 shows the force vs. indentation curves and Table 7.4 the key results for the four runs.

The point of first plastic strain is used as a measure of the linear capacity[3] of the vessel hull. After the linear capacity is reached, the effect of the stiffener is gradually diminished and membrane stresses develop in the plate (and stiffener).

Table 7.4: Response of vessel hull to different load levels with indentation, plastic strain, dissipated strain energy and the corresponding pressure and force. A normalized force F/F_{demand} show the force level normalized to the force estimation found in Table 7.2.

	Indentation [m]	$\varepsilon_{plastic}$ [−]	Energy [kJ]	Pressure [MPa]	Force [MN]	F/F_{demand} [−]
RUN 1						
Linear	0.005	0.000	3.91	0.77	1.76	20%
2x thickness	0.059	0.042	165	2.49	5.8	65%
End of impact	0.107	0.083	448	3.83	8.97	100%
Web frame collapse	0.436	0.226	5510	13.02	30.9	340%
RUN 2						
Linear	0.006	0.0008	5.00	0.84	2.59	25%
2x thickness	0.062	0.064	185	2.51	7.84	75%
End of impact	0.096	0.115	378	3.35	10.5	100%
Web frame collapse	0.237	0.1867	2230	7.0	21.9	220%
RUN 3						
Linear	0.007	0.0006	6.75	0.69	3.81	30%
2x thickness	0.056	0.041	195	1.73	9.47	75%
End of impact	0.094	0.0718	423	2.31	12.6	100%
Web frame collapse	0.281	0.2208	2420	5.08	27.7	220%
RUN 4						
Linear	0.006	0.001	12.8	0.61	7.18	40%
2x thickness	0.057	0.042	257	1.23	14.3	79%
End of impact	0.087	0.069	471	1.53	18	100%
Web frame collapse	0.234	0.1611	2170	3.17	36.8	200%

For a permanent deformation of 60 mm (two times the plate thickness), the res-

---

[3]Due to the chosen interval between each plot state used in the analysis, the exact point of first plastic strain is not captured and a small plastic strain is present in some of the marked points in Table 7.4.
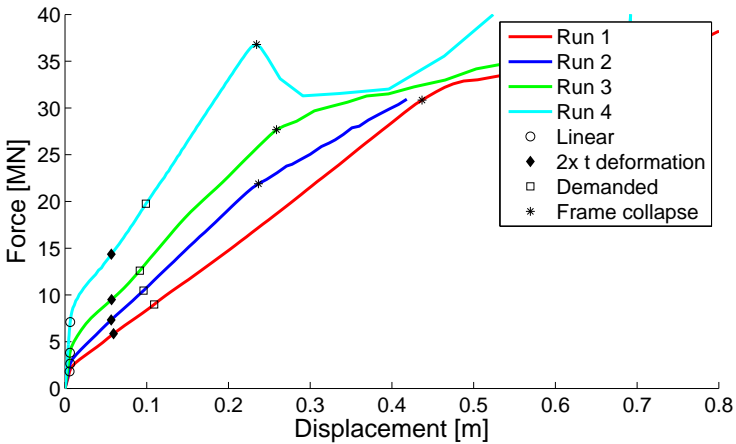
Figure 7.16: Force vs. displacement curves. Points marked *demanded* represent the prediction of indentation at the demanded load level from Table 7.2.

istance is increased by a factor of 2 to 3 compared to the elastic capacity. Plastic hinges in the stiffeners are under development, see Figure 7.17.

(a) Equivalent stress [MPa], from 0 (blue) to 400 (red)

(b) Plastic strain [-], from 0 (blue) to 0.03 (red)
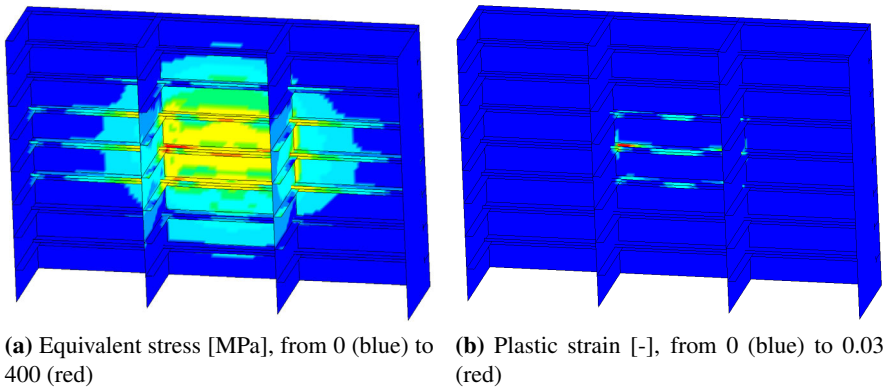
Figure 7.17: Structural response at an indentation of two times plate thickness, run 3

At the full load level from Table 7.2, the contact force is increased to between 2.5 and 5 times the linear capacity. The deformations were in the range of 100 mm. For an ALS event, this is acceptable and far from any progressive collapse. Repairs would however be required, and further transit in ice not recommended.

When the loading is increased further, the indentation level in the stiffener for the different runs increase up to between 0.23 and 0.44 m, with significant energy

dissipation in the structure. After this point the web frame collapses, with rapid deformation of the double side structure, see Figure 7.18. Contact force levels are between 5 and 17 times the linear capacity, with higher maximum load factors for the smaller contact areas. High plastic strains are observed, but fracture is not predicted according to the RTCL criterion.

(a) Equivalent stress [MPa], from 0 (blue) to 500 (red)

(b) Plastic strain [-], from 0 (blue) to 0.15 (red)
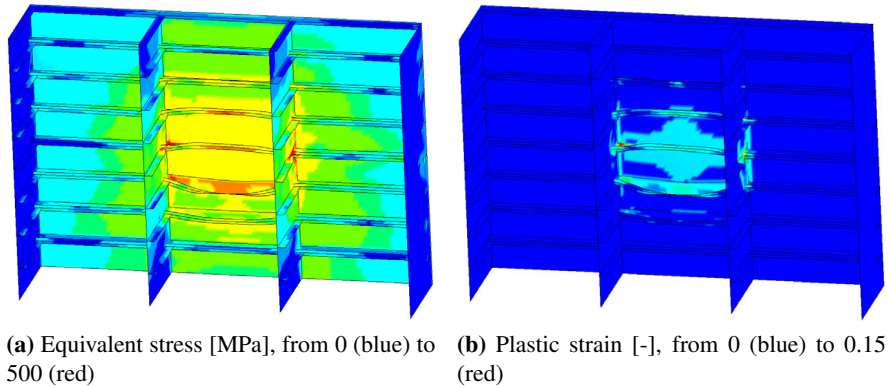
Figure 7.18: Structural response at webframe collapse, run 3

This numerical experiment is useful for several reasons. First, it demonstrates that the ultimate resistance of the vessel side is far greater than the elastic capacity. Even limited damage of 2 times the plate thickness can increase the resistance with a factor of 2-3. Second, the analyses show that the mechanisms involved are simple to describe analytically using existing idealized mechanism models (such as those in Sections 2.3.2 and 6.5.1).

The smallest impact scenarios (run 1 and 2) represent relatively small ice masses. A mass of 250 tons is could arise from a circular ice sheet with a global radius of 19 m and a thickness of 1.0 m, which is commonly observed. Such an ice mass would also get significant wave-induced motions (ref. Section 7.2.5). Hence, this is a relevant design scenario for both vessels in transit and stationary platforms.

It was assumed in the load application herein that the ice impacts midway between webframes. Thus, the total force up to frame collapse mobilizes two web frames, and might thus overpredict the collapse force for a direct impact on a frame. The studied load scenario maximizes the plate indentation, but if the web frames are the primary focus, the impact load should be assumed to act over one rather than between two web frames. For design, both scenarios have to be investigated.

7.3.3   Calculations of Plastic Resistance

Daley (2002a) derived plastic framing requirements for stiffeners subjected to patch loads from ice, ratified in IACS-UR-I (2011). Daley used a three-hinge collapse mechanism for the stiffener, with reduction in the plastic section capacity for shear in the end hinges of the mechanism. For a uniformly loaded stiffener, the pressure to form a three-hinge mechanism p_{3h} was expressed as

$$p_{3h} = \frac{(2 - k_w) + k_w\sqrt{1 - 48Z_{pns}(1 - k_w)}}{12Z_{pns}k_w^2 + 1} \frac{Z_p\sigma_0 8}{sL^2} \tag{7.14}$$

where k_w is the ratio of the plastic modulus of the web Z_w compared to the full plastic modulus Z_p, ($k_w = Z_w/Z_p$), s the stiffener spacing and L the loaded length. The term Z_{pns} was given as

$$Z_{pns} = \left[\frac{2Z_p}{A_w L}\right]^2 \tag{7.15}$$

where A_w is the cross-sectional area of the web.

If the shear capacity is exceeded, the limiting pressure is found as

$$p_{lim} = 2\frac{A_w\sigma_0}{\sqrt{3}sL} \tag{7.16}$$

Using Daley (2002a)'s approach, the stiffener capacity for the ship side in Figure 7.14a is 0.45 MPa in shear. This is in the same range as the values of first yield for run 2 in Table 7.4 (0.84 MPa), which is the investigated loading that is closest to a uniform load over one stiffener. If a uniform pressure following $p = 7.4A^{-0.7}$ acts over one stiffener, the resulting pressure is 3.5 MPa. Consequently, large indentation is expected when the stiffener fails at 0.45 MPa.

To investigate the large-indentation response, the rooftop model in Section 6.5.2 was used. A uniform load was assumed to act over the span between two stiffeners (n=1 in Eq. 6.7). The load was assumed to be carried by stiffener shear and membrane stresses in the plate. If large indentations are assumed ($w \gg t$), the predicted indentation by the method is 0.21 m for the given pressure.

NLFEA is used to simulate the same scenario, with the same assumption of pressure and loaded area. To comply with the material assumption in the roof-top model, the NLFEA material is set as linear elastic - perfectly plastic. Figure 7.19 shows the predicted indentation from the simulations. A maximum value of 0.135

m is observed, compared to 0.21 m for the roof-top model. The deformed area is limited by the stiffeners, similar to the assumptions in Eq. 6.7.
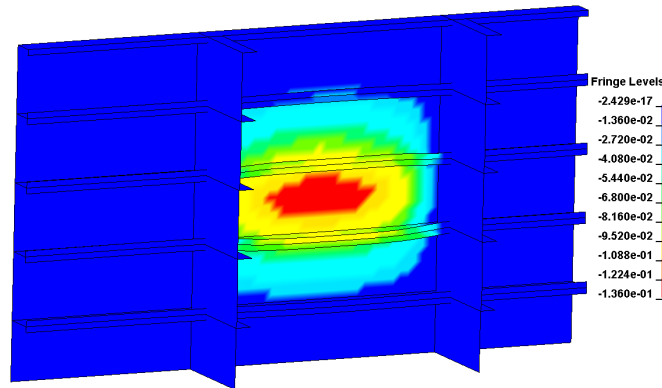
Figure 7.19: Indentation for the ICE-1A ship side subjected to uniform loading over one stiffener. Fringes are indentation in meters.

The observed response of the hull in NLFEA is suitable for plastic analysis methods. It should be noted that such methods does not guarantee that rupture of the vessel shell plating does not occur, as small very hard ice features or embedded rocks in glacial ice can produce local damage not captured by the assumed distributed load.

7.4 Assessment of Structural Resistance using Integrated NLFEA Simulations

As a more advanced alternative to using pressure-area curves, the structural resistance to ice impacts can be evaluated using integrated NLFEA simulations, in which both the ice and the structure are modeled explicitly. For this purpose, we need a continuum mechanics description of the ice, which ideally can cover the main mechanisms governing ice failure including rate and time dependence, pure crushing, microcracking, spalling, splitting, damage degradation and interaction effects due to shape and confinement. However, such a model does not exist, and simplified approaches are necessary. The end result is a *design load* model, whose purpose is to transfer a decent design ice load to the structure, and calculate the associated energy dissipation in the ice. Safety margins should normally be introduced so that the achieved load is conservative. To maintain a similar level of structural reliability, the ice load model should generate a pressure-area response in the same range as what would have been employed in a simpler assessment.

There are substantial benefits to utilizing integrated analysis for ice collision. Primar-

ily, the external mechanics of the impact can be assessed more accurately, such that glancing impacts can be treated differently than perpendicular impacts. During a glancing impact the structure may deform and the direction of the impact force may thus change significantly. Such effects can only be captured with integrated analysis. Hence, utilizing integrated analysis can solve more complicated scenarios and remove some of the conservative assumptions that are enforced when using simplified methods (such as assuming a perpendicular impact).

7.4.1   Continuum Material Models for Glacial Ice

Several researchers attempt numerical modeling of the behavior of glacial ice in compression. The simplest continuum approach is to use a linear elastic-perfectly plastic material (Kim et al. 2006). Gagnon (2007) used a crushable foam to replicate full scale iceberg impact experiments. A more advanced model was proposed by Liu et al. (2011a), based on a Tsai-Wu yield surface and a hydrostatic erosion criterion.

Pralong et al. (2006); Xiao and Jordaan (1996) used visco-elastic material combined with damage mechanics to model glacial ice. Singh and Jordaan (1999) modeled the behavior of the crushed layer of ice by considering damage and porosity as state variables. Using visco-elastic damage theory is claimed to be closer to the actual behavior of glacial ice, though this is a debated statement in the ice community. These works have gained much appraisal, but little practical use for design.

In the following, the crushable foam material models from Gagnon (2007, 2011), and plasticity based model from Liu et al. (2011a) are investigated. They have to some extent been used by other researchers and industry (Gao et al. 2015; Lee et al. 2010). The models are based on a design load principle. The behavior of each model was investigated with NLFEA, specifically the effect of local geometry of the ice mass on the collision response.

Gagnon and Derradji-Aouat (2006) and Gagnon (2007) used a crushable foam material model in LS-DYNA that was tuned to behave analogous to ice. The model was calibrated towards the *CCGS Terry Fox* impact runs in 2001 by trial and error (Gagnon et al. 2008), and not to the physical behavior of ice in general.

The primary input variable for the crushable foam model is the stress vs. volumetric strain curve. It describes how each foam element will respond to deformation. Figure 7.20 shows the employed curve; with a low initial hardening followed by a sharp linear hardening up to half of the assumed Young's modulus at a strain of 1. With this curve and a mesh discretization of about 2 m, the *CCGS Terry Fox* impact runs were simulated with good representation of both the total impact load and the

impact duration. The crushable foam model was further motivated by the fact that impact on corner of an ice mass gives a high pressure zone in the contact element (high fractional volumetric strain) and low pressure in the surrounding elements with less volumetric strain. This was claimed to represent the soft and hard zones of contact by Gagnon and Derradji-Aouat (2006). In essence, the steep hardening gives a near rigid response after a predefined volumetric strain.
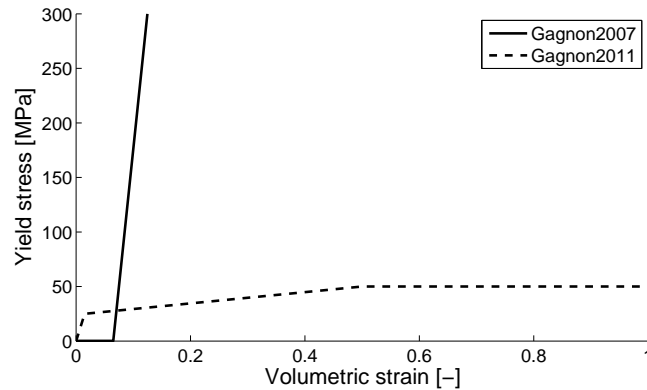
Figure 7.20: Volumetric strain vs. stress curve for Gagnon (2007, 2011)

In Gagnon (2011) spalling behavior of ice was investigated by a layered material setup with two different crushable foam material curves. A cutoff value of the maximum stress of 50 MPa for hard and 10 MPa for soft ice material was applied. An eroding contact definition between the soft and hard material types was defined to produce load peaks at predetermined intervals. After sufficient strain in a material layer, the cutout value was reached, and further deformation would not increase the element stress. The eroding contact definition further ensured that the hardened pieces of ice were disregarded in the contact definition. Thus, the material is no longer rigid for large deformations. The hard ice parameters were chosen for comparison herein, with volumetric strain vs. stress curve as in Figure 7.20. The layered approach with eroding contact surfaces was not used, as that imposes too stringent assumptions on the results, and is thus not suited for investigative analyses with an unknown solution.

To compare the stress-strain curve in Gagnon (2007) with the new curve in Gagnon (2011), both are run in the subsequent analysis. The latter curve will behave less rigid, thereby allowing energy absorption in the ice also after the first strains. In the following, the crushable foam with steep hardening is referred to as *Gagnon2007*, and the crushable foam with a stress cutoff at 50 MPa is referred to as *Gagnon2011*.

Liu et al. (2011a) proposed a material model based on plasticity theory. The model

is dependent on the hydrostatic pressure, and thereby the triaxial loading state of the ice. The purpose of the model was to provide reasonable pressure-area relationships for a strength-design case, for which validation data was available. It was then assumed that the triaxial calibration would also yield valid results in shared-energy design, in which the coupled effect of ice-structure becomes important. No experimental data are available to validate brittle ice crushing in a shared-energy regime. A Tsai-Wu yield surface[4] was fitted to experimental data sets. The yield surface is a function of both the second invariant of the deviatoric stress tensor J_2 and the hydrostatic pressure p as

$$f(p, J_2) = J_2 - (a_0 + a_1 p + a_2 p^2) = 0 \qquad (7.17)$$

with coefficients a_0, a_1 and a_2. When an element reaches plasticity in compression, it follows the yield surface until failure.

Due to the low tension capacity of ice, an element is removed by erosion if the tensile stress surpass 2 MPa. For compressive stress-states, failure by element erosion was activated if the equivalent plastic strain ε_{eq} (compressive) reaches the failure curve ε_f, defined by

$$\varepsilon_f = \varepsilon_0 + (\frac{p}{p_2} - 0.5)^2 \qquad (7.18)$$

in which ε_0 is the initial failure strain and p_2 is the larger root of the yield function (Eq. 7.17). The Tsai-Wu criterion is plotted in Figure 7.21. In the following, this plasticity based model is referred to as *Liu2011*.

For all material models the density is set to $\rho = 900 kg/m^3$, Young's modulus $E = 9.5 GPa$ and Poisson ratio of $\nu = 0.3$ for *Liu*'s model and 0.0 for *Gagnon*'s models. The material constants for *Liu*'s model are $a_0 = 22.93$ MPa^2, $a_1 = 2.06$ MPa, $a_2 = -0.023$ and $\varepsilon_0 = 0.02$. These parameters are in line with the parameters used by the individual authors. Gagnon calibrated towards full-scale impacts of icebergs, whereas Liu calibrated towards triaxial testing of iceberg ice.

7.4.2   Simulation of Ice Crushing against a Rigid Plate

To compare the material models in a simple manner, a spherical ice model was impacted against a rigid plate at a constant velocity of 1 m/s. The sphere had a radius of 1.5 m and a mesh size of about 50 mm. This allowed for sufficiently fine discretization of the model compared to the relevant structural models, and is in

---

[4]Technically, the Tsai-Wu yield surface is for anisotropic materials. A simpler isotropic elliptical yield surface was used by Liu et al. (2011a), but the reference to Tsai-Wu was maintained

(a) Yield surface

(b) Erosion criteria
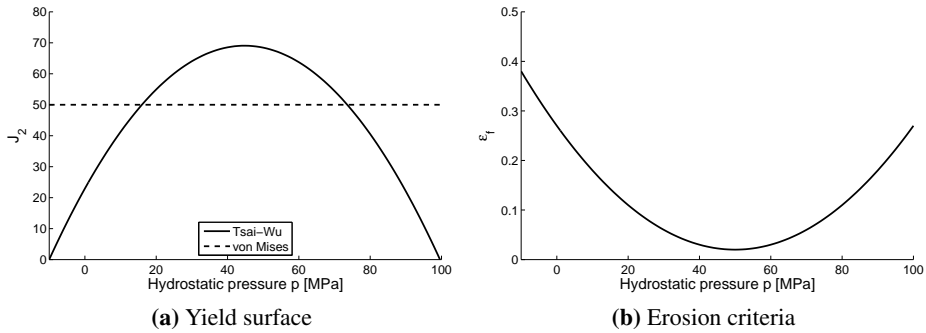
Figure 7.21: Tsai-wu yield surface and erosion limit with the parameters used herein.

(a) Definitions

(b) Force-displacement curves
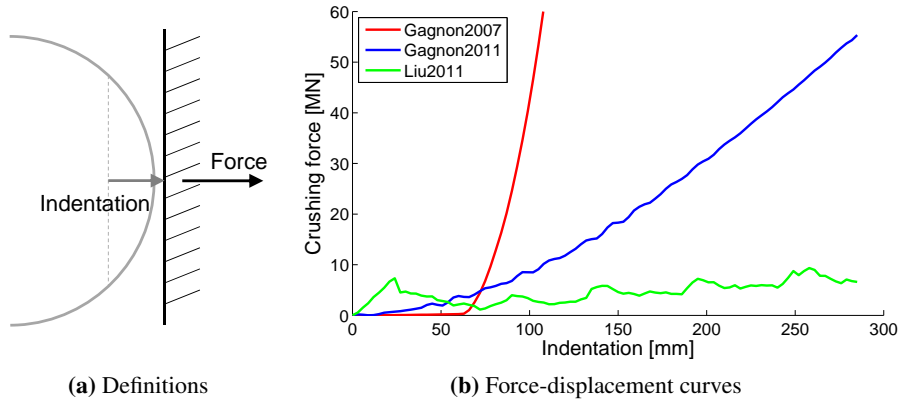
Figure 7.22: Total reaction force vs. crushing depth for rigid plate vs. spherical ice model

line with the validation performed in Liu et al. (2011a). The total crushing length was about 270 mm, giving a maximum obtainable contact area of about 2 m^2.

Figure 7.22 shows the total contact force from the different material models. The *Gagnon2007* model show low initial force, but then reach the limit fractional volumetric strain and the contact force quickly increases to unphysical values (thereby behaving rigidly). The *Gagnon2011* model shows a less extreme response. The *Liu2011* model exhibits a response more similar to the expected crushing behavior in glacial ice, with force peaks and a slight increase in total force as the contact area increases.

Figure 7.23 shows the pressure-area contours after 270 mm of deformation for the different material models (a-c), and an envelope of the maximum pressure over

the entire impact event (d-f). The magnitudes of the pressure differ significantly between the models, from 1800 MPa for *Gagnon2007* to 25 MPa for *Liu2011*. All models show a large spatial variation in the pressure values, but this is mainly due to discretization, numerics and erosion and not input material parameters. At the selected time step, the *Liu2011* model has just eroded massively and the contact area is very small. Comparing the plot of one time step with the time envelope of the maximum pressures reveals that the crushable foam models exhibit steadily increasing pressures, whereas the Tsai-Wu model exhibit a larger spatial and temporal variation with the highest pressures at the center of the ice contact (where the confinement is the largest). Kim (2014) shows similar plots of the envelope of the peak pressures over an indentation event using Liu's material model, which compared well with experimental measurements obtained using pressure-sensitive film.

(a) Gagnon2007   (b) Gagnon2011   (c) Liu2011

(d) Gagnon2007   (e) Gagnon2011   (f) Liu2011
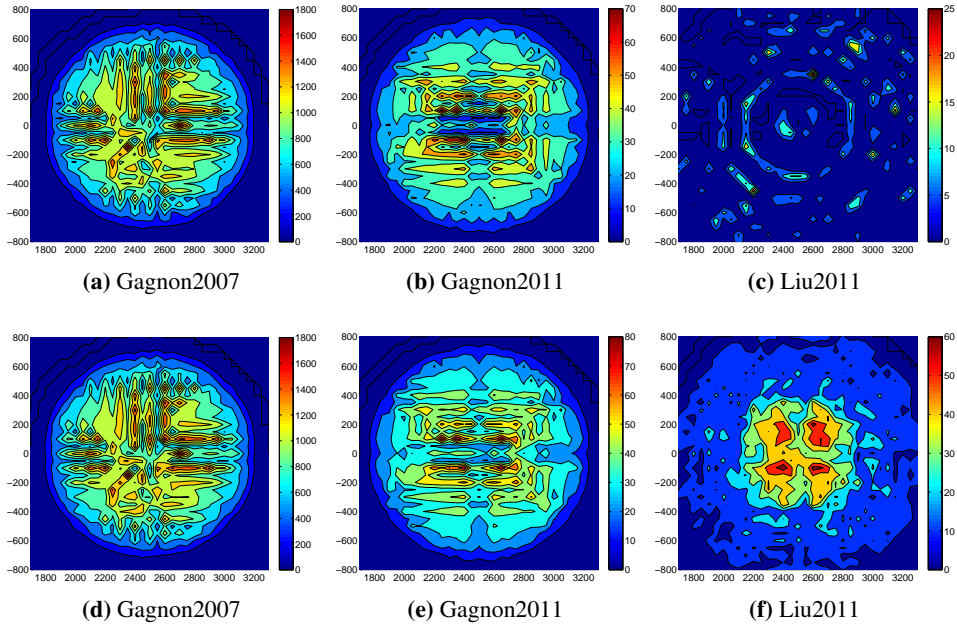
Figure 7.23: Pressure contours at maximum deformation (a-c) and envelope of maximum pressures during the entire indentation (d-f). Axes units [mm] and contour unit [MPa]

Figure 7.24 shows the pressure area points plotted together with a pressure curve with $p = 7.4A^{-0.7}$ from ISO-19906 (2010). Pressure-area from the analysis is calculated as the total force over the actual contact area[5]. Both *Gagnon2007* and

---

[5]Areas not in contact was disregarded compared to a nominal area (that would enclose all the area inside the contact surface)

Gagnon2011 models show low pressures initially, but as the hardening takes effect the pressures increase rapidly. The *Liu2011* model is more aligned with the pressure-area curve from ISO-19906 (2010), with initial high pressures stabilizing on a near constant pressure as the area increases.
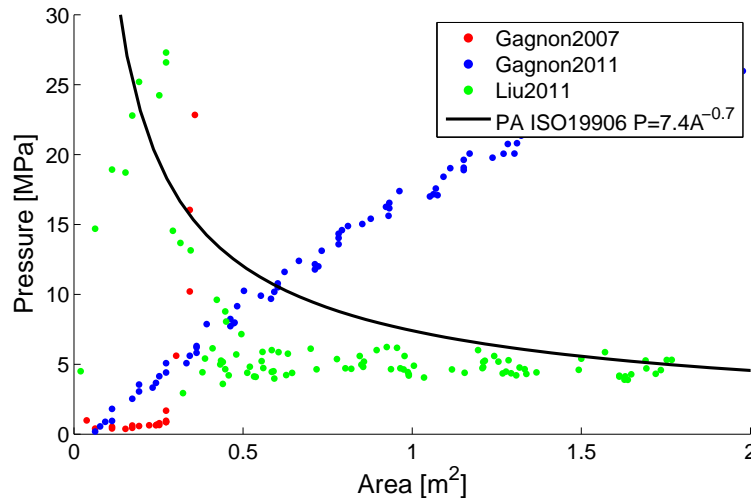
Figure 7.24: Pressure-area relationship for ice sphere vs. rigid plate. Pressure calculated as actual area in contact.

7.4.3 Simulation of Ice Crushing against a Deformable Ship Side

An integrated analysis model was established to investigate the effect of the local shape and size of the ice with the different continuum ice models. Only internal collision mechanics was considered. The membrane LNG tanker in Section 3.8 was used. Figure 7.25 shows the stiffening system used in the vessel side.

The ship material was assumed to have a yield strength of 285 MPa. J_2 plasticity and the RTCL fracture criterion were employed. Four node Belytschko-Tsay shell elements with five integration points over the thickness were used. The mesh size was roughly 250 mm, totaling at around 150 000 shell elements. This implied only two elements over the height of the stiffeners, thus somewhat overestimating their bending strength.

Several local ice geometry models were created. The models represented different local shapes of the iceberg features which gave different interaction regimes. Physical considerations suggest that a sharp ice feature should crush easily, whereas a blunt ice feature can mobilize sufficiently large forces to deform the ship prior to ice crushing. The transition between crushing of ice and deformation of ship is likely a function of the ice properties and its triaxial behavior as well as the ship
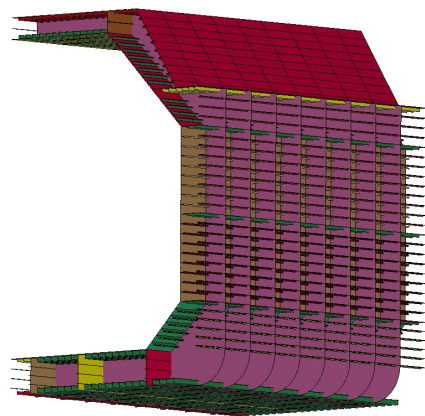
Figure 7.25: FE model of membrane tanker. Outer shell removed for clarity.

structural layout and strength. Due to melting induced by the sea temperature and wave and current action, mathematically sharp or flat ice surfaces are not found in nature. Most ice features exhibit rounded features over time (McKenna 2015).

Table 7.5: Ice models used for study of shape dependence.
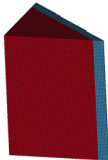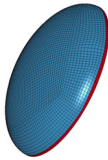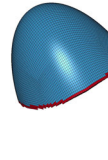
1	2	3	4	5
Cube	Ellipsoid blunt	Sphere	Ellipsoid sharp	Cone vertical
5 × 5 × 5 m, corner impact	3 m diameter, 0.75 m radius in forward direction	3 m diameter, 1.5 m radius in forward direction	3 m diameter, 3 m radius in forward direction	5 m diameter top, 2.8 m diameter bottom, 3.8 m high

Table 7.5 show the different geometries of the ice models analyzed. To limit calculation time, only part of the iceberg was modeled. A rigid surface was attached aft of each iceberg to supply an even force distribution into the local part of the iceberg. All ice elements were eight node constant stress brick elements (solid element option 1 in LS-DYNA). The mesh size was between 50 and 60 mm. The same mesh was used for all material models.

Liu et al. (2011b) describes numerical calculation of ship-ice collision and the estimated energy to be dissipated, based on the external mechanics approach outlined in Liu and Amdahl (2010). With a 150 000 ton vessel and a 5 000 and 10 000 ton iceberg impacting at a relative velocity of 5 m/s, the need for energy dissipation is 18.2 MJ and 35.2 MJ respectively for a perpendicular impact up until a common velocity is reached. These numbers illustrate an energy range that an iceberg material model should absorb easily in an impact analysis. The energy levels are comparable to supply ship collision events (Chapter 6).

Each ice model in Table 7.5 was combined with the various material models, giving 15 simulations in total. Only one contact location was investigated for each ice shape, all in the same vertical area close to the waterline and midway between two web frames.

Figure 7.26 shows the force vs. hull indentation curves for crushing of each ice model against the side structure of the membrane LNG carrier. Significant differences can be observed for the various material models; the crushable foam models show a steadily increasing force, whereas the Tsai-Wu model shows large force fluctuations with some elastic restitution of the structure for each force drop.

(a) Gagnon2007   **(b)** Gagnon2011   **(c)** Liu2011
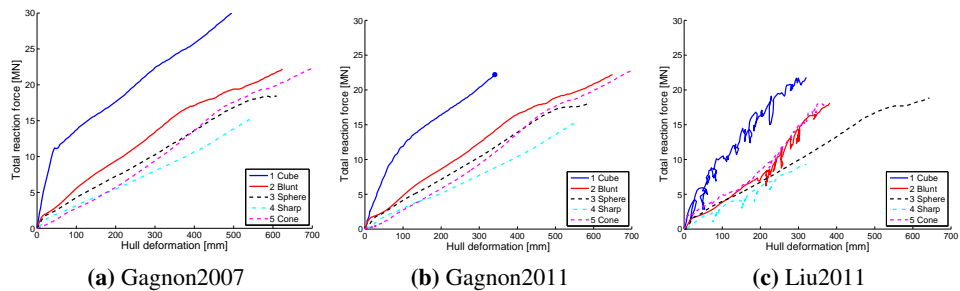
Figure 7.26: Force-deformation plots of crushing of each ice model against the ship structure. The cube shape with Gagnon2011 model failed prematurely due to negative volume, failure point marked with circle in the figure.

Figure 7.27a shows the deformation of the vessel after impact with the spherical ice model (model 3). All material models yield essentially the same deformation in the vessel, though with somewhat more deformation of the ice with the *Gagnon2007* model. No significant ice erosion occurs for *Liu2011*.

Figure 7.27b shows the deformation of the vessel after impact with the conical ice model (model 5). This geometric model has a sharp edge at the top. All the glacial ice material models show significant deformation of the top of the ice cone, but the structural damage varies significantly. With *Gagnon*'s models, the sharp edge

acts fairly rigid and creates significant deformations in the hull structure. With *Liu*'s model the sharp edge of the cone crushes more easily, and creates a softer contact with less total deformation and a more even vertical distribution of the deformation.

For all the models, the deformation in the ship structure is sufficient to cause increased confinement of the ice. This is not explicitly accounted for in either of the ice material models, but the pressure dependence in *Liu2011* may mitigate this somewhat.

(a) Ice model 3   (b) Ice model 5
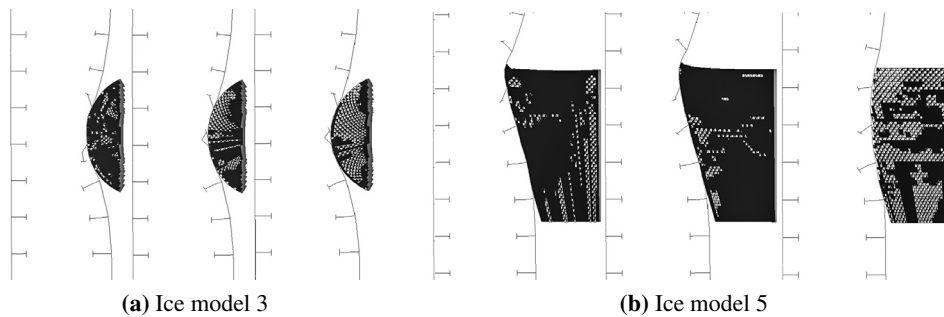
Figure 7.27: Deformation plot of ice vs. structure with varying ice shape for the tested ice material models, Gagnon2007 (left), Gagnon2011 (mid) and Liu2011 (right).

Figure 7.28 shows the total dissipated energy and the ratio of energy dissipation in the ice vs. total energy dissipation for all the models. The energy level was in the same range for the different ice models except for the sharp ellipsoidal ice model (model 4). Here the *Liu2011* model results in more pronounced ice crushing, with about half the total energy compared to the crushable foam models. The *Liu2011* model shows significantly less deformation in the vessel hull for all ice models except the sphere.

Comparing the ratio of dissipated energy in the ice vs. the total dissipated energy, both the crushable foam models show initial crushing of the ice, but the ice then hardens and mainly deforms the vessel hull. The *Liu2011* ice model shows a larger spread in the results, but in general a lot more energy is dissipated in the ice (thus with lower structural deformations for the same collision event).

The pressure-area relation from crushing of the spherical ice mass (model 3) against a rigid wall in Figure 7.24 can be compared to the same ice mass impacted against the vessel model in Figure 7.29. The vessel hull is weaker than the ice mass, and the unrealistic high pressures observed from crushing against a rigid plate is therefore naturally not observed for the crushable foam models during integrated

(a) Total energy, Gagnon2007

(b) Energy ratio, Gagnon2007

(c) Total energy, Gagnon2011

(d) Energy ratio, Gagnon2011

(e) Total energy, Liu2011

(f) Energy ratio, Liu2011
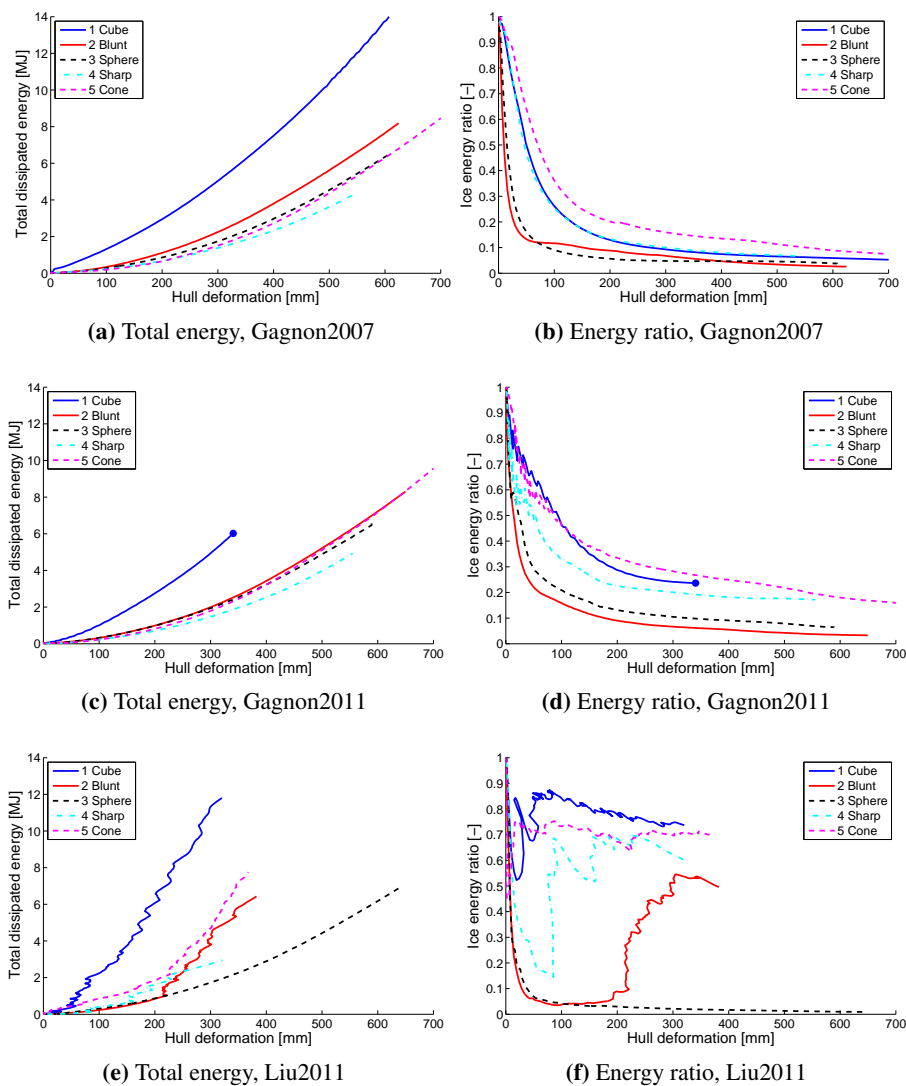
Figure 7.28: Total energy dissipation (left) and ratio of ice deformation energy over total deformation energy (right), plotted against maximum hull indentation for the material models. The cube shape with Gagnon2011 model failed prematurely due to negative volume, failure point marked with circle in the figure.

analysis. It is the resistance of the side shell that governs the contact pressure. The interaction can then be characterized as being in the ductile energy regime, and the differences between the ice material models are small.

It should be noted that the vessel side structure was not heavily reinforced, thus the difference between the strength of the ice and the vessel will be different if the vessel was designed to withstand such iceberg impacts (having a sufficient strength to crush the ice without significant structural deformations). The crushable foam models are not able to capture this difference, and will behave rigidly virtually regardless of any strengthening of the ship side.
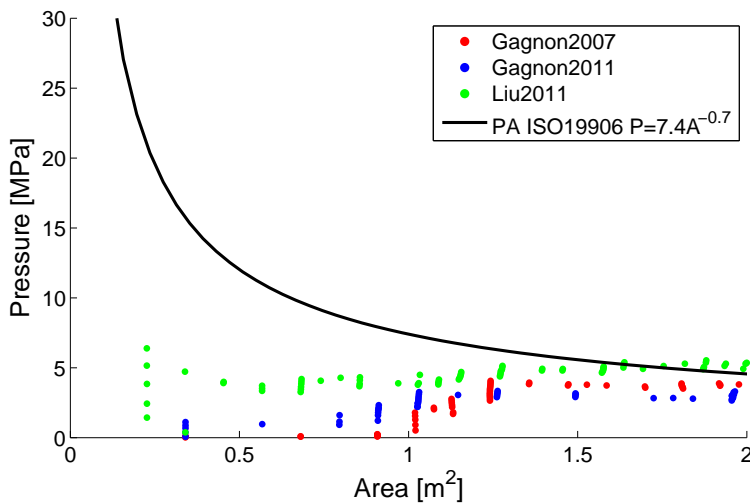
Figure 7.29: Pressure-area relationship for spherical ice vs. deformable vessel. Pressure calculated as actual area in contact.

7.4.4   Discussion

The local shape dependence of iceberg interaction was investigated by existing material models. For blunt objects (Figure 7.27a) and moderate deformations the models agree well, and show a similar range of energy vs. hull deformation. For sharper objects (Figure 7.27b) the material models deviate strongly. Using the material model from *Liu2011*, the ice was crushed easily, whereas with *Gagnon2007* and *Gagnon2011* the ice penetrated the hull. All material models yields significant structural deformations which cannot be disregarded. In Figure 7.27b, the structural damage from the crushable foam models could be realistic if the relative strength of the ice was large compared to the ships strength. On the other hand, results from *Liu*'s model give a softer response at large deformations. The different models could thus all represent realistic icebergs for the given structure. However,

if the structural resistance is increased significantly, the crushable foam models will continue to act rigidly, whereas the plasticity model will crush (erode) more ice, in line with expected behavior in an actual impact. Thus, using crushable foam to represent the ice does not give any value in an integrated analysis, and the ice could just as well be treated as rigid.

Further experiments are needed to study the energy dissipation when crushing ice, especially sharp features. This should consider realistic strain-rates and the coupled effect that develops during mutual crushing of ice and structure, ideally at large scale. This will enable the material models to be calibrated towards an energy criterion, and yield more coherent results. At the moment it is difficult to conclude if any of the continuum ice models behave in a physically correct manner, but the results from the *Liu2011* model seems to be more plausible for large deformations in the ice, and adheres to the pressure-area response commonly assumed for ice crushing.

7.5   Concluding Remarks

Many challenges have to be addressed when designing a structure against impacts from ice masses; most importantly iceberg shape, strength and velocity relative to the motion of the structure. Using data resources from various full-scale measurements, the ice shapes, frequency of occurrence and impact velocities can be established.

Using impulse integration techniques, realistic loaded areas can be determined based on assumptions of shape and a certain pressure-area curve (often defined in rules). The loads can be applied in simplified models, or through application of NLFEA, and the structural resistance is efficiently evaluated. The investigations herein shows both that the structural response of low-ice class vessels is suitable for simplified mechanism models, and that there is a significant capacity from the elastic load limit until large plastic deformations are obtained.

Investigations using integrated NLFEA revealed that the available continuum material models for crushing of glacial ice show large variations in the predicted response. They are not sufficiently validated against experiments, and to a large degree calibrated to the same data for which they are validated. This may yield useful simulation results for the specific calibration cases, but serve more as an illustration rather than a calculation of the ice behavior.

The behavior of ice during crushing is complex, and not fully understood. The available experimental data is sufficient to design structures according to strength design principles. For shared-energy and ductile interaction regimes, the interaction effects with load redistribution and change of the local ice confinement due

to changing shape of the structure will be important due to larger indentations. Exactly when this becomes important has yet to be understood by the research community.

The local confinement depends on the actual deformation state of the structure, and may vary during the impact. Its effect on the collision outcome can be large, causing a *progressive increase* in the severity of the impact event. Further experimental work is needed in order to develop sufficient knowledge of this phenomenon.

If the confinement dependence of the ice was known, it could be included in a simplified calculation routine as well as in continuum models for use with NLFEA. This would enable increased reliability in validation of continuum material models for ice. Further, it can help to understand what types of ice features that can be expected to crush, and what features that can be expected to indent the structure. A better understanding of this will help to provide improved operational constraints for vessels operating in ice, so that risks to life, environment and property can be lowered.

Two experimental campaigns that address the coupled ice-structure interaction in the shared-energy regime are presented in the following chapter.

Chapter 8

Experimental Studies on Ice-structure Interaction

As identified in Chapter 7, there is a need for deeper understanding of the behavior of brittle ice during impacts in which both the ice and structure undergo large inelastic deformations, and where contact surfaces does not remain flat.

Two experimental campaigns have been performed during the PhD work to investigate the coupled interaction process between ice and a structure when they both undergo significant damage; the first was done at the *Aalto Ice Basin* in Helsinki in 2012 under the lead of Dr. Ekaterina Kim, and the second performed at the *SIMLab* research facilities at NTNU, Trondheim, in 2014 under my lead.

8.1 Floating Impact Experiments at Aalto

The first laboratory test campaign on shared-energy collisions was carried out to provide experience of modeling of shared-energy collisions in laboratory conditions, and to support the development of the testing procedure for a full-scale ice-structure collision scenario. Experimental methodology, setup, instrumentation and some key results are described in the following. A full description of these tests, results and discussion of results can be found in JP-5, CP-7, CP-8 and Kim (2014).

8.1.1 Experimental Goal

The key focus was to obtain shared-energy impacts between iceberg ice (granular freshwater ice) and a floating structure, similar to what can be expected in an actual collision in which the ship sustains damage. The tests were not scaled by any

similitude law. Steel structures and granular freshwater ice were used - ice of significantly higher strength than model ice. The following goals were defined:

- The ice behavior during impact should approximate that of glacial ice (freshwater granular ice).
- The steel panel should have dimensions so as to undergo permanent deformations, with deformation modes as can be expected at full-scale.
- Both the ice and the structure should deform during the collision event. The ice block should be strong and have sufficient energy to cause permanent deformations in the steel structure.

8.1.2   Test Setup

The tests were conducted in the 40×40 m Aalto Ice Tank facility, which has a depth of 2.8 m. Figure 8.1 shows the experimental setup.

A system of ropes and pulleys was used to tow an approximately 900-kg ice block into a purpose-built target at speeds of 1.0 and 2.0 m/s. The ice basin carriage was used to tow the rope. Transverse motions of the ice block were controlled by a steering rope to obtain a direct impact on the target. An auxiliary rope was used to position the ice block before each test. The ice was towed against the moored structure shown in Figure 8.1a, to which either a rigid or deformable panel was attached.

The towing test was conducted using the following procedure: the ice block was manually positioned at the desired location using the auxiliary rope. This location was selected to enable the towing carriage to reach the desired steady-state velocity and to enable the ice block to reach the designated impact position. The ice block was controlled by a steering rope to ensure that the impact occurred near the centre of the target structure and reduce possible fishtailing motions. A V-towing scheme (Figure 8.2) was used to prevent the towing hook from hitting the impacted structure.
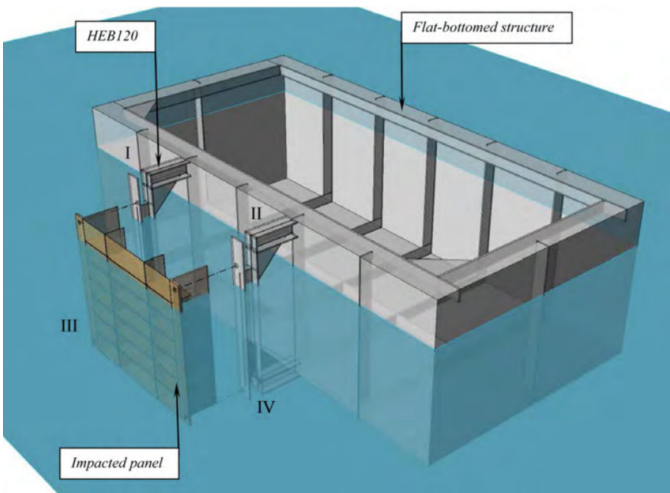
(a) Floater with attached panel
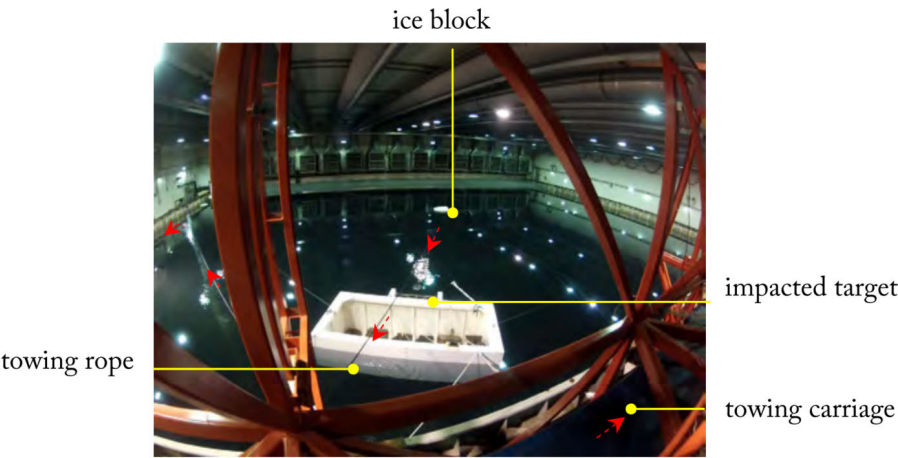
(b) Towing setup overview

Figure 8.1: Experimental setup at the Aalto ice basin.
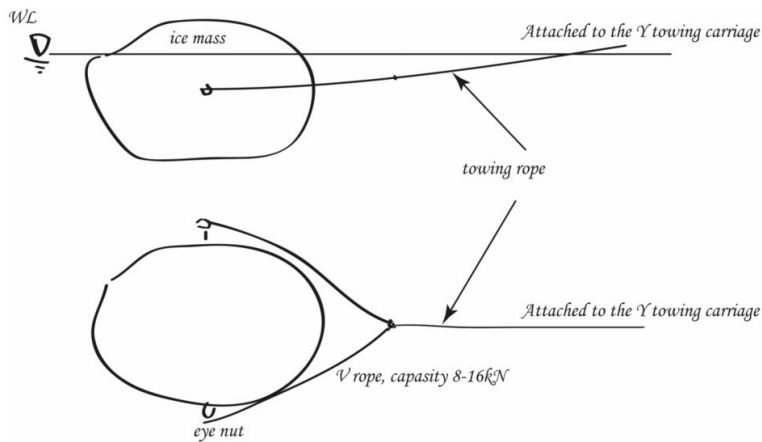
Figure 8.2: Side and plan view schematics of the towing arrangement.

8.1.3   The Impacted Structure

A barge with HEB beams (Figure 8.1a) allowed for attaching a rigid or deformable panel (Figure 8.3). The floater was moored with soft mooring to prevent large displacements but without affecting the measurements of the response due to the impact. In the fully loaded condition, the barge displacement was about 7500 kg on even keel.
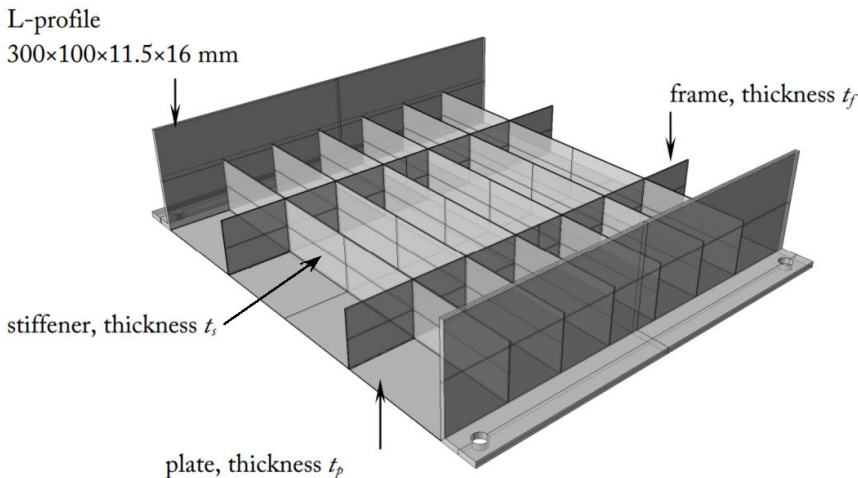
Figure 8.3: Panel configuration used in the experiments.

Four steel panels of different configurations were used to simulate the desired inter-action between the ice block and the structure (Table 8.1). The overall dimensions

of the panel were 1.1×1.3 m. The panel was supported by six transverse flatbar stiffeners and two longitudinal flatbar frames. The test panels were not scale models of any particular ship structure, but a representative panel that could behave similar to a ship structure at the given experimental scale, i.e., with local plate denting between the stiffeners and possible collapse of the stiffeners for severe impacts.

Table 8.1: Panel dimensions and initial yield strength of plate.

Panel	t_p [mm]	t_s [mm]	t_f [mm]	σ_0 [MPa]
A	4	2	4	300
B	2	2	2	190
C	4	4	4	300
D	12	12	12	-

8.1.4   The Ice

Iceberg ice had a predominant granular structure and no salinity except for intrusion of saline water in cracks in the ice. To best resemble iceberg ice, freshwater granular ice was made. The ice blocks were manufactured in plastic containers with dimensions of $1.0\times1.2\times0.9$ m. The container molds were filled up with crushed ice and water. To facilitate specimen handling, a threaded metal rod was frozen into the ice. The threaded rod, with eye nuts attached to both ends, provided connection points for the system of ropes that was used during lifting and towing of ice. A total of ten containers were filled and packed with commercially available crushed ice. The crushed ice was ordered from a third-party company and had a piece size of approximately 10-40 mm (Figure 8.4a). Subsequently, freshwater was added from the bottom to avoid air entrapment. The containers, filled with the mixture of water and crushed ice (Figure 8.4b), were stored at $-20°C$ to freeze completely. The freezing process was monitored by two temperature sensors in the ice at depths of approximately 0.4 m and 0.1 m. Furthermore, the freezing process was accelerated and the internal stresses in the ice (due to multiaxial freezing) were decreased by drilling holes, approximately 0.3 m deep, into the ice near the threaded bar. These holes enabled unfrozen water to flow to the surface of the block, releasing some of the internal pressure.

The ice blocks were considered to be frozen once the temperature at both sensors attained the ambient temperature of $-20°C$. It took approximately 5 days to completely freeze the samples. One to two days before testing, visible cracks that had formed during the freezing process were sealed with freshwater where possible.

Prior to testing, the ice block was examined for signs of open cracks and unfrozen water pockets. In case of detecting long cracks which might endanger the integrity

(a) Ice seeds from crushed ice   **(b)** Containers filled with water and crushed ice
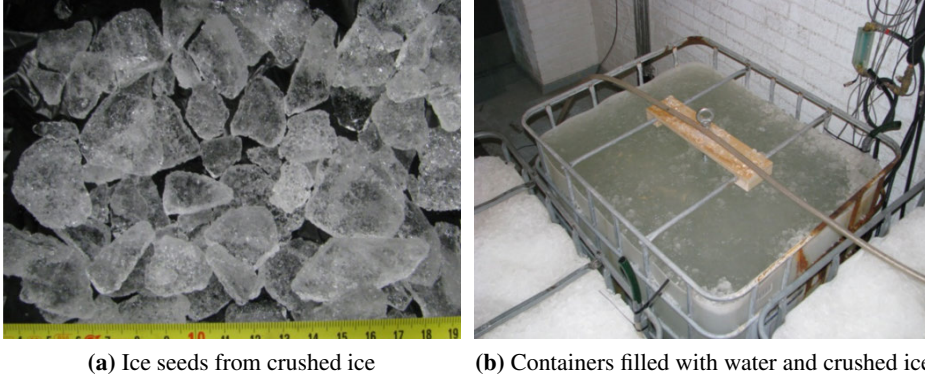
Figure 8.4: Ice seeds and molds used in the ice manufacturing process.

of the ice block, the block was discarded. Solid ice blocks were cut into the final shape (a truncated prism) using a large chain-saw. Figure 8.5 presents idealized geometry and a photograph of a typical ice block used in the impact tests.

(a) Idealized geometry   **(b)** Actual ice shape
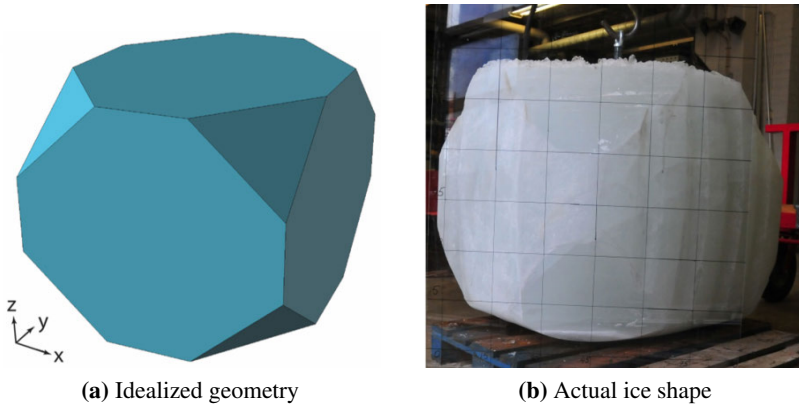
Figure 8.5: Idealized truncated prism geometry and actual ice shape. Grid in (b) is 0.15x0.15 m.

Ice samples were cut from the produced ice and tested in uniaxial compression. The ice samples exhibited a density of 901 ± 11 kg/m^3 (indicating an average porosity of approximately 2%) and a compressive strength of 0.80 ± 0.10 MPa in brittle-like failure mode under near uniaxial loading conditions. Note that the obtained compressive strength only serves as an indication of the strength due to limitations with the test rig.

To examine the undamaged ice microstructure, thin sections were produced from the manufactured ice blocks. The pieces were collected from both virgin ice and ice that was tempered in the ice basin (block C). These pieces were stored at $-10°C$ before their microstructure was examined. Thin sections of all of the ice samples were obtained using a microtome. Figures 8.6a and 8.6b show close-up photographs of the manufactured ice.

The internal structure of the ice specimens did not exhibit large variations in texture, except for the top most layer of the ice block (not shown in Figure 8.6). The manufactured ice was relatively homogeneous in all of the thin sections, with grain sizes varying from 2-10 mm. Air bubbles with diameters of 1 mm or less were mainly found along the boundaries of the ice pieces which were used to manufacture ice blocks (see Figure 8.6a).

(a) Air inclusions
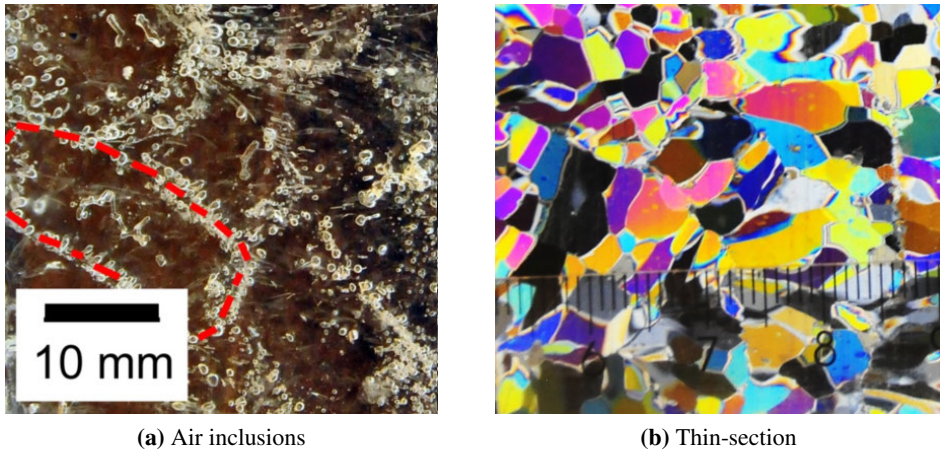
(b) Thin-section

Figure 8.6: Air inclusions and a thin section under cross-polarized light of the produced ice.

8.1.5 Instrumentation

Each impact event was recorded from five different angles using a high-speed FASTCAM-APX video camera and four GoPro HD Hero 2 video cameras. Additionally, a video camera was mounted on the upper right side of the floating structure to record an oblique angle view of the impact zone and to provide additional information about the eccentricity of the impact and the orientation of the ice block prior to impact. The high-speed video camera was mounted on the side of the ice basin and recorded images at 500 frames per second.

The impact force transferred through each of the four HEB beams (denoted I-IV

in Figure 8.1a) was measured by three uniaxial strain gages (SG) in each beam, which were attached along the beam flange, across the beam flange and at an angle of $45°$ to the beam web neutral axis.

A dynamic motion unit (DMU) recorded accelerations and the angular rates of the floater and the attached stiffened panel. The strains, accelerations and angular rates were recorded using a data acquisition system at a sampling frequency of 523 Hz, which was the highest sampling frequency possible with this equipment. The system ensured that the strain and acceleration measurements were synchronized.

The plate deflection profiles were manually recorded before and after each test. Readings of the surface profiles were done on a flat, vibration-free surface by using a plunger-type dial gage on a three-axis stand (Figure 8.7). Final deformations of the deformable panels (A-C) were computed as the difference between the measured plate deflections before and after the impact.

Figure 8.7: Deformation measurement of deformed panel after drop test 2 using a plunger-type gage on a three-axis stand.

8.1.6 Laboratory Tests Results

A total of 18 impact tests were conducted in water. Of these, 16 impacts were conducted using the 12-mm-thick panel (D panel) to determine whether reproducible results could be obtained with the experimental configuration. There was a significant scatter in impact location. Repetitions of a single test revealed difficulties in ensuring the exact impact conditions for each test, e.g., with respect to the horizontal impact location on the panel and the rotation of the ice block during

towing.

Two drop tests in dry conditions were conducted in addition to the towing tests. A detailed description of the drop tests can be found in CP-8. The drop tests can be used to investigate the interaction between the ice and the stiffened panel in the absence of hydrodynamic effects. In Drop Test no. 1, a 706-kg ice block is dropped onto panel B from a height of 0.5 m (similar kinetic energy as in the floating tests), and in Drop Test no. 2, a 601-kg ice block is dropped onto panel C from a height of 3.0 m to investigate the behavior with a significantly increased kinetic energy.

From 18 tests, only the four most interesting runs are presented herein. Results from the two towing tests with damage and the two drop tests are shown. More data on the drop tests can be found in CP-8.

Figure 8.8 shows the measured damage of the panels. Local plate dents were obtained for all the impacts on deformable panels. In drop test 1, the plate deflection of more than 12 mm can be normalized against the stiffener spacing (150 mm), which gives a normalized indentation of 0.087. This is comparable to plate dents observed at full-scale from impact with hard ice features (Hänninen 2005).

Figure 8.7 shows a picture of the most damaged plate, from the second drop test with the highest kinetic energy. The stiffeners are in general strong enough to withstand the impact, but the plate now suffers major damage. The indentations may have been large enough to locally change the confinement of the ice, thereby increasing its crushing strength. However, the lack of force measurements makes it impossible to substantiate such conclusions.

8.1.7 Ice Damage

The ice behavior was governed either by local crushing or by splitting. This classification was made through visual observations of ice blocks after impact. During crushing, the ice block remained intact except for the crushed region; the ice crushing was localized specifically at the contact zone, consisting of microcracks and a damaged layer with weakened ice. The splitting-dominated failure resulted in complete shattering of the ice block upon impact. The local ice crushing failure dominated in the impact tests in water (Test nos. 8 and 9) and in Drop Test no. 1. The splitting failure dominated in Drop Test no. 2, i.e., the test with the largest kinetic energy of ice before impact. Figure 8.9a and Figure 8.9b are close-up photographs of ice damage after Drop Test no. 2 and tow test no. 8, respectively.

See JP-5 for a full description of results and post-processing, including a quantification of the energy dissipation in the steel and ice respectively.

(a) Tow 8

(b) Tow 9

(c) Drop 1

(d) Drop 2
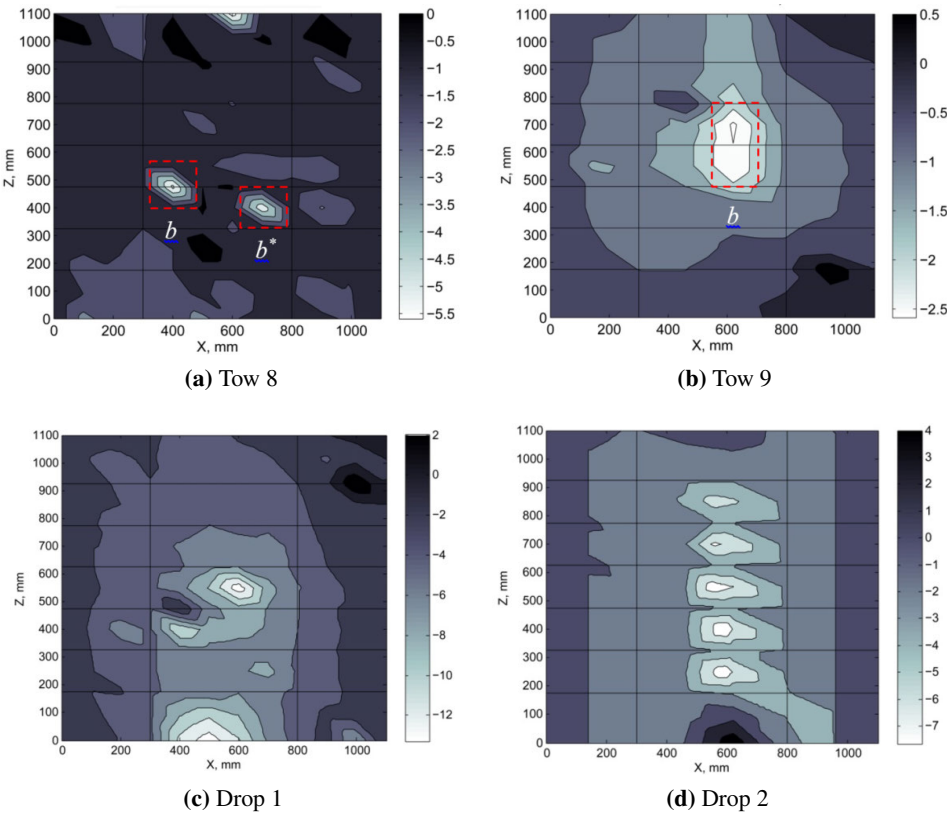
Figure 8.8: Plots of deformations on the four tests in shared-energy design regime.

(a) After drop test 2   (b) After tow impact 8
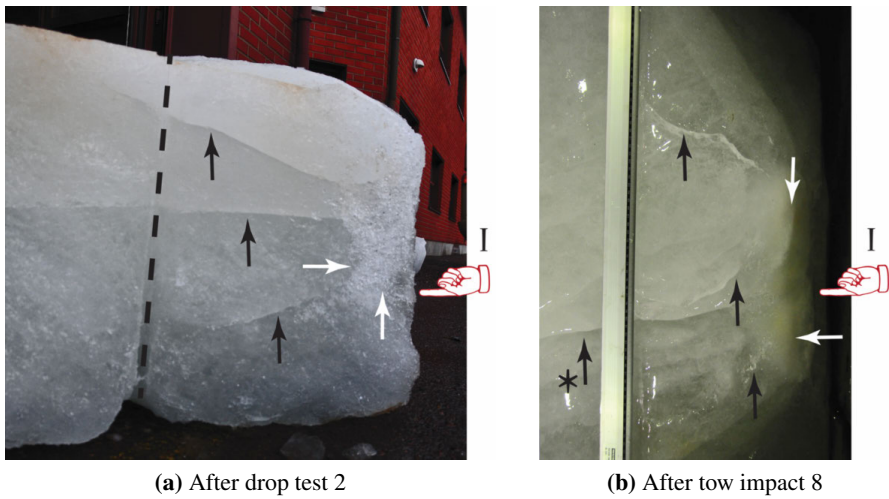
Figure 8.9: Photographs of ice damage. Black arrows indicate freshly-formed splitting cracks, and white arrows indicate crushed ice. The arrow with a star indicates an 'old' crack (i.e., the crack that was healed using freshwater before the freezing process of the ice block was completed). The dashed line indicates the position of the metal rod, which was frozen into the ice to facilitate specimen handling. A hand symbol with label 'I' indicates the direction of impact.

8.1.8 Lessons Learned

The *Aalto* experiments were successful in achieving multiple examples of shared-energy impacts, in which both the ice and the structure underwent permanent deformations and dissipated significant energy. The test setup was in part limited by the possibilities at the basin (max safe towing speed, avoid large impact forces to basin walls etc.), and in part by a cautious approach due to the novelty of the test type and setup. It proved to be a great challenge to obtain satisfactory control of the towing to ensure consistent impact location and ice orientation, and the presence of water limited visual observations of the actual impact event.

It is possible that the shared-energy impacts gave sufficiently large damage to the steel structure so that the changed structural topography gave rise to a changed local stress state (confinement) of the ice. However, the limitations in measurements and repeatability prevented both a qualitative and quantitative assessment of these aspects.

The most important lessons learned are listed below:

- Unidirectional freezing is preferable to avoid large cracks during the freezing process (not possible at in these tests due to time limitations)
- Better control of the local contact shape of the ice is needed. Either prevent rotations or measure the actual impact shape better.
- The size of the ice block relative to the available kinetic energy should have been maximized to avoid premature splitting, or measures taken to increase confinement of the free ice boundaries.
- The inertia of ice block should have been large so as to create larger damage and increased the coupled ice-structure interaction. This was limited, however, by the safe towing speed and the practical handling size of the ice block.
- Impact location under water resulted in difficulty in controlling and documenting the actual local shape of the ice at impact and the actual impact location
- Direct force measurements would have been preferable compared to indirect (DMU og SG)
- Measurements should have been sampled at higher frequencies. This was not possible with the available measurement system and high-speed camera.
- The dimensions of the steel panels could have been reduced slightly to allow larger deformations for the same impact energy. However, considering the uncertainty in ice properties and the rapid transition often observed from shared-energy to ductile design, it is very difficult to design experimental models that will result in shared-energy dissipation regimes.

Detailed analysis of hydrodynamic interaction was outside the initial scope of this study. However, as the experiments were the first shared-energy ice impact experiments conducted with a floating body, the obtained results can be used for assessment of the hydrodynamic interaction during the collision with methods such as fluid-structure-interaction (FSI). Song et al. (2015) used ALE modeling is LS-DYNA together with the Tsai-Wu-based glacial ice model from Liu et al. (2011a) to simulate the experiments. The added mass of the barge found with the ALE method was verified against potential theory with good agreement, and the force-time results from the FSI simulation agreed well with the experiments.

8.2 Impact Experiments at SIMLab

Based on the experience gained and the lessons learned from the *Aalto* experiments, a new set of experiments were devised to better study the coupled ice-structure interaction in the shared-energy regime. Now, the movement of the ice and the local contact shape and location could be controlled, and the measurement system was significantly improved by adaptation of an existing test rig.

The experimental focus could then be placed directly on the coupling effect from changed contact geometry due to deformation of the steel structure and the effect this has on the local stress state (confinement) of the ice. In turn, the increased ice confinement increases the crushing pressure of the ice, giving a greater potential for a progressive increase in the severity of the impact event.

Attempts have been made to study this before, e.g., the tests reported in Kim et al. (2015b); Manuel et al. (2013, 2015) and the planned extension of the tests in Gagnon et al. (2015); Oldford et al. (2014), but no published data exists for successful tests that demonstrate this coupling effect for realistic indentations speeds (thus with brittle behavior of the ice).

8.2.1 Experimental Setup

The experiments were conducted in the pendulum accelerator impact rig at the SIMLab laboratory facilities at NTNU, Trondheim. A pendulum arm is used to accelerate a trolley along a set of rails towards an impacted structure. The impacted structure is attached to a 150 ton concrete reaction wall on rubber foundations to resist the impact. The impact rig can be used with varying trolley mass and impact speeds. The pendulum impact rig is thoroughly described in Hanssen et al. (2003).

In these experiments, the trolley mass was 711.5 kg and the impact velocity 8 m/s. An ice piece was attached to the front of the trolley through a steel adapter (Figure 8.10), which also provided boundary conditions for the aft end of the ice. The kinetic energies for the experiments were in the range of 24 kJ. If all kinetic

energy was not absorbed by the ice impact, a secondary barrier system stopped the trolley and prevented damage to the impact rig and measurement equipment.

No model scale was defined as such for the experiments; the focus was rather to obtain results from impacts between freshwater granular ice and steel in a realistic impact scenario causing structural damage and a coupled ice-structure response.

8.2.2 Ice Sample Preparation

Glacial ice, and to some extent multi-year ice, have a predominant granular structure and low or no salinity. To get ice behavior close to this, granular freshwater ice was manufactured using commercially available crushed ice and cooled freshwater. The ice manufacturing was influenced by the recommendations from the STePS2-program reported in Gudimetla et al. (2012) and the lessons learned in the *Aalto* experiments.

Figure 8.10: Ice sample mounted to the trolley.

Circular cross-section of the ice specimens were preferred to attach the specimen to the impact trolley and to reduce effects of sharp boundaries on the ice response. The steel adapter connecting the ice sample to the trolley (Figure 8.10) consists of a bolt plate, a cylindrical spacer and a 20 mm thick backing plate, which act as the end support of the ice specimen. Forward of the backing plate, a steel cylinder with internal diameter of 320 mm, a thickness of 4 mm and a height of 100 mm (impacts 1-3) and 200 mm (impact 4) served to hold the cantilevered ice sample in place prior to impact, as well as adding some confinement to the aft end of the ice sample. Six 50 mm bolts were inserted radially in the top of the confining steel cylinder to better anchor the ice to the adapter.

In the ice manufacturing procedure, the steel adapter was resting vertically on the cold room floor. A thin plastic pipe was attached above the steel adapter using water and duct tape to create a mold for the freezing process, giving a maximum

sample height of around 500 mm. The mold assembly was left to cool prior to the ice sample manufacturing. Once cooled, the mold was filled with layers of commercially available crushed ice, commonly used for fish storage, mixed with cooled freshwater. The crushed ice had a seed size varying from 2 to 20 mm (Figure 8.11). The larger pieces were not complete crystals, but rather smaller ice pieces sintered together. The mixture was stirred throughout the filling process to prevent large air entrapments.
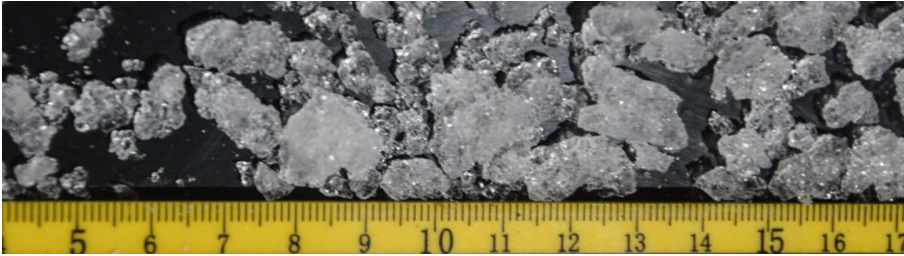
Figure 8.11: Commercially available crushed ice.

Once the samples were fully mixed, sample 1-3 were insulated on the sides and partly on the top to obtain a near unidirectional freezing from the bottom towards the ice tip, thereby reducing thermal stresses and cracks. Sample 4 was left without insulation. The samples were then left to freeze for three days.

When the samples were completely frozen, the plastic bucket was carefully cut away using an angle grinder. Due to time limitations a proper shaping apparatus was not available, in which a symmetric easily defined shape could be obtained. The ice was shaped using an angle grinder with a wood sander disc of grade 80. The grinding was very suitable for the ice shaping, but the manual control resulted in slightly asymmetric ice shapes.

A bullet-like shape was targeted, with a free cylindrical portion of the ice still intact to limit the confining effect of the steel cylinder on the ice response. The four samples are shown in Figure 8.12a. Ice sample 2 had a visible circumferential healed crack at the tip of the sample (Figures 8.10 and 8.12b). The other samples showed no visible cracks. Figure 8.12b shows the measured shape of the specimens, extracted from images from a high-speed camera directly above the impact location prior to impact. The ice was stored for two days after shaping at $-24°C$ prior to the experiments.

Figure 8.13 shows a thin-section of the intact ice. The grain size is around 1-5 mm (Figure 8.13a). Small air bubbles were distributed in the ice (Figure 8.13b), remnants of the original crushed ice structure. The amount of air bubbles indicate

(a) Ice sample 4 (left) to 1 (right)   (b) Shape of ice specimens, [mm].
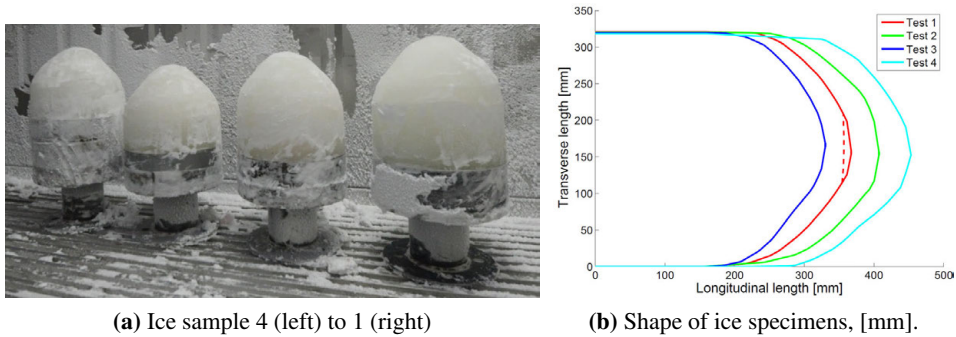
Figure 8.12: Shape of ice samples after shaping. Dashed line in b) indicate initial circumferential crack in specimen 2 (test 1).

a lower density of the ice compared to pure freshwater ice, but the density was not specifically measured. The ice microstructure has many similarities to iceberg ice, but the shape of the grains and their interlocking as well as the character of air bubble accumulation differs, see Gagnon and Gammon (1995a) and Barrette and Jordaan (2001) for details of iceberg ice properties.

(a) Thin-section   (b) Air inclusions
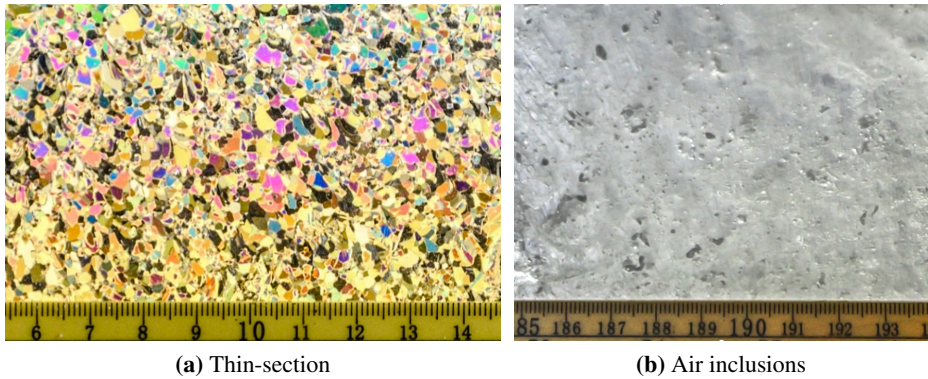
Figure 8.13: Air inclusions and a thin-section under cross-polarized light of ice as produced. Ruler scale in [cm].

8.2.3 Impacted Structure

The target of the experiment was to achieve a coupled ice-structure interaction. Thus, the steel should be strong enough to crush the ice, but weak enough to also dissipate plastic energy itself. The width of the rail system in the impact rig prevented the use of a plate structure as the struck object. Instead, a hollow profile beam with dimensions $140 \times 80 \times 6$ mm was selected, wide enough to cover most

of the expected contact area of the collision. The beam was mounted on simple supports in which the span length could be varied (Figure 8.14).

The steel grade was S355J2H. Four uniaxial tensile samples, two from each side of the beam, were tested at a speed of 2.1 mm/min. The cross-section varied from 5.83-5.94 by 12.43-12.57 mm. Two extensometers with gauge length 35 mm, one on either side of the specimen, measured the axial displacements accurately up to 4.5 mm elongation (13% strain, maximum stroke of extensometer). In addition, the stroke of the uniaxial test apparatus was measured (which includes the complete specimen and elastic response of the clamping system). The latter was used to estimate the response after 13% strain, calibrated to match the extensometer response. Figure 8.15 shows the test results in engineering stress vs. strain. The material response was found to be well represented by a Young's modulus E=194 GPa, a yield stress of 460 MPa, and power law modulus K=798 MPa and exponent n=0.157. No strain-rate tests were performed, but this is recommended for a more elaborate impact study.
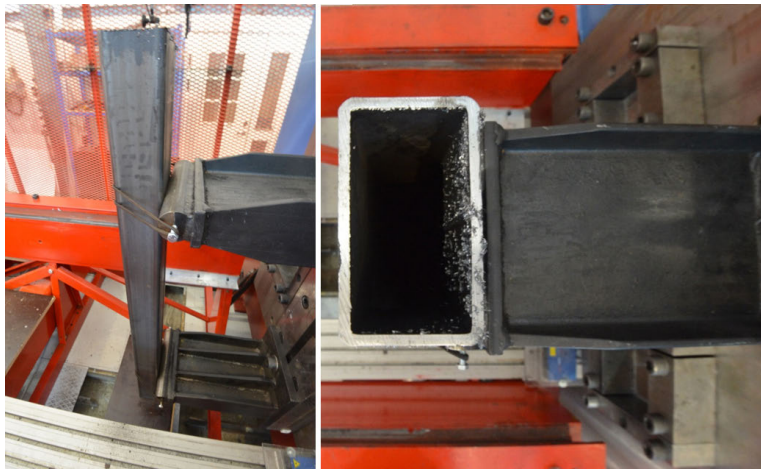
Figure 8.14: Hollow profile beam mounted on two simple supports. Rubber bands attach the beam to the supports.

The steel beam was designed weak enough to be able to deform plastically, but strong enough to also crush the ice. This resulted in a natural period of vibration of the beam in the same order of magnitude as the impact event, with the first global natural period of the simply supported beam of around 2 ms.

8.2.4 Measurements

The impact force was measured by a load cell between the trolley and the ice adapter. The load cell was calibrated statically up to 500 kN, though its capacity
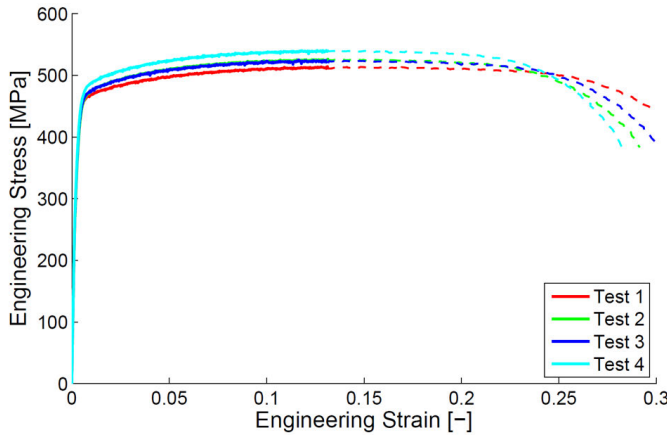
Figure 8.15: Engineering stress-strain from four uniaxial tensile tests. Solid lines are measured with the extensometers, dashed lines from the stroke of the testing machine (less accurate).

was far greater. The position of the carriage was measured by a laser distance meter mounted on the rail system. In addition, a laser measured the deflection of the reaction wall. The wall deflection was found to be negligible during the impacts. The force and distances were recorded at 100 kHz, but the laser measuring the position of the trolley only supplied new data every 2.5 kHz, thereby creating a stepped load signal.

Two Phantom v1610 high-speed cameras recorded the impacts, one from above and one from approximately $45°$ to the side. The cameras recorded at 18 kHz with a resolution of 1280×720 pixels. The measured force and distance signals were also supplied to the camera system to synchronize the measurements and video recordings. A laser trigger was activated by the trolley to start the measurements at a fixed distance prior to impact. This triggered both the force and distance measurements as well as the high-speed cameras.

8.2.5   Test Matrix

Four impacts were performed using the four ice samples. All impacts had the same trolley mass and the same impact velocity, but the span of the beam and the ice mass were varied. The temperature in the lab was approximately $+20°C$. In order to minimize the time the ice specimens were exposed to the warm air, they were shielded by a double layer of bubble wrap plastic. This insulation was removed some minutes prior to impact. The ice core temperature was around $-24°C$. The mass, kinetic energy, beam span and time exposed to the $+20°C$ in the lab (warm exposure) are given in Table 1.

Table 8.2: Test matrix with key parameters.

Test #	Ice sample	Mass of ice and adapter [kg]			Kinetic energy [kJ]	Beam span [mm]	Warm exposure [min]
		before	after	crushed			
1	2	47.7	33.2	-14.5	24.3	700	16
2	1	49.2	33.0	-16.2	24.3	900	10
3	3	45.8	33.5	-12.3	24.2	800	15
4	4	54.4	42.0	-12.4	24.5	800	9

8.2.6   Experimental Results

The measured force-time histories are shown in Figure 8.16a for all four tests and for the entire impact duration. An initial large load peak (first 10 ms) was observed, at the end of which the ice sample was fractured into individual fragments and contact was partially lost (marked with dashed line in Figure 8.16a). Some of the tests then obtained a secondary impact, when remaining intact ice regained contact. Large oscillations were observed for all the tests with a period of around 1 ms.

Test 1 showed a significantly larger force peak than the other tests. Figure 8.16b shows the corresponding force-displacement curve for the first 10 ms of impact. Displacement is here the change in position of the trolley from first contact. Points of interest are marked with letters, and the corresponding deformation of the ice and beam are shown in Figure 8.17.

The high contact force in test 1 was partially due to a circumferential initial crack on the tip of the specimen (Figure 8.12b and Figure 8.17a), that crushed early in the interaction (first 10 mm in Figure 8.16b). After this, the contact area between the ice and steel was larger, and the ice could withstand a larger force prior to global comminuted fracture of the specimen (starts after point c). At point d in Figure 8.16b, the ice strength degraded due to accumulation of cracks, and the load level dropped while more and more of the ice lost its integrity and contact. The remaining ice pieces started to move outwards, while some ice blocks still maintained contact between the steel adapter and the steel beam. After point e, no solid ice pieces remained in contact, and the force level dropped significantly while the remaining ice was cleared away.

All four tests showed the same large oscillations with a period of around 1 ms. These are very different from the saw tooth-pattern typically observed in ice crushing events. During the first two large load peaks (from b to c in Figure 8.16b) no visible damage was observed in the bulk ice other than pulverization at the tip of the sample and small cracks radiating away from the contact zone. At the second large peak (point c), global fractures from the tip to the bottom of the specimens were observed for all tests. The main difference between test 1 and tests 2-4 was

the circumferential initial crack, which crushed without causing visible damage to the rest of the ice (a to b in Figure 8.16b), thereby creating a larger contact area capable of higher force before the sample failed globally.

The oscillations are probably due to interaction with the deflection modes of the impacted beam, both globally as beam vibrations ($\approx$ 2 Hz) and locally as vibrations of the beam flange ($\approx$ 1 Hz). However, the measurement setup of the beam response was not sufficient to substantiate this. Further, some oscillatory response may have been present in the ice and load cell system due to stress waves and the dynamic load cell response. An investigation of the dynamic parameters of the coupled ice and load cell system was not conducted to verify this.

Figure 8.18 shows the plastically deformed configuration of the steel beam, measured after impact 1. A global deflection with amplitude of around 10 mm was combined with a local deflection of the beam flange around the impact with an additional 14 mm indentation. The total global deflection during the impact (elastic + plastic) was about 60% larger, and occurred after approximately 45 mm displacement of the trolley in Figure 8.16b, somewhat out of phase from the force signal.

The deflection of the beam should be combined with the displacement of the trolley to obtain an estimate of the crushing distance of the ice. The global beam deflection was extracted through processing of the high-speed video files, and an updated force-displacement curve is shown in Figure 8.19. The corrected curve now represents a better estimate of the actual indentation into the ice, but the local deflection of the beam flange has not been accounted for. This would additionally reduce the estimate of indentation into the ice.

The crushing distance of the ice was estimated. Using the shape data in Figure 8.12b, the nominal contact area was calculated by assuming a circular contact, and used to establish the process pressure-area relation in the right of Figure 8.19 for impact 1. For the other impacts, the elastic deflection of the beam was smaller, and was not accounted for in the area calculation.

For impact test no. 1, crushing of the ice cap gave a high initial pressure. As the larger contact area was established, the nominal pressure peaked at 12 MPa. After large fractures were visible in the ice, the rate of increase in pressure vs. area decreased as a result of the accumulated ice damage, both micromechanical and global comminuted fractures. For impacts 2-4, a higher peak pressure was observed at a lower force, after which the pressure capacity of the ice samples decreased quickly. Impact 1 showed a slower decrease in pressure capacity, likely due to the confining effect from the plastically deformed beam.
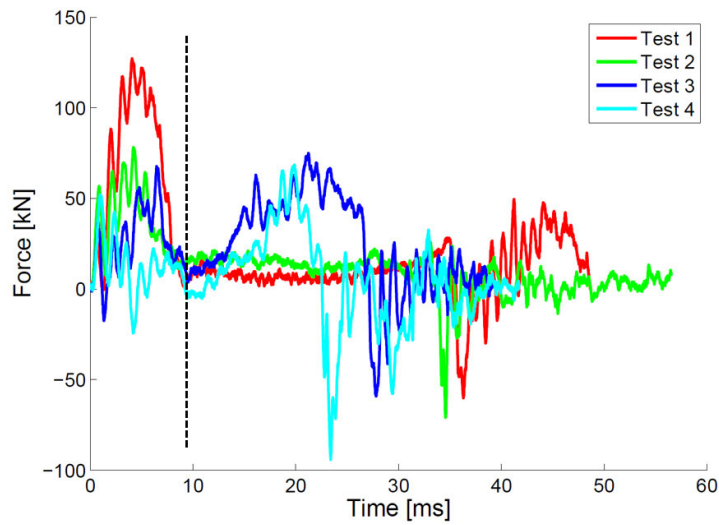
(a) Force-time for entire impact event. Partially lost contact after dashed vertical line
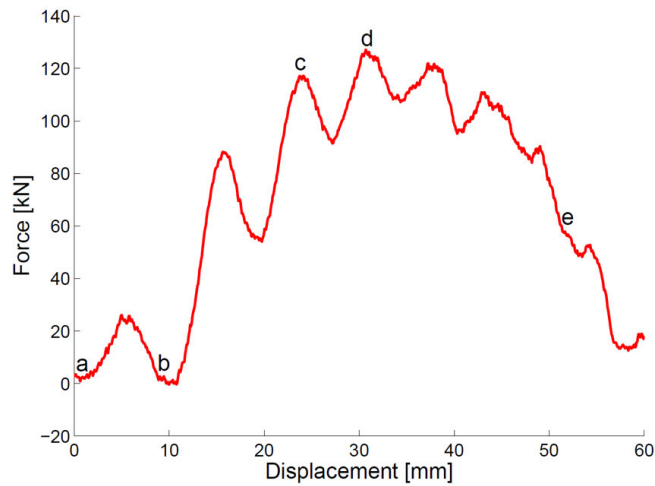
(b) Force-displacement for first global peak in test 1. Points of interest marked

Figure 8.16: Force-time histories of all tests (left) and force vs. trolley displacement (right) for the first large load peak.

(a)   (b)   (c)   (d)   (e)
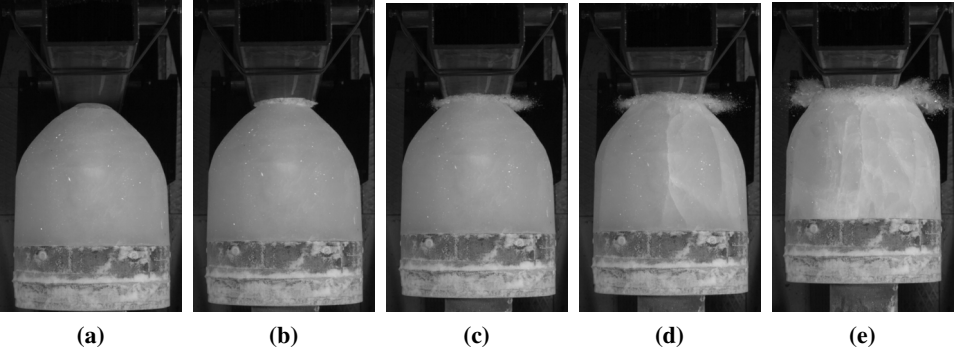
Figure 8.17: Deformation pattern at marked points in Figure 8.16b for impact 1.
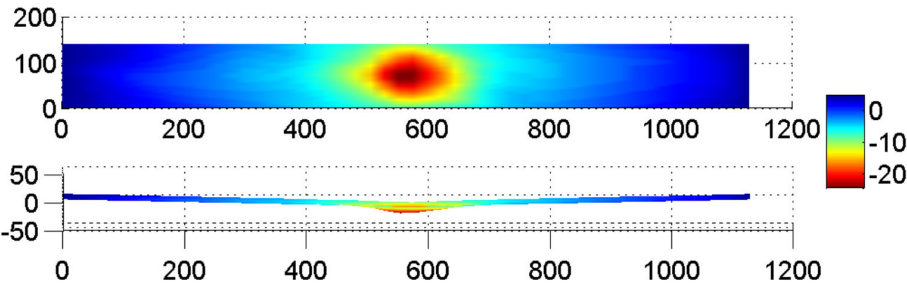
Figure 8.18: Deformation of steel beam from impact 1. Values in [mm].
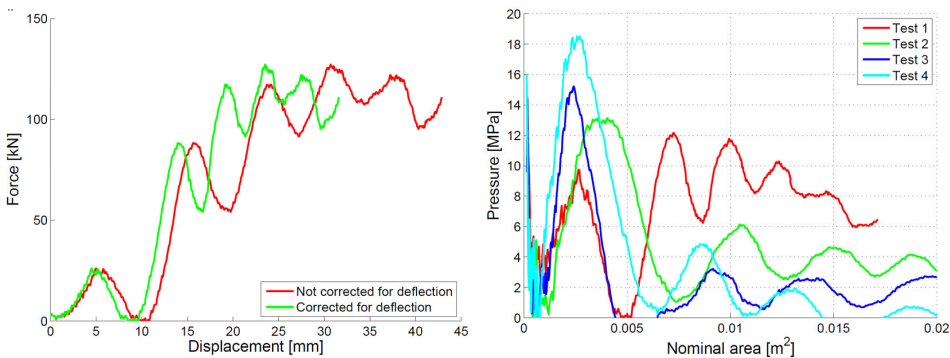
(a) Force-displacement relation corrected for beam deflection for impact test 1

(b) Process pressure-area plot for the first 50 mm displacement for all impact tests

Figure 8.19: Force-displacement and pressure-area plots. Note that the area for impact 2 -4 is not corrected for the beam deflection.

A section of damaged ice was extracted from the contact zone of the secondary force peak in impact 1, and shaved into a thin-section (Figure 8.20) using a microtome. A compacted crushed layer of ice was present in the top layer, extending about 25 mm into the ice. Inwards of this, the crystal structure is similar to the intact ice in Figure 8.13.
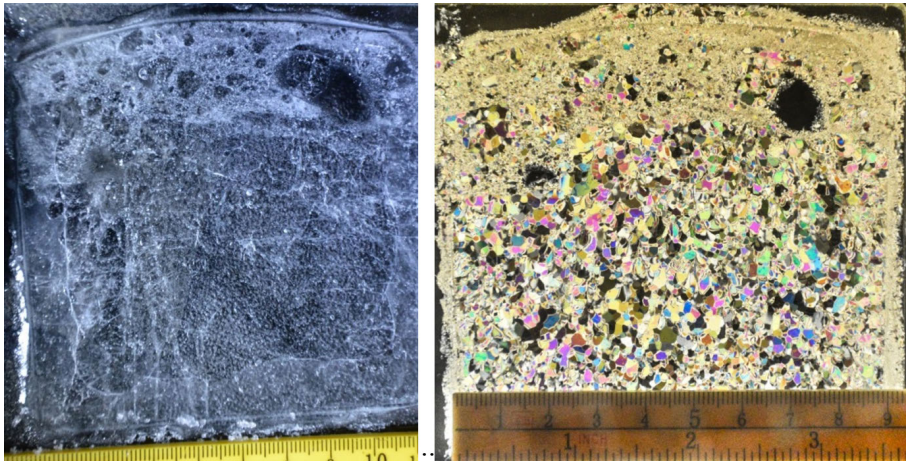
Figure 8.20: Thin-section of damaged section of ice under side-light (left) and cross-polarized light (right).

8.2.7 Capacity Evaluation of the Impacted Beam

The elastic moment capacity of the beam was 160 kN for test 1, i.e. well above the obtained force. Thus, the global deformation was due to local damage at the contact point causing contractions on one side of the beam. To better understand the experimental results, the beam response was investigated through finite element analysis. The beam was modelled on simple supports using shell elements with a refined mesh. Power law hardening without strain-rate effects was adopted.

The shape of the ice indenter was represented by rigid solid elements based on Figure 8.12. Integrated simulations was not performed, as the pilot study did not involve sufficient triaxial material tests to characterize the behavior of the manufactured ice.

The ice indenter was subjected to the transient load history measured in impact test 1, applied to the aft of the ice sample. The applied load and the simulated indentation are shown in Figure 8.21a. The local indentation into the beam flange matches the experimental deformation in Figure 8.18 closely, while the global deflection is somewhat underestimated.

Comparing the applied force vs. indentation, it is also clear that impact tests no. 2-4, in which the ice failed globally at less than 75 kN, caused no significant permanent damage to the beam in the experiments. Further, as the failure mode was local indentation to the beam flange which then caused global deformation of the beam, extending the beam span from 700 mm in test 1 to 900 and 800 mm in tests 2-4 reduced the strength of the beam, thereby giving smaller local damage.
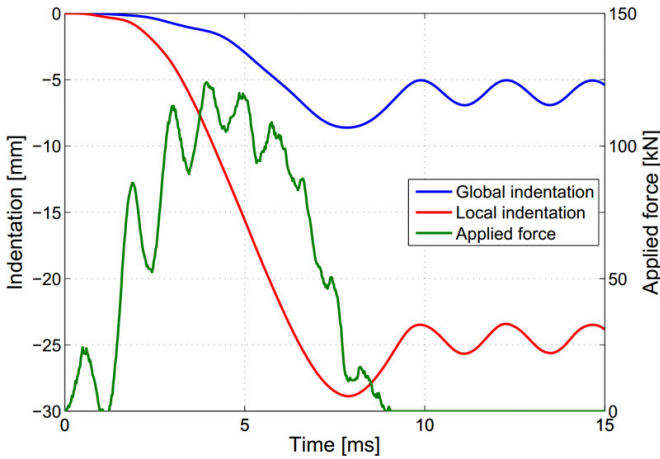
(a) Applied load and simulated global and local indentations to the beam for test 1.
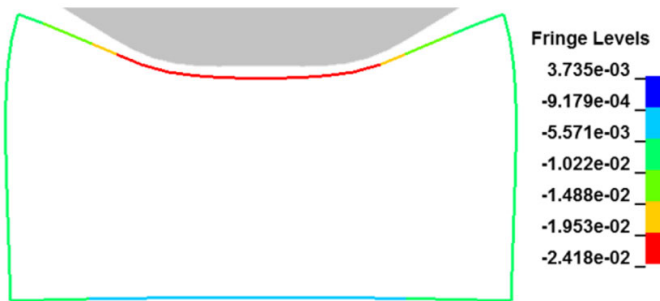
(b) Deformation of beam in numerical simulation at the point of maximum plastic damage. Fringes are in [mm].

Figure 8.21: Results of numerical evaluation of beam strength.

Figure 8.21b shows a cross-section of the beam response to the collision load at the point at which the indentation into the beam match the permanent damage as in Figure 8.18. As the beam wraps around the ice tip it confines the ice locally, thereby increasing its crushing strength even for small levels of indentation. Further experimental data are needed to assess at what level of indentation the

coupled effect becomes important, which was not feasible within the scope of the pilot study.

Amplified force fluctuations were observed in the beam simulations at the simply supported boundary. Thus, the simple numerical simulation supports that the force oscillations with a period of around 1 ms observed in all the impact tests was due to the coupled ice crushing and the beam vibration (both local flange and global beam). After the applied load signal, the beam vibrates freely with a period of 2.35 ms, close to the first natural vibration mode. Further studies are needed to investigate the coupled vibrational response, and refined measurements should be employed in future experiments if the natural frequency of the impacted structure is not increased significantly.

8.2.8   Discussion

Experiments on coupled ice-structure interaction with freshwater granular ice in the brittle ice regime were successfully conducted. Permanent damage of both the ice and the steel structure was obtained, and the experimental setup and procedure were found to be suitable for further studies of the coupled ice-structure behavior. The high sampling rates of both the forces and high-speed video proved very useful for observations of the ice response. For example, a crack propagating through the specimen took between two to four video frames, thereby having a propagation speed between 1500 and 3000 m/s.

Comparing the obtained pressure-area relationships with data from literature shows that the ice behavior is in line with previous measurements of crushing of freshwater ice, see Figure 8.22. Ulan-Kvitberg et al. (2011) investigated the effect of constrained and unconstrained ice cones (thereby different levels of local confinement of the ice) on ice with a "high degree of variability in grain orientation". The constrained samples had a conical shape extending outside from a confining metal cylinder. The unconstrained samples had a cylindrical extension of ice outwards of the confining cylinder before the conically shaped section. The unconstrained samples thus resembled the ice shapes in this study (Figure 8.12) which also has a cylindrical extension between the shaped tip and the confining cylinder. The results of the present study in test 1 are in line with the values from the constrained tests, indicating that the level of confinement from the deforming steel beam was sufficient to increase the crushing strength of the ice significantly. For tests 2-4, the steel beam did not provide increased confinement and the trend of decreasing pressure vs. area matches that of the unconstrained tests by Ulan-Kvitberg et al.

The present experiments give pressures in the same range as other experiments with actual glacial ice, as the Pond Inlet experiments with a 0.1 m^2 spherical in-

denter into an ice wall from Masterson et al. (1993). The impacts from the double pendulum swing in Oldford et al. (2014) are in the same pressure range, but for lower areas. Note that the impact velocity varies significantly between the reported experiments, with 100 mm/s in Ulan-Kvitberg et al. and the Pond Inlet tests, 2.3-4.7 m/s in Oldford et al. and 8 m/s in the present study.
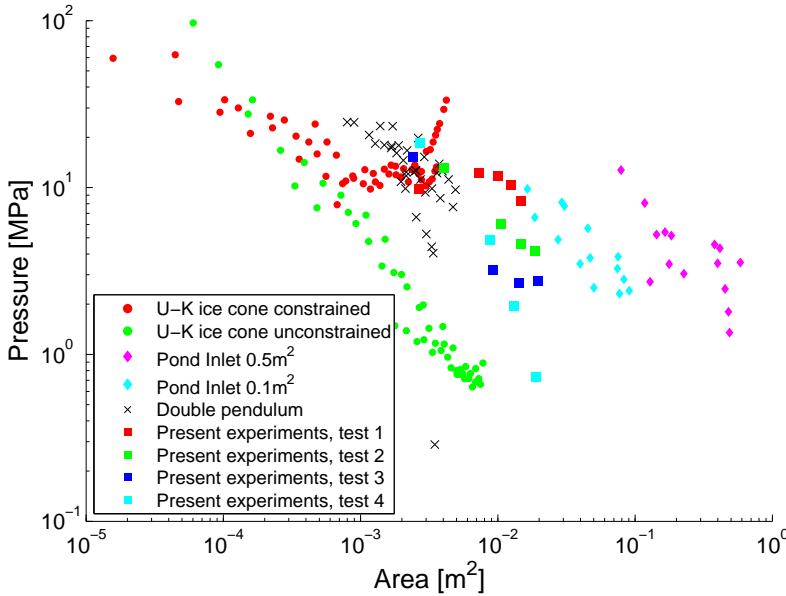
Figure 8.22: Process pressure-area from impact test 1 compared with data from Pond Inlet-tests (Masterson et al. 1993), constrained and unconstrained ice cones (Ulan-Kvitberg et al. 2011) and medium scale impact tests in a double pendulum swing (Oldford et al. 2014). The pressures represent peaks in force-displacement relation, thus giving multiple points pr. experiment.

Plastic damage to the beam was only observed for impact test 1. This was likely due to a combination of two factors. Firstly, the pre-existing circumferential crack allowed for a larger contact area to be established prior to global failure of the ice. This could also have been achieved with a flat tip of the ice specimen. Secondly, when the beam flange deformed, its confining effect increased the crushing strength of the ice, thereby causing even larger damage to the beam. This emphasizes that the transition between a near rigid structure and large inelastic deformations (strength design vs. shared energy design) is very narrow, and small changes in the collision scenario may significantly change the outcome in terms of structural deformation, similar to ship-ship collisions.

Further investigations of this coupled effect are vital to improve the understanding

of ice in a realistic impact scenario, and to establish additional requirements to limit catastrophic damage on vessels with design loads with high probabilities (less than 100 year return period).

8.2.9 Lessons Learned

Compared to the first shared-energy ice collision campaign, the test setup used at the SIMLab facilities greatly improved the control of the impact and the quality of the measurements. Though only a few tests were performed, the results highlight the importance of the coupled behavior of ice and structure, especially how the changing steel geometry during an impact with damage in turn increases the crushing strength of the ice due to the created confinement.

Further research is needed to fully understand the interaction effects and validate material models capable of simulating this behavior. With better knowledge, it is possible to prevent catastrophic damage to ships that are not designed to withstand the loads from ALS level ice impact events, such as the commonly used lighter ice classes.

The quality of the data can be further enhanced by improvements to the experimental setup :

- Obtaining better control of the shape of the ice specimen by a shaping apparatus
- Use a flatter tip of the ice specimens to get a larger load transferred prior to global ice failure
- Perform ice impacts to a "rigid" beam to study the ice without structural interaction
- Quantify the mechanical and physical properties of the tested ice, and compare them with full-scale glacial ice data
- Investigate different shapes to see how this affects the pressure-area relation (will a given shape be crushed or cause structural damage?)
- Investigate impacts with similar ice and structure at different velocities (while maintaining the same level of kinetic energy)
- Investigate the effect of ice temperature on the impact response

Further, the measurements could be improved by :

- Measuring the obtained shape in a more robust manner
- Providing direct measurement by high-speed laser on the structural deformation
- Measure forces also at the beam supports (in addition to trolley interface)
- Investigating the dynamic response of the measurement system

- Apply visual trackers on the beam and ice for digital image correlation (DIC) measurements of motions and strains through high-speed video
- If possible, utilize a spatial measurement system to investigate the crushing pressures distributed over the contact zone.

With these modifications, the test setup gives the opportunity to study the ice-structure interaction in an efficient and controlled manner.

8.3   Conclusion of Experimental Studies

Two experimental campaigns were carried out to study shared-energy ice-structure interaction and the effect of increased local confinement due to structural deformation. Both aspects are highly relevant for full-scale ice encounters with damage to the ship, and both aspects are yet to be properly understood by the research community. These experiments represents the first of its kind to provide data from shared-energy ice-structure collisions at realistic indentation velocities.

The experiments have gained new insight, and paved the way for further studies that better can quantify these aspects and contribute to increased understanding of the behavior of granular ice in general and specifically in a collision scenario. This can prove important in future revisions of rules, in which damage to the vessels can be both expected and allowed provided that the impact event does not develop into a scenario disproportionate its original cause.

With the experimental setup and suggested improvements, an effective test bench was established to study the ice-structure interaction in an efficient manner.

Chapter 9

Conclusions and Suggestions for Future Work

9.1 Conclusion

Collision events may have severe consequences, and it is important to design both ships and offshore structures so that they have sufficient resistance to such events. The main purpose of this Thesis work is to improve the methods for description of the material behavior in NLFEA, and to study the physics of the collision process through numerical simulations of both experiments and full-scale scenarios.

9.1.1 Steel Material Behavior

The steel material behavior controls the outcome of the collision event. The effect of the shape of the stress-strain curve was investigated, and found to have a large influence of the predicted outcome of a collision event. The slope of the curve, especially in the initial phase of straining, is important as this controls how strains spread out or localize.

Strain-rate hardening was identified as challenging with shell elements. The accuracy of the simulation was found to be better if strain-rate effects were disregarded compared to if they were included in a simplified manner. If strain-rate hardening is used with shell elements, the dynamic fracture strain should be set to less than the diffuse necking strain to avoid erroneous fracture prediction, unless the stabilizing effect of strain-rate hardening on the necking process is accounted for in the prediction of the true dynamic fracture strain limit.

Both nominal rule values and statistical distributions of material parameters were

investigated. The *design material* concept was introduced as a method to ensure that the materials representing load and resistance are given appropriate safety factors. A realistic shape of the stress-strain curve is required, both for upper and lower bound material strength (for the striking and struck ship respectively).

A new way of separating two different mesh scale effects termed *geometric* and *material* mesh dependence was proposed. The geometric mesh dependence accounts for strain concentrations not properly captured by the mesh prior to diffuse necking (a strain concentration factor relative to element discretization). The material mesh dependence accounts for the localization of strains after necking (as the length of the local neck is related to the plate thickness, whereas the simulated local neck occur over one element length). Both mesh scale effects should be addressed in a robust fracture criterion.

9.1.2   Fracture in Steel Structures

The micromechanical process of fracture was related to the macromechanical process that can be captured with coarse shell elements. Many of the commonly used fracture criteria were implemented in LS-DYNA and a large simulation program was conducted. The various fracture criteria were tested against several types of experiments, each simulated with different mesh sizes. The simulation results were normalized to their experimental equivalent, and the overall robustness of each fracture criterion with varying strain-state and mesh size was investigated. Strain-state dependent fracture criteria gave the best estimates of first fracture of the shell plating (low-energy impacts), whereas simpler strain-state independent criteria were sufficient for large-scale fracture and damage (high-energy impacts).

An extension of the BWH criterion has been developed in which post-necking effects are included. A virtual neck is assumed to form after the onset of local instability, with initial length equal to the plate thickness. This resulted in a damage model that was coupled to the element response in the post-necking phase, thereby allowing for treatment of local necking in larger shell elements. Material tests show that the post-necking ductility varies with the strain state. A pragmatic erosion criterion was developed, dependent on both the strain state and the virtual necking damage. The combined extension of the BWH criterion with damage and erosion gave increased robustness of fracture prediction with changing structural layout, strain state and mesh size. The fracture path converges to experimental results with decreasing mesh size.

9.1.3   Full-scale Numerical Simulations

NLFEA was used as virtual experiments to study the full-scale behavior of the collision process of supply vessels impacting stiffened panel structures (such as semi-

sub platforms) and jacket structures. Based on the simulations, a new pressure-area relation was established for pressures sufficient to initiate crushing of a modern supply vessel with a bulbous bow. If the structure can resist these loads, the striking supply vessel will crush and dissipate the majority of the energy in a collision event.

A simplified calculation model was developed for strength-design of stiffened panels, combining a roof-top yield-line mechanism with the stiffener shear capacity in an incremental approach. The relation between load vs. indentation vs. extension of the indented zone compared well between the method and integrated NLFEA simulations.

A refined method for strength-design of jacket legs and braces was proposed. If the brace/leg complies with a local strength requirements ($R_c \geq \eta$), a collision will cause limited local denting to the brace/leg and the striking vessel dissipates most of the energy. This distributes the load over a larger region, in turn increasing the capacity of the jacket to further deformation.

9.1.4   Collisions with Ice Masses

Challenges related to simulation of ice collision events were discussed, especially the material behavior of ice during fast compressive loading. For NLFEA simulations of abnormal ice events, it is extremely challenging to define a robust continuum mechanics material representation of ice, both due to the large variability in ice properties observed from experimental testing and due to the limited knowledge of the actual processes causing the mechanical ice response.

The link between the crushing load and the local confinement of the ice was identified as particularly challenging. During a collision where the ship sustains substantial damage, the changed geometry of the ship side will increase the confinement of the ice, thereby increasing its crushing pressure. Confinement effects are reported to some extent in literature, but few experiments have investigated this coupled deformation process, and it is disregarded in current rules and standards.

Two experimental campaigns have been performed to study the coupled deformation process as both ice and structure deforms. Such tests were found to be complex, and it was difficult to achieve mutual damage to ice and structure. The second experimental campaign was successful in achieving both coupled and non-coupled response. It was observed that the load exerted from the ice increased significantly when the structure was deforming plastically, indicating that the coupled effect is strong and should be included in revised rules.

9.2   Further Work

The doctoral work leaves many questions unanswered. Some of the points that should be further studied are listed below:

Material modeling and fracture of steel :

- A robust approach to determine *design material* parameters should be defined, based on material statistics and a total probability of exceedance (similar to 5% and 95% percentiles adopted in NORSOK N-001). The shape of the stress-strain curve used for NLFEA should be realistic, both for upper and lower bound material strength.
- Geometric mesh scaling should be studied in more detail. Large variations were observed when simulating fracture experiments in the strain concentrations not captured in a coarse mesh with varying structural configuration, shape of indenter etc. Could the geometric mesh-scaling be defined as a function of strain state?
- Many of the common fracture criteria significantly overestimate the capacity of the struck structure. Appropriate safety factors for design rules should be determined to ensure conservative results.
- The thesis work has focused on steel materials. Other materials, such as aluminum, should also be investigated in a similar manner.

Collision simulations :

- The numerical studies covers only a few actual designs. Further studies of the crushing characteristics of e.g. other vessels bows should be performed.
- The combination of stiffener shear and roof-top membrane capacity seems like a viable option for assessing the resistance and expected damage to stiffened panels with moderate indentations. Further development and verification of the method is encouraged.
- The capacity of jacket structures against ship impacts at the midspan of legs and braces was investigated. Further studies of the deformation mechanisms and possible measures for strength design of brace/leg intersections should be conducted. Can the requirement of $R_c > \eta$ to avoid local crushing of the brace/leg be applied also for intersections?
- The influence of external mechanics on the collision response should be further studied in an integrated manner. How does e.g. the vessel roll affect the damage to a jacket leg during sideways impact?

Ice-structure collisions :

- Further experiments to study the coupled ice-structure interaction should be performed in the pendulum accelerator test rig. This should include a thorough set of material tests to calibrate the material parameters to the ice behavior.
- Numerical investigations of the impact experiments should be performed.
- The effect of the local ice shape on the structural damage should be investigated, ideally through a combination of experimental and numerical testing.
- Design rules should be updated to include the effect of coupling between ice and structure during mutual deformation. This would in effect increase the accidental ice pressures defined for low ice class vessels.

References

ABAQUS. *ABAQUS/Standard 6.12 user's manual*. Dassault Systèmes, Providence, RI, USA., 2012.

Accident Investigation Board Norway. Report on Marine Accident MV FULL CITY grounding at Såstein 31. July 2009. Report, Report Sjø 2013/08, Lillestrøm, Norway, 2013.

Alsos, H. S. *Analysis of Ductile Fracture, Bottom Damage and Hull Girder Response*. Phd, NTNU, 2008.

Alsos, H. S. and Amdahl, J. On the resistance to penetration of stiffened plates, Part I : Experiments. *International Journal of Impact Engineering*, 36(6):799–807, 2009.

Alsos, H. S., Hopperstad, O. S., Törnqvist, R., and Amdahl, J. Analytical and numerical analysis of sheet metal instability using a stress based criterion. *International Journal of Solids and Structures*, 45(78):2042–2055, 2008.

Alsos, H. S., Amdahl, J., and Hopperstad, O. S. On the resistance to penetration of stiffened plates, Part II: Numerical analysis. *International Journal of Impact Engineering*, 36(7):875–887, 2009.

Altmeyer, G. Theoretical and numerical comparison of Limit Point Bifurcation and Maximum Force criteria. Application to the prediction of diffuse necking. 2013.

Alves, M. and Jones, N. Influence of hydrostatic stress on failure of axisymmetric notched specimens. *Journal of the Mechanics and Physics of Solids*, 47(3): 643–667, 1999.

Amdahl, J. Impact Capacity of Steel Platforms and Tests on Large Deformations on Tubes under Transverse Loading. Technical report, Det Norske Veritas, Progress Report No. 10 on Impacts and Collisions Offshore, Report No. 80-0036, Høvik, Norway, 1980.

Amdahl, J. *Energy absorption in ship-platform impacts*. PhD thesis, Department of Marine Technology, NTH, 1983.

Anderson, D., Winkler, S., Bardelcik, A., and Worswick, M. J. Influence of stress triaxiality and strain rate on the failure behavior of a dual-phase DP780 steel. *Materials and Design*, 60(0):198–207, 2014.

Aretz, H. Numerical analysis of diffuse and localized necking in orthotropic sheet metals. *International Journal of Plasticity*, 23(5):798–840, 2007.

Arunachalam, V. M., Murray, J. J., and Muggeridge, D. B. Short term motion analysis of icebergs in linear waves. *Cold Regions Science and Technology*, 13 (3):247–258, 1987.

Bai, Y. and Wierzbicki, T. A new model of metal plasticity and fracture with pressure and Lode dependence. *International Journal of Plasticity*, 24(6):1071 – 1096, 2008. ISSN 0749-6419.

Bai, Y. and Wierzbicki, T. Application of extended Mohr–Coulomb criterion to ductile fracture. *International Journal of Fracture*, 161(1):1–20, 2010. ISSN 0376-9429. doi: 10.1007/s10704-009-9422-8.

Bala, S. and Day, J. General guidelines for crash analysis in LS-DYNA. *Livermore Software Technology Corporation*, 2012.

Barba, M. Resistance a la traction et allongements des meteaux apres rupture. *Memoires de la Societe des ingenieurs civils de France, Part I*, page 682, 1880.

Barrette, P. D. and Jordaan, I. J. Beam bending and fracture behaviour of iceberg ice. Technical report, National Research Council Canada; NRC Canadian Hydraulics Centre. PERD/CHC Report 4-78, 2001.

Bazant, Z. P. and Xiang, Y. Size effect in compression fracture: splitting crack band propagation. *Journal of Engineering Mechanics*, 123(2):162–172, 1997.

Billingham, J., Sharp, J. V., Spurrier, J., and Kilgallon, P. J. *Research Report 105 : Review of the performance of high strength steels used offshore*. Health and Safety Executive, Bedfordshire, UK, 2003.

Bressan, J. D. and Williams, J. A. The use of a shear instability criterion to predict local necking in sheet metal deformation. *International Journal of Mechanical Sciences*, 25(3):155–168, 1983.

Broekhuijsen, J. *Ductile failure and energy absorption of Y-shape test section*. Master thesis, Delft University of Technology, 2003.

Brown, A. J. Collision scenarios and probabilistic collision damage. *Marine Structures*, 15(4):335–364, 2002.

Bundesstelle für Seeundfalluntersuchung. Collision between the ro-pax ferry NILS HOLGERSSON and the ro-pax ferry URD in the port of Lübeck-Travemünde on 3 May 2012. Report, Investigation Report 154/12, Federal Bureau of Maritime Casualty Investigation, Germany, 2012.

Canadian Coast Guard. *Ice Navigation in Canadian Waters*. Icebreaking Program, Maritime Services, Canadian Coast Guard, Ottawa, Canada, revised august 2012 edition, 2012.

Choung, J., Cho, S.-R., and Kim, K. S. Impact test simulations of stiffened plates using the micromechanical porous plasticity model. *Ocean Engineering*, 37 (8–9):749 – 756, 2010. ISSN 0029-8018. doi: 10.1016/j.oceaneng.2010.02.015.

Choung, J., Shim, C.-S., and Song, H.-C. Estimation of failure strain of EH36 high strength marine structural steel using average stress triaxiality. *Marine Structures*, 29(1):1–21, 2012.

Choung, J., Nam, W., and Lee, J.-Y. Dynamic hardening behaviors of various marine structural steels considering dependencies on strain rate and temperature. *Marine Structures*, 32:49–67, 2013. doi: 10.1016/j.marstruc.2013.02.001.

Cockcroft, M. and Latham, D. Ductility and the workability of metals. *Journal of the Institute of Metals*, 96:33–39, 1968.

Colla, V., De Sanctis, M., Dimatteo, A., Lovicu, G., Solina, A., and Valentini, R. Strain hardening behavior of dual-phase steels. *Metallurgical and Materials Transactions A*, 40(11):2557–2567, 2009.

Countryman and McDaniel. 2003 Nightmare: T-boned, 2003. URL http://www.cargolaw.com/2003nightmare_t-bone.html. [Online; accessed 27-March-2015].

Cowper, J. and Symonds, P. Strain-hardening and strain-rate effects in the impact loading of cantilever beams. technical report no. 28. Report, Contract Nonr-562(10),NR-064-406, Division of Applied Mathematics, Brown University, USA, 1957.

Daley, C. and Kim, H. Ice collision forces considering structural deformation. *ASME Conference Proceedings*, 2010(49125):817–825, 2010.

Daley, C. G. Derivation of plastic framing requirements for polar ships. *Marine Structures*, 15(6):543–559, 2002a.

Daley, C. G. Application of plastic framing requirements for polar ships. *Marine Structures*, 15(6):533–542, 2002b.

Daley, C. G. and Liu, J. Safe speeds for ships in pack ice. volume 118 of *Transactions - Society of Naval Architects and Marine Engineers*, pages 94–102, 601 Pavonia Avenue, Jersey City, NJ 07306, United States, 2010. Society of Naval Architects and Marine Engineers.

de Borst, R. Chapter 10 : Damage, material instabilites, and failure. In Stein, E., Borst, R. d., and Hughes, T. J., editors, *Encyclopedia of Computational Mechanics*, volume Volume 2 : Solids and Structures, pages 335–373. 2004.

de Jonge, T. and Laukeland, L. Collision between a spar tanker and a platform.

6th International Conference on Collision and Grounding of Ships and Offshore Structures, ICCGS 2013, pages 267–280, Trondheim, 2013.

Dempsey, J., Adamson, R., and Mulmule, S. Scale effects on the in-situ tensile strength and fracture of ice. Part II: First-year sea ice at Resolute, NWT. *International journal of fracture*, 95(1-4):347–366, 1999.

Det Norske Veritas. Rules for Classification of Ships, Part 5 Chapter 1 : Ships for Navigation in Ice, July 2011.

Det Norske Veritas. DNV-OS-B101 : Metallic Materials, 2009.

Det Norske Veritas. DNV-RP-C204 : Design Against Accidental Loads, 2010.

Det Norske Veritas. DNV-OSS-201 : Verification for Compliance with Norwegian Shelf Regulations, 2013a.

Det Norske Veritas. DNV-RP-C208 : Determination of Structural Capacity by Non-linear FE Analysis Methods, 2013b.

Ehlers, S. Strain and stress relation until fracture for finite element simulations of a thin circular plate. *Thin-Walled Structures*, 48(1):1–8, 2010a.

Ehlers, S. The influence of the material relation on the accuracy of collision simulations. *Marine Structures*, 23(4):462–474, 2010b.

Ehlers, S. and Varsta, P. Strain and stress relation for non-linear finite element simulations. *Thin-Walled Structures*, 47(11):1203–1217, 2009.

Ehlers, S., Broekhuijsen, J., Alsos, H. S., Biehl, F., and Tabri, K. Simulating the collision response of ship side structures: A failure criteria benchmark study. *International Shipbuilding Progress*, 55(1-2):127–144, 2008.

Ehlers, S., Tabri, K., Romanoff, J., and Varsta, P. Numerical and experimental investigation on the collision resistance of the x-core structure. *Ships and offshore structures*, 7(1):21–29, 2012.

Erhart, T. and Borrvall, T. Drilling rotation constraint for shell elements in implicit and explicit analyses. Technical report, 9th European LS-DYNA Conference 2013, 2013.

EURONCAP. Ncap test procedures : The tests explained, Cited Dec. 10. 2013. URL http://www.euroncap.com/testprocedures.aspx.

Fricke, W., Schöttelndreyer, M., and Tautz, I. *Validierung von Kollisionsberechnungen durch Großversuche an Konstruktionsvarianten von Seitenhüllen*. Technische Universität Hamburg-Harburg, Hamburg, Germany, 2014. ISBN 978-3-89220-676-7.

Fuglem, M., Jordaan, I., and Crocker, G. Iceberg-structure interaction probabilities for design. *Canadian Journal of Civil Engineering*, 23(1):231–241, 1996.

Fuglem, M., Muggeridge, K., and Jordaan, I. Design load calculations for iceberg impacts. *International Journal of Offshore and Polar Engineering*, 9(4), 1999.

Fylling, I. J. Accidental collisions for offshore platforms - influence from wave-induced motions of drifting ships. *International Conference of Ship and Marine Research - NAV'94*, 1994.

Gagnon, R. and Derradji-Aouat, A. First results of numerical simulations of bergy bit collisions with the ccgs terry fox icebreaker. *The 18th IAHR International Symposium on Ice*, pages 9–16, 2006.

Gagnon, R. and Gammon, P. Characterization and flexural strength of iceberg and glacier ice. *Journal of Glaciology*, 41(137):103–111, 1995a.

Gagnon, R., Cumming, D., Ritch, R., Browne, R., Johnston, M., Frederking, R., McKenna, R., and Ralph, F. Overview accompaniment for papers on the bergy bit impact trials. *Cold Regions Science and Technology*, 52(1):1–6, 2008.

Gagnon, R., Daley, C., and Colbourne, B. A large double-pendulum device to study load, pressure distribution and structure damage during ice impact tests in the lab. In *Proceedings of the International Conference on Port and Ocean Engineering Under Arctic Conditions*, 2015.

Gagnon, R. E. Results of numerical simulations of growler impact tests. *Cold Regions Science and Technology*, 49(3):206–214, 2007.

Gagnon, R. E. A numerical model of ice crushing using a foam analogue. *Cold Regions Science and Technology*, 65(3):335–350, 2011.

Gagnon, R. E. and Gammon, P. H. Triaxial experiments on iceberg and glacier ice. *Journal of Glaciology*, 41(139):528–540, 1995b.

Gagnon, R. E. and Gammon, P. H. In situ thermal profiles and laboratory impact experiments on iceberg ice. *Journal of Glaciology*, 43(145):569–582, 1997.

Gao, X., Zhang, G., and Roe, C. A study on the effect of the stress state on ductile fracture. *International Journal of Damage Mechanics*, 19:75–94, 2009.

Gao, Y., Hu, Z., Ringsberg, J. W., and Wang, J. An elastic–plastic ice material model for ship-iceberg collision simulations. *Ocean Engineering*, 102:27–39, 2015.

Garrison Jr, W. and Moody, N. Ductile fracture. *Journal of Physics and Chemistry of Solids*, 48(11):1035 – 1074, 1987. doi: 10.1016/0022-3697(87)90118-1.

Goodwin, G. M. Application of strain analysis to sheet metal forming problems in the press shop. *La Metallurgia Italiana*, 8, 1968.

Gruben, G., Hopperstad, O., and Børvik, T. Evaluation of uncoupled ductile fracture criteria for the dual-phase steel Docol 600DL. *International Journal of Mechanical Sciences*, 62(1):133–146, 2012.

Gruben, G., Hopperstad, O., and Børvik, T. Simulation of ductile crack propagation in dual-phase steel. *International Journal of Fracture*, 180(1):1–22, 2013a.

Gruben, G., Vysochinskiy, D., Coudert, T., Reyes, A., and Lademo, O.-G. De-

termination of Ductile Fracture Parameters of a Dual-Phase Steel by Optical Measurements. *Strain*, 49(3):221–232, 2013b.

Gudimetla, S., Colbourne, B., Daley, C., Bruneau, S., and Gagnon, R. Strength and pressure profiles from conical ice crushing experiments. In *International Conference and Exhibition on Performance of Ships and Structures in Ice, ICETECH12, September*, pages 17–20, 2012.

Guo, W.-G. and Gao, X. On the constitutive modeling of a structural steel over a range of strain rates and temperatures. *Materials Science and Engineering: A*, 561(0):468–476, 2013.

Gurson, A. L. Continuum theory of ductile rupture by void nucleation and growth: Part I—Yield criteria and flow rules for porous ductile media. *Journal of engineering materials and technology*, 99(1):2–15, 1977.

Habib, K. B., Taylor, R. S., Jordaan, I. J., and Bruneau, S. Experimental Investigation of Compressive Failure of Truncated Conical Ice Specimens. In *ASME 2014 33rd International Conference on Ocean, Offshore and Arctic Engineering*, 2014.

Hallquist, J. O. LS-DYNA theory manual. *Livermore Software Technology Corporation*, 3, 2006.

Hänninen, S. Incidents and accidents in winter navigation in the baltic sea, Winter 2002 - 2003. Technical report, Winter Navigation Research Board, Research Report No. 54, 2005.

Hanssen, A., Auestad, T., Tryland, T., and Langseth, M. The kicking machine: A device for impact testing of structural components. *International Journal of Crashworthiness*, 8(4):385–392, 2003.

Haufe, A., Schweizerhof, K., and DuBois, P. Properties & Limits: Review of Shell Element Formulations. *Livermore Software Technology Corporation*, 2013.

Hill, R. On discontinuous plastic states, with special reference to localized necking in thin sheets. *Journal of the Mechanics and Physics of Solids*, 1(1):19–30, 1952.

Hillerborg, A., Modéer, M., and Petersson, P.-E. Analysis of crack formation and crack growth in concrete by means of fracture mechanics and finite elements. *Cement and concrete research*, 6(6):773–781, 1976.

Hogström, P., Ringsberg, J. W., and Johnson, E. An experimental and numerical study of the effects of length scale and strain state on the necking and fracture behaviours in sheet metals. *International Journal of Impact Engineering*, 36 (10-11):1194–1203, 2009.

Hogström, P. and Ringsberg, J. W. An extensive study of a ship's survivability after collision–A parameter study of material characteristics, non-linear FEA and damage stability analyses. *Marine Structures*, 27(1):1–28, 2012.

Hong, L. *Simplified analysis and design of ships subjected to collision and grounding*. PhD Thesis, 2008.

Hong, L. and Amdahl, J. Crushing resistance of web girders in ship collision and grounding. *Marine Structures*, 21(4):374–401, 2008.

Hong, L., Amdahl, J., and Wang, G. A direct design procedure for fpso side structures against large impact loads. *Journal of Offshore Mechanics and Arctic Engineering*, 131(3), 2009.

Hosford, W. F. and Caddell, R. M. *Metal forming : mechanics and metallurgy*. Englewood Cliffs, N.J. : Prentice-Hall, 1983. ISBN 0-13-577700-3, 0-13-577214-1.

IACS-UR-I. Unified Requirements Polar Class, International Association of Classification Societies, 2011.

International Maritime Organization. *SOLAS: consolidated text of the International Convention for the Safety of Life at Sea, 1974, and its Protocol of 1988 : articles, annexe- s and certificates : incorporating all amendments in effect from 1 July 2014*. International Convention for the Safety of Life at Sea, London, 2014. ISBN 978-92-801-1594-9. Consolidated ed. 2014, 6th ed.

International Maritime Organization. GISIS: Marine Casualties and Incidents, Cited 05. May 2015. URL https://gisis.imo.org/Public/MCI/Default.aspx.

ISO-19902. ISO-19902:2007 Petroleum and natural gas industries – Fixed steel offshore structures, 2007.

ISO-19906. ISO-19906:2010 Petroleum and natural gas industries – Arctic offshore structures, 2010.

Jernkvist, L. O., Massih, A. R., and Rudling, P. A strain-based clad failure criterion for reactivity initiated accidents in light water reactors. Technical report, Swedish Nuclear Power Inspectorate, Stockholm (Sweden), 2004.

Johnson, G. R. and Cook, W. H. A constitutive model and data for metals subjected to large strains, high strain rates and high temperatures. In *Proceedings of the 7th International Symposium on Ballistics*, volume 21, pages 541–547. The Netherlands, 1983.

Jones, N. A theoretical study of the dynamic plastic behavior of beams and plates with finite-deflections. *International Journal of Solids and Structures*, 7(8): 1007–1029, 1971.

Jones, N. On the dynamic inelastic failure of beams. In *Structural Failure*, chapter 5, pages 133–159. Wiley, New York, 1989a.

Jones, N. Some comments on the modelling of material properties for dynamic structural plasticity. In *Proceedings of the International Conference on the*

Mechanical Properties of Materials at High Rates of Strain,Oxford. Institute of Physics Conference Series No. 102., pages 435–445, 1989b.

Jones, N. Some recent developments in the dynamic inelastic behaviour of structures. *Ships and Offshore Structures*, 1(1):37–44, 2006.

Jones, N. *Structural Impact, 2nd Edition*. Cambridge University Press, New York, USA, 2012. ISBN 9781107010963.

Jones, N. The credibility of predictions for structural designs subjected to large dynamic loadings causing inelastic behaviour. *International Journal of Impact Engineering*, 53:106–114, 2013.

Jordaan, I. J. and Timco, G. W. Dynamics of the ice-crushing process. *Journal of Glaciology*, 34:318–326, 1988.

Jordaan, I. J., Stone, B. M., McKenna, R. F., and Fuglem, M. K. Effect of microcracking on the deformation of ice. *Canadian Geotechnical Journal*, 29(1): 143–150, 1992.

Jordaan, I. J., Matskevitch, D. G., and Meglis, I. L. Disintegration of ice under fast compressive loading. *International Journal of Fracture*, 97:279–300, 1999.

Karlsson, U. B., Ringsberg, J. W., Johnson, E., Hoseini, M., and Ulfvarson, A. Experimental and numerical investigation of bulb impact with a ship side-shell structure. *Marine Technology*, 46(1):16–26, 2009.

Keeler, S. and Backhofen, W. Plastic instability and fracture in sheet stretched over rigid punches. *ASM Transactions Quarterly*, 56:25–48, 1964.

Kim, E. *Experimental and numerical studies related to the coupled behavior ofice mass and steel structures during accidental collisions*. PhD Thesis, Doctoral dissertations 2014:135, NTNU, Trondheim, Norway, 2014.

Kim, E. and Schulson, E. M. A phenomenological explanation of the pressure–area relationship for the indentation of ice: Two size effects in spherical indentation experiments. *Cold Regions Science and Technology*, 115:48–55, 2015.

Kim, E., Golding, N., Schulson, E. M., Løset, S., and Renshaw, C. E. Mechanisms governing failure of ice beneath a spherically-shaped indenter. *Cold Regions Science and Technology*, 78(0):46–63, 2012a.

Kim, E., Storheim, M., und Polach, R. v. B., and Amdahl, J. Design and modelling of accidental ship collisions with ice masses at laboratory-scale. In *ASME 2012 31st International Conference on Ocean, Offshore and Arctic Engineering*, pages 495–505, 2012b.

Kim, E., Storheim, M., Amdahl, J., Løset, S., and von Bock und Polach, R. Drop tests of ice blocks on stiffened panels with different structural flexibility. In *Proceedings of the 6th International Conference on Collision and Grounding of Ships and Offshore Structures*, pages 241–250, 2013.

Kim, E., Amdahl, J., Storheim, M., and Løset, S. Understanding the Effect of Assumptions on Shell Plate Thickness for Arctic Ships. In *Proceedings of the International Conference on Port and Ocean Engineering Under Arctic Conditions*, 2015a.

Kim, E., Storheim, M., Amdahl, J., Løset, S., and von Boch und Polach, R. Laboratory experiments on shared-energy collisions between freshwater ice blocks and a floating steel structure. In Review.

Kim, H., Dolny, J., and Daley, C. An experimental study of the design and overload capacity of structural grillages subjected to ice loads. In *Proceedings of the International Conference on Port and Ocean Engineering Under Arctic Conditions*, 2015b.

Kim, W. S., Shin, S. H., Urm, H. S., Hysing, T., Sannes, L., and Che, J. Safety of cargo containment system and support structure in spherical tank type lng carrier under iceberg-ship collision. Technical report, Hyunday Heavy Industries Co., Ltd, Det Norske Veritas AS, Moss Maritime and InnoQual Co., LTd, 2006.

Kivisild, H. Iceberg impact effects on drillships. Technical report, EPOA, Eastcoast Petroleum Operators Association, 1971.

Kõrgesaar, M., Remes, H., and Romanoff, J. Size dependent response of large shell elements under in-plane tensile loading. *International Journal of Solids and Structures*, 51(21):3752–3761, 2014.

Körgesaar, M. and Romanoff, J. Influence of mesh size, stress triaxiality and damage induced softening on ductile fracture of large-scale shell structures. *Journal of Marine Structures*, 38:1–17, 2014.

Körgesaar, M., Tabri, K., Naar, H., and Reinhold, E. Ship collision simulations using different fracture criteria and mesh size. In *Proceedings of the ASME 2014 33rd International Conference on Ocean, Offshore and Arctic Engineering*, 2014.

Kujala, P. and Ehlers, S. Limit State Identification for Ice-Strengthened Hull Structures Using Measured Long-Term Loads. In *Proceedings of the International Conference on Port and Ocean Engineering Under Arctic Conditions*, 2013.

Kvitrud, A. Collisions between platforms and ships in norway in the period 2001-2010. In *ASME 2011 30th International Conference on Ocean, Offshore and Arctic Engineering*, pages 637–641. American Society of Mechanical Engineers, 2011.

Lee, S., Zhao, T., and Nam, J. Structural safety assessment of ship collision and grounding using FSI analysis technique. 6th International Conference on Collision and Grounding of Ships and Offshore Structures, ICCGS 2013, pages 197–204, Trondheim, 2013.

Lee, S.-G., Lee, I., Baek, Y., Nicolas, C., Le Goff, S., and Quenez, J.-M.

Membrane-type lng carrier side collision with iceberg. *Arctic Shipping 2010*, 2010.

Lehmann, E. and Yu, X. Progressive folding of bulbous bows. PRADS 95, 6th Intl Symposium on Practical Design of Ships and Mobile Units; 17-22 Sept 1995, page 1048, Soul, Korea, 1995. ISBN 89-950016-2-3.

Li, M. and Chandra, A. Influence of strain-rate sensitivity on necking and instability in sheet metal forming. *Journal of Materials Processing Technology*, 96 (1–3):133–138, 1999. doi: 10.1016/s0924-0136(99)00321-0.

Li, Y., Luo, M., Gerlach, J., and Wierzbicki, T. Prediction of shear-induced fracture in sheet metal forming. *Journal of Materials Processing Technology*, 210(14): 1858–1869, 2010.

Liu, Z. and Amdahl, J. A new formulation of the impact mechanics of ship collisions and its application to a ship–iceberg collision. *Marine Structures*, 23(3): 360–384, 2010.

Liu, Z., Amdahl, J., and Løset, S. Plasticity based material modelling of ice and its application to ship-iceberg impacts. *Cold Regions Science and Technology*, 65(3):326–334, 2011a.

Liu, Z., Amdahl, J., and Løset, S. Integrated numerical analysis of an iceberg collision with a foreship structure. *Marine Structures*, 24(4):377–395, 2011b.

Lützen, M. *Ship collision damage*. PhD thesis, Technical University of Denmark, Department of Mechanical Engineering, 2001.

Lützen, M., Simonsen, B. C., and Pedersen, P. T. Rapid prediction of damage to struck and striking vessels in a collision event. *Proceedings of Ship Structures for the New Millennium: Supporting Quality in Shipbuilding, Arlington*, 2000.

MacLean, C. G. *Fracture and plasticity characterization of DH-36 Navy steel*. Master thesis, Massachusetts Institute of Technology, 2012.

Maker, B. N. and Zhu, X. Input parameters for metal forming simulation using ls-dyna. *Livermore Software Technology Corporation*, 4:43–46, 2000.

Manuel, M., Gudimelta, P. S. R., Daley, C., and Colbourne, B. Controlled plastic deformation of a grillage using artificial freshwater ice at a large scale. In *Proceedings of the International Conference on Port and Ocean Engineering Under Arctic Conditions*, 2013.

Manuel, M., Colbourne, B., and Daley, C. Ship Structure Subjected to Extreme Ice Loading : Full Scale Laboratory Experiments used to Validate Numerical Analysis. In *Proceedings of the International Conference on Port and Ocean Engineering Under Arctic Conditions*, 2015.

Marchenko, N. Navigation in the Russian Arctic. Sea ice caused difficulties and accidents. *Proceedings of the 32nd International Conference on Ocean, Offshore and Arctic Engineering, OMAE2013*, pages OMAE2013–10546, 2013.

Marchenko, N. Floating Ice Induced Ship Casualties. *The 22nd IAHR International Symposium on Ice*, pages 908–915, 2014.

Marciniak, Z. and Kuczyiski, K. Limit strains in the processes of stretch-forming sheet metal. *International Journal of Mechanical Sciences*, 9(9):609–620, 1967.

Marinatos, J. and Samuelides, M. Towards a unified methodology for the simulation of rupture in collision and grounding of ships. *Marine Structures*, 42:1 – 32, 2015. doi: 10.1016/j.marstruc.2015.02.006.

Marinatos, J. N. and Samuelides, M. S. Material modeling for finite-element simulation of ship impacts. In *Proceedings of the 4th International Conference on Marine Structures*, pages 187–198, 2013a.

Marinatos, J. N. and Samuelides, M. S. Material characterization and implementation of the rtcl, bwh and shear failure criteria to finite element codes for the simulation of impacts on ship structures. 6th International Conference on Collision and Grounding of Ships and Offshore Structures, ICCGS 2013, pages 267–280, Trondheim, 2013b. ISBN 978-1-138-00059-9.

Marine Accident Investigation Section. Report of investigation into the Collision between the Hong Kong Registered ship "Heibei Spirit" and Korean Crane Barge "Samsung no. 1" on 7 December 2007. Report, The Hong Kong Special Administrative Region Marine Department, 2009.

Martens, I. *Konstruktive Aspekte beim Entwurf von Bugwülsten zur Verbesserung des Energieaufnahmevermögens bei Schiffskollisionen*. PhD Thesis, Schriftenreihe Schiffbau, Bericht 679, Technical University of Hamburg, Germany, 2014.

Masterson, D., Jordaan, I. J., Frederking, R., and Spencer, P. A. Description of multi-year ice indentation tests at Hobson's choice ice island- 1990. In *the 12 th International Conference on Offshore Mechanics and Arctic Engineering 1993, Glasgow, Engl, 06/20-24/93*, pages 145–155, 1993.

McKenna, R. Refinement of iceberg shape characterization for risk to grand banks installations. Technical report, National Research Council Canada; NRC Canadian Hydraulics Centre. PERD/CHC Report 20-77, 2005.

McKenna, R. Iceberg climate, morphology, and design situations. In *Proceedings of the International Conference on Port and Ocean Engineering Under Arctic Conditions*, 2015.

Minorsky, V. An analysis of ship collisions with reference to protection of nuclear power plants. *Journal of Ship Research*, 3(2):1–4, 1959.

Moan, T. The Progressive Structural Failure of the Alexander L. Kielland Platform. In Maier, G., editor, *Case Histories in Offshore Engineering*, volume 283 of *International Centre for Mechanical Sciences*, pages 1–42. Springer Vienna, 1985. ISBN 978-3-211-81817-6. doi: 10.1007/978-3-7091-2742-1_1.

Määttänen, M., Marjavaara, P., Saarinen, S., and Laakso, M. Ice crushing tests

with variable structural flexibility. *Cold Regions Science and Technology*, 67 (3):120–128, 2011.

Muggeridge, K. J. and Jordaan, I. J. Microstructural change in ice: Iii. observations from an iceberg impact zone. *Journal of Glaciology*, 45(151):449–455, 1999.

Mulmule, S. and Dempsey, J. LEFM size requirements for the fracture testing of sea ice. *International journal of fracture*, 102(1):85–98, 2000.

Nahshon, K. and Hutchinson, J. Modification of the gurson model for shear failure. *European Journal of Mechanics-A/Solids*, 27(1):1–17, 2008.

National Transportation Safety Board. Grounding of the U.S. tankship Exxon Valdez on Bligh Reef, Prince William Sound nead Valdez, Alaska. March 24, 1989. Marine Accident Report NTSB/MAR-90/04, Washington, US, 1990.

Nemat-Nasser, S. and Guo, W.-G. Thermomechanical response of DH-36 structural steel over a wide range of strain rates and temperatures. *Mechanics of Materials*, 35(11):1023–1047, 2003.

Notaro, G. DNVGL, Private communication, 2015.

Notaro, G., Brinchmann, K., Steen, E., and Oma, N. Evaluation of the fendering capabilities of the *sps* for an offshore application. *6th International Conference on Collision and Grounding of Ships and Offshore Structures, ICCGS 2013, June 17, 2013 - June 19, 2013*, pages 85–92, 2013.

Notaro, G., Johansen, A., Selås, S., and Nybø, T. Estimation of high energy collision response for jacket structures. In *Proceedings of the 34th International Conference on Ocean, Offshore and Arctic Engineering*, St. Johns, Newfoundland, Canada, May 31-June 5 2015.

NSIDC. International Ice Patrol (IIP) Iceberg Sightings Database. Technical report, Boulder, Colorado USA: National Snow and Ice Data Center. DOI:10.7265/N56Q1V5R., 1995(updated annualy).

Nurcheshmeh, M. and Green, D. E. Prediction of sheet forming limits with marciniak and kuczynski analysis using combined isotropic–nonlinear kinematic hardening. *International Journal of Mechanical Sciences*, 53(2):145–153, 2011.

Oldford, D., Sopper, R., and Daley, C. Impact Ice Loads on Spherical Geometries. In *the ICETECH2014 conference, July 28.-31., ICETECH14-120-RF, Banff, Alberta, Canada*, pages 145–155, 2014.

Ortiz, M. and Simo, J. An analysis of a new class of integration algorithms for elastoplastic constitutive relations. *International Journal for Numerical Methods in Engineering*, 23(3):353–366, 1986.

Paik, J. Practical techniques for finite element modeling to simulate structural crashworthiness in ship collisions and grounding (Part I: Theory). *Ships and Offshore Structures*, 2(1):69–80, 2007.

Paik, J. K. and Pedersen, P. T. Ultimate and crushing strength of plated structures. *Journal of ship research*, 39(3):250–261, 1995.

Paik, J. K. and Thayamballi, A. K. *Ultimate limit state design of steel-plated structures*. Wiley, Chichester, England, 2003.

Palmer, A., Dempsey, J., and Masterson, D. A revised ice pressure-area curve and a fracture mechanics explanation. *Cold regions science and technology*, 56(2): 73–76, 2009.

Paul, S. K. Theoretical analysis of strain-and stress-based forming limit diagrams. *The Journal of Strain Analysis for Engineering Design*, 48(3):177–188, 2013.

Pedersen, P. T. Review and application of ship collision and grounding analysis procedures. *Marine Structures*, 23(3):241–262, 2010.

Pedersen, P. T. and Zhang, S. On impact mechanics in ship collisions. *Marine Structures*, 11(10):429–449, 1998.

Pedersen, P. T. and Zhang, S. Absorbed energy in ship collisions and grounding: Revising Minorsky's empirical method. *Journal of Ship Research*, 44(2):140–154, 2000.

Pedersen, P. T., Valsgård, S., Olsen, D., and Spangenberg, S. Ship impacts: Bow collisions. *International Journal of Impact Engineering*, 13(2):163 – 187, 1993. ISSN 0734-743X. doi: http://dx.doi.org/10.1016/0734-743X(93)90091-K.

Peschmann, J. *Energy absorption computations of ship steel structures under collision and grounding (translated from German language)*. PhD Thesis, Institute for Ship Structural Design and Analysis, Hamburg University of Technology, Germany, 2001.

Petrie, C. J. Considère reconsidered: Necking of polymeric liquids. *Chemical Engineering Science*, 64(22):4693–4700, 2009.

Petroleum Safety Authority. Investigation of Big Orange XVIII's collision with Ekofisk 2/4 - W 8 June 2009 . Accident investigation report, Stavanger, Norway, 2009.

Pettersen, E. and Soegaard, L. M. A study of a collision incident evaluated against ruling. *OTC 17156, Offshore Technology Conference*, 2005. doi: 10.4043/17156-MS.

Pettersen, T. Tanker accident on Northern Sea Route., Cited 15. Dec 2014. 2013. URL http://barentsobserver.com/en/nature/2013/09/tanker-accident-northern-sea-route-09-09.

Popov, Y. N., Faddeyev, O., Ye, D., Kheysin, A., and Yakovlev, A. *Strength of Ships Sailing in Ice*. Sudostroyeniye Publishing House, Leningrad, USSR, 1967.

Pralong, A., Hutter, K., and Funk, M. Anisotropic damage mechanics for viscoelastic ice. *Continuum Mechanics and Thermodynamics*, 17(5):387–408, 2006.

Radon, M. DNVGL, Private communication, 2014.

Redhe, M. DYNAMORE Nordic AB , Private communication, 2014.

Rice, J. R. and Tracey, D. M. On the ductile enlargement of voids in triaxial stress fields*. *Journal of the Mechanics and Physics of Solids*, 17(3):201–217, 1969.

Riska, K. and Kämäräinen, J. A review of ice loading and the evolution of the finnish-swedish ice class rules. In *Proceedings of the SNAME Annual Meeting and Expo. November*, pages 16–18, 2011.

Roth, C. C. and Mohr, D. Effect of strain rate on ductile fracture initiation in advanced high strength steel sheets: Experiments and modeling. *International Journal of Plasticity*, 56(0):19–44, 2014.

Russian Maritime Register of Shipping. Rules for the Classification and Construction of Sea-Going Ships. Volume 1., Sept. 2014.

Saeki, H., Hamanaka, K., and Ozaki, A. Experimental study on ice force on a pile. Technical report, Proceedings of the 4th International Conference on Port and Ocean Engineering under Arctic Conditions (POAC 77), Newfoundland Memorial University, Canada, September 26-30., 1977.

Sajdak, J. and Brown, A. Modeling longitudinal damage in ship collisions. *Report SSC-437, Ship Structure Committee*, 2005.

Samuelides, M. Recent advances and future trends in structural crashworthiness of ship structures subjected to impact loads. *Ships and Offshore Structures*, (10): 1–10, 2015.

Sawczuk, A. On initiation of the membrane action in rigid-plastic plates. *Journal de Mecanique*, 3(1):15–23, 1964a.

Sawczuk, A. Large deflections of rigid-plastic plates. In *Applied Mechanics*, pages 224–228. Springer, 1964b.

Scharrer, M., Zhang, L., and Egge, E. D. Kollisions-berechnungen in schiffbau-lichen entwurfssystemen (collision calculation in naval design systems). Report, Bericht ESS 2002.183, Germanischer Lloyd, 2002.

Schulson, E. M. The brittle failure of ice under compression. *The Journal of Physical Chemistry B*, 101(32):6254–6258, 1997.

Schulson, E. M. Brittle failure of ice. *Engineering Fracture Mechanics*, 68(17-18): 1839–1887, 2001.

Schulson, E. M. and Duval, P. *Creep and fracture of ice*. Cambridge University Press Cambridge, 2009.

Shazly, M., Prakash, V., and Lerch, B. A. High strain-rate behavior of ice under uniaxial compression. *International Journal of Solids and Structures*, 46(6): 1499–1515, 2009.

Simonsen, B. C. and Törnqvist, R. Experimental and numerical modelling of

ductile crack propagation in large-scale shell structures. *Marine Structures*, 17 (1):1–27, 2004.

Singh, S. and Jordaan, I. Constitutive behaviour of crushed ice. *International journal of fracture*, 97(1-4):171–187, 1999.

Skallerud, B. and Amdahl, J. *Nonlinear analysis of offshore structures*. Research Studies Press Baldock, Hertfordshire,, England, 2002. ISBN 0863802583.

Sohdi, D. S. Crushing failure during ice–structure interaction. *Engineering Fracture Mechanics*, 68(17-18):1889–1921, 2001.

Solland, G. Beregning av konstruksjonskapasitet med ikke-lineær FE analyse - Anbefalinger fra DNV-RP-C208 (In Norwegian only). Presented at Konstruksjonsdagen 2014, PTIL, Stavanger, Norway, 2014.

Song, M., Kim, E., and Amdahl, J. Fluid-structure-interaction analysis of an ice block - structure collision. In *Proceedings of the International Conference on Port and Ocean Engineering Under Arctic Conditions, Paper 235*, 2015.

Sopper, R., Gagnon, R., Daley, C., and Colbourne, B. Measurements of spatial and temporal variations in ice impact pressures. In *Proceedings of the International Conference on Port and Ocean Engineering Under Arctic Conditions*, 2015.

SSAB. SSAB Steelfacts database, Cited 04. Dec 2014 2014. URL http://www.ssab.com/en/Products--Services/Service--Support/Technical-Tools-and-films/Steelfacts/Steelfacts/.

Standard Norge. NORSOK-N003: Actions and Actions Effects. Rev. 2, Sept. 2007.

Standard Norge. NORSOK-N004: Design of steel structures. Rev. 2, Oct., 2004.

Standard Norge. NORSOK M120: Material Data Sheets for Structural Steels, 2008.

Standard Norge. NORSOK-N001: Integrity of offshore structures. Rev. 8, Sept., 2012.

Storheim, M. *Analysis of Structural Damage of Tankers subjected to Collision*. Master thesis, Norwegian University of Science and Technology, Trondheim, Norway, 2008.

Storheim, M. and Amdahl, J. Accidental ice management–platform vs. ice breaking supply vessel collision. In *Proceedings of The Twenty-third International Offshore and Polar Engineering Conference*, pages 1195–1202, ISOPE-I-13-046, 30 June-5 July, Anchorage, Alaska, 2013.

Storheim, M. and Amdahl, J. Non-conservative consequences of "conservative" assumptions in ship-platform collision analysis. In *Proceedings of the 33rd International Conference on Ocean, Offshore and Arctic Engineering*, pages OMAE2014–24457, San Francisco, California, USA, June 2014a.

Storheim, M. and Amdahl, J. Design of offshore structures against accidental ship collisions. *Marine Structures*, 37:135–172, 2014b.

Storheim, M. and Amdahl, J. On the effect of work hardening on strain-localization and fracture initiation in collision simulations. In *Proceedings of the 34rd International Conference on Ocean, Offshore and Arctic Engineering*, St. Johns, Newfoundland, Canada, June 2015a.

Storheim, M. and Amdahl, J. On the sensitivity to work hardening and strain-rate effects in nonlinear fem analysis of ship collisions. *Ships and Offshore Structures*, 2015b. doi: 10.1080/17445302.2015.1115181.

Storheim, M., Kim, E., Amdahl, J., and Ehlers, S. Iceberg shape sensitivity in ship impact assessment in view of existing material models. In *Proceedings of the ASME 2012 31st International Conference on Ocean, Offshore and Arctic Engineering OMAE2012 Volume 6.*, 2012.

Storheim, M., Alsos, H., Hopperstad, O., and Amdahl, J. An extension of the BWH instabilitiy criterion - Numerical study. In *Proceedings of the 34rd International Conference on Ocean, Offshore and Arctic Engineering*, St. Johns, Newfoundland, Canada, June 2015a.

Storheim, M., Alsos, H. S., Hopperstad, O. S., and Amdahl, J. A damage-based failure model for coarsely meshed shell structures. *International Journal of Impact Engineering*, 83:59–75, 2015b.

Storheim, M., Nord, T., Kim, E., Høyland, K., Langseth, M., Amdahl, J., and Løset, S. Pilot Study of Ice-Structure Interaction in a Pendulum Accelerator. In *Proceedings of the International Conference on Port and Ocean Engineering Under Arctic Conditions*, 2015c.

Storheim, M., Amdahl, J., and Martens, I. On the Accuracy of Fracture Estimation in Collision Analysis of Ship and Offshore Structures. *Journal of Marine Structures*, 44:254–287, 2015. doi: 10.1016/j.marstruc.2015.09.006.

Stoughton, T. B. Stress-based forming limits in sheet-metal forming. *Journal of Engineering Materials and Technology, Transactions of the ASME*, 123(4): 417–422, 2001.

Stronge, W. J. *Impact mechanics*. Cambridge university press, UK, 2004.

Su, J., Guo, W., Meng, W., and Wang, J. Plastic behavior and constitutive relations of dh-36 steel over a wide spectrum of strain rates and temperatures under tension. *Mechanics of Materials*, 65(0):76–87, 2013.

Swift, H. Plastic instability under plane stress. *Journal of the Mechanics and Physics of Solids*, 1(1):1–18, 1952.

Tabri, K., Määttänen, J., and Ranta, J. Model-scale experiments of symmetric ship collisions. *Journal of marine science and technology*, 13(1):71–84, 2008.

Tabri, K., Broekhuijsen, J., Matusiak, J., and Varsta, P. Analytical modelling of

ship collision based on full-scale experiments. *Marine Structures*, 22(1):42–61, 2009.

Tautz, I., Schottelndreyer, M., Lehmann, E., and Fricke, W. Collision tests with rigid and deformable bulbous bows driven against double hull side structures. *6th International Conference on Collision and Grounding of Ships and Offshore Structures, ICCGS 2013, June 17, 2013 - June 19, 2013*, pages 93–100, 2013.

Timco, G. Compilation of iceberg shape and geometry data for the Grand Banks region. Technical report, National Research Council Canada, PERD/CHC Report 20-43, 24 June, 1999 1999.

Travanca, J. and Hao, H. Numerical analysis of steel tubular member response to ship bow impacts. *International Journal of Impact Engineering*, 64:101–121, 2014.

Törnqvist, R. *Design of Crashworthy Ship Structures*. PhD thesis, Technical University of Denmark, Department of Mechanical Engineering.

Ulan-Kvitberg, C., Kim, H., Daley, C., et al. Comparison of pressure-area effects for various ice and steel indenters. In *Proceedings of the 21st International Offshore and Polar Engineering Conference Maui, Hawaii, USA*, 2011.

VanDerHorn, E. and Wang, G. A statistical study on the material properties of shipbuilding steels. *Sustainable Maritime Transportation and Exploitation of Sea Resources*, pages 371–378, 2011.

Varsta, P. and Riska, K. Measurement of ice pressures and forces on canmar kigoriak during repeated trials in 1981. Technical report, Report LAI-332/82, Dome Petroleum Limited, Technical Research Centre of Finland, Finland, 1982.

Walker, S. Mumbai High North Accident. In *Presentation to Marine Safety Forum. Merseyside, UK: Health and Safety Executive (HSE). Available online at www. npchse. net/safety/pdf/useful% 20information/Mumbai-north-Blow-outreport. pdf (accessed 20 October 2013)*, 2005.

Walters, C. L. Framework for adjusting for both stress triaxiality and mesh size effect for failure of metals in shell structures. *International Journal of Crashworthiness*, 2013. doi: 10.1080/13588265.2013.825366.

Walters, C. L. and Voormeeren, L. O. Consequences of using the plane stress assumption for damage calculations in crash analyses, OMAE2014-23946. In *Proceedings of the ASME 2014 33rd International Conference on Ocean, Offshore and Arctic Engineering*, 2014.

Weck, A. Ductile fracture, Cited Aug. 4. 2015. URL http://www.weck.ca/index.php?mode=7.

Wevers, L. and Vredeveldt, A. W. Full scale ship collision experiments 1998. TNO-report 98-CMC-R0359, TNO, Delft, 1999.

Widianto, Khalifa, J., Younan, A., Karlsson, T., Stuckey, P., and Gjorven, A.

Design of Hebron Gravity Based Structure for Iceberg Impact. *The Twenty-third International Offshore and Polar Engineering Conference, June 30 - July 5, 2013 , Anchorage, Alaska*, 2013.

Wierzbicki, T. and Driscoll, J. C. Crushing damage of web girders under localized static loads. *Journal of Constructional Steel Research*, 33(3):199–235, 1995.

Wierzbicki, T. and Suh, M. Indentation of tubes under combined loading. *International Journal of Mechanical Sciences*, 30(3):229–248, 1988.

Willock, R. T. S. *Research Report 108 : Yield : Tensile Ratio and Safety of High Strength Steels*. Health and Safety Executive, Bedfordshire, UK, 1992.

Woelke, P., Hiriyur, B., Benowitz, B., and Hutchinson, J. W. Ductile fracture prediction for marine structures, OMAE2015-42295. In *Proceedings of the 34th International Conference on Ocean, Offshore and Arctic Engineering*, St. Johns, Newfoundland, Canada, May 31-June 5 2015.

Xiao, J. and Jordaan, I. Application of damage mechanics to ice failure in compression. *Cold Regions Science and Technology*, 24(3):305–322, 1996.

Xue, Z., Pontin, M., Zok, F., and Hutchinson, J. W. Calibration procedures for a computational model of ductile fracture. *Engineering Fracture Mechanics*, 77 (3):492–509, 2010.

Yamada, Y. and Pedersen, P. A benchmark study of procedures for analysis of axial crushing of bulbous bows. *Marine Structures*, 21(2):257–293, 2008.

Yamada, Y. and Pedersen, P. T. Simplified analysis tool for ship-ship collision. In *Proceedings of The Seventeenth 2007 International Offshore and Polar Engineering Conference (ISOPE 2007)*, pages 3760–3767, 2007.

Yamada, Y., Endo, H., and Terndrup-Pedersen, P. Numerical study on the effect on buffer bow structure in ship-ship collision. *Proceedings of the 15th international offshore and polar engineering conference 2005. Seoul, Korea*, pages 604–611, 2005.

Yoshida, K., Kuwabara, T., and Kuroda, M. Path-dependence of the forming limit stresses in a sheet metal. *International Journal of Plasticity*, 23(3):361–384, 2007.

Zhang, L., Egge, E. D., and Bruhms, H. Approval procedure concept for alternative arrangements. In *Proceedings of the Third International Conference on the Collision and Grounding of Ships (ICCGS)*, pages 87–97, 2004.

Appendix A

Numerical Setup

In the following, recommendations for numerical simulations of ship collisions are given. A sensitivity study is conducted to investigate the effect of different physical and numerical parameters on the collision outcome, both from simulations of a crushing experiment with severe folding and from crushing of a full-scale bulbous bow.

A.1 Recommendations for Simulations in LS-DYNA

The following recommendations are compiled based on data from Bala and Day (2012); Haufe et al. (2013); Maker and Zhu (2000); Redhe (2014); Sajdak and Brown (2005) and experiences gained during the course of the PhD.

A.1.1 General Recommendations

- Minimize the number of nodes and elements to reduce computational time (but maintaining sufficient computational accuracy)
- Minimize complexity
- Minimize ratio of triangular to quadrilateral elements
- Minimize numerical instabilities by using a consistent uniform mesh
- Have a minimum of three elements per side in any section of the model (e.g., over the stiffener web height)
- Have a minimum of six elements per buckle in the energy absorbing parts of the structure
- Have a time step sufficiently small to capture proper behavior and sufficiently large to minimize computational cost
- Minimize element warpage

A.1.2   Material

- If strain-rate effects are included, use the visco-plastic formulation (VP=1)
- Avoid the use of pure elastic materials
- Never use artificially high stiffness
- Use physical yield values
- Always use smooth stress-strain curves
- Avoid rigid material as connections
- Avoid the DEFORMABLE_TO_RIGID-option
- Use DAMPING_PART_STIFFNESS with damp=0.05 for all materials
- Avoid brittle failure if possible
- For shell failure care must be taken that never a single integration point may remain. Typically, the number of failed integration points required for element erosion should be less than the total number of integration points through the thickness.
- Use smooth constitutive curves - especially for foams

Of these, contact damping and DAMPING_PART_STIFFNESS was not used during the thesis work.

A.1.3   Contact

- Avoid redundant contact definitions
- Reduce the number of contacts
- Use automatic contacts
- Avoid edge-to-edge penetrations (intersections)
- Avoid initial penetrations if possible
- Use IGNORE=1 for initial penetrations
- Use a uniform mesh in the contact zone
- Avoid increasing the contact stiffness
- Account for shell thicknesses (set ISTUPD=1)
- For contact always use contact damping VDC=20-40%
- Use soft contact (type 1)
- Use DTSTIF=0.5-1.0 millisecond in contact with SOFT=1 or 2

Of these recommendations, contact damping and soft contacts was generally not used during the thesis work.

A.1.4   MPP Analysis

- Reduce the number of contacts
- Distribute large contacts
  CONTROL_MPP_DECOMPOSITION_CONTACT_DISTRIBUTE

- Distribute expensive features (SPH, ALE etc.)
  CONTROL_MPP_DECOMPOSITION_DISTRIBUTE_ALE
- Use a local file system
- Use RCBLOG - same decomposition of model for several simulations
- Use LSTC_REDUCE - arithmetic order during summation etc.

A.1.5   Checking of Numerical Stability

- Check for initial penetrations
- Check for and remove untied nodes
- Avoid conflicting / multiple constraints on nodes
- Run the simulation without loading and check if the model is stable?
- The energy ratio should be close to 1 (requires that all energy components are included in *CONTROL_ENERGY)
- Check that the ratio of hourglass/internal energy is less than 10% for every part
- Check the ratio of (hourglass+sliding)/internal energy for the system
- Check that the sliding energy is > 0
- Check that the sliding energy $<<$ internal energy
- Check the velocity field (e.g. at cycle 2) when initial velocity is applied
- Check for noise (e.g. by velocity field) after initial loads are applied
- Check for noise (e.g. by velocity field) after dynamic relaxation (if used)
- If quasi-static loading - check that the kinetic energy is less than 1% of internal energy

A.1.6   Selective Mass Scaling

If selective mass scaling is applied, the elements with time steps below a set minimum will be mass-scaled during the simulation. This will allow for larger time steps, thereby significantly reducing the computational cost. However, simulations of ship-ship collisions have shown that this may affect the energy balance negatively, and only small time-step improvements can be obtained without it affecting the results.

Selective mass scaling is thus not recommended for ship collisions, but may be an efficient option for applications such as sheet metal forming or quasi-static indentation.

A.1.7   Relevant Elements

The elements used throughout the thesis simulations are all based on Reissner-Mindlin kinematic equations, i.e., cross section remains straight and unstretched and shear deformations through-the-thickness are allowed.

Belytschko-Lin-Tsay Shell Element, ELFORM=2

The Belytschko-Lin-Tsay shell element has a very effective co-rotational formulation, and is the default element in LS-DYNA. The element uses reduced integration. Its warping stiffness is by default to low. Warping stiffness can be added through the BWC-flag in *CONTROL_SHELL. This will apply for all parts in the simulation. Set BWC=1 and PROJ=1.

As warpage may be an issue, it is not recommended to use this element for coarse meshes. What a coarse mesh is for a stiffened panel structure is not well defined.

Belytschko-Wong-Chiang Shell Element, ELFORM=10

This element is similar to the Belytschko-Lin-Tsay, but without shortcomings in the warped configuration. The computational cost is about 10% higher than for the Belytschko-Lin-Tsay element. Using this rather than BWC=1 and PROJ=1 can give warping stiffness only to selected parts (e.g. stiffeners and girders subjected to warpage).

Fully Integrated Shell elements, ELFORM=16

The full integration element uses 2x2 integration points in the plane. If using hourglass stiffness type 8, warping stiffness is added to the element. The computational cost is 2-3 times higher than the reduced integration Belytschko-Lin-Tsay element. Objective stress update is used by default.

(a) Reduced integration shell   (b) Full integration shell

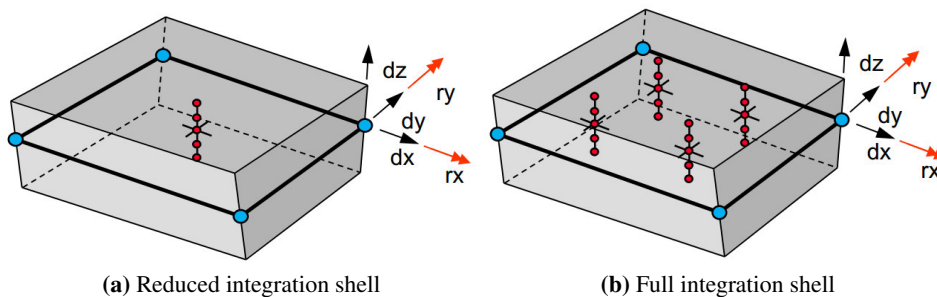**Figure A.1:** Shell elements in LS-DYNA, from Haufe et al. (2013).

A.1.8   Hourglass and Drilling Stiffness

Reduced integration shell elements suffers from two spurious energy modes (hourglass and drilling), in which deformation can occur without being resisted from the element stiffness.

Hourglass stiffness is added to the reduced integration elements using the stiffness-

based form (option 4 in LS-DYNA). This is very efficient and gives low dissipation of spurious hourglass energy, typically less than 2-3%. For some simulations, the stiffness based form fails, and the viscous hourglass stiffness (option 1) was used. This gives a somewhat higher hourglass energy.

Drilling stiffness constraints for explicit analysis was recently included in LS-DYNA, see Erhart and Borrvall (2013) for details. Drilling stiffness controls a spurious deformation mode similar to hourglass stiffness, the drilling mode being rotation around the normal axis of the element (Figure A.2b). This deformation mode is automatically constrained for curved shells, but may be significant for flat unstiffened panels.

A limitation to the current implementation in LS-DYNA is that the energy associated with the added artificial drilling stiffness is not calculated, thus the numerical effect cannot be checked similar to what can be done for hourglass energy. Directly, the drilling stiffness will affect the shear behavior, and will thus influence the stiffness and energy dissipation in the structure.
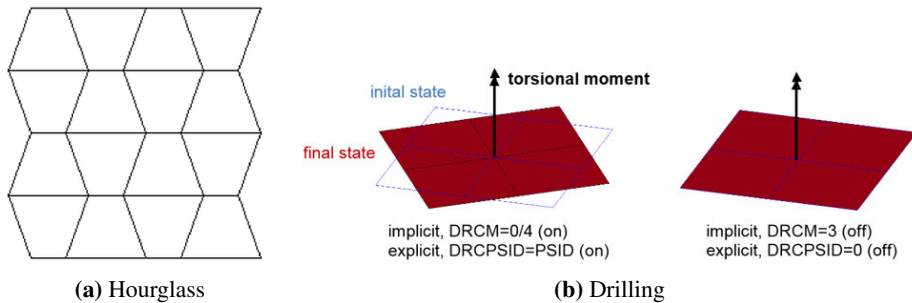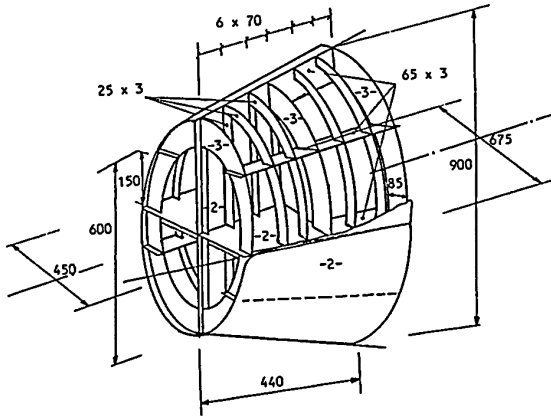

(a) Hourglass   (b) Drilling

Figure A.2: Spurious energy modes for shell elements, from Erhart and Borrvall (2013).

A.2 Sensitivity to Warping and Drilling in Simulations of a Crushing Experiment

A.2.1 Experimental and Simulation Setup

Amdahl (1983) investigated energy absorption mechanisms by conducting scale experiments of crushing of various ship features such as bulbous bows and forecastle structures. Herein, a conical bulb model is investigated (Figure A.3) to study the effect of different numerical parameters.

The conical model consisted of two different sections; the forward part of the model included a deck and a bulkhead, whereas in the aft part only stringers were used as longitudinal stiffening. A ring stiffening system was applied throughout

the model. The deck, outer shell and bulkheads were made of 2 mm thick mild steel and the stiffeners of 3 mm thick steel, with material properties as listed in Table A.1. The different structural elements were assembled by continuous double sided fillet welding, and after welding the structure was stress-relieved by heating it to $550\,^\circ$C.

Figure A.3: Sketch of Bulbous Bow Model, from Amdahl (1983)

Table A.1: Material parameters for the experiments in Amdahl (1983)

	σ_0 [MPa]	E [GPa]	K [MPa]	n	$\varepsilon_{plateau}$
Plate 2 mm	220	201	626	0.304	0.045
Stiffener 3 mm	260	201	720	0.247	0.04

The crushing experiment was performed quasi-statically, and the crushing force was plotted against the crushing distance. For the conical model, the crushing was a two-step process. In the first step the structure was supported at both the inner decks in the middle of the structure as well as at the rear end. This was to test the part of the model with inner decks separate from the rear part of the structure, which only included ring and longitudinal stiffeners. The last part of the crushing was done by supporting only the rear end of the model. The simulated boundaries are shown in Figure A.4. The aft boundary was assumed to act during the entire simulation, whereas the internal only for the first 152 mm of indentation.

Both reduced and full integration elements were used in the following simulations, with three different mesh sizes of 5, 10 and 15 mm (l_e/t_e =2.5, 5 and 7.5). The effect of warping and drilling stiffness is compared.

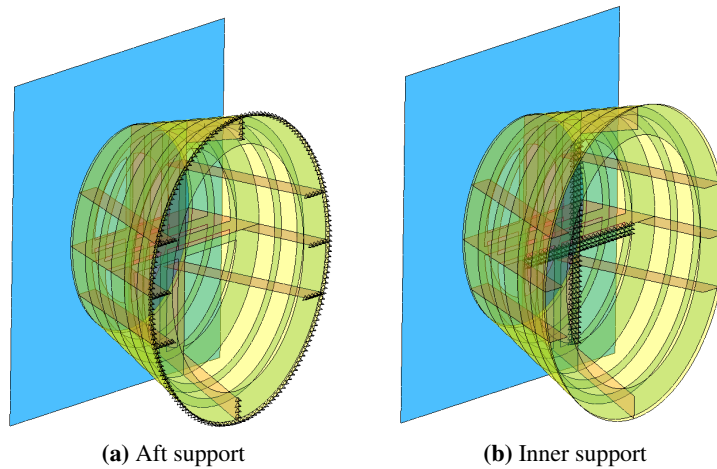(a) Aft support   (b) Inner support

Figure A.4: Boundary conditions for the model

A.2.2   Simulated Deformation

Figure A.5 compares the deformation pattern in the experiment with the simulations. The pattern compares well for all mesh sizes, though the folding events are more accurately represented with refined meshes. The coarsest mesh, with 15 mm elements, is too coarse to capture the folding event accurately, and diverges from the experiment. The distance between each ring stiffener in the conical model is 72 mm center to center. Subtracting plate thickness and welds, about 60-65 mm remains of free plate to form a fold. 15 mm mesh size gives only 4.5 elements over one fold, whereas 10 and 5 mm give respectively 6.5 and 13 elements pr. fold. Six elements are generally recommended over each fold.
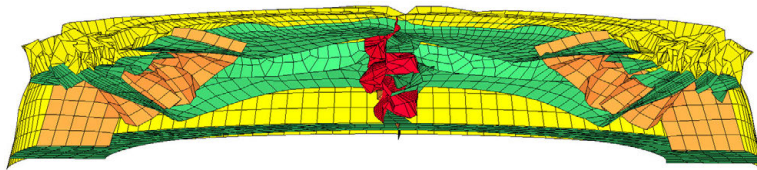
Figure A.6 shows a top view. The simulated folding pattern was similar to the experiment, also in the more complicated intersections between longitudinal stiffeners and plastic folds. Strains in these connections quickly reach 1.0, but not in a bi-axial tensional mode.
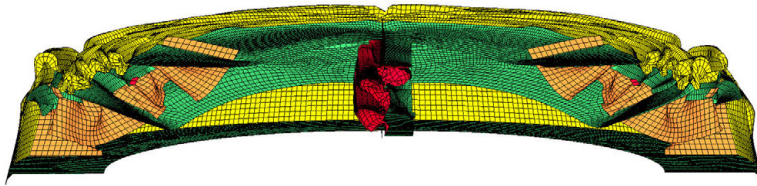
(a) L=5mm
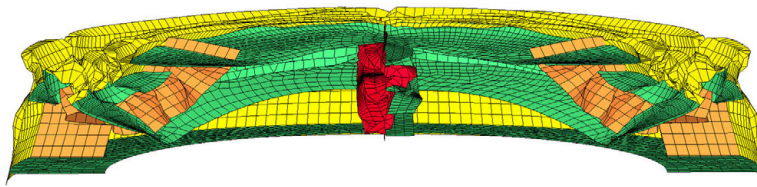
(b) L=10mm

(c) L=15mm

(d) experiment

Figure A.5: Comparison of simulation and experiment, cut of section after testing

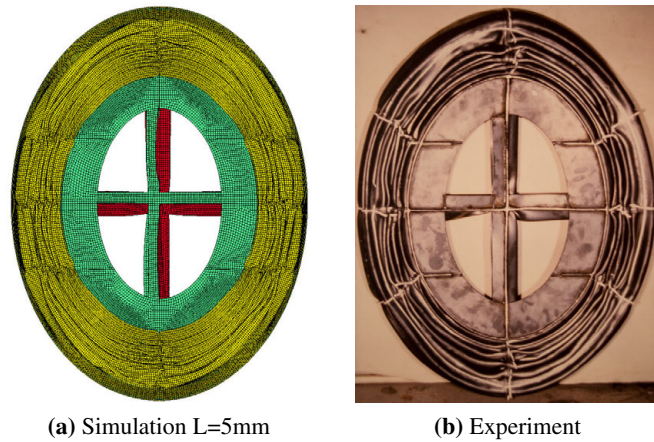(a) Simulation L=5mm   (b) Experiment

Figure A.6: Comparison of simulation with 5mm elements and experiment, top view after testing

A.2.3 Effect of Warping Stiffness

Figure A.7 shows the simulated force-displacement curves from the folding experiment for the different mesh sizes. In Figure A.7, solid lines are without warping stiffness and dashed lines are with. The addition of warping stiffness to the element formulation is minimal for this comparison. It should however be included in full-scale simulations, as warped reduced integration Belytschko-Lin-Tsay elements are too weak in warping by default.

The results are quite comparable between reduced and full integration, although full integration captures the force peaks from folding better, especially after the internal supports have been removed from the simulation.

The initial load peak is overestimated for all meshes used. This is likely due to imperfections in the experiment which were not recorded, and not included in the simulation model. Decreasing mesh size gives a softer response.

A.2.4 Effect of Drilling Stiffness in LS-DYNA

Analysis with drilling stiffness has been conducted for all mesh sizes, and the resulting force-displacement curves are shown in Figure A.8. A drilling stiffness factor DRCPRM=10000 was used. Adding a high drilling stiffness affects the results by increasing the overall stiffness. The force peaks are captured better, but the force troughs are now overestimated. Consequently, the energy dissipation is overestimated compared to the experiments.
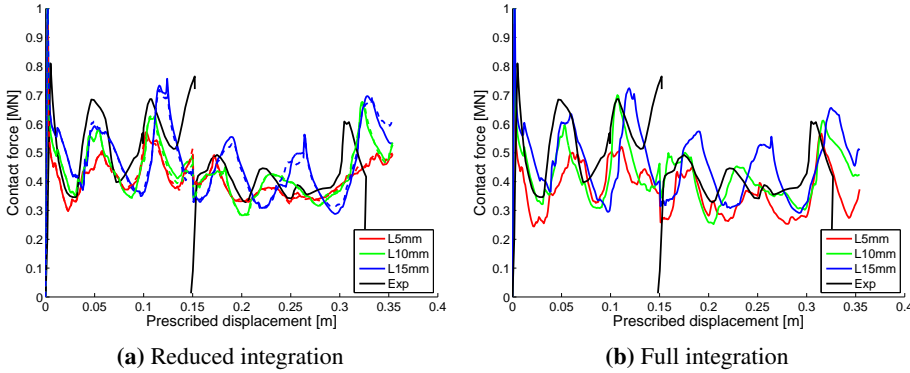
(a) Reduced integration

(b) Full integration

Figure A.7: Effect of warping stiffness on force-displacement relation. Solid lines are without warping stiffness, dashed lines are with

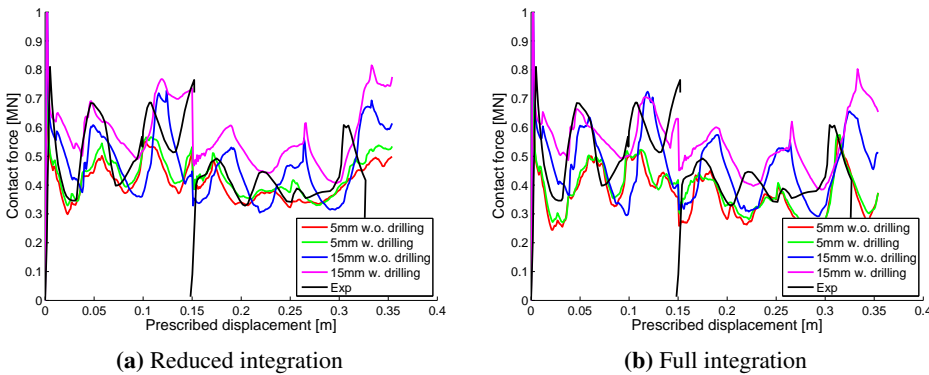**(a)** Reduced integration

(b) Full integration

Figure A.8: Effect of drilling stiffness for two mesh sizes in LS-DYNA.

Figure A.9 shows the effect of drilling stiffness on the shape of the folds during deformation of the stiffened cone. For the smallest mesh size, the differences are negligible. For 10 mm elements, the drilling stiffness changes the fold shape to something closer to the 5 mm solution, which looks like a reasonable improvement.
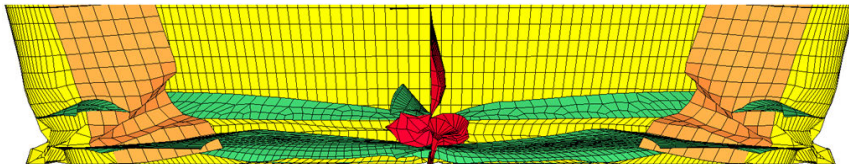
In the current drilling simulations, a high value (10000) is set to the constraint. It has not been investigated at which value the drilling constraint is sufficient, which could occur at a smaller level. It can also be observed in Figure A.8 that the drilling stiffness is mesh dependent; its effect increases with increasingly coarse mesh.
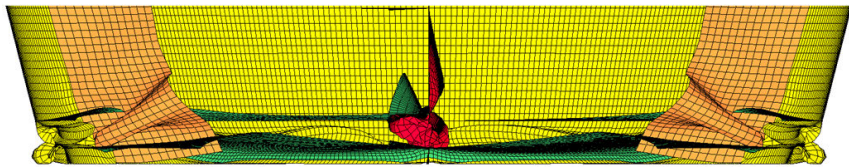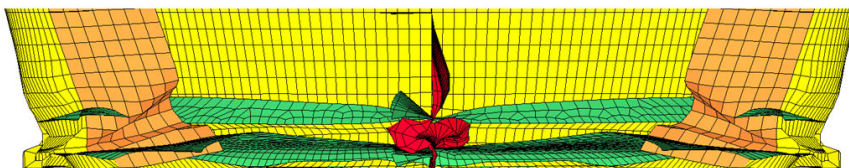
(a) L=5mm
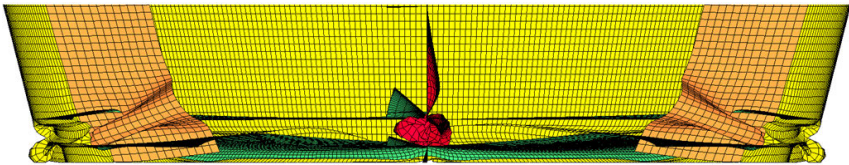
(b) L=5mm drilling

(c) L=10mm

(d) L=10mm drilling

Figure A.9: Comparison of effect of drilling stiffness on folding mechanism

A.2.5   Effect of Drilling Stiffness in ABAQUS

Simulations of the folding experiment were performed in ABAQUS by Notaro (2015) with and without drilling stiffness by controlling the ABAQUS section controls. In ABAQUS, drilling stiffness is on by default, and can only be deactivated through manipulation of the input file. The numerical value of the stiffness parameter in ABAQUS is 1, compared to the much higher numbers used in LS-DYNA to obtain a similar drilling stiffness effect.

Figure A.10 shows the effect of the drilling stiffness in ABAQUS with full and reduced integration elements. A similar behavior as in LS-DYNA is observed (Figure A.8 vs. A.10), with increasing effect of the drilling stiffness with increasing mesh size.
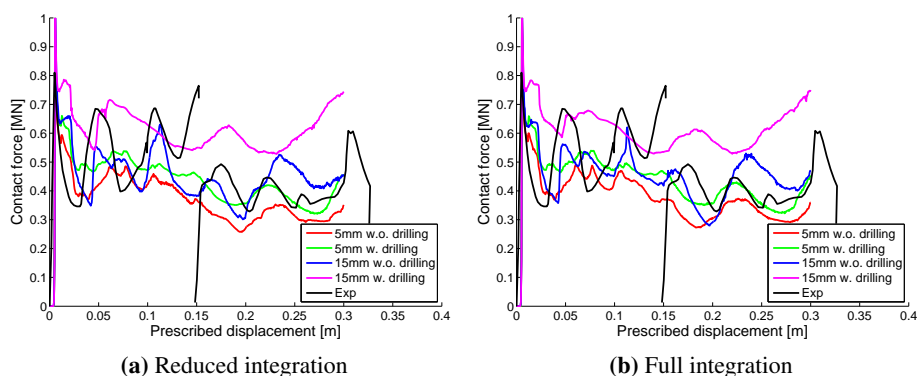

| (a) Reduced integration | (b) Full integration |

Figure A.10: Effect of drilling stiffness for two mesh sizes in ABAQUS.

Using a high drilling stiffness seems to overestimate the crushing force in both ABAQUS and LS-DYNA, especially for large element. A more in-depth study is needed to check whether drilling stiffness should be applied for ship collisions, and how to determine the drilling stiffness parameter in either code in relation to the mesh size and deformation mode.

A.3   Sensitivity of Numerical Parameters in Crushing of a Full-scale Bulbous Bow

The effect of a wide range of numerical parameters on a full-scale bow crushing simulation is investigated in the following. The bow model described in Section 3.8 is used. Two meshes are tested; a coarse mesh with 130 mm elements in the bow ($l_e/t = 10$), and a 65 mm mesh ($l_e/t = 5$). The element size is in similar range over the entire shell model.

A.3.1   Base Case for Comparison

The base case for comparison is based on the control parameters in Appendix A.4, except for warping stiffness, which is included as a separate comparison in the following. A bi-linear hardening curve is used. Both a coarse and a refined mesh are investigated for all parameters.

A.3.2   Warping Stiffness

As the standard Belytschko-Lin-Tsay element has reduced warping stiffness, corrections may be added. The Belytschko-Wong-Chiang stiffness is added in Figure A.11. Some minor differences are seen for the peak bulb crush force, but significant differences occur for the folding events following the initial crushing of the bulb tip. The change is more pronounced with refined mesh.
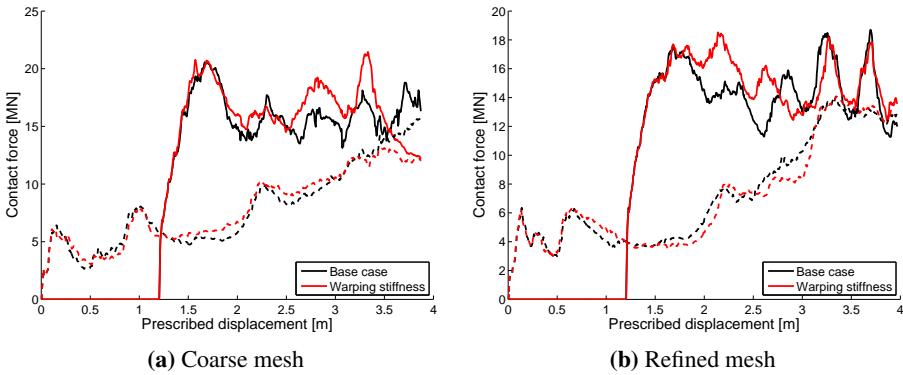

(a) Coarse mesh   **(b)** Refined mesh

Figure A.11: Effect of warping stiffness on force-displacement relation. Solid lines from bulb, dashed lines from forecastle

A.3.3   Full Integration Elements

Figure A.12 shows the effect of using full integration elements. As the full integration elements include warping stiffness, the reduced integration base case is compared with and without warping. Full integration gives a significantly different force than reduced integration. The change is more significant for the coarser mesh in terms of energy dissipation.
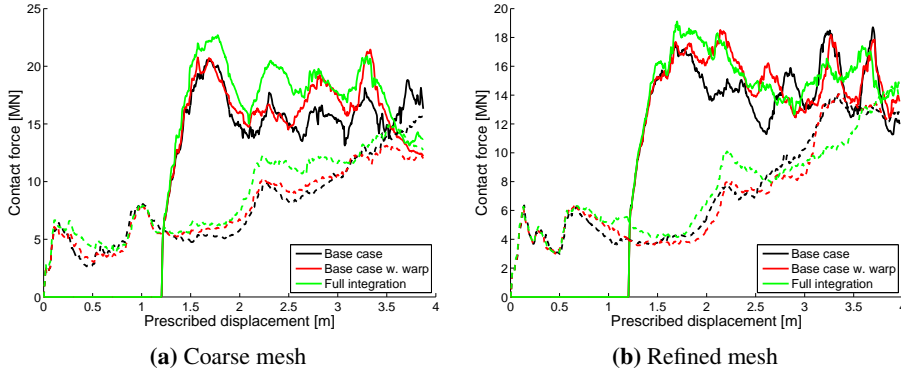
(a) Coarse mesh   **(b)** Refined mesh

Figure A.12: Effect of full integration on force-displacement relation. Solid lines from bulb, dashed lines from forecastle

A.3.4   Single or Double precision

Figure A.13 shows the effect of using double precision on the calculation. The first load peak is captured well, but the subsequent folding events are more sensitive to the selected precision.

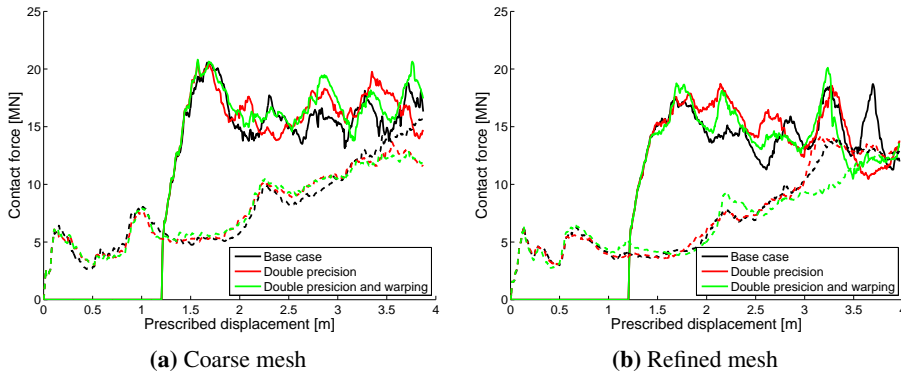**(a)** Coarse mesh   **(b)** Refined mesh

Figure A.13: Effect of double precision on force-displacement relation. Solid lines from bulb, dashed lines from forecastle

Figure A.14 shows the effect of using full integration and double precision on the calculation. Double precision gives a negligible change for full integration elements.
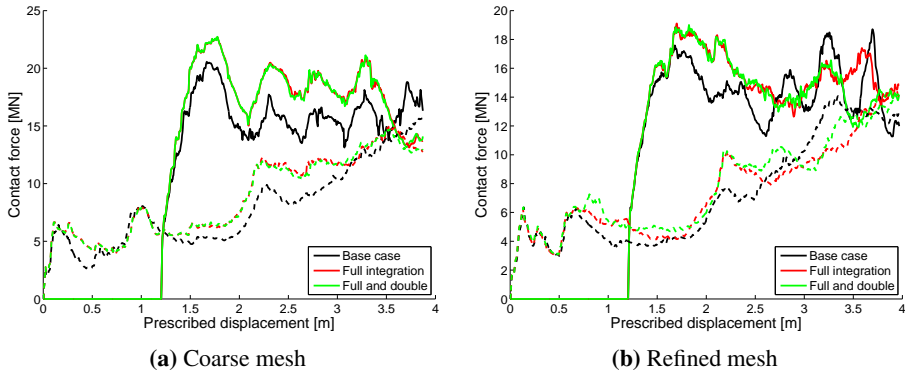
(a) Coarse mesh   **(b)** Refined mesh

Figure A.14: Effect of full integration and double precision on force-displacement relation. Solid lines from bulb, dashed lines from forecastle

A.3.5   Objective Stress Update

Figure A.15 shows the effect of using objective stress update on reduced integration elements. Objective stress update includes second order terms in the stress-rate during explicit calculations, thus increasing both accuracy and cost. It can be important with large rotation, or for high velocity impacts generating large strains in a few time steps. Some changes in the subsequent folding are observed.
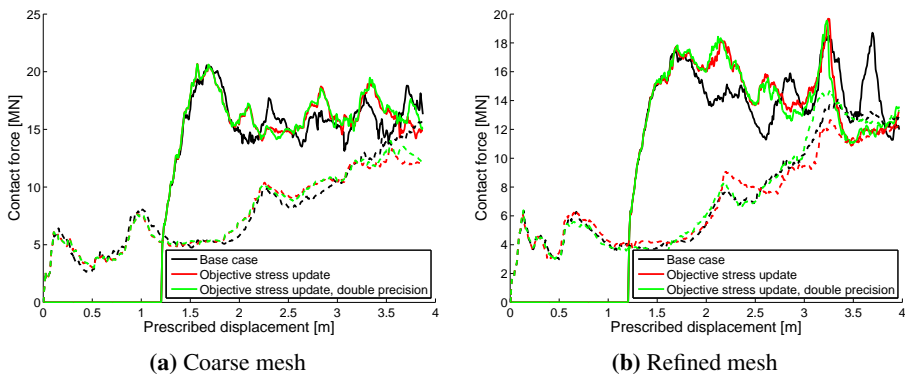

(a) Coarse mesh   **(b)** Refined mesh

Figure A.15: Effect of objective stress update on force-displacement relation. Solid lines from bulb, dashed lines from forecastle

Objective stress update is included in the formulation of the full-integration elements, and is not checked further.

A.3.6   Drilling Stiffness

Figure A.16 shows the effect of using drilling stiffness on reduced integration elements with warping stiffness. A drilling stiffness parameter DRCPRM of 100 and 10000 is investigated. A drilling stiffness of 100 gives some changes to the simulation results, but to obtain large differences (comparable to the drilling effect in ABAQUS) the stiffness parameter needs to be increased even more.

Even a small drilling stiffness increases the gradient of the bulb crushing force prior to the first peak. This may give significant effects in an integrated analysis.
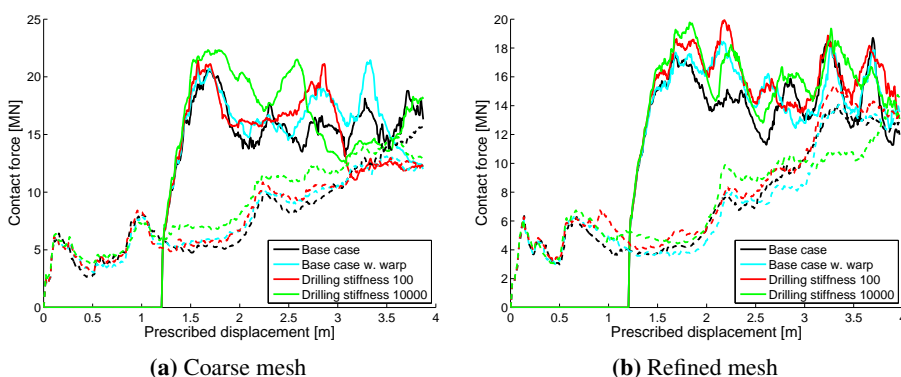

(a) Coarse mesh   (b) Refined mesh

Figure A.16: Effect of drilling stiffness on force-displacement relation. Solid lines from bulb, dashed lines from forecastle

A.3.7   Comparison with ABAQUS

ABAQUS simulations of the same model with the same material and contact parameters have been performed by DNV (Notaro 2015) for benchmarking.

Figure A.17 shows the comparison without drilling stiffness. With the coarse mesh, the first load peak is in a similar range, but the resistance after this is higher in ABAQUS compared to LS-DYNA. The same applies for refined mesh, with ABAQUS giving somewhat higher peaks of the subsequent folds.

Figure A.18 shows the comparison with drilling stiffness. With coarse mesh, a drilling stiffness factor of 10000 in LS-DYNA approach the ABAQUS simulation with drill stiffness of 1, but an even higher LS-DYNA factor is necessary to match ABAQUS. The same holds for the refined mesh, but the LS-DYNA and ABAQUS solutions with high drilling stiffness are closer to each other. It may be that the absolute value of drilling stiffness should be related to the mesh-size, and it may scale differently in the two codes.

(a) Coarse mesh

(b) Refined mesh

Figure A.17: LS-DYNA vs. ABAQUS for analysis without drilling stiffness. Solid lines from bulb, dashed lines from forecastle

(a) Coarse mesh

(b) Refined mesh

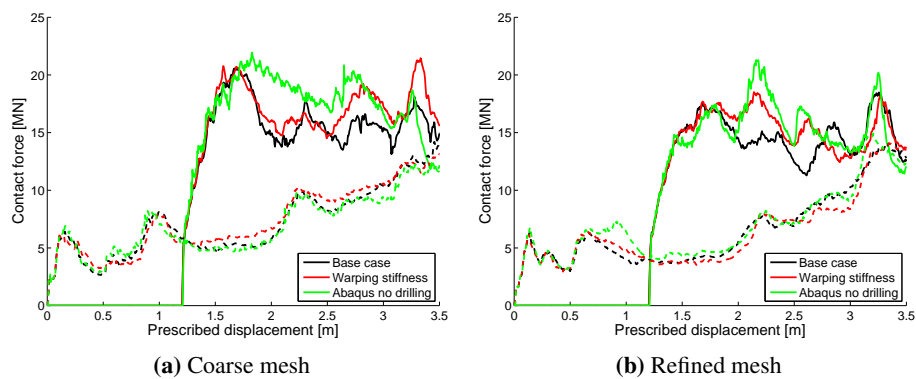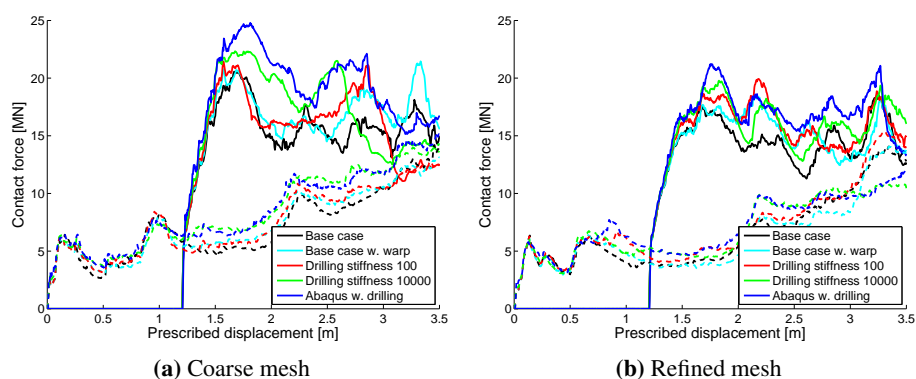**Figure A.18:** LS-DYNA vs. ABAQUS for analysis with drilling stiffness. Solid lines from bulb, dashed lines from forecastle

Figure A.19 shows the comparison with coarse mesh and full integration elements. With full integration elements, the two softwares give a more similar response than with reduced integration elements.
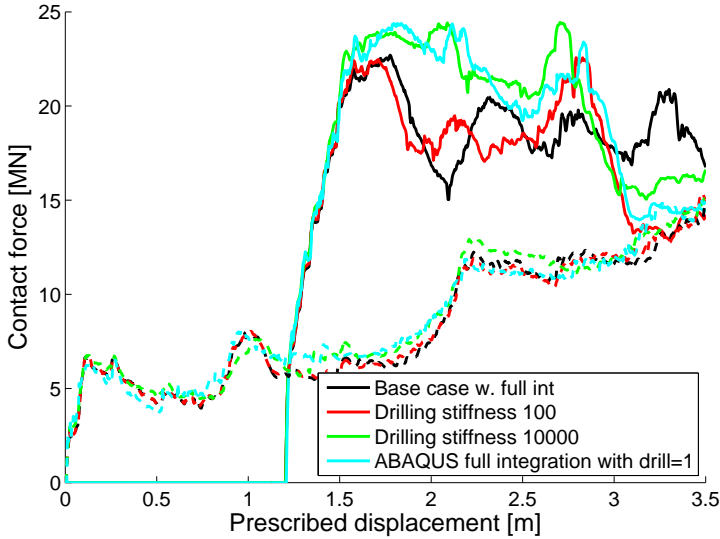
Figure A.19: LS-DYNA vs. ABAQUS for analysis with full integration elements and drilling stiffness. Solid lines from bulb, dashed lines from forecastle

A.3.8   Sensitivity to Solver Type

Figure A.20 shows LS-DYNA simulations using the SMP solver (shared memory processing, one node with X cpus) vs. the MPP (massive parallel processing, Y nodes, each with X cpus). There is a small difference in the force-displacement when changing from SMP to MPP, but no difference when scaling the simulations over an increasing number of nodes with the MPP version. Some of the difference between SMP and MPP is due to the contact formulation, which is rewritten for the MPP version of LS-DYNA.

Most simulations herein are performed with the MPP solver, typically between 16 and 240 CPU's per simulation.

Figure A.20: SMP vs. MPP solver with varying number of CPUs

A.4   Control Card Input to LS-DYNA Developed During the PhD Work

Due to the complexity of NLFEA simulations, the method for analysis has continued to improve during the Thesis work as new problems have been encountered or 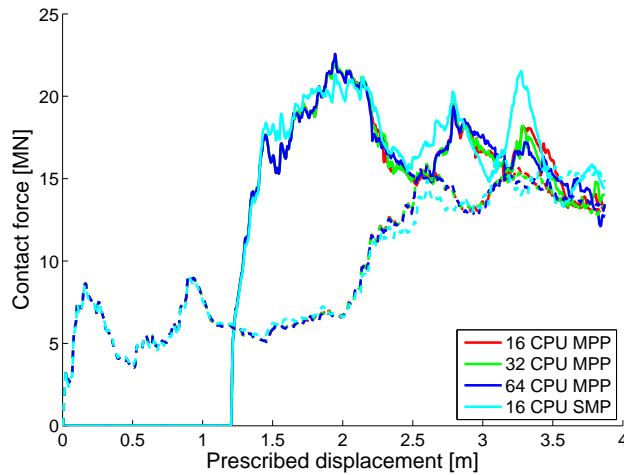new input gained from discussions with other analysts. The control parameters below represent the final setup used in JP-2, JP-3 and JP-4. The setup is in line with most of the recommendations discussed above.

```
1   *KEYWORD
    *CONTROL_ACCURACY
3   $#       osu        inn     pidosu
             0          2          0
5   *CONTROL_BULK_VISCOSITY
    $#        q1         q2       type      btype
7    1.500000   0.060000         -1          0
    *CONTROL_CONTACT
9   $#    slsfac     rwpnal     islchk     shlthk     penopt     thkchg      orien     enmass
     0.100000   1.000000          2          2          1          0          1          0
11  $#    usrstr     usrfrc      nsbcs     interm      xpene      ssthk       ecdt    tiedprj
             0          0          0          0   4.000000          0          0          0
13  $#     sfric      dfric        edc        vfc         th      th_sf     pen_sf
     0.000      0.000      0.000      0.000      0.000      0.000      0.000
15  $#    ignore     frceng     skiprwg     outseg    spotstp    spotdel    spothin
             2          1          1          0          0          1      0.000
17  $#      isym     nserod     rwgaps     rwgdth      rwksf       icov     swradf     ithoff
             0          0          0      0.000      0.000          0      0.000          0
19  $#    shledg     pstiff     ithcnt     tdcnof      ftall     unused     shltrw
             0          0          0          0          1                 0.000
21  *CONTROL_DYNAMIC_RELAXATION
    $#    nrcyck      drtol     drfctr     drterm     tssfdr     irelal      edttl     idrflg
23         250   0.001000   0.995000      0.000      0.000          0   0.040000       -999
    *CONTROL_ENERGY
25  $#      hgen       rwen     slnten      rylen
             2          2          2          2
27  *CONTROL_HOURGLASS
    $#       ihq         qh
29           4   0.030000
    *CONTROL_MPP_IO_LSTC_REDUCE
```

```
31  *CONTROL_MPP_IO_NODUMP
    *CONTROL_OUTPUT
33  $#    npopt    neecho    nrefup    iaccop     opifs    ipnint     ikedit    iflush
             1         3         0         1     0.000         0       1000       5000
35  $#    iprtf     ierode     tet10    msgmax    ipcurv
             0         1         2     10000         1
37  *CONTROL_PARALLEL
    $#     ncpu    numrhs     const      para
             1         0         1         0
39  *CONTROL_RIGID
41  $#      lmf      jntf    orthmd     partm    sparse    metalf     plotel     rbsms
             0         0         0         0         0         0          0         0
43  *CONTROL_SHELL
    $#   wrpang     esort     irnxx    istupd    theory       bwc      miter      proj
45  20.000000         1        -1         1         2         1          1         1
    $# rotascl    intgrd    lamsht    cstyp6    tshell
47  1.000000         0         0         1         0
    $# psstupd   sidt4tu     cntco    itsflg    irquad
49          0         0         0         0         2
    $#   nfail1    nfail4   psnfail    keepcs     delfr   drcpsid     drcprm
51          1         1         0         0         0         0   1.000000
    *CONTROL_SOLID
53  $#    esort   fmatrix   niptets    swlocl    psfail
             1         0         0         2         0
55  $#      pm1       pm2   pm3   pm4       pm5       pm6   pm7   pm8       pm9      pm10
             0         0     0     0         0         0     0     0         0         0
57  *CONTROL_SOLUTION
    $#     soln       nlq     isnan     lcint
             0         0         1      1001
59  *CONTROL_TIMESTEP
61  $#   dtinit    tssfac      isdo    tslimt     dt2ms      lctm      erode     ms1st
         0.000  0.900000         0     0.000   0.0e-6         0          0         0
63  $#   dt2msf    dt2mslc     imscl    unused    unused     rmscl
         0.000         0         0                         0.000
65  *DAMPING_GLOBAL
    $#     lcid    valdmp       stx       sty       stz       srx        sry       srz
67          0     0.000     0.000     0.000     0.000     0.000      0.000     0.000
    *END
```

Appendix B

Conversion Formulas for Plane Stress

$$\varepsilon_1 = \varepsilon_{eq}\left(\frac{2\sigma_1 - \sigma_2}{2\sigma_{eq}}\right) = \varepsilon_{eq}\frac{1 - \alpha/2}{\sqrt{1 - \alpha + \alpha^2}} \tag{B.1}$$

$$\varepsilon_2 = \varepsilon_{eq}\left(\frac{2\sigma_2 - \sigma_1}{2\sigma_{eq}}\right) = \varepsilon_{eq}\frac{\alpha - 1/2}{\sqrt{1 - \alpha + \alpha^2}} \tag{B.2}$$

$$\sigma_1 = \frac{\sigma_{eq}}{\sqrt{1 - \alpha + \alpha^2}} \tag{B.3}$$

$$\sigma_1 = \sigma_{eq}\frac{2}{\sqrt{3}}\frac{1 + \beta/2}{\sqrt{1 + \beta + \beta^2}} \tag{B.4}$$

$$\alpha = \frac{\sigma_2}{\sigma_1} = \frac{\dot{\sigma}_2}{\dot{\sigma}_1} = \frac{2\beta + 1}{2 + \beta} \tag{B.5}$$

$$\beta = \frac{\dot{\varepsilon}_2}{\dot{\varepsilon}_1} = \frac{2\alpha - 1}{2 - \alpha} \tag{B.6}$$

$$T = \frac{1}{\sqrt{3}}\frac{\beta + 1}{\sqrt{1 + \beta + \beta^2}} \tag{B.7}$$

$$\varepsilon_{eq}^2 = \frac{4}{3}\left(\varepsilon_1^2 + \varepsilon_1\varepsilon_2 + \varepsilon_2^2\right) = \varepsilon_1^2\frac{4}{3}\left(1 + \beta + \beta^2\right) \tag{B.8}$$

$$d\varepsilon_{eq} = \left[\frac{2}{3}\left(d\varepsilon_1^2 + d\varepsilon_2^2 + d\varepsilon_3^2\right)\right]^{1/2} \tag{B.9}$$

$$\sigma_1 = \left[T + \frac{2}{3}\cos\left(\theta_L\right)\right]\sigma_{eq} \tag{B.10}$$

Appendix C

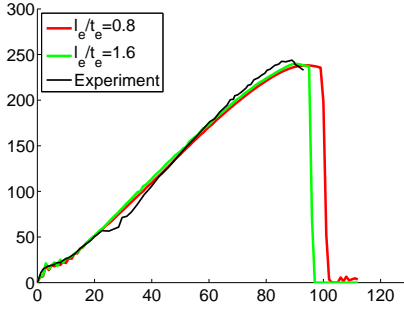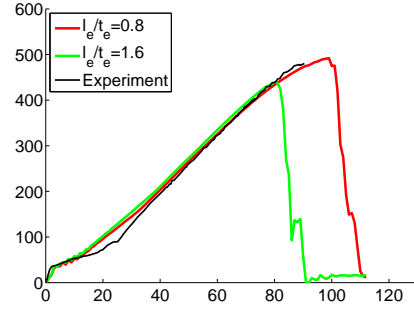# Force-displacement Curves for Simulations in Chapter 5

C.1   Formability Tests

(a) FLD 1, $\beta = -0.2$

(b) FLD 2, $\beta = 0.0$

(c) FLD 3, $\beta = 0.28$

(d) FLD 4, $\beta = 0.43$

(e) FLD 5, $\beta = 0.44$
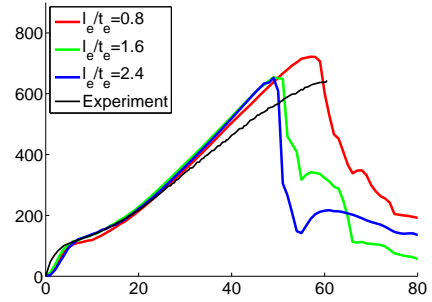
(f) FLD 6, $\beta = 0.66$

Figure C.1: Force-displacement relation from formability tests and simulations with varying mesh size vs. thickness ratio l_e/t_e. Fracture criterion : BWH w. damage
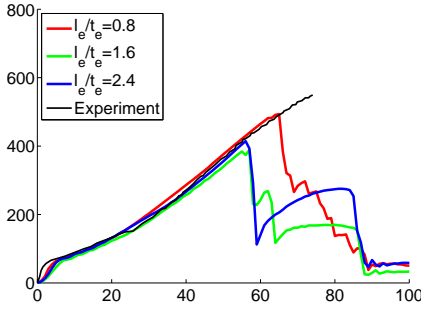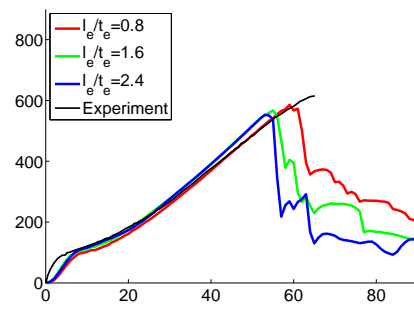
(a) FLD 1, $\beta = -0.2$

(b) FLD 2, $\beta = 0.0$

(c) FLD 3, $\beta = 0.28$

(d) FLD 4, $\beta = 0.43$

(e) FLD 5, $\beta = 0.44$

(f) FLD 6, $\beta = 0.66$

Figure C.2: Force-displacement relation from formability tests and simulations with varying mesh size vs. thickness ratio l_e/t_e. Fracture criterion : BWH no dam

Figure C.3: Force-displacement relation from formability tests and simulations with varying mesh size vs. thickness ratio l_e/t_e. Fracture criterion : RTCL
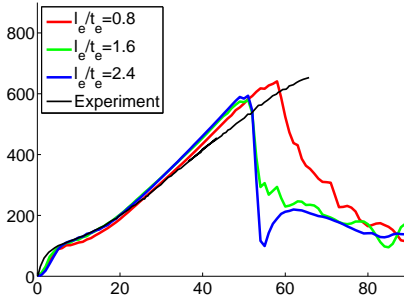
(a) FLD 1, $\beta = -0.2$

(b) FLD 2, $\beta = 0.0$

(c) FLD 3, $\beta = 0.28$

(d) FLD 4, $\beta = 0.43$

(e) FLD 5, $\beta = 0.44$

(f) FLD 6, $\beta = 0.66$

Figure C.4: Force-displacement relation from formability tests and simulations with varying mesh size vs. thickness ratio l_e/t_e. Fracture criterion : GL

(a) FLD 1, $\beta = -0.2$
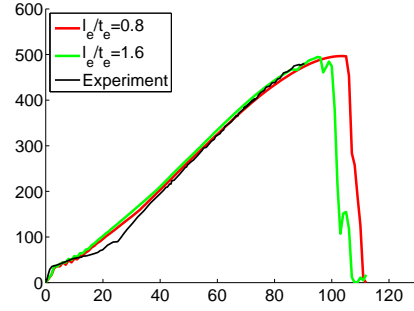
(b) FLD 2, $\beta = 0.0$
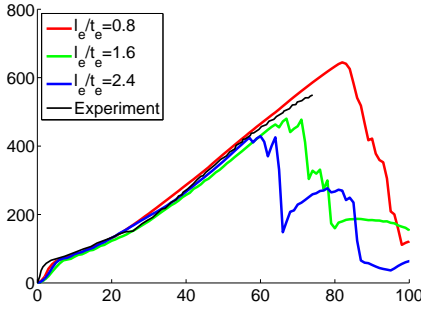
(c) FLD 3, $\beta = 0.28$

(d) FLD 4, $\beta = 0.43$

(e) FLD 5, $\beta = 0.44$
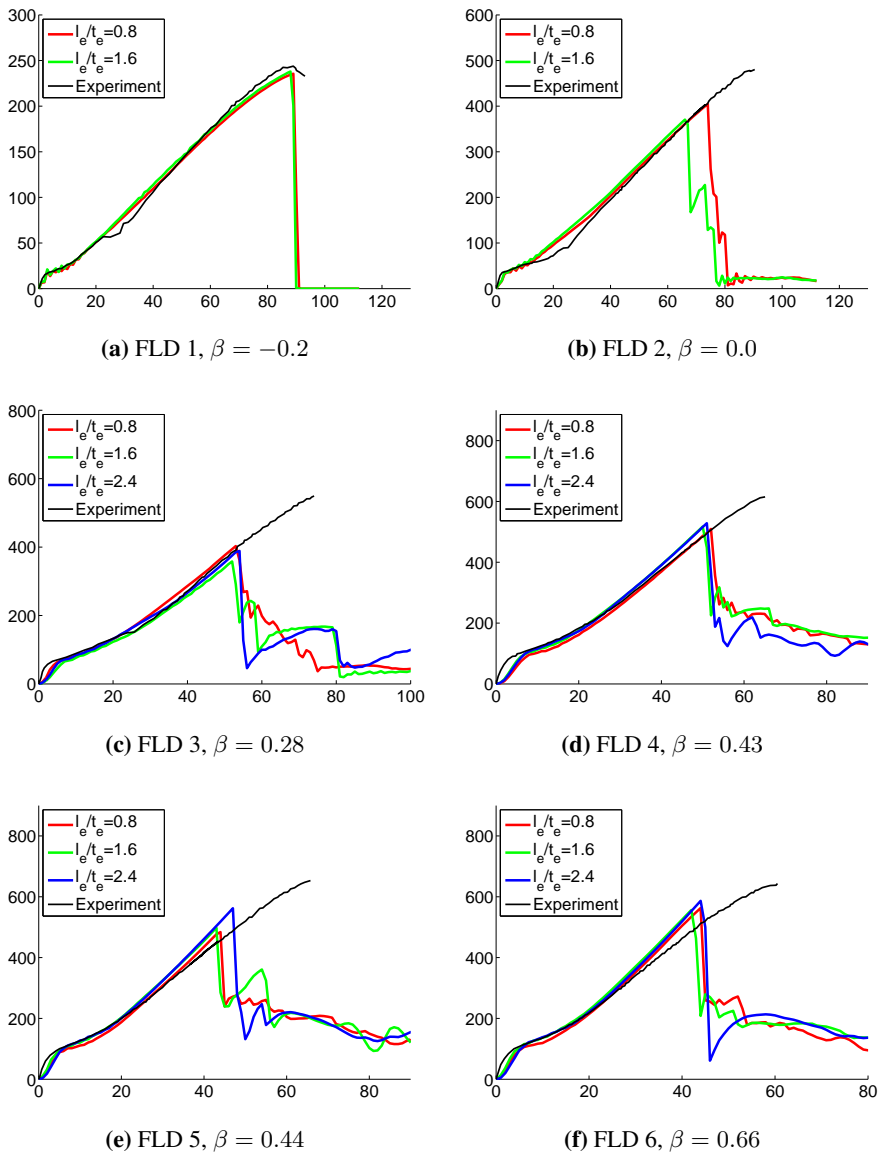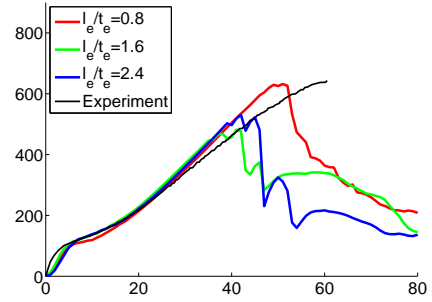
(f) FLD 6, $\beta = 0.66$

Figure C.5: Force-displacement relation from formability tests and simulations with varying mesh size vs. thickness ratio l_e/t_e. Fracture criterion : SHEAR

(a) FLD 1, $\beta = -0.2$

(b) FLD 2, $\beta = 0.0$

(c) FLD 3, $\beta = 0.28$

(d) FLD 4, $\beta = 0.43$

(e) FLD 5, $\beta = 0.44$
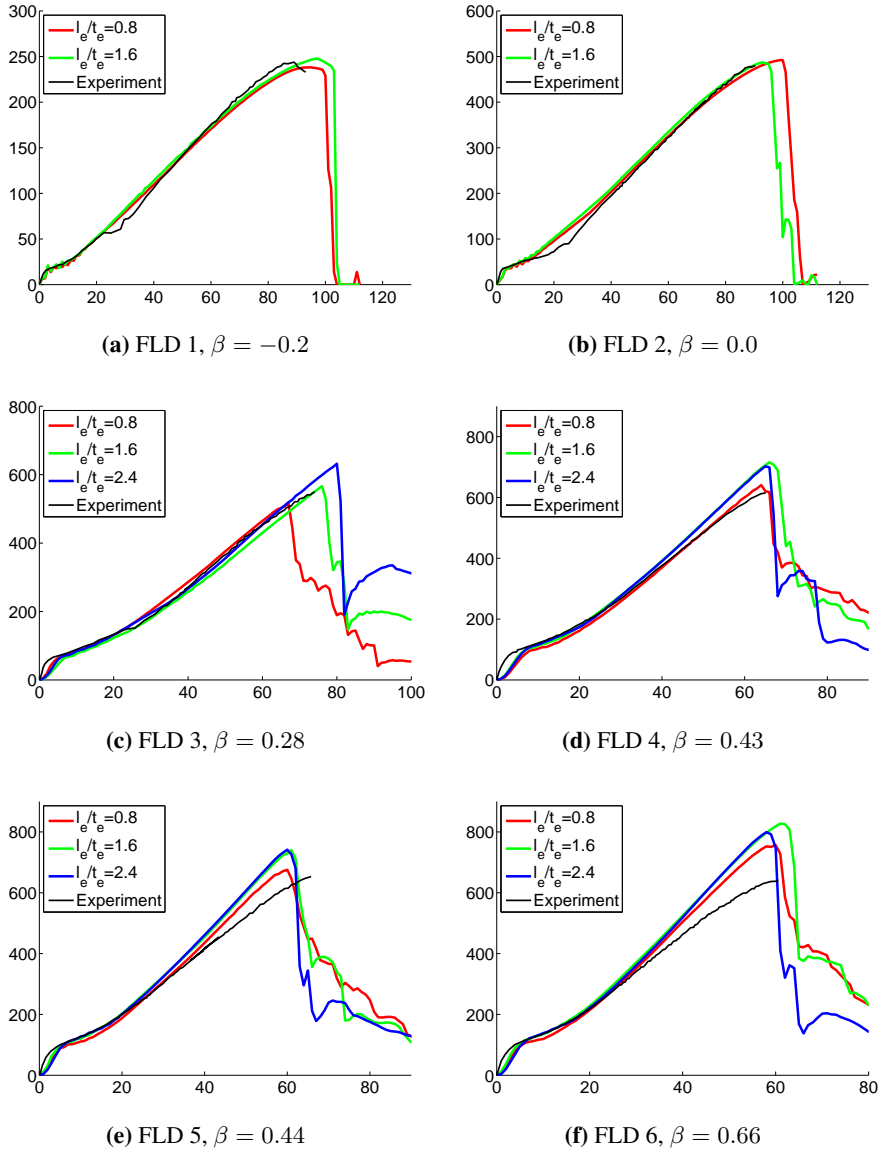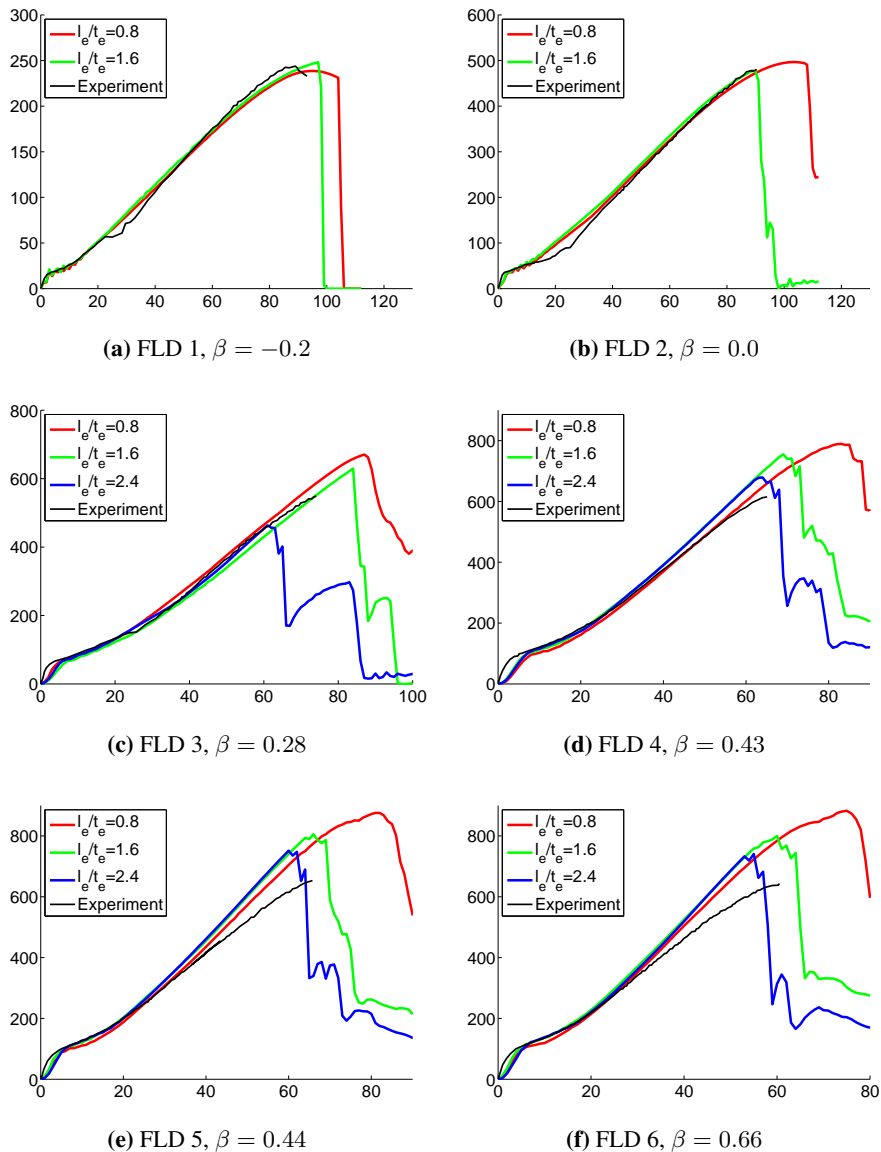
(f) FLD 6, $\beta = 0.66$
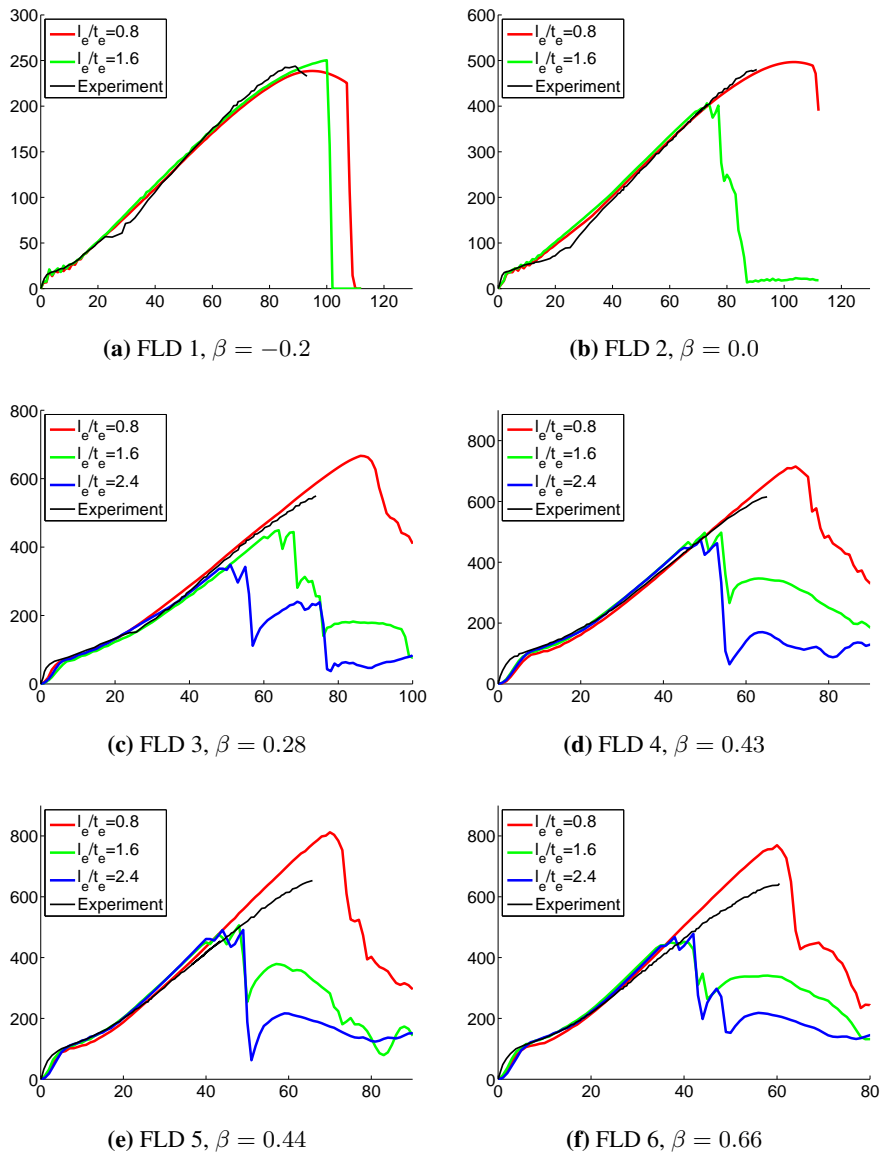
Figure C.6: Force-displacement relation from formability tests and simulations with varying mesh size vs. thickness ratio l_e/t_e. Fracture criterion : RPC204

(a) FLD 1, $\beta = -0.2$

(b) FLD 2, $\beta = 0.0$

(c) FLD 3, $\beta = 0.28$

(d) FLD 4, $\beta = 0.43$

(e) FLD 5, $\beta = 0.44$

(f) FLD 6, $\beta = 0.66$
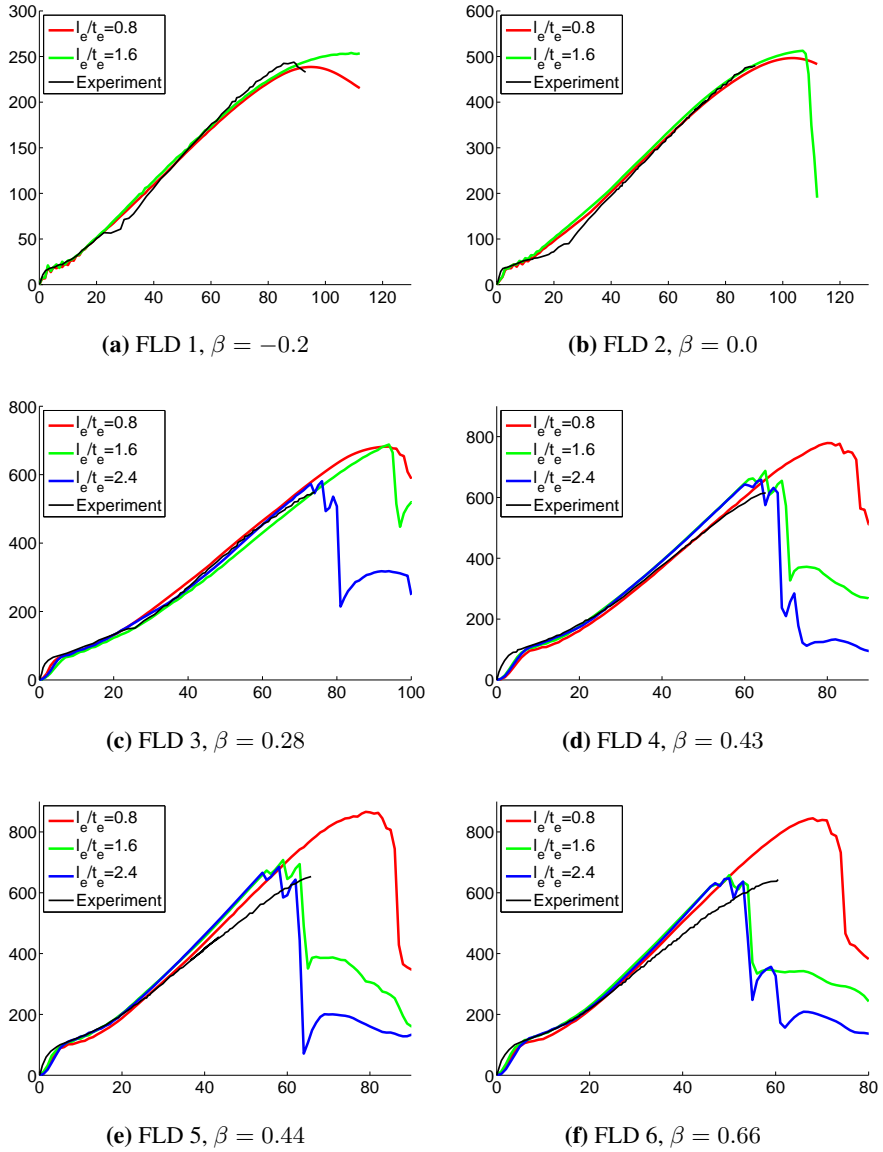
Figure C.7: Force-displacement relation from formability tests and simulations with varying mesh size vs. thickness ratio l_e/t_e. Fracture criterion : Peschmann
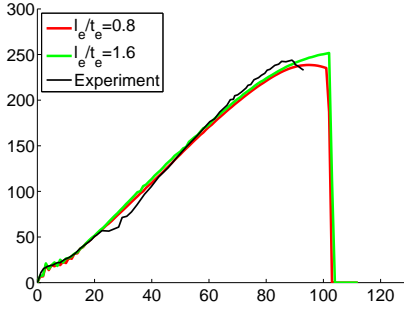
(a) FLD 1, $\beta = -0.2$

(b) FLD 2, $\beta = 0.0$

(c) FLD 3, $\beta = 0.28$

(d) FLD 4, $\beta = 0.43$

(e) FLD 5, $\beta = 0.44$

(f) FLD 6, $\beta = 0.66$
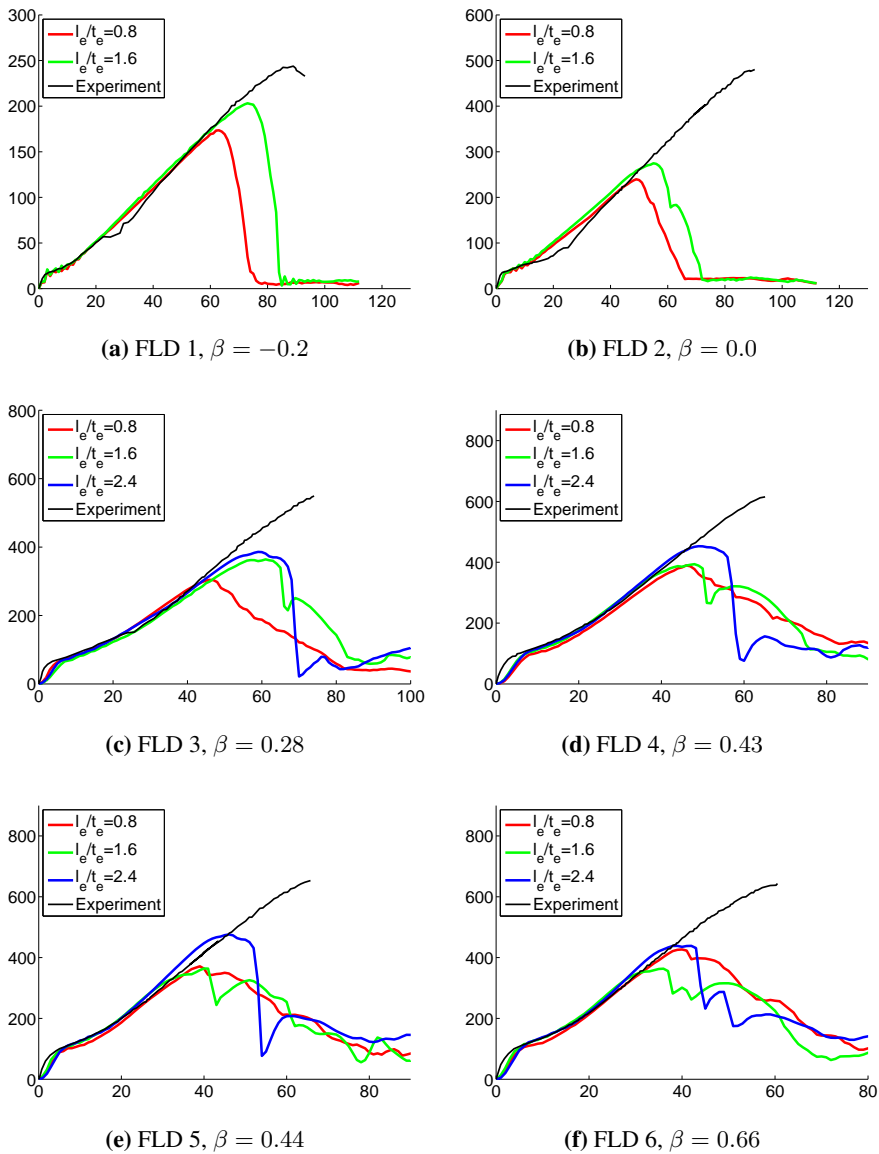
Figure C.8: Force-displacement relation from formability tests and simulations with varying mesh size vs. thickness ratio l_e/t_e. Fracture criterion : Ductile damage

C.2   Plate Tearing Tests

(a) 5 mm plate   **(b)** 10 mm plate

Figure C.9: Force-displacement relation from Simonsen and Törnqvist tearing tests and simulations with varying mesh size vs. thickness ratio l_e/t_e. Fracture criterion : BWH w. damage
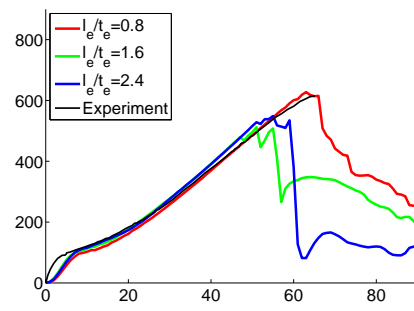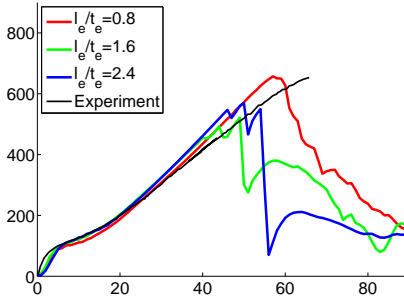
(a) 5 mm plate

(b) 10 mm plate

Figure C.10: Force-displacement relation from Simonsen and Törnqvist tearing tests and simulations with varying mesh size vs. thickness ratio l_e/t_e. Fracture criterion : BWH no damage

(a) 5 mm plate

(b) 10 mm plate

Figure C.11: Force-displacement relation from Simonsen and Törnqvist tearing tests and simulations with varying mesh size vs. thickness ratio l_e/t_e. Fracture criterion : RTCL

Figure C.12: Force-displacement relation from Simonsen and Törnqvist tearing tests and simulations with varying mesh size vs. thickness ratio l_e/t_e. Fracture criterion : GL

Figure C.13: Force-displacement relation from Simonsen and Törnqvist tearing tests and simulations with varying mesh size vs. thickness ratio l_e/t_e. Fracture criterion : SHEAR

(a) 5 mm plate

(b) 10 mm plate

Figure C.14: Force-displacement relation from Simonsen and Törnqvist tearing tests and simulations with varying mesh size vs. thickness ratio l_e/t_e. Fracture criterion : RPC204

(a) 5 mm plate

(b) 10 mm plate

Figure C.15: Force-displacement relation from Simonsen and Törnqvist tearing tests and simulations with varying mesh size vs. thickness ratio l_e/t_e. Fracture criterion : Peschmann

(a) 5 mm plate

(b) 10 mm plate
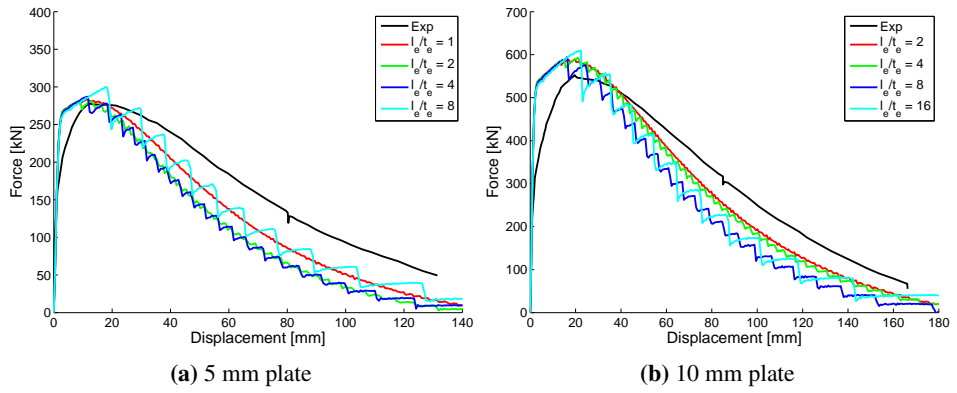
Figure C.16: Force-displacement relation from Simonsen and Törnqvist tearing tests and simulations with varying mesh size vs. thickness ratio l_e/t_e. Fracture criterion : Damage

C.3   Alsos and Amdahl Indentation Tests

(a) Plate US

(b) Plate 1FB

(c) Plate 2FB

Figure C.17: Force-displacement relation from Alsos and Amdahl tests and simulations with varying mesh size vs. thickness ratio l_e/t_e. Fracture criterion : BWH w. dam

(a) Plate US

(b) Plate 1FB

(c) Plate 2FB

Figure C.18: Force-displacement relation from Alsos and Amdahl tests and simulations with varying mesh size vs. thickness ratio l_e/t_e. Fracture criterion : BWH no dam
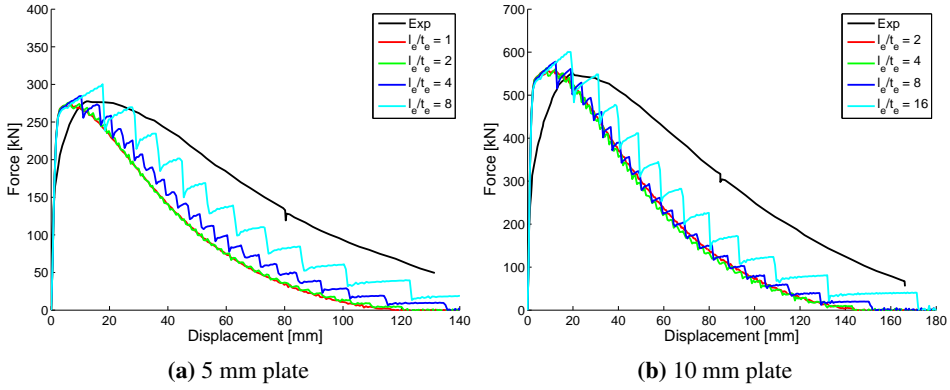
(a) Plate US

(b) Plate 1FB

(c) Plate 2FB

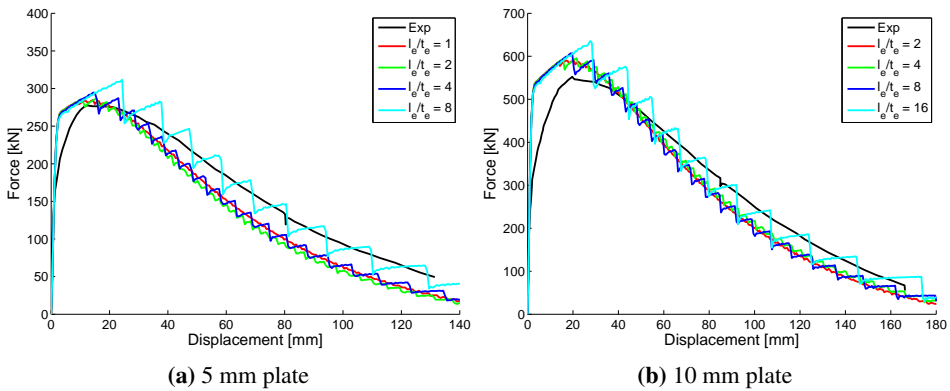**Figure C.19:** Force-displacement relation from Alsos and Amdahl tests and simulations with varying mesh size vs. thickness ratio l_e/t_e. Fracture criterion : RTCL

(a) Plate US

(b) Plate 1FB

(c) Plate 2FB

Figure C.20: Force-displacement relation from Alsos and Amdahl tests and simulations with varying mesh size vs. thickness ratio l_e/t_e. Fracture criterion : GL

(a) Plate US

(b) Plate 1FB

(c) Plate 2FB

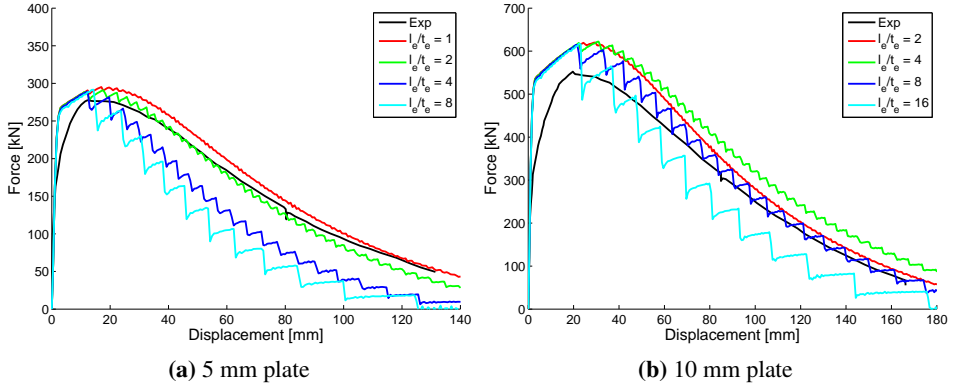**Figure C.21:** Force-displacement relation from Alsos and Amdahl tests and simulations with varying mesh size vs. thickness ratio l_e/t_e. Fracture criterion : SHEAR

(a) Plate US

(b) Plate 1FB

(c) Plate 2FB
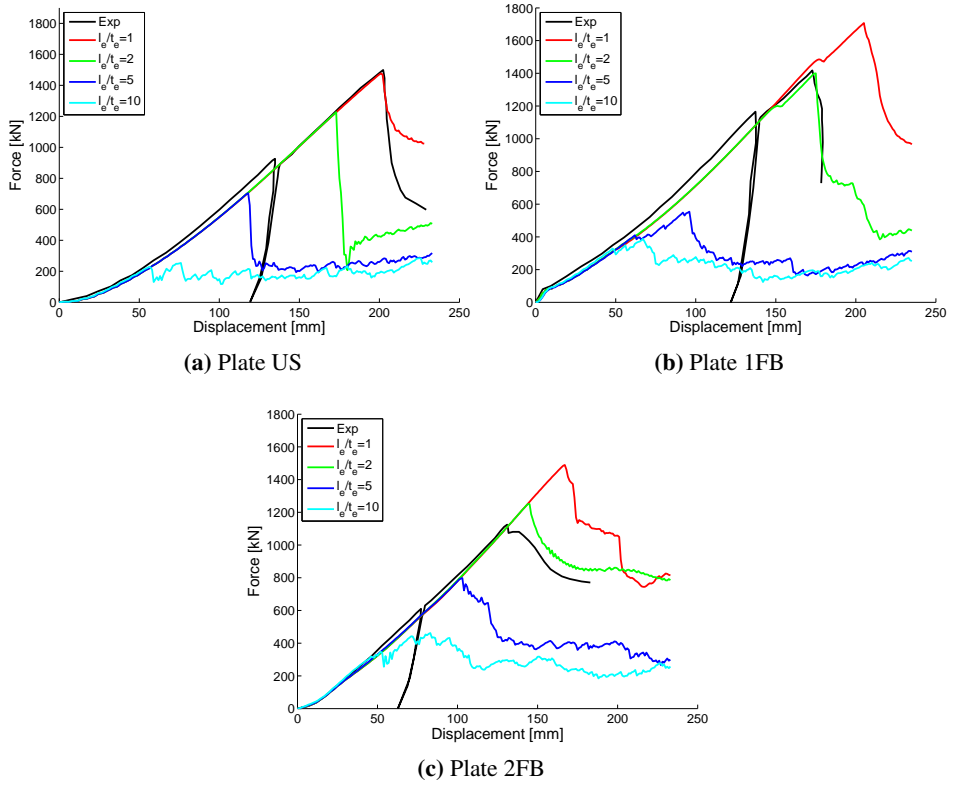
Figure C.22: Force-displacement relation from Alsos and Amdahl tests and simulations with varying mesh size vs. thickness ratio l_e/t_e. Fracture criterion : RPC204
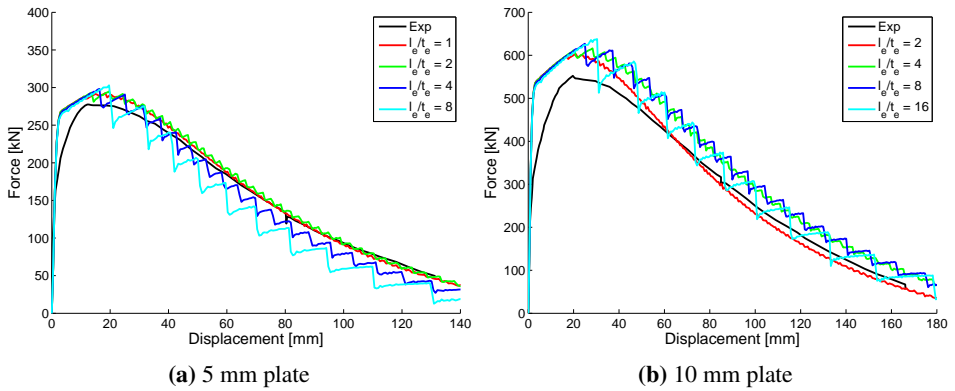
(a) Plate US

(b) Plate 1FB

(c) Plate 2FB
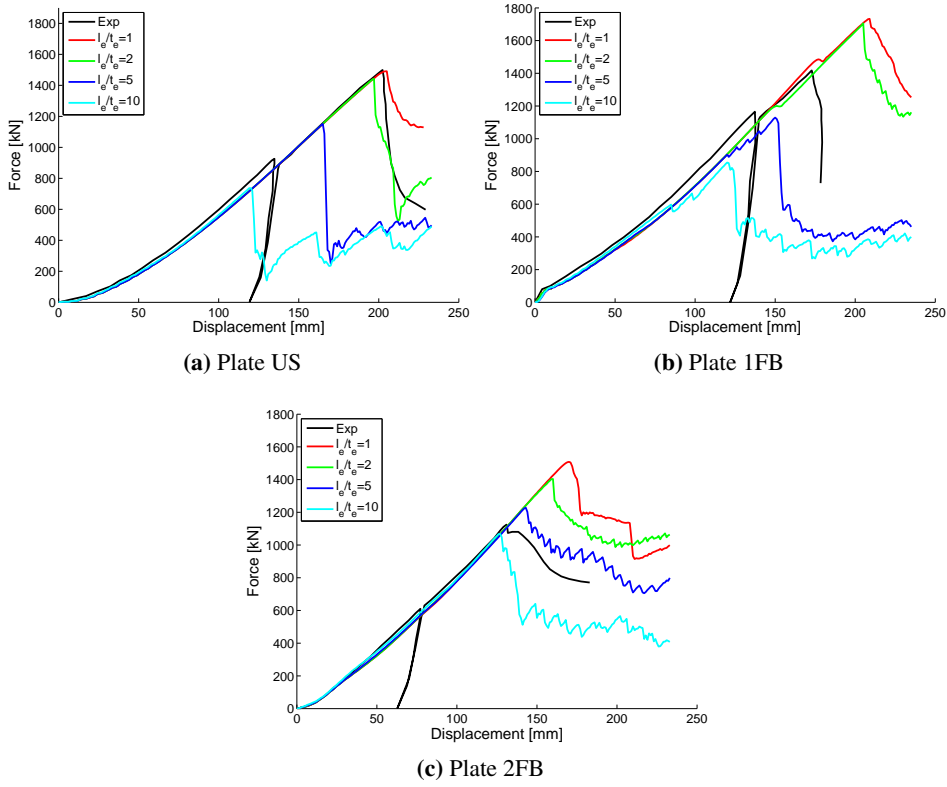
Figure C.23: Force-displacement relation from Alsos and Amdahl tests and simulations with varying mesh size vs. thickness ratio l_e/t_e. Fracture criterion : Peschmann
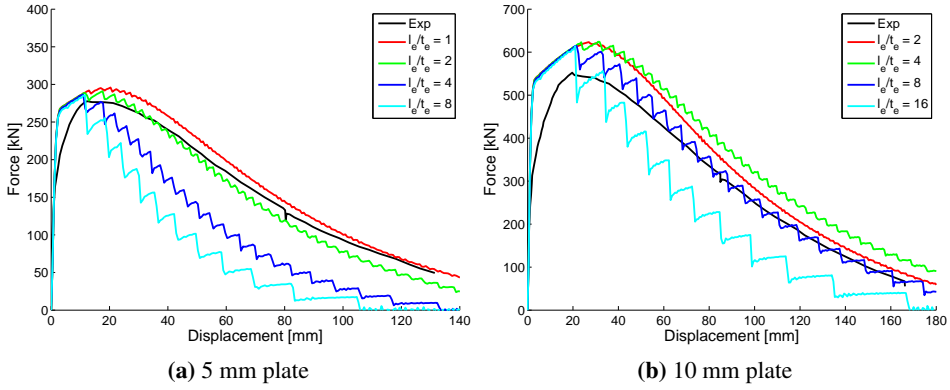
(a) Plate US

(b) Plate 1FB

(c) Plate 2FB
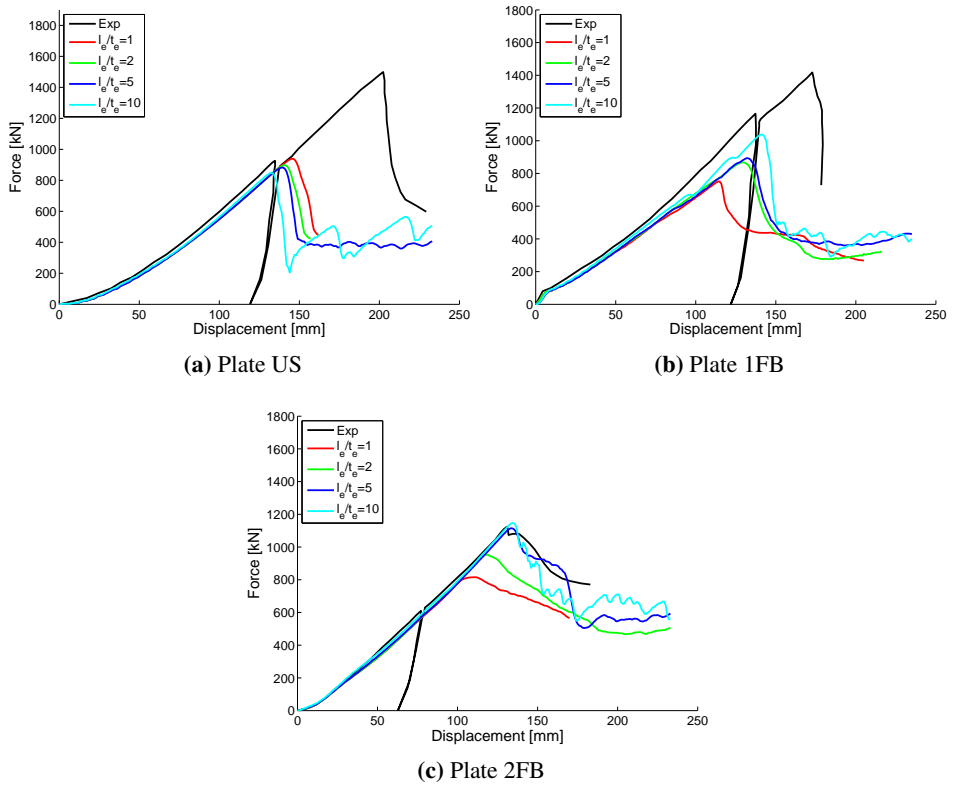
Figure C.24: Force-displacement relation from Alsos and Amdahl tests and simulations with varying mesh size vs. thickness ratio l_e/t_e. Fracture criterion : Ductile damage

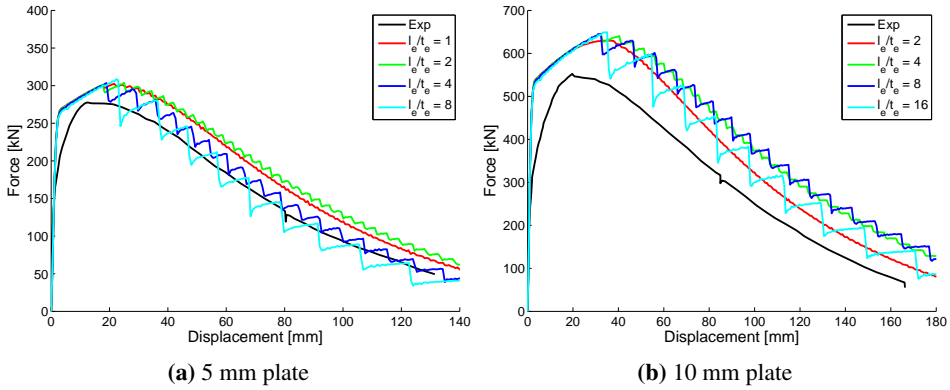## C.4   Tautz et al. Indentation Tests

(a) With cutouts

(b) Without cutouts

Figure C.25: Force-displacement relation from Tautz et al. tests and simulations with varying mesh size vs. thickness ratio l_e/t_e. Fracture criterion : BWH w. dam

(a) With cutouts

(b) Without cutouts

Figure C.26: Force-displacement relation from Tautz et al. tests and simulations with varying mesh size vs. thickness ratio l_e/t_e. Fracture criterion : BWH no dam

(a) With cutouts

(b) Without cutouts

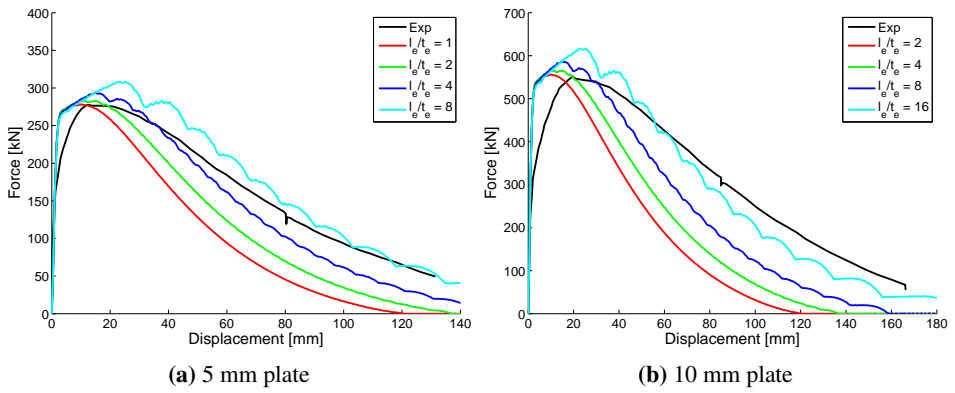**Figure C.27:** Force-displacement relation from Tautz et al. tests and simulations with varying mesh size vs. thickness ratio l_e/t_e. Fracture criterion : RTCL
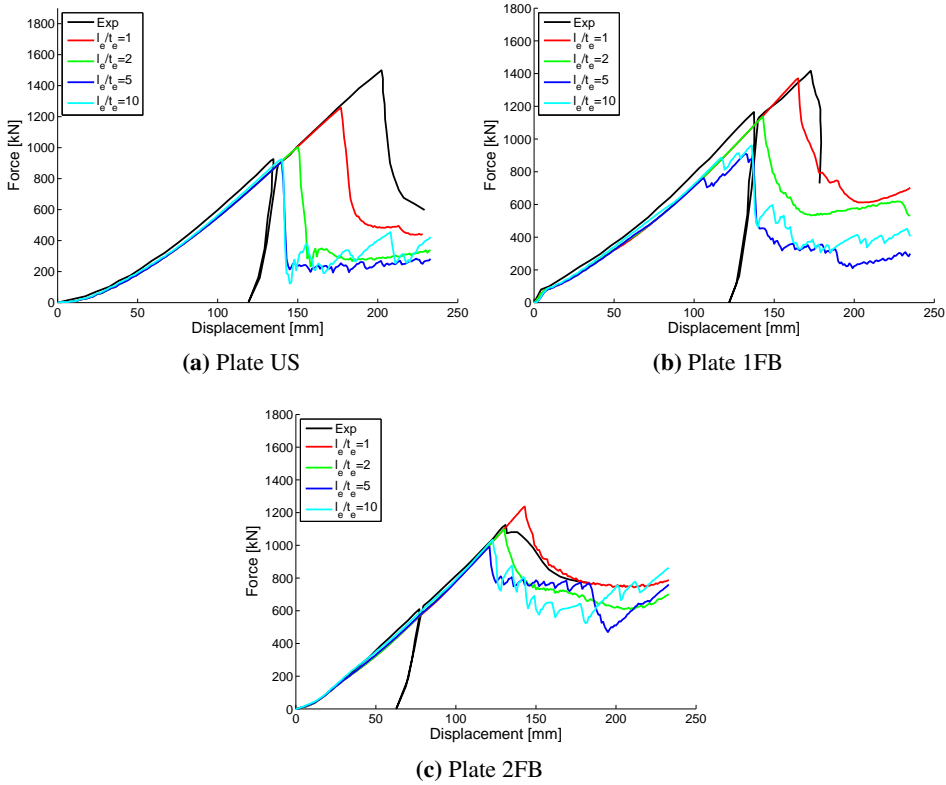

(a) With cutouts

(b) Without cutouts
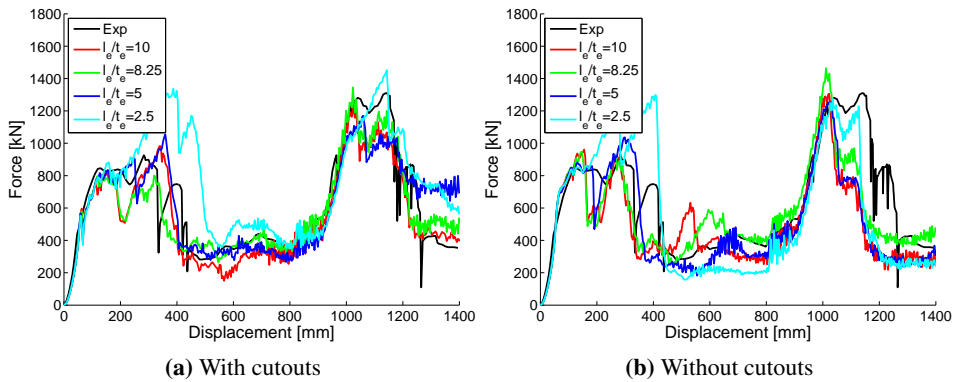
Figure C.28: Force-displacement relation from Tautz et al. tests and simulations with varying mesh size vs. thickness ratio l_e/t_e. Fracture criterion : GL

(a) With cutouts

(b) Without cutouts
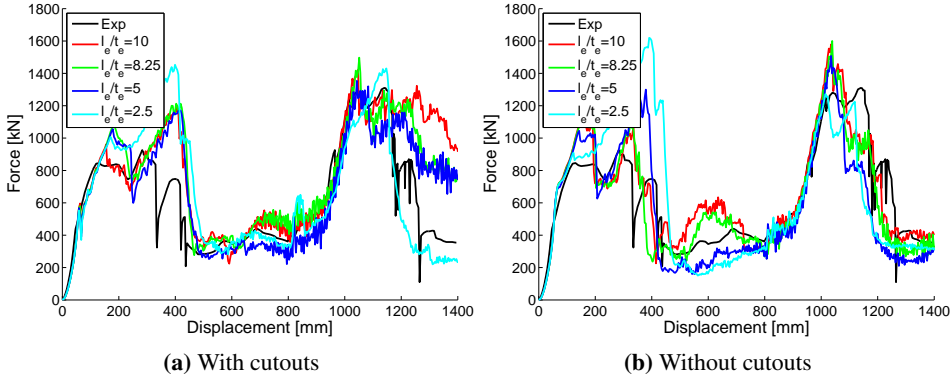
Figure C.29: Force-displacement relation from Tautz et al. tests and simulations with varying mesh size vs. thickness ratio l_e/t_e. Fracture criterion : SHEAR
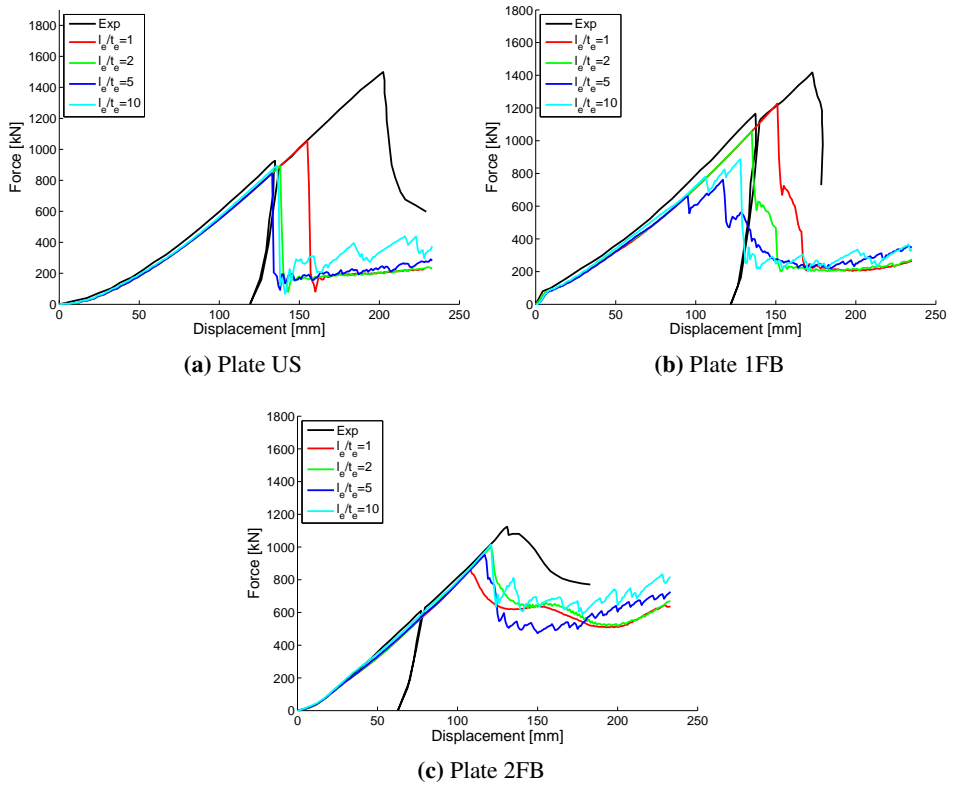

(a) With cutouts

(b) Without cutouts

Figure C.30: Force-displacement relation from Tautz et al. tests and simulations with varying mesh size vs. thickness ratio l_e/t_e. Fracture criterion : RPC204
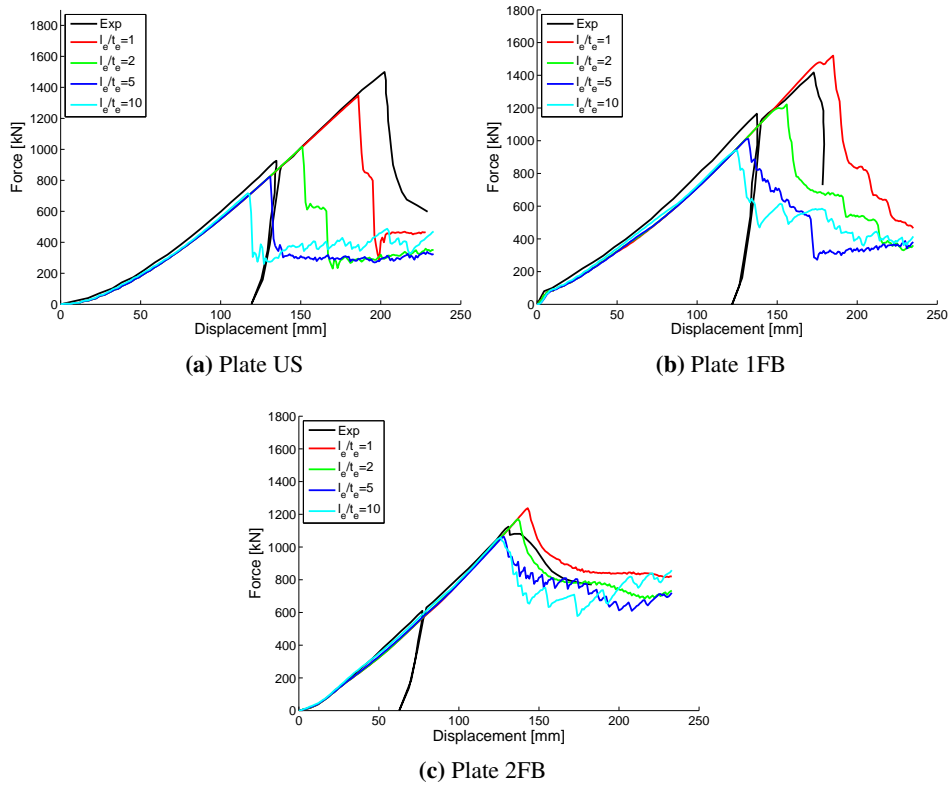
(a) With cutouts

(b) Without cutouts

Figure C.31: Force-displacement relation from Tautz et al. tests and simulations with varying mesh size vs. thickness ratio l_e/t_e. Fracture criterion : Peschmann
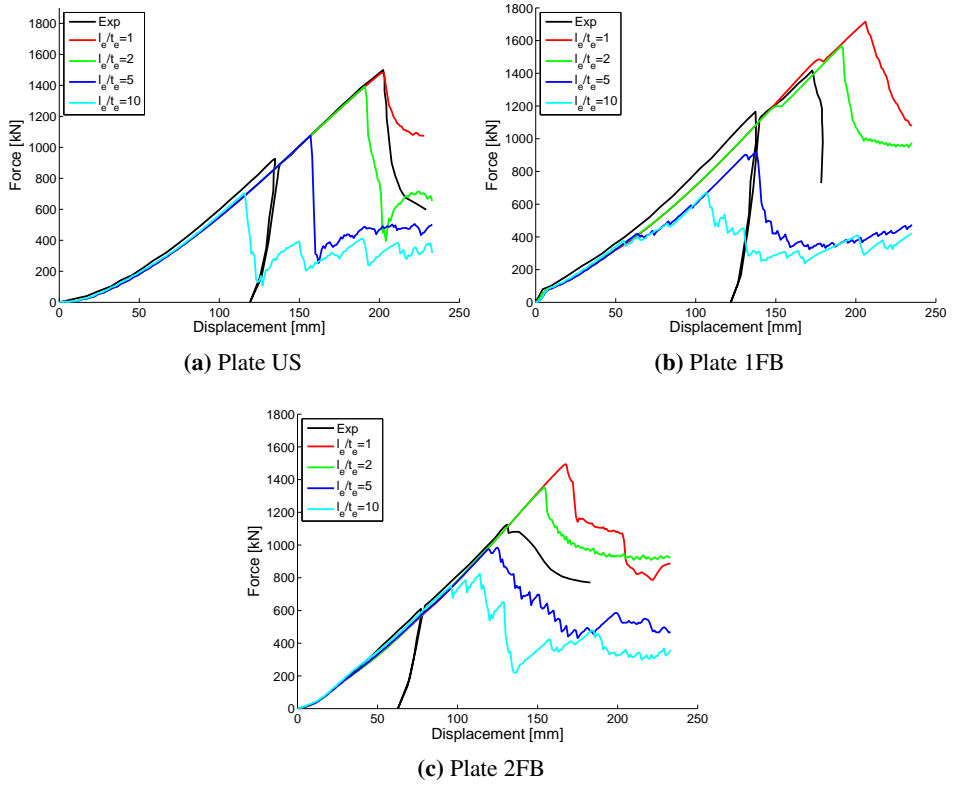

(a) With cutouts

(b) Without cutouts

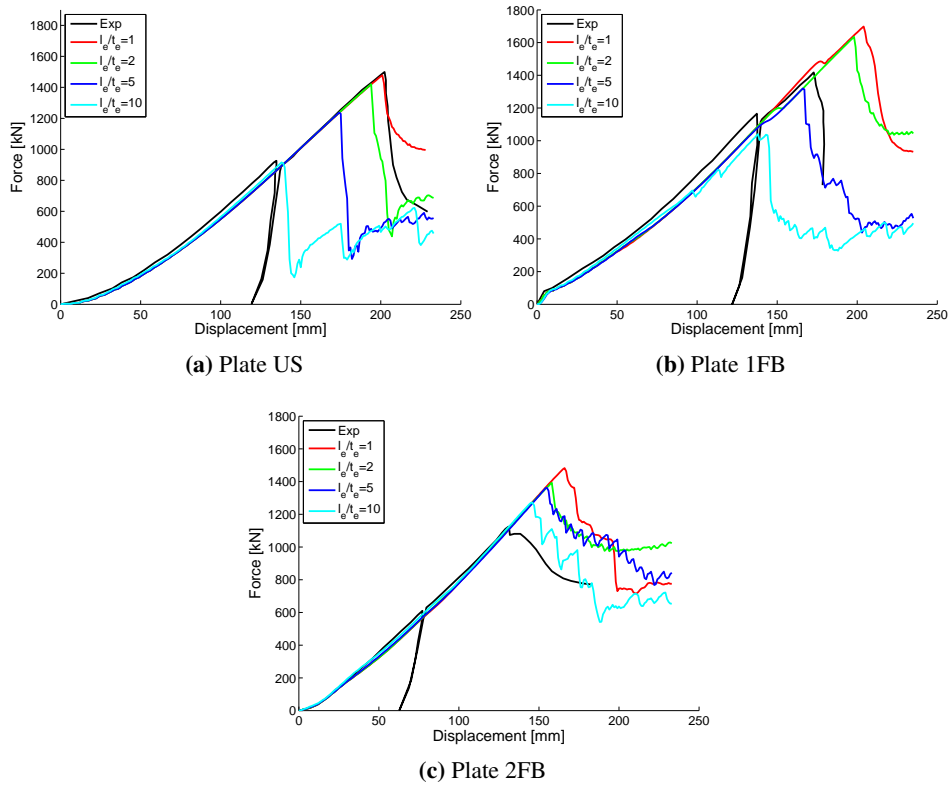**Figure C.32:** Force-displacement relation from Tautz et al. tests and simulations with varying mesh size vs. thickness ratio l_e/t_e. Fracture criterion : Ductile damage

C.5 Peschman Impact Tests

(a) BWH w. dam   **(b)** BWH1 no dam   **(c)** RTCL

(d) GL   **(e)** SHEAR   **(f)** RPC204

(g) Peschmann   **(h)** Ductile damage
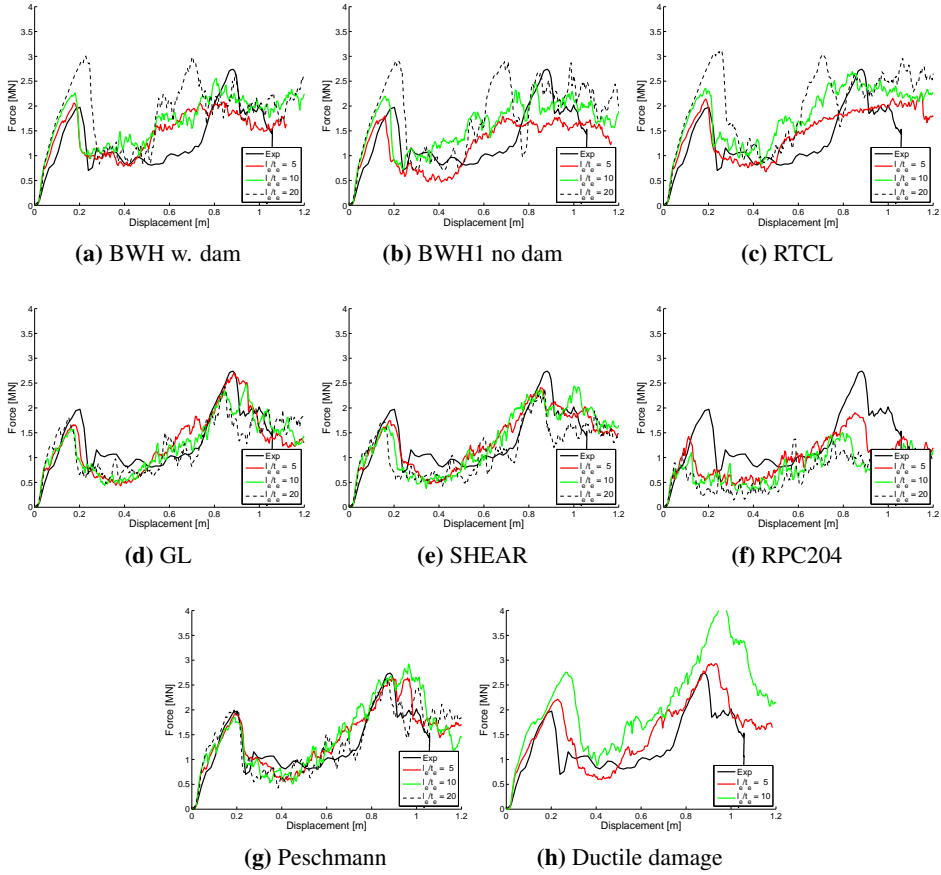
Figure C.33: Force-displacement relation from Peschmann tests and simulations with varying mesh size vs. thickness ratio l_e/t_e

C.6   Travemünde Collision

(a) BWH w. dam

(b) BWH1 no dam

(c) RTCL

(d) GL
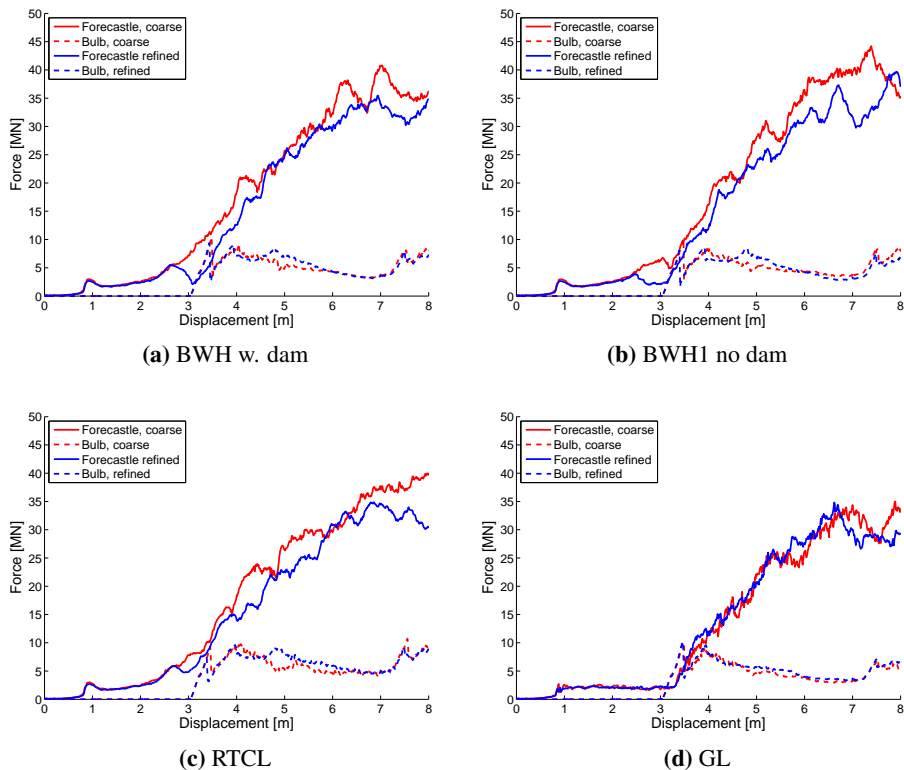
Figure C.34: Force-displacement relation from simulations of the Travemunde collision with two mesh sizes.

(a) SHEAR

(b) RPC204

(c) Peschmann

(d) Ductile damage
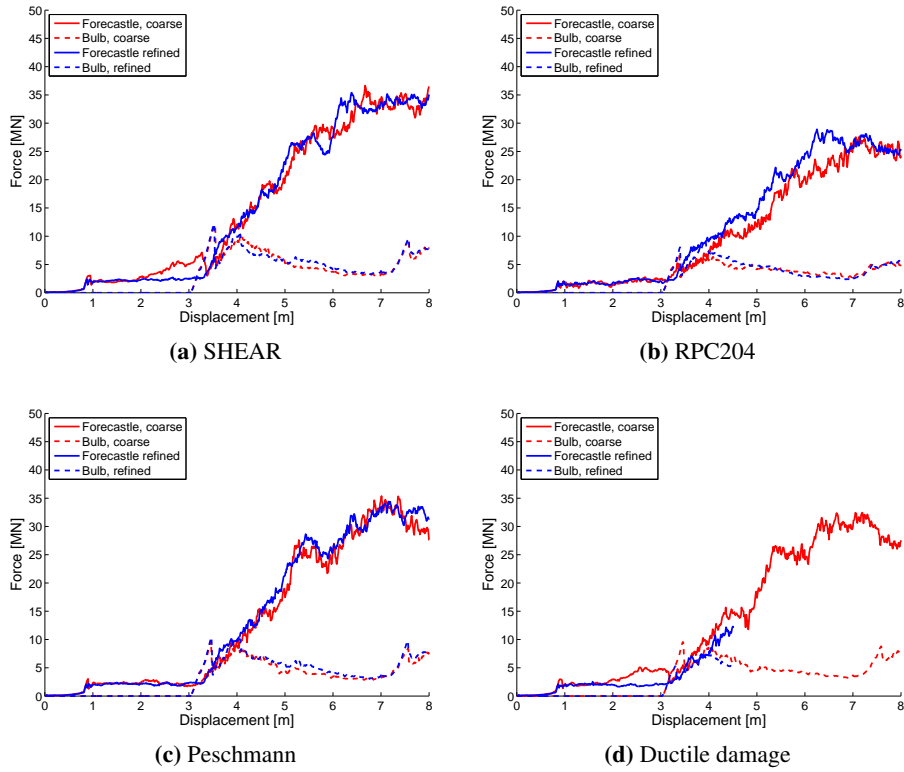
Figure C.35: Force-displacement relation from simulations of the Travemunde collision with two mesh sizes.

Appendix D

Derivation of Roof-top Collapse Model

This appendix contains the derivation of the roof-top model in Section 6.5.1.

D.1   Rooftop Model

Shell plating generally deforms between the various supporting members, such as frames, stringers or stiffeners. For a local load on one panel, and provided that the boundaries are strong enough to support the deforming plate, the boundaries can be considered clamped rather than free. This is valid especially for large indentations, as significant rotations of plastic hinges are observed at the boundaries of the plate. Further, the edges will normally be able to support the membrane forces that develop as the plate undergoes finite deformations. In the following, clamped boundaries with full membrane capacity is assumed. This will give an upper bound value of the collapse resistance of a pressure-loaded plate.

A simple roof-top mechanism may be derived based on the postulated yield line pattern in Figure D.1. All plastic deformation takes place in the yield lines, and that the material otherwise behave rigidly. The increment of internal virtual work δW_i is composed of a bending and a membrane component, and is found by integrating along each yield line m as

$$\delta W_i = \sum_{m=1}^{n} \int_{l_m} (Nw - M)\, \delta\theta_m dl_m \tag{D.1}$$

where $M_p = \sigma_0 h^2 / 4$ is the plastic bending moment in the plate, h the plate thick-
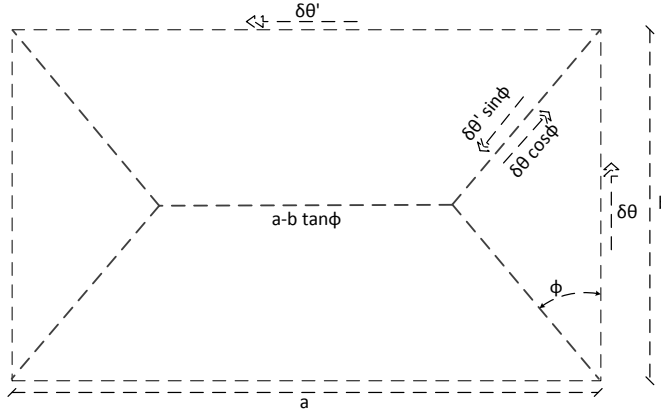
Figure D.1: Simple rooftop model

ness, $\delta\theta_m$ the increment of virtual rotation of a yield line, N the membrane force and δu_m the increment of virtual elongation. Through a lengthy derivation (see Jones (1971) for details), the internal virtual work including bending and membrane effects and with clamped boundaries is given as

$$\frac{\delta W_i}{M_p} = \frac{w}{h} \left\{ 8a \tan\phi - 4b \tan^2\phi + 4b \right\} \delta\theta + \frac{1}{3w/h} \left\{ 4b \tan\phi + 4b \right\} \delta\theta \quad \text{(D.2)}$$

where w is the plate deflection, h the plate thickness, a and b the width and height of the roof top model and ϕ the angle of the yield lines to the height direction (along b).

The next step is to find the angle ϕ such that the collapse load of the plate is minimized. For a uniform load, this gives ϕ as

$$\tan\phi = \sqrt{3 - 2\alpha}, \qquad \alpha = \frac{b}{a} \left\{ \sqrt{3 + (b/a)^2} - b/a \right\} \quad \text{(D.3)}$$

A different approach is selected herein. Motivated by the local damage commonly observed in simulation of impacts of sharp bulbous bows against a stiffened panel, the angle ϕ is assumed to follow the stiffener layout (as in Figure D.2) rather than the angle of minimum load for an unstiffened panel. The loaded area U is assumed to be constant, as this is determined by the contact area of the bulb. Further, the yield hinges are assumed to start outside of the loaded area.
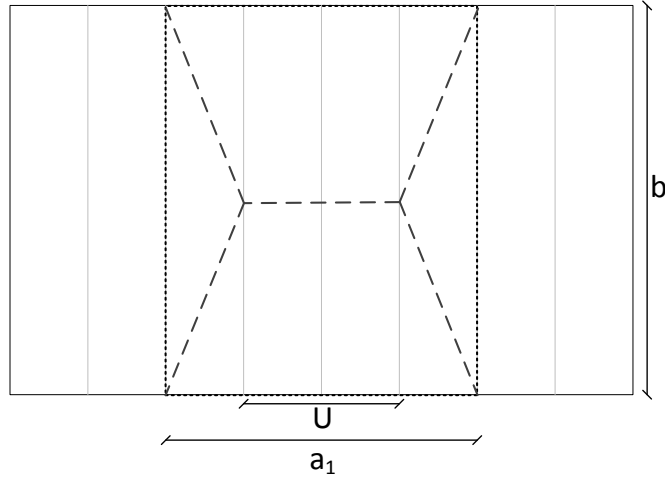
Figure D.2: Roof top collapse mechanism between frames: top and bottom of model are stiff frames; grey lines indicate stiffeners; dashed lines indicate plastic hinges.

Initially, the plate deflection is assumed to be constrained by the neighboring stiffener[1], such that ϕ is given as

$$\tan \phi = \frac{2s}{b} \tag{D.4}$$

Upon indentation, membrane effects in the plate loads the neighboring stiffener up to collapse. Once this fails, the roof top mechanism expands to a wider width a_i, increasing with one stiffener span on each side (as in Figure D.3). It is assumed that the plate deflection is linear in the triangular area. Hence, ϕ evolves with the number of loaded neighboring stiffeners i as

$$\tan \phi_i = \frac{2is}{b} \tag{D.5}$$

Assuming the contact load from the collision to be uniformly distributed on the plate between n stiffeners ($n+1$ stiffeners in contact), the total loaded width U is given as

$$U = ns \tag{D.6}$$

---

[1]The neighboring stiffener is defined as the stiffener that constrains the roof top mechanism, not including stiffeners that are in contact (within the loaded area U).
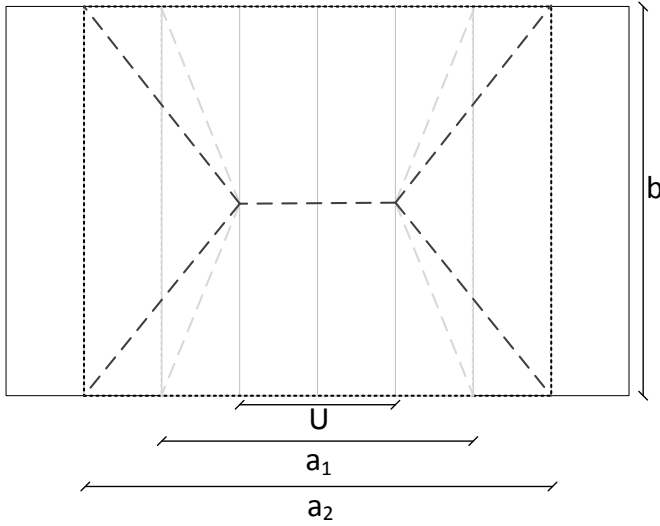
Figure D.3: Roof top collapse mechanism between frames, spreading out due to failure of stiffeners outside of the loaded area. In the figure, $i = 2$ in Eq. D.5.

and the total mechanism width as

$$a_i = (n + 2i)s \tag{D.7}$$

The mechanism length b follows the frame spacing. The internal work in Eq. D.2 can then be modified by inserting for a and $\tan \phi_i$

$$
\begin{aligned}
\frac{\delta W_i}{M_p} &= \frac{w}{h} \left\{ 8(n + 2i)s \frac{2is}{b} - 4b \left(\frac{2is}{b} \right)^2 + 4b \right\} \delta\theta + \frac{1}{3w/h} \left\{ 4b \frac{2is}{b} + 4b \right\} \delta\theta \\
&= \left[\frac{w}{h} \left\{ 16 \left(ni + i^2 \right) \frac{s^2}{b} + 4b \right\} + \frac{1}{3w/h} \left\{ 8is + 4b \right\} \right] \delta\theta \tag{D.8}
\end{aligned}
$$

If large indentations are assumed ($w \gg h$) the term $1/(3w/h)$ can be neglected. In the derivation, the energy dissipation from rolling of yield lines as i increases are disregarded.

The external work can be calculated from the volume V of the loaded rooftop area A as

$$\delta W_e = \int_A Q_{rt} \delta w(x, y) \tag{D.9}$$

where Q_{rt} is the mechanism load. If the entire rooftop is loaded with a uniform pressure, we get

$$\delta W_e = \frac{Q_{rt}}{12} \left\{ 3ab - b^2 \tan \phi \right\} b \tan \phi \delta \theta \tag{D.10}$$

With the assumed loading, only the central part of the rooftop mechanism contributes to the virtual external work (U wide, b long), and δW_e simplifies to

$$\delta W_e = Q_{rt} V = Q_{rt} \left(Ub \frac{1}{2} \delta w \right) = \frac{1}{4} Q_{rt} Ub^2 \tan \phi \delta \theta = \frac{Q_{rt}}{2} nibs^2 \delta \theta \tag{D.11}$$

Solving for $\delta W_i = \delta W_e$ gives the load Q_{rt}

$$
\begin{aligned}
Q_{rt} &= \frac{2M_p \left[\frac{w}{h} \left\{ 16 \left(ni + i^2 \right) \frac{s^2}{b} + 4b \right\} + \frac{1}{3w/h} \left\{ 8is + 4b \right\} \right]}{nibs^2} \\
&= M_p \left[\frac{w}{h} \left\{ 32 \frac{(1 + i/n)}{b^2} + \frac{8}{nis^2} \right\} + \frac{2}{3w/h} \left\{ \frac{8}{nbs} + \frac{4}{nis^2} \right\} \right] \tag{D.12}
\end{aligned}
$$

The derivation assumes that the angular change over the plastic hinges is sufficiently small so that $\tan \delta \theta_m$ can be replaced by $\delta \theta_m$ when relating the indentation w to the yield line rotation $\delta \theta_m$. Thus, for large indentations w, this assumption may be a limitation, and a refined derivation is necessary. For the intended use of the derived equation (early-phase strength design with moderate indentations), the simplification is valid.

D.2   Plots from NLFEA Simulations in Section 6.5.4

Figure D.4 shows the indentation histories for three stiffeners during the integrated simulations with the four different scantling models. Model 1 - 3 exhibit large indentations, but sufficient plate membrane capacity was mobilized to crush the bulb after a finite indentation. Model 4 exhibit small indentations, and large force fluctuations. The response was primarily elastic, but some deflections in the plate between stiffeners were observed, with plastic strains of 1-2%.

Figure D.5 shows the force-indentation histories plotted for the three stiffener locations. The sequential failure of stiffeners 1-3 as assumed in the roof-top pattern is evident for model 1-3.

(a) Model 1

(b) Model 2

(c) Model 3

(d) Model 4
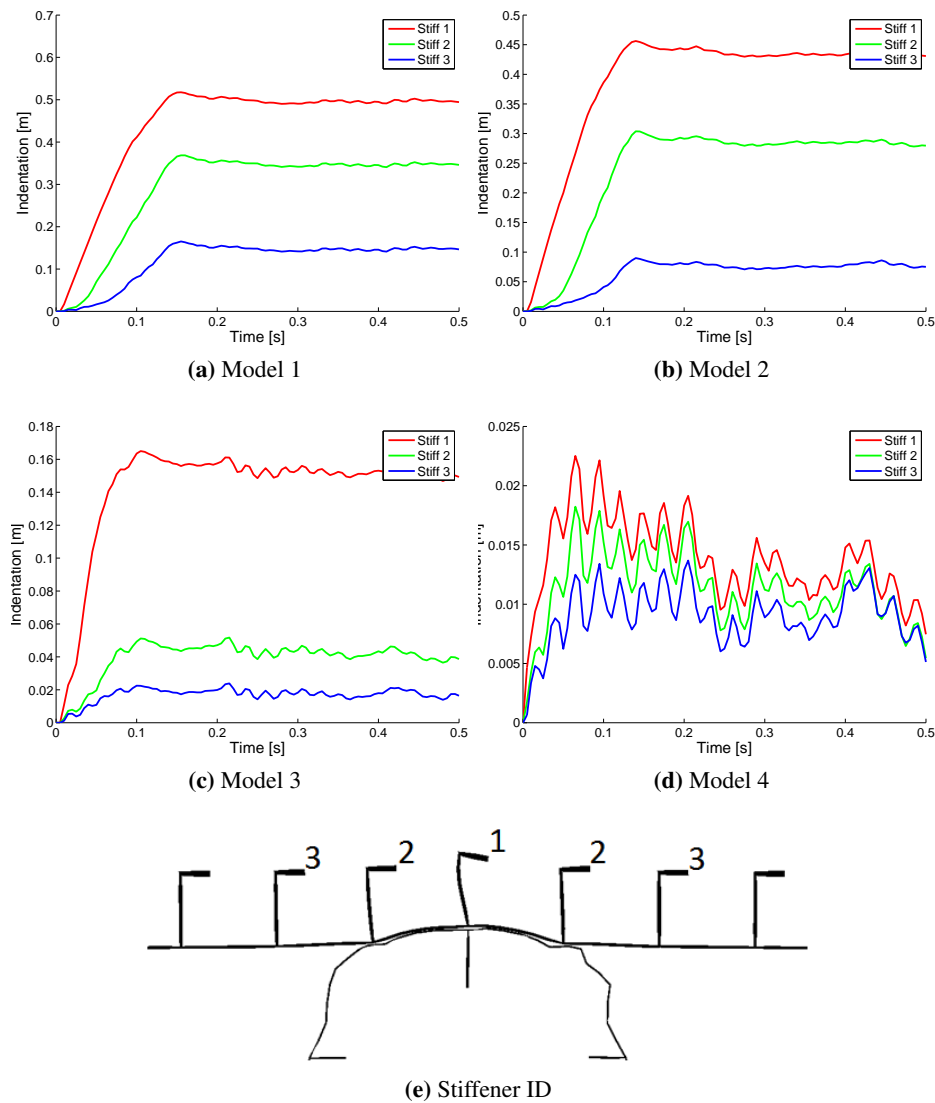
(e) Stiffener ID

Figure D.4: Time vs. indentation at three stiffeners for simulations of bulb vs. generic side

(a) Model 1

(b) Model 2

(c) Model 3

(d) Model 4
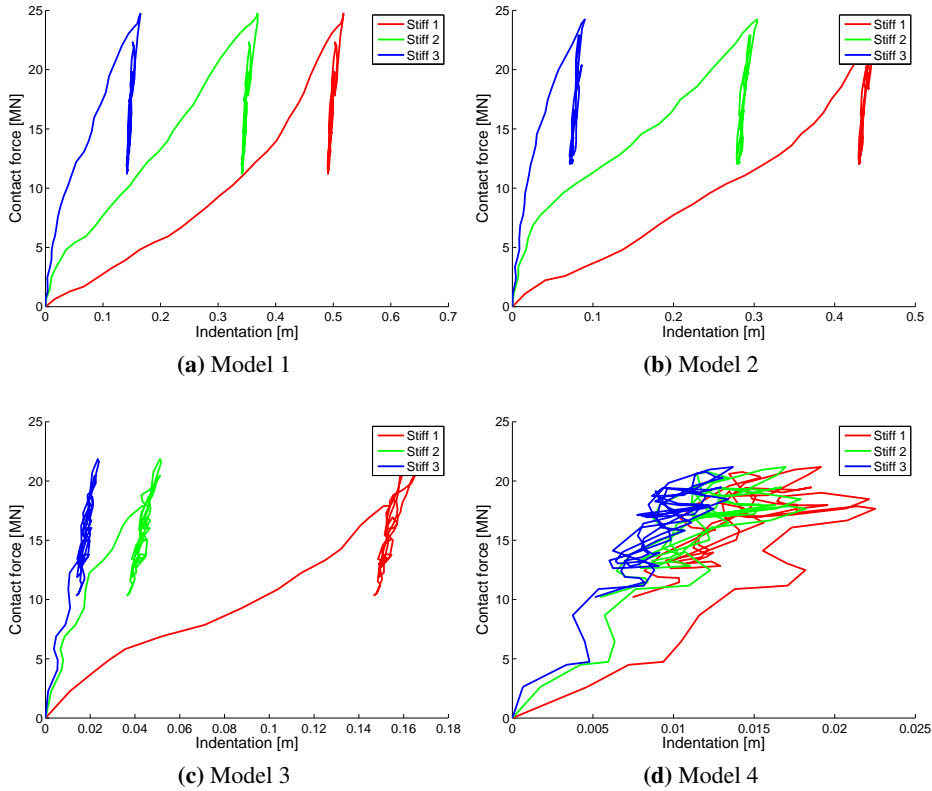
Figure D.5: Force vs. indentation at three stiffeners for simulations of bulb vs. generic side

Appendix E

Previous PhD Theses published at the Department of Marine Technology

Previous PhD theses published at the Departement of Marine Technology
(earlier: Faculty of Marine Technology)
NORWEGIAN UNIVERSITY OF SCIENCE AND TECHNOLOGY

Report No.	Author	Title
	Kavlie, Dag	Optimization of Plane Elastic Grillages, 1967
	Hansen, Hans R.	Man-Machine Communication and Data-Storage Methods in Ship Structural Design, 1971
	Gisvold, Kaare M.	A Method for non-linear mixed -integer programming and its Application to Design Problems, 1971
	Lund, Sverre	Tanker Frame Optimalization by means of SUMT-Transformation and Behaviour Models, 1971
	Vinje, Tor	On Vibration of Spherical Shells Interacting with Fluid, 1972
	Lorentz, Jan D.	Tank Arrangement for Crude Oil Carriers in Accordance with the new Anti-Pollution Regulations, 1975
	Carlsen, Carl A.	Computer-Aided Design of Tanker Structures, 1975
	Larsen, Carl M.	Static and Dynamic Analysis of Offshore Pipelines during Installation, 1976
UR-79-01	Brigt Hatlestad, MK	The finite element method used in a fatigue evaluation of fixed offshore platforms. (Dr.Ing. Thesis)
UR-79-02	Erik Pettersen, MK	Analysis and design of cellular structures. (Dr.Ing. Thesis)
UR-79-03	Sverre Valsgård, MK	Finite difference and finite element methods applied to nonlinear analysis of plated structures. (Dr.Ing. Thesis)
UR-79-04	Nils T. Nordsve, MK	Finite element collapse analysis of structural members considering imperfections and stresses due to fabrication. (Dr.Ing. Thesis)
UR-79-05	Ivar J. Fylling, MK	Analysis of towline forces in ocean towing systems. (Dr.Ing. Thesis)
UR-80-06	Nils Sandsmark, MM	Analysis of Stationary and Transient Heat Conduction by the Use of the Finite Element Method. (Dr.Ing. Thesis)
UR-80-09	Sverre Haver, MK	Analysis of uncertainties related to the stochastic modeling of ocean waves. (Dr.Ing. Thesis)
UR-81-15	Odland, Jonas	On the Strength of welded Ring stiffened cylindrical Shells primarily subjected to axial Compression
UR-82-17	Engesvik, Knut	Analysis of Uncertainties in the fatigue Capacity of

Welded Joints

UR-82-18	Rye, Henrik	Ocean wave groups
UR-83-30	Eide, Oddvar Inge	On Cumulative Fatigue Damage in Steel Welded Joints
UR-83-33	Mo, Olav	Stochastic Time Domain Analysis of Slender Offshore Structures
UR-83-34	Amdahl, Jørgen	Energy absorption in Ship-platform impacts
UR-84-37	Mørch, Morten	Motions and mooring forces of semi submersibles as determined by full-scale measurements and theoretical analysis
UR-84-38	Soares, C. Guedes	Probabilistic models for load effects in ship structures
UR-84-39	Aarsnes, Jan V.	Current forces on ships
UR-84-40	Czujko, Jerzy	Collapse Analysis of Plates subjected to Biaxial Compression and Lateral Load
UR-85-46	Alf G. Engseth, MK	Finite element collapse analysis of tubular steel offshore structures. (Dr.Ing. Thesis)
UR-86-47	Dengody Sheshappa, MP	A Computer Design Model for Optimizing Fishing Vessel Designs Based on Techno-Economic Analysis. (Dr.Ing. Thesis)
UR-86-48	Vidar Aanesland, MH	A Theoretical and Numerical Study of Ship Wave Resistance. (Dr.Ing. Thesis)
UR-86-49	Heinz-Joachim Wessel, MK	Fracture Mechanics Analysis of Crack Growth in Plate Girders. (Dr.Ing. Thesis)
UR-86-50	Jon Taby, MK	Ultimate and Post-ultimate Strength of Dented Tubular Members. (Dr.Ing. Thesis)
UR-86-51	Walter Lian, MH	A Numerical Study of Two-Dimensional Separated Flow Past Bluff Bodies at Moderate KC-Numbers. (Dr.Ing. Thesis)
UR-86-52	Bjørn Sortland, MH	Force Measurements in Oscillating Flow on Ship Sections and Circular Cylinders in a U-Tube Water Tank. (Dr.Ing. Thesis)
UR-86-53	Kurt Strand, MM	A System Dynamic Approach to One-dimensional Fluid Flow. (Dr.Ing. Thesis)
UR-86-54	Arne Edvin Løken, MH	Three Dimensional Second Order Hydrodynamic Effects on Ocean Structures in Waves. (Dr.Ing. Thesis)
UR-86-55	Sigurd Falch, MH	A Numerical Study of Slamming of Two-Dimensional Bodies. (Dr.Ing. Thesis)
UR-87-56	Arne Braathen, MH	Application of a Vortex Tracking Method to the Prediction of Roll Damping of a Two-Dimension Floating Body. (Dr.Ing. Thesis)

UR-87-57	Bernt Leira, MK	Gaussian Vector Processes for Reliability Analysis involving Wave-Induced Load Effects. (Dr.Ing. Thesis)
UR-87-58	Magnus Småvik, MM	Thermal Load and Process Characteristics in a Two-Stroke Diesel Engine with Thermal Barriers (in Norwegian). (Dr.Ing. Thesis)
MTA-88-59	Bernt Arild Bremdal, MP	An Investigation of Marine Installation Processes – A Knowledge - Based Planning Approach. (Dr.Ing. Thesis)
MTA-88-60	Xu Jun, MK	Non-linear Dynamic Analysis of Space-framed Offshore Structures. (Dr.Ing. Thesis)
MTA-89-61	Gang Miao, MH	Hydrodynamic Forces and Dynamic Responses of Circular Cylinders in Wave Zones. (Dr.Ing. Thesis)
MTA-89-62	Martin Greenhow, MH	Linear and Non-Linear Studies of Waves and Floating Bodies. Part I and Part II. (Dr.Techn. Thesis)
MTA-89-63	Chang Li, MH	Force Coefficients of Spheres and Cubes in Oscillatory Flow with and without Current. (Dr.Ing. Thesis
MTA-89-64	Hu Ying, MP	A Study of Marketing and Design in Development of Marine Transport Systems. (Dr.Ing. Thesis)
MTA-89-65	Arild Jæger, MH	Seakeeping, Dynamic Stability and Performance of a Wedge Shaped Planing Hull. (Dr.Ing. Thesis)
MTA-89-66	Chan Siu Hung, MM	The dynamic characteristics of tilting-pad bearings
MTA-89-67	Kim Wikstrøm, MP	Analysis av projekteringen for ett offshore projekt. (Licenciat-avhandling)
MTA-89-68	Jiao Guoyang, MK	Reliability Analysis of Crack Growth under Random Loading, considering Model Updating. (Dr.Ing. Thesis)
MTA-89-69	Arnt Olufsen, MK	Uncertainty and Reliability Analysis of Fixed Offshore Structures. (Dr.Ing. Thesis)
MTA-89-70	Wu Yu-Lin, MR	System Reliability Analyses of Offshore Structures using improved Truss and Beam Models. (Dr.Ing. Thesis)
MTA-90-71	Jan Roger Hoff, MH	Three-dimensional Green function of a vessel with forward speed in waves. (Dr.Ing. Thesis)
MTA-90-72	Rong Zhao, MH	Slow-Drift Motions of a Moored Two-Dimensional Body in Irregular Waves. (Dr.Ing. Thesis)
MTA-90-73	Atle Minsaas, MP	Economical Risk Analysis. (Dr.Ing. Thesis)
MTA-90-74	Knut-Aril Farnes, MK	Long-term Statistics of Response in Non-linear Marine Structures. (Dr.Ing. Thesis)
MTA-90-75	Torbjørn Sotberg, MK	Application of Reliability Methods for Safety Assessment of Submarine Pipelines. (Dr.Ing.

Thesis)

MTA-90-76	Zeuthen, Steffen, MP	SEAMAID. A computational model of the design process in a constraint-based logic programming environment. An example from the offshore domain. (Dr.Ing. Thesis)
MTA-91-77	Haagensen, Sven, MM	Fuel Dependant Cyclic Variability in a Spark Ignition Engine - An Optical Approach. (Dr.Ing. Thesis)
MTA-91-78	Løland, Geir, MH	Current forces on and flow through fish farms. (Dr.Ing. Thesis)
MTA-91-79	Hoen, Christopher, MK	System Identification of Structures Excited by Stochastic Load Processes. (Dr.Ing. Thesis)
MTA-91-80	Haugen, Stein, MK	Probabilistic Evaluation of Frequency of Collision between Ships and Offshore Platforms. (Dr.Ing. Thesis)
MTA-91-81	Sødahl, Nils, MK	Methods for Design and Analysis of Flexible Risers. (Dr.Ing. Thesis)
MTA-91-82	Ormberg, Harald, MK	Non-linear Response Analysis of Floating Fish Farm Systems. (Dr.Ing. Thesis)
MTA-91-83	Marley, Mark J., MK	Time Variant Reliability under Fatigue Degradation. (Dr.Ing. Thesis)
MTA-91-84	Krokstad, Jørgen R., MH	Second-order Loads in Multidirectional Seas. (Dr.Ing. Thesis)
MTA-91-85	Molteberg, Gunnar A., MM	The Application of System Identification Techniques to Performance Monitoring of Four Stroke Turbocharged Diesel Engines. (Dr.Ing. Thesis)
MTA-92-86	Mørch, Hans Jørgen Bjelke, MH	Aspects of Hydrofoil Design: with Emphasis on Hydrofoil Interaction in Calm Water. (Dr.Ing. Thesis)
MTA-92-87	Chan Siu Hung, MM	Nonlinear Analysis of Rotordynamic Instabilities in Highspeed Turbomachinery. (Dr.Ing. Thesis)
MTA-92-88	Bessason, Bjarni, MK	Assessment of Earthquake Loading and Response of Seismically Isolated Bridges. (Dr.Ing. Thesis)
MTA-92-89	Langli, Geir, MP	Improving Operational Safety through exploitation of Design Knowledge - an investigation of offshore platform safety. (Dr.Ing. Thesis)
MTA-92-90	Sævik, Svein, MK	On Stresses and Fatigue in Flexible Pipes. (Dr.Ing. Thesis)
MTA-92-91	Ask, Tor Ø., MM	Ignition and Flame Growth in Lean Gas-Air Mixtures. An Experimental Study with a Schlieren System. (Dr.Ing. Thesis)
MTA-86-92	Hessen, Gunnar, MK	Fracture Mechanics Analysis of Stiffened Tubular Members. (Dr.Ing. Thesis)

MTA-93-93	Steinebach, Christian, MM	Knowledge Based Systems for Diagnosis of Rotating Machinery. (Dr.Ing. Thesis)
MTA-93-94	Dalane, Jan Inge, MK	System Reliability in Design and Maintenance of Fixed Offshore Structures. (Dr.Ing. Thesis)
MTA-93-95	Steen, Sverre, MH	Cobblestone Effect on SES. (Dr.Ing. Thesis)
MTA-93-96	Karunakaran, Daniel, MK	Nonlinear Dynamic Response and Reliability Analysis of Drag-dominated Offshore Platforms. (Dr.Ing. Thesis)
MTA-93-97	Hagen, Arnulf, MP	The Framework of a Design Process Language. (Dr.Ing. Thesis)
MTA-93-98	Nordrik, Rune, MM	Investigation of Spark Ignition and Autoignition in Methane and Air Using Computational Fluid Dynamics and Chemical Reaction Kinetics. A Numerical Study of Ignition Processes in Internal Combustion Engines. (Dr.Ing. Thesis)
MTA-94-99	Passano, Elizabeth, MK	Efficient Analysis of Nonlinear Slender Marine Structures. (Dr.Ing. Thesis)
MTA-94-100	Kvålsvold, Jan, MH	Hydroelastic Modelling of Wetdeck Slamming on Multihull Vessels. (Dr.Ing. Thesis)
MTA-94-102	Bech, Sidsel M., MK	Experimental and Numerical Determination of Stiffness and Strength of GRP/PVC Sandwich Structures. (Dr.Ing. Thesis)
MTA-95-103	Paulsen, Hallvard, MM	A Study of Transient Jet and Spray using a Schlieren Method and Digital Image Processing. (Dr.Ing. Thesis)
MTA-95-104	Hovde, Geir Olav, MK	Fatigue and Overload Reliability of Offshore Structural Systems, Considering the Effect of Inspection and Repair. (Dr.Ing. Thesis)
MTA-95-105	Wang, Xiaozhi, MK	Reliability Analysis of Production Ships with Emphasis on Load Combination and Ultimate Strength. (Dr.Ing. Thesis)
MTA-95-106	Ulstein, Tore, MH	Nonlinear Effects of a Flexible Stern Seal Bag on Cobblestone Oscillations of an SES. (Dr.Ing. Thesis)
MTA-95-107	Solaas, Frøydis, MH	Analytical and Numerical Studies of Sloshing in Tanks. (Dr.Ing. Thesis)
MTA-95-108	Hellan, Øyvind, MK	Nonlinear Pushover and Cyclic Analyses in Ultimate Limit State Design and Reassessment of Tubular Steel Offshore Structures. (Dr.Ing. Thesis)
MTA-95-109	Hermundstad, Ole A., MK	Theoretical and Experimental Hydroelastic Analysis of High Speed Vessels. (Dr.Ing. Thesis)
MTA-96-110	Bratland, Anne K., MH	Wave-Current Interaction Effects on Large-Volume Bodies in Water of Finite Depth. (Dr.Ing. Thesis)
MTA-96-111	Herfjord, Kjell, MH	A Study of Two-dimensional Separated Flow by a Combination of the Finite Element Method and

Navier-Stokes Equations. (Dr.Ing. Thesis)

MTA-96-112	Æsøy, Vilmar, MM	Hot Surface Assisted Compression Ignition in a Direct Injection Natural Gas Engine. (Dr.Ing. Thesis)
MTA-96-113	Eknes, Monika L., MK	Escalation Scenarios Initiated by Gas Explosions on Offshore Installations. (Dr.Ing. Thesis)
MTA-96-114	Erikstad, Stein O., MP	A Decision Support Model for Preliminary Ship Design. (Dr.Ing. Thesis)
MTA-96-115	Pedersen, Egil, MH	A Nautical Study of Towed Marine Seismic Streamer Cable Configurations. (Dr.Ing. Thesis)
MTA-97-116	Moksnes, Paul O., MM	Modelling Two-Phase Thermo-Fluid Systems Using Bond Graphs. (Dr.Ing. Thesis)
MTA-97-117	Halse, Karl H., MK	On Vortex Shedding and Prediction of Vortex-Induced Vibrations of Circular Cylinders. (Dr.Ing. Thesis)
MTA-97-118	Igland, Ragnar T., MK	Reliability Analysis of Pipelines during Laying, considering Ultimate Strength under Combined Loads. (Dr.Ing. Thesis)
MTA-97-119	Pedersen, Hans-P., MP	Levendefiskteknologi for fiskefartøy. (Dr.Ing. Thesis)
MTA-98-120	Vikestad, Kyrre, MK	Multi-Frequency Response of a Cylinder Subjected to Vortex Shedding and Support Motions. (Dr.Ing. Thesis)
MTA-98-121	Azadi, Mohammad R. E., MK	Analysis of Static and Dynamic Pile-Soil-Jacket Behaviour. (Dr.Ing. Thesis)
MTA-98-122	Ulltang, Terje, MP	A Communication Model for Product Information. (Dr.Ing. Thesis)
MTA-98-123	Torbergsen, Erik, MM	Impeller/Diffuser Interaction Forces in Centrifugal Pumps. (Dr.Ing. Thesis)
MTA-98-124	Hansen, Edmond, MH	A Discrete Element Model to Study Marginal Ice Zone Dynamics and the Behaviour of Vessels Moored in Broken Ice. (Dr.Ing. Thesis)
MTA-98-125	Videiro, Paulo M., MK	Reliability Based Design of Marine Structures. (Dr.Ing. Thesis)
MTA-99-126	Mainçon, Philippe, MK	Fatigue Reliability of Long Welds Application to Titanium Risers. (Dr.Ing. Thesis)
MTA-99-127	Haugen, Elin M., MH	Hydroelastic Analysis of Slamming on Stiffened Plates with Application to Catamaran Wetdecks. (Dr.Ing. Thesis)
MTA-99-128	Langhelle, Nina K., MK	Experimental Validation and Calibration of Nonlinear Finite Element Models for Use in Design of Aluminium Structures Exposed to Fire. (Dr.Ing. Thesis)
MTA-99-	Berstad, Are J., MK	Calculation of Fatigue Damage in Ship Structures.

129 (Dr.Ing. Thesis)

MTA-99-130	Andersen, Trond M., MM	Short Term Maintenance Planning. (Dr.Ing. Thesis)
MTA-99-131	Tveiten, Bård Wathne, MK	Fatigue Assessment of Welded Aluminium Ship Details. (Dr.Ing. Thesis)
MTA-99-132	Søreide, Fredrik, MP	Applications of underwater technology in deep water archaeology. Principles and practice. (Dr.Ing. Thesis)
MTA-99-133	Tønnessen, Rune, MH	A Finite Element Method Applied to Unsteady Viscous Flow Around 2D Blunt Bodies With Sharp Corners. (Dr.Ing. Thesis)
MTA-99-134	Elvekrok, Dag R., MP	Engineering Integration in Field Development Projects in the Norwegian Oil and Gas Industry. The Supplier Management of Norne. (Dr.Ing. Thesis)
MTA-99-135	Fagerholt, Kjetil, MP	Optimeringsbaserte Metoder for Ruteplanlegging innen skipsfart. (Dr.Ing. Thesis)
MTA-99-136	Bysveen, Marie, MM	Visualization in Two Directions on a Dynamic Combustion Rig for Studies of Fuel Quality. (Dr.Ing. Thesis)
MTA-2000-137	Storteig, Eskild, MM	Dynamic characteristics and leakage performance of liquid annular seals in centrifugal pumps. (Dr.Ing. Thesis)
MTA-2000-138	Sagli, Gro, MK	Model uncertainty and simplified estimates of long term extremes of hull girder loads in ships. (Dr.Ing. Thesis)
MTA-2000-139	Tronstad, Harald, MK	Nonlinear analysis and design of cable net structures like fishing gear based on the finite element method. (Dr.Ing. Thesis)
MTA-2000-140	Kroneberg, André, MP	Innovation in shipping by using scenarios. (Dr.Ing. Thesis)
MTA-2000-141	Haslum, Herbjørn Alf, MH	Simplified methods applied to nonlinear motion of spar platforms. (Dr.Ing. Thesis)
MTA-2001-142	Samdal, Ole Johan, MM	Modelling of Degradation Mechanisms and Stressor Interaction on Static Mechanical Equipment Residual Lifetime. (Dr.Ing. Thesis)
MTA-2001-143	Baarholm, Rolf Jarle, MH	Theoretical and experimental studies of wave impact underneath decks of offshore platforms. (Dr.Ing. Thesis)
MTA-2001-144	Wang, Lihua, MK	Probabilistic Analysis of Nonlinear Wave-induced Loads on Ships. (Dr.Ing. Thesis)
MTA-2001-145	Kristensen, Odd H. Holt, MK	Ultimate Capacity of Aluminium Plates under Multiple Loads, Considering HAZ Properties. (Dr.Ing. Thesis)
MTA-2001-146	Greco, Marilena, MH	A Two-Dimensional Study of Green-Water

Loading. (Dr.Ing. Thesis)

MTA-2001-147	Heggelund, Svein E., MK	Calculation of Global Design Loads and Load Effects in Large High Speed Catamarans. (Dr.Ing. Thesis)
MTA-2001-148	Babalola, Olusegun T., MK	Fatigue Strength of Titanium Risers – Defect Sensitivity. (Dr.Ing. Thesis)
MTA-2001-149	Mohammed, Abuu K., MK	Nonlinear Shell Finite Elements for Ultimate Strength and Collapse Analysis of Ship Structures. (Dr.Ing. Thesis)
MTA-2002-150	Holmedal, Lars E., MH	Wave-current interactions in the vicinity of the sea bed. (Dr.Ing. Thesis)
MTA-2002-151	Rognebakke, Olav F., MH	Sloshing in rectangular tanks and interaction with ship motions. (Dr.Ing. Thesis)
MTA-2002-152	Lader, Pål Furset, MH	Geometry and Kinematics of Breaking Waves. (Dr.Ing. Thesis)
MTA-2002-153	Yang, Qinzheng, MH	Wash and wave resistance of ships in finite water depth. (Dr.Ing. Thesis)
MTA-2002-154	Melhus, Øyvin, MM	Utilization of VOC in Diesel Engines. Ignition and combustion of VOC released by crude oil tankers. (Dr.Ing. Thesis)
MTA-2002-155	Ronæss, Marit, MH	Wave Induced Motions of Two Ships Advancing on Parallel Course. (Dr.Ing. Thesis)
MTA-2002-156	Økland, Ole D., MK	Numerical and experimental investigation of whipping in twin hull vessels exposed to severe wet deck slamming. (Dr.Ing. Thesis)
MTA-2002-157	Ge, Chunhua, MK	Global Hydroelastic Response of Catamarans due to Wet Deck Slamming. (Dr.Ing. Thesis)
MTA-2002-158	Byklum, Eirik, MK	Nonlinear Shell Finite Elements for Ultimate Strength and Collapse Analysis of Ship Structures. (Dr.Ing. Thesis)
IMT-2003-1	Chen, Haibo, MK	Probabilistic Evaluation of FPSO-Tanker Collision in Tandem Offloading Operation. (Dr.Ing. Thesis)
IMT-2003-2	Skaugset, Kjetil Bjørn, MK	On the Suppression of Vortex Induced Vibrations of Circular Cylinders by Radial Water Jets. (Dr.Ing. Thesis)
IMT-2003-3	Chezhian, Muthu	Three-Dimensional Analysis of Slamming. (Dr.Ing. Thesis)
IMT-2003-4	Buhaug, Øyvind	Deposit Formation on Cylinder Liner Surfaces in Medium Speed Engines. (Dr.Ing. Thesis)
IMT-2003-5	Tregde, Vidar	Aspects of Ship Design: Optimization of Aft Hull with Inverse Geometry Design. (Dr.Ing. Thesis)
IMT-	Wist, Hanne Therese	Statistical Properties of Successive Ocean Wave

2003-6		Parameters. (Dr.Ing. Thesis)
IMT-2004-7	Ransau, Samuel	Numerical Methods for Flows with Evolving Interfaces. (Dr.Ing. Thesis)
IMT-2004-8	Soma, Torkel	Blue-Chip or Sub-Standard. A data interrogation approach of identity safety characteristics of shipping organization. (Dr.Ing. Thesis)
IMT-2004-9	Ersdal, Svein	An experimental study of hydrodynamic forces on cylinders and cables in near axial flow. (Dr.Ing. Thesis)
IMT-2005-10	Brodtkorb, Per Andreas	The Probability of Occurrence of Dangerous Wave Situations at Sea. (Dr.Ing. Thesis)
IMT-2005-11	Yttervik, Rune	Ocean current variability in relation to offshore engineering. (Dr.Ing. Thesis)
IMT-2005-12	Fredheim, Arne	Current Forces on Net-Structures. (Dr.Ing. Thesis)
IMT-2005-13	Heggernes, Kjetil	Flow around marine structures. (Dr.Ing. Thesis
IMT-2005-14	Fouques, Sebastien	Lagrangian Modelling of Ocean Surface Waves and Synthetic Aperture Radar Wave Measurements. (Dr.Ing. Thesis)
IMT-2006-15	Holm, Håvard	Numerical calculation of viscous free surface flow around marine structures. (Dr.Ing. Thesis)
IMT-2006-16	Bjørheim, Lars G.	Failure Assessment of Long Through Thickness Fatigue Cracks in Ship Hulls. (Dr.Ing. Thesis)
IMT-2006-17	Hansson, Lisbeth	Safety Management for Prevention of Occupational Accidents. (Dr.Ing. Thesis)
IMT-2006-18	Zhu, Xinying	Application of the CIP Method to Strongly Nonlinear Wave-Body Interaction Problems. (Dr.Ing. Thesis)
IMT-2006-19	Reite, Karl Johan	Modelling and Control of Trawl Systems. (Dr.Ing. Thesis)
IMT-2006-20	Smogeli, Øyvind Notland	Control of Marine Propellers. From Normal to Extreme Conditions. (Dr.Ing. Thesis)
IMT-2007-21	Storhaug, Gaute	Experimental Investigation of Wave Induced Vibrations and Their Effect on the Fatigue Loading of Ships. (Dr.Ing. Thesis)
IMT-2007-22	Sun, Hui	A Boundary Element Method Applied to Strongly Nonlinear Wave-Body Interaction Problems. (PhD Thesis, CeSOS)
IMT-2007-23	Rustad, Anne Marthine	Modelling and Control of Top Tensioned Risers. (PhD Thesis, CeSOS)
IMT-2007-24	Johansen, Vegar	Modelling flexible slender system for real-time simulations and control applications
IMT-2007-25	Wroldsen, Anders Sunde	Modelling and control of tensegrity structures.

(PhD Thesis, CeSOS)

IMT-2007-26	Aronsen, Kristoffer Høye	An experimental investigation of in-line and combined inline and cross flow vortex induced vibrations. (Dr. avhandling, IMT)
IMT-2007-27	Gao, Zhen	Stochastic Response Analysis of Mooring Systems with Emphasis on Frequency-domain Analysis of Fatigue due to Wide-band Response Processes (PhD Thesis, CeSOS)
IMT-2007-28	Thorstensen, Tom Anders	Lifetime Profit Modelling of Ageing Systems Utilizing Information about Technical Condition. (Dr.ing. thesis, IMT)
IMT-2008-29	Refsnes, Jon Erling Gorset	Nonlinear Model-Based Control of Slender Body AUVs (PhD Thesis, IMT)
IMT-2008-30	Berntsen, Per Ivar B.	Structural Reliability Based Position Mooring. (PhD-Thesis, IMT)
IMT-2008-31	Ye, Naiquan	Fatigue Assessment of Aluminium Welded Box-stiffener Joints in Ships (Dr.ing. thesis, IMT)
IMT-2008-32	Radan, Damir	Integrated Control of Marine Electrical Power Systems. (PhD-Thesis, IMT)
IMT-2008-33	Thomassen, Paul	Methods for Dynamic Response Analysis and Fatigue Life Estimation of Floating Fish Cages. (Dr.ing. thesis, IMT)
IMT-2008-34	Pákozdi, Csaba	A Smoothed Particle Hydrodynamics Study of Two-dimensional Nonlinear Sloshing in Rectangular Tanks. (Dr.ing.thesis, IMT/ CeSOS)
IMT-2007-35	Grytøyr, Guttorm	A Higher-Order Boundary Element Method and Applications to Marine Hydrodynamics. (Dr.ing.thesis, IMT)
IMT-2008-36	Drummen, Ingo	Experimental and Numerical Investigation of Nonlinear Wave-Induced Load Effects in Containerships considering Hydroelasticity. (PhD thesis, CeSOS)
IMT-2008-37	Skejic, Renato	Maneuvering and Seakeeping of a Singel Ship and of Two Ships in Interaction. (PhD-Thesis, CeSOS)
IMT-2008-38	Harlem, Alf	An Age-Based Replacement Model for Repairable Systems with Attention to High-Speed Marine Diesel Engines. (PhD-Thesis, IMT)
IMT-2008-39	Alsos, Hagbart S.	Ship Grounding. Analysis of Ductile Fracture, Bottom Damage and Hull Girder Response. (PhD-thesis, IMT)
IMT-2008-40	Graczyk, Mateusz	Experimental Investigation of Sloshing Loading and Load Effects in Membrane LNG Tanks Subjected to Random Excitation. (PhD-thesis, CeSOS)
IMT-2008-41	Taghipour, Reza	Efficient Prediction of Dynamic Response for Flexible amd Multi-body Marine Structures. (PhD-

thesis, CeSOS)

IMT-2008-42	Ruth, Eivind	Propulsion control and thrust allocation on marine vessels. (PhD thesis, CeSOS)
IMT-2008-43	Nystad, Bent Helge	Technical Condition Indexes and Remaining Useful Life of Aggregated Systems. PhD thesis, IMT
IMT-2008-44	Soni, Prashant Kumar	Hydrodynamic Coefficients for Vortex Induced Vibrations of Flexible Beams, PhD thesis, CeSOS
IMT-2009-45	Amlashi, Hadi K.K.	Ultimate Strength and Reliability-based Design of Ship Hulls with Emphasis on Combined Global and Local Loads. PhD Thesis, IMT
IMT-2009-46	Pedersen, Tom Arne	Bond Graph Modelling of Marine Power Systems. PhD Thesis, IMT
IMT-2009-47	Kristiansen, Trygve	Two-Dimensional Numerical and Experimental Studies of Piston-Mode Resonance. PhD-Thesis, CeSOS
IMT-2009-48	Ong, Muk Chen	Applications of a Standard High Reynolds Number Model and a Stochastic Scour Prediction Model for Marine Structures. PhD-thesis, IMT
IMT-2009-49	Hong, Lin	Simplified Analysis and Design of Ships subjected to Collision and Grounding. PhD-thesis, IMT
IMT-2009-50	Koushan, Kamran	Vortex Induced Vibrations of Free Span Pipelines, PhD thesis, IMT
IMT-2009-51	Korsvik, Jarl Eirik	Heuristic Methods for Ship Routing and Scheduling. PhD-thesis, IMT
IMT-2009-52	Lee, Jihoon	Experimental Investigation and Numerical in Analyzing the Ocean Current Displacement of Longlines. Ph.d.-Thesis, IMT.
IMT-2009-53	Vestbøstad, Tone Gran	A Numerical Study of Wave-in-Deck Impact usin a Two-Dimensional Constrained Interpolation Profile Method, Ph.d.thesis, CeSOS.
IMT-2009-54	Bruun, Kristine	Bond Graph Modelling of Fuel Cells for Marine Power Plants. Ph.d.-thesis, IMT
IMT 2009-55	Holstad, Anders	Numerical Investigation of Turbulence in a Sekwed Three-Dimensional Channel Flow, Ph.d.-thesis, IMT.
IMT 2009-56	Ayala-Uraga, Efren	Reliability-Based Assessment of Deteriorating Ship-shaped Offshore Structures, Ph.d.-thesis, IMT
IMT 2009-57	Kong, Xiangjun	A Numerical Study of a Damaged Ship in Beam Sea Waves. Ph.d.-thesis, IMT/CeSOS.
IMT 2010-58	Kristiansen, David	Wave Induced Effects on Floaters of Aquaculture Plants, Ph.d.-thesis, CeSOS.

IMT 2010-59	Ludvigsen, Martin	An ROV-Toolbox for Optical and Acoustic Scientific Seabed Investigation. Ph.d.-thesis IMT.
IMT 2010-60	Hals, Jørgen	Modelling and Phase Control of Wave-Energy Converters. Ph.d.thesis, CeSOS.
IMT 2010- 61	Shu, Zhi	Uncertainty Assessment of Wave Loads and Ultimate Strength of Tankers and Bulk Carriers in a Reliability Framework. Ph.d. Thesis, IMT/ CeSOS
IMT 2010-62	Shao, Yanlin	Numerical Potential-Flow Studies on Weakly-Nonlinear Wave-Body Interactions with/without Small Forward Speed, Ph.d.thesis,CeSOS.
IMT 2010-63	Califano, Andrea	Dynamic Loads on Marine Propellers due to Intermittent Ventilation. Ph.d.thesis, IMT.
IMT 2010-64	El Khoury, George	Numerical Simulations of Massively Separated Turbulent Flows, Ph.d.-thesis, IMT
IMT 2010-65	Seim, Knut Sponheim	Mixing Process in Dense Overflows with Emphasis on the Faroe Bank Channel Overflow. Ph.d.thesis, IMT
IMT 2010-66	Jia, Huirong	Structural Analysis of Intect and Damaged Ships in a Collission Risk Analysis Perspective. Ph.d.thesis CeSoS.
IMT 2010-67	Jiao, Linlin	Wave-Induced Effects on a Pontoon-type Very Large Floating Structures (VLFS). Ph.D.-thesis, CeSOS.
IMT 2010-68	Abrahamsen, Bjørn Christian	Sloshing Induced Tank Roof with Entrapped Air Pocket. Ph.d.thesis, CeSOS.
IMT 2011-69	Karimirad, Madjid	Stochastic Dynamic Response Analysis of Spar-Type Wind Turbines with Catenary or Taut Mooring Systems. Ph.d.-thesis, CeSOS.
IMT - 2011-70	Erlend Meland	Condition Monitoring of Safety Critical Valves. Ph.d.-thesis, IMT.
IMT – 2011-71	Yang, Limin	Stochastic Dynamic System Analysis of Wave Energy Converter with Hydraulic Power Take-Off, with Particular Reference to Wear Damage Analysis, Ph.d. Thesis, CeSOS.
IMT – 2011-72	Visscher, Jan	Application of Particla Image Velocimetry on Turbulent Marine Flows, Ph.d.Thesis, IMT.
IMT – 2011-73	Su, Biao	Numerical Predictions of Global and Local Ice Loads on Ships. Ph.d.Thesis, CeSOS.
IMT – 2011-74	Liu, Zhenhui	Analytical and Numerical Analysis of Iceberg Collision with Ship Structures. Ph.d.Thesis, IMT.
IMT – 2011-75	Aarsæther, Karl Gunnar	Modeling and Analysis of Ship Traffic by Observation and Numerical Simulation. Ph.d.Thesis, IMT.

Imt – 2011-76	Wu, Jie	Hydrodynamic Force Identification from Stochastic Vortex Induced Vibration Experiments with Slender Beams. Ph.d.Thesis, IMT.
Imt – 2011-77	Amini, Hamid	Azimuth Propulsors in Off-design Conditions. Ph.d.Thesis, IMT.
IMT – 2011-78	Nguyen, Tan-Hoi	Toward a System of Real-Time Prediction and Monitoring of Bottom Damage Conditions During Ship Grounding. Ph.d.thesis, IMT.
IMT- 2011-79	Tavakoli, Mohammad T.	Assessment of Oil Spill in Ship Collision and Grounding, Ph.d.thesis, IMT.
IMT- 2011-80	Guo, Bingjie	Numerical and Experimental Investigation of Added Resistance in Waves. Ph.d.Thesis, IMT.
IMT- 2011-81	Chen, Qiaofeng	Ultimate Strength of Aluminium Panels, considering HAZ Effects, IMT
IMT- 2012-82	Kota, Ravikiran S.	Wave Loads on Decks of Offshore Structures in Random Seas, CeSOS.
IMT- 2012-83	Sten, Ronny	Dynamic Simulation of Deep Water Drilling Risers with Heave Compensating System, IMT.
IMT- 2012-84	Berle, Øyvind	Risk and resilience in global maritime supply chains, IMT.
IMT- 2012-85	Fang, Shaoji	Fault Tolerant Position Mooring Control Based on Structural Reliability, CeSOS.
IMT- 2012-86	You, Jikun	Numerical studies on wave forces and moored ship motions in intermediate and shallow water, CeSOS.
IMT- 2012-87	Xiang ,Xu	Maneuvering of two interacting ships in waves, CeSOS
IMT- 2012-88	Dong, Wenbin	Time-domain fatigue response and reliability analysis of offshore wind turbines with emphasis on welded tubular joints and gear components, CeSOS
IMT- 2012-89	Zhu, Suji	Investigation of Wave-Induced Nonlinear Load Effects in Open Ships considering Hull Girder Vibrations in Bending and Torsion, CeSOS
IMT- 2012-90	Zhou, Li	Numerical and Experimental Investigation of Station-keeping in Level Ice, CeSOS
IMT- 2012-91	Ushakov, Sergey	Particulate matter emission characteristics from diesel enignes operating on conventional and alternative marine fuels, IMT
IMT- 2013-1	Yin, Decao	Experimental and Numerical Analysis of Combined In-line and Cross-flow Vortex Induced Vibrations, CeSOS

IMT-2013-2	Kurniawan, Adi	Modelling and geometry optimisation of wave energy converters, CeSOS
IMT-2013-3	Al Ryati, Nabil	Technical condition indexes doe auxiliary marine diesel engines, IMT
IMT-2013-4	Firoozkoohi, Reza	Experimental, numerical and analytical investigation of the effect of screens on sloshing, CeSOS
IMT-2013-5	Ommani, Babak	Potential-Flow Predictions of a Semi-Displacement Vessel Including Applications to Calm Water Broaching, CeSOS
IMT-2013-6	Xing, Yihan	Modelling and analysis of the gearbox in a floating spar-type wind turbine, CeSOS
IMT-7-2013	Balland, Océane	Optimization models for reducing air emissions from ships, IMT
IMT-8-2013	Yang, Dan	Transitional wake flow behind an inclined flat plate-----Computation and analysis, IMT
IMT-9-2013	Abdillah, Suyuthi	Prediction of Extreme Loads and Fatigue Damage for a Ship Hull due to Ice Action, IMT
IMT-10-2013	Ramìrez, Pedro Agustìn Pèrez	Ageing management and life extension of technical systems- Concepts and methods applied to oil and gas facilities, IMT
IMT-11-2013	Chuang, Zhenju	Experimental and Numerical Investigation of Speed Loss due to Seakeeping and Maneuvering. IMT
IMT-12-2013	Etemaddar, Mahmoud	Load and Response Analysis of Wind Turbines under Atmospheric Icing and Controller System Faults with Emphasis on Spar Type Floating Wind Turbines, IMT
IMT-13-2013	Lindstad, Haakon	Strategies and measures for reducing maritime CO2 emissons, IMT
IMT-14-2013	Haris, Sabril	Damage interaction analysis of ship collisions, IMT
IMT-15-2013	Shainee, Mohamed	Conceptual Design, Numerical and Experimental Investigation of a SPM Cage Concept for Offshore Mariculture, IMT
IMT-16-2013	Gansel, Lars	Flow past porous cylinders and effects of biofouling and fish behavior on the flow in and around Atlantic salmon net cages, IMT
IMT-17-2013	Gaspar, Henrique	Handling Aspects of Complexity in Conceptual Ship Design, IMT
IMT-18-2013	Thys, Maxime	Theoretical and Experimental Investigation of a Free Running Fishing Vessel at Small Frequency of Encounter, CeSOS
IMT-19-2013	Aglen, Ida	VIV in Free Spanning Pipelines, CeSOS

IMT-1-2014	Song, An	Theoretical and experimental studies of wave diffraction and radiation loads on a horizontally submerged perforated plate, CeSOS
IMT-2-2014	Rogne, Øyvind Ygre	Numerical and Experimental Investigation of a Hinged 5-body Wave Energy Converter, CeSOS
IMT-3-2014	Dai, Lijuan	Safe and efficient operation and maintenance of offshore wind farms ,IMT
IMT-4-2014	Bachynski, Erin Elizabeth	Design and Dynamic Analysis of Tension Leg Platform Wind Turbines, CeSOS
IMT-5-2014	Wang, Jingbo	Water Entry of Freefall Wedged – Wedge motions and Cavity Dynamics, CeSOS
IMT-6-2014	Kim, Ekaterina	Experimental and numerical studies related to the coupled behavior of ice mass and steel structures during accidental collisions, IMT
IMT-7-2014	Tan, Xiang	Numerical investigation of ship's continuous- mode icebreaking in leverl ice, CeSOS
IMT-8-2014	Muliawan, Made Jaya	Design and Analysis of Combined Floating Wave and Wind Power Facilities, with Emphasis on Extreme Load Effects of the Mooring System, CeSOS
IMT-9-2014	Jiang, Zhiyu	Long-term response analysis of wind turbines with an emphasis on fault and shutdown conditions, IMT
IMT-10-2014	Dukan, Fredrik	ROV Motion Control Systems, IMT
IMT-11-2014	Grimsmo, Nils I.	Dynamic simulations of hydraulic cylinder for heave compensation of deep water drilling risers, IMT
IMT-12-2014	Kvittem, Marit I.	Modelling and response analysis for fatigue design of a semisubmersible wind turbine, CeSOS
IMT-13-2014	Akhtar, Juned	The Effects of Human Fatigue on Risk at Sea, IMT
IMT-14-2014	Syahroni, Nur	Fatigue Assessment of Welded Joints Taking into Account Effects of Residual Stress, IMT
IMT-1-2015	Bøckmann, Eirik	Wave Propulsion of ships, IMT
IMT-2-2015	Wang, Kai	Modelling and dynamic analysis of a semi-submersible floating vertical axis wind turbine, CeSOS
IMT-3-2015	Fredriksen, Arnt Gunvald	A numerical and experimental study of a two-dimensional body with moonpool in waves and current, CeSOS
IMT-4-2015	Jose Patricio Gallardo Canabes	Numerical studies of viscous flow around bluff bodies, IMT

IMT-5-2015	Vegard Longva	Formulation and application of finite element techniques for slender marine structures subjected to contact interactions, IMT
IMT-6-2015	Jacobus De Vaal	Aerodynamic modelling of floating wind turbines, CeSOS
IMT-7-2015	Fachri Nasution	Fatigue Performance of Copper Power Conductors, IMT
IMT-8-2015	Oleh I Karpa	Development of bivariate extreme value distributions for applications in marine technology, CeSOS
IMT-9-2015	Daniel de Almeida Fernandes	An output feedback motion control system for ROVs, AMOS
IMT-10-2015	Bo Zhao	Particle Filter for Fault Diagnosis: Application to Dynamic Positioning Vessel and Underwater Robotics, CeSOS
IMT-11-2015	Wenting Zhu	Impact of emission allocation in maritime transportation, IMT
IMT-12-2015	Amir Rasekhi Nejad	Dynamic Analysis and Design of Gearboxes in Offshore Wind Turbines in a Structural Reliability Perspective, CeSOS
IMT-13-2015	Arturo Jesùs Ortega Malca	Dynamic Response of Flexibles Risers due to Unsteady Slug Flow, CeSOS
IMT-14-2015	Dagfinn Husjord	Guidance and decision-support system for safe navigation of ships operating in close proximity, IMT
IMT-15-2015	Anirban Bhattacharyya	Ducted Propellers: Behaviour in Waves and Scale Effects, IMT
IMT-16-2015	Qin Zhang	Image Processing for Ice Parameter Identification in Ice Management, IMT
IMT-1-2016	Vincentius Rumawas	Human Factors in Ship Design and Operation: An Experiential Learning, IMT
IMT-2-2016	Martin Storheim	Structural response in ship-platform and ship-ice collisions, IMT